

KfK 3311/1
UWFDM-500
Juni 1982

TASKA -

**Tandem Spiegelmaschine Karlsruhe
A Tandem Mirror Fusion Engineering
Test Facility**

Volume 1

**TASKA-Team
Institut für Technische Physik**

Kernforschungszentrum Karlsruhe

KERNFORSCHUNGSZENTRUM KARLSRUHE

INSTITUT FÜR TECHNISCHE PHYSIK

KfK 3311

UWFDM-500

- T A S K A - Tandem Spiegelmaschine Karlsruhe

A Tandem Mirror Fusion Engineering Test Facility

Volume 1

B. Badger ^(a)	W. Köhler ^(d)	K.E. Plute ^(a)
F. Arendt ^(b)	P. Komarek ^(b)	U. Quade ^(c)
H.M. Attaya ^(a)	G.L. Kulcinski ^(a)	G. Ries ^(l)
K. Audenaerde ^(a)	M. Kuntze ^(h)	H. Runge ^(c)
H. Avci ^(a)	E.M. Larsen ^(a)	J.F. Santarius ^(a)
J.B. Beyer ^(a)	T. Lechtenberg ⁽ⁱ⁾	M.E. Sawan ^(d)
E. Bogusch ^(c)	H.G. Leiste ^(d)	J.E. Scharer ^(a)
G. Böhme ^(d)	X.Z. Li ^(a)	D.C. Schluderberg ^(g)
D. Bruggink ^(a)	W. Link ^(d)	H. Schütz ^(c)
L. Buth ^(e)	B.M. Manes ^(b)	A. Suppan ^(d)
L. Dietz ^(f)	W. Maurer ^(b)	I.N. Sviatoslavsky ^(a)
H. Dittrich ^(b)	C.W. Maynard ^(a)	D.K. Sze ^(a)
L. El-Guebaly ^(a)	F. Mehren ^(c)	W. Tischler ^(c)
G.A. Emmert ^(a)	E. Montalvo ^(a)	M.A. Vogel ^(j)
J. Erb ^(b)	D. Mundt ^(c)	W.F. Vogelsang ^(a)
H. Frey ^(b)	Z. Musicki ^(a)	A.M. White ^(a)
B. Glaser ^(d)	E. Opperman ^(j)	W.G. Wolfer ^(a)
G. Grant ^(g)	J.E. Osher ^(k)	K.Y. Yuan ^(a)
W. Heinz ^(b)	L.J. Perkins ^(a)	D.B. Young ^(g)
W. Hennhöfer ^(d)	R.R. Peterson ^(a)	

(a) UW/FPA

(b) KfK-ITP

(c) Interatom

(d) KfK-IT

(e) KfK-INR

(f) Grumman Aerospace

(g) Babcock and Wilcox

(h) KfK-IK

(i) General Atomic

(j) HEDL

(k) LLNL

(l) Siemens

Als Manuskript vervielfältigt
Für diesen Bericht behalten wir uns alle Rechte vor

Kernforschungszentrum Karlsruhe GmbH
ISSN 0303-4003

Abstract:

TASKA (Tandem Spiegelmaschine Karlsruhe) is a near term engineering test facility based on a tandem mirror concept with thermal barriers. The main objectives of this study were to develop a preconceptual design of a facility that could provide engineering design information for a Demonstration Fusion Power Reactor. Thus TASKA has to serve as testbed for technologies of plasma engineering, superconducting magnets, materials, plasma heating, breeding and test blankets, tritium technology, and remote handling.

Zusammenfassung:

TASKA - Eine Tandem-Spiegel-Fusions-Testanlage

TASKA (Tandem Spiegelmaschine Karlsruhe) ist eine Testanlage für Technologien, die sich auf das plasmaphysikalische Konzept eines Tandem Spiegels mit thermischer Barriere stützt. Hauptziel der Studie war, eine Anlage zu entwerfen, die Auslegungsinformationen für einen Demonstrationsfusionsreaktor liefern soll. Daher muß TASKA als Testbett für Technologien dienen, wie etwa Plasmaengineering, supraleitende Magnete, Materialien, Plasmaheizung, Brut- und Testblankets, Tritium-technologie und Fernbedienung.

PREFACE

TASKA (Tandem Spiegelmaschine Karlsruhe) is a near term engineering test facility based on the tandem mirror concept with thermal barriers. The study was essentially completed in December 1981 after approximately one year of study.

The main objectives of this study were to develop a pre-conceptual design of a facility that could provide engineering design information for a Demonstration Power Reactor. Another objective of this study was to design a facility that would be within financial reach of a single country's fusion budget. Trying to achieve both of these objectives was indeed a challenge but we feel that TASKA does come close to meeting both objectives. It must also be noted that this report was completed in only one year and normally, a second or even third year would be required to pass from the pre-conceptual to conceptual design phase. Therefore, the level of detail in this report is not consistent with that in the INTOR or US-ETF/FED activities which have been in progress for several years. However, we do think that the basic features of TASKA are so attractive as to warrant early exposure and early publication.

The project was carried out and financed by KfK together with the University of Wisconsin in Madison, USA. Further financial support came from the Wisconsin Electric Utilities Research Foundation and Fusion Power Associates. A subcontract was awarded to the INTERATOM company.

We wish to acknowledge the technical assistance that we received from Dr. Grant Logan of the Lawrence Livermore National Laboratory, and the donation of scientific staff from the Grumman Corporation, the Hanford Engineering Development Laboratory, General Atomic Corporation, Lawrence Livermore National Laboratory, and Babcock and Wilcox Corporation, all in USA, and the Institut für Plasmaphysik Garching, the KFA Jülich and the Siemens AG in the Federal Republic of Germany. These efforts were vital to the final success of this program.

Finally, we wish to acknowledge the superb job that was done by the secretarial staffs at both KfK and the University of Wisconsin in preparing this report.

Table of Contents for TASKA

	<u>Page</u>	
I Introduction and Objectives of TASKA	I-1	1
II Overview of TASKA	II.1-1	4
1 Introduction	II.1-1	4
2 Objectives	II.2-1	6
3 Physics Basis for TASKA	II.3-1	7
4 General Survey and Basic Reactor Parameters of TASKA	II.4-1	9
4.1 Design Philosophy	II.4-1	9
4.2 General Survey and Parameters	II.4-1	9
5 Plasma Physics	II.5-1	16
6 Magnet System of TASKA	II.6-1	20
7 Plasma Heating Technology	II.7-1	26
7.1 Neutral Beam Injection	II.7-1	26
7.2 ECRH and ICRF Heating	II.7-4	29
8 Blanket Design	II.8-1	33
8.1 Permanent Breeding Blanket	II.8-1	33
8.2 Test Blanket Module	II.8-1	33
9 Materials Testing	II.9-1	37
10 Maintenance	II.10-1	44
11 Cost Analysis	II.11-1	49
12 Conclusions	II.12-1	51
References for Chapter II	II.12-2	52
III Plasma Physics	III.1-1	54
1 Physics Background for TASKA	III.1-1	54
1.1 Overview of Tandem Mirror Concepts	III.1-1	54
1.2 Experimental Results with Tandem Mirrors	III.1-15	68
1.3 Future Major Tandem Mirror Experiments	III.1-22	75
1.4 Physics Issues Related to TASKA	III.1-26	79
References for Section III.1	III.1-46	99
Appendix III.1-A Reprint: "Summary of TMX Results"	III.1-A	103
2 Power Balance Model	III.2-1	112
2.1 Introduction	III.2-1	112
2.2 General Formulas	III.2-2	113
2.3 Barrier Physics	III.2-6	117
2.4 Central Cell Physics	III.2-9	120
2.5 Plug Physics	III.2-13	124
2.6 Input Power	III.2-14	125
2.7 Numerical Solution of the System of Equations	III.2-15	126
References for Section III.2	III.2-15	126
3 Special Cases and Parametric Analysis	III.3-1	128
References for Section III.3	III.3-23	150
Appendix III.3-A Radial Transport Due to Central Cell Flux Tube Asymmetry	III.3-24	151
4 TASKA Design Point	III.4-1	154
5 The DT Fuel Density in the Thermal Barrier and Plug	III.5-1	161
References for Section III.5	III.5-9	169

	<u>Page</u>	
6 Plasma Wall Interactions and the "Halo" Plasma	III.6-1	170
References for Section III.6	III.6-8	177
IV Heating, Fueling and Exhaust	IV.1-1	178
1 Electron Cyclotron Resonance Heating	IV.1-1	178
1.1 Introduction	IV.1-1	178
1.2 The Plasma	IV.1-2	179
1.3 The Gyrotron Microwave Power Source	IV.1-20	197
1.4 Beam Waveguide Launcher	IV.1-21	198
References for Section IV.1	IV.1-32	209
2 ICRF Heating in Central Cell	IV.2-1	210
2.1 Introduction	IV.2-1	210
2.2 ICRF Physics and Design Considerations	IV.2-1	210
2.3 Antenna Layout	IV.2-5	214
2.4 Materials Considerations	IV.2-7	216
References for Section IV.2	IV.2-9	218
3 Neutral Beam Injection	IV.3-1	219
3.1 General	IV.3-1	219
3.2 Typical Positive Ion Source/Beam Line System	IV.3-5	223
3.3 Specific NBI Design Parameters for TASKA	IV.3-17	235
3.4 Design Considerations for a Positive Ion Source (Options)	IV.3-21	239
3.5 Negative Ion Source Based NBI	IV.3-26	244
References for Section IV.3	IV.3-29	247
4 Vacuum System	IV.4-1	250
4.1 Introduction	IV.4-1	250
4.2 Vacuum Pumping of the Discharge Chamber	IV.4-1	250
4.3 Evacuation System for the Dumps	IV.4-5	254
4.4 Evacuation System for the Neutral Beam Injectors	IV.4-6	255
4.5 Roughing Pump System	IV.4-9	258
4.6 Control of Vacuum Parameters	IV.4-10	259
References for Section IV.4	IV.4-11	260
5 Tritium Fuel Cycle	IV.5-1	261
5.1 Overview	IV.5-1	261
References for Section IV.5	IV.5-21	281
V Magnet System	V.1-1	283
1 Introduction	V.1-1	283
1.1 Magnet Design Philosophy	V.1-1	283
1.2 General Description of the Magnet System	V.1-2	284
References for Section V.1	V.1-10	292
2 Central Cell Magnets	V.2-1	293
References for Section V.2	V.2-1	293
3 The Barrier Mirror Coil	V.3-1	296
3.1 The Superconducting Solenoid Set	V.3-1	296
3.2 The Normal Conducting Insert Coil	V.3-7	302
References for Section V.3	V.3-12	307
4 End Plug Coils	V.4-1	308
References for Section V.4	V.4-1	308

	<u>Page</u>	
5	Field Shaping Coils	V.5-1 313
6	Magnetic Shielding	V.6-1 316
	References for Section V.6	V.6-3 318
7	Superconductors for TASKA	V.7-1 319
	7.1 Introduction	V.7-1 319
	7.2 Stresses	V.7-1 319
	7.3 Fast Discharge	V.7-2 320
	7.4 Cryogenic Stability	V.7-3 321
	7.5 Design Procedure	V.7-4 322
	7.6 Conductor Parameters	V.7-5 323
8	Coil Support	V.8-1 330
	8.1 Central Cell	V.8-1 330
	8.2 Plug Region	V.8-2 331
	References for Section V.8	V.8-3 332
9	The Impact of the Magnetic Properties of Ferritic Steels	V.9-1 341
10	Conclusions	V.10-1 342
	Appendix: The Impact of Magnetic Properties of Ferritic Steels	V.9-1 343
VI	Central Cell	VI.1-1 378
1	General Design	VI.1-1 378
	1.1 Introduction	VI.1-1 378
	1.2 Description of Central Cell	VI.1-1 378
	1.3 Evolution of TASKA Blanket Design	VI.1-9 387
	1.4 Mechanical Description of Central Cell Components	VI.1-12 390
	References for Section VI.1	VI.1-30 409
2	Neutronics	VI.2-1 410
	2.1 Design Goals	VI.2-1 410
	2.2 Central Cell Permanent Blanket	VI.2-1 410
	2.3 Barrier Region	VI.2-10 419
	2.4 Radioactivity	VI.2-19 428
	2.5 Test Blanket	VI.2-32 441
	References for Section VI.2	VI.2-40 449
3	Thermal Hydraulics	VI.3-1 450
	3.1 MHD Effects	VI.3-1 450
	3.2 Heat Transfer Calculations	VI.3-5 454
	3.3 Cooling of the Reflector and the Shield	VI.3-14 463
	References for Section VI.3	VI.3-18 467
4	Structural Materials for TASKA	VI.4-1 468
	4.1 General Considerations	VI.4-1 468
	4.2 Physical and Thermal Properties of HT-9	VI.4-4 471
	4.3 Use of Martensitic Steels	VI.4-9 476
	4.4 Mechanical Properties of HT-9	VI.4-11 478
	4.5 Thermal Stress Factor	VI.4-17 483

	<u>Page</u>	
4.6	Compatibility of HT-9 with Pb-Li Alloys	VI.4-20 486
4.7	Magnetic Properties of HT-9	VI.4-28 494
4.8	Effects of Irradiation on HT-9 Type Alloys	VI.4-31 497
4.9	Fabrication of TASKA Blanket Module	VI.4-59 525
4.10	Expected Irradiation Performance of HT-9 in TASKA	VI.4-67 530a
	References for Section VI.4	VI.4-72 536
5	Tritium Extraction and Purification	VI.5-1 539
5.1	Blanket and Heat Exchange Systems	VI.5-1 539
5.2	Purification Systems	VI.5-13 551
5.3	Summary of the Total Tritium Inventory and Comments	VI.5-18 556
	References for Section VI.5	VI.5-21 559
6	Heat Removal Cycle	VI.6-1 562
6.1	Introduction	VI.6-1 562
6.2	TASKA Power Cycle	VI.6-1 562
6.3	Future Steam Cycle Improvements	VI.6-2 563
7	Electricity Production	VI.7-1 571
7.1	Introduction	VI.7-1 571
7.2	General System Requirements	VI.7-1 571
7.3	Steam Generation System	VI.7-4 574
7.4	Components	VI.7-5 574a
7.5	Component Costs	VI.7-11 580
VII	Testing Program	VII.1-1 582
1	Overview	VII.1-1 582
2	Materials Testing	VII.2-1 585
2.1	Introduction	VII.2-1 585
2.2	Neutronics Survey Analysis	VII.2-2 586
2.3	Test Matrix and Test Module Design Considerations	VII.2-15 599
2.4	Neutronics Analysis for the REGAT Module of TASKA	VII.2-44 628
	References for Section VII.2	VII.2-65 649
	Appendix VII.2-A Materials Test Specimens Specified in the TASKA Test Matrix	VII.2-66 650
	Appendix VII.2-B Test Module and Specimen Capsule Design Details	VII.2-72 655
3	Test Module with Liquid Lithium Blanket	VII.3-1 658
3.1	General Considerations	VII.3-1 658
3.2	Concept of a Test Module with Liquid Lithium Blanket	VII.3-2 659
VIII	End Plug Design	VIII.1-1 722
1	General Features	VIII.1-1 722
2	Neutron Environment	VIII.2-1 723
	References for Section VIII.2	VIII.2-27 749
3	Beam Dumps	VIII.3-1 751
3.1	Introduction	VIII.3-1 751
3.2	Design Philosophy	VIII.3-4 754
3.3	Engineering Design	VIII.3-7 757
3.4	Dump Location and Vacuum Pumping Considerations	VIII.3-12 762
3.5	Sputtering and Lifetime Considerations	VIII.3-16 767

	<u>Page</u>	
3.6 DT and DD Neutron Generation from the Dump Surfaces	VIII.3-21	772
References for Section VIII.3	VIII.3-35	786
4 Direct Convertor	VIII.4-1	788
4.1 Particle and Energy Flow to the Direct Convertor and Thermal Dumps	VIII.4-4	791
4.2 Grid and Collector System	VIII.4-7	794
4.3 Comparison to a Full Scale Reactor Direct Convertor	VIII.4-13	800
References for Section VIII.4	VIII.4-15	802
5 Ion and Electron Thermal Dumps	VIII.5-1	803
5.1 Thermal Hydraulics	VIII.5-1	803
5.2 Tritium Considerations	VIII.5-2	804
References for Section VIII.5	VIII.5-7	809
6 Surface Erosion on Components of the Plasma Direct Convertor and Thermal Dump	VIII.6-1	810
6.1 Introductory Remarks	VIII.6-1	810
6.2 Concentration Profiles of Implanted Ions	VIII.6-5	814
References for Section VIII.6	VIII.6-14	823
7 End Plug Coils Arrangement	VIII.7-1	824
 IX Operations	 IX.1-1	 827
1 Plasma Startup	IX.1-1	827
1.1 Introduction	IX.1-1	827
1.2 Initial Target Plasma	IX.1-2	828
1.3 Rate Code Calculations	IX.1-4	830
1.4 Conclusions	IX.1-29	855
2 Diagnostics, Instrumentation, and Control	IX.2-1	858
2.1 Introduction	IX.2-1	858
2.2 General Instrumentation and Control	IX.2-1	858
2.3 Neutron Diagnostics	IX.2-7	864
2.4 Plasma Diagnostics	IX.2-10	867
References for Section IX.2	IX.2-18	875
 X Maintenance	 X.1-1	 876
1 General Aspects and Plant Layout	X.1-1	876
2 Handling Equipment for Repair and Operation	X.2-1	884
2.1 Generalities	X.2-1	884
2.2 Elevated Working Platform	X.2-3	886
2.3 Manipulator Unit	X.2-5	888
2.4 Shielded Cabin with Manipulators	X.2-10	893
2.5 Television Camera System	X.2-13	897
2.6 Tools for Manipulators	X.2-14	900
2.7 Concluding Remarks	X.2-21	904
3 Maintenance Classification	X.3-1	905
4 Short Lifetime Components	X.4-1	911
4.1 Blankets	X.4-1	911
4.2 Neutral Beam Injectors	X.4-6	916
5 Large Sized Components	X.5-1	925
5.1 Central Cell Coils	X.5-1	925

	<u>Page</u>	
5.2 Barrier Coil	X.5-7	931
6 Barrier Coil	X.6-1	937
6.1 Requirement and Objective	X.6-1	937
6.2 Approach	X.6-1	937
6.3 Configuration Description	X.6-2	938
6.4 Alternate Designs and Procedures	X.6-20	956
6.5 Description of Selected Procedure	X.6-23	959
6.6 Facility Requirements	X.6-25	961
6.7 Special Equipment Requirements	X.6-26	962
6.8 Recommendations for Further Study	X.6-31	967
7 Availability and Maintainability	X.7-1	970
7.1 Introduction and Summary	X.7-1	970
7.2 Main Subsystems in TASKA and Their Logic Interconnection	X.7-2	971
7.3 The Computer Code for Analysis of Availability	X.7-2	971
7.4 Data	X.7-8	977
7.5 Results	X.7-8	977
7.6 Maintainability	X.7-8	977
References for Section X.7	X.7-10	979
8 Conclusion	X.8-1	980
XI Costs	XI.1-1	981
1 Introduction	XI.1-1	981
2 Costs in Individual Accounts	XI.2-1	983
3 Summary of Accounts	XI.3-1	991
4 Annual Operating Costs	XI.4-1	992
TASKA Parameter List	A-1	993

I Introduction and Objectives of TASKA

There has been considerable progress in the plasma physics field during the last decade. It is expected that at least one of the major experiments to come into operation in the 1980's (e.g., TFTR, JET, JT-60, MFTF-B) will approach or even surpass the Lawson criterion. Some of these experiments may even reach ignition. If such positive expectations are realized, we will then be at a major turning point in fusion research where the main interest will switch from plasma physics to plasma engineering and fusion technology for a DT demonstration reactor.

There are a large number of scientists in the fusion community who feel that only one large device needs to be built before a DT demonstration reactor (DEMO) operates. This single device should be the maximum reasonable step beyond the experiments of this decade and considerable effort has been invested in defining the nature of that step.

The most advanced confinement concept at the present time is that of the tokamak and it is expected that tokamaks will demonstrate ignition first. Nevertheless, doubts continue to be expressed as to whether the tokamak line will lead to the most attractive commercial power reactor. Due to the complex and toroidally interlinked structure of the magnet system and its pulsed operation, intrinsic engineering difficulties are anticipated; e.g., restricted accessibility, material fatigue problems, pulsed power cycle. In principle, a linear device and steady state operation can avoid such problems. It will lead to a reactor with improved accessibility, thus easing exchange or repair of key components. Without the dynamic loads from pulsing, the mechanical behavior of the materials will be improved.

The present optimism for the successful design and operation of a major DT fusion experiment has initiated a considerable effort on studies of an engineering test facility with all the features mentioned above. A worldwide endeavor for such a conceptual design is the study of the International Tokamak Reactor, INTOR. Recent advances in the physics of tandem mirrors have caused us to examine the potential of a tandem mirror device with thermal barriers serving as such an engineering test facility. Therefore we limited our study, TASKA (Tandem Spiegelmaschine Karlsruhe), to be the maximum reasonable step beyond the next generation of large mirror machines (AMBAL, TMX-Upgrade, GAMMA-10, TARA, and MFTF-B). The objective of the study is to demonstrate that all key technologies required for this step (and later on for DEMO) can be integrated into one machine and adequately tested. Thus TASKA has to serve as test bed (e.g., it should have a reactor-relevant neutron flux, at least 1 MW/m^2) for technologies of plasma engineering, superconducting magnets, existing materials, plasma heating (neutral beam and RF-heating), breeding and test blankets, tritium technology and remote handling. It has to prove that such a facility can operate safely and reliably as a DT burner. We have also limited the direct capital cost to 800 million dollars or less, and an operating cost of less than 80 million dollars per year.

The physics basis for TASKA has partly been verified on GAMMA-6 and TMX, and is partly expected to be proven by TMX-Upgrade during 1982. In addition MFTF-B, currently under construction, should demonstrate by 1986 long pulse operation (≈ 30 seconds) in the TMR-thermal barrier mode.

The main objectives of the overall TASKA study are twofold: (1) the study of a feasible tandem mirror engineering test facility, and (2) the comparison of the technologies required for a tokamak based solution with a

solution based on the tandem mirror with thermal barriers. This report mainly addresses the first point and subsequent reports will concentrate more on the mirror/tokamak comparisons. It is felt that by such a "friendly" competition between the two major magnetic fusion concepts, we may arrive at the optimum facility to be built by the world fusion community.

II. Overview of TASKA

II.1 Introduction

The rapid progress in plasma physics during the past 10 years and the expectations of positive results from the major experiments to come into operation this decade (e.g., TFTR, JET, T-15, JT-60, MFTF-B) suggest that the next large device to be built before the Demonstration Reactor (DEMO) operates will be a DT Technology Test Facility. This point of view has initiated many studies directed towards the next step in the world fusion program which is envisaged to be an engineering test facility where all of the key technologies required for a Demonstration Reactor can be successfully integrated into, and tested in, one machine. One such worldwide endeavor for the conceptual design of a tokamak is the study of the International Tokamak Reactor, INTOR.⁽¹⁾ Indeed, tokamaks presently represent the most advanced fusion concept and are expected to demonstrate ignition and the behavior of an ignited DT-plasma in the late 1980's. Nevertheless there are some doubts that tokamaks may in fact lead to a commercial power reactor mainly because of their complex and toroidally interlinked magnet structure.⁽²⁾

In principle, a linear device could avoid such complexity. It can lead to a device which gives better access and the linear geometry allows for modular construction of the major components. This configuration is also a definite advantage for the exchange or repair of key components within the reactor vessel. The physics concept with the best chance for a linear geometry is the mirror and recent advances in the physics of mirrors give rise to the expectation that the difficulties in the plasma physics performance of minimum B mirror machines can be overcome by the tandem mirror concept with thermal barriers.⁽³⁾ Conceptual designs of power plants have already shown

such configurations to be economically competitive with tokamaks.⁽⁴⁾ In addition to the favorable possibilities of the tandem mirror, it was also evident that such a device might be a very attractive engineering test facility. Thus, the TASKA study was initiated in late 1980 to see if our optimistic expectations were justified from an engineering point of view.

II.2 TASKA Objectives

The main objective of TASKA is to provide an engineering test bed to qualify and test materials and blanket concepts for a Demonstration Fusion Power Reactor. TASKA must also demonstrate that superconducting magnets, heating technologies, tritium handling equipment, remote handling equipment, etc., can all operate in an intense neutron environment with reliabilities that will allow ~ 50% availabilities to be achieved. It must do all of this in a timely, but yet cost effective manner which is consistent with the safe operation of a nuclear facility. To be more specific, TASKA must be the maximum reasonable physics and technology step beyond the next generation of large mirror machines (AMBAL,⁽⁵⁾ TMX-Upgrade,⁽⁶⁾ GAMMA-10,⁽⁷⁾ TARA,⁽⁸⁾ and MFTF-B⁽⁹⁾). It should be able to operate in the early 1990's (similar to INTOR⁽¹⁰⁾) and provide at least 5 MW-y/m² of large scale test volume in no more than 10 years of full power operation (exclusive of check-out and initial low power tests). Finally, the overall direct cost of TASKA should be \leq 800 million dollars and the yearly operating cost (including personnel, power, T₂, etc.) should be less than 50 million dollars.

II.3 Physics Basis for TASKA

The tandem mirror physics concept has been previously verified on GAMMA-6⁽¹¹⁾ and TMX.⁽¹²⁾ Some aspects of electron heating with ECRH in the end plugs of TMR's have been recently demonstrated on Phaedrus⁽¹³⁾ and ICRH heating of plasmas has been demonstrated in PLT.⁽¹⁴⁾ The key experiment to demonstrate operation with thermal barriers on a tandem mirror will be performed in 1982 on TMX-U.⁽⁶⁾ This device will also advance the understanding of electron heating and the central cell region will be operated in the collisionless diffusion regime.

The MFTF-B⁽⁹⁾ and its axicell upgrade⁽¹⁵⁾, currently under construction, should demonstrate long pulse operation (30 seconds) in the TMR-thermal barrier mode in the 1985-1986 time period. The limits on central cell beta will also be investigated in that device. High power, continuous (30 sec) 80 keV neutral beams will be used to achieve a D-T equivalent $Q \sim 1$ in the same time period. MFTF-B will be the first tandem mirror machine to use all superconducting magnets, including high field barrier and yin-yang coils.

The physics relationship of TASKA to past, present, and future devices is shown in Fig. II.3-1. The anticipated performance of WITAMIR-I⁽⁴⁾ is also included and the collection of parameters shows that TASKA lies on a reasonable projection of the aforementioned devices. More discussion on the physics basis of TASKA is given below and in Ref. 16. It is important to note that while the optimism about achieving the TASKA physics goals is high, the success of any device after MFTF-B depends on the degree to which current physics models can be verified. Progress through the TARA/AMBAL/TMX-U/GAMMA-10/MFTF-B series must therefore be closely monitored.

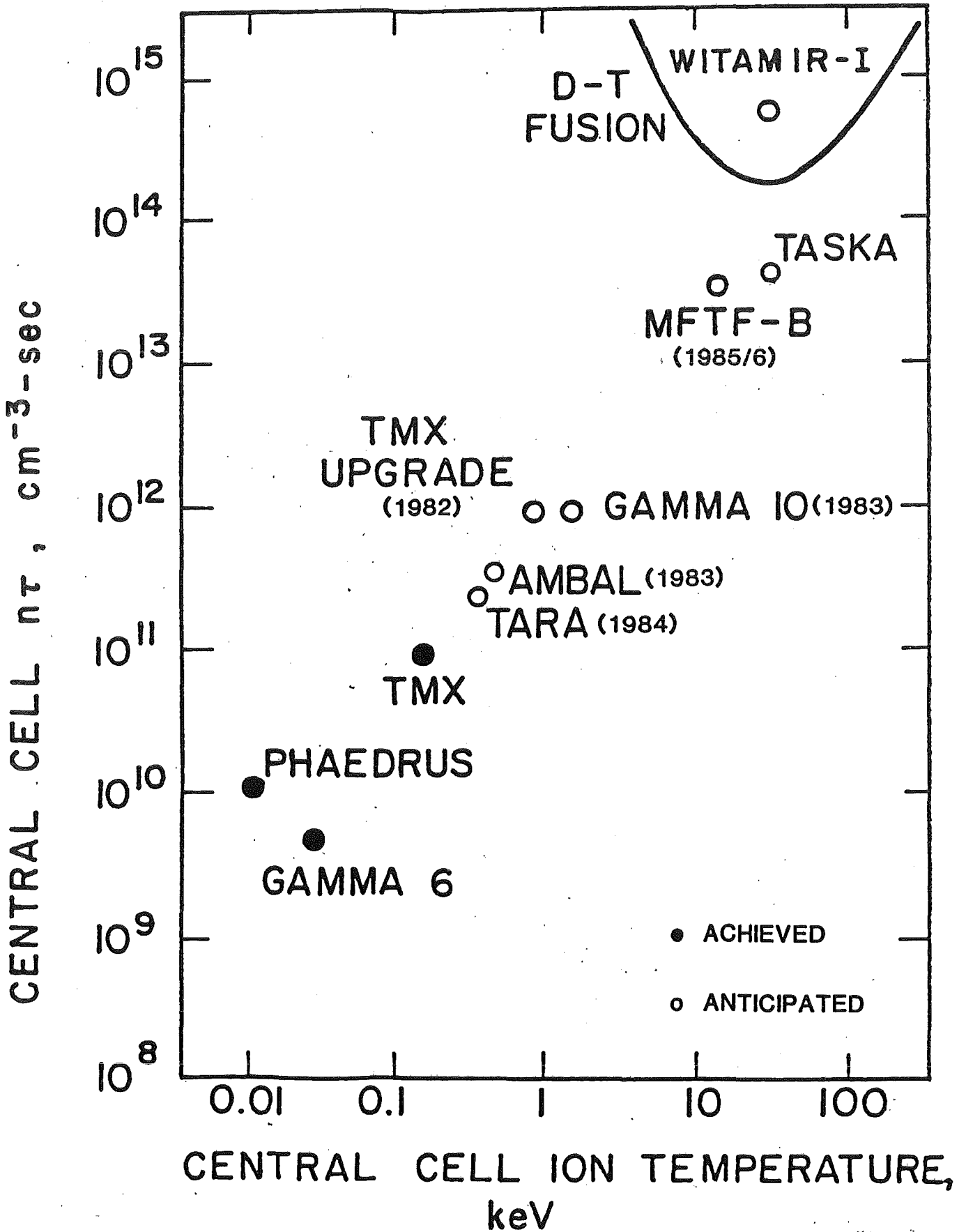


Fig. II.3-1 Critical physics parameters for present and future tandem mirrors.

II.4 General Survey and Basic Reactor Parameters of TASKA

II.4.1 Design Philosophy

TASKA is based on the concept of a tandem mirror with an inside thermal barrier. The design uses existing technologies or those which may be expected to be available in the near future. A net power gain is not required, therefore Q is not an important parameter and will be slightly less than unity. However, a main consideration is that the neutron wall loading should be high enough to achieve a significant neutron flux and fluence for materials and blanket tests. The central cell length is minimized because of the modest requirements of the test blankets, thus reducing costs without losing scalability. A tritium breeding ratio of 1.0 or more is foreseen so that there will be no net tritium consumption over the lifetime of the machine. Electric power production, direct energy conversion, or fission fuel breeding are options that can be examined during the life of TASKA.

II.4.2 General Survey and Parameters

Schematic views of TASKA are shown in Figs. II.4-1 and II.4-2. The positions of the magnets, the test blankets, the neutral beam injectors and the generators for ECRH and ICRH are indicated along with the power and energy levels for NBI power and frequency for the RF heating systems. A selective list of TASKA general operating parameters is given in Table II.4-1. In Fig. II.4-3 the confining magnetic fields and electric potentials are shown. The end plugs consist of an inside thermal barrier, and a minimum-B yin-yang coil set. There are 3 central cell solenoids.

Some key features of TASKA are listed below:

- The DT power level is 86 MW, far below the 620 MW of INTOR⁽¹⁾ or the 180 MW of FED.⁽¹⁰⁾ This lower power level greatly eases the tritium requirements

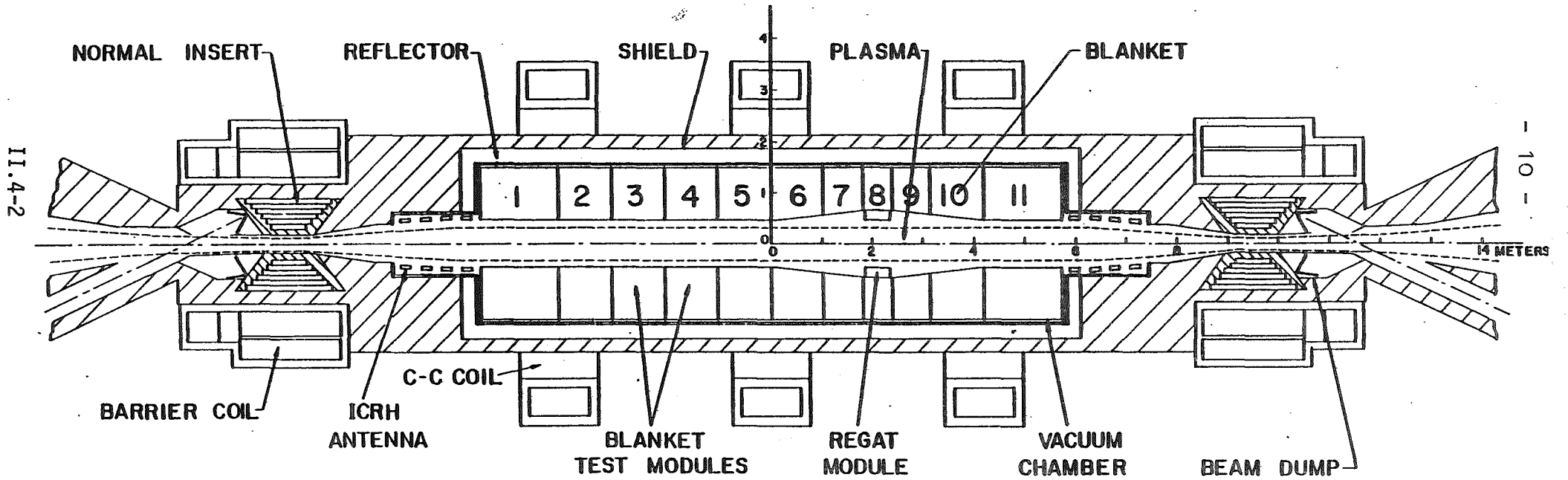


Fig. II.4-1 TASKA central cell layout.

II.4-3

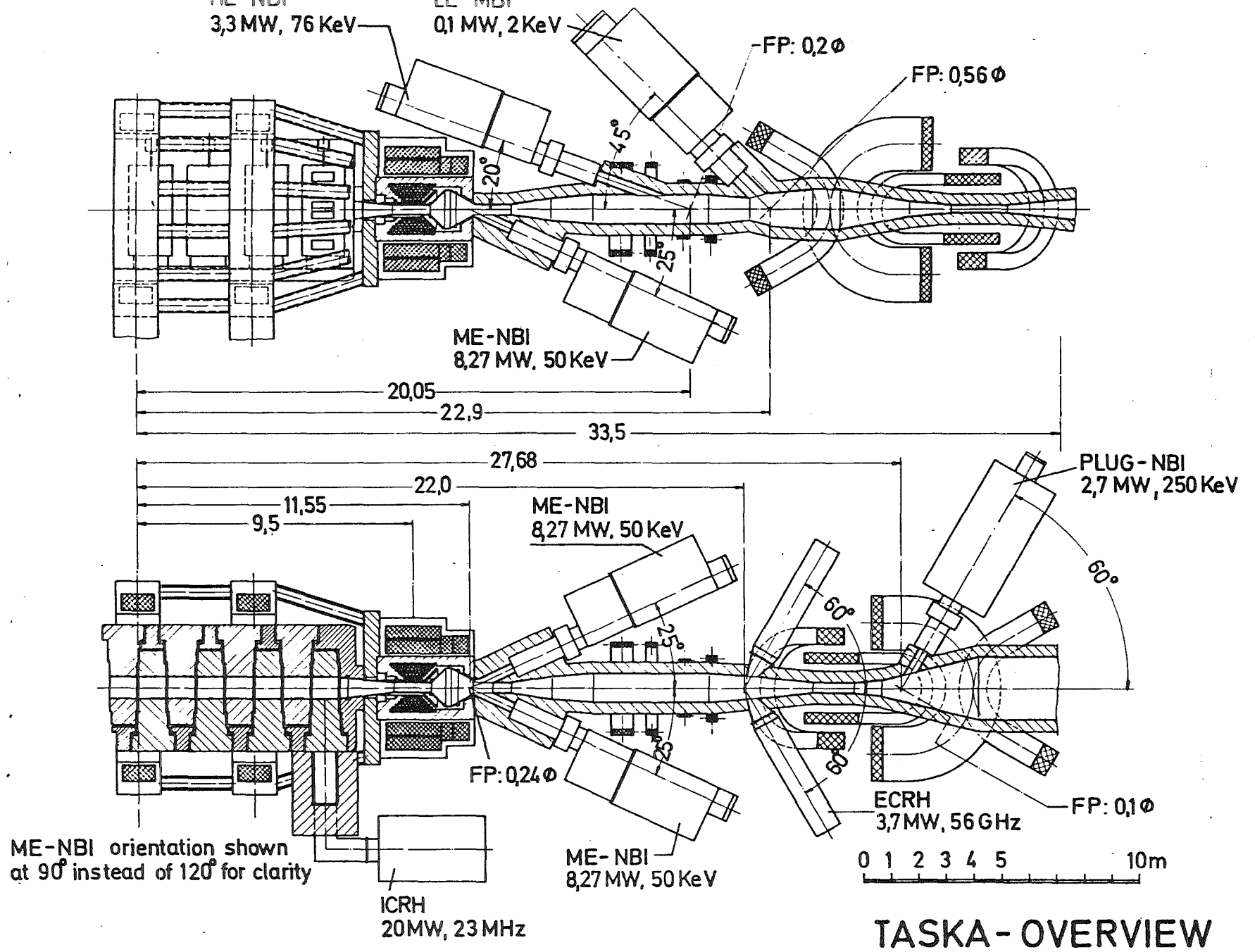
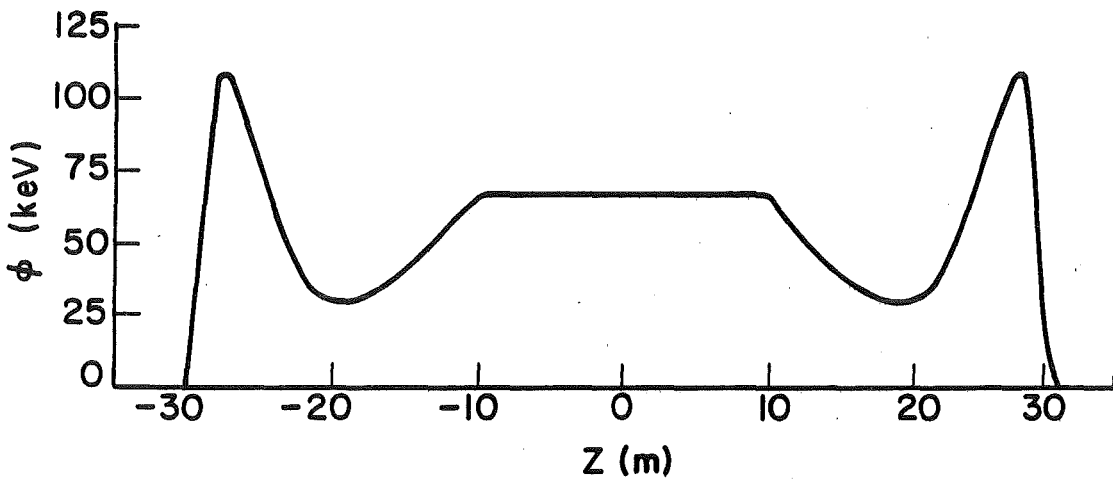
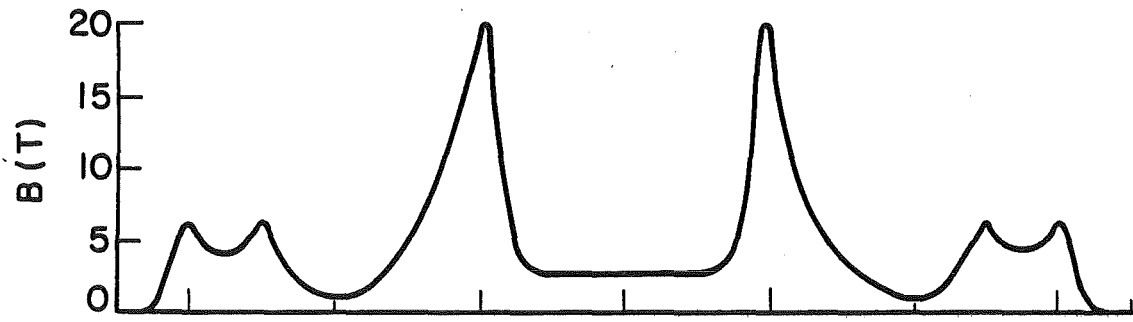


Fig. II.4-2

Table II.4-1. General Operating Parameters - TASKA

DT Power Level		86 MW
First Wall Neutron Wall Loading		1.5 MW/m ²
Total Heating Power		110 MW
Central Cell Magnetic Field (On-Axis)		2.7 T
Central Cell Length		21 m
Structure/Breeder		HT-9/Pb ₈₃ Li ₁₇
Number/Total Volume of Test Modules		1-Material/493 liters 2-Blanket/5700 liters
Operating Lifetime		15 years
Operating Scenario	<u>Year</u>	<u>% Availability</u>
H ₂ Check Out	1	10
DT Check Out	2	15
Short Term Test Phase	4	25
Long Term Test Phase	8	50



| Plug | Barrier | Central Cell | Barrier | Plug |

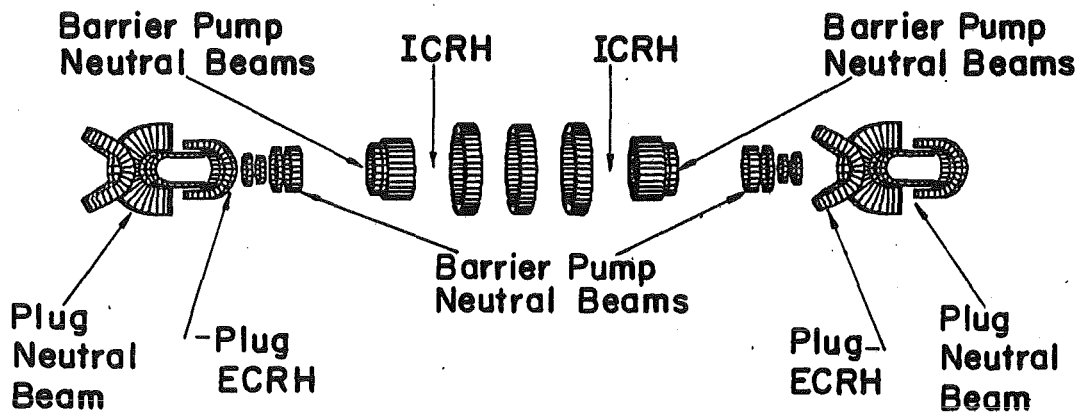


Fig. II.4-3 Magnet and electrostatic configuration of TASKA.

- and reduces the overall costs compared to previous test devices.
- The neutron wall loading is 1.5 MW/m^2 . This relatively high wall loading will allow reactor relevant testing to be performed in both blanket and materials modules. Coupled with reactor availabilities of 25 to 50%, this flux will also allow reactor relevant fluences to be obtained.
 - The barrier region is pumped with neutral deuterium and tritium beams and the electrons in the end plug region are heated with ECRH at 56 GHz. The plug ions are sustained by H^0 beams of 250 keV. The use of the very high barrier magnetic fields and ECRH requires selective ion pumping and the proposed design uses two stage charge exchange pumping⁽¹⁷⁾ to reduce these requirements.
 - One of the key features of the machine that allows such a favorable performance is the use of a high field, room temperature copper insert which raises the field in the barrier coil from 14 T produced by the superconducting coil to 20 T. The life limiting feature of this coil is radiation damage to the ceramic insulation conservatively assumed to be 10^{12} rad. The projected life is then 10 years at 25% availability or 5 years at 50% availability.
 - The tritium for this device is provided by circulating a $\text{Pb}_{83}\text{Li}_{17}$ alloy in HT-9 ferritic steel tubes (see Fig. II.8-1). The localized breeding ratio is 1.65 and the overall breeding ratio of the machine (including test sections as well as leakage) is 1.0 so that no net tritium consumption is incurred over the life of the machine. The low solubility of T_2 in $\text{Pb}_{83}\text{Li}_{17}$ ⁽¹⁸⁾ results in only a 20 g inventory in the blanket.
 - There are two modules devoted to blanket testing and one module devoted to materials testing. These test modules are placed between the central cell

coils for ease of access and maintenance.

- The secondary heat transfer loop contains an organic material, HB-40. Normally, the approximately 60 MW from the central cell breeding blanket are dumped to cooling towers but provisions have been made to generate electricity with 350°C steam. Roughly 15 MW_e can be generated in this manner.
- Normally, the energy of the plasma ions and electrons leaking from the plasma is deposited in heat dumps at either end of the machine but provisions have been made to test various direct convertor modules on one end. The operation of TASKA does not depend on the successful operation of the direct convertor.

II.5 Plasma Physics

The end plug configuration used in TASKA consists of an inboard thermal barrier, generated by a high field hybrid solenoid, and the electrostatic plug located in a min-B yin-yang magnetic mirror (see Fig. II.4-3). The potential peak in the plug provides axial confinement of the central cell ions; the good magnetic curvature of the min-B mirror provides MHD stability of the entire system. The thermal barrier provides thermal isolation of the plug and central cell electrons and allows the plug electrons to be heated substantially without heating the central cell electrons. This also allows the positive confining potential of the plug to be achieved at lower density, which thereby reduces the required neutral beam power to sustain the plug. The central cell ion temperature is maintained by ICRF heating and the power input from the barrier pump beams. This reduces the power requirements for "pumping" of the thermal barriers.

The physics parameters of TASKA are given in Table II.5-1 and the heating parameters are given in Table II.5-2. The central cell beta of 50% is an assumed value, but is considered to be conservative in light of recent theoretical developments concerning finite Larmor radius stabilization of ballooning modes; this is discussed further in Section III.1. Microstability of the mirror-confined plug plasma is an unresolved issue with the TASKA configuration. The TASKA design utilizes "sloshing" ions in the plug to create a local electrostatic well and trap warm plasma. This can, in principle, provide microstability against the drift cyclotron loss cone (DCLC) mode and the Alfvén ion cyclotron mode, but stability against the axial loss cone mode (which has not yet been observed experimentally) is harder to obtain.

Table II.5-1. TASKA Plasma Physics Parameters

Central Cell

Magnetic field	2.7 T
Density	$1.94 \times 10^{14} \text{ cm}^{-3}$
Alpha particle density	$1.6 \times 10^{12} \text{ cm}^{-3}$
Ion temperature	30. keV
Electron temperature	11.5 keV
Beta	0.5
$(n\tau)_{iC}$	$5.4 \times 10^{13} \text{ cm}^{-3} \text{ s}$
$(n\tau)_{eC}$	$5.3 \times 10^{13} \text{ cm}^{-3} \text{ s}$
Potential, ϕ_C	42.8 keV

Barrier

Barrier peak magnetic field	20 T
Barrier minimum magnetic field	.8 T
Potential, ϕ_b	37.5 keV
Pumping parameter, g_b	2.

Plug

Midplane magnetic field	4 T
Vacuum mirror ratio	1.56
Midplane density	$6.3 \times 10^{13} \text{ cm}^{-3}$
Mean ion energy	388. keV
Electron temperature	59.3 keV
Beta	0.64
$(n\tau)_{ip}$	$2.9 \times 10^{13} \text{ cm}^{-3} \text{ s}$
$(n\tau)_{ep}$	$7.5 \times 10^{11} \text{ cm}^{-3} \text{ s}$
Potential, $\phi_C + \phi_e$	109. keV
Cohen parameter, ν_C	0.5

Table II.5-2. TASKA Heating Parameters

Neutral Beams

Plug:	power	5.4 MW
	energy	250. keV
	angle	60°
	species	p
	trapping fraction	0.21
Barrier:	power	6.6 MW
	energy	76 keV
	angle	20°
	species	d
	trapping fraction	0.42
Barrier:	power	49.7 MW
	energy	50 keV
	angle	25°
	species	0.44 d/0.56 t
	trapping fraction	0.95
Barrier:	power	0.2 MW
	energy	2. keV
	angle	45°
	species	d
	trapping fraction	0.99

ECRF

Plug:	power	14.9 MW
	frequency	56. GHz
	absorption efficiency	1.

ICRF

Central cell:	power	40. MW
	frequency	30 MHz
	absorption efficiency	0.8

Total Injected Power 117. MW

NB: Plug and barrier powers are total powers for both sides.

Maintaining the thermal barrier requires removal ("pumping") of the ions which become trapped in the barrier. TASKA utilizes neutral beam pumping for this purpose; this process occurs by charge exchange between the barrier trapped ions and the neutral atoms which have been injected with the appropriate energy and angle relative to the magnetic field. The required energies and power for neutral beam pumping of the barrier and for sustaining the plug are given in Table II.5-2.

Alpha particle accumulation in the central cell is a general problem with tandem mirror reactors. Accumulation in the central cell of TASKA is not a problem because the ion confining potential is relatively low compared with the ion temperature ($\phi_C/T_{iC} \approx 1.4$); the steady state alpha concentration in the central cell is about 1%. Alpha accumulation in the thermal barriers is a potential problem that requires further study. Fueling of the central cell is done entirely by ionization of the neutral beams which pump the thermal barriers; a separate fueling mechanism is not required, except perhaps during startup.

II.6 Magnet System of TASKA

The total magnet system of TASKA consists of:

- 3 solenoids in the central cell to give the required central cell field;
- 2 barrier mirror hybrid coils to provide the magnetic mirror field;
- 2 transition coils for plasma cross section shaping;
- 2 yin-yang systems to provide plasma stability;
- 2 recirculating coils for plasma cross section shaping; and
- 8 coils for field shaping in the thermal barrier region.

The (arrangement) position of the coils is given in Figs. II.4-1, II.4-2, and II.6-1, and the magnetic field generated by those magnets is shown in Fig. II.4-3. Table II.6-1 gives the general operating parameters of the magnet system.

The three central cell magnets have an inner radius of 2.8 m and a winding cross section of 1.2 x 0.58 meters and 1.2 x 0.50 meters. The technology for these coils is available and is based on the experience with large coils already existing. The current density in the two outside coils is 1350 A/cm² and it is 1160 A/cm² in the center coil which is necessary to reduce the field ripple to 5 % or less. The maximum field at the conductor is less than 6.0 T and the conductor consists of NbTi with copper and/or aluminum stabilizer and stainless steel reinforcement.

The most complicated coil is the barrier mirror hybrid coil. It consists of a superconducting outer part and a normal conducting inner part; each of these is built up by six solenoids with different current densities and different winding cross sections. The design goes to the limits of the technology which can be expected in the near future; the majority of the field is provided by the Nb₃Sn superconductor with a maximum field of ~ 15 T at the

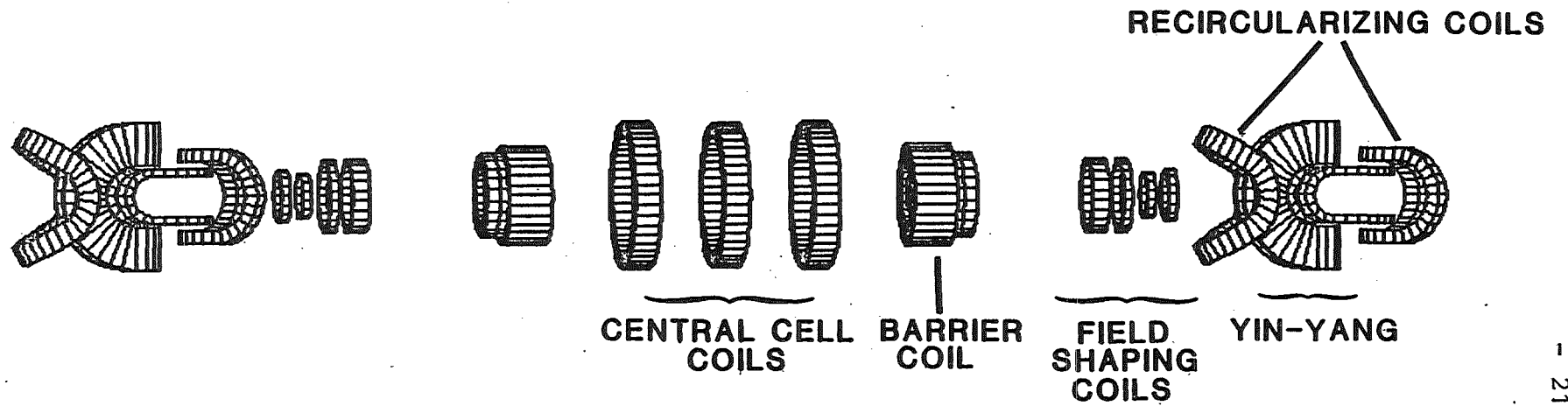


Fig. II.6-1 TASKA magnet configuration.

Table II.6-1. Main Parameters of the TASKA-Magnet System

	<u>Central Cell Solenoids</u>	<u>Barrier Coil S.C. Part</u>	<u>Barrier Coil N.C. Part</u>	<u>Transition and Recirculating Coils</u>	<u>Yin-Yangs</u>	<u>Field Shaping Coils</u>
Conductor	NbTi, Al- stabilized	NbTi/Nb ₃ Sn Cu and Al- stabilized	Hard Cu	NbTi, Cu- stabilized	NbTi, Cu- stabilized	Hard Cu
Overall current density in the winding (A/cm ²)	1350/1160	1600/2400	480-2800	1900	1630	450-795
Maximum field at the conductor (T)	6	15	20.7	7	7.9	0.5
Stored energy (MJ)	368/202	2600	12	487	411	0.013-2.25
Weight of the winding (tonnes)	68/72.5	177	20.5	84	117	1-12.9
Operating temperature (K)	4.2	4.2/1.8	300	4.2	4.2	300

II.6-3

22

coil winding and a stored energy of ~ 2 GJ. The design of the normal conducting part is made to be most power effective and is based on the experience of high field coils of the Bitter or polyhelix type already in operation at various High Magnetic Field Laboratories.

The general design of the normal Cu insert coils includes six nested cylinders, each 10 cm thick, but with a length which increases with increasing radius. Figure II.6-2 shows a cross section of the coil with the lines of constant magnetic field superimposed on it. The inner radius of the coil is 0.3 m to provide space for radiation shielding. The current density drops from 2800 A/cm^2 in the inner cylinder to 480 A/cm^2 in the outermost cylinder. The field contribution of the normal copper coil is about 6 T. The outer superconducting coil is limited by stress requirements and by the maximum allowable magnetic field at conductor of 15 T. The coil is graded in the NbTi region for conductor fields of about 8 T and in the Nb_3Sn region for higher fields. The current densities vary from 1600 A/cm^2 to 2400 A/cm^2 due to the stress limitation.

The end plug magnets (transition coil, yin-yang, recircularizer) are C-shaped with current densities less than 1900 A/cm^2 . The design of these magnets was straightforward because they are similar in geometry and electrical data to those of the MFTF-B machine which has already operated under similar conditions. Characteristic dimensions for the yin-yang system are an overall height of 7.0 m and for a transition coil about 5 m. These are comparable with the MFTF-B dimensions of ~ 6 m overall height for the yin-yang and ~ 12 m for the outside A-cell coil. This coil was successfully tested in February 1982.

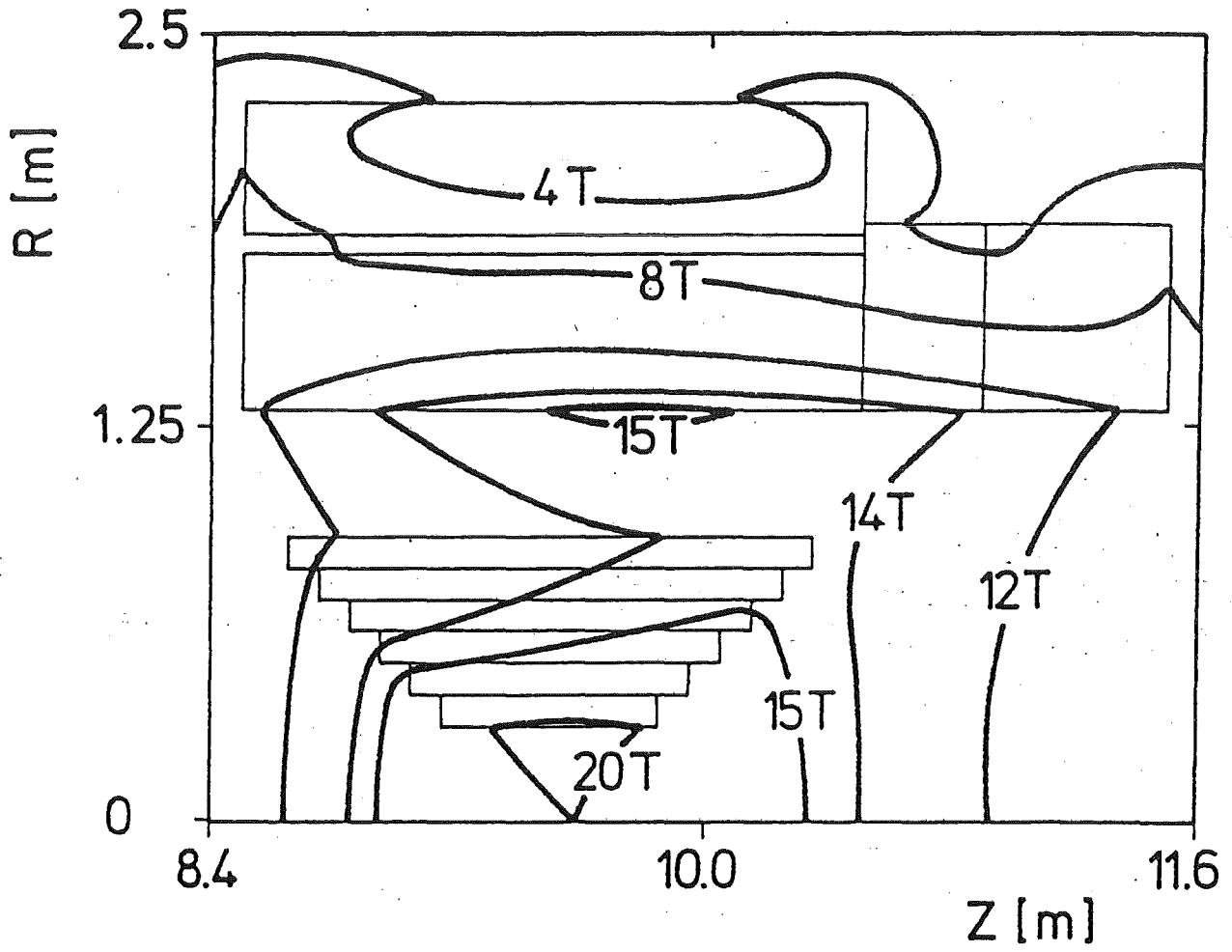


Fig. II.6-2 Cross section of the barrier coil with 4 T, 8 T, 12 T, 14 T, 15 T, and 20 T B-contours.

In addition, access for neutral beam injectors which provide the barrier pumping has to be included. The neutral beam injection angles, dictated by plasma physics requirements, are small which means that the present magnet design is the result of a trade-off between the magnetic fields from the plasma physics requirements and the access requirements for neutral beam injection. To fulfill these requirements, the barrier coil is built up by several parts with different thicknesses and different current densities. In addition, the end plug has been moved away from the barrier coil to enhance NBI access. However, the minimum field in the thermal barrier region is then lower than the required 0.8 T. This requires that field shaping coils (in this case normal conducting) be placed on each end of the device to increase the field to the required level. These coils are integrated in the shield as shown in Fig. II.4-2.

II.7 Plasma Heating Technology

II.7.1 Neutral Beam Injection

Neutral beam injection (NBI) is used as the primary means for plasma heating, plasma fueling, and selective ion charge exchange pumping in the TASKA materials test tandem mirror reactor design. Computational studies⁽¹⁹⁾ of the equilibrium plasma parameters needed to attain the desired neutron wall loading of 1.5 MW/m^2 in the central cell yield the preliminary NBI design and heating requirements (see Table II.7-1). For simplicity in present parameter studies, each neutral beam is assumed to consist only of the full energy component.

The NBI performance parameters (listed in Table II.7-1) are based upon a present capability or scaling of existing ion source technology. However, the application to steady state D-T operation for TASKA will require a further level of special technological development particularly in the following areas:

- The design of high power level steady state NBI/ion sources with high reliability and compatibility with remote NBI component changeout. Operation of NBI hardware in a high neutron fluence with a tritium loaded system will also require some form of remote handling for maintenance (the aim is for a minimum of 1 year normal lifetime before required maintenance).
- Special cooling technology will be required because of locally high beam power loading on the charged ion dump, on the remnant neutral beam dump, on associated diagnostics, on the ion source grids, and on the machine end walls. Solutions such as thin channel-cooled surfaces⁽²⁰⁾ or direct energy recovery for ion dump and end walls⁽²¹⁾ are feasible.

Table II.7-1. TASKA Neutral Beam Injector and Heating Requirements

<u>Location</u>	<u>Injection Angle</u>	<u>V₀ (kV)</u>	<u>NBI Power Per Injector (MW)</u>	<u># Ion Sources Per Injector</u>	<u>Total # Injectors</u>	<u>I⁰ (Equiv.) Per Injector</u>	<u>I[±] (EST) Per Injector</u>
P-NBI (plugs)	60°	250	2.7	1/H ⁻ est.	2	10.8 AH ⁰	29 AH ⁻
HE-NBI (barriers)	20°	76	3.3	1	2	43 AD ⁰	108.8 AD ⁺
ME-NBI (barriers)	25°	50	8.3	3	6	3 x 65 A D ⁰ + T ⁰	3 x 362 A D ⁺ + T ⁺
LE-NBI (barriers)	45°	2	.1	1	2	50 AD ⁰	97.5 AD ⁺
ECRH (plugs and barriers)	~ 56 GHz 4 units each 3.7 MW to plasma						
ICRH (central cell)	~ 21 MHz 1 unit yielding ~ 40 MW to plasma						

II.7-2

- The development of steady state vacuum pumping schemes for the H_2 , D_2 or D_2/T_2 gas flow in the ion source and neutralizer is required. Sufficient local pumping speed is required to reduce the line density of gas beyond the ion dump to low enough values to limit re-ionization loss to less than 10% and eliminate duct choking. The low injection angles for the high energy and medium energy pump beams tend to require long ducts and careful baffling to avoid direct beam impingement on the walls. The cooling of duct walls (to avoid any thermal desorption) is also essential. Initial studies⁽²²⁾ with a long duct NBI system possessing a small thermal desorption term of .005 T-l/s-kJ, revealed that we may have a duct choking problem. To overcome this, present plans call for H_2 , D_2 and T_2 gas pumping using panels of solid getter material arranged in a full surface folded panel configuration which allows cyclic regeneration. A short cold wall/hot exit neutralizer is being considered to reduce the neutralizer gas flow.⁽²³⁾
- The relatively high plug-NBI energy requirements and the need to avoid neutron production in the plugs call for the use of H^0 injection at 250 keV. This will require H^- ion source technology for a reasonable neutralization efficiency. Such a source is also desirable for other fusion devices.
- Magnetic shielding for the NBI's in the high fringe magnetic field from TASKA (particularly for beam lines at low injection angles) is required. While such shielding is difficult to include in the small space allowed, it is feasible.

It is obvious that TASKA represents a challenge to NBI technology, but no insurmountable problems have been identified. Testing of advanced neutral beam injectors and heating systems in an integrated system can be one of the key applications for TASKA.

II.7.2 ECRH and ICRF Heating *

The plug electrons are maintained at a temperature of 59 keV with 7.5 MW of ECRH power per plug. The frequency chosen is 56 GHz, which corresponds to resonance at a magnetic field of 2 T. The resonance surface is located between the minimum field point in the barrier and the mirror throat of the plug. Electrons reaching the resonance surface are primarily plug electrons; heating the plug electrons there heats the entire plug electron population because of their bounce motion along B, drift motion in the flux surface, and collisional transfer to electrons which don't reach the resonance surface. The 56 GHz frequency corresponds to the upper limit of high power cw gyrotron sources considered to be available on the TASKA time scale.

The ECRH power is delivered to the plasma using a quasi-optical offset Cassegrain beam waveguide transport system, as shown in Fig. II.7-1. Using a set of hyperbolic-parabolic mirrors, the microwave power is reflected and focussed onto the plasma at the desired angle. An array of gyrotrons feeds a single launcher system. Up to 4 MW can be focussed onto a reasonable spot size at the plasma with reasonable electric field intensity. Consequently, two launcher systems are required per plug.

Forty megawatts of ICRF heating of central cell ions is used to maintain the ion temperature at 30 keV; this allows a considerable reduction of the neutral beam energy and power required for pumping of the thermal barrier. The fundamental deuterium frequency at the beta-corrected magnetic field in the central cell is 15 MHz. In this frequency range, and because of the 32 cm hot plasma radius, we are constrained to using antennas to couple the ICRF power to the plasma. In order to improve antenna coupling, second harmonic heating (at 30 MHz) is used. To protect the antennas from alpha particle

* ECRH = Electron Cyclotron Resonance Heating
ICRF = Ion " range of Frequencies (sometimes ICRH)

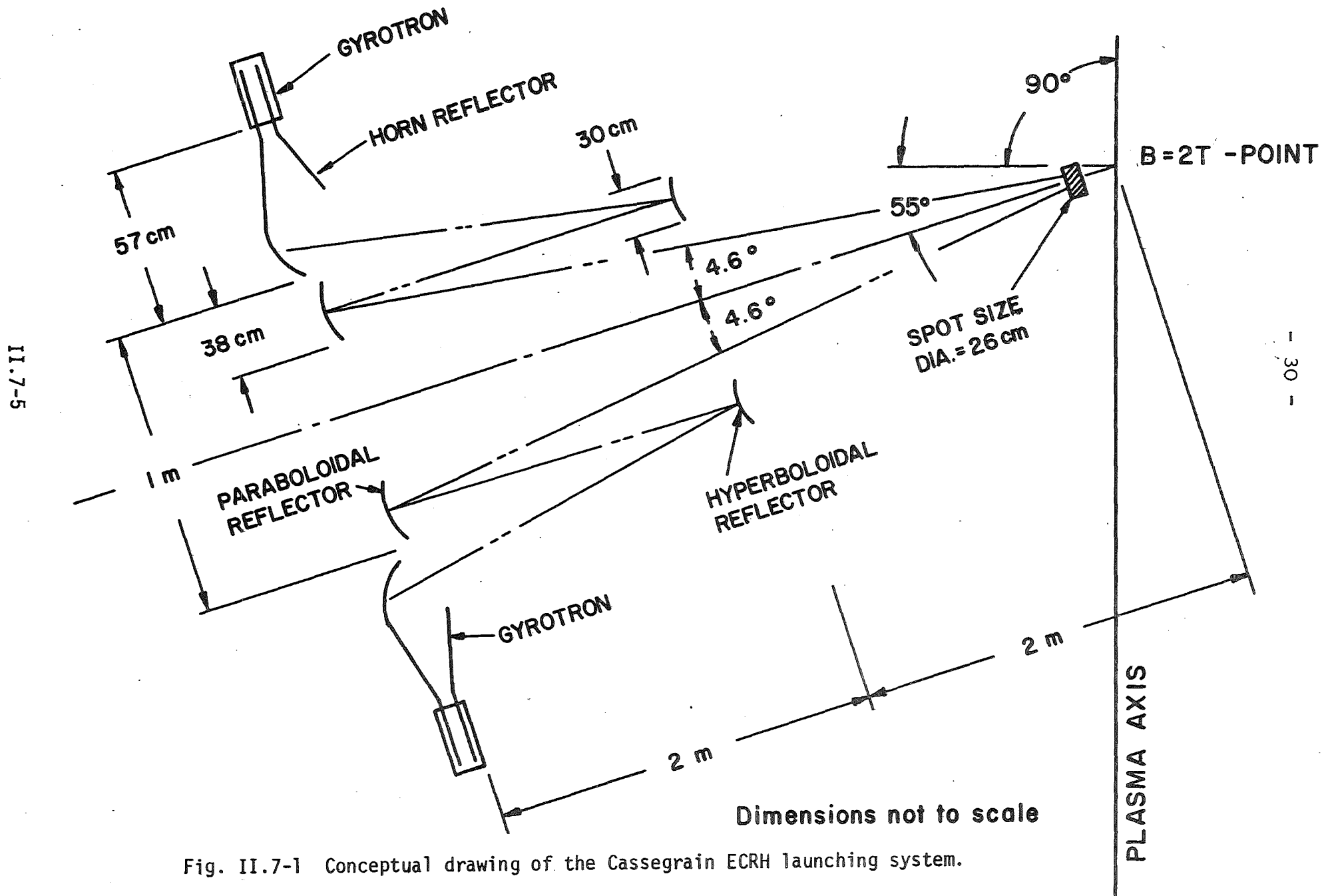
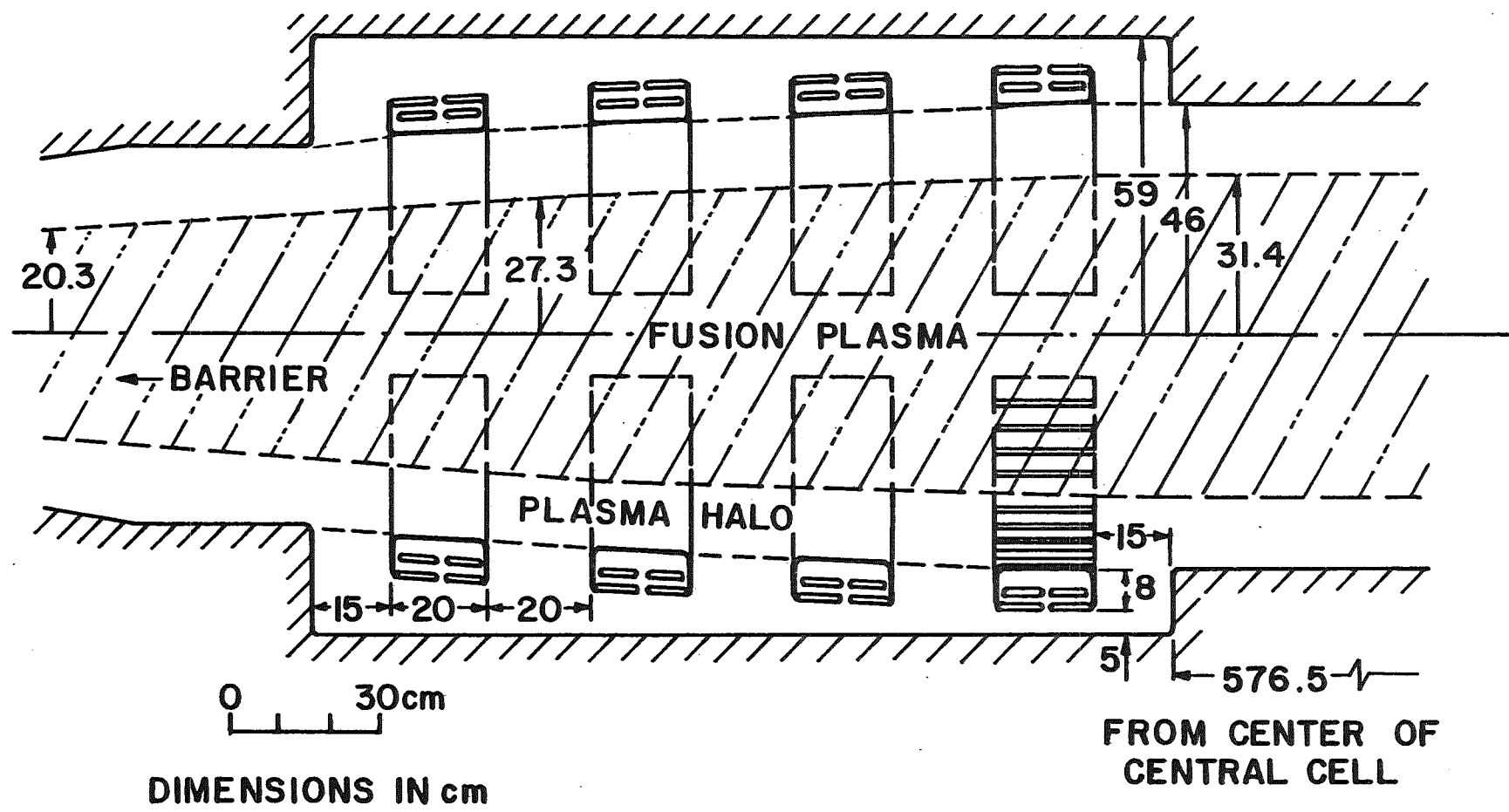


Fig. II.7-1 Conceptual drawing of the Cassegrain ECRH launching system.

bombardment and to improve the coupling to the hot plasma, a warm plasma halo between the hot plasma and the antennas is proposed. The antennas are located at each end of the central cell in order to leave the central region free for test modules. The four 2-coil sets (see Fig. II.7-2) take up 1.4 m of axial length at each end. The antennas are austenitic stainless steel with a high conductivity copper surface layer and cooled by water. The Faraday shields are made of molybdenum and radiation cooled.

II.7-7



- 32 -

CENTRAL CELL ICRF ANTENNA LAYOUT

Figure II.7-2

II.8 Blanket Design

The TASKA central cell region has two main types of blankets: (1) the permanent tritium breeding and heat removal blanket, and (2) test blanket modules. The first blanket system is designed to last the lifetime of TASKA (15 years), while the second blanket system is designed to be changed rather frequently to test a variety of breeding materials. There are completely separate coolant systems for each system, but they are based on the same design principles as shown in Fig. II.8-1.

II.8.1 Permanent Breeding Blanket

The coolant-breeder is $Pb_{83}Li_{17}$ which enters the U-shaped tubes at 300°C and leaves at 400°C. The tubes are made from a martensitic alloy, HT-9, which has displayed a great resistance to radiation damage in fission reactor tests. The design of the blanket is such that all welded joints are protected by roughly 1 meter of $Pb_{83}Li_{17}$ /HT-9 material which reduces the radiation damage in the weld region.

The localized tritium breeding ratio is calculated to be ~ 1.65 which more than compensates for the lack of breeding in the materials test modules and the loss of neutrons out the ends of the machine. When the overall tritium breeding ratio is calculated, it is ~ 1.0 (including a nominal breeding ratio of 1 from the test blanket region). The low solubility of tritium in the $Pb_{83}Li_{17}$ alloy gives an inventory of only ~ 20 grams. This low inventory, coupled with the reduced chemical activity of this liquid metal, makes it very attractive from a safety standpoint.

II.8.2 Test Blanket Module

A breeder test module with liquid lithium as coolant and breeding material has been designed (Fig. II.8-2). On the basis of neutronic calculations,

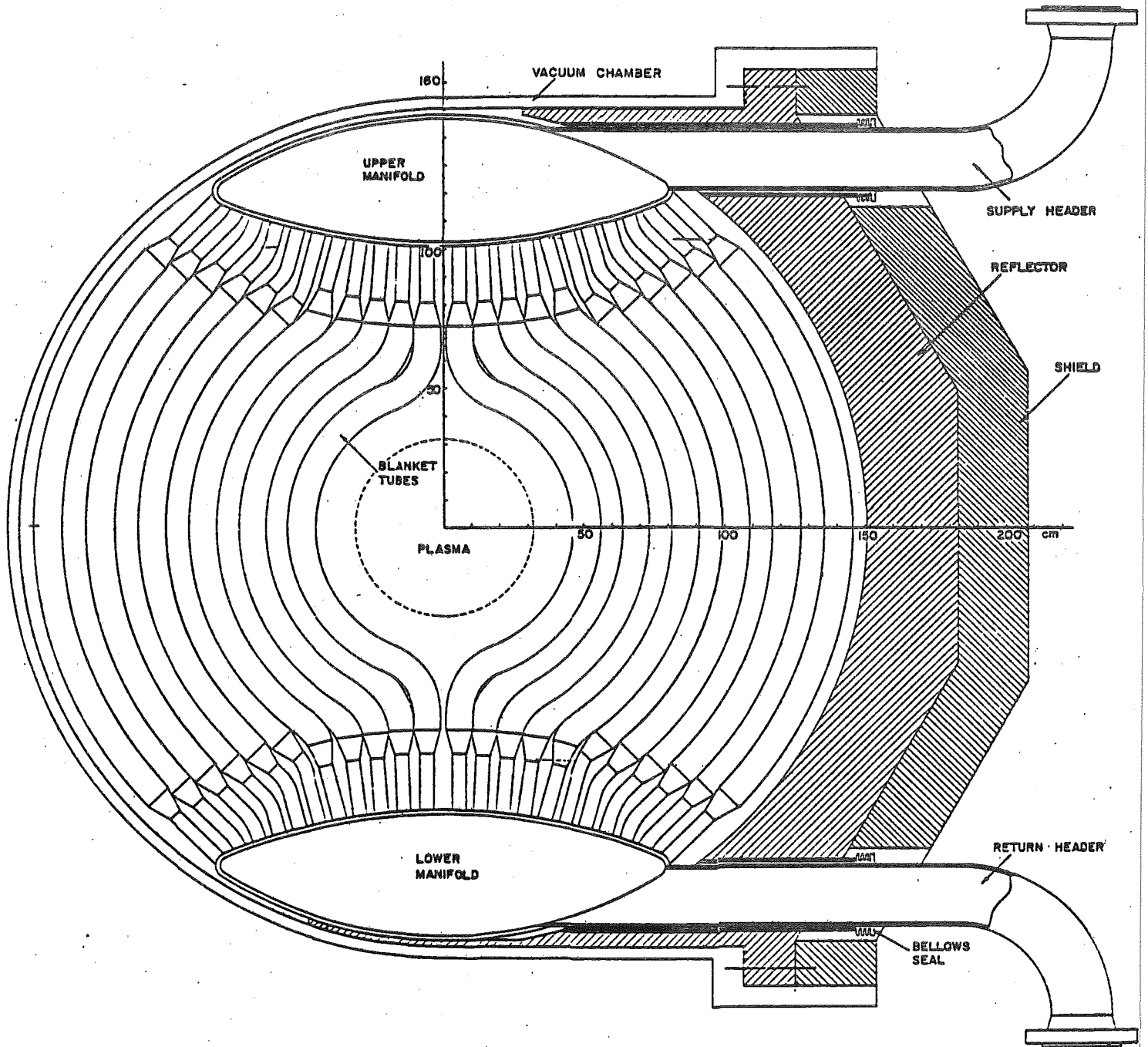


Fig. II.8-1 Vertical section of TASKA blanket

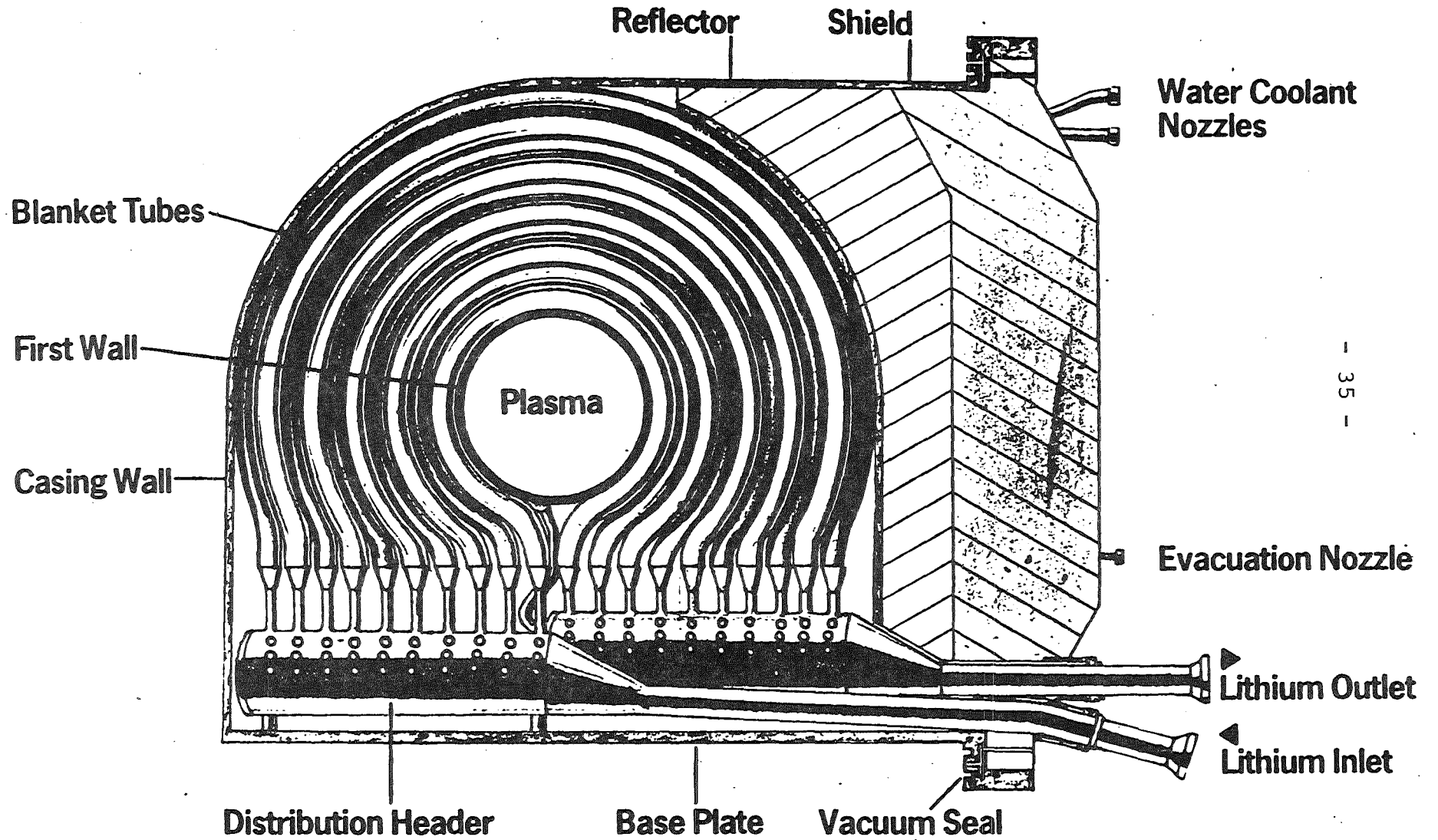


Fig. II.8-2

Taska-Test Module

0 1m

the test module will be provided with a liquid lithium blanket using natural lithium as breeding material. This will result in a blanket power of about 3 MW (design value) at a maximum neutron wall loading of 1.5 MW/m^2 . The operation target of one test module is expected to be 2 full power years (2.5 years at a load factor of 80 %).

The test module consists of three main components: casing, blanket with headers and main coolant pipes, and reflector and shield.

The casing of the test module is constructed such as to shield the vacuum vessel wall completely against the direct 14 MeV neutron flux.

In the blanket liquid lithium is circulating in tubes bent around the first wall cylinder. The blanket tubes are connected to one inlet and one outlet header by nozzles of the required size and length. Spacers keep the tubes in a fixed distance from each other.

The main coolant pipes are stacked one above the other to achieve a closer access to the coolant supply lines. Headers and main coolant pipes can be heat isolated by ceramic materials.

Reflector and shield are designed as a water-cooled plug unit, which is inserted into the module casing behind the blanket.

II.9 Materials Testing

One of the main functions of TASKA is to test structural materials for the fusion Demonstration Power Reactor which should operate shortly after the turn of the century. To satisfy this function, we require three main features of TASKA. The first is a high neutron wall loading to reduce the time needed to accumulate significant damage levels; TASKA is designed to give 1.5 MW/m^2 . The second is a high reactor availability to make the most effective use of the irradiation time. In this respect we used the proposed operating sequence for INTOR (1) (see Table II.4-1), but because (1) the duty cycle of TASKA is 1 versus 0.7 to 0.8 for INTOR, (2) the wall loading is higher (1.5 versus 1.3 MW/m^2), and (3) the samples can be placed closer to the vacuum surface in TASKA than in INTOR, we obtain even higher cumulative damage levels in TASKA than in INTOR. It should also be noted that maintenance of TASKA is much simpler than for a tokamak so that if INTOR can attain an availability of $\sim 50\%$, TASKA should be able to attain an even larger value (however, we did not take credit for that in this study). The third requirement for the materials test program is for a large testing volume and in that respect we have designed for more than $3 \times 10^5 \text{ cm}^3$ of high flux test volume in TASKA.

Analyses of the special test module REGAT (Reduced Damage Gradient Test) design as well as types and numbers of samples to be irradiated are given elsewhere^(24,25) and we will only present the results of that discussion here. Figure II.9-1 shows the general design of the test module and one of the 354 test capsules that can be used to irradiate over 27,000 specimens in 10 years (see Table II.9-1) The REGAT modules are either He or H_2O cooled and provide test environments ranging from 300 to 600°C at damage levels up to $\sim 100 \text{ dpa}$.

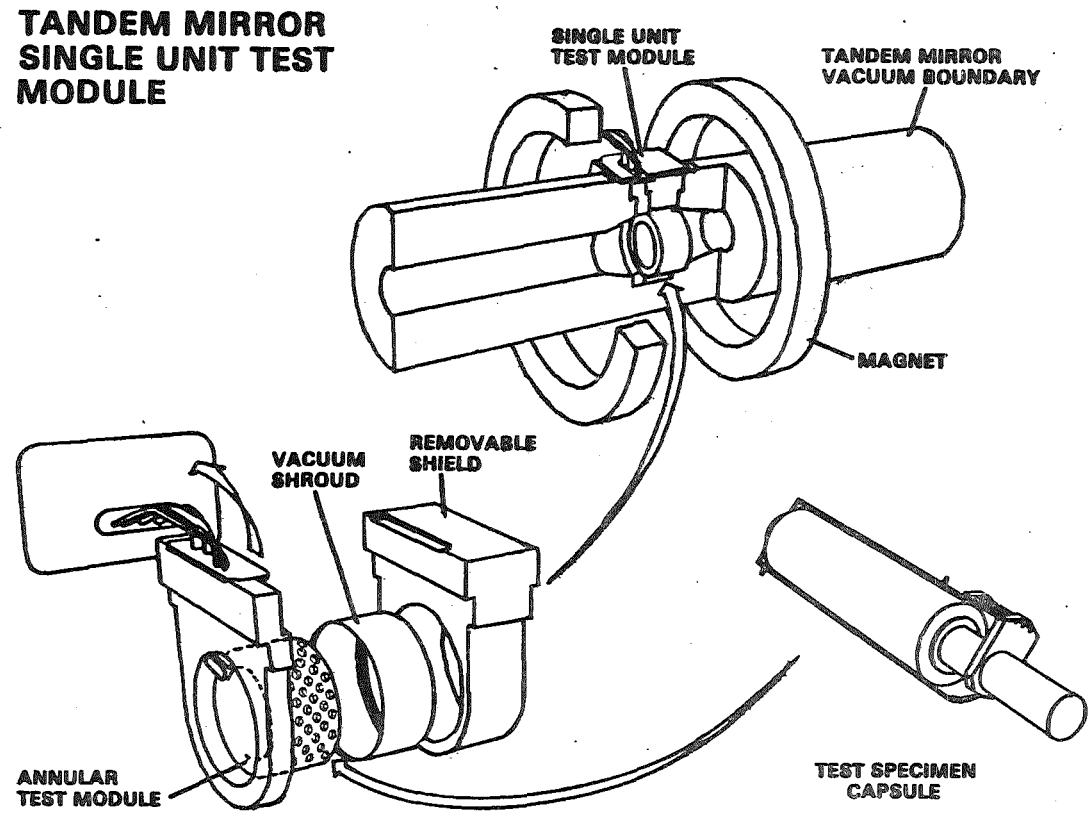


Fig. II.9-1

TABLE II.9-1

Proposed Materials Test Matrix -TASKA

	Mat. Var. ^a	Dup. ^b	Temp. ^c	Fluence ^d	Conditions	Total Specimens		Total Capsule ^g	
						Mirror ^e	Tokamak ^f	Mirror ^e	Tokamak ^f
<u>Materials Surveillance</u>									
Tensile	3	2	2	2	2 rate/temp.	48	48	3	3
Fatigue	0(3)	0(2)	0(2)	0(2)	0(4) stress	0	96	0	4
Crack growth	1(2)	2	2	3	3 stress levels	36	72	1	2
Fracture	2	2	2	2	2 temp.	32	32	4	4
					Subtotal	116	248	8	13
<u>Structural Materials</u>									
Tensile	5	3	6	5	6 rate/temp.	2700	2700	10	10
Fatigue (High Cycle)	0(8)	0(3)	0(2)	0(4)	0(4) stress	0	768	0	29
Crack growth	3(6)	2	4	4	3 stress levels	288	576	3	6
Fracture	4	3	4	2	2 temp.	192	192	5	5
Swelling	10	5	10	5	4 post irr. tests	10,000	10,000	5	5
Stress relax.	6	4	6	-	5 stresses	720	720	3	3
Creep-rupture	6	2	6	-	5 stresses	360	360	2	2
In situ-cyclic	0(4)	0(2)	0(2)	-	0(4) stress levels	0	64	0	64
					Subtotal	14,260	15,380	28	124
<u>Other Materials^h</u>									
Fatigue	5	3	4	4	2 strain range	480	960	11	22
Tensile	15	3	6	4	4 rate/temp.	4,320	4,320	15	15
Dimensional stab.	15	5	6	4	4 post tests	7,200	7,200	4	4
Creep	10	2	6	-	4 stresses	480	480	2	2
In situ-cyclic	0(6)	0(2)	0(2)	-	0(4) stresses	0	96	0	96
Fracture	3	2	2	2	6 temp.	144	144	7	7
Elect. prop.	6	3	2	4	3 tests	432	432	18	18
Therm. Cond.	6	3	4	4	---	288	288	12	12
					Subtotal	13,344	13,920	69	176
					Total	27,720	29,548	105	313

II.9-6

^aMaterials x variations
^bDuplication
^cNumber of irradiation temperatures
^dFluence levels
^eSpecifically for the Mirror Program
^fRequired for both Mirror and Tokamak Programs
^gCapsule volume-390 cm³
^hCeramics, electrical, and heat dump materials
() Addition for tokamak program

In order to compare the performance of TASKA to other test facilities we show in Fig. II.9-2 the cumulative damage in four devices of interest to fusion materials scientists: the RTNS-II at LLNL, the proposed FMIT device at HEDL, TASKA, and the INTOR test reactors. The main points from this figure are:

1. The accumulated damage rate and test volume is too small in RTNS to be of importance for the Demo.
2. The FMIT will produce high damage levels by the early 1990's, but the test volumes are rather small, 10-100's of cm³.
3. If TASKA and INTOR have exactly the same starting dates and operating schedules, reactor relevant damage levels (~ 50 dpa) can be achieved in TASKA by the year 2000, whereas it will take 5-10 years longer to achieve such levels in INTOR. The test volume in both devices is reasonably large (~ 10's of liters).

There is an even better way to represent the testing capabilities of fusion materials test devices and this is by multiplying the damage level times by the test volume at that damage level. Mathematically, this can be stated by:

$$\text{dpa-l} = \int \text{dpa}(v) \, dv \quad ,$$

where the volume, v , of test space that can give a dpa level in a given time is represented by $\text{dpa}(v)$.

A graphical representation of the dpa-l values for the test devices is given in Fig. II.9-3. It clearly shows, along with the previous figure, that if one wants to achieve the largest damage times volume product, then clearly

CUMULATIVE DAMAGE IN FUSION MATERIALS TEST FACILITIES

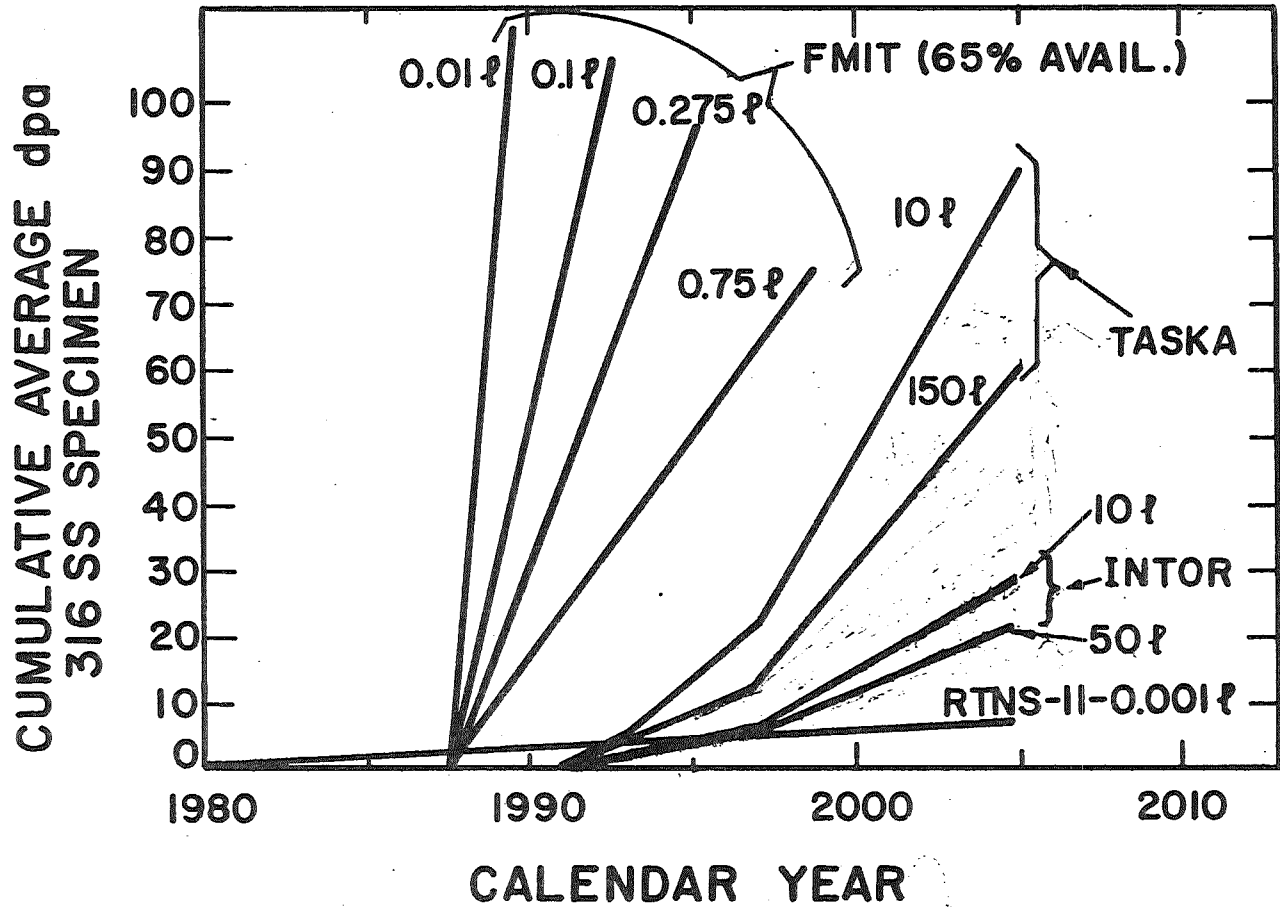


Fig. II.9-2 Cumulative damage in fusion materials test facilities.

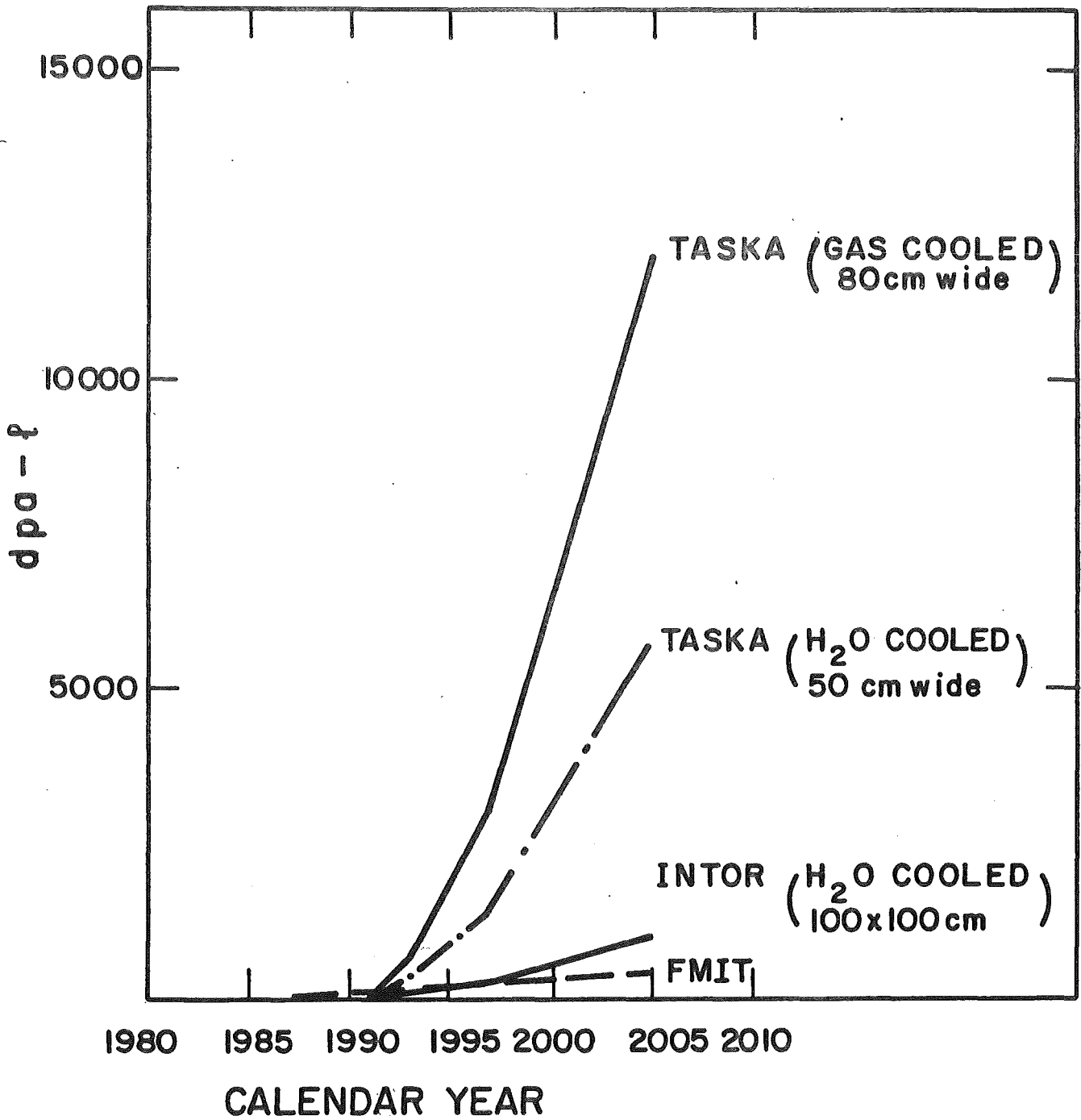


Fig. II.9-3 Cumulative damage times test volume for fusion material test facilities.

the TASKA device is superior to INTOR or FMIT (RTNS data is not discernible on this scale).

II.10 Maintenance

Successful operation of TASKA can be achieved if the downtime can be maintained at a level consistent with the assumed availability. The TASKA reactor equipment is divided into four classes, depending on the anticipated replacement or repair frequency.

Class 1 - Designed for full lifetime such as buildings, support structure and parts of the vacuum vessel.

Class 2 - Lifetime $>$ 5 years, such as shield, magnets, etc.

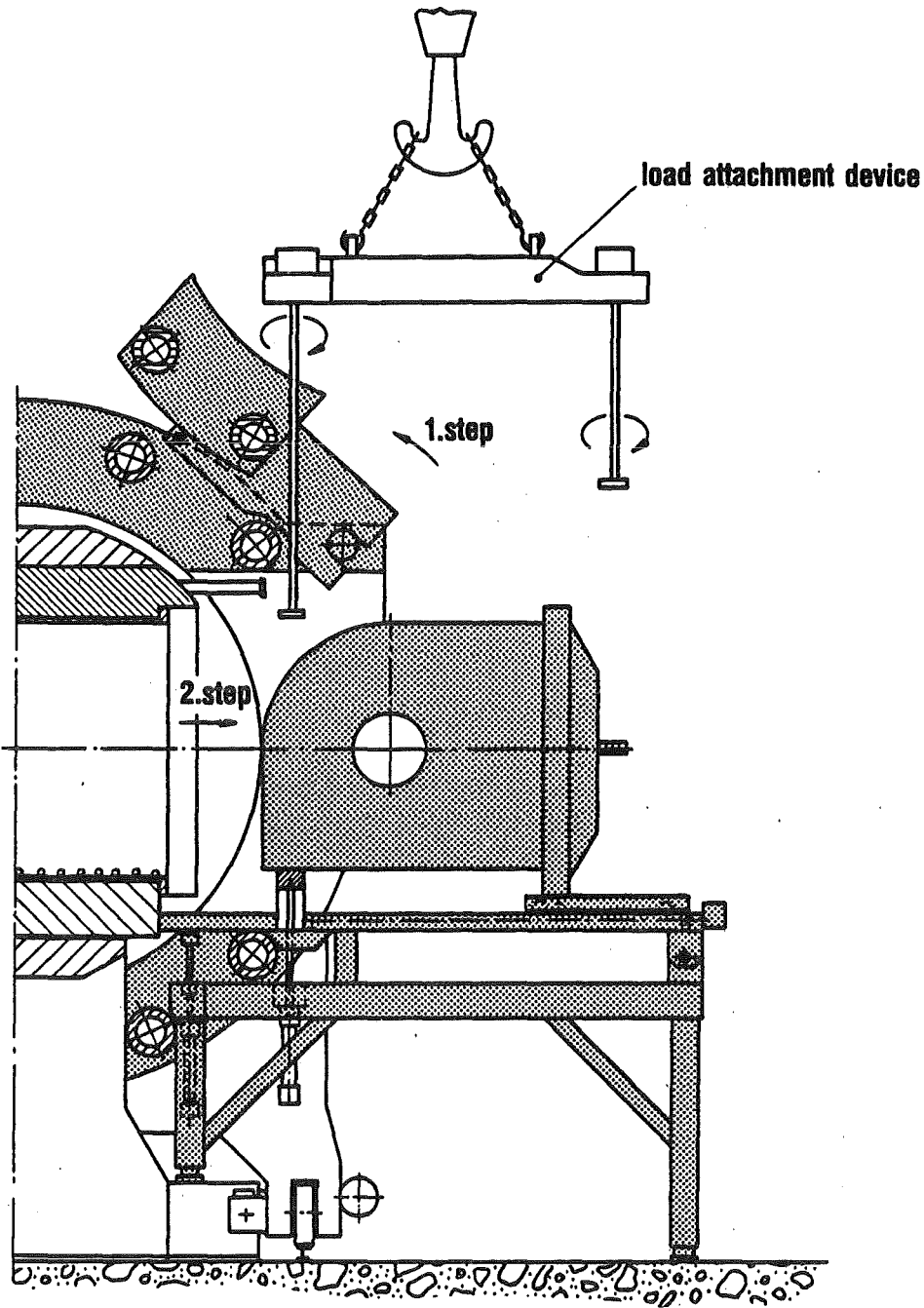
Class 3 - Average lifetime, such as blanket and material test modules, neutral beam components.

Class 4 - Short lifetime, such as handling and experimental equipment.

It is felt that at the minimum the following general purpose remote handling systems will be required:

1. Component handling machine and manipulator carrier attached to the overhead bridge crane.
2. Shielded cabin with manipulator.
3. Elevated work platform.
4. Stereo television viewing system.
5. Various tools adapted for remote handling use.
6. Moveable shields.

The maintenance concepts also address the changeout and repair of blanket modules (as shown in Fig. II.10-1), neutral beam injector components such as ion sources and getter panels, central cell coils and the barrier coils. Displacement of the barrier coil perpendicular to the axis of the reactor (as shown in Fig. II.10-2) is needed to provide access for maintaining the normal insert



Blanket exchange

Fig. II.10-1

II.10-2

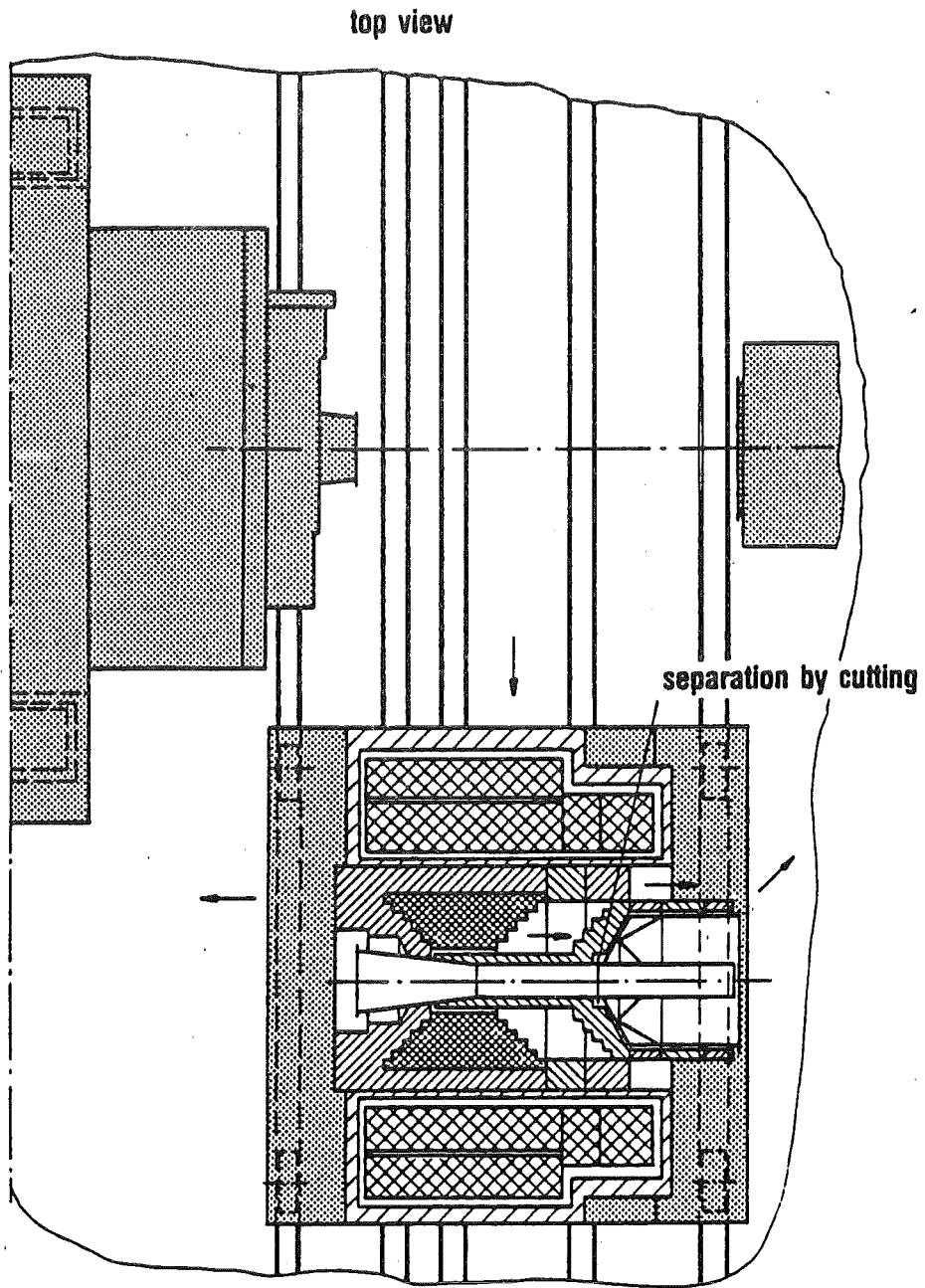


Fig. II.10-2 Components exchange at barrier region-components dismantling

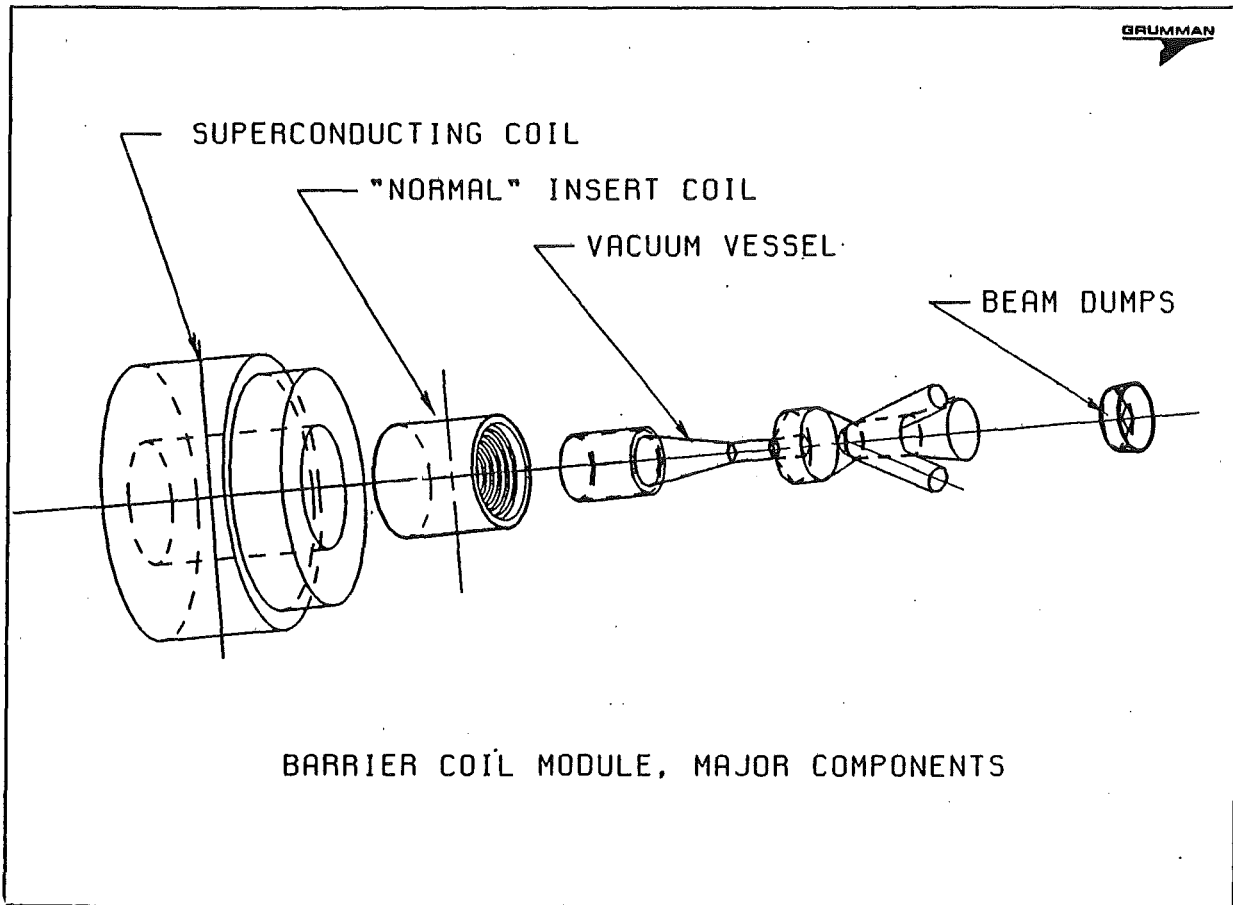
II.10-3

and the thermal barrier dumps (an exploded view of the barrier coil and vacuum vessel is shown in Fig. II.10-3). This operation requires the following special purpose remote systems:

1. Special transportable carriage support structure with hydraulic adjustments and a lifting traverse.
2. Turnover device for use in maintaining getter panels.
3. A cutting and welding machine adapted for separating or joining vacuum chamber sections.
4. Auxiliary support structure used in removing the barrier coil.

Although only several critical maintenance operations have been addressed, it is felt that the remaining numerous maintenance tasks can be performed with the general purpose equipment provided and some additional special purpose fixtures.

Fig. II.10-3



II.11 Cost Analysis

The costs developed for TASKA follow the format adopted for INTOR. The accounts are divided into blanket/shield, magnets, plasma heating, reactor support systems, and buildings. Indirect costs (ID) are engineering (45% of direct costs (DC)), installation/assembly (15% of DC), and contingency (30% of DC and IC). Unit costs and cost algorithms were taken from INTOR (FEDC-M-81-SE-062), PNL-2987, and ORNL (WFPS-TN-057) in that order of information availability. A summary of the costs for TASKA are given below in Table II.11-1:

Table II.11-1. Summary of Direct Costs for TASKA

	<u>\$ x 10⁶ (1981\$)</u>
1.1 Blanket/Shield	46.3
1.2 Magnets	227.9
1.3 Plasma Heating	269.6
2.0 Reactor Support Systems	163.8
3.0 Buildings	<u>80.4</u>
Total Direct Costs	788.0

It can be seen from Table II.11-1 that we were able to meet our objective of < 800 million dollars in direct costs. The main cost drivers are the high costs of ECRH and neutral beams. If some improvement in the ECRH costs can be made, the total cost of TASKA would be proportionately reduced. The other major cost driver is the magnets with the end plug and barrier coils accounting for roughly 1/3 each of the total cost. The intercoil support structure accounts for ~ 28% of the total coil costs. It is obvious that more intense effort to reduce the magnet costs would also be important to reducing the overall cost of TASKA.

In addition to the direct costs, certain percentages for indirect costs such as engineering, assembly and contingency have to be accounted for. As an example, in INTOR these consisted of 45% and 15% of the direct costs for engineering and assembly respectively, and 30% of the direct and indirect costs for contingency.

The operating costs for TASKA are composed of three main items:

1. Annual O & M (including salaries, administrative expenses, etc.).
2. Costs for continuously required power.
3. Additional electrical power costs needed during reactor operation.

The first item is usually taken as 3% of the direct costs, or 24 million dollars per year. It is important to note that this does not include the experimentalists or special equipment used in the blanket or test modules. The second item amounts to 8.7 MW_e continuously or ~3.4 million dollars per calendar year. The third item includes 189 MW_e of power during the burning plasma phase and that is ~37 million dollars per year (at 50% availability).

The total O & M cost for 15 years is 360 million dollars and the total electrical power costs are 455 million dollars. The levelized annual costs are 54 million dollars per year and will be below our target of 80 million dollars per year.

II.12 Conclusions

The purpose of the TASKA study was to identify the potential of a tandem mirror device as a technology test bed in a next generation of fusion experiments. This preliminary conceptual design has shown that TASKA can provide meaningful tests of heating technologies, superconducting magnets, remote maintenance equipment, etc., as well as blanket and material tests and that all these reactor relevant technologies could be integrated into one machine of moderate size and with relatively low costs. In particular, the materials testing capabilities are very attractive. A large volume (> 300 liter) of high damage level (up to ~ 100 dpa) testing space is available in TASKA and it can accommodate all the specimens needed to qualify alloys and non-metallic materials for a demonstration plant operating shortly after the turn of the century.

References for Chapter II

1. INTOR - International Tokamak Reactor - Zero Phase, IAEA, Vienna (1980).
2. See for example, "NUWMAK - A Tokamak Reactor Design Study," University of Wisconsin Fusion Engineering Program Report UWFD-330 (1979); "STARFIRE," Argonne National Laboratory Report, ANL/FPP-80-1 (1981).
3. D.E. Baldwin and B.G. Logan, "Improved Tandem Mirror Fusion Reactor," *Phy. Rev. Let.* 43, (1979) 1318.
4. B. Badger et al., "WITAMIR-I, A University of Wisconsin Tandem Mirror Reactor Design," University of Wisconsin Fusion Engineering Program Report UWFD-400 (1980).
5. Mirror Fusion Newsletter, Lawrence Livermore National Laboratory, July 1981.
6. F.H. Coensgen, T.C. Simonen, A.K. Chargin, and B.G. Logan, Lawrence Livermore National Laboratory, LLL-PROP-172, April 1980.
7. M. Inutaki et al., "Conceptual Design of the GAMMA-10 Tandem Mirror," Symposium on Open Systems and Related Problems, Nagoya University, Dec. 1980.
8. J. Kesner, B.D. McVey, R.S. Post, and D.K. Smith, "A Tandem Mirror with Axisymmetric Central Cell Ion Confinement," MIT Report PFC/JA81-11 (submitted to *Nucl. Fusion*) (1981).
9. D.E. Baldwin, B.G. Logan, and T.C. Simonen, UCID-18496 (1980).
10. "INTOR - U.S. Contribution to the International Tokamak Reactor Phase-1 Workshop," USA INTOR/80-1 (June 1980).
11. S. Miyoshi et al., 7th Int. Conf. on Plasma Physics and Controlled Nuclear Fusion Research, Innsbruck, Austria, (1978), Vol. II, (1979) 437.
12. T.C. Simonen, UCRL-53120, Lawrence Livermore National Laboratory, (in preparation).
13. R.S. Post et al., Proc. 8th Int. Conf. on Plasma Physics and Controlled Nuclear Fusion Research, Brussels (1980), paper IAEA-CN-38/F-2-1.
14. W.D. Getty, "RF Heating of Plasmas," a Report on the Fourth Topical Conference held in Austin, Texas, Feb. 1981, in *Nucl. Fus.* 21(7), (July 1981) 891-897.
15. K. Fowler, private communication.

16. G.A. Emmert, "Physics Background for TASKA," Chapter III, University of Wisconsin Fusion Engineering Program Report UWFDM-500 (also FPA-82-1/KfK-3311) (March 1982).
17. J. Santarius, private communication.
18. E. Velekis, Argonne National Laboratory, to be published.
19. J.F. Santarius, to be published.
20. J. Hemmerick, P. Kupschus, private communication.
21. W.L. Barr, R.W. Moir, G.W. Hamilton, Lawrence Livermore National Laboratory, UCRL-84432 (1980).
22. J.H. Feist, private communication.
23. J. Hemmerich, to be published.
24. G.L. Kulcinski, G.A. Emmert, J.F. Santarius, M.E. Sawan, E.K. Opperman, "TASKA, A Fusion Engineering Test Facility for the 1990's," University of Wisconsin Fusion Engineering Program Report UWFDM-427 (August 1981).
25. M.E. Sawan, D.K. Sze and G.L. Kulcinski, to be published in the Proc. of 9th Symp. on Eng. Probl. of Fusion Research, Oct. 26-29, 1981.

III Plasma Physics

III.1 Physics Background for TASKA

III.1.1 Overview of Tandem Mirror Concepts

The tandem mirror as a confinement scheme was invented in 1976 by Fowler and Logan,⁽¹⁾ and independently in the U.S.S.R. by Dimov.⁽²⁾ The basic tandem mirror configuration is shown in Fig. III.1-1. A magnetic mirror cell, commonly called a "plug", is located at each end of a central cell in which the magnetic field is uniform. The fundamental concept is to use the positive ambipolar potential of the mirror-confined plasma to provide axial confinement of plasma in the central cell. The central cell ions are confined by the potential ϕ_c and the electrons by the potential ϕ_e . The idea of using mirrors at the ends of a central cell, but without the potential peak in the end mirrors to improve the axial confinement of the central cell plasma, was first suggested by Kelley⁽³⁾ in 1967. The positive potential peak, however, is important for achieving high Q operation in a power reactor.

Maintaining the axial potential profile shown in Fig. III.1-1 implies, through the Boltzmann relation for electrons, i.e.

$$\phi(z) - \phi_e = T_e \ln \left(\frac{n(z)}{n_c} \right) , \quad (\text{III.1-1})$$

that there is also an axial (z) density variation. In Eq. (III.1-1) it is assumed that, in the central cell, $n = n_c$, $\phi = \phi_e$. T_e is the electron temperature; it is assumed here to be constant along the magnetic field line. The plug density, n_p , is then related to the confining potential, ϕ_c , by

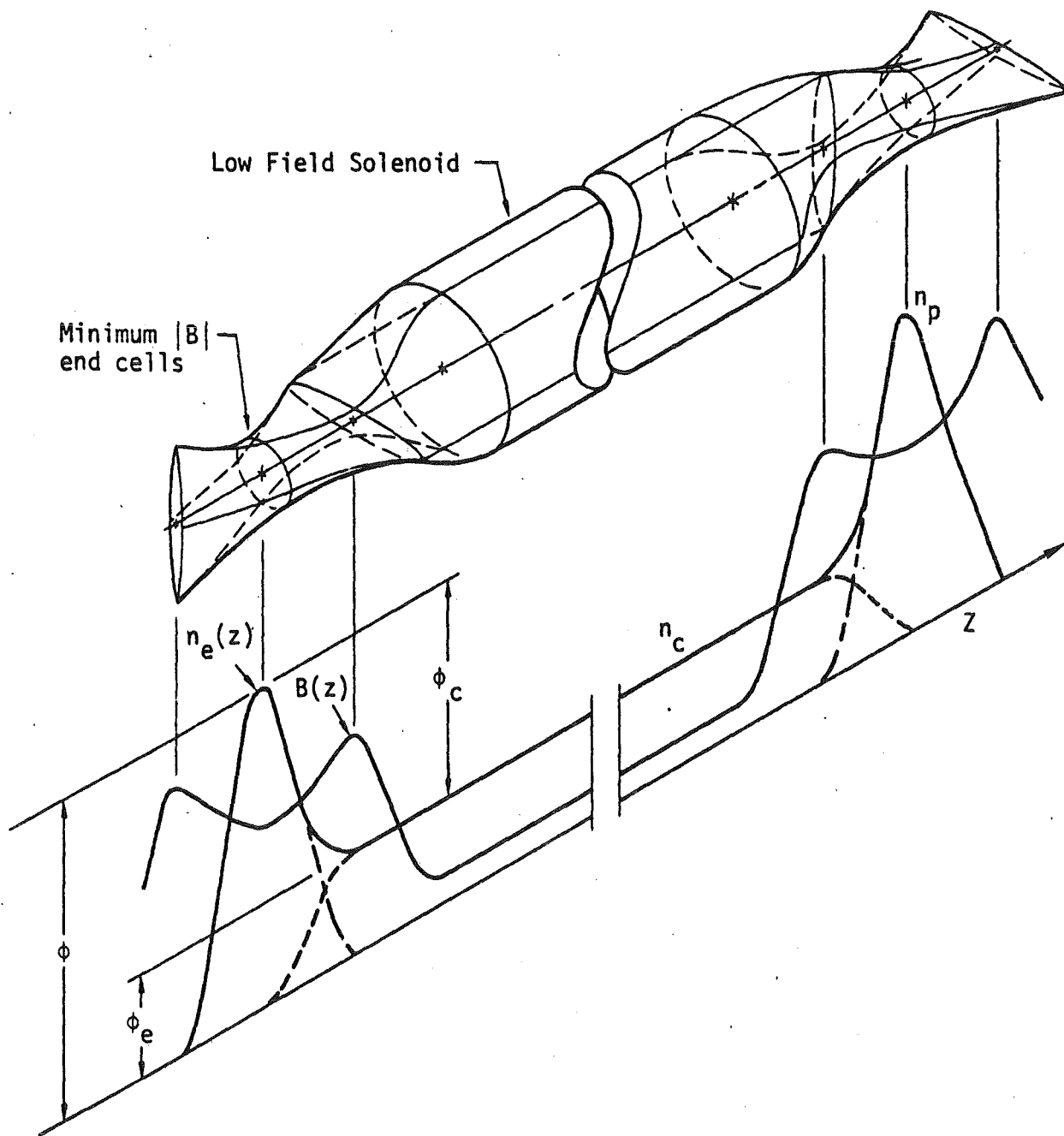


Fig. III.1-1. Tandem mirror with ambipolar plugs at the ends.

$$n_p = n_c \exp\left(\frac{\phi_c}{T_e}\right) . \quad (\text{III.1-2})$$

The axial confinement time of the central cell ions is related to ϕ_c by an expression originally derived by Pastukhov⁽⁴⁾ for electron confinement in mirrors; further corrections have been obtained by Cohen.⁽⁵⁾ The confinement time is

$$\tau_i = \tau_{ij} \frac{g(R)}{I\left(\frac{\phi_c}{T_{ic}}\right)} \left(\frac{\phi_c}{T_{ic}}\right) \exp\left(\frac{\phi_c}{T_{ic}}\right) \quad (\text{III.1-3})$$

where

$$I(x) = 1 + \frac{\sqrt{\pi x}}{2} \exp\left(\frac{1}{x}\right) \operatorname{erfc}\left(\frac{1}{\sqrt{x}}\right) ,$$

$$g(R) = \sqrt{\pi} (2R + 1) \ln \frac{(4R + 2)}{4R} ,$$

τ_{ij} is the ion-ion collision time, T_{ic} is the central cell ion temperature, and R is the central cell mirror ratio. Equation (III.1-3) is valid in the collisionless regime, which is the TASKA regime. For current experiments, which are in a more collisional regime, there is an additional term which is not shown. Typically $\phi_c \approx 2.5 T_{ic}$ for good axial ion confinement, so that $n_p/n_c \approx 10$. The high density in the end plug is sustained by neutral beam injection into the end plug.

The potential, ϕ_e , of the central cell relative to the end wall is determined by equating the total ion loss rate to the total electron loss rate. If the radial transport is non-ambipolar, then the radial loss rate + axial loss rate is needed to determine ϕ_e . Normally, $\phi_e \approx 5 T_e$.

The plug magnetic field has good curvature for MHD stability. The central cell has zero curvature, but the connection of the central cell to the minimum-B plug introduces bad curvature so that the total system is no longer a minimum-B system but minimum-average B, if the plugs provide enough good curvature. The contribution of the plugs to the overall stability is increased by operating the plugs at high β ; consequently stability against interchange modes is easy to obtain. Ballooning modes, which localize in regions of bad magnetic curvature, are a potential problem, but present indications are that finite gyroradius corrections to ideal MHD theory are sufficient to stabilize them. The MHD aspects of tandem mirrors are discussed in more detail in Section III.1.4.

The high density in the end plugs makes them rather collisional and thus increases the ion scattering rate into the loss-cone unless the mean ion energy is rather high. The high density coupled with the high mean energy implies high plasma pressure and high magnetic field strength in the plug to contain the end plug plasma. The high mean ion energy requires a high energy neutral beam to sustain the end plug plasma. Consequently the technological problems of the end plugs in a reactor based on the standard configuration can be severe. The reactor implications of the standard tandem mirror configuration have been studied at Livermore,⁽⁶⁾ Wisconsin, and elsewhere. These studies found that very high magnetic field strengths in the plugs ($\sim 15-17$ T) and very high energy neutral beams (~ 1 MeV) were required for the reasons discussed above. Even with these requirements, the Q (ratio of fusion power to injected power) was marginal ($\sim 5-10$) and the neutron wall loading in the central cell was low ($\sim .5-1$ MW/m²). (A low neutron wall loading generally implies a high capital cost per unit power.) Using RF in the plugs to heat

the plug ions allowed the neutral beam energy to be reduced to ≈ 500 keV, but the other characteristics remained.

The difficulty with the standard tandem mirror configuration is easily seen from Eq. (III.1-1). Since T_e is assumed to be constant along a field line, the potential, which provides the confinement, varies only logarithmically with the density. Furthermore, the central cell has the lowest density, where one wants high density in order to get high fusion power density. Raising the electron temperature everywhere gives more potential for a given density variation, but increases the electron pressure in the central cell. For a given central cell β and field, the central cell ion density has to be reduced if the electrons are heated. This reduces the fusion power.

A solution to the difficulties with the tandem mirror is to heat the plug electrons to high temperature in order to get a high confining potential, but avoid heating the central cell electrons so that their contribution to the central cell β is not increased. The thermal barrier, introduced by Baldwin and Logan⁽⁷⁾ in 1979, allows one to do this by introducing a potential dip between the central cell and the plug. This potential dip reflects most central cell electrons and does not allow them to enter the plug. This allows the plug electron temperature to be decoupled from the central cell electron temperature. The hotter plug electron temperature, achieved by ECRH or other forms of heating, allows one to reduce the plug density relative to the central cell density. This also reduces the collisionality of the plug ions and allows one to use lower energy neutral beam injection. The reduced plug pressure reduces the required magnetic field in the plug for a given β . The reactor implications are striking;^(8,9) the net effect of the thermal barrier is substantially higher Q ($\sim 20-30$) and neutron wall loading ($\sim 2-3$ MW/m²),

with a peak plug magnetic field of the order of 9 T at the coil and neutral beam injection energy ~ 400-500 keV.

The original thermal barrier configuration, now called an "inboard" barrier, introduces an additional mirror between the plug and central cell, as shown in Fig. III.1-2. The density of ions streaming from the central cell through the barrier, where the magnetic field is low, is reduced by the expansion of the flux tube, and by the increase of the parallel velocity due to expanding magnetic field and falling potential. An approximate expression for the passing ion density at the minimum field of the barrier

$$n_b^{\text{passing}} = \frac{n_c}{R_b} \sqrt{\frac{T_{ic}}{\pi\phi_b + T_{ic}}} \quad (\text{III.1-4})$$

if $\phi_b > T_{ic}$. Here, R_b is the barrier mirror ratio,

$$R_b = \frac{B_{mb}}{B_b} .$$

In this expression the distribution function of ions in the central cell is assumed to be Maxwellian and these ions pass through the barrier without collisions. Particle sources localized in velocity space, e.g., due to ionization and charge exchange of the pump beams (discussed in Section III.4.1.4.2), will produce a distortion of the distribution function and therefore modify the passing ion density and the trapping rate in the barrier; these effects are ignored in this discussion. A factor g_b is introduced to phenomenologically account for ions trapped in the barrier; g_b is the total ion density/passing ion density and is usually assumed ≈ 2 . The electron density is assumed to be a Boltzmann relation with the central temperature,

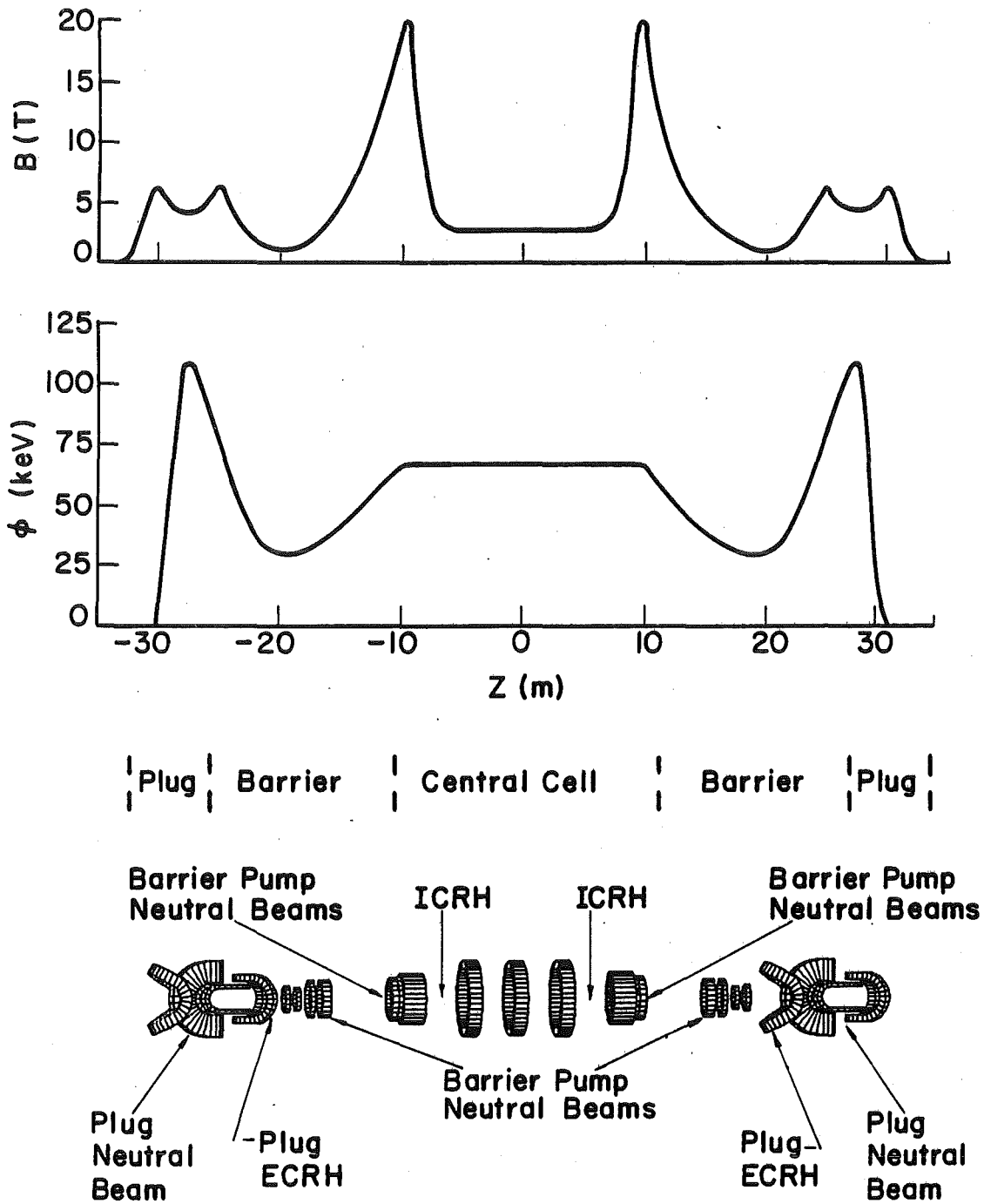


Fig. III.1-2 TASKA magnetic field and potential profiles. TASKA coil set also shown.

T_{ec} , and density;

$$n_b = n_c \exp \left(- \frac{\phi_b}{T_{ec}} \right) . \quad (\text{III.1-5})$$

Equating the electron and ion densities determines the barrier potential ϕ_b ,

$$\exp \left(- \phi_b / T_{ec} \right) = \frac{g_b}{R_b} \sqrt{\frac{T_{ic}}{\pi \phi_b + T_{ic}}} . \quad (\text{III.1-6})$$

In Ref. 7 it was assumed that a Boltzmann relation at the plug electron temperature, T_{ep} , also applied between the barrier magnetic field minimum and the plug. Cohen⁽¹⁰⁾ has found from both analytical and Fokker-Planck calculations that a modified Boltzmann relationship applies,

$$\phi_b + \phi_c = T_{ep} \ln \left[\frac{n_p}{n_b} \left(\frac{T_{ec}}{T_{ep}} \right)^\nu \right] , \quad (\text{III.1-7})$$

where the parameter ν is approximately .5 when the plug electrons are confined inside a magnetic mirror but can be larger when the magnetic field is attempting to eject the electrostatically confined plug electrons. The latter case corresponds to the potential peaking at a magnetic hill or in a region of rising magnetic field. The effect of the temperature ratio, T_{ec}/T_{ep} , in the modified Boltzmann relation is to reduce the benefit of the thermal barrier by reducing ϕ_c for a given density ratio, n_p/n_b . The modified relationship, Eq. (III.1-5), was used in the WITAMIR-I reactor design;⁽⁸⁾ the benefits of the thermal barrier are still substantial relative to the standard tandem mirror configuration so that current reactor designs continue to incorporate thermal barriers.

The effectiveness of the thermal barrier can be increased by using microwave power at the minimum field point in the barrier to create a population of hot, magnetically trapped electrons⁽¹¹⁾ in the barrier. For a given total electron density, this reduces the density of Maxwellian electrons. Consequently in Eqs. (III.1-5) and (III.1-7)

$$n_b \rightarrow n_b - n_b^{\text{Hot}},$$

where n_b^{Hot} is the density of the magnetically confined electrons. Equations (III.1-6) and (III.1-7) are then modified to become

$$\exp\left(\frac{-\phi_b}{T_{ec}}\right) + \frac{n_b^{\text{Hot}}}{n_c} = \frac{g_b}{R_b} \sqrt{\frac{T_{ic}}{\pi\phi_b + T_{ic}}} \quad (\text{III.1-8})$$

and

$$\phi_b + \phi_c = T_{ep} \ln \left[\frac{n_p}{n_b - n_b^{\text{Hot}}} \left(\frac{T_{ec}}{T_{ep}}\right)^{\nu} \right] \quad (\text{III.1-9})$$

This increases ϕ_b (deepens the barrier) and increases the effective density ratio in Eq. (III.1-9) for a given plug density, which compensates for the temperature ratio in the argument of the logarithm. Producing a hot, magnetically trapped electron population requires more careful tailoring of the electron distribution function by the use of microwave power than simply heating a Maxwellian distribution. This is an as yet untested concept; there are also questions concerning the penetration and absorption of the microwave power.

Maintaining the thermal barrier requires that ions trapped in the barrier by collisional scattering be "pumped out" in some manner. The LLNL⁽⁹⁾ and

WITAMIR-I⁽⁸⁾ designs used neutral beam pumping to remove these ions. The neutral beams injected into the passing ion part of the velocity space "pump" trapped ions by charge exchange between the trapped ions and the neutral atoms. Ionization of these beams also provides refuelling of the central cell plasma. The neutral beams for barrier pumping also contribute to the heating of the central cell. Although the principles of neutral beam pumping of the barrier are based on atomic physics and appear straightforward, there are technological problems with this method of pumping. The neutral beams require considerable amounts of power, and providing space for beam lines at small angles relative to the magnetic field can be difficult. The ion sources need to be shielded from the magnetic field, but they cannot be too far away or choking of the beam duct becomes a problem.

Alternative schemes for pumping thermal barriers have been proposed. Kesner⁽¹²⁾ suggested using nonaxisymmetric barriers and used the drift orbits of trapped ions to pump them from the barrier. Calculations by Braun and Emmert⁽¹³⁾ indicate that the electric drift due to the ambipolar potential make the excursion of a trapped ion from a flux surface too small for this effect to be significant. Baldwin⁽¹⁴⁾ proposed using AC magnetic fields in the barrier to enhance the radial diffusion of the trapped ions and thereby cause them to be pumped. Hamilton⁽¹⁵⁾ proposed DC perturbation fields in the elliptical fan of the plug to cause radial drifts of the barely trapped ions; this could provide some pumping and reduce the requirement for neutral beam pumping. These latter schemes have not yet been sufficiently analyzed to assess their utility.

A variety of alternative plug and thermal barrier configurations have been proposed. The MFTF-B⁽¹¹⁾ configuration uses an outboard "A-cell", as

shown in Fig. III.1-3. The yin-yang minimum-B mirror provides good curvature for MHD stability, while the outboard mirror cell contains the thermal barrier and potential peak for central cell confinement. The barrier and plug can be placed in one mirror cell by injecting a neutral beam at an angle to the magnetic field. The trapping of this beam produces a "sloshing" ion distribution with density peaks near the turning points of the ions. Microwave power is applied at the outer density peak to heat the electrons there and produce the potential peak which confines the central cell ions. Microwave power is also used at the density minimum to produce a population of hot, magnetically confined electrons and thereby deepen the potential dip. This forms the thermal barrier. Ions which trap in the thermal barrier are removed by neutral beam pumping. The minimum-B mirror between the central cell and the A-cell provides the good curvature needed for MHD stability.

The barrier and potential peak can also be located in the minimum-B mirror cell, as shown in Fig. III.1-4, so that an additional mirror cell is not required; this is the TMX-Upgrade configuration.⁽¹⁶⁾ In order to obtain good confinement of the sloshing ions, a deeper mirror ratio is required. Providing access for beam injection also complicates the coil configuration.

Both the outboard A-cell and TMX-Upgrade configuration, and the inboard barrier to a lesser extent, suffer from nonaxisymmetric magnetic fields in the transition region and end plug. Nonaxisymmetry causes radial drifts of central cell ions as they approach the plug; this enhances radial transport⁽¹⁷⁾ in the central cell. One way of eliminating the radial drift and associated enhanced radial diffusion is to move the thermal barrier and potential peak to an axisymmetric mirror cell between the central cell and minimum-B cell (see Fig. III.1-5). Central cell ions are then reflected by

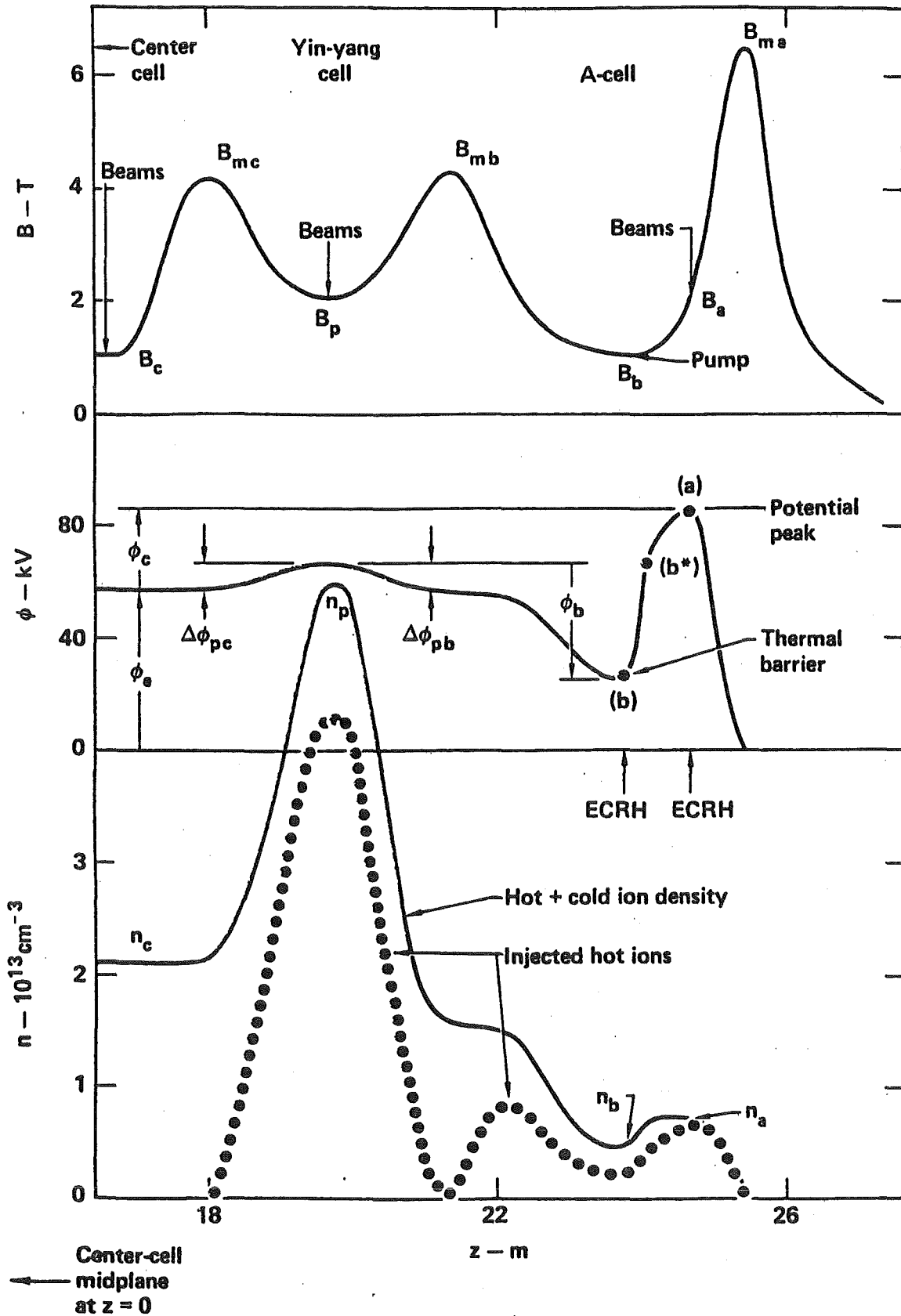


Fig. III.1-3. Profiles of field B , potential ϕ , and density n vs. distance z at one end of MFTF-B operated with A-cell-type thermal barriers. (Taken from Ref. 11)

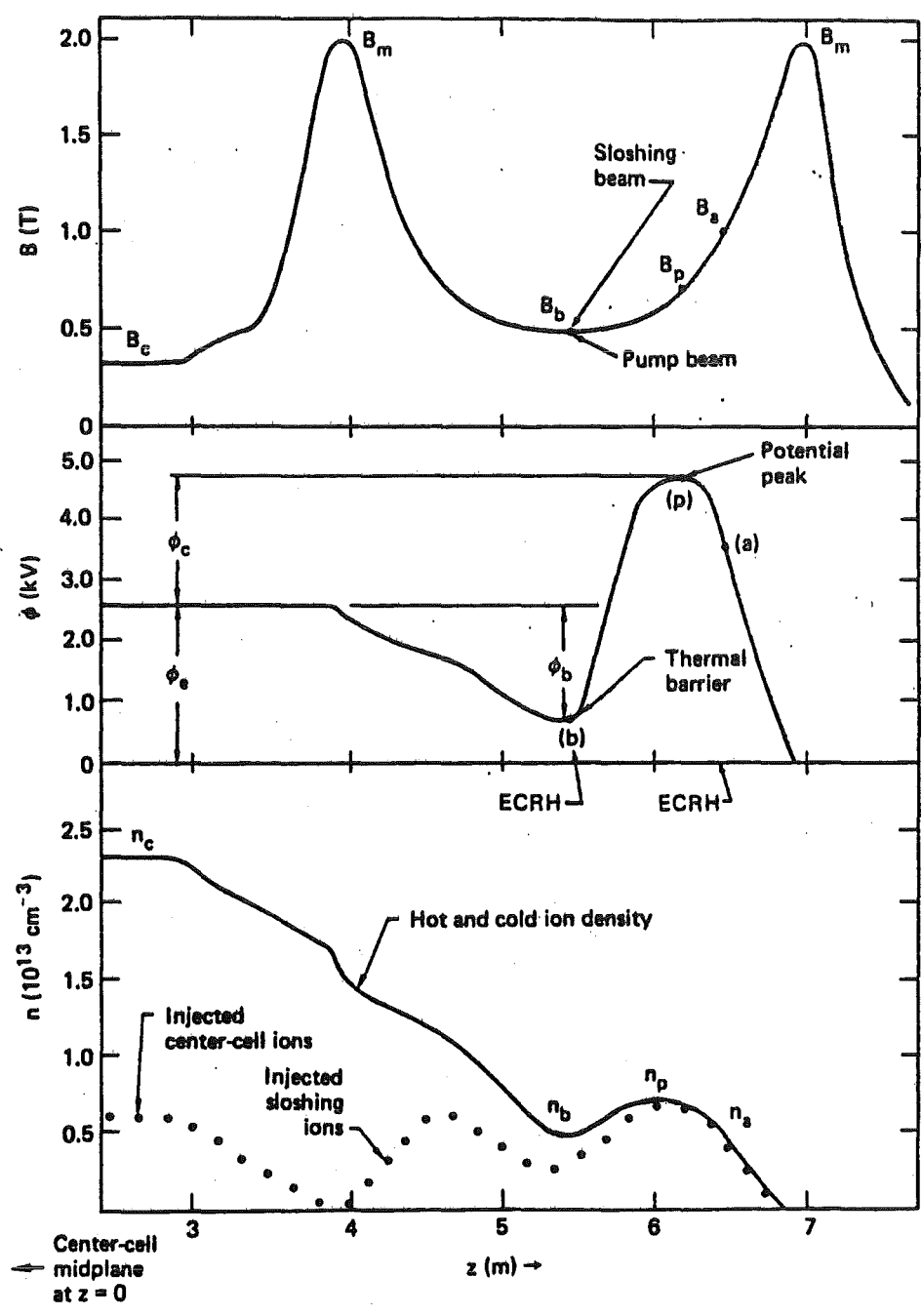


Fig. III.1-4. Profiles of magnetic field B , potential ϕ , and density n versus distance z at one end of TMX Upgrade operated with thermal barriers (Reference case A). The subscripts refer to c, central cell; m, maximum; a and b, points where ECRH is applied; and p, peak. (Taken from Ref. 16)

III.1-14

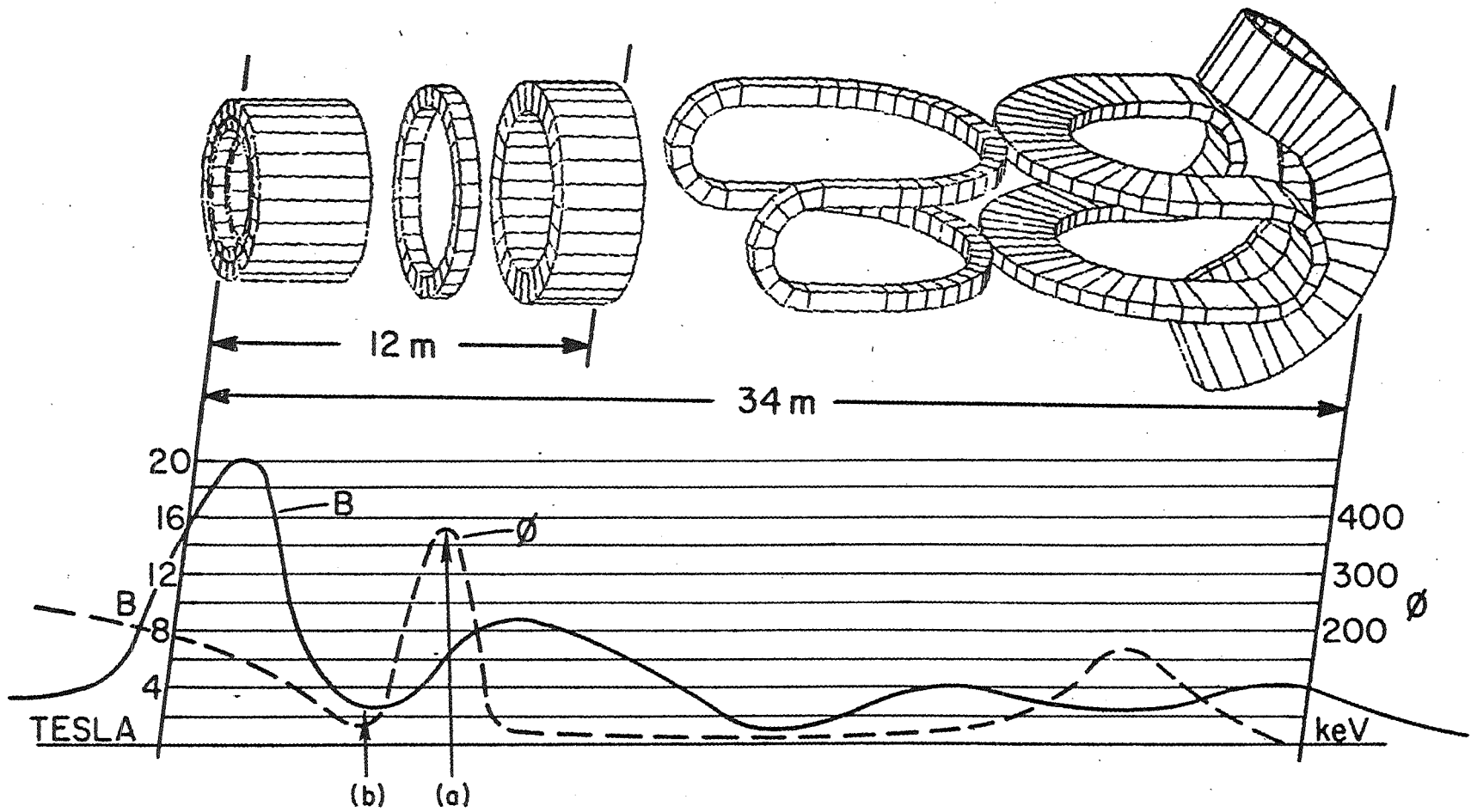


Fig. III.1-5. The magnetic field and potential profile and magnet set for the axi-cell end plug configuration. The central cell is to the left.

the potential peak before they can experience the nonaxisymmetric fields. This is the configuration to be used in the proposed TARA device.⁽¹⁸⁾

Another solution to the enhanced radial transport problem is to make the end plug purely axisymmetric. Good magnetic curvature can then be obtained by using a hot electron ring⁽¹⁹⁾ in the end-cell as in EBT, using internal rings,⁽²⁰⁾ or a magnetic cusp configuration.⁽²¹⁾

All of these configurations are further removed from standard mirror and tandem mirror experience and their reactor implications are not yet well assessed. There is, however, considerable experience with hot electron rings in the EBT device and predecessor mirror experiments at Oak Ridge and Nagoya.

III.1.2 Experimental Results with Tandem Mirrors

Results from three different tandem mirror experiments have been reported to date. These are the GAMMA 6⁽²²⁾ device at the University of Tsukuba, Japan, TMX⁽²³⁾ at Lawrence Livermore National Laboratory, and Phaedrus⁽²⁴⁾ at the University of Wisconsin. These devices are all of the standard configuration without thermal barriers. Their major design parameters are listed in Table III.1-1.

The first test of the tandem mirror concept was in the GAMMA 6 device,^(22,25) although the achieved parameters of the experiment are modest ($T_e \approx 10-15$ eV, $n_p \approx 1.7 \times 10^{13}$ cm⁻³, $n_c \approx 3 \times 10^{12}$ cm⁻³), the fundamental concept of a potential peak in the plugs relative to the central cell was established. This potential peak was sustained by neutral beam injection into the plugs and found to be in agreement with the Boltzmann relation. The Pastukhov formula for the end-loss has also been tested and found to be in agreement.

Table III.1-1. Summary of Operating Design Parameters of Tandem Mirror Experiments in Operation or Construction (Taken from Ref. 30)

	Gamma 6	TMX	Phaedrus	AMBAL-1
Plug:				
B_0 (T)	0.4	1.0	.3	1.2
B_{mirror} (T)	1.0	2.0	.57	---
R_p (cm)	4	10	7	12
L_m mirror-mirror (cm)	---	75	105	---
Heating method	Beam, RF, REB	Beam	ICRF, Beam	Beam
Heating Power (MW)	0.5	7	0.1	1.0
Duration (ms)	2.5	25	1	---
n (cm^{-3})	5×10^{13}	4×10^{13}	5×10^{12}	3×10^{13}
W_i (keV)	0.4-10	13	2	20
T_e (eV)	20-2000	260 max	40	1000
Solenoid:				
B (T)	0.15	0.05-0.2	0.05	0.2
$L_{\text{plug-to-plug}}$ (cm)	315	640	390	---
R_p (cm)	2 x 20	30	30	30
n (cm^{-3})	1.0×10^{13}	1×10^{13}	2×10^{12}	1×10^{13}
W_i (eV)		250 max	15	500-1000

The TMX device, shown schematically in Fig. III.1-6, began operation in July 1979. It is based upon favorable results found earlier with the 2XIIB⁽²⁶⁾ single mirror cell experiment. In 2XIIB, a plasma stream flowing through the mirror cell was found to be effective in stabilizing the drift cyclotron-loss-cone (DCLC) mode. This instability is driven by the loss-cone nature of the ion distribution function in the mirror and can seriously degrade mirror confinement if allowed to be present. TMX was designed so that the plasma stream leaving the central cell and flowing through the end plugs was sufficient to stabilize the DCLC mode.

TMX has also demonstrated the basic principles of tandem mirror confinement. The density in the plug has been maintained higher than in the central cell by neutral beam injection. The potential in the plug is also higher than in the central cell so that the central cell plasma is confined electrostatically by the potential generated by the end plug plasma. A confining potential, ϕ_c , of up to 300 V and plug potentials exceeding 1 kV relative to the end wall have been measured.⁽²⁷⁾ Axial profiles of density and potential are shown in Fig. III.1-6. Axial confinement has also been demonstrated directly by turn-off of one end plug and observing the end-loss and decay. When both end plugs are present, the axial confinement is enhanced of up to a factor of 9 over what it would have been without the plug plasmas. The measured parameters are within a factor of 2 of theoretical calculations if the density ratio, n_p/n_c , does not exceed 3. In this case the end-loss from the central cell is sufficient to stabilize the ion cyclotron fluctuations in the plugs at a low level. At larger values of n_p/n_c , RF fluctuations in the plug increase due presumably to microinstabilities and central cell confinement is degraded. Depending on the mode of operation, RF fluctuations in the

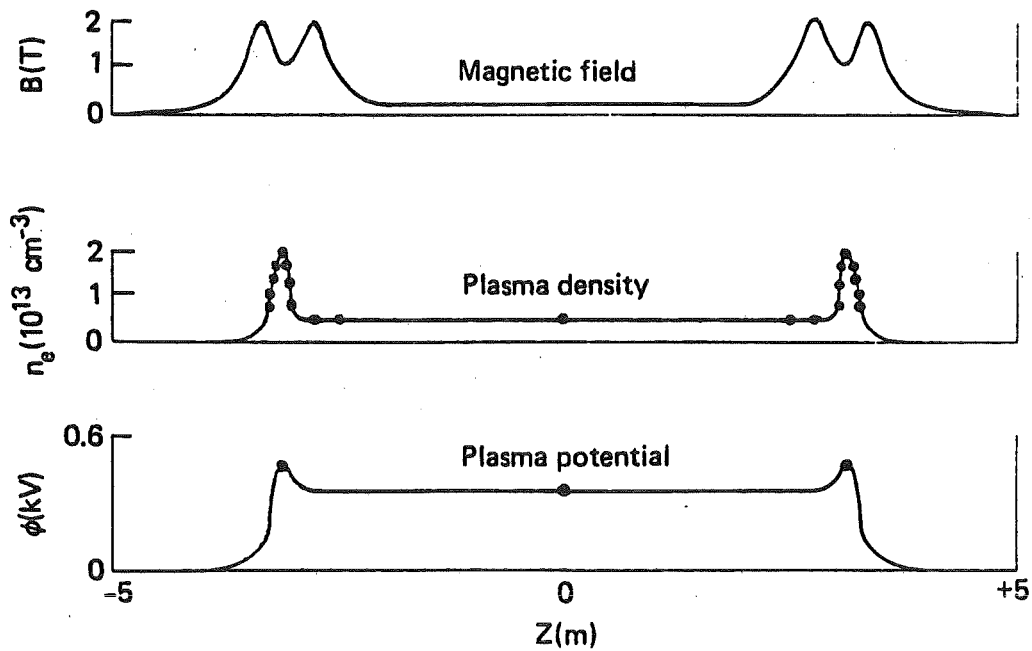
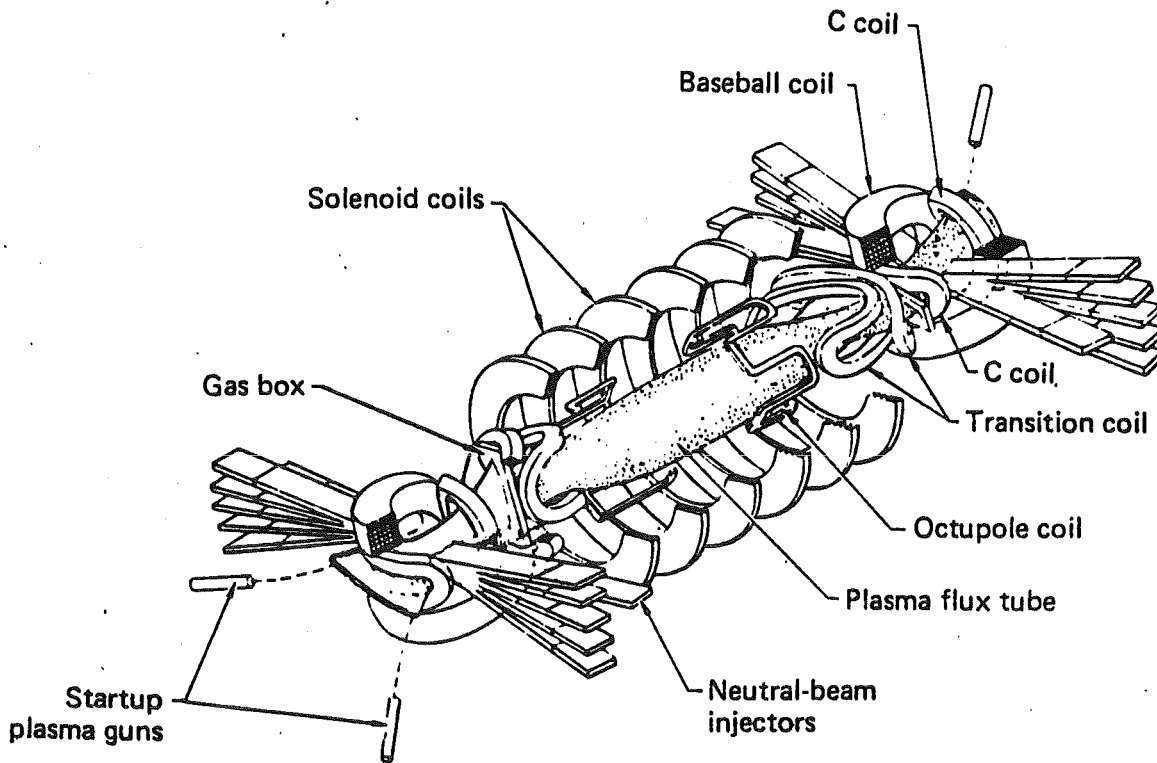


Fig. III.1-6. TMX magnet geometry and measured axial plasma profiles (Taken from Ref. 30)

plug have the characteristics of the DCLC or Alfvén-ion-cyclotron (AIC) instabilities. The latter instability is an electromagnetic mode driven by the pressure anisotropy in the plug.

A study of radial transport⁽²⁸⁾ in TMX indicated that the axial loss rate exceeds the radial loss rate in the core ($r \lesssim 15-20$ cm) of the central cell, but at larger radii, radial losses exceed axial losses. The radial transport appears to be non-ambipolar with the ion radial flux exceeding the electron radial flux. This results in a net negative electrical current to the end walls; this was observed directly. Within the uncertainty of the data, the radial transport was equal to or greater than the transport predicted by resonant neoclassical theory.

Low frequency oscillations have been observed in the central cell of TMX. Both an $m = 0$, 13 kHz and an $m = 1$, 7 kHz oscillation have been found and studied. The $m = 0$ mode appears to be an acoustic wave and is locked to RF "bursting" in the plugs. The $m = 1$ mode is localized near the edge of the plasma and its amplitude is a function of the method and rate of gas fueling of the central cell. Gas box fueling in the elliptical fans of the plugs produces a larger mode amplitude than puffing into the central cell. For gas box fueling the mode is absent at low gas input rates, coherent at intermediate rates, and perhaps turbulent at high rates. There is some indirect evidence for radial transport caused by the $m = 1$ mode. Its characteristics have been compared to rotational instabilities, drift waves, and Kelvin-Helmholtz instabilities. None of these adequately describe the observed oscillation. Consequently, it remains unidentified at this time.

The axial energy transport between central cell and plug electrons has been studied in TMX by attempting to assess all the power flows into and out

of the electrons.⁽²⁹⁾ Within the uncertainties of the measurements and the analysis, it was concluded that the energy transfer between the plug and central cell electrons is equal to or less than the classical rate,⁽¹⁰⁾ depending on operating conditions. Measurement of the electron temperature, T_{ew} , near the end wall also indicates reduced energy transport to the end walls. The measured temperature was $T_{ew} \approx 7-10$ eV when $T_{ec} \approx 50$ eV. From Monte Carlo calculations and the Pastukhov analysis, one expects $T_{ew} \approx T_{ec}$. Good isolation of the confined plasma from the end wall is achieved when the startup guns are turned off. The external plasma density near the end wall is 3 to 4 orders of magnitude less than in the plug.

The maximum plasma parameters achieved in TMX are listed in Table III.1-2. Of particular interest to TASKA is the central cell β of 40%, achieved by neutral beam injection into the central cell. This result is discussed further in Section III.1.3. A summary of TMX results has been published.⁽³⁰⁾ The executive summary of that report is reprinted in Appendix III.1-A.

The Phaedrus experiment has concentrated on ICRF heating in the plug and in the central cell to produce hot ion plasmas.⁽³¹⁾ Experiments with neutral beam injection into the plugs are in their initial phases. At the fundamental resonance, 50 kW of RF power was coupled to the plug with 30% efficiency. Increase of the mean ion energy to 700 eV at high density (10^{13} cm⁻³) or 1 keV at low density (10^{12} cm⁻³) was observed.⁽³²⁾ Heating at the first harmonic ($2\omega_{ci}$) with 30 kW of power produced a bulk ion energy of 200 eV and a 700 eV hot ion tail. This tail could be localized in pitch angle so as to produce a "sloshing ion" tail distribution.

Experiments with ICRF heating of the central cell plasma have also demonstrated good heating. Central cell plasmas with $n \approx 10^{12}-10^{13}$ cm⁻³,

Table III.1-2 Maximum Plasma Parameters in TMX

(Achieved with deuterium and 0.1 T, central-cell magnetic field strength. These parameters were not all achieved simultaneously.) (Taken from Ref. 30.)

Plug density	$4 \times 10^{13} \text{ cm}^{-3}$
Plug ion energy	13 keV
Plug electron temperature	0.26 keV
Plug radius	10 cm
Central-cell density	$3 \times 10^{13} \text{ cm}^{-3}$
Central-cell ion energy	0.25 keV
Central-cell radius	30 cm
Plug plasma potential	1 keV
Central-cell confining potential	0.3 keV
Central-cell axial confinement parameter	$10^{11} \text{ cm}^{-3} \cdot \text{s}$
Electrostatic enhancement in confinement	9
Central-cell beta (0.07 without central-cell neutral beam injection)	0.40

$T_i \approx 300-100$ eV and $\beta_c \approx 10-20\%$ have been produced. These ICRF heated plasmas have been useful for the investigation of the MHD stability characteristics of Phaedrus. Flute-like oscillations propagating in the ion diamagnetic direction with a dominant $m = 1$ azimuthal mode number are observed at high beta. The threshold central cell beta, β_c , is 3-10 times the plug beta, β_p , and decreases with reduced plug quadrupole field. The observed threshold value of β_c/β_p is 2-5 times the theoretical value from ideal MHD theory. Line tying plays a role at the higher values of β_c/β_p , but is not believed to be significant at the lower values.

The rate of energy transfer between plug electrons and central cell electrons in a thermal barrier tandem mirror is an important element in determining the effectiveness of thermal barriers. This problem has been analyzed by Cohen.⁽¹⁰⁾ The theoretical result was tested in Phaedrus by operating the central cell at low density relative to the plugs. The electron temperature in one plug was changed rapidly with a short high power microwave pulse. The rise of the electron temperature in the central cell and in the other plug was then monitored. The results are in reasonable agreement with point model theoretical calculations using the theoretical energy transfer ratio.⁽¹⁰⁾ As indicated above, TMX showed less than the theoretical energy transfer under some conditions.

III.1.3 Future Major Tandem Mirror Experiments

Three major tandem mirror experiments are under construction and should produce results relevant to TASKA. These are TMX-Upgrade,⁽¹⁶⁾ which is expected to be operational at LLNL in early 1982, GAMMA 10,⁽³³⁾ which is to be operational in 1983 at the University of Tsukuba, Japan, and MFTF-B,⁽¹¹⁾ which

is to begin operation in 1985. The design parameters for these devices are shown in Table III.1-3.

The plug configuration of TMX-Upgrade was discussed in Section III.1.1 and is shown in Fig. III.1-4. This device is expected to provide a test of several physics concepts important to tandem mirrors. Among these are the thermal barriers and the use of ECRH to increase the barrier potential, ECRH heating of plug electrons, the creation of a sloshing ion distribution in the plug, and a test of the microstability of sloshing ion distributions. This concept is discussed further in Section III.1.4. In addition, TMX-Upgrade is expected to improve the performance of TMX by about an order of magnitude and to operate in the collisionless central cell regime appropriate to MFTF-B and reactors. Because of its lower central cell temperatures, TMX operated on the borderline between the collisional and collisionless regimes.

GAMMA 10 is a successor to the GAMMA 6 device in Japan. Current planning calls for it to operate in three different phases. Phase I utilizes a standard tandem mirror configuration with a minimum-B mirror as the end plug. Phase II is similar to MFTF-B in that it uses a mirror cell outboard of the minimum-B mirror. In GAMMA 10, this mirror is axisymmetric, however. The outboard simple mirror can be used to study sloshing ion distributions and thermal barriers with ECRH heating. Phase III will utilize an end plug which has only an axisymmetric simple mirror with hot electron rings to provide MHD stability. The parameters shown in Table III.1-3 are for Phase II operation.

MFTF-B started as a large single yin-yang mirror experiment, MFTF, which was approved and construction of the yin-yang magnet was begun. Following the successful results with TMX and the invention of the thermal barrier, it was modified to become a tandem mirror with an outboard A-cell thermal barrier.

Table III.1-3. Summary of Design Parameters of Major Future Tandem Mirror Experiments

	<u>TMX-Upgrade</u>	<u>GAMMA 10</u>	<u>MFTF-B</u>
Begin Operation	1982	1983	1985
<u>Central Cell</u>			
Density (cm ⁻³)	2.3 x 10 ¹³	10 ¹³	2.1 x 10 ¹³
Ion Temperature (keV)	.9	1	15
Electron Temperature (keV)	.6	1	9
Beta	.25 ⁽⁴⁾	.05	.2
Axial Confinement, nτ (sec/cm ³)	10 ¹²	10 ¹²	5 x 10 ¹³
Radial Confinement, nτ (sec/cm ³)	5 x 10 ¹¹	---	---
Magnetic Field (T)	.3	.4	1
Radius (cm)	20	26	54
Length (m)	8	30	32
<u>Plug (or A-cell)</u>			
Density ⁽¹⁾ (cm ⁻³)	7 x 10 ¹²	10 ¹³	7 x 10 ¹²
Mean Ion Energy ⁽²⁾ (keV)	10	15	84
Electron Temperature ⁽³⁾ (keV)	1.4	3	30
Magnetic Field (T)	2 - 4	.5 - 3	1 - 6.5

1. In A-cell if used.

2. Hottest component present in yin-yang or A-cell.

3. Warm component if magnetically trapped barrier electrons are used.

4. Includes hot ion component.

It utilizes, however, the original MFTF yin-yang magnet; this placed substantial constraints on the design of the end plugs. As with other devices, this machine can be tested in various modes of operation. The parameters given in Table III.1-3 are the reference case with thermal barriers. For this case the primary research objectives are:

1. Generate central cell ion confining potentials, ϕ_c , via electron heating and ion pumping in A-cells at densities lower than the central cell density.
2. Increase central cell electrostatic confinement ($n\tau$) and ion temperature sufficient to test radial transport in the appropriate collisionless reactor regimes.
3. Confine sufficient plasma pressure in the central cell to test MHD beta limits at relatively high central cell magnetic fields ($B_c \gtrsim B_p/2$).
4. Maintain steady-state density depression with sloshing ions in the A-cell midplane to test cold-ion stabilization of loss-cone modes at high potential.

Theoretical analysis of the expected sloshing-ion distribution function in the A-cell of MFTF-B indicates that all known mirror-related microinstabilities should be stabilized. This is discussed further in Section III.1.4. The relevant parameters for MFTF-B are expected to be about an order of magnitude more advanced than in TMX-Upgrade.

In addition to these devices, an "axisymmetric" tandem mirror, called TARA,⁽¹⁸⁾ is under consideration for construction at MIT. As discussed in Section III.1.1, its end plug configuration places the potential peak and thermal barrier in an axisymmetric mirror cell between the central cell and

the MHD anchor, which is a minimum-B cell. This eliminates the enhanced ion radial diffusion associated with the quadrupole fields in the anchor. TARA will provide a test of this concept and of the microstability of sloshing ion distributions in the plug, along with a test of the thermal barrier concept and the use of ECRH to heat the electrons and increase the barrier potential.

The projected central cell ion temperature and ion confinement parameter, $n\tau$, are shown in Fig. III.1-7 for these three devices along with experimental results from GAMMA 6, Phaedrus, and TMX, and the projected values for TASKA. This graph is often used as a simplified way of presenting progress and distance to go to reach the objective of a thermonuclear fusion reactor; it should be remembered, however, that this type of graph ignores a lot of important physics questions and, if taken out of context, can give an erroneous impression of progress, or lack thereof, in fusion physics.

III.1.4 Physics Issues Related to TASKA

III.1.4.1 Plug Configuration

The TASKA plug configuration, shown in Fig. III.1-2, consists of an inside thermal barrier between the central cell and the minimum-B mirror, which provides good curvature for MHD stability and contains the ambipolar potential peak for confinement of central cell ions. In order to provide microstability in the hot, mirror-confined ion plug, a sloshing ion distribution with trapped warm plasma is used. A detailed schematic of the end plug is shown in Fig. II.4-2 and the plasma parameters are given in Table III.4-3.

This configuration has a number of advantages and disadvantages relative to possible alternatives. Of all the configurations proposed, it is closest to current tandem mirror experiments in the plug configuration. Consequently, there is a somewhat better experimental foundation for the physics analysis.

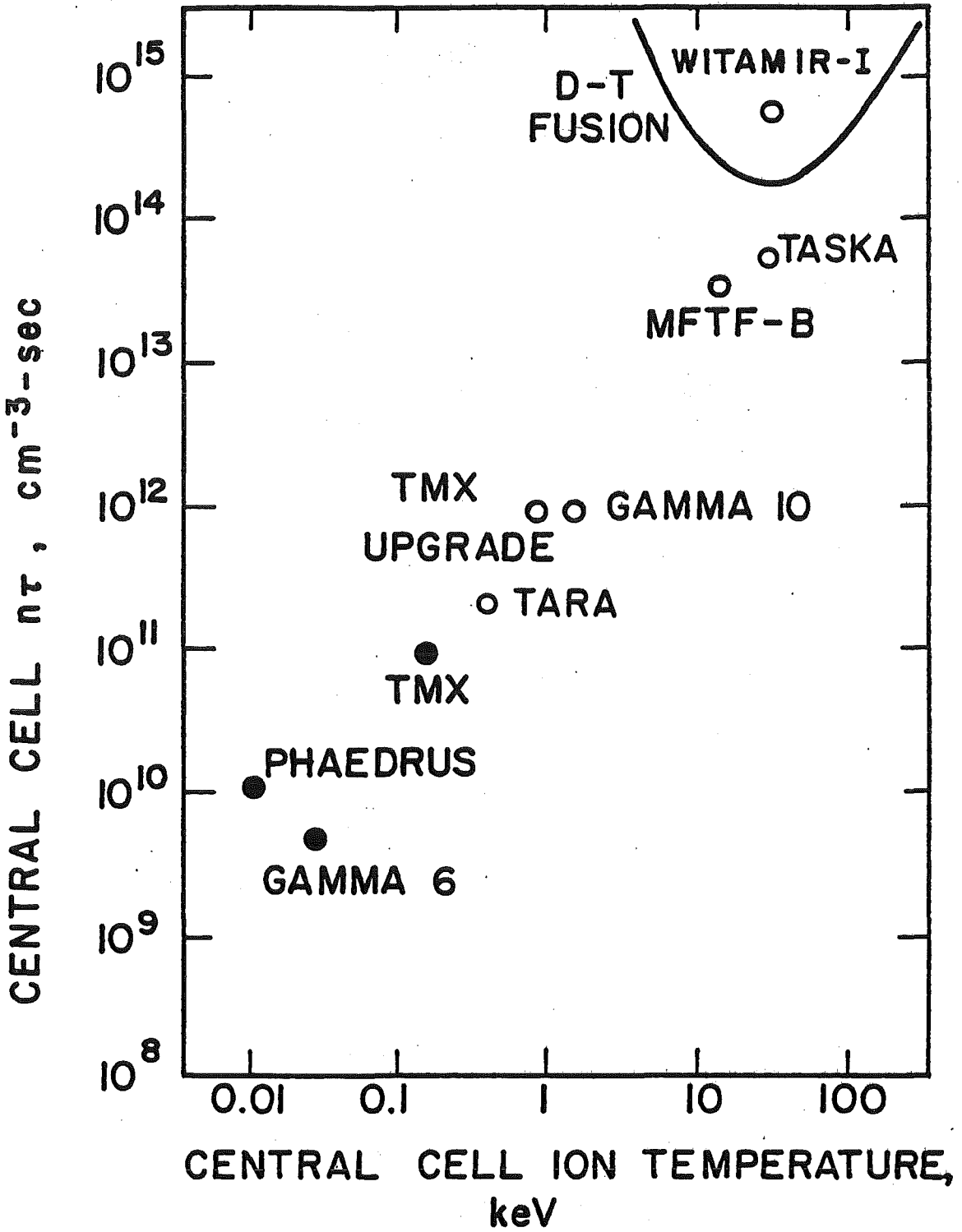


Fig. III.1-7. $n\tau$ versus central cell ion temperature for present (●) and future (○) tandem mirrors.

In addition, less subtle plasma physics is required in this configuration than in the more advanced configurations, TMX-Upgrade and MFTF-B. As a result, the probability of the plug operating as planned should be increased. An example of simpler plasma physics is the decision to not incorporate hot, magnetically trapped electrons in the barrier to further depress the potential there. This would improve the performance of TASKA but is an as yet untested concept.

Since the performance objectives of TASKA can be achieved without it, it was decided to design TASKA without this improvement. An experimental test of the use of hot, magnetically trapped electrons in the barrier will be made in TMX-Upgrade and MFTF-B. If successful, this concept could be incorporated into an upgraded version of TASKA.

The high magnetic field at the barrier throat in TASKA produces a number of desirable effects. The large central cell mirror ratio, B_{mb}/B_c , reflects a larger fraction of ions and electrons approaching the barrier. Consequently fewer central cell ions experience the nonaxisymmetric fields in the transition region and plug; this reduces the central cell radial diffusion caused by radial drifts in these nonaxisymmetric fields. The larger central cell mirror ratio also improves the confinement of unthermalized alpha particles in the central cell by decreasing their loss-cone for axial escape. The larger local barrier mirror ratio, B_{mb}/B , reduces the plasma pressure in the bad curvature regions in the barrier and transition region between the barrier and minimum-B plug. This reduced pressure decreases the driving term for MHD instabilities.

The axisymmetric plug-barrier configuration used in TARA⁽¹⁸⁾ would have even better properties relative to radial transport but its MHD characteristics are not as good, since the high pressure associated with the potential

peak is in a region of bad curvature. It also requires the use of hot, magnetically trapped electrons to generate the thermal barrier. Completely axisymmetric configurations utilizing electron rings⁽¹⁹⁾ seem too untested to be incorporated in TASKA at this time. Axisymmetric configurations with internal rings⁽²⁰⁾ present technological questions which have not yet been fully analyzed.

The inside barrier configuration with a high field barrier coil also has a neutronics advantage. The plug plasma can be nonfusion-reacting (e.g., protons). This, coupled with the low density of deuterium and tritium in the barrier and transition region, has the effect of reducing substantially the neutron production rate in the end plug and thereby reduces the shielding requirements for the yin-yang and transition coils and reduces neutron streaming into the direct convertor and down beam lines and other penetrations of the end plug and barrier shields.

III.1.4.2 Thermal Barrier Pumping

Pumping of the trapped ions in the thermal barrier is done in TASKA by charge exchange pumping using neutral beam injection, as discussed in Section III.1.1. This method is chosen because it is based on relatively straightforward atomic physics considerations. Although it appears to be manageable from a technological viewpoint, there are distinct disadvantages with charge exchange pumping. The associated hardware is expensive and is still in a stage of development. Present limits on beam current density and divergence dictate a minimum size for the plasma in the barrier, which then determines the plasma radius in the central cell. A larger neutron wall loading can be obtained, however, by operating with a smaller central cell radius for a given input power. Furthermore the space requirements for the beam sources,

magnetic shielding, neutralizers, beam lines, and vacuum pumping equipment conflict with other requirements.

It would be highly advantageous to utilize alternative barrier pumping schemes. Some alternatives have been proposed; these are discussed in Section III.1.1. They generally operate by removing trapped ions from the system, instead of "pumping" them back into the central cell. Rather than being an energy input, these schemes drain energy from the plasma so that they affect the stationary operating point in a thermal power balance sense. The hardware associated with them, however, ought to be minimal in comparison with neutral beam pumping. Since these alternative schemes are not yet thoroughly analyzed and are totally untested in experiments, we decided to design TASKA with neutral beam pumping. If these schemes prove successful, they could be implemented in TASKA with only a minor redesign. The converse, however, is not true. Designing for an alternative pumping scheme and having to shift to neutral beam pumping would require a major redesign of the machine.

III.1.4.3 MHD Stability

It has been recognized since about 1979 that ideal MHD stability theory places a severe constraint on the allowable beta in the central cell. The limiting instability is thought to be the ballooning mode driven by bad curvature. In the inboard thermal barrier configuration this occurs in the transition region between the thermal barrier and the minimum-B plug, in the thermal barrier itself, and in the connection between the thermal barrier and the central cell. Predicted ideal MHD beta limits are in the range of 10-25%.⁽¹¹⁾ The most unstable modes have high azimuthal mode number, n . The central cell, however, is a region with large volume, zero curvature, and relatively large gyroradius ρ in relation to the radial scale length, r_c . In TASKA, for

example, $r_c = 32$ cm, $\rho = 2$ cm. One might expect a substantial finite gyroradius correction to ideal MHD stability theory in these circumstances. Recent analysis^(34,35) confirms this result. A model analytical calculation gave an increase in the limiting central cell beta from 27%, at the zero gyroradius limit at high n , to $\beta > 1$ for all $n > 5$.⁽³⁵⁾ In this calculation, the finite gyroradius parameter Γ ,

$$\Gamma \approx n \left(\frac{L}{r_c}\right) \left(\frac{\rho}{r_c}\right)$$

was equal to .5. Since L (the parallel scale length) $\gg r_c$, this corresponds to rather modest values of ρ/r_c .

Finite gyroradius stabilization is most effective at high mode number, n , and vanishes for the $n = 1$ mode if one uses a sharp boundary model for the plasma. Allowing for diffuse radial profiles will give some finite gyroradius stabilization at $n = 1$, but this may not be sufficient. Wall stabilization is most effective, however, for low n ,^(36,37) so this may provide the needed stability for small values of n , including $n = 1$. In TASKA, the wall to plasma radius is only 1.4, so significant wall effects can be expected.

The calculations in Refs. 33 and 34 use model magnetic fields; the necessary revisions to MHD codes which calculate stability with real magnetic fields are under development at LLNL but not yet operational. Consequently, one has to assume a beta value for the design of TASKA. The choice of 50% for the central cell beta seems entirely reasonable in light of these calculations.^(35,36)

Experience with tokamaks⁽³⁸⁾ and multipoles⁽³⁹⁾ also supports this conclusion. Both have operated at beta values in excess of theoretical ideal MHD

beta limits for ballooning modes. Experimental encouragement is also found in the Phaedrus tandem mirror experiment, which has exceeded the theoretical interchange stability limits.

The interchange instability and instabilities driven by plasma rotation give much higher beta limits⁽¹¹⁾ even without finite gyroradius corrections, so they are not a design consideration.

III.1.4.4 Plug Microstability

The minimum-B plug has to contain a hot ion, mirror-confined plasma. The distribution function of these hot ions will be definitely non-Maxwellian and hence will be a source of free energy to drive plasma instabilities. These instabilities will have the effect of seriously degrading the confinement time (by orders of magnitude) of the hot ions and hence must be avoided. The most dangerous of these modes are currently believed to be:⁽¹¹⁾

1. The drift cyclotron loss-cone mode (DCLC).
2. The Alfvén ion cyclotron mode (AIC).
3. The axial loss-cone mode (ALC), which is the absolute version of the convective loss-cone mode.
4. The negative energy wave (NEW).

To date, the DCLC mode was identified as the dominant mode in the 2XIIB⁽²⁶⁾ experiment and believed to be one of the modes seen in TMX.⁽²⁸⁾ The AIC mode should have been unstable in 2XIIB but was not observed. It has been tentatively identified in TMX, however.⁽³⁰⁾ The ALC model should have been the dominant mode⁽¹¹⁾ in the PR-6 experiment⁽⁴⁰⁾ in the U.S.S.R., but the instability seen there was identified as the DCLC mode. The NEW mode has not been seen experimentally.

The linear theory of these modes, and the experimental evidence for them, is reviewed in Ref. 41.

The DCLC mode, which was the major consideration in the 2XIIB experiment and in the design of TMX can be stabilized by a sufficient amount of warm (unconfined) plasma in the mirror. In 2XIIB, this was produced by a plasma streaming through the mirror; this plasma stream was produced by external plasma guns or by ionization in a gas box. This method is undesirable in tandem mirrors because it keeps the electron temperature, and therefore the confining potential, low. TMX was designed so that the classical loss rate of central cell plasma was sufficient to provide enough plasma stream to stabilize the DCLC mode. This was only partially successful in actual practice.⁽³⁰⁾ For hotter plasmas, however, this method is inadequate since the loss rate goes down as the temperature goes up. Hence reactor relevant plasmas need to obtain stability in other ways.

The end plug in the WITAMIR-I reactor design⁽⁸⁾ was calculated to be stable against the DCLC mode because of the combination of low end plug density, high beta, and large plasma radius. This, however, does not give stability against the other modes, which can exist in an infinite plasma or depend on the axial variation of the density and magnetic field.

TMX-Upgrade and MFTF-B are designed to avoid these instabilities by the use of a sloshing ion distribution in the end plug (or A-cell). This sloshing ion distribution, which is produced by injection of a neutral beam at an angle to the magnetic field (see Fig. III.1-8), causes the hot ion density to peak off the midplane, as shown in Fig. III.1-9. Corresponding to this density peak, the potential will also peak off the midplane. The local potential "valley" created in the plug can then trap low-energy ions which can partially

WARM - ION
NEUTRAL BEAM

- 87 -

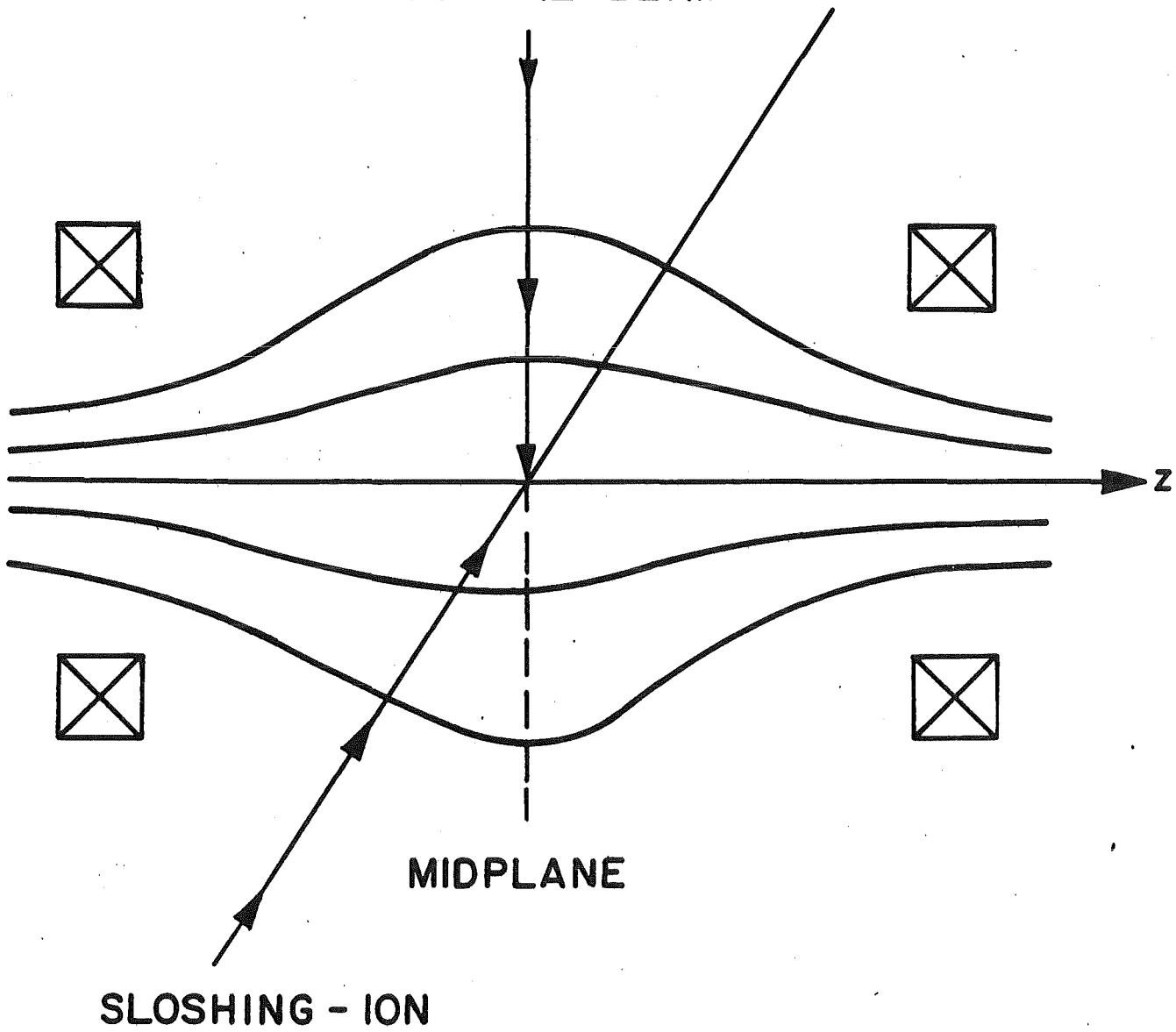


Fig. III.1-8. Neutral beam configuration for a sloshing ion mirror cell.

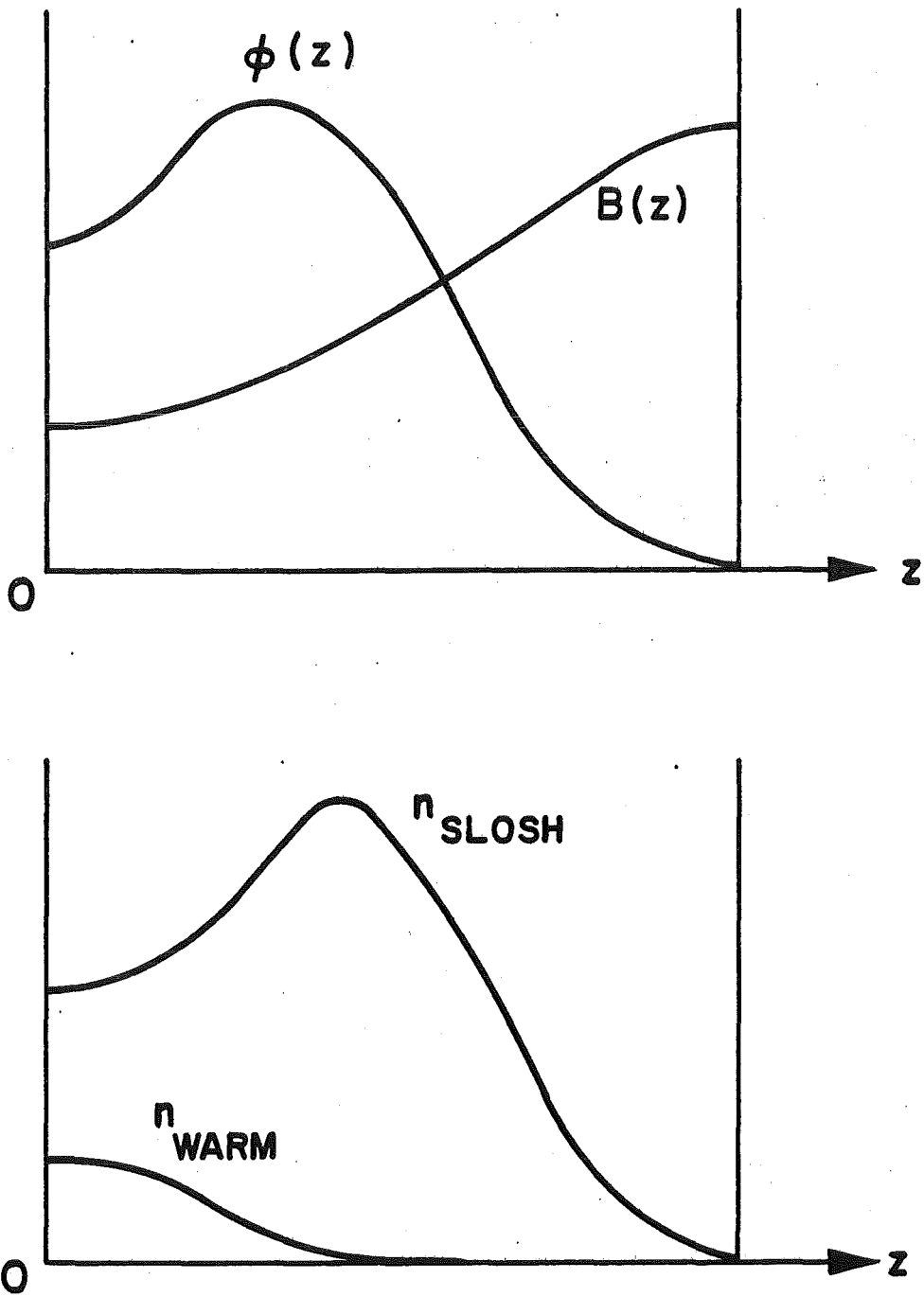


Fig. III.1-9. Axial profiles of density, potential, and magnetic field in a sloshing ion mirror cell.

fill in the hole in the ion distribution function at low energy. This is shown schematically in Fig. III.1-10. The central cell plasma streaming through the sloshing ion plasma also helps to fill in the ion distribution. In this manner, one obtains stability against the DCLC mode. The AIC mode is also stabilized by the increase in T_{\parallel}/T_{\perp} associated with the sloshing ion distribution and by reduced ion beta. The warm plasma coupled with the finite length along the magnetic field and the low density can also provide stability against the ALC and NEW modes, as well. As a result, both MFTF-B and TMX-Upgrade are expected to be stable against all of these modes.⁽⁴²⁾

The design philosophy in TASKA is to utilize the sloshing ion beam concept in the end plug to provide stability against at least the DCLC and AIC modes, since these have been seen experimentally. Ignoring the other modes may be dangerous if they occur at a sufficient level to degrade plug ion confinement. On the other hand, designing TASKA to satisfy all existing theoretical stability criteria is difficult and may be overly restrictive if the modes turn out to be figments of the theorists' imagination. Given the weakness of the theory (both linear and non-linear) and the lack of experimental corroboration, we have chosen to put more priority on the DCLC and AIC modes. There is some precedence for this philosophy in the tokamak community. The trapped particle instabilities, and the dissipative trapped ion mode in particular, were used as design criteria for tokamak reactors until PLT⁽⁴³⁾ with beam heating produced plasmas which should have been unstable to the trapped ion mode, but only low level fluctuations were seen and plasma confinement was not significantly degraded. Currently, trapped particle instabilities are ignored in the design of tokamak reactors, although there is no theoretical justification for this, other than the realization that all theoretical models

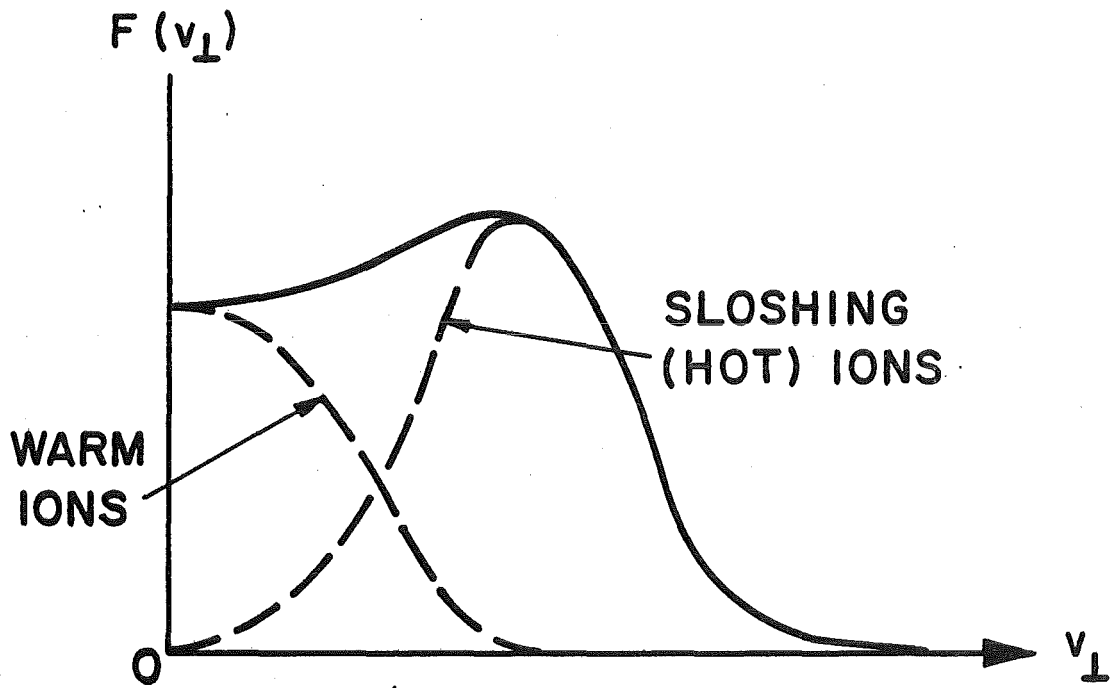


Fig. III.1-10. Ion distribution function; $f(v_{\perp}) = \int f(\vec{v}) dv_{\parallel}$.

are only an approximation to reality. On the other hand, it should be noted that near-classical plug ion confinement is required in tandem mirrors, while the radial transport in toroidal devices can be much larger in relation to the neo-classical rate and still be acceptable.

III.1.4.5 Radial Transport

In a tandem mirror central cell the problem of radial transport is of special importance because longitudinal losses are greatly reduced by the ambipolar potential of the end plugs. It was recognized by Ryutov and Stupakov⁽⁴⁴⁾ that the nonaxisymmetric fields of the end plugs can cause radial drifts of the central cell ions so that their drift surfaces are no longer circular. In most tandem mirror designs, the quadrupole fields at opposite ends are rotated by 90° relative to each other. This produces a lowest order cancellation⁽⁴⁵⁾ but higher order deviations of the drift surfaces from circular remain.

An important parameter determining the character of the radial diffusion is the azimuthal drift, $\Delta\psi$, of an ion in one axial transit of the central cell. This azimuthal drift arises from the grad-B drift in the central cell, the $\vec{E} \times \vec{B}$ drift in the central cell, and azimuthal drifts in the end plugs. Three modes of diffusion have been identified, depending on the magnitude of $\Delta\psi$. If $\Delta\psi \ll 1$, one gets enhanced diffusion due to the step size per collision being determined by the ion stepping from one drift surface to another. This is called neoclassical diffusion and is analogous to neoclassical diffusion in toroidal devices. If $\Delta\psi \approx 1$ then certain classes of particles in phase space experience a resonance with the radial drifts. Those particles for which $\Delta\psi$ is an odd multiple of $\pi/2$ experience the same sign of the radial drift at each end of the central cell and can have large radial excursions.

This is known as resonant diffusion. The third mode occurs when $\Delta\psi \gg 1$ and $a \frac{\partial}{\partial r} \Delta\psi \gg 1$. The parameter a is the maximum radial displacement of an ion due to a single reflection in the end plug. In this case the diffusion is called "stochastic", in analogy to nonlinear oscillation theory. Of course, the ions have different $\Delta\psi$ corresponding to their velocity, so that a sum over these "modes" is needed to get the net particle transport rate.

Elaborate theoretical calculations of the transport coefficients resulting from these effects have been made.^(44,46) They are highly non-linear, however, with a complicated dependence on the plasma properties, including the radial electric field. Furthermore, the radial transport is non-ambipolar and therefore plays a role in determining the electric field. Consequently, one needs self-consistent profiles of n , T_i , T_e , and ϕ to get an accurate calculation of the radial transport.

A qualitative picture of the diffusion coefficient for these different modes is shown in Fig. III.1-11. Here r_c is the central cell radius and t_{dr} is the time required for an ion to drift azimuthally by 2π in the central cell,

$$t_{dr} \approx \frac{r_c^2}{\rho_c^2 \Omega_c} ,$$

where ρ_c is the ion gyroradius and Ω_c is the ion cyclotron frequency in the central cell. The small parameter α is a measure of the noncircularity of the drift surfaces. An order of magnitude estimate⁽¹¹⁾ for α is

$$\alpha \sim \frac{r_c^4}{L_c L_t^3} ,$$

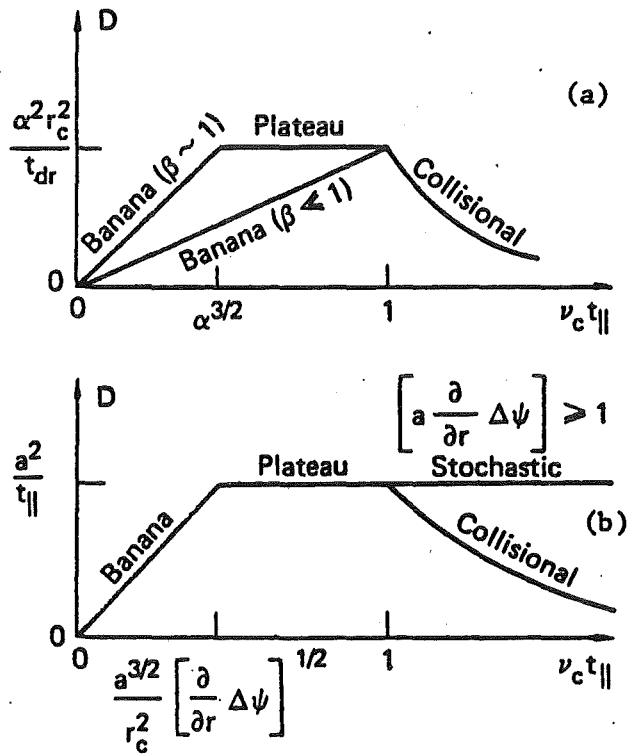


Fig. III.1-11. (a) Neoclassical diffusion and (b) Resonant diffusion. (Taken from Ref. 11)

where L_c is the central cell length and L_t is the transition length for the quadrupole magnetic field. The longitudinal transit time is t_{\parallel} , $t_{\parallel} = L_c/v_{\parallel}$, and ν_c is the ion-ion collision frequency. An order of magnitude estimate of a is⁽¹¹⁾

$$a \approx \frac{\rho_c r_c}{L_t} .$$

The significance of radial transport in TASKA can be determined using these order of magnitude estimates. For the TASKA design parameters, the appropriate diffusion regime is at the border between banana and plateau diffusion for resonant neoclassical diffusion. The estimated radial confinement time is ≈ 1.4 sec, which is to be compared with the axial confinement time of .3 sec. Furthermore, this is most likely a low estimate of the radial confinement time. The circular barrier magnet in TASKA produces an axisymmetric mirror field which reflects most central cell ions before they experience the nonaxisymmetric fields in the plug. This should reduce the radial transport (this effect has been seen in detailed MFTF-B calculations⁽¹¹⁾) but no credit was given for this in the above estimate. We conclude from this, that radial transport in TASKA may play a role, but should not seriously affect the design operating point.

III.1.4.6 Alpha and Impurity Accumulation

The potential peak in the plugs confines higher-Z ions, such as fusion-born alpha particles and impurities, even better than the D-T fuel. Consequently one can get accumulation of alphas and impurities in the central cell. One of the advantages of single mirrors, namely that the positive potential expels impurities from the plasma, has been lost. The steady-state level of

these $Z > 1$ ions is determined by a balance between sources and losses. In this section we consider only alpha particles, which are an irreducible minimum impurity source. The same considerations apply to other impurities as well.

The fusion produced alpha particles are born at 3.5 MeV energy. A small fraction of these are born inside the loss-cone of the high barrier field, B_{mb} , at the entrance to the barrier (see Fig. III.1-2) and escape immediately. The remaining alphas are trapped by the central cell mirror ratio and slow down in the plasma, first by electron drag, and later by ion-alpha collisions. Some of these alphas will scatter into the loss-cone during the slowing-down process and be lost. The remaining alphas scatter down in energy and become trapped by the electrostatic potential of the plugs. They can be lost by radial transport or by upscattering in energy to above the confining potential as they attempt to establish a Maxwell-Boltzmann distribution.

A rough estimate of the alpha accumulation level in the central cell can be obtained by using the Pastukhov formula to estimate the axial loss rate of alpha particles by upscattering in energy. The source rate is determined by the fusion power density. One gets

$$\frac{n_{\alpha}}{n_c} \approx \frac{f_b}{5} e^{\phi_c/T_{ic}} \quad . \quad (III.1-10)$$

In this result, the alphas have been assumed to thermalize to the central cell ion temperature, T_{ic} . The parameter f_b is the fractional burnup (ion "burned" per ion injected), the factor 5 arises from the higher collisionality of the alphas ($Z = 2$, mass = 4 amu). For TASKA, the fractional burnup, f_b , is low, and $\phi_c/T_{ic} \approx 1.5$ so that n_{α}/n_c is on the order of 1%. This steady-state alpha

accumulation level will have only a minor effect on the performance. For a reactor, however, $f_b \approx 20\%$ and $\phi_c/T_{ic} \sim 3$ so that alpha accumulation to the level given by Eq. (III.1-10) is unacceptable. Alpha accumulation in the thermal barrier has a serious effect at lower levels. If the alpha particles are not pumped out of the barrier, then the alpha density can be expected to satisfy a Boltzmann relation between the central cell and the barrier minimum;

$$n_{\alpha}^b = n_{\alpha}^{cc} e^{2\phi_b/T^*}$$

where T^* is some effective parallel temperature for alpha particles in the barrier and n_{α}^b , n_{α}^{cc} are the alpha densities in the barrier and central cell, respectively. One might take $T^* = T_{ic}$, which is equivalent to assuming the alphas have established a Maxwellian distribution at the ion temperature, T_{ic} . This would occur primarily by alpha-ion collisions. The ions in the barrier, however, are essentially two interpenetrating streams with temperature T_{ic} and streaming energy ϕ_b . The streaming motion should cause an increase in the mean alpha parallel energy in the barrier. Consequently, another possible choice is $T^* = 2\phi_b$. For both of these choices n_{α} (barrier) $\gtrsim n_{\alpha}$ (cc). The ion density in the barrier, n_b , is much less than n_c , and the total ion density, after summing over species, needs to be kept small in order to maintain the potential dip of the barrier. In thermal barrier tandem mirrors, the first effect of alpha particles is to cause "quenching" of the thermal barrier. To avoid quenching of the barrier, one wants $n_{\alpha}^b \ll n_b$, which is a more stringent requirement than $n_{\alpha}^{cc} \ll n_c$.

In TASKA the resulting alpha density in the barrier would be $n_{\alpha}^b/n_b \approx 100$ or $n_{\alpha}^b/n_b \approx 1$ depending on the choice for T^* . Either case is

unacceptable so some form of alpha particle removal from the barrier is needed. Since alpha particles get trapped in the barrier by pitch angle scattering, it would seem that classical cross-field diffusion in the barrier is too slow to keep n_{α}^b small. An active means of removing alpha particles from the barrier is required. An early proposal⁽⁴⁷⁾ for removing alpha particles from standard tandem mirrors was to drop the potential in one end plug and allow some fraction of the central cell plasma to flow out; the potential peak is then re-established and the central cell plasma is brought back to its original operating point by fueling and heating. This technique will work in principle but the investment in energy in each cycle to re-establish the plasma is substantial and the degradation of Q is severe.⁽⁴⁷⁾ Using this procedure in a thermal barrier tandem mirror would be even more undesirable since it is only the barrier that needs to be purged, but this purging technique drains the entire central cell as well.

An alternative scheme for pumping alpha particles has been proposed by Hamilton and Logan.⁽⁴⁸⁾ This method uses the neutral beams which pump the barrier to convert He^{+2} to He^{+1} by charge exchange. If this occurs at the right point in the potential profile the kinetic energy acquired by the alpha particle is sufficient to allow it to escape through the end plug. In order that the alpha particle escape before re-ionization to He^{+2} , the neutral beam has to be directed towards the end plug. Estimates indicate that this can be a viable scheme for removing alpha particles in a reactor.

The same process can also be used to pump barrier trapped alpha particles back into the central cell. Figure III.1-12 shows the velocity space for alphas at the bottom of the barrier. Trapped He^{+2} ions in the cross-hatched region become untrapped and return to the central cell if they undergo charge

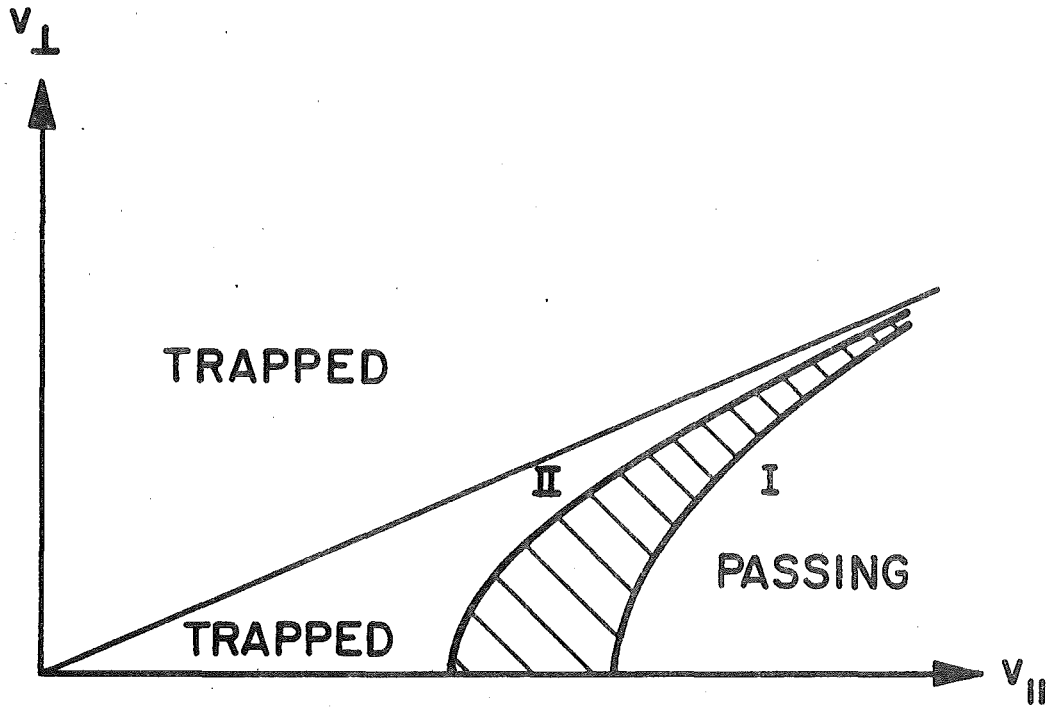


Fig. III.1-12. Velocity space for alpha particles at the barrier minimum. Curve I is the trapped-passing boundary for He^{+2} ; curve II is for He^{+1} . Charge exchange ($\text{He}^{+2} \rightarrow \text{He}^{+1}$) causes alpha particles in the cross-hatched region to be pumped into the central cell. The diagram is symmetric in v_{\parallel} .

exchange to the +1 state. Alpha particles more deeply trapped than the cross-hatched area cannot be pumped by a single charge exchange event. All alpha particles, in scattering from passing to trapped in the barrier, pass through the cross-hatched region in Fig. III.1-12 and hence have a finite probability for being pumped. Estimates of the magnitude of this effect for alpha particle removal from the thermal barrier have not yet been made.

The alternative barrier pumping schemes described in Section III.1.4.2 remove barrier trapped ions by enhanced radial loss; they would appear to be equally effective for removing alpha particles as well from the barrier. Consequently, if these methods prove suitable for barrier pumping in TASKA, then they may also solve the problem of alpha particle accumulation in the barrier.

References for Section III.1

1. T. K. Fowler and B. G. Logan, Comments on Plasma Physics and Controlled Fusion 2, 167 (1977).
2. G. I. Dimov, V. V. Zakaidakov, and M. E. Kishinevskii, Fizika Plasma 2, 597 (1976).
3. G. G. Kelley, Plasma Physics 9, 503 (1967).
4. V. P. Pastukhov, Nucl. Fusion 14, 3 (1974).
5. R. H. Cohen, M. E. Rensink, T. A. Cutler, A. A. Mirin, Nucl. Fusion 18, 1229 (1978).
6. B. G. Logan et al., "Tandem Mirror Reactors," Proc. 7th International Conf. on Plasma Physics and Controlled Nuclear Fusion Research, Innsbruck 1978, Vol. III, 401 (1979).
7. D. E. Baldwin and B. G. Logan, Phys. Rev. Lett. 43, 1318 (1979).
8. B. Badger et al., "WITAMIR-I, A Tandem Mirror Reactor Study," University of Wisconsin Report, UWFDM-400 (1980).

9. G. A. Carlson et al., "Tandem Mirror Reactor with Thermal Barriers," Lawrence Livermore National Laboratory, Report UCRL-52836 (1979).
10. R. H. Cohen, I. B. Bernstein, J. J. Dorning, G. Rowlands, Nucl. Fusion 20, 1421 (1980).
11. "Physics Basis for MFTF-B," edited by D. E. Baldwin, B. G. Logan, T. C. Simonen, Lawrence Livermore National Laboratory Report, UCID-18496 (1980).
12. J. Kesner, Comments on Plasma Physics and Controlled Fusion 5, 123 (1979).
13. D. G. Braun and G. A. Emmert, "Drift Orbits and Drift Orbit Pumping in Thermal Barriers," University of Wisconsin Report, UWFDM-403 (1981).
14. D. E. Baldwin, "Pumping of Thermal Barriers by Induced Radial Transport," Lawrence Livermore National Laboratory Mirror Theory Monthly, May 15, 1981.
15. G. Hamilton, "DC Gradient-B Pumping of Tandem-Mirror Thermal Barriers," Lawrence Livermore National Laboratory Report UCRL-85936 (1981).
16. F. H. Coensgen, T. C. Simonen, A. K. Chargin, and B. G. Logan, "TMX Upgrade Major Project Proposal," Lawrence Livermore National Laboratory Report LLL-PROP-172 (1980).
17. D. D. Ryutov and G. V. Stupakov, S. J. Plasma Physics 4, 278 (1978); R. H. Cohen, Nucl. Fusion 19, 1579 (1979).
18. J. Kesner, B.D. McVey, R.S. Post, D.K. Smith, "A Tandem Mirror with Axisymmetric Central Cell Ion Confinement," Mass. Inst. of Tech. PFC/JA-81-11 (1981).
19. B. G. Logan, "Stability and Power Loss Constraints for E-Ring TMR's," Lawrence Livermore National Laboratory Mirror Theory Monthly, Sept. 15, 1980.
20. G. W. Shuy, Y. C. Lee, F. Kantrowitz, Comments on Plasma Physics and Controlled Fusion 6, 155 (1981).
21. B. G. Logan, Mirror League Workshop, Lawrence Livermore National Laboratory, Feb. 1980.
22. S. Miyoski et al., Proc. 7th Int. Conf. on Plasma Physics and Controlled Nuclear Fusion Research, Innsbruck, Austria, 1978, Vol. II, 437 (1979); Proc. 8th Int. Conf. on Plasma Physics and Controlled Nuclear Fusion Research, Brussels, 1980, paper CN-381/F-2-2.
23. F. H. Coensgen, "TMX Major Project Proposal," Lawrence Livermore National Laboratory Report LLL-PROP-148 (1977).

24. R. S. Post et al., Proc. 8th Int. Conf. on Plasma Physics and Controlled Nuclear Fusion Research, Brussels, 1980 paper IAEA-CN-38/F-2-1; J. Kesner, Nucl. Fusion 20, 557 (1980).
25. K. Yatsu et al., Phys. Rev. Lett. 43, 627 (1979).
26. F. H. Coensgen et al., Proc. 6th Int. Conf. on Plasma Physics and Controlled Nuclear Fusion Research, Berchtesgaden, Germany, 1976, Vol. III, 135 (1977).
27. T. C. Simonen et al., Proc. 8th Int. Conf. on Plasma Physics and Controlled Nuclear Fusion Research, Brussels, 1980; paper IAEA-CN-38/F-1.
28. R.P. Drake et al., "A Detailed Study of Radial Transport in the TMX Central Cell," Lawrence Livermore National Laboratory Report, UCRL-85872 (1981).
29. D.P. Grubb, "Power Flow in TMX," in preparation.
30. "Summary of TMX Results," edited by T. C. Simonen, Lawrence Livermore National Laboratory, Report UCRL-53120.
31. D. K. Smith et al., Bull. Amer. Phys. Soc. 25, 859 (1980).
32. S. N. Golovato et al., Bull. Amer. Phys. Soc. 25, 859 (1980).
33. M. Inutake et al., "Tandem Mirror GAMMA 10 and its Contribution to Reactor Design," Third IAEA Tech. Comm. Meeting and Workshop on Fusion Reactor Design and Technology, 5-16 October 1981, Tokyo, Japan.
34. W. M. Tang and P. J. Catto, "Kinetic Effects on Ballooning Modes in Mirror Machines," Phys. Fluids 24, 1314 (1981).
35. D. A. D'Ippolito, G. L. Francis, J. R. Myra, and W. M. Tang, "Finite-Larmor-Radius Stabilization of Ballooning Modes in an Axisymmetric Tandem Mirror," Science Applications, Inc., PRI-18 (1980).
36. T. E. Cayton, "Finite Ion Larmor Radius Effects and Wall Effects on $m=1$ Instabilities," Los Alamos Scientific Laboratory, LA-8650-MS (1980).
37. D.A. D'Ippolito and B. Hafizi, "Low- m Ballooning Stability of an Axisymmetric Sharp-Boundary Tandem Mirror," Science Applications, Inc., PRI-26 (1981).
38. N. Suzuki et al., "Recent Results on the Modified JFT-2 Tokamak," paper IAEA-CN-38/T-2-3; J.J. Ellis et al., "Critical β and Magnetic Island Studies on the TOSCA Tokamak," paper IAEA-CN-38/X4-4; M. Murakami et al., "Neutral Beam Injection Experiments in the ISX-B Tokamak," paper IAEA-CN-38/N-1, 8th International Conference on Plasma Physics and Controlled Nuclear Fusion Research (Brussels, 1980).

39. S.C. Prager et al., Nucl. Fus. 20, 635 (1980); J.H. Halle et al., Phys. Rev. Lett. 46, 1394 (1981).
40. B. I. Kanaev, Nuclear Fusion 19, 347 (1979).
41. "Status of Mirror Fusion Research 1980," B. I. Cohen, Ed., Lawrence Livermore National Laboratory Report UCAR-10049-80 (1980).
42. W. Nevins, Bull. Amer. Phys. Soc. 25, 920 (1980).
43. H. Eubank et al., "PLT Neutral Beam Heating Results," Plasma Physics and Controlled Nuclear Fusion Research 1978 (Proc. Seventh Int. Conf. Innsbruck, 1978) Vol. 1, p. 167.
44. D. D. Ryutov and G. V. Stupakov, Soviet Physics JETP Lett. 26, 174 (1977); Sov. J. Plasma Physics 4, 278 (1978).
45. L. L. Lao, R. W. Conn, J. Kesner, Nucl. Fusion 18, 1308 (1978).
46. R. H. Cohen, Nucl. Fusion 19, 1579 (1979).
47. R. H. Cohen, Nucl. Fusion 19, 1295 (1979).
48. G. W. Hamilton and B. G. Logan, Comments on Plasma Physics and Controlled Fusion 6, 139 (1981).


Appendix III.1-A

Reprint of the executive summary of UCRL-53120, "Summary of TMX Results,"
T.C. Simonen, editor.

Summary of TMX Results Executive Summary

TMX Group
T. C. Simonen, Editor

Manuscript date: February 26, 1981

LAWRENCE LIVERMORE LABORATORY 
University of California • Livermore, California • 94550

Available from: National Technical Information Service • U.S. Department of Commerce
5285 Port Royal Road • Springfield, VA 22161 • \$5.00 per copy • (Microfiche \$3.50)

CONTRIBUTORS

TMX Experimental Physicists, LLNL

S. L. Allen, T. A. Casper, J. F. Clauser, F. H. Coengen, W. Condit, D. L. Correll,
W. C. Cummins, J. C. Davis, R. P. Drake, J. H. Foote, A. H. Futch, R. K. Goodman,
D. P. Grubb, E. B. Hooper, R. S. Hornady, A. L. Hunt, C. V. Karmendy, A. W. Molvik,
W. E. Nexsen, W. L. Pickles, P. Poulsen, T. C. Simonen, B. W. Stallard

M Division Experimental and Computational Physicists, LLNL

W. L. Barr, J. M. Gilmore, G. E. Gryczkowski, G. W. Leppelmeier,
A. A. Mirin, M. E. Rensink, G. D. Porter

L Division X-Ray/Optics Diagnostics Team, LLNL

C. A. Anderson, G. A. Burginyan, R. Crabb, A. M. Frank, C. E. Frerking,
H. Koehler, M. E. McGee, L. B. Olk, H. D. Snyder, J. P. Stoering, A. Toor

E Division Spectroscopy and Neutron Diagnostic Teams, LLNL

D. D. Dietrich, R. J. Fortner, D. R. Slaughter

Surface Studies Team, Sandia National Laboratories

M. J. Baskes, R. Bastasz, W. Bauer, L. G. Haggmark, A. E. Pontau, W. R. Wampler, K. L. Wilson

Department of Applied Science, UC Davis—Livermore Campus

S. Fallabella, T. J. Nash

Rensselaer Polytechnic Institute

G. A. Hallock

Johns Hopkins University

O. T. Strand

University of Iowa

P. Coakley

Participating Scientists

D. Boyd, University of Maryland; A. L. Gardner, Brigham Young University; W. Getty, University of Michigan; N. Hershkowitz, University of Iowa; R. L. Hickock, Rensselaer Polytechnic Institute; T. Kawabe, Tsukuba University, Japan; H. W. Moos, Johns Hopkins University; M. P. Paul, Alcorn State University; M. Siedel, Stevens Institute of Technology; R. S. Post, University of Wisconsin; K. Yatsu, Tsukuba University, Japan.

Summary of TMX Results Executive Summary

INTRODUCTION

This report summarizes results from the successful experimental operation of the Tandem Mirror Experiment (TMX) over the period October 1978 through September 1980. The experimental program, summarized by the DOE milestones given in Table 1, had three basic phases: (1) an 8-month checkout period, October 1978 through May 1979, (2) a 6-month initial period of operation, June through November 1979, during which the basic principles of the tandem configuration were demonstrated (i.e., plasma confinement was improved over that of a single-cell mirror), and (3) a 10-month period, December 1979 through September 1980, during which the initial TMX results were corroborated by additional diagnostic measurements and many detailed physics investigations

were carried out. This report summarizes the early results, presents results of recent data analysis, and outlines areas of ongoing research and data analysis which will be reported in future journal publications.

The TMX experiments demonstrated the fundamental tandem mirror principles, as summarized in Table 2. Table 3 lists the maximum plasma parameters achieved in TMX. The main result was that TMX generated electrostatic confining potentials that significantly improved central-cell plasma confinement. These data established a new scaling of ion confinement by ambipolar potential in magnetic mirror systems and provided the impetus for the initiation of both TMX Upgrade, a tandem mirror in which potential confinement is increased through the use of thermal barriers, and MFTF-B, a larger tandem mirror that will extend the TMX Upgrade results to thermonuclear temperatures.

TABLE 1. Summary of TMX milestones.

Milestones	Date achieved	Reference
1. Begin TMX checkout.	Oct 1978	Direct communication to DOE
2. Begin plasma-buildup experiments.	Jul 1979	Direct communication to DOE
3. Determine density and beta of plug and solenoid.	Sep 1979	Direct communication to DOE
4. Demonstrate electrostatic plugging of solenoid ions in a measured well.	Sep 1979	Direct communication to DOE
5. Submit draft report evaluating initial TMX performance.	Oct 1979	<i>Phys. Rev. Letters</i> 44, 1132 (1980)
6. Begin neutral-beam heating experiments in solenoid with two beams.	Nov 1979	Section III.E ^a
7. Submit final report evaluating initial TMX performance.	Jan 1980	UCID-18496
8. Submit a plan for modification of TMX, based on TMX data, that will address issues most appropriate to MFTF-B.	Jan 1980	Mirror Senior Review Panel
9. Begin plug-optimization experiments.	May 1980	Section III.G ^a
10. Submit report on measurements of initial electron-beam experiments in TMX.	May 1980	Section III.G, ^a UCID-18725
11. Submit report evaluating impurities in TMX including types and origins of impurities.	Oct 1980	Section III.I, ^a UCID-18883
12. Obtain Thomson-scattering measurements of TMX solenoid electron temperature.	Sep 1980	Section III.A ^a
13. Initiate procurement of hardware to improve TMX performance.	Aug 1980	Initiation of TMX Upgrade construction
14. Submit report summarizing TMX results.	Feb 1981	UCRL-53120
15. Submit report on radial transport of plasma in the solenoid of TMX.	Feb 1981	Section III.F ^a
16. Submit report on initial TMX central-cell ICRH experiments.	Dec 1980	UCID-18866

^aSection of this report (UCRL-53120).

TABLE 2. Summary of TMX results.

- Generated tandem mirror configuration:
 - Configuration sustained for full 25-ms shot duration.
 - Plug microstability maintained with solenoid outflow.
 - Central-cell MHD stability (40% maximum beta with neutral-beam injection).
- Demonstrated central-cell electrostatic plugging:
 - Measured electrostatic potential well.
 - Direct evidence by measurements made when one end plug was turned off.
 - Measured factor-of-9 electrostatic enhancement.
 - Radial confinement exceeds axial confinement.
- Improved electron confinement:
 - Electron temperature higher than in 2XIIB.
 - Low density at end wall.
 - Dominant power loss to end walls.
 - Low levels of impurities.

TABLE 3. Maximum plasma parameters achieved in TMX with deuterium and a central-cell magnetic field strength of 0.1 T. These parameters were not achieved simultaneously on the same shot.

Plug density	$4 \times 10^{13} \text{ cm}^{-3}$
Plug ion energy	13 keV
Plug electron temperature	0.26 keV
Plug radius	10 cm
Central-cell density	$3 \times 10^{13} \text{ cm}^{-3}$
Central-cell ion energy	0.25 keV
Central-cell radius	30 cm
Plug plasma potential	1 kV
Central-cell confining potential	0.3 kV
Central-cell axial-confinement parameter	$10^{11} \text{ cm}^{-3} \cdot \text{s}$
Electrostatic enhancement in confinement	9
Central-cell beta (0.07 without central-cell neutral-beam injection)	0.40

INITIAL TMX RESULTS

Tandem Mirror Configuration

● One of the expected tandem mirror characteristics verified by TMX was that the density of the plasma in the end plug could be sustained at a higher level than that of the central-cell plasma, and that this produced higher electric potentials in the end plugs than in the central cell. These densities were controlled by varying the end-plug neutral-beam current and the central-cell gas-feed current. The density peaks generate potential peaks, as shown in Fig. 1, which also shows that relatively small end-plug plasmas can electrostatically confine a much larger central-cell plasma.

● The density and temperature of the TMX plasma are within a factor of 2 of those predicted by theoretical codes. Calorimeter measurements showed that most of the neutral-beam power deposited on the axis is carried to the end walls by ions.

● Gross MHD stability and microstability were achieved. Finite-beta plasma was confined in the central cell with minimum-B end-plugs. The outflow of central-cell plasma provided end-plug microstability.

Improved Plasma Confinement

● The TMX end plugs improve confinement of the central-cell plasma by up to a factor of 9 over

that which would have been attained if the end-plug plasmas had not been present. Typical enhancements were in the range of 3 to 7 times. Central-cell axial confinement of ions is near that predicted by our theoretical models.

● TMX plasma confinement can be explained by classical Coulomb theoretical models, over a certain range of parameters. However, there must be sufficient warm plasma to stabilize the plugs. If insufficient low-energy plasma flows through the end plug, then fluctuating electric fields develop at the end-plug ion-cyclotron frequency and confinement of central-cell ions is reduced. Theoretical models describing TMX performance over a wide range of operation have been developed on the basis of these experiments.

● A second measure of improvement in the tandem mirror over the single mirror is the electron temperature that can be achieved with a given amount of input neutral-beam power. TMX end plugs achieved electron temperatures up to 260 eV, three to four times higher than the electron temperatures of the similar single-cell mirror machine 2XIIB when operated with comparable neutral-beam input power. Since TMX has such a large central-cell plasma, this electron temperature increase indicates a hundred-fold improvement in electron energy confinement. This improvement arises from the fact that the low-energy plasma required for end-plug microstability is supplied from

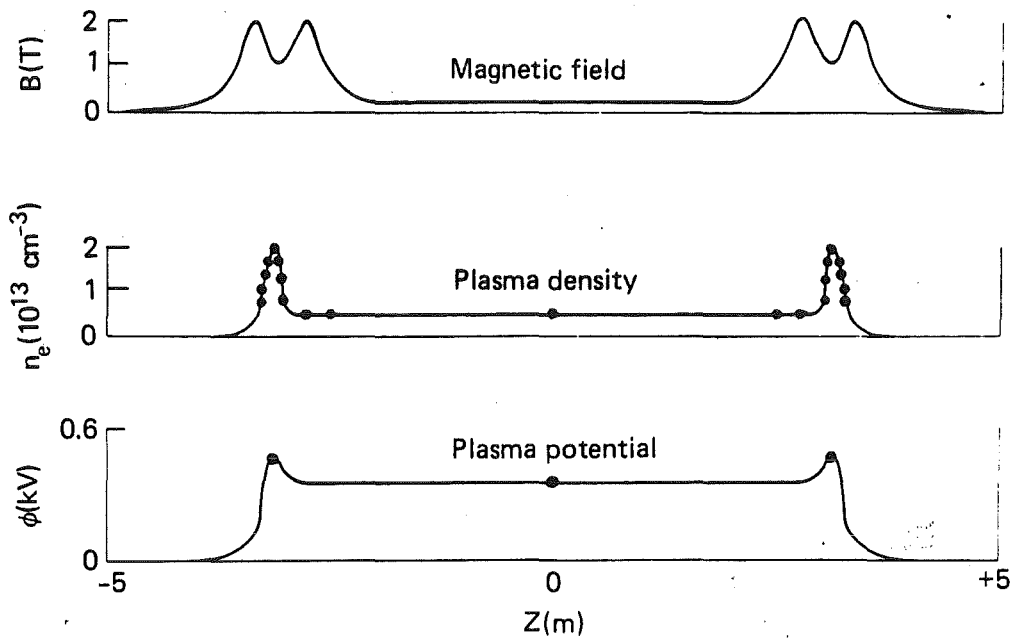
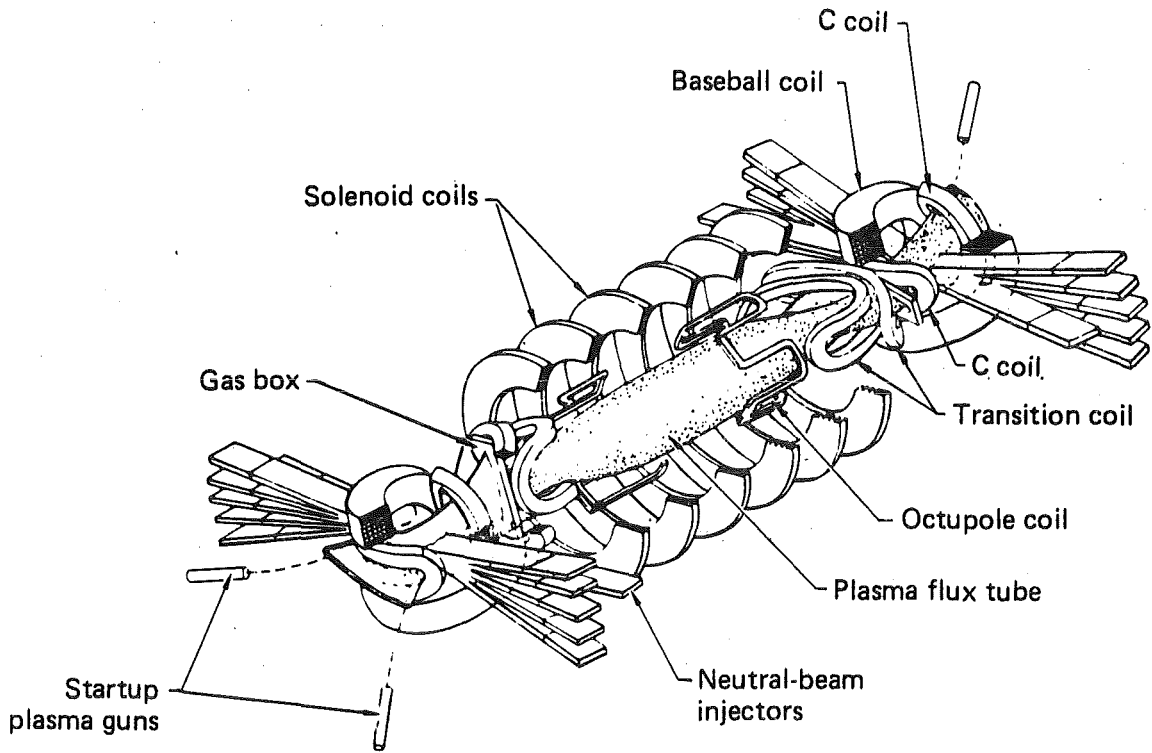


FIG. 1. TMX magnet geometry and measured axial plasma profiles.

the TMX central cell rather than from the ends, as in 2XIIB, thus reducing the electron energy loss to the end walls.

NEW RESULTS PRESENTED IN THIS REPORT

During much of the last period of TMX operation (December 1979 through September 1980), poor vacuum conditions caused lower electron temperatures than had been achieved earlier (although sometimes temperatures above 200 eV were still observed). Therefore, our progress during the later phases of TMX operation was in physics understanding rather than in increasing plasma parameters. This increase in understanding resulted from more extensive diagnostic instrumentation, new data analysis, and improved theoretical understanding. Highlights of these recent results are summarized below.

Tandem Configuration

- Plasma potential measurements carried out as a function of radius have shown that the electrostatic potential well is not just localized near the axis but extends across the central cell. The well-diagnosed plasmas had 150-V well depths, as expected for the measured electron temperature and densities. Other cases had well depths about twice as high.

- End-plug potentials exceeding 1 kV have been generated and maintained in TMX.

- Methods for controlling the radial profiles have been demonstrated. Operation of TMX over a wide range of central-cell gas feeds has shown that the radial density profiles can be changed from peaked on-axis to inverted profiles peaked off-axis. Additional diagnostic channels allowed us to measure these radial density profiles in more detail than was previously possible.

Plasma Confinement

- Under proper operating conditions, the confinement of the central-cell plasma is in agreement with the theoretical Coulomb values. The highest confinement parameter achieved was $n\tau = 10^{11} \text{ cm}^{-3} \cdot \text{s}$. When end-plug fluctuation levels are significant, confinement is degraded in agreement with Monte-Carlo calculations. These fluctuations limited the range over which TMX could be

operated but did not prevent us from demonstrating the basic features of tandem mirrors.

Power Balance

- We have been able to account for the neutral-beam power input by using multiple diagnostic arrays.

- Near the axis, most of the trapped neutral-beam power is lost axially, indicating good radial confinement. Near the edge, more power is lost radially. Radial arrays of calorimeters on the TMX end wall show that the power is more concentrated on the axis than was previously assumed. Radial end-loss analyzer measurements indicate that this concentration is due to the radial profiles of both the end-loss current and the plasma potential.

Plasma Beta Measurements

- After TMX was shut down, an extensive calibration of the diamagnetic loops was carried out. With this new calibration, we determined that a maximum central-cell beta of 0.4 was achieved with neutral-beam injection.

- This calibration has also enabled us to conclude that the central-cell ion distribution has a non-Maxwellian component, as we had expected, because of ion-cyclotron heating by plug fluctuations.

Radial Transport

- In TMX, radial particle confinement exceeds axial confinement near the axis. Near the edge, radial transport processes are more important.

- Resonant-neoclassical-ion-transport theory is consistent with the experimental measurements, but the measurements cannot resolve factor-of-3 uncertainties in the theory nor can we resolve comparable amounts of ambipolar radial transport.

Radio-Frequency Measurements

- Wavelength and polarization measurements of the end-plug ion-cyclotron fluctuations indicate wave properties more similar to the Alfvén ion-cyclotron (AIC) mode than to the drift-cyclotron loss-cone (DCLC) mode. In comparison to 2XIIB, the AIC mode is theoretically more unstable in TMX, while the DCLC mode is less unstable. Theoretically, the AIC mode is expected to be much more stable in the low-ion-beta end plugs

of TMX Upgrade and MFTF-B, as is the DCLC mode.

- Turbulent noncoherent central-cell fluctuations extending up to 0.5 MHz, possibly associated with drift waves, have been detected in the central cell. No correlation with plasma confinement has been identified.

- Coherent low-frequency 7 kHz ($m = 1$) and 12 kHz ($m = 0$) oscillations have been observed in the central cell. The $m = 0$ mode is correlated with bursting of end-plug ion-cyclotron fluctuations and thus would not be expected in TMX Upgrade with microstable sloshing-ion end plugs. The $m = 1$ mode exists at large amplitude near the edge when sufficient central-cell gas input causes large density gradients near the edge. The $m = 1$ mode can be controlled by modifying central-cell radial profiles by controlled central-cell fueling and heating.

Impurity Studies

- Further analysis continues to indicate remarkably low central-cell impurity levels (0.5%), resulting in less than 10% power loss by impurity radiation. Recent data analysis shows that the lower ionization states of the prevalent oxygen impurity are localized near the edge and the higher ionization states near the axis, as expected.

- High-resolution spectroscopy has provided Doppler-broadening measurements of impurity radiation that corroborate the 100-to-200-eV diamagnetic-loop measurements of central-cell ion temperature.

Sandia Surface-Probe Studies

- Surface probes have been employed to characterize plasma-wall interactions and to determine TMX plasma properties. Passive solid-state

probe measurements of particle fluxes and energies at the central-cell walls corroborate other central-cell diagnostic measurements.

- The probes collected the expected number of particles on the end walls. The major component of end losses comes from the central cell. The end-plug contribution is also in agreement with theoretical calculations.

End-Wall Plasma Characteristics

- We have succeeded in decoupling the TMX plasma from the end walls. This was a necessary accomplishment for future higher-temperature machines. A very low density ($2 \times 10^9 \text{ cm}^{-3}$) and cool (5 eV) plasma exists near the end wall. This density is four orders of magnitude less and this electron temperature 40 times cooler than the density and electron temperature of the end plug plasmas.

- Secondary electrons emitted from the end wall are detected but the power losses are small, consistent with a model developed for MFTF-B end-wall processes.

ONGOING RESEARCH

The full report, UCRL-53120, describes many major new findings that will subsequently be reported in individual journal publications. Several questions have been raised and are the subject of ongoing research. Many of these questions will be answered by further data analysis and analytic modeling, while others can only be resolved experimentally in the TMX Upgrade, Phaedrus, or other tandem mirror machines. We expect to obtain more quantitative information about power balance, fluctuation studies, and radial transport.

MAJOR TMX PUBLICATIONS

1. F. H. Coensgen, *TMX Major Project Proposal*, Lawrence Livermore National Laboratory, Livermore, CA, LLL-PROP-148 (1977).
2. F. H. Coensgen, C. A. Anderson, T. A. Casper, J. F. Clauser, W. C. Condit, D. L. Correll, W. F. Cummins, J. C. Davis, R. P. Drake, J. H. Foote, A. H. Futch, R. K. Goodman, D. P. Grubb, G. A. Hallock, R. S. Hornady, A. L. Hunt, B. G. Logan, R. H. Munger, W. E. Nexsen, T. C. Simonen, D. R. Slaughter, B. W. Stallard, and O. T. Strand, "Electrostatic Plasma-Confinement Experiments in a Tandem Mirror System," *Phys. Rev. Lett.* **44**, 1132-35 (1980).
3. Papers presented at the session on the TMX experiment at the 21st Annual Meeting of the Division Plasma Physics of the American Physical Society, *Bull. Am. Phys. Soc.* **24**, 1017 (1979).
4. D. P. Grubb et al., in *Proc. Intl. Symp. Physics of Open-Ended Fusion Systems, Tsukuba University, Japan 1980*; in preparation.
5. D. E. Baldwin, B. G. Logan, and T. C. Simonen, Eds., *Physics Basis for MFTF-B*, Lawrence Livermore National Laboratory, Livermore, CA, UCID-18496 (1980).
6. T. C. Simonen, C. A. Anderson, T. A. Casper, J. F. Clauser, F. J. Coensgen, W. C. Condit, D. L. Correll, W. F. Cummins, J. C. Davis, R. P. Drake, J. H. Foote, R. J. Fortner, A. H. Futch, R. K. Goodman, D. P. Grubb, E. B. Hooper, R. S. Hornady, A. L. Hunt, C. V. Karmendy, B. G. Logan, R. H. Munger, W. E. Nexsen, W. L. Pickles, P. Poulsen, D. R. Slaughter, B. W. Stallard, G. A. Hallock, and O. T. Strand, "Plasma Confinement Experiments in the TMX Tandem Mirror," in *Proc. Intl. Conf. Plasma Physics and Controlled Nucl. Fusion Research, 8th, Brussels, 1980* (IAEA-CN-38/F-1, Vienna, 1981).
7. R. P. Drake, G. Deis, M. Richardson, and T. C. Simonen, "Gas Control and Wall Conditioning in TMX," *J. Nucl. Mat.* **93/94**, 291 (1980).
8. R. P. Drake, T. A. Casper, J. F. Clauser, F. H. Coensgen, D. L. Correll, W. F. Cummins, J. C. Davis, J. H. Foote, A. H. Futch, R. K. Goodman, D. P. Grubb, R. S. Hornady, W. E. Nexsen, T. C. Simonen, and B. W. Stallard, "The Effect of End-Cell Stability on the Confinement of the Central-Cell Plasma in TMX," UCRL-84558 Rev. 1 (1980); submitted to *Nucl. Fusion*.
9. T. D. Rognlien and Y. Matsuda, "Tandem Mirror Confinement in the Presence of Ion Cyclotron Fluctuations," UCRL-84571 (1980); submitted to *Nucl. Fusion*.
10. Papers presented at the session on TMX experiments at the 22nd Annual Meeting of the Division of Plasma Physics of the American Physical Society, *Bull. Am. Phys. Soc.* **25**, 878 (1980).
11. D. L. Correll and R. P. Drake, Eds., *Results of TMX Operations: January-July 1980*, Lawrence Livermore National Laboratory, Livermore, CA, UCID-18803 (1980).
12. T. C. Simonen, "Experimental Progress in Magnetic Mirror Fusion Research," Lawrence Livermore National Laboratory, Livermore, CA, UCRL-85494 (1981); submitted to *Proc. IEEE*.
13. T. C. Simonen, "Comparison of Tandem Mirror Confinement with Single Mirror Experiments," Lawrence Livermore National Laboratory, Livermore, CA, UCRL-85834, (1981); to be submitted to *Nucl. Fusion*.

III.2 Power Balance Model

III.2.1 Introduction

The basic performance of TASKA has been calculated using a zero-dimensional model for the power and particle balance of the plasma. It treats three distinct regions of the machine (central cell, barrier, and plug) and includes power and particle flows between these regions as well as losses to the walls and absorption of injected power.

A zero-dimensional model was chosen for this study since, while tractable, it allows quick solution of the system of equations. It is, therefore, well-suited to parametric studies. This approach necessitates some approximations which will be discussed where appropriate. All formulas are written in the cgs system, except that energies and temperatures will be in keV.

The present work expands on the plasma physics analysis of Ref. 1, which was a major conceptual tandem mirror reactor study including engineering details. A rudimentary version of the analysis was given in Ref. 2. Most of the foundation of the physics of tandem mirrors with thermal barriers was laid at Lawrence Livermore National Laboratory^(3,4,5). Reference 3 is especially helpful, although it treats A-cell tandem mirrors, since much of the physics is the same or similar. Many of the equations and much of the notation in this paper is based on Ref. 3. For completeness, a full set of consistent equations will be given here.

There are two electron populations; their densities and temperatures or average energies are: 1) central cell (n_c, T_{ec}) and 2) potential-trapped in the plug (n_{ew}, T_{ep}). Electrons passing through both central cell and plug are counted in group 1. The three ion populations are: 1) central cell (n_c, T_{ic}); 2) barrier, which includes both passing (n_{pass}^i, T_{ic}) and trapped (n_{bt}, T_{ic}); and

3) plug, which are mirror-trapped (n_p, E_p). The central cell density n_c includes the density, n_α , of thermalized alpha particles. These will be discussed in detail in the appropriate places. It has been assumed that alpha particles are removed from the barrier and do not contribute to the barrier density.

The exposition of the physics included here will begin with discussions of the details of the three main plasma regions. These details will then be combined into a set of power balance equations. First, some general considerations and essential formulas are given, perhaps most useful for reference.

III.2.2 General Formulas

The plasma radius at a given $B(z)$ follows from flux conservation:

$$r(z) = r_c \left\{ \frac{B_c}{B(z)} \left[\frac{1-\beta_c}{1-\beta(z)} \right]^{1/2} \right\}^{1/2} \quad (\text{III.2-1})$$

where $\beta(z) \equiv$ perpendicular plasma pressure/magnetic field pressure, values are referenced to the central cell, and the long-thin approximation has been used for beta correction of the magnetic fields.

Betas are given by

$$\beta_c = \frac{n_c (T_{ec} + T_{ic} + T_\alpha)}{2.5 \times 10^7 B_c^2} \quad (\text{III.2-2})$$

for the central cell,

$$\beta_b = \frac{n_b \left[T_{ic} \frac{B_b}{B_{maxb}} + T_{ec} \right]}{2.5 \times 10^7 B_b^2} \quad (\text{III.2-3})$$

for the barrier, and

$$\beta_p = \frac{n_p (0.9 E_p + T_{ep})}{2.5 \times 10^7 B_p^2} \quad (\text{III.2-4})$$

for the plug, where B_p/B_{max} corrects for the constancy of $u \equiv V_{\perp}^2/2B$ of barrier ions, the coefficient 0.9 in β_p approximately corrects for the average plug ion energy being mainly perpendicular, and alpha particles are assumed to contribute to β_c with an equivalent temperature of⁽⁵⁾

$$T_{\alpha} = 8.3 \times 10^{10} \langle \sigma v \rangle_{DT} E_{\alpha} f_{e\alpha} T_{ec}^{3/2} \quad (\text{III.2-5})$$

where $\langle \sigma v \rangle_{DT}$ is the fusion reaction rate, and the alpha particle energy, E_{α} , is assumed to be distributed to the central cell ions and electrons as follows: the fraction $f_{e\alpha}$ goes to electrons, $f_{i\alpha}$ goes to ions, and the remainder is lost out the ends. The values $f_{e\alpha}$ and $f_{i\alpha}$ depend on a variety of parameters, and the values used for TASKA are generated numerically by an analysis given in Ref. 6.

The collisional energy transfer rate $\nu^{\gamma/\beta}$ from species β to species γ is approximated by assuming both species are Maxwellian and using standard formulas:⁽⁷⁾

$$\nu^{\gamma/\beta} = 5.7 \times 10^{-24} \frac{(m_{\gamma} m_{\beta})^{1/2} Z_{\gamma}^2 Z_{\beta}^2 n_{\beta} \Lambda_{\gamma\beta}}{(m_{\gamma} T_{\beta} + m_{\beta} T_{\gamma})^{1.5}} \quad (\text{III.2-6})$$

where m_j is the mass, Z_j is the atomic number, n_j is the density, and T_j is the temperature of species j ; $\Lambda_{\gamma\beta}$ is a Coulomb logarithm, also given in Ref.

7. The assumption of Maxwellian distribution functions is inaccurate for

streaming components, but collisional terms tend to be small, and no serious consequences of this approximation are anticipated.

The Logan-Rensink model is used for $(n\tau)_{ip}$ of ions in the plug⁽⁸⁾, giving

$$(n\tau)_{ip} = \left[\frac{\Lambda_{iip} (m_D/m_{ip})^{1/2}}{3.9 \times 10^{12} E_{inj}^{1.5} \log_{10} R_{eff}} + \frac{\Lambda_{eip} (m_H/m_{ip})}{10^{13} T_{ep}^{1.5} \ln(E_{inj}/E_{out})} \right]^{-1} \quad (III.2-7)$$

where m_D is the mass of deuterium, m_H is the mass of hydrogen, m_{ip} is the plug ion mass, Λ_{iip} and Λ_{eip} are Coulomb logarithms given by $\Lambda_{iip} = 28 + 1/2 (\ln T_{ep} + \ln E_p - \ln n_p)$ and $\Lambda_{eip} = 24 + \ln T_{ep} - 1/2 \ln n_p$, E_{inj} is the neutral beam injection energy. The mean ion escape energy, E_{out} , is given by

$$E_{out} = \frac{E_{inj}}{1 + \frac{\tau_i}{\tau_{dr}}} + \frac{(\phi_c + \phi_e)}{R_p \sin^2 \theta} \frac{\tau_i/\tau_{dr}}{[(1 - \beta_p)^{1/2} - 1]} \left(1 + \frac{\tau_i}{\tau_{dr}}\right) \quad (III.2-8)$$

where R_p is the plug vacuum mirror ratio, θ is the beam injection angle, β_p is the plug beta, and τ_i/τ_{dr} , the ratio of ion collision time to electron drag time, is given by

$$\frac{\tau_i}{\tau_{dr}} = .11 \left(\frac{E_{inj}}{T_{ep}}\right)^{1.5} \frac{\Lambda_{eip}}{\Lambda_{iip}} \frac{\log_{10} R_{eff}}{\ln\left(\frac{E_{inj}}{E_{out}}\right)} \left(\frac{m_D}{m_{ip}}\right)^{1/2} \quad (III.2-9)$$

where T_{ep} is the plug electron temperature. The effective mirror ratio, R_{eff} , is

$$R_{eff} = \frac{R_p / (1 - \beta_p)^{1/2}}{1 + \frac{(\phi_e + \phi_c)}{E_{inj}}} \sin^2 \theta \quad (III.2-10)$$

For ions in the central cell, $(n\tau)_{ic}$ is given by Pastukhov's analysis as corrected and expanded by Cohen, et al.^(9,10)

$$(n\tau)_{ic} = \frac{(m_i/2)^{1/2}}{Z_{ic} \pi e^4 \Lambda_{iic}} \frac{G(Z_{ic} R_c)}{I(\frac{ic}{\phi_c})} T_{ic}^{1/2} \phi_c e^{\phi_c/T_{ic}} \quad (\text{III.2-11})$$

where m_i is the ion mass, Λ_{iic} is the ion Coulomb logarithm given by $\Lambda_{iic} = 24 + \ln T_{ic} - 1/2 \ln n_c$, $Z_{ic} = 0.5$ for ions because they scatter only slightly off of electrons, $R_c = B_{\max b}/B_c$ is the central cell mirror ratio,

$$G(x) \equiv \frac{\pi^{1/2}}{4} \left(1 + \frac{1}{x}\right)^{1/2} \ln \left[\frac{\left(1 + \frac{1}{x}\right)^{1/2} + 1}{\left(1 + \frac{1}{x}\right)^{1/2} - 1} \right] \quad (\text{III.2-12})$$

and

$$I(x) \equiv \frac{1 + \frac{x}{2}}{1 + \frac{x^2}{4}} \quad (\text{III.2-13})$$

For electrons in the central cell, similar analysis gives

$$(n\tau)_{ec} = \frac{(m_e/2)^{1/2}}{Z_{ec} \pi e^4 \Lambda_{eec}} \frac{G(Z_{ec} R_c)}{I(\frac{ec}{\phi_e})} T_{ec}^{1/2} \phi_e e^{\phi_e/T_{ec}} \quad (\text{III.2-14})$$

where m_e is the electron mass, Λ_{eec} is the electron Coulomb logarithm, given by $\Lambda_{eec} = 24 + \ln T_{ec} - 1/2 \ln n_c$, and $Z_{ec} = 1$ for electrons because they scatter off both ions and electrons.

Synchrotron power for a given density n , electron temperature T_e , plasma radius r , magnetic field B , volume V , and reflection coefficient R_s is given by⁽¹¹⁾

$$P_s = 4.2 \times 10^{-23} \left(\frac{n}{r}\right)^{1/2} (BT_e)^{5/2} (1 - R_s)^{1/2} \text{ V watts (III.2-15)}$$

and Bremsstrahlung power is given by⁽⁷⁾

$$P_B = 5.34 \times 10^{-31} n^2 T_e^{1/2} \text{ V watts . (III.2-16)}$$

III.2.3 Barrier Physics

The barrier potential, ϕ_b , arises from a dip in ion density (and therefore electron density) through the equation

$$e\phi_b = T_{ec} \ln \frac{n_c}{n_b} \quad (\text{III.2-17})$$

assuming Maxwellian electrons.

This density decrease is caused by the expansion of the magnetic field flux tube as the B field drops and by acceleration of the ions as they fall down the potential hill. To maintain the density dip, passing central cell ions which collisionally scatter into trapped orbits must be pumped out of the barrier region. The pumping mechanism considered here is charge exchange pumping. Neutral beam particles injected into the barrier loss cone become central cell ions when they charge exchange. The resulting neutrals tend to have fairly large perpendicular velocities and should quickly leave the machine; thus, reionization of these particles is neglected. For a trapped barrier ion with zero parallel energy at a point where the potential is ϕ_{in} , relative to the central cell, the injection energy necessary to create a passing ion by overcoming that potential and the ∇B forces is

$$E_{in} = \frac{\phi_{in}}{1 - \frac{B_{maxb}}{B_{in}} \sin^2 \theta_{in}} \quad (\text{III.2-18})$$

where B_{in} is the magnetic field at the injection point and θ_{in} is the injection angle. When the potential ϕ_{in} is positive relative to the central cell, the effective injection angle is actually smaller than θ_{in} because ϕ_{in} increases $v_{||}$ at the $\phi = 0$ point. The result is

$$\theta_{eff} = \arctan \left[\frac{\sin \theta_{in}}{\cos \theta_{in} + (\phi_{in}/E_{in})^{1/2}} \right] \quad (\text{III.1-19})$$

Charge exchange with passing ions is neglected since the resulting neutral can still pump the barrier. Since each charge exchange event, which does the pumping, is accompanied by $\langle \sigma v \rangle_{ion} / \langle \sigma v \rangle_{cx}$ ionization events, the total energy change per pumped ion is

$$(E_{in} - \phi_{in}) \left(1 + \frac{\langle \sigma v \rangle_{ion}}{\langle \sigma v \rangle_{cx}} \right) - \frac{3}{2} T_{ic} \quad (\text{III.2-20})$$

where $\langle \sigma v \rangle_{ion}$ includes ionization on both trapped and passing ions. If the electron from an ionization event enters the central cell, it will add energy ϕ_{in} to the central cell electrons. If the electron enters the plug, it will add energy $\phi_{in} + \phi_c$, but a plug electron must then become a passing electron in order to maintain quasi-neutrality, carrying an energy $\phi_b + \phi_c + T_{ep}$ from the plug and adding $\phi_b + T_{ep}$ to the central cell.

Achieving a high barrier potential while keeping the total barrier density to a minimum is important. The lower limit on barrier density is the density of central cell ions passing through the barrier,

$$n_{\text{pass}}^i(z) = n_c \frac{B(z)}{B_{\text{maxb}}} \left[\frac{\tau_{ic}}{\pi \phi_b(z) + \tau_{ic}} \right]^{1/2}. \quad (\text{III.2-21})$$

The total barrier density is normalized to n_{pass}^i through the relation

$$n_b = g_b n_{\text{pass}}^i. \quad (\text{III.2-22})$$

The calculation of g_b is difficult; a reasonable value of $g_b = 2$ is generally used in this report.

The current per unit volume of passing ions which trap in the barrier at z is given by a formula fitted to Fokker-Planck studies⁽⁵⁾:

$$J_{\text{trap}}(z) = \frac{[n_{\text{pass}}^i(z)]^2}{5.5 \times 10^9 \tau_{ic}^{3/2}} \left[1 + 0.185 \frac{B_{\text{maxb}}}{B(z)} \right]. \quad (\text{III.2-23})$$

Average B and ϕ values for the barrier are found assuming parabolic profiles,

$$\langle B \rangle_b = \frac{2}{3} B_b + \frac{1}{6} (B_{\text{maxb}} + B_{\text{maxp}}) \quad (\text{III.2-24})$$

and
$$\langle \phi \rangle_b = \frac{2}{3} \phi_b, \quad (\text{III.2-25})$$

then these are inserted into J_{trap} and also used to find the effective barrier volume $V_b = \pi \langle r \rangle_b^2 L_b$. $\langle r \rangle_b$ is calculated using $\langle B \rangle_b$ in Eq. (III.2-1). The total current of ions scattering into the barrier is then

$$I_{\text{trap}} \approx \frac{2V_b n_c^2}{5.5 \times 10^9 \tau_{ic}^{1/2} B_{\text{maxb}}^2} \left[\frac{\langle B \rangle_b^2 + 0.185 B_{\text{maxb}} \langle B \rangle_b}{\pi \langle \phi \rangle_b + \tau_{ic}} \right]. \quad (\text{III.2-26})$$

This approach agrees well with the values from Ref. 12, Table 1, after compensating for the use in Ref. 12 of 0.55 instead of the more accurate 0.185 in J_{trap} . Total currents tend to be a factor of one to two higher than the Ref. 12 currents, in harmony with the philosophy used here of being slightly pessimistic when estimating uncertain effects.

III.2.4 Central Cell Physics

The calculation of the potential ϕ_c , which confines central cell ions, has been examined in Ref. 13. Passing electrons scattering into the plug and electrons from neutral beam ionization balance the loss of electrons by collisional scattering to parallel energies above the potential $\phi_b + \phi_c$ to give

$$\frac{n_{ew}^2(p)}{(n\tau)_{ep}} \left[1 - \frac{n_{ec}(b)}{n_{ew}(p)} \left(\frac{T_{ep}}{T_{ec}} \right)^{v_c} \exp \left(\frac{\phi_b + \phi_c}{T_{ep}} \right) \right] = \frac{n_p^2}{(n\tau)_{ip}} \quad (\text{III.2-27})$$

$$+ I_{\text{trap}} \sum_{k=1}^3 f_{nk} f_{pk} \frac{\langle \sigma v \rangle_{ionk}}{\langle \sigma v \rangle_{cxk}}$$

where $n_{ew}(p)$ is the density of warm (plug) electrons at point p, $n_{ec}(b)$ is the density of passing central cell electrons at point b, the subscript $k = 1, 2, 3$ labels the barrier pumping neutral beams in order of descending energy, f_{ck} and f_{pk} are the fractions of beam k lying to central cell or plug side of the barrier, $\langle \sigma v \rangle_{ionk}$ and $\langle \sigma v \rangle_{cxk}$ are ionization and charge exchange rates, and f_{nk} is the fraction of trapping current which beam k must pump. When the ions resulting from one beam are pumped into a region where another beam can pump them into the central cell (two stage pumping), f_{nk} for the second region increases and $f_{n1} + f_{n2} + f_{n3} > 1$. The amount of increase is (for beam 1 pumping to the beam 3 region)

$$\Delta f_{n3} = f_{n1} \left(\frac{g_b}{g_b - 1} + \frac{\langle \sigma v \rangle_{ion1}}{\langle \sigma v \rangle_{cx1}} \right) . \quad (\text{III.2-28})$$

Plug electron confinement time is given by

$$(n\tau)_{ep} = \frac{8.2 \times 10^9}{\Lambda_{ep}} \frac{G\left(\frac{B_{maxp}}{B_p}\right)}{I\left(\frac{T_{ep}}{\phi_b + \phi_c}\right)} T_{ep}^{3/2} \exp\left(\frac{\phi_b + \phi_c}{T_{ep}}\right) , \quad (\text{III.2-29})$$

where Λ_{ep} is the plug electron Coulomb logarithm. The first term on the RHS of Eq. (III.2-27) gives the source of plug electrons due to ionization of the plug neutral beam. The second RHS term gives the plug electron source due to pump beam ionization events occurring on the plug side of the barrier potential. The parameter ν_c is 0.5. Unfortunately, $\nu_c = 0.5$ requires, as can be seen in Eq. (III.2-27), a higher value of $n_{ew}(p)$ for a given $n_{ec}(b)$ than $\nu_c = 0$ does, and plug power varies approximately as $n_{ew}^2(p)$.

The main contributors to central cell power are the collisional slowing of fusion alpha particles on ions and electrons, and power from pump beam particles which ionize and enter the central cell. These are chiefly balanced by end loss. The central cell electron power balance is given by

$$\begin{aligned}
 & \frac{n_c^2}{4} \langle \sigma v \rangle_{DT} f_{e\alpha} E_\alpha \left(1 + \frac{E_r}{E_{fus}}\right) V_c + \frac{3}{2} n_c v^{ec/ic} (T_{ic} - T_{ec}) V_c \\
 & + n_c v^{ec/ip} \left(E_p - \frac{3}{2} T_{ec}\right) V_c + \frac{n_p^2}{(n\tau)_{ip}} (\phi_b + T_{ep}) 2V_p \\
 & + 3 \frac{n_{ec}(b) n_{ew}(p)}{(n\tau)_{ep}} \left(\frac{T_{ep}}{T_{ec}}\right)^{v_c} (T_{ep} - T_{ec}) \exp\left(\frac{\phi_b + \phi_c}{T_{ep}}\right) V_p \\
 & + 2 I_{trap} \sum_{k=1}^3 f_{nk} [f_{ck} \phi_{ink} + f_{pk} (\phi_b + T_{ep})] \frac{\langle \sigma v \rangle_{ionk}}{\langle \sigma v \rangle_{cxk}} \\
 & = \left[\frac{n_c^2}{(n\tau)_{ec}} + \frac{n_c^2}{(n\tau)_{xfe}} \right] (\phi_e + T_{ec}) V_c + P_{sc} + P_{br}
 \end{aligned} \tag{III.2-30}$$

where ϕ_{ink} is the potential at which the beam k is aimed, and $(n\tau)_{xfe}$ is the $(n\tau)$ product for electron cross-field diffusion. The equilibrium central cell alpha particle density, n_α , is found by equating alpha particle production to end loss. That is,

$$\frac{(n_c - 2n_\alpha)^2}{4} \langle \sigma v \rangle_{DT} V_c = \frac{n_\alpha^2}{(n\tau)_{\alpha c}} V_c \tag{III.2-31}$$

where, similar to Eq. (III.2-11),

$$(n\tau)_{\alpha c} = \frac{(m_\alpha/2)^{1/2}}{Z_{\alpha c} \pi e^4 \Lambda_\alpha} \frac{G(R_c/2)}{I(T_{ic}/Z_\alpha \phi_c)} T_{ic}^{1/2} z_\alpha \phi_c e^{z_\alpha \phi_c / T_{ic}} \tag{III.2-32}$$

with m_α the alpha particle mass, $\Lambda_\alpha = 20$ the alpha particle Coulomb logarithm, $Z_\alpha \approx .33$, and $z_\alpha = 2$. E_{fus} is the energy output per fusion, and E_r is the average reacting ion energy, taken to be (5)

$$E_r = 45 + \frac{3}{2} T_{ic} \tag{III.2-33}$$

The first term in Eq. (III.2-30) is power from fusion; the second and third terms come from collisional energy transfer; the fourth and fifth terms from conduction and convection of energy between the plug and central cell⁽³⁾; the sixth term from ionization of barrier pumping neutral beams; the seventh term from end loss and cross-field transport; the eighth term from synchrotron radiation; and the last term from Bremsstrahlung.

Central cell ion power balance is given by

$$\begin{aligned} & \frac{(n_c - n_\alpha)^2}{4} \langle \sigma v \rangle_{DT} [f_{i\alpha} E_\alpha (1 + \frac{E_r}{E_{fus}}) - E_r] V_c + P_{ICRH} \\ & + 2 I_{trap} \sum_{k=1}^3 f_{nk} [(1 + \frac{\langle \sigma v \rangle_{ionk}}{\langle \sigma v \rangle_{cxk}}) (E_{ink} - \phi_{ink}) - \frac{3}{2} T_{ic}] \\ & = [\frac{n_c^2}{(n\tau)_{ic}} + \frac{n_c^2}{(n\tau)_{xfi}}] (\phi_c + T_{ic}) V_c + \frac{3}{2} n_c v^{ic/ec} (T_{ic} - T_{ec}) V_c \end{aligned} \quad (III.2-34)$$

where $(n\tau)_{xfi}$ is the ion cross-field $(n\tau)$.

The first term gives power distributed to the ions from alpha particles; the second term gives heating due to ion cyclotron range of frequencies (ICRF) power; the third term comes from neutral beam barrier pumping; the fourth term gives end loss and cross-field transport; and the fifth term gives collisional energy transfer.

Fueling of the central cell must compensate for end loss, cross-field transport, and loss of ions to fusion events. Since TASKA is a relatively low power device, operating points were chosen where ionization events of the barrier pumping neutral beams supply the entire fueling needs of the central cell. This alleviates the requirement of fueling by gas puffing or pellet injection, which are difficult and not well understood. The ion particle

balance is governed by

$$\left[\frac{n_c^2}{(n\tau)_{ic}} + \frac{n_c^2}{(n\tau)_{xfi}} + \frac{n_c^2}{2} \langle \sigma v \rangle_{DT} \right] V_c = 2 I_{\text{trap}} \sum_{k=1}^3 f_{nk} \frac{\langle \sigma v \rangle_{ionk}}{\langle \sigma v \rangle_{cxk}} \quad (\text{III.2-35})$$

III.2.5 Plug Physics

Plug electron power balance is given by

$$\begin{aligned} \frac{P_{\text{eaux}}}{2} + n_{\text{ew}}(p) v^{ep/ip} (E_p - \frac{3}{2} T_{ep}) V_p &= I_{\text{trap}} \sum_{k=1}^3 f_{nk} f_{pk} \frac{\langle \sigma v \rangle_{ionk}}{\langle \sigma v \rangle_{cxk}} (\phi_b - \phi_{ink} \\ &+ T_{ep}) + \frac{3}{2} \frac{n_{ec}(b)n_{\text{ew}}(p)}{(n\tau)_{ep}} \left(\frac{T_{ep}}{T_{ec}} \right)^{v_c} (T_{ep} - T_{ec}) \exp \left(\frac{\phi_b + \phi_c}{T_{ep}} \right) V_p \\ &+ \frac{n_p^2}{(n\tau)_{ip}} (\phi_b + \phi_c + T_{ep}) V_p + P_{sp} + P_{bp} \end{aligned} \quad (\text{III.2-36})$$

P_{eaux} is the total auxiliary heating of plug electrons for both plugs; the second term gives collisional energy transfer; the third term comes from ionization events of the barrier pumping neutral beams; the fourth and fifth terms arise from conduction and convection of energy between the plug and the central cell; P_{sp} is synchrotron power, given by Eq. (III.2-15); and P_{bp} is Bremsstrahlung power, given by Eq. (III.2-16).

Plug ion power balance is given by

$$\begin{aligned} \frac{n_p^2}{(n\tau)_{ip}} (E_{\text{inj}} - E_{\text{out}}) V_p &= \frac{n_p^2}{(n\tau)_{ip}} \frac{\langle \sigma v \rangle_{cxp}}{\langle \sigma v \rangle_{ionp}} (E_p - E_{\text{inj}}) V_p \\ &+ n_p v^{ip/ep} (E_p - \frac{3}{2} T_{ep}) V_p + n_p v^{ip/ec} (E_p - \frac{3}{2} T_{ec}) V_p \end{aligned} \quad (\text{III.2-37})$$

where $\langle\sigma v\rangle_{cxp}$ and $\langle\sigma v\rangle_{ionp}$ are the plug charge exchange and ionization rates. The first term is the power deposited by neutral beams; the second term represents energy lost to charge exchange; and the third and fourth terms give collisional energy transfer.

III.2.6 Input Power

The power required to sustain a single plug is

$$P_{nb}^p = \frac{n_p^2}{(n\tau)_{ip}} E_{inj} V_p \quad (III.2-38)$$

while barrier pumping powers are given by

$$P_{nk}^b = f_{nk} I_{trap} \left(1 + \frac{\langle\sigma v\rangle_{ionk}}{\langle\sigma v\rangle_{cxnk}}\right) E_{ink} \quad (III.2-39)$$

where $k = 1,2,3$ is the beam index. These give the absorbed beam power. Beam trapping fractions are then found using

$$f_{tr} = 1 - \exp \left[\frac{-4.52 \times 10^{-8} n \ell (\langle\sigma v\rangle_{ion} + \langle\sigma v\rangle_{cx})}{(E_{in}/m_i)^{1/2}} \right]. \quad (III.2-40)$$

The expression in square brackets is the ratio of beam path length in the plasma to the mean free path. n is density, ℓ is path length, $\langle\sigma v\rangle_{ion}$ is ionization rate, $\langle\sigma v\rangle_{cx}$ is charge exchange rate, E_{in} is injection energy, and m_i is the ratio of ion mass to proton mass. Injected powers are then given by

$$P_{nk}^{inj} = \frac{P_{nk}}{f_{trk}} \quad (III.2-41)$$

where k is again the beam index.

III.2.7 Numerical Solution of the System of Equations

The equations are solved by conventional iterative methods.⁽¹⁴⁾ The power balance equations, Eqs. (III.2-30), (III.2-36), and (III.2-37) are written as time rate of change equations for temperature or energy. For a given set of input guesses, standard methods are used to simultaneously iterate equations until $dT_{ec}/dt = 0 = dE_p/dt$. Then, the other quantities allowed to vary are updated and the process is repeated until a relative accuracy of about 10^{-4} is reached. Time is thus used as a dummy variable; more care must be exercised if the truly time-dependent behavior is desired. A time-dependent code for solution of this system is presented in Sec. IX.1.

References for Section III.2

1. B. Badger et al., "WITAMIR-I, A Tandem Mirror Reactor Study," University of Wisconsin Fusion Engineering Program Report UWFDM-400 (1980).
2. J.F. Santarius and R.W. Conn, "Power Balance in a Tandem Mirror Reactor with Thermal Barriers," University of Wisconsin Fusion Engineering Program Report UWFDM-340 (1980).
3. D.E. Baldwin, B.G. Logan, and T.C. Simonen, Editors, "Physics Basis for MFTF-B," Lawrence Livermore National Laboratory Report UCID-18496 (1980).
4. F.H. Coensgen, T.C. Simonen, A.K. Chargin, and B.G. Logan, "TMX Upgrade Major Project Proposal," Lawrence Livermore National Laboratory Proposal LLL-PROP-172 (1980).
5. G.A. Carlson et al., "Tandem Mirror Reactor with Thermal Barriers," Lawrence Livermore National Laboratory Report UCRL-52836 (1979).
6. J.F. Santarius and J.D. Callen, "Alpha Particle Ion and Energy Deposition in Tandem Mirrors," University of Wisconsin Fusion Engineering Program Report UWFDM-425 (1981).
7. D.L. Book, NRL Plasma Formulary (1980).
8. B.G. Logan, A.A. Mirin, and M.E. Rensink, "An Analytic Model for Classical Ion Confinement in Tandem Mirror Physics," Nucl. Fus. 20, 1613 (1980).

9. V.P. Pastukhov, "Collisional Losses of Electrons from an Adiabatic Trap in a Plasma with a Positive Potential," Nucl. Fus. 14, 3 (1974).
10. R.H. Cohen, M.E. Rensink, T.A. Cutler, and A.A. Mirin, "Collisional Loss of Electrostatically Confined Species in a Magnetic Mirror," Nucl. Fus. 18, 1229 (1978).
11. B.A. Trubnikov, "Yield Coefficient of Cyclotron Radiation from a Thermonuclear Plasma," ZhETF Pis Red 16, 37 (1972).
12. B.M. Boghosian, D.A. Lappa, and B.G. Logan, "Physics Parameter Calculations for a Tandem Mirror Reactor With Thermal Barriers," Lawrence Livermore National Laboratory Report UCID-18314 (1979).
13. R.H. Cohen, I.B. Bernstein, J.J. Dorning, and G. Rowlands, "Particle and Energy Exchange Between Untrapped and Electrostatically Confined Populations in Magnetic Mirrors," Nucl. Fus. 20, 1421 (1980).
14. IMSL Library Reference Manual, IMSL LIB-008 (1980).

III.3 Special Cases and Parametric Analysis

This section will discuss some of the modes of operation which were considered as alternatives to the TASKA reference design presented in Section III.4. Also, the dependence of selected important parameters on a variety of variables will be examined.

For the reference case, in this section only, the parameters of Tables III.3-1 and III.3-2 are used. This case is very close to the TASKA design point given in Section III.4, but reflects some minor mistakes corrected in the computer program since the plasma physics parameters were frozen on July 31, 1981. The changes were: 1) the central cell ion power balance coefficients for two stage pumping were corrected so as not to subtract the two stage pumped ion twice from the central cell power; and 2) the neutral beam trapping fraction was corrected by dividing the injection energy by particle mass in order to get the correct particle velocity. Parameters not given here are equal to those given in Section III.4 for the TASKA reference case.

The methodology of the parametric variation was that as few parameters as possible were varied when investigating a given variable. When necessary, the ICRF power and occasionally the medium energy neutral beam energy were altered to give beam fueling equal to particle loss. In a few instances, central cell magnetic field had to be lowered slightly in order to reach an equilibrium state.

One of the most difficult problems faced in the TASKA study was finding a suitable means of pumping out ions which become trapped in the barrier region. The most straightforward means is to inject neutral beams into the barrier loss cone so that charge exchange events will give ions which travel into the central cell, and this was chosen for TASKA. Some alternatives are discussed

Table III.3-1. Section III.3 Reference Case Power and Machine Parameters

CC neutral wall load	1.50 MW/m ²
Fusion power	86. MW
CC plasma radius	0.32 m
Average barrier radius	0.20 m
Midplane plug radius	0.29 m
CC magnetic field	2.7 T
<u>Neutral Beams</u>	
Plug: power	5.2 MW
energy	75 keV
angle	20°
Barrier: power	48.6 MW
energy	50 keV
angle	25°
Barrier: power	48.6 MW
energy	50 keV
angle	25°
Barrier: power	0.2 MW
energy	2 keV
angle	45°
ECRF power	15.3 MW
ICRF power	38.5 MW
Total injected power	113 MW

Table III.3-2. Section III.3 Reference Case Plasma Parameters

Central Cell

Density	$1.95 \times 10^{14} \text{ cm}^{-3}$
Alpha particle density	$2.78 \times 10^{12} \text{ cm}^{-3}$
Ion temperature	30. keV
Electron temperature	11.4 keV
$(n\tau)_{ic}$	$5.3 \times 10^{13} \text{ cm}^{-3} \text{ sec}$
$(n\tau)_{ec}$	$5.3 \times 10^{13} \text{ cm}^{-3} \text{ sec}$
Potential, ϕ_c	43 keV

Barrier

Minimum density	$6.8 \times 10^{12} \text{ cm}^{-3}$
Potential, ϕ_b	37.3 keV
High energy pumping fraction	0.025
Medium energy pumping fraction	0.975
Low energy pumping fraction (two stage)	0.109

Plug

Midplane density	$6.3 \times 10^{13} \text{ cm}^{-3}$
Mean ion energy	388 keV
Electron temperature	59.4 keV
$(n\tau)_{ip}$	$2.9 \times 10^{13} \text{ cm}^{-3} \text{ sec}$
$(n\tau)_{ep}$	$7.4 \times 10^{11} \text{ cm}^{-3} \text{ sec}$
Potential, $\phi_c + \phi_e$	109 keV

in Section III.1. However, a number of different neutral beam configurations in the barrier still had to be evaluated. The reference case uses three barrier beams, given in Table III.3-1. The distinctive feature of this method is the use of two stage pumping whereby trapped ions are pumped from the bottom of the barrier to a region where a low energy beam can pump them into the central cell. Parameters for three other possible configurations are given in Tables III.3-3 and III.3-4.

Case A describes a situation where the high energy neutral beam pumping the bottom of the barrier is at a sufficiently small angle with respect to the magnetic field so that charge exchange ions are in the barrier loss cone and reach the central cell in a single step (cf. Eq. III.2-18). Although the parameters for case A are attractive in some respects, engineering considerations effectively prohibit reaching the small angle required for pumping the bottom of the barrier, especially at the required high power. This one stage scheme was used in the WITAMIR-I tandem mirror reactor study⁽¹⁾, but beam lines were very long and central cell blanket access was hampered for over ten meters on each end; this is unacceptable for a test device such as TASKA.

In case B, the low energy beam is eliminated and its function in two stage pumping is assumed by the medium energy beam. Required input power rises dramatically and, since the low energy beam needs only relatively easy technology, the trade-off greatly favors the reference case. Also, the high energy beam now needs a 16° injection angle.

Case C investigates the possibility of aiming the high energy beam into the loss cone from barrier bottom to plug. The mirror ratio involved is then 7.8 instead of 25, although the potential to be overcome is approximately doubled. The charge exchange ions then leave the machine entirely for

Table III.3-3. Power and Machine Parameters

A. HEPB Pumps Directly Into the Central Cell

B. HEPB Pumps to MEPB Region

C. HEPB Pumps Out Over Plug Potential

	<u>Case A</u>	<u>Case B</u>	<u>Case C</u>
CC neutron wall load, MW/m ²	1.50	1.53	1.50
Fusion power, MW	87.	86.	92.
CC plasma radius, m	0.34	0.31	0.36
Average barrier radius, m	0.21	0.19	0.22
Midplane plug radius, m	0.31	0.27	0.32
CC magnetic field, T	2.8	2.6	2.7
<u>Neutral Beams</u>			
Plug: power, MW	7.3	4.8	7.8
energy, keV	250.	250.	250.
angle	60°	60°	60°
Barrier: power, MW	51.6	92.2	58.4
energy, keV	200.	207.	190.
angle	10°	16°	15°
Barrier: power, MW	14.4	80.3	48.4
energy, keV	20.	50.	50.
angle	25°	25°	25°
ECRF power, MW	11.7	14.2	13.6
ICRF power, MW	35.	45.	32.5
Total injected power, MW	120.	237.	161.

Table III.3-4. Plasma Parameters

A. HEPB Pumps Directly Into the Central Cell

B. HEPB Pumps to MEPB Region

C. HEPB Pumps Out Over Plug Potential

	<u>Case A</u>	<u>Case B</u>	<u>Case C</u>
<u>Central Cell</u>			
Density, cm^{-3}	1.93×10^{14}	2.00×10^{14}	1.85×10^{14}
Alpha density, cm^{-3}	4.8×10^{12}	1.1×10^{12}	3.9×10^{12}
Ion temperature, cm^{-3}	30.	30.	30.
Electron temperature, cm^{-3}	13.8	8.7	12.9
$(n\tau)_{iC}$, $\text{cm}^{-3} \text{ sec}$	7.7×10^{13}	3.0×10^{13}	6.9×10^{13}
$(n\tau)_{eC}$, cm, sec	7.5×10^{13}	2.9×10^{13}	6.4×10^{13}
Potential, ϕ_C , keV	49.1	32.8	47.1
<u>Barrier</u>			
Minimum density, cm^{-3}	6.2×10^{12}	8.0×10^{12}	6.2×10^{12}
Potential, ϕ_B , keV	46.2	27.2	42.7
HEPB fraction	0.025	0.025	.025
MEPB fraction	0.975	1.37	.975
		(two stage)	
<u>Plug</u>			
Midplane density, cm^{-3}	6.2×10^{13}	7.0×10^{13}	6.4×10^{13}
Mean ion energy, keV	388.	357.	383.
Electron temperature, keV	63.5	45.1	58.1
$(n\tau)_{ip}$	2.5×10^{13}	3.2×10^{13}	2.6×10^{13}
$(n\tau)_{ep}$	9.6×10^{11}	4.9×10^{11}	8.9×10^{11}
Potential, $\phi_C + \phi_e$, keV	130	81.3	121.7

sufficiently energetic ions. Unfortunately, as seen in Table III.3-3, the required total power is very large, primarily because the high energy beam pumps energy from the barrier and thus from the central cell while giving no energy to the central cell. The injection angle of 15° is even more of a problem, as it is very difficult to reach.

A disadvantage shared by cases A, B, and C is that the high energy pump beam is both high energy and high power, in contrast to the moderate energy, low power beam of the reference case two stage pumping scheme. Construction of the reference case is thus far easier.

The low energy pump beam is very efficient, and some tandem mirror designs do a large fraction of the barrier pumping by this beam.⁽²⁾ There is a disadvantage associated with the low energy beam, however: electrons resulting from ionization events are born on the plug side of the barrier bottom. These electrons eventually must be heated to the ambient plug electron temperature, resulting in an increase in required plug electron cyclotron range of frequencies (ECRF) heating. This is shown in Fig. III.3-1, where total input power and plug ECRF power are plotted vs. fraction of pumping done by the low energy pump beam. Two stage ions are not counted in this graph. For the same reason, although the powers involved are relatively small for the reference case, it is advantageous to aim the footprint of the beam pumping the barrier bottom to overlap the central cell side of the potential to as great a degree as possible.

The medium energy pump beam, which does the majority of the barrier pumping, plays a large role in central cell ion energy and particle balance. If, as in the case where there is no auxiliary heating of central cell ions, it functions as the primary source controlling each of those processes, there

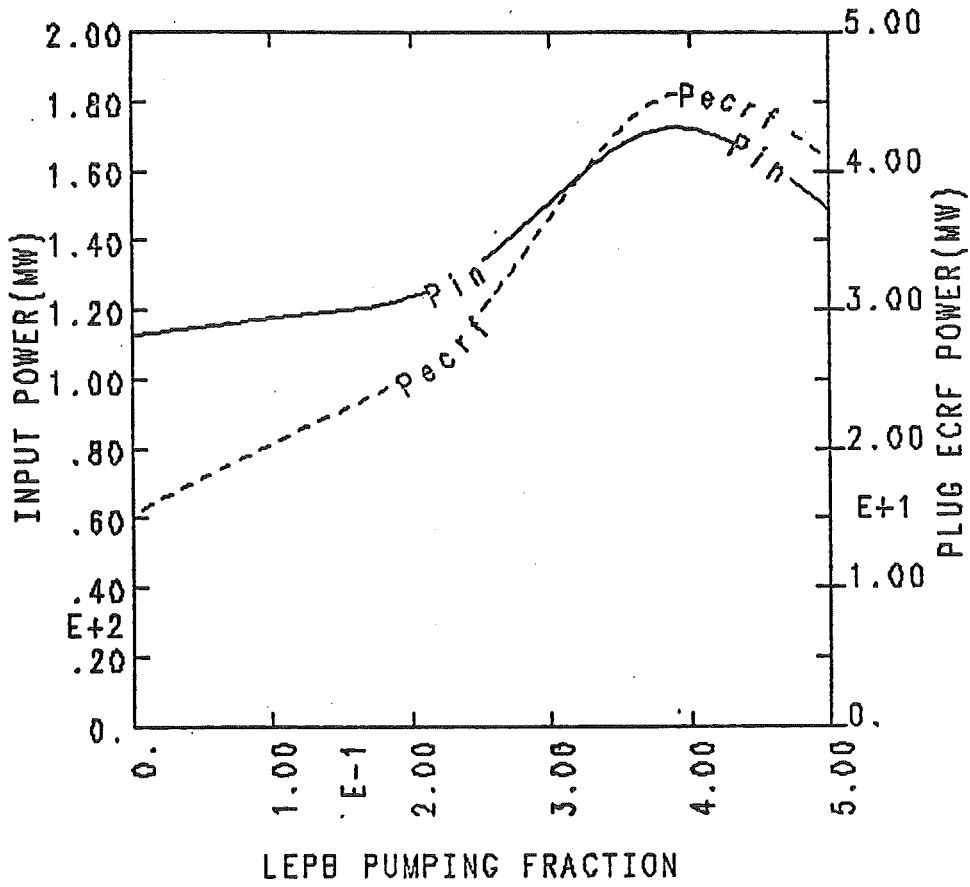


Fig. III.3-1. Total input power and plug ECRF power vs. fraction of pumping done by the low energy pump beam.

exists little flexibility in choosing an operating point and it is difficult to find an attractive reference case. Figure III.3-2 shows the trade-off between total input power, medium energy pump beam energy, and central cell ion cyclotron range of frequencies (ICRF) heating power. In addition, there is a tradeoff between the complexity of adding an ICRF launching system and the difficulties of building a very high power neutral beam system in a region where space is limited.

The high energy beam which pumps the bottom of the barrier is very difficult to fit physically into the machine, as discussed in Section IV.3. This is chiefly due to the small angle with respect to the magnetic field which the beam must achieve. In order to reach the low energy pumping point at a magnetic field of 3 T, the beam must fit within a loss cone of 31° . Since the energy required for the beam is governed by Eq. (III.2-18), values approaching the loss cone are difficult to achieve. Figure III.3-3 shows the dependence of input power on high energy beam angle.

Injection of neutral beams into the plug is somewhat easier in terms of access, but achieving the required energy is very difficult without invoking negative ion technology. High energy is required in order to overcome the effective potential $(\phi_c + \phi_e)/(R_p \sin^2 \theta_{in} - 1) = 114 \text{ keV}$. R_p is the beta-corrected plug mirror ratio. For reasonable plug beam input power, neutral beam energies greater than 200 keV are required. The dependence of total input power and plug power on injection energy for injection at a 90° angle is shown in Fig. III.3-4. Injection angle is also critical since a sloshing ion distribution is necessary for plug microstability as discussed in Section III.1. Powers do not vary greatly until the loss cone is approached; they then rise sharply. Total input power and plug neutral beam power are given as a

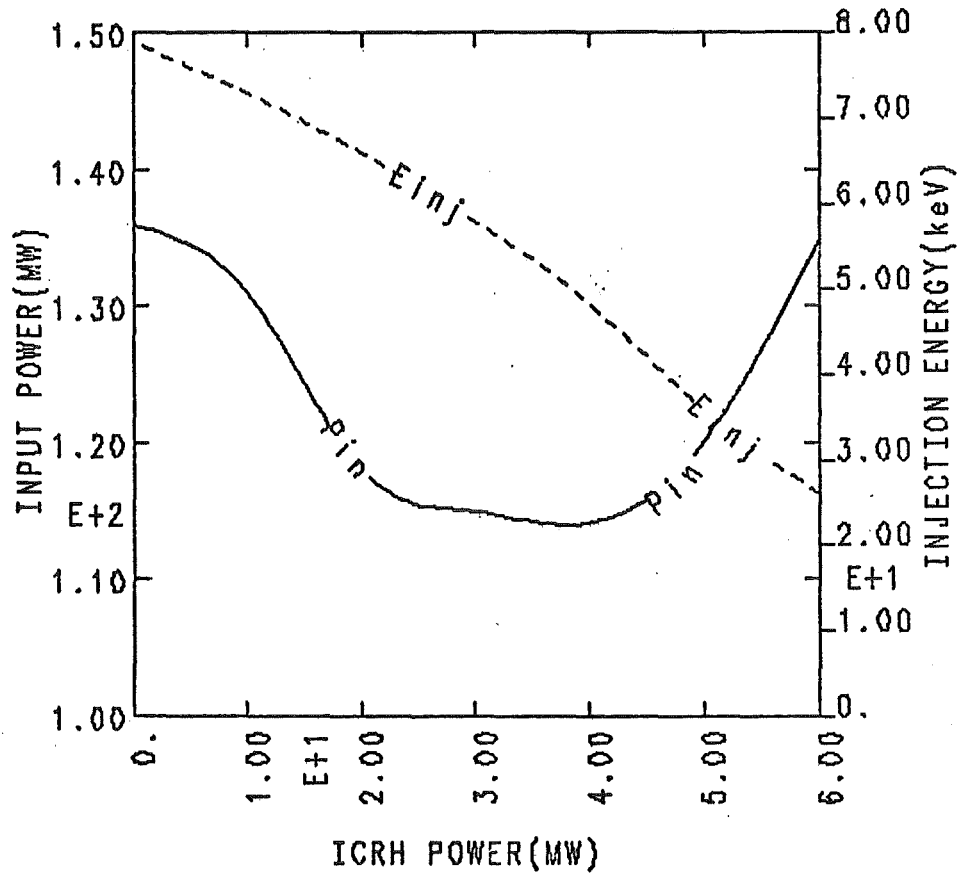


Fig. III.3-2. Total input power and medium energy pump beam energy vs. ICRF power.

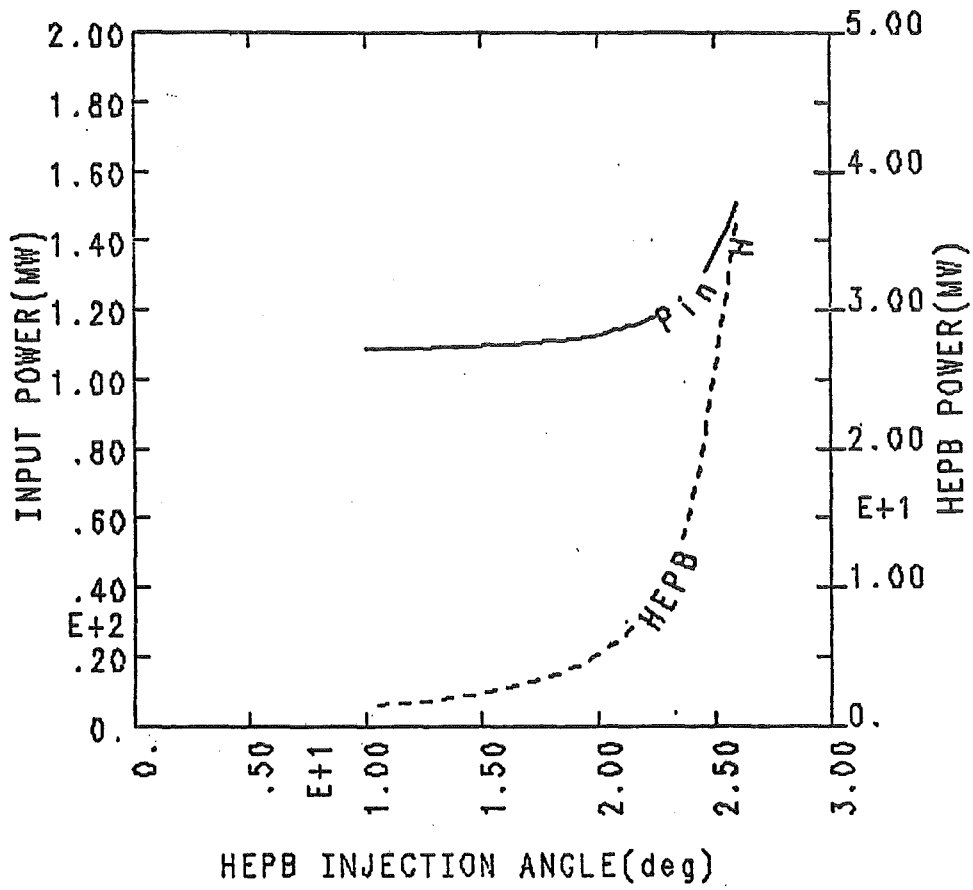


Fig. III.3-3, Total input power and high energy pump beam power vs. high energy beam injection angle.

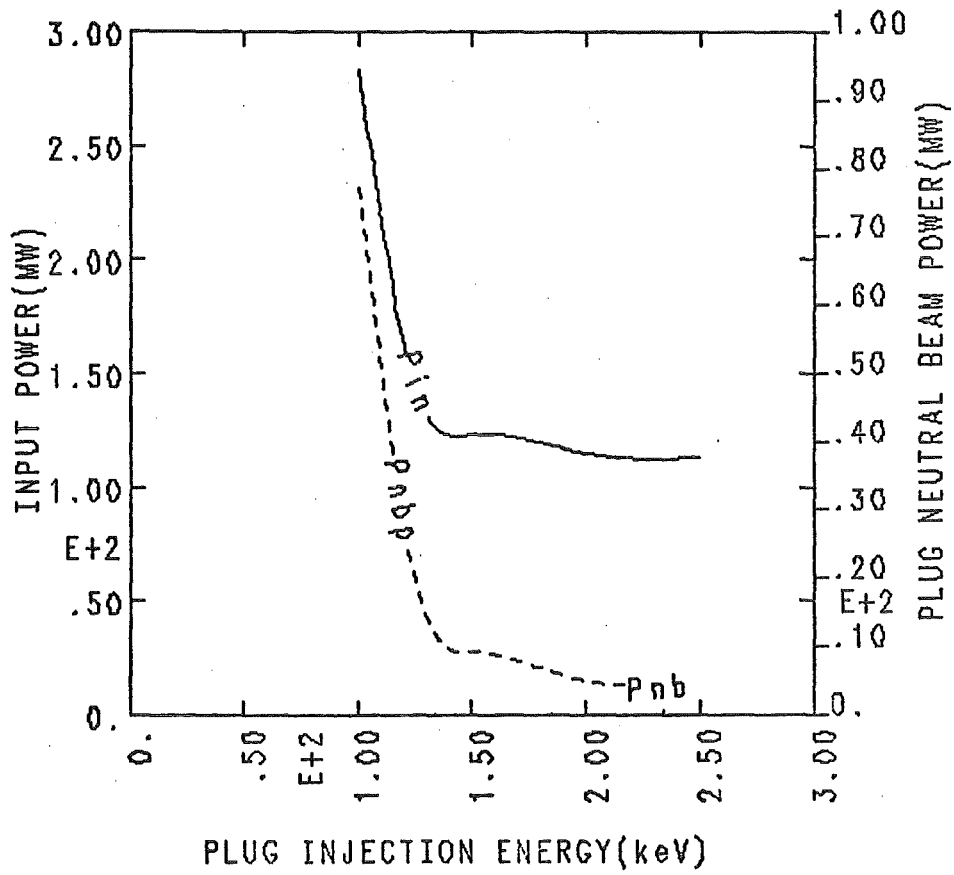


Fig. III.3-4. Total input power and plug beam power vs. plug injection energy for injection at a 90° angle.

function of plug beam injection angle in Fig. III.3-5. A possible means of achieving high plug beam energy without invoking negative ion technology is the use of non-hydrogen beams. Since approximately 100 keV/amu is attainable with positive ion technology, even helium could reach the desired energies. Suitably modifying the plug physics,⁽³⁾ helium beams lead to a total machine input power of about 135 MW. As discussed in Section III.1 and Ref. 3, there is little chance for the He atoms to contaminate the central cell since the plug ions are well-separated from the rest of the machine in phase space.

Flexibility exists in choosing an operating point in terms of total input power and wall loading. The maximum wall loading attainable depends, to a great extent, on how high an input power level is allowed by economic or engineering constraints. The trade-off is shown in Fig. III.3-6 for barrier mirror ratios of 32.5, 25, and 17.5. The minimum barrier field is kept constant at 0.8 T here. To achieve the reference case mirror ratio of 25, a copper insert has been added to the superconducting barrier coil as discussed in Chapter V. Thus, the penalties for using a high barrier mirror ratio are that the technology becomes more complicated and difficult, and that power must now be expended to run the normal-conducting copper insert. Figure III.3-6 shows that there is a net gain in going from the $R_b = 17.5$ case where no copper insert is needed to the $R_b = 25$ case where approximately 60 MW of extra line power is needed, since the power needed to run the copper inserts is much lower grade and less expensive than that needed for neutral beams or RF sources.

Two other variations of barrier fields have been investigated. First, $B_{\max b}$ was held constant while B_b was lowered. The resulting higher mirror ratios give a smaller trapping rate into the potential well since barrier

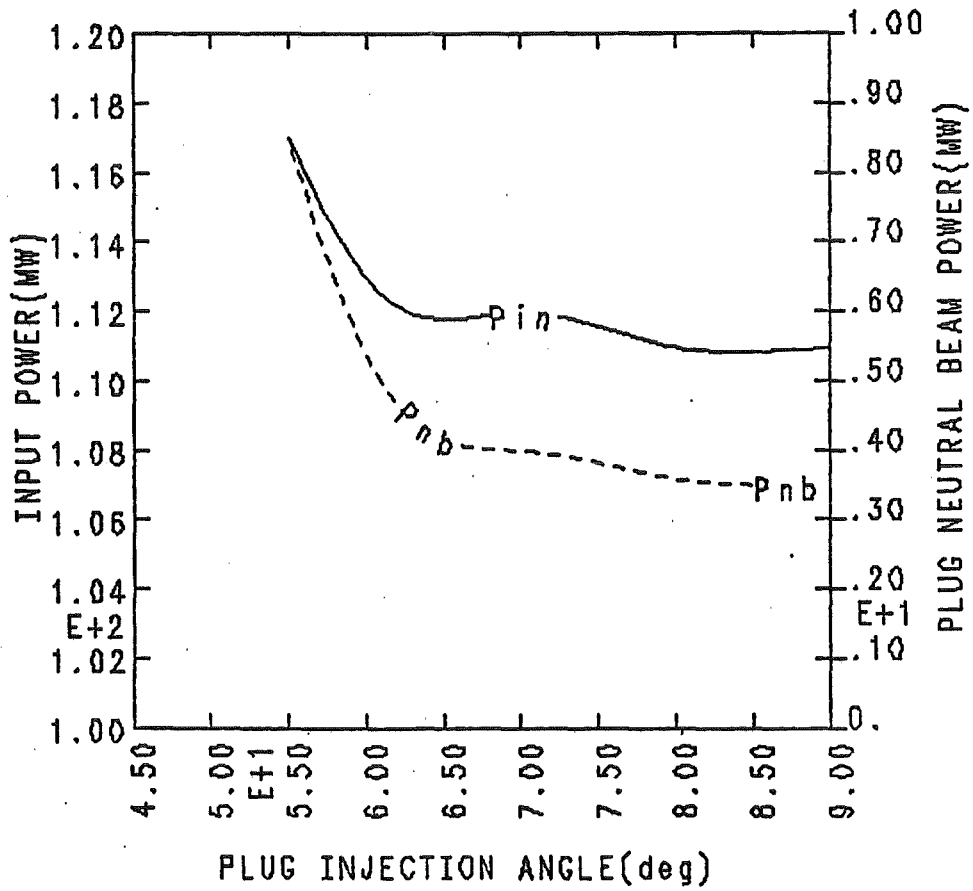


Fig. III.3-5. Total input power and plug beam power vs. plug injection angle.

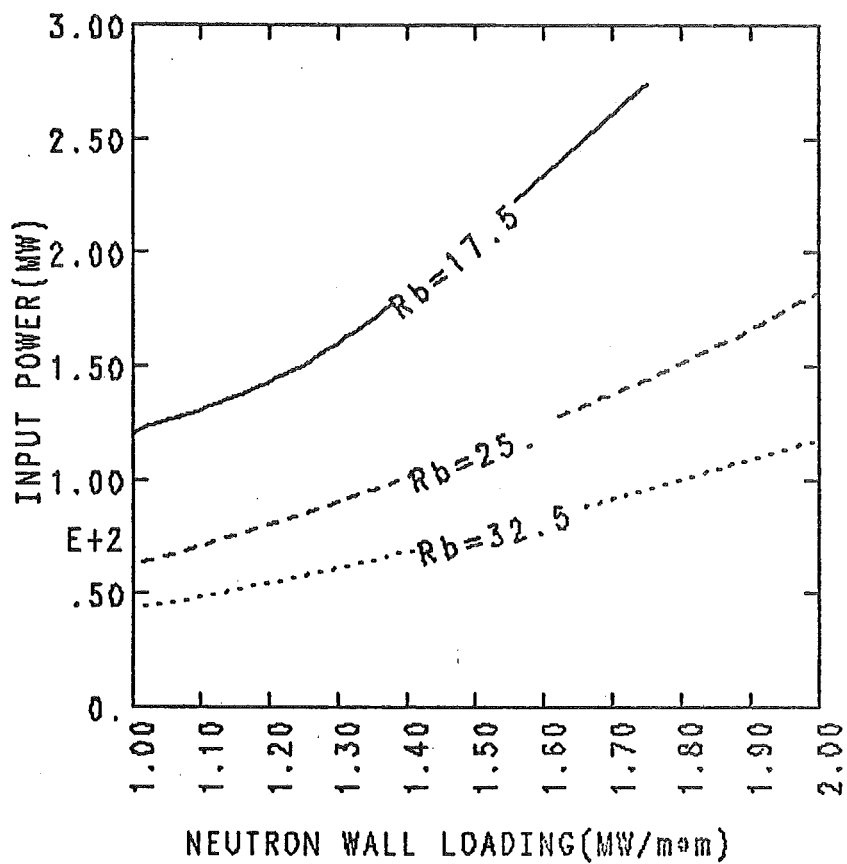


Fig. III.3-6. Total input power vs. neutron wall loading for barrier mirror ratios of 17.5, 25, and 32.5

density is reduced but, unfortunately, the beam trapping fraction is likewise reduced and no total power savings is achieved. Second, the barrier mirror ratio was held constant while varying the magnitudes of B_{maxb} and B_{b} . Changing these from 20 T and 0.8 T to 17.5 T and 0.7 T led to an increase in total input power of 11 MW. Lower field cases required even more power. This result is due to slightly poorer mirror confinement of central cell particles and to the larger mirror ratio which the two-stage pumping process must then overcome.

Central cell beta is important because high beta allows efficient utilization of the magnetic field. As central cell beta rises, total input power drops, as shown in Fig. III.3-7. Similar behavior occurs as B_{c} varies, a low B_{c} implying low density by Eq. (III.2-2). Input power and central cell density vs. B_{c} are plotted in Fig. III.3-8.

Central cell alpha particle density is allowed to reach an equilibrium level as described in Section III.2. Figure III.3-9, where the alpha particle fraction is legislated to various values, shows that only a few percent of alpha particles are tolerable before machine performance is seriously degraded.

The reference point design assumes that essentially all central cell particle loss will be end loss. A very small amount of classical, collisional radial transport will also occur. Some resonant transport⁽⁴⁾ may take place but, since this is driven by magnetic flux tube azimuthal asymmetry in particle bounce regions and most central cell ions turn near the barrier solenoids, little effect is expected. Another possible cause of transport is that the use of ferritic steel in central cell blanket regions of finite length gives non-circular flux tubes, as discussed in Section V.9. When mapped into the

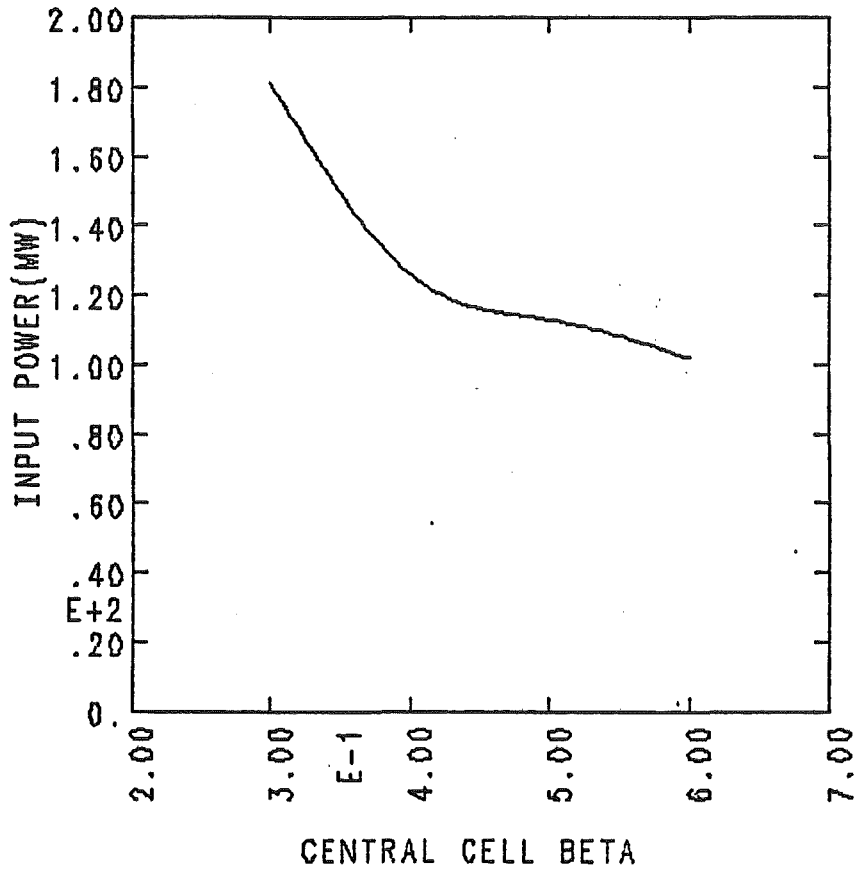


Fig. III.3-7. Total input power vs. central cell beta.

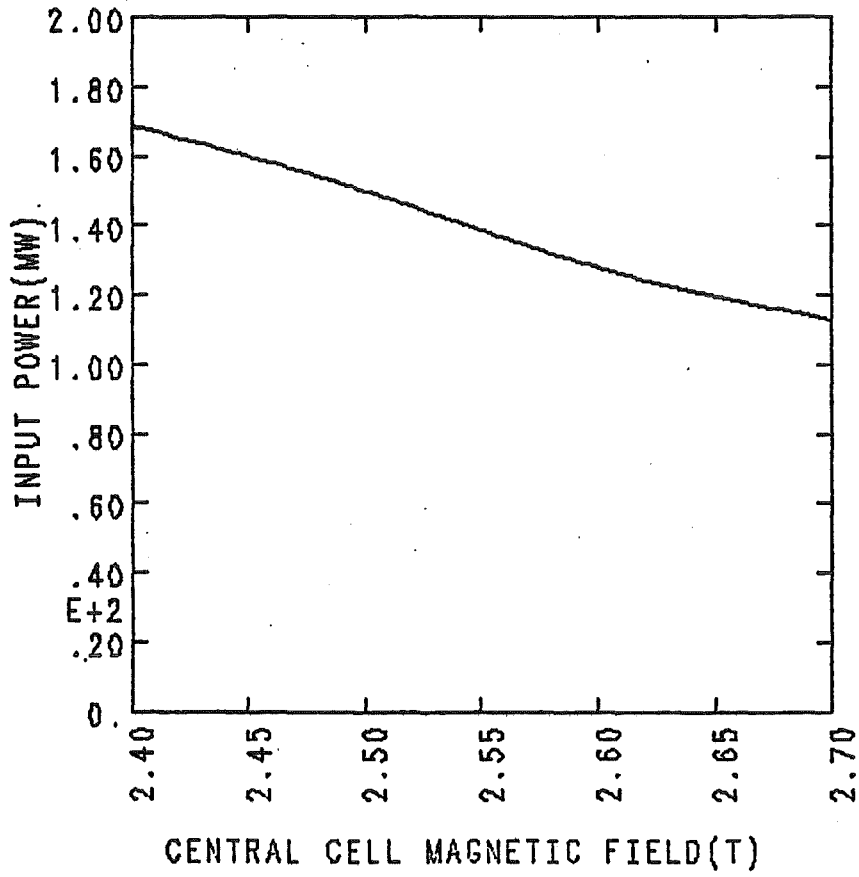


Fig. III.3-8. Total input power vs. central cell magnetic field.

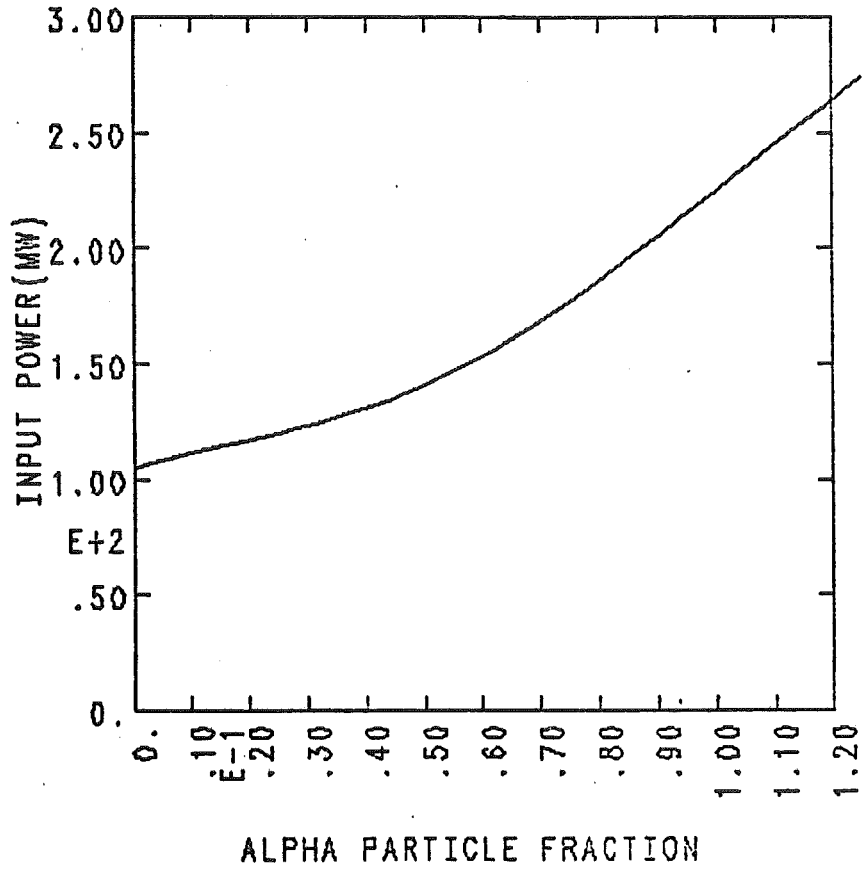


Fig. III.3-9. Total input power versus central cell alpha particle fraction.

bounce regions, this asymmetry is a small perturbation of the magnetic field and thus should have a small effect on resonant transport.⁽⁵⁾ However, the large radial excursions due to flux tube asymmetry can lead to enhanced diffusion since the random walk step size is proportional to the excursion. Estimates of the diffusion and allowed asymmetry are discussed in Appendix III.3-A. The effect of cross field transport on total input power is shown in Fig. III.3-10. Surprisingly, a cross field loss time equal to only four times the end loss time does not lead to a large increase in input power.

The central cell ion temperature has a broad optimum at about 30 keV. Two major effects are involved: 1) For low temperatures, the trapping rate into the barrier is high and barrier pumping power becomes excessive; and 2) for high temperatures, required neutral beam injection energies become large since potentials vary approximately as temperatures. The dependence of total input power and plug injection energy on central cell ion temperature is shown in Fig. III.3-11.

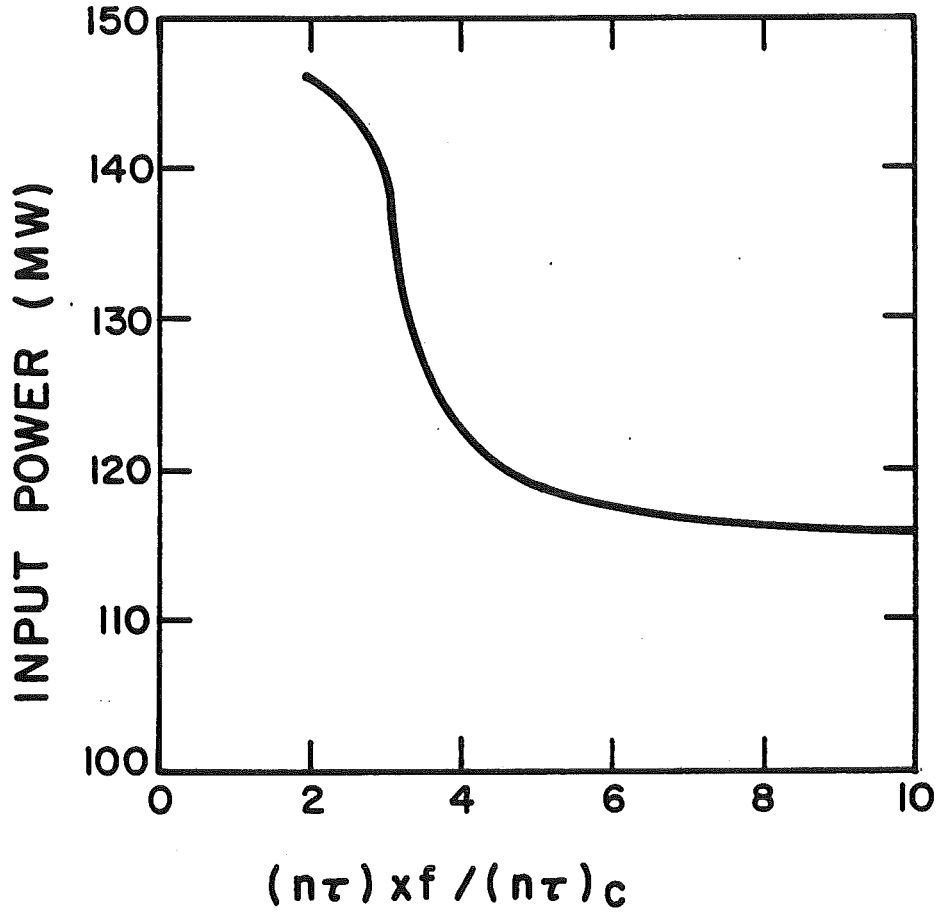


Fig. III.3-10. Total input power versus $(n\tau)_{xf}/(n\tau)_c$ (\equiv cross field diffusion time/end loss time).

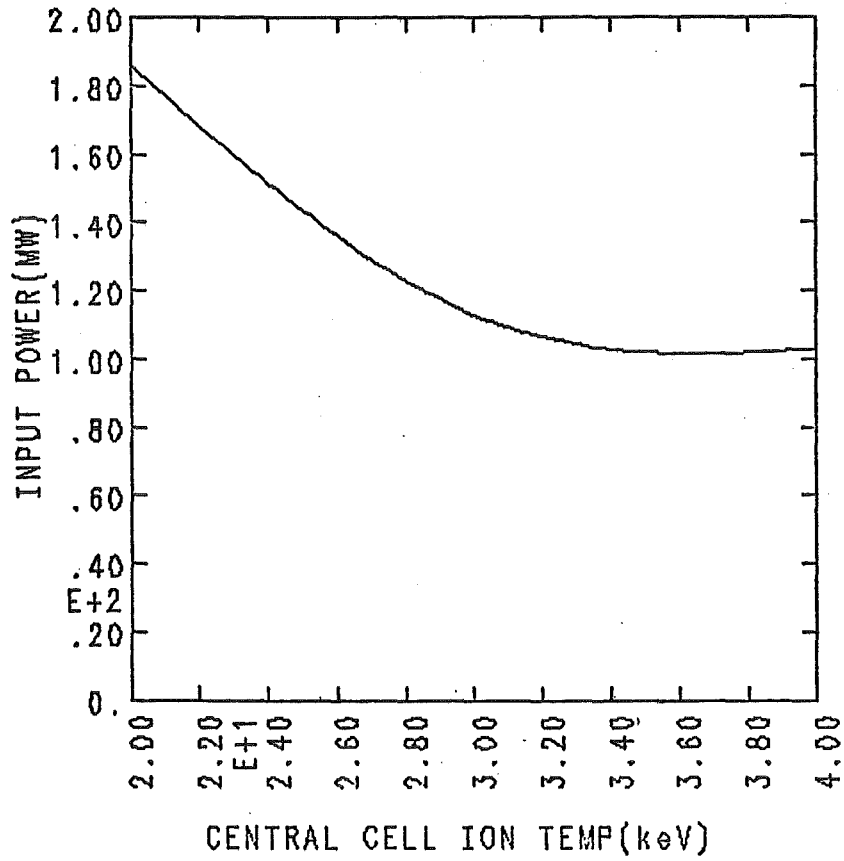


Fig. III.3-11. Total input power and plug injection energy vs. central cell ion temperature.

References for Section III.3

1. B. Badger, et al., "WITAMIR-I, A Tandem Mirror Reactor Design Study," University of Wisconsin Fusion Engineering Program Report UWFD-400 (1980).
2. D.E. Baldwin, B.G. Logan, and T.C. Simonen, "Physics Basis for MFTF-B," Lawrence Livermore National Laboratory Report UCID-18496 (1980).
3. D.E. Post, T.R. Grisham, J.F. Santarius, and G.A. Emmert, "Heavy Atom Neutral Beams for Tandem Mirror End Plugs," Princeton Plasma Physics Laboratory Report PPPL-1786 (1981) (submitted to Nuclear Fusion).
4. R.H. Cohen, "Analytic Approximation to Resonant Plateau Transport Coefficients for Tandem Mirrors," Nucl. Fus. 19, 1579 (1979).
5. B.G. Logan, private communication.

Appendix III.3-A

Radial Transport Due to Central Cell Flux Tube Asymmetry

Some central cell asymmetry is expected due to ferritic steel in the blanket module, as discussed in Section V.9. This can enhance collisional diffusion since, while following a flux surface, a particle may experience an appreciable radial excursion between collisions. A rough estimate for diffusion due to a general asymmetry, plus a calculation for a TASKA blanket will be presented here.

For the reference case,

$$\tau_{\theta} \lesssim \tau_b \ll \tau_i \quad (1)$$

where τ_{θ} is the azimuthal drift time, τ_i is the central cell ion collision time, τ_b is the ion bounce time. A gradient of the magnetic field, B , then gives a radial drift velocity of

$$V_{dr} = \frac{T_{ic} c}{q} \left(\frac{\tilde{B} \times \nabla B}{B^3} \right)_r \sim \frac{\mu c}{qr_c} \frac{\tilde{B}}{B} \quad (2)$$

where μ is the ion magnetic moment, q is the ion charge, c is the speed of light, and \tilde{B} is the magnetic field perturbation over an angle of $\theta \sim 1$. For TASKA parameters,

$$V_{dr} \sim 4.8 \times 10^6 \frac{\tilde{B}}{B} \text{ cm/sec} . \quad (3)$$

Since $\tau_{\theta} \lesssim \tau_b$, the random walk radial diffusion process can be looked at as occurring with step size

$$\delta r \sim \frac{V_{dr}}{4} \tau_{\theta} \sim 7.7 \frac{\tilde{B}}{B} \text{ cm} \quad (4)$$

where the factor of 4 is a crude attempt at averaging. Then, assuming the randomization occurs on the collisional time scale, the diffusion coefficient due to \tilde{B} may roughly be taken to be

$$D \sim \frac{(\delta r)^2}{\tau_i} \sim 2.1 \times 10^3 \left(\frac{\tilde{B}}{B}\right)^2 \frac{\text{cm}^2}{\text{sec}} \quad (5)$$

and the radial loss time is

$$\tau_r \sim \frac{r_c^2}{2D} \sim 0.24 \left(\frac{B}{\tilde{B}}\right)^2 \text{ sec} . \quad (6)$$

The axial loss time is

$$\tau_{ic} = \frac{(n\tau)_{ic}}{n_c} = 0.28 \text{ sec} . \quad (7)$$

For good confinement, a rough estimate is $\tau_r \sim 10 \tau_{ic}$ which leads to an allowed value of

$$\frac{\tilde{B}}{B} \lesssim 0.29 .$$

This should be easy to satisfy, although a more detailed analysis is needed before definite conclusions are drawn.

In any case, the TASKA blanket designs lead to much lower values of V_{dr} , as shown by $\tilde{B} \times \nabla B/B^3$ values presented in Section V.9. The reference case,

almost-symmetric blanket module leads to a maximum $D \sim 10^{-5} \text{ cm}^2/\text{sec}$. This is less than the estimate given in Eq. (5) unless $\tilde{\delta}/B$ is negligibly small.

Thus, radial diffusion due to central cell magnetic flux tube asymmetry induced by ferritic steel blanket modules seems to be of little concern for TASKA or similar devices.

III.4 TASKA Design Point

The plasma physics reference point parameters were set on July 31, 1981 so that work on related engineering systems could proceed. TASKA design point parameters are given in Tables III.4-1, III.4-2, and III.4-3. Note that the physics model is based on present theoretical knowledge of mirror plasmas, some of which has not yet been completely experimentally verified. Experiments currently under construction will address these questions. Major changes in theoretical understanding would, of course, alter the design point significantly.

The basic philosophy behind the choice of these parameters was to find the simplest, least expensive system which would achieve the technological goals. Since one of the primary functions of TASKA is materials testing, a central cell neutron wall loading of at least 1 MW/m^2 was sought while an attempt was made to minimize input power, magnet technology, physical size, beam technology, and ECRF technology. Because TASKA reaches the reactor regime for temperature and density, achieving a high plasma Q value is not a concern; large Q's are obtained primarily by using a long central cell.

Thus, the search for a TASKA operating point was constrained within fairly well-defined parametric boundaries by a number of variables. The chief boundaries were defined by the following considerations:

- 1) For economic reasons, the neutron wall loading of $> 1 \text{ MW/m}^2$ had to be achieved by using on the order of or less than 100 MW of input power. Minimizing ECRF power is particularly important, since its cost seems likely to be higher than that for other sources.

- 2) For magnetic field coils on the 1990's time scale (see Chap. V) a maximum of 6.25 T on the yin-yang axis was deemed possible. The minimum of

Table III.4-1. TASKA Power and Machine Parameters

CC neutron wall load	1.52 MW/m ²
Fusion power	86. MW
CC plasma power density	17. MW/m ³
Q (fusion power/injected power)	0.74

Central Cell

Length (peak to peak B)	19.2 m
Plasma radius	0.32 m
Minimum wall radius	0.46 m

Barrier

Physical length	15.6 m
Effective length	9.0 m
Minimum plasma radius	0.099 m
Average plasma radius	0.20 m
Maximum plasma radius	0.50 m

Plug

Length	5.0 m
Midplane radius	0.28 m

Magnetic Fields

Central cell	2.7 T
Barrier maximum	20. T
Barrier minimum	0.8 T
Plug maximum	6.25 T
Plug minimum	4. T

Table III.4-2. TASKA Heating Parameters

Neutral Beams

Plug:	power	5.4 MW
	energy	250. keV
	angle	60°
	species	p
	trapping fraction	0.21
Barrier:	power	6.6 MW
	energy	76 keV
	angle	20°
	species	d
	trapping fraction	0.42
Barrier:	power	49.7 MW
	energy	50 keV
	angle	25°
	species	0.44 d/0.56 t
	trapping fraction	0.95
Barrier:	power	0.2 MW
	energy	2. keV
	angle	45°
	species	d
	trapping fraction	0.99

ECRF

Plug:	power	14.9 MW
	frequency	56. GHz
	absorption efficiency	1.

ICRF

Central cell:	power	40. MW
	frequency	30 MHz
	absorption efficiency	0.8

Total Injected Power 117. MW

NB: Plug and barrier powers are total powers for both sides.

Table III.4-3. TASKA Plasma Physics Parameters

Central Cell

Density	$1.94 \times 10^{14} \text{ cm}^{-3}$
Alpha particle density	$1.6 \times 10^{12} \text{ cm}^{-3}$
Ion temperature	30. keV
Electron temperature	11.5 keV
Beta	0.5
$(n\tau)_{ic}$	$5.4 \times 10^{13} \text{ cm}^{-3} \text{ sec}$
$(n\tau)_{ec}$	$5.3 \times 10^{13} \text{ cm}^{-3} \text{ sec}$
Potential, ϕ_c	42.8 keV

Barrier

Minimum density	$6.8 \times 10^{12} \text{ cm}^{-3}$
Beta	0.054
Potential, ϕ_b	37.5 keV
Pumping parameter, g_b	2.
High energy pumping fraction	0.025
Medium energy pumping fraction	0.975
Low energy pumping fraction (two stage ions)	0.109

Plug

Midplane density	$6.3 \times 10^{13} \text{ cm}^{-3}$
Mean ion energy	388. keV
Electron temperature	59.3 keV
Beta	0.64
$(n\tau)_{ip}$	$2.9 \times 10^{13} \text{ cm}^{-3} \text{ sec}$
$(n\tau)_{ep}$	$7.5 \times 10^{11} \text{ cm}^{-3} \text{ sec}$
Potential, $\phi_c + \phi_e$	109. keV
Cohen parameter, v_c	0.5

4 T was chosen to give a reasonably high mirror ratio at which to aim the sloshing ion neutral beam, while allowing a fairly high plug density which allows a high central cell density. On the solenoidal barrier coil, 14 T on axis is created by the superconductor; the total possible barrier maximum field then depends on trade-offs between the field desired, power costs in the normal conducting insert coil, and neutron shielding needed. An operating point of 20 T was chosen as a suitable compromise, for reasons discussed in Chapter V and Section III.3.

3) Constraints are also associated with the neutral beam systems. As mentioned in Sections III.3 and IV.3, injection angles are extremely critical. The medium energy pump beam requires a 10 cm plasma radius for all of the beam to intersect the plasma; when magnetic flux tube conservation is taken into account, this translates into a central cell plasma radius of at least 32 cm for $B_c = 2.7$ T. Injection energy is also a problem, particularly for the plug beam where energies greater than 200 keV are required (cf. Fig. III.3-4). The use of helium plug beams was considered because positive ion neutral beam technology could be used, as mentioned in Section III.3, but was rejected, primarily because of vacuum pumping difficulties.

4) Fueling the plasma also creates something of a dilemma, since the high plasma densities and temperatures make source penetration very difficult. For TASKA, since neutral beam ionization does a large amount of fueling, plasma and power parameters are adjusted to give particle loss equal to neutral beam fueling. This somewhat limits flexibility in choosing operating points, but more than balances difficulties with gas puff or pellet fueling. Since the low energy and high energy pump beams do only a small amount of the fueling, only the medium energy beam contains significant amounts of tritium,

with the percentage of tritium to deuterium set to give 50% total fueling of each species. This obviates the necessity of handling large amounts of tritium in the low and high energy pump beam systems.

A central cell neutron wall loading of 1.5 MW/m^2 was chosen since the total input power requirement of 117 MW is not prohibitive. The central cell length was set by consideration of space requirements for materials testing and tritium breeding.

Because of magnetic flux tube conservation, the plasma radius decreases in the central cell end regions, thus decreasing fusion power output and neutron wall loading there. This is modelled here by using an effective central cell length of 15.7 m to compute central cell volume.

Central cell wall radius was defined by the requirement that there be a distance of two 3.5 MeV alpha particle Larmor radii between the plasma and the wall; this insures that alpha particle orbits do not intersect the wall. Unfortunately, after the plasma physics parameters were set, it was discovered that the Larmor radius used was too small by a factor of $\sqrt{2}$. For a flat density profile, the resultant flux of alpha particles' can seriously damage the first wall. However, increasing the first wall radius by 4 cm removes the problem without greatly modifying the design.

Central cell ion cyclotron range of frequencies heating (ICRF) is used because, as shown in Fig. III.3-2, it reduces total power and beam injection energy. Also, ICRF technology needed for TASKA is state-of-the-art and would require very little development (see Section IV.2). Reducing power requirements for the medium energy pump beam is a significant advantage, too, since even the reference case beams for TASKA are non-trivial.

The central cell ion temperature was chosen as a compromise between low temperature, where the barrier ion trapping rate becomes formidable, and high temperature, where required pumping energies become very high.

Plug beta was chosen as a typical value for this type of magnetic field configuration. Central cell beta was chosen somewhat conservatively, since finite Larmor radius MHD theory is still in a state of flux.

The barrier pumping parameter, g_b , was chosen equal to two as a reasonable value, but detailed calculations of g_b are very difficult and have not been attempted here.

In summary, the TASKA design point is a major step beyond present devices, but is an achievable and reasonable one. The inside-barrier tandem mirror configuration thus appears to possess good potential as an engineering and materials test facility.

III.5 The DT Fuel Ion Density in the Thermal Barrier and Plug

The TASKA tandem mirror configuration utilizes an inboard thermal barrier with a yin-yang plug. The plug ions were chosen to be protons in order to avoid fusion reactions in the plug and thereby reduce the neutron shielding requirements for the yin-yang magnets and the degree of neutron streaming through penetrations, such as neutral beam lines, and into the direct converter. The fuel ions, deuterium and tritium, from the central cell pass through the thermal barrier and are reflected by the rising potential in the plug. This will produce some rate of DT fusion in the barrier and plug; the 14 MeV neutron source in the plug cannot be entirely eliminated by choosing a non-reacting plug plasma. In this section we estimate the density of deuterium and tritium in the barrier and plug in order to provide a neutron source for neutronics calculations.

In a previous report,⁽¹⁾ we calculated the potential profile in the thermal barrier. Implicit in this was the calculation of the ion density profile, although explicit results were not obtained. Here we utilize the same formalism to calculate explicitly the fuel density (deuterium plus tritium) in the barrier and plug.

The barrier and plug region is divided axially into three regions, as shown in Fig. III.5-1. Region I spans from the barrier throat (peak magnetic field) to the point of minimum field. In this region the electrons are assumed to be Maxwellian with temperature T_{ec} , which is the same as in the central cell. The passing ions are assumed to be Maxwellian in the appropriate region of velocity space. The trapped ions in the barrier will not be calculated explicitly, although their effect is discussed later.

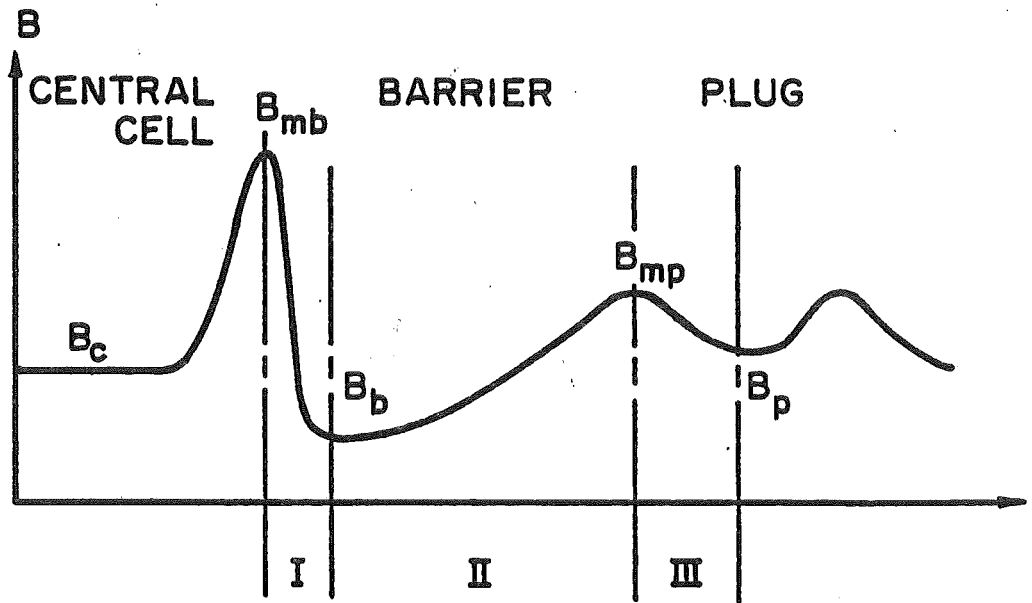


Fig. III.5-1. Axial profile of the magnetic field in the inboard thermal barrier and plug.

Region II spans from the barrier minimum to the throat of the plug. The ion distribution function in this region is determined by the choice in Region I; it cannot be chosen independently. The electrons in this region consist of three "classes": electrons coming from the central cell, from the plug, and electrons trapped by the barrier potential at one end and by the magnetic field, B_{mp} , at the other end. The latter class is analogous to Yushmanov⁽²⁾ trapped ions in mirrors, and are referred to here as Yushmanov electrons. The phase space for electrons in Region II is shown in Fig. III.5-2. The electron distribution function is taken to be piece-wise Maxwellian at different temperatures. Electrons in zones M and N of Fig. III.5-2 come from Region I and are therefore assigned the temperature, T_{ec} . Electrons in zone K come from the plug and are therefore assigned the plug temperature, T_{ep} . Electrons in zone L are the Yushmanov electrons; they are assigned the temperature T_{ec} under the assumption that their energy exchange is more rapid with central cell electrons than with plug electrons.

Region III is between the plug mirror throat and the plug midplane. As long as the potential profile in Region III is not calculated, we need not specify the hot ion distribution function in the plug. The midplane electron density and potential are needed, however, to calculate the contribution of plug electrons to Region II. These are taken as input data.

The calculational procedure is to integrate over the ion and electron distribution functions to obtain the local electron and ion density as functions of the local magnetic field and potential. These are shown in Figs. III.5-3 and III.5-4. The assumption of quasi-neutrality ($n_i(\phi, B) = n_e(\phi, B)$) then determines explicitly the potential and ion density as functions of B .

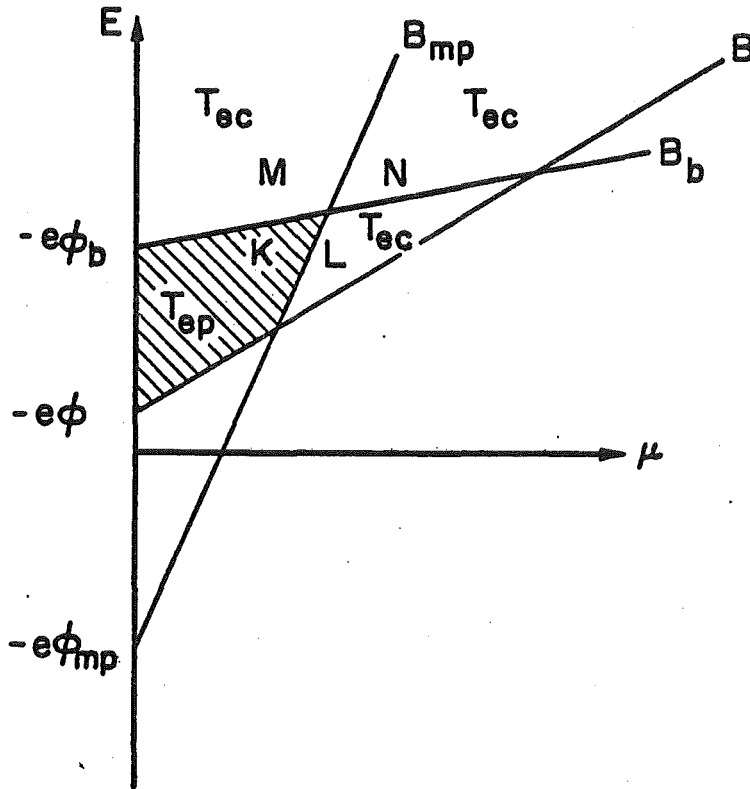


Fig. III.5-2. Phase space for electrons in Region II.

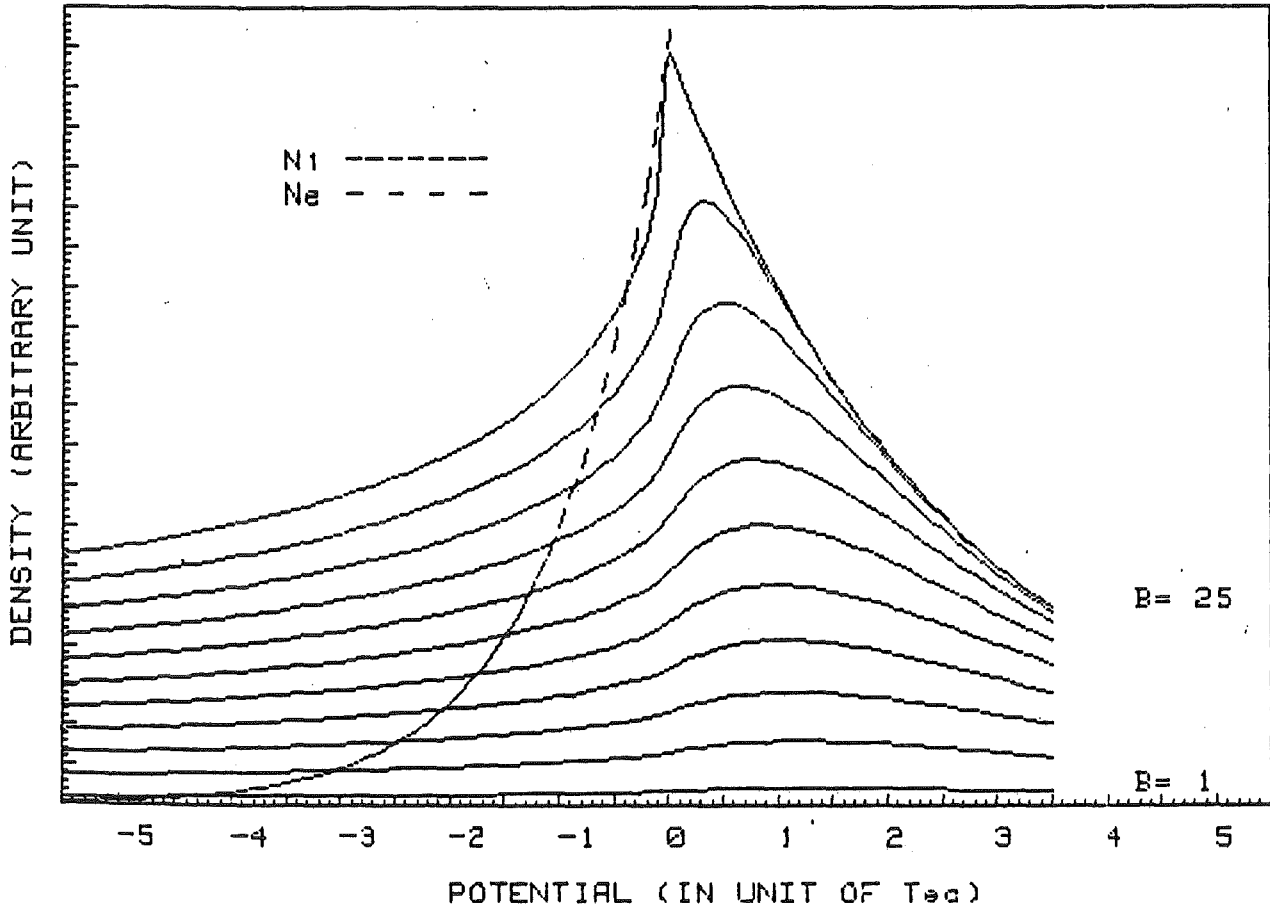


Fig. III.5-3. Ion and electron density versus potential and magnetic field strength (normalized to B_b ; increment in $B = 2.4$) in Region I.

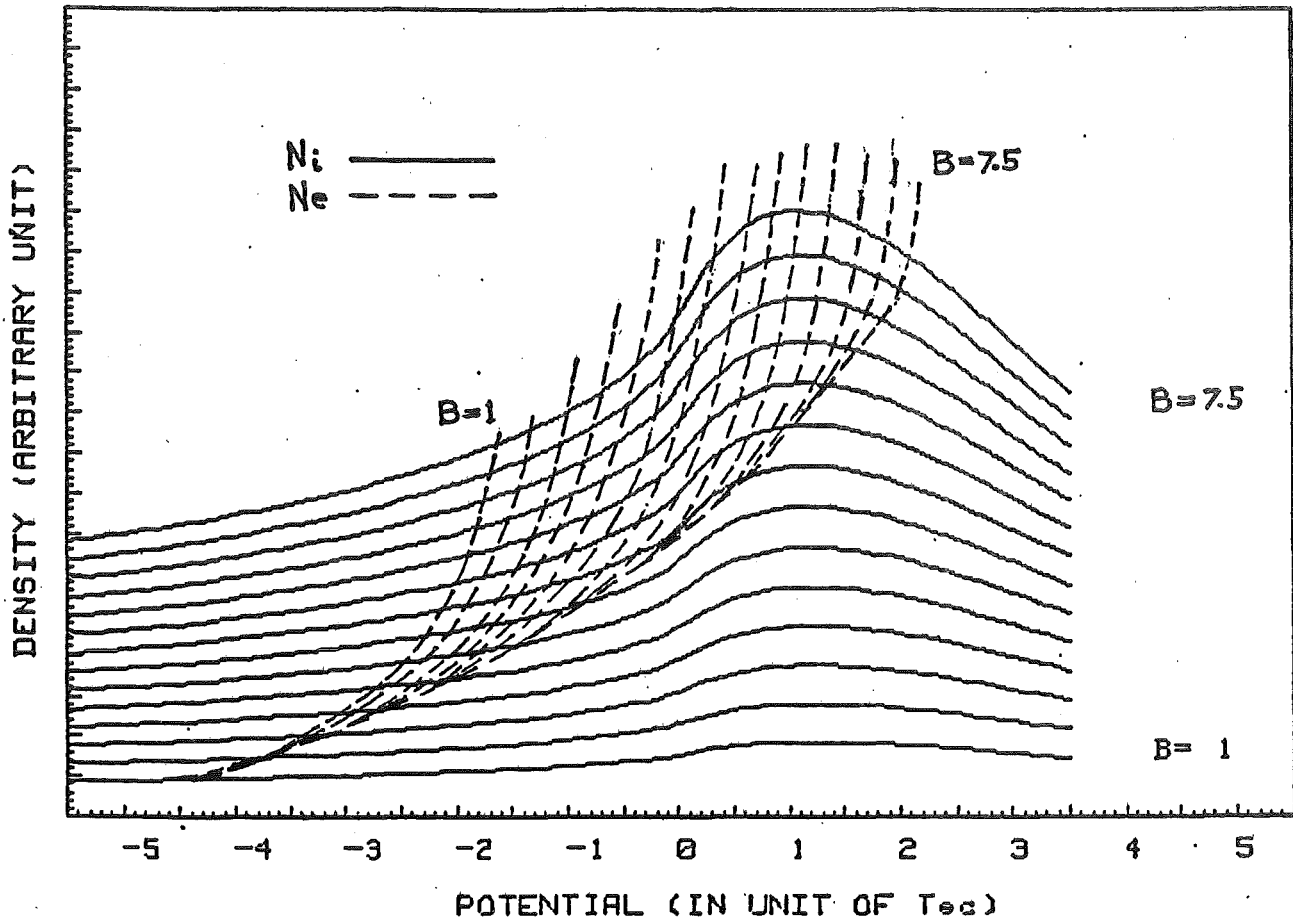


Fig. III.5-4. Ion and electron density versus potential and magnetic field strength (normalized to B_b ; increment in $B = .5$) in Region II.

Note that the spatial coordinate does not enter explicitly, but only implicitly through $B(z)$.

The total ion density (deuterium plus tritium) and electrostatic potential profile are shown in Fig. III.5-5 for TASKA for the two choices for the ion distribution function. The ion density drops in Region I because of the expanding magnetic field and the falling potential, as expected. In Region II the ion density first rises, because of the increasing magnetic field and potential, but then peaks and starts to fall while the potential continues to rise. When the potential becomes positive ($\phi = 0$ in the central cell is the reference value) passing ions from the central cell are reflected; this causes the density to fall. Since $n_i = n_e$, it is clear that the potential and electron density in Region II do not satisfy the Boltzmann relation. This is because the electron distribution function is non-Maxwellian; it is only piece-wise Maxwellian with the "colder" (i.e. temperature equal to T_{ec}) electrons at the higher kinetic energy than the "hotter" electrons at temperature T_{ep} .

Ions trapped in the thermal barrier will add to the ion density shown in Fig. III.5-5. They will contribute most near the bottom of the barrier but should not contribute much where $\phi > 0$, since the trapped ions are mostly trapped by the potential. Consequently the trapped ions should not affect the magnitude or location of the density peak near the throat of the yin-yang magnet. Since the neutron source rate is proportional to the square of the density, the peak value and location are more important for neutronics calculations. The peak density in the barrier is about one-fifth the central cell density. The density at the barrier minimum is a factor of 70 lower than the central cell density. The significance of this density peak as a neutron

AXIAL DT DENSITY PROFILE TASKA

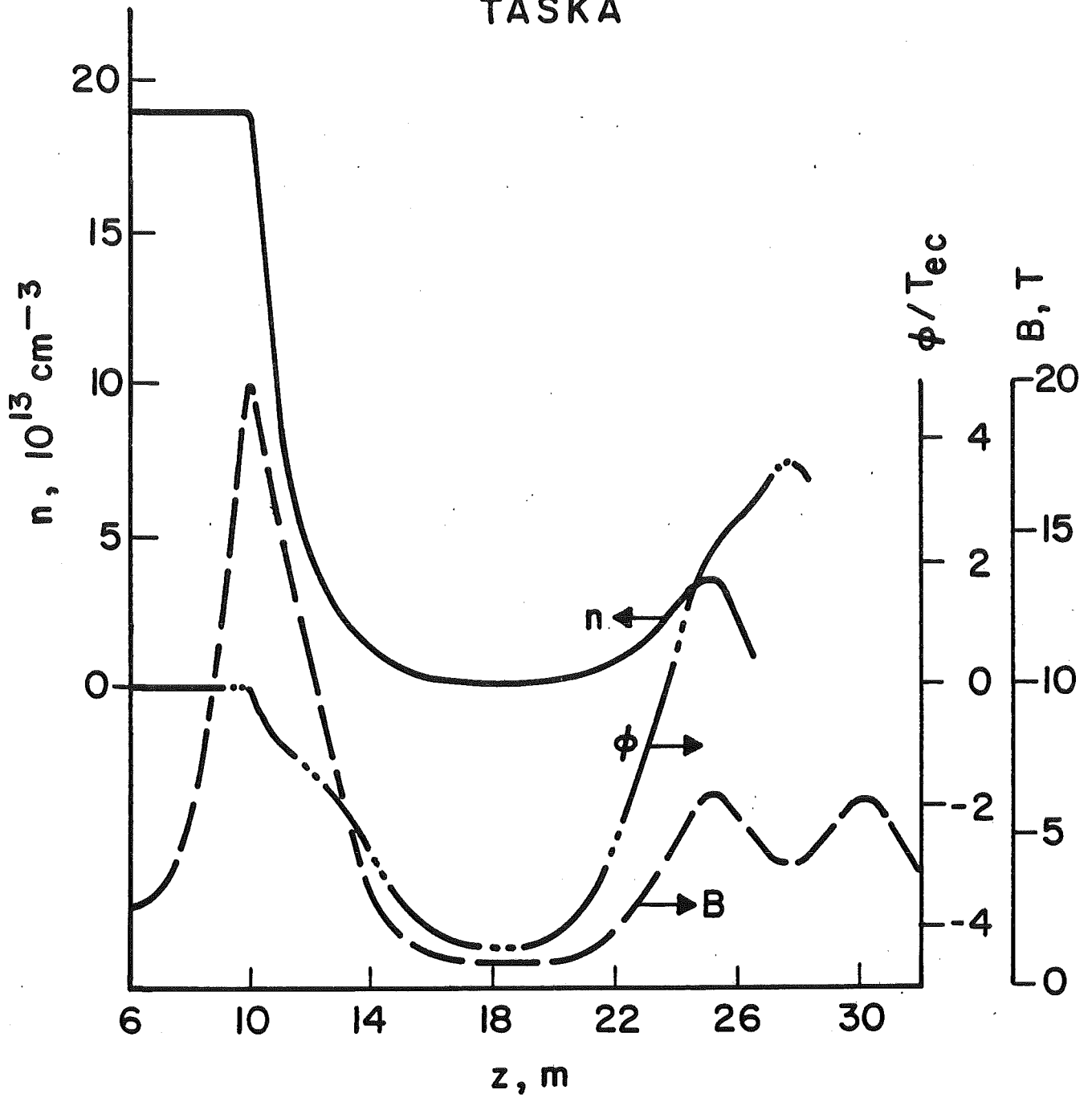


Fig. III.5-5. Axial profile of the potential and passing ion density in the thermal barrier and plug of TASKA.

source depends on its location relative to beam lines and other penetrations and is determined by detailed three-dimensional neutronic calculations.

A similar calculation⁽³⁾ has been done for the WITAMIR-I⁽⁴⁾ tandem mirror power reactor, which utilizes the same basic end-plug configuration. The density profile in TASKA is similar to that in WITAMIR-I except that the density peak in TASKA is shifted towards the throat of the yin-yang mirror. This is because the ion confining potential, ϕ_c , in TASKA is smaller relative to the central cell ion temperature, and consequently the central cell ions can penetrate further into the plug.

In addition to the neutron production in the barrier/plug due to fusion reactions between passing central cell deuterium and tritium ions, there is also neutron production due to fusion between the non-thermalized deuterium and tritium ions produced by the barrier pump beams and the plasma ions in the barrier. One can also get neutron production in the beam dump because of buildup of D and T in the surface of the beam dump. This is evaluated in Section VIII.3.

References for Section III.5

1. X.Z. Li and G.A. Emmert, "The Electrostatic Potential Profile in a Tandem Mirror Thermal Barrier," University of Wisconsin Fusion Engineering Program Report UWFDM-392 (1980).
2. E.E. Yushmanov, Sov. Phys. - JETP 22, 409 (1966).
3. X.Z. Li and G.A. Emmert, "The DT Fuel Density in the Thermal Barrier of a Tandem Mirror Reactor", University of Wisconsin Fusion Engineering Program Report UWFDM-419 (1981).
4. B. Badger, et al., "WITAMIR-I, A Tandem Mirror Reactor Design Study," University of Wisconsin Fusion Engineering Program Report UWFDM-400 (1980).

III.6 Plasma Wall Interactions and the "Halo" Plasma

In open-ended devices, such as mirrors and tandem mirrors, the primary plasma loss is parallel to the magnetic field (i.e., out the ends). Consequently the primary location for plasma-wall interaction problems is at the ends where the plasma is neutralized at thermal dumps or in a direct convertor. With sufficient expansion of the magnetic field between the plugs and the thermal dumps and with adequate pumping near the thermal dumps, the thermal contact between the main plasma and the wall can be kept small, so that cooling of the hot plug electrons by parallel heat flow to the thermal dumps is not a problem. This has been achieved in TMX;⁽¹⁾ theoretical calculations⁽²⁾ also support this conclusion.

Impurities generated by plasma bombardment at the end walls are unable to enter the main plasma because of their relatively low energy and the positive potential of the plasma. This assumes they are ionized in the plasma stream before reaching the peak potential in the plug plasma. Impurities generated at the walls of the central cell (by charge exchange neutral atom bombardment or a residual ion flux hitting the central cell walls) have only to cross a short distance before entering the electrostatic well of the central cell plasma. If ionized there, the impurities are well-confined by the electrostatic potential; accumulation of such impurities in the central cell is a potential problem that needs to be addressed.

Fortunately, the tandem mirror has a natural divertor action which can, in principle, alleviate the problem of impurity accumulation in the central cell. The radius of the plug plasma is determined by the footprint of the plug neutral beam and the gyroradius of the hot plug ions. This radius determines the radius over which there is a sufficiently positive confining

potential for the central cell. Following the field lines from the edge of the plug plasma back to the central cell determines the central cell radius for which there is adequate axial confinement. In TASKA, this is 32 cm, which is what we define to be the plasma radius in the central cell. Plasma on magnetic field lines outside this radius is not axially confined and can flow to the end walls. This region is analogous to the scrape-off layer due to divertors or limiters in tokamaks. The plasma between the central cell wall and the axially confined plasma radius is sometimes called a "halo" plasma. We will use that terminology here.

The halo plasma can play an important role in preventing impurity accumulation in the main confined plasma in the central cell. Impurity atoms released from the wall have to traverse the halo plasma before reaching the main plasma. If the line density of the halo plasma is sufficiently dense ($\int n dr \gtrsim 10^{13} \text{ cm}^{-2}$) then the impurity atoms are ionized in the halo plasma and swept out the ends before they can diffuse into the main plasma and become confined. The halo plasma is maintained by cross-field transport from the main plasma and by ionization of gas in the halo. An upper limit for the loss rate of the halo plasma can be estimated⁽³⁾ by the transit time of the ions (at temperature T_i) modified by the mirror ratio, R_C , between the central cell and the peak field of the barrier;

$$\tau_{\parallel} \approx \frac{R_C L}{2v_{\parallel}}$$
$$v_{\parallel} \approx \sqrt{\frac{2kT_i}{\pi m_i}} .$$

Using a "slab" model for the halo region, the particle conservation equation

is

$$\frac{\partial \Gamma}{\partial r} = - \frac{n}{\tau_{\parallel}},$$

where Γ is the cross-field flux and the parallel loss is treated as an absorption process. Assuming $\tau_{\parallel} \approx \text{constant}$, one gets an expression for the line density of the halo plasma,

$$\int ndr = \tau_{\parallel} \Gamma_r.$$

Here Γ_r is the radial flux at the boundary between the halo and the main confined plasma.

The value of Γ_r is unknown since it depends sensitively on details concerning radial transport in the central cell. For estimation purposes, we can normalize Γ_r to the total loss \dot{N}_T of the main plasma with a factor f ;

$$\Gamma_r = \frac{f \dot{N}_T}{2\pi r_c L} = \frac{f}{1-f} \frac{\dot{N}_a}{2\pi r_c L}$$

where \dot{N}_a is the total axial end loss (particle/sec) from the main central cell plasma. Putting these results together, one gets an estimate for the line density in the halo plasma

$$\int ndr \approx \frac{R_c \dot{N}_a}{\pi r_c} \sqrt{\frac{\pi m_i}{2kT_i}} \frac{f}{1-f}.$$

For TASKA, $\dot{N}_a = 3.5 \times 10^{21}$ ions/sec, $R_c = 7.4$, and $r_c = .32$ m. If we assume $f = .2$ and $T_i = 100$ eV, then

$$\int ndr \approx 1.3 \times 10^{13} \text{ cm}^{-2}$$

which is a marginally adequate line density for the halo plasma. This line density is comparable to that sought in the scrape-off layer of divertor tokamaks. This value, however, depends on the assumption for f and T_i in the halo; both of these are unknown at this time. The factor f depends on the details of radial transport, and T_i is determined by a power balance for the halo plasma, which remains an unsolved problem (in the tokamak scrape-off layer, $f = 1$, but the value of T_i is very poorly known).

One contribution to the power balance for the halo plasma is line radiation from partially stripped atoms. These could be helium or impurity atoms entering the plasma from the outside. This problem has been well studied for impurity radiation in tokamaks⁽⁴⁻⁶⁾ and for the case of high density z-pinch plasmas.⁽⁷⁾ In this section, the populations of the ionization states and the line radiation are calculated for helium and a possible impurity, oxygen, in a halo plasma with an electron density of 10^{13} cm^{-3} and an electron temperature of 100 eV. In both cases, the losses from line radiation are found to be insignificant in the power balance of the halo plasma if the impurity density is $\leq 1\%$ of the hydrogen ion density in the halo.

In order to estimate the power from line radiation, the populations of atoms with each of the ionization states must be calculated. Since the density of electrons is 10^{13} cm^{-3} and the temperature is 100 eV, the equilibrium ionization populations may be calculated in the Coronal model.⁽⁸⁾ In this model, if the recombination rate for Z-times ionized atoms, α_Z , and the ionization rate, S_Z , obey the relation

$$\alpha_z N_z = S_{z-1} N_{z-1} ,$$

where N_z is the density of ions in ionization state z , then

$$\frac{\alpha_{z+1}}{S_z} = 7.87 \times 10^{-9} \frac{I_z^2}{n_z} \left(\frac{I_z}{T}\right)^{.75} \exp\left(\frac{I_z}{T}\right) .$$

In this expression, I_z is the ionization potential in eV for ions moving from state Z to $Z+1$, n_z is the degeneracy of electrons doing this ionization and T is the electron temperature in eV. Using the ionization potentials calculated by Carlson,⁽⁹⁾ the densities of atoms in each possible ionization state for helium and oxygen are determined for total impurity densities of 10^{11} cm^{-3} and are shown in Table III.6-1. It may be noted that the helium is almost fully stripped and should not emit much line radiation while most oxygen ions still have electrons bound to them and may emit significant amounts of line radiation.

The power of line radiation may be estimated with the analysis of Mosher,⁽⁷⁾ where the power is given as

$$P_L = \frac{3.5 \times 10^{-25}}{T^{1/2}} N_z N_e \langle \exp\left(-\frac{E_{N1}^2}{T}\right) \rangle \text{ (W/cm}^3\text{)}$$

where

$$E_{N1}^2 = \left(\frac{Z}{137}\right)^2 \frac{m_e c^2}{2} \left[\frac{1}{N^2} - \frac{1}{(N+1)^2} \right]$$

is a typical energy of a line if N is the principal quantum number of the electrons involved in the transition. The electron and ion densities are in

Table III.6-1. Ionization State Densities (cm⁻³)

<u>Z</u>	<u>He</u>	<u>0</u>
0	2.82	1.71×10^{-17}
1	$.53 \times 10^6$	1.07×10^{-10}
2	$.99997 \times 10^{11}$	3.91×10^{-5}
3	---	2.14
3	---	1.99×10^4
5	---	8.64×10^7
6	---	8.98×10^{10}
7	---	9.97×10^9
8	---	8.63×10^7

The plasma temperature in the "halo" is 100 eV.

The plasma density in the "halo" is 10^{13} cm⁻³.

The total density of He is 10^{11} cm⁻³.

The total density of 0 is 10^{11} cm⁻³

units of cm^{-3} while the temperature and energies are in eV. Using the densities in Table III.6-1, the line radiation powers are found to be

$$P_L \approx 5.89 \times 10^{-7} \text{ W/cm}^3$$

for helium and

$$P_L \approx 1.64 \times 10^{-2} \text{ W/cm}^3$$

for oxygen. For the halo plasma, the power loss due to parallel flow is .2 W/cm^3 at $n = 10^{13} \text{ cm}^{-3}$ and 100 eV. Both values for the line radiation are small compared to the total power of the system and should not be important to the power balance.

Post et al.⁽⁴⁾ have done more detailed calculations which lead to an even lower power for oxygen ($3 \times 10^{-4} \text{ W/cm}^3$) and approximately the same value for helium ($2 \times 10^{-6} \text{ W/cm}^3$). Though the resulting powers are somewhat different than those calculated herein, the general statement that line radiation is not an important effect for oxygen and helium impurities is supported.

References for Section III.6

1. R.P. Drake, "Control of Plasma-Wall Interactions in Tandem Mirrors," Lawrence Livermore National Laboratory Report UCRL-86273 (1981).
2. G.D. Porter, "Effect of Gas Recycling and Secondary Electron Emission," in Physics Basis for MFTF-B, edited by D.E. Baldwin, B.G. Logan, and T.C. Simonen, Lawrence Livermore National Laboratory Report UCID-18496, Part 2 (1980).
3. G.A. Emmert, "Modeling of Bundle Divertors," University of Wisconsin Fusion Engineering Program Report UWFDM-343 (1981).
4. D.E. Post, R.V. Jensen, C.B. Tarter, W.H. Grasberger, and W.A. Lokke, "Steady-State Radiative Cooling Rates for Low Density, High Temperature Plasmas," Atomic Data and Nuclear Data Tables 20, (1977) 397.
5. D.E.T.F. Ashby and M.H. Hughes, "A Study of Impurity Radiation From the Peripheral Plasma of a Tokamak Reactor," Culham Laboratory Memo (CLM-P625), November 1980.
6. L.L. Lengyel, "Analysis of Radiating Plasma Boundary Layers," IPP Report IPP 1/191, Sept. 1981.
7. D. Mosher, "The Coronal Equilibrium of High Atomic Number Plasmas," NRL Memorandum Report 2563, March 1973.
8. R.W.P. McWhirter and T.F. Stratton in "Plasma Diagnostic Techniques," (R.H. Huddleston and S.L. Leonard, Eds.), Academic Press, New York, 1965.
9. T.A. Carlson, C.W. Nestor, Jr., N. Wasserman, and J.D. McDowell, "Calculated Ionization Potentials for Multiply Charged Ions," Atomic Data 2, 63 (1970).

IV Heating, Fueling and Exhaust

IV.1 Electron Cyclotron Resonance Heating

IV.1.1 Introduction

Continuous direct heating of the potentially trapped electron population in the TASKA end plugs is necessary to maintain the excess potential ϕ_c required to confine the central cell ions.⁽¹⁾ This excess plug potential is a nearly linear function of the plug electron temperature T_{ep} :

$$\phi_c = T_{ep} \ln \left(\frac{n_e}{n_b} \sqrt{\frac{T_{ec}}{T_{ep}}} \right) - \phi_b \quad (IV.1-1)$$

Here T_{ec} is the central cell electron temperature, ϕ_b is the barrier potential dip, and n_e and n_b are the plug and barrier electron densities, respectively. The desired excess potential of 43 keV requires a plug electron temperature of 59 keV.

A detailed study of the barrier/plug plasma physics reveals that good confinement can be achieved if the heating zone is centered around the 2 tesla-point, i.e., at an axial distance of 2200 cm outwards from the midplane of the central cell. This is because the plug electron population is electrostatically confined by the total potential $\phi_b + \phi_c$, and heating anywhere within the electrostatic well should heat the bulk electron population.

Following criteria were used to define a feasible solution of the heating problem:

- a. No variation of the signal frequency should be required during the startup phase of the reactor.
- b. The launching direction should be constant, too, and should not be close to tangential to the plasma surface.

- c. Penetration of the plasma should be good, i.e., most of the wave energy should be absorbed by the bulk of the plasma (as opposed to surface absorption, which approaches 100% when the plasma appears as a blackbody at the local electron cyclotron resonance frequency).
- d. Absorption should be near 100% for a single pass through the plasma. To a certain extent this criterion is in contradiction to c), and one has to expect a fairly narrow window in parameter space where both requirements are satisfied - if such a window exists at all.
- e. The transport system between wave source and plasma should have low losses and show a low susceptibility to neutron damage.
- f. The wave source should require only a slight extrapolation of existing technology. We will discuss in detail the solutions we propose, starting from the plasma requirements.

IV.1.2 The Plasma

Propagation and absorption of electromagnetic waves close to the electron cyclotron frequency of the plasma was studied numerically using the general purpose code ECNAG.⁽²⁾ This code is characterized by:

- a. Numerical solution of the geometric optics equations

$$\frac{d\bar{r}}{dt} = - \frac{\partial D / \partial \bar{k}}{\partial D / \partial \omega} ; \frac{\partial \bar{k}}{\partial t} = \frac{\partial D / \partial \bar{r}}{\partial D / \partial \omega} \quad (\text{IV.1-2})$$

using a cold-plasma dispersion relation

$$D(\bar{k}, \omega) = 0 . \quad (\text{IV.1-3})$$

Here \bar{r} and \bar{k} represent the position of the wave front along the ray and the wave vector, respectively, while t and ω are time and frequency. Because we are interested in spatial absorption in a stable plasma ω is held constant while \bar{k} is allowed to vary according to the requirements of the dispersion relation.

It has been shown that using a hot plasma dispersion relation does not affect the calculated wave trajectories⁽³⁾ as long as the characteristic distance of the absorption is significantly larger than the wavelengths involved.

- b. An analytic absorption model. We would have preferred to use a more generally valid numerical model, but at present such a model is not available for absorption around the fundamental frequency. The choice of the resonance at 2 T excludes the use of harmonics (the cyclotron frequency ω_c at B = 2 T is 56 GHz, i.e., at the limit of available power sources).

The model consists of the following expressions for the absorption coefficient α , correct to lowest significant order in v_{th}/c :

*oblique propagation, low density, (4)

$$\alpha^{x,0} = \frac{\sqrt{\pi}}{2} \frac{\omega_p^2}{\omega} \frac{\omega}{c} (1 + \cos^2\theta) \frac{c}{v_{th}} \frac{e^{-\left(\frac{c}{v_{th}} \frac{\omega - \omega_c}{ck \cos\theta}\right)^2}}{|\cos\theta|} \quad (IV.1-4)$$

*oblique propagation, high density, (5)

$$\alpha^{x,0} = 2\sqrt{2} R^{x,0} \frac{v_{th}}{c} \frac{\omega}{c} \operatorname{Im}\left[-\frac{1}{Z(\zeta)}\right] \quad (IV.1-5)$$

where $R^{X,0}$ represents a complicated function of ω_p , ω_c , $\frac{ck}{\omega}$ and θ (which scales as $\frac{\omega^2}{\omega_p^2} \sim \frac{1}{n_e}$!), $\zeta = \frac{\sqrt{2}}{2} \frac{c}{v_{th}} \frac{\omega - \omega_c}{ck \cos \theta}$ and $Z(\zeta)$ represents the familiar plasma dispersion function.

*quasi-perpendicular propagation, low density^(5,6)

$$\alpha^0 = \frac{1}{\sqrt{2}} \left(1 - \frac{\omega_p^2}{\omega_c^2}\right)^{1/2} \frac{\omega_p^2}{\omega_c^2} \frac{\omega}{c} [-F_{7/2}''(z)] \quad (IV.1-6)$$

$$\alpha^X = \frac{\omega_p^2}{\omega_c^2} \left(\frac{c}{v_{th}}\right)^2 \frac{\omega}{c} [-\frac{1}{2} F_{5/2}''(z)] \quad (IV.1-7)$$

*quasi-perpendicular propagation, high density⁽⁵⁾

$$\alpha^0 = \frac{1}{\sqrt{2}} \left(1 - \frac{\omega_p^2}{\omega_c^2}\right)^{1/2} \frac{\omega_p^2}{\omega_c^2} \frac{\omega}{c} \frac{-F_{7/2}''(z)}{|G_{7/2}| + \sqrt{|G_{7/2}|^2 + |G_{7/2}|}} \quad (IV.1-8)$$

$$\alpha^X = \sqrt{2} \left(1 - \frac{\omega_p^2}{2\omega_c^2}\right)^{3/2} \frac{\omega_c^2}{\omega_p^2} \left(\frac{v_{th}}{c}\right) \frac{\omega}{c} \frac{-F_{5/2}''(z)}{|F_{5/2}(z)|^2} \cdot \quad (IV.1-9)$$

The function $F_q(z)$ is the relativistic counterpart of the plasma dispersion function and is defined by⁽⁷⁾

$$F_q(z) = F_q'(z) + iF_q''(z) = -i \int_0^{\infty} \frac{e^{izt}}{(1-it)^q} dt \quad (IV.1-10)$$

with $z = \frac{c^2}{v_{th}^2} \frac{\omega - \omega_c}{\omega_c}$. $G_q(z)$ is a shorthand for $1 + \frac{1}{2} \frac{\omega_p^2}{\omega_c^2} F_q(z)$.

Remarkable is the inverse dependence on the squared plasma frequency ω_p^2 (i.e. on the electron density n_p) of the absorption coefficient for the extraordinary mode in a high density plasma. The ordinary mode does not show this anomalous behavior, and Eq. (IV.1-6) is simply the low density limit of Eq. (IV.1-8). The code selects between oblique (where Doppler broadening prevails) and quasi-perpendicular (where a relativistic mechanism is dominant) regimes by comparing the quantities $\frac{ck}{\omega} |\cos\theta|$ and v_{th}/c . Both high and low-density absorptivities are calculated, and the lowest value is used. Finally, the choice between X and O-mode depends on the user and is dictated by the polarization of the incoming signal. The code is completed by user supplied models for the confining magnetic field and the plasma equilibrium.

IV.1.2.1 Magnetic Field and Plasma Model

We use a field model based on quadratic regression of data from an exact field calculation with EFFI:

$$B_x = [.0085 z^2 - 4.35 z + 512] x$$

$$B_y = [-.0028 z^2 + 1.22 z - 198] y \quad (IV.1-11)$$

$$B_z = [B_p + 100 (z - 300)] (1 + 1.8 \times 10^{-5} x^2) (1 - 1.2 \times 10^{-5} y^2) .$$

This model does not satisfy $\nabla \cdot \vec{B} = 0$ at every point (x,y,z) where the model holds, but $\nabla \cdot \vec{B} \ll |\nabla B|$. The point $z = 300$ cm where $B_z = B_p = 2$ T on axis is an arbitrary chosen coordinate, corresponding to $z = 2200$ cm in the regular system. Distances and fields are in cm and gauss, respectively, and the model holds for $|x,y| \leq 30$ cm and $250 \text{ cm} < z < 350$ cm. The plasma electron density and temperature are represented by

$$n_e = n_{e0} e^{-\left(\frac{r^2}{a^2}\right)^5} \quad (\text{IV.1-12})$$

$$T_e = T_{e0} e^{-\left(\frac{r^2}{a^2}\right)^5} \quad (\text{IV.1-13})$$

where T_{e0} and n_{e0} are the central electron temperature and density, respectively, $r^2 = x^2 + y^2$ and a is the plasma radius. The β -factor, i.e., the ratio between kinetic and magnetic pressure, is calculated for every point along the ray trajectories and the vacuum magnetic field calculated by means of Eq. IV.1-11 is corrected accordingly.

IV.1.2.2 Results

Preliminary calculations showed that the extraordinary mode (wave electric vector in a plane perpendicular to the confining magnetic field at perpendicular prop.) cannot be used for the following reasons.

A complication typical of linear confinement systems is that the resonant layer roughly has the shape of a disc perpendicular to the machine axis. As a consequence the ray trajectory needs to have a substantial axial component if one is to achieve absorption in the central plasma area. For an X-polarized wave the plasma acts as a dielectric with a refractive index larger than unity, i.e., with a high permittivity. This implies that a ray is bent towards

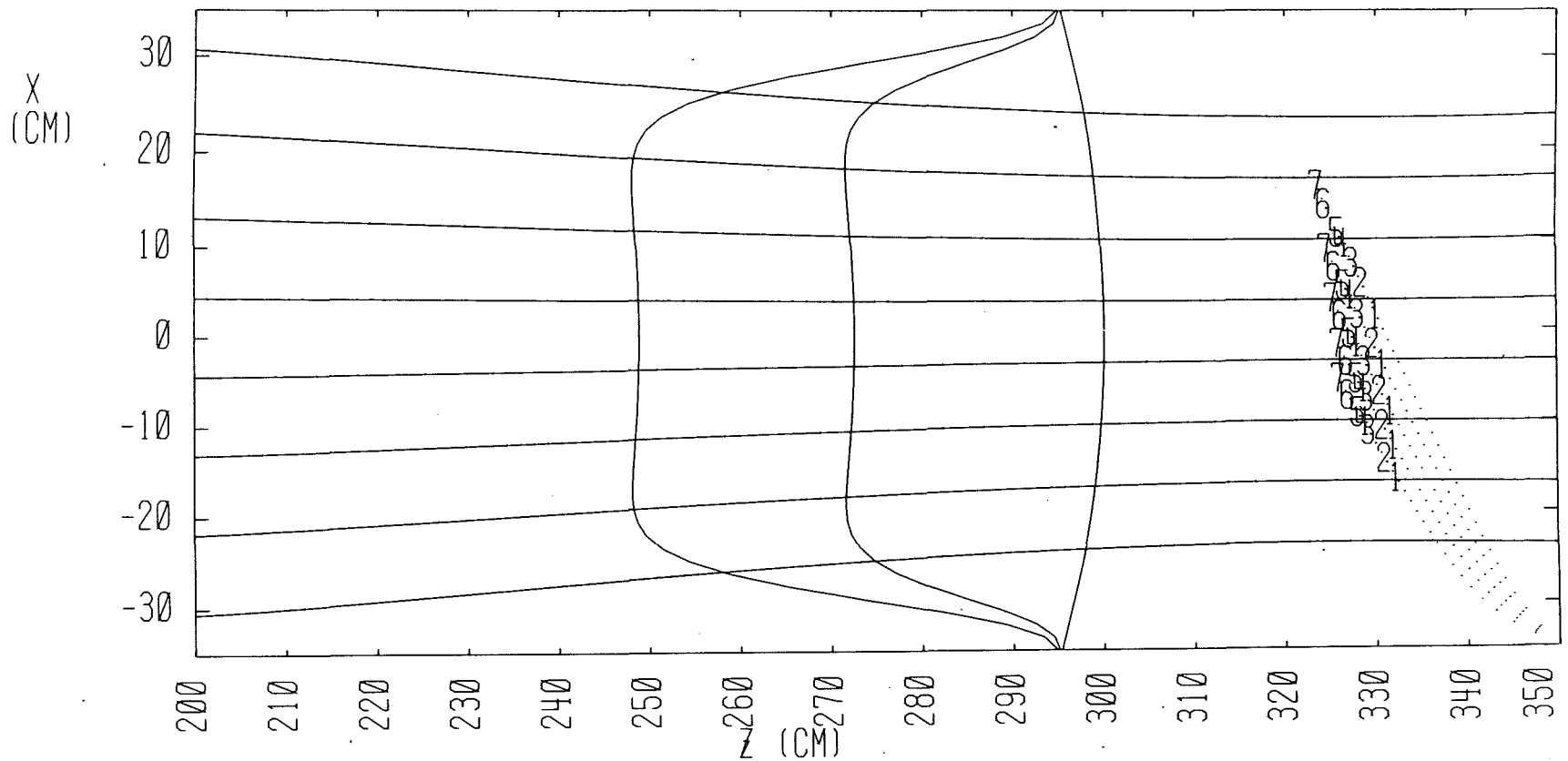
the normal and will have to enter the plasma at a grazing angle to allow for any penetration in the axial direction. There simply is not enough room to mount the launching structure parallel to the axis of the reactor. Furthermore, such a mounting would make the structure very vulnerable to neutron damage.

The extraordinary mode as a rule has a very high absorption coefficient. While this is an attractive feature during the early startup phase and, in general, for devices with a low operating temperature, it turns the plasma into a black body which totally absorbs the wave at the plasma surface. Therefore, X-mode heating of a mirror plug can only be useful during the earliest startup phase. This would, however, require separate sources for startup and steady-state operation. For this reason the use of waves with X-polarization has been rejected altogether. Figure IV.1-1 shows typical ray trajectories and absorption patterns for the X-mode.

The ordinary mode has its wave electric vector oriented parallel to the direction of the confining magnetic field (for propagation perpendicular to the field) and, therefore, displays little or no refraction. One expects no penetration problems with the ordinary mode until high electron densities or very high temperatures are reached. If the density is sufficiently high, then the condition

$$\omega = \omega_p \quad (\text{IV.1-13})$$

is satisfied on a closed surface in the plasma. Because the plasma frequency ω_p is a cut-off for the ordinary mode the wave cannot penetrate inside this closed surface. A total electron density of $1.1 \times 10^{13} \text{ cm}^{-3}$ in the center



EXTRAORDINARY MODE
 FREQUENCY 56. GHZ
 B FIELD AT (0,0,300.0) 1.9970E+04 GAUSS
 DENSITY AT (0,0,300.0) 1.0000E+13 1/CM**3
 EL. TEMP AT (0,0,300.0) 2.00 KEV
 INCIDENCE : FROM -65. TO -45. DEGREES (5.)

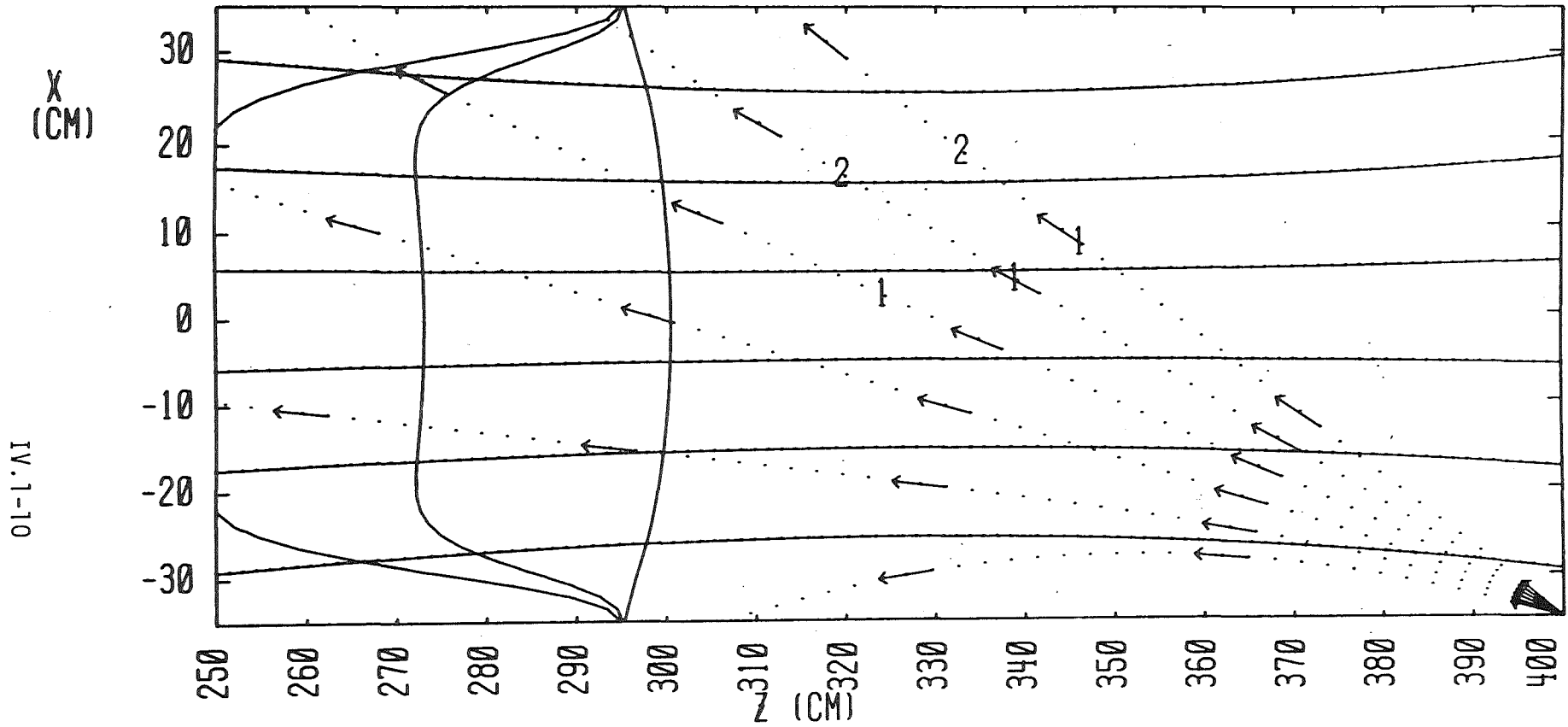
Fig. IV.1-1 Typical ray trajectories for the X-mode.

implies a lower limit for the wave frequency of 29.8 GHz, which is well below the electron cyclotron frequency of 56 GHz. The flat density profile (Eq. IV.1-12) causes the $\omega = \omega_p$ surface to be ill defined in the bulk of the plasma and prevents the use of reflection at this surface to enhance the effective optical depth of the plasma.

Figures IV.1-2a through 2g show ray trajectories and absorption levels for various temperatures representative for both startup and steady-state. The launching point is chosen .5 m outwards from the $B_0 = 2$ T point and the frequency is kept at 56 GHz. Although it is certain that a different frequency may lead to improved results, it was felt that the commercial availability of a 56 GHz tube was too important an asset to be sacrificed for slightly better plasma physical performance. The dots representing the ray trajectories are plotted at fixed time intervals (of 10^{-10} s) and, therefore, their separation can be used as a measure for the phase velocity. The numbers 1-7 represent the percentage of incident energy absorbed up to the point where they are printed; they stand for 25, 50, 75, 90, 95, 99 and 100% absorption, respectively.

Other features of the plot are the quasi-axial field lines and, from right to left, the electron cyclotron resonance, the right-hand cyclotron cut-off and the cold plasma resonance surfaces; the latter two only affect the extraordinary mode. The angles of incidence are measured from the upwards vertical, in clockwise direction. Linear scales are the same in both directions.

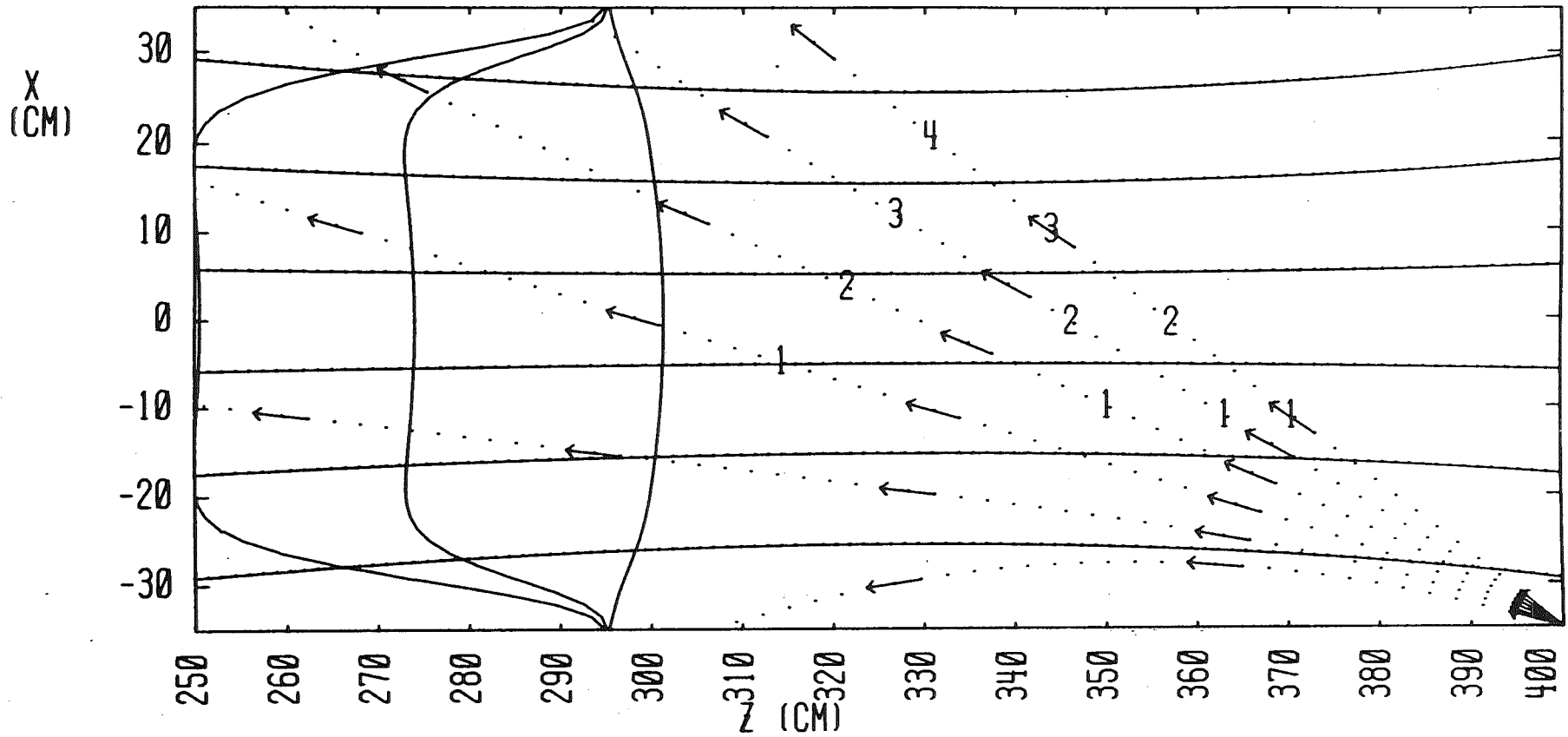
At 5 keV absorption of the ordinary mode is already considerable: the rays with a 60° , 55° , and 50° incidence reach 46, 66 and 68 percent absorption, respectively. At 10 keV the corresponding percentages are 68, 88 and



ORDINARY MODE
 FREQUENCY 56. GHZ
 B FIELD AT (0.0,300.0) 1.9925E+04 GAUSS
 DENSITY AT (0.0,300.0) 1.0000E+13 1/CM³
 EL. TEMP AT (0.0,300.0) 5.00 KEV
 INCIDENCE : FROM -75. TO -50. DEGREES (5.)

Fig. IV.1-2a. Ray trajectories and absorption profiles for the 0-mode at 5 keV.

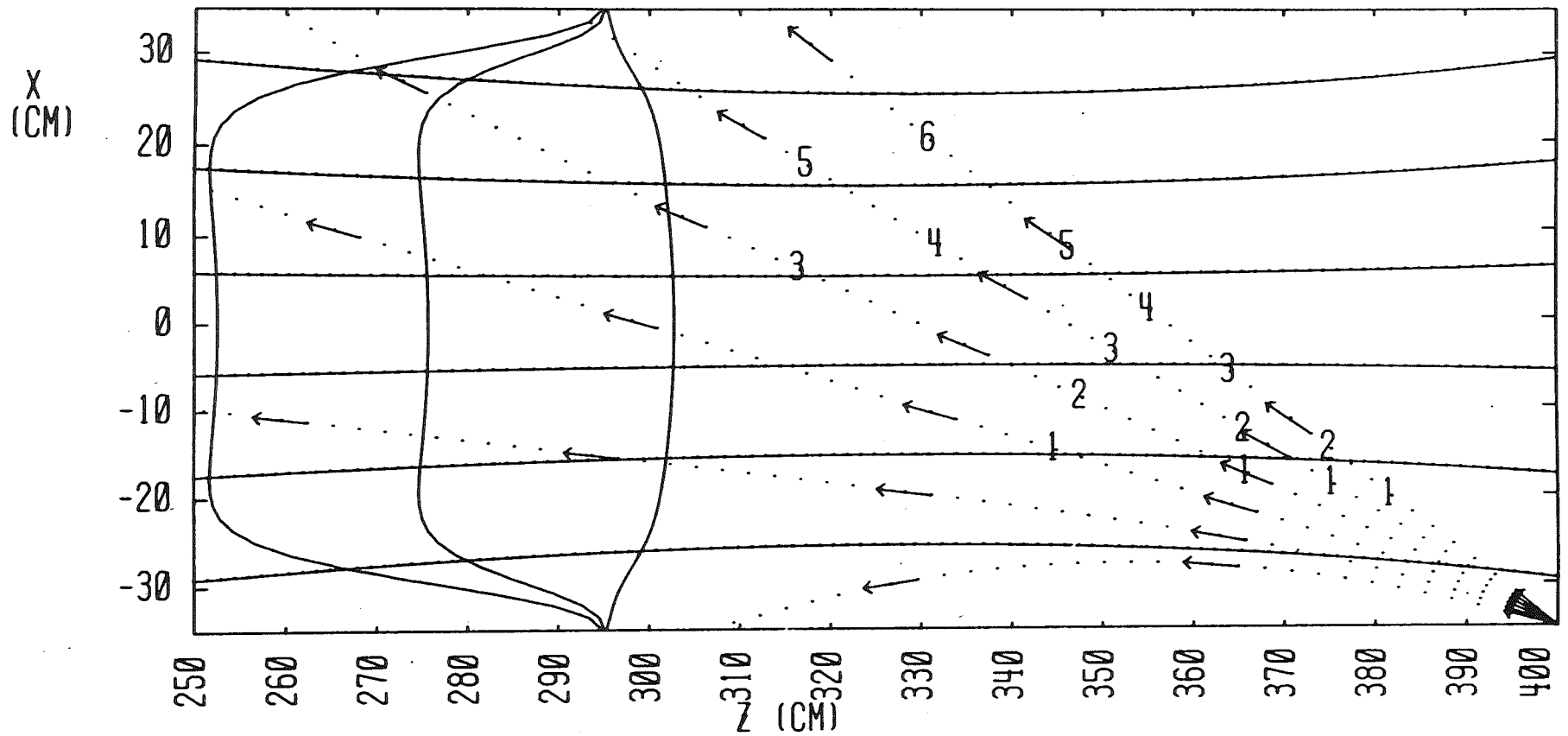
IV.1-11



ORDINARY MODE
 FREQUENCY 56. GHZ
 B FIELD AT (0,0,300.0) 1.9849E+04 GAUSS
 DENSITY AT (0,0,300.0) 1.0000E+13 1/CM³
 EL. TEMP AT (0,0,300.0) 10.00 KEV
 INCIDENCE : FROM -75. TO -50. DEGREES (5.)

Fig. IV.1-2b Ray trajectories and absorption profiles for the 0-mode at 10 keV.

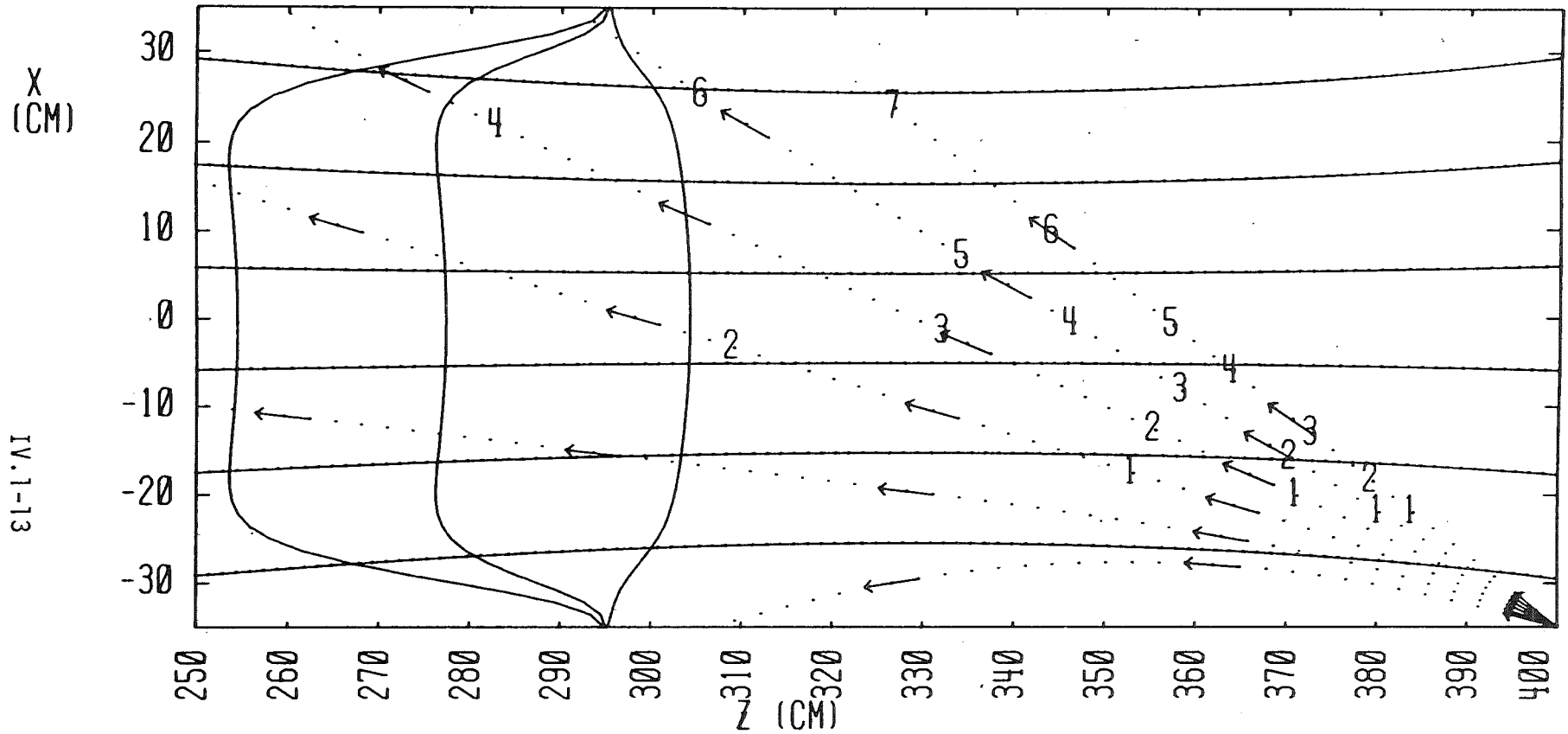
IV.1-12



- 189 -

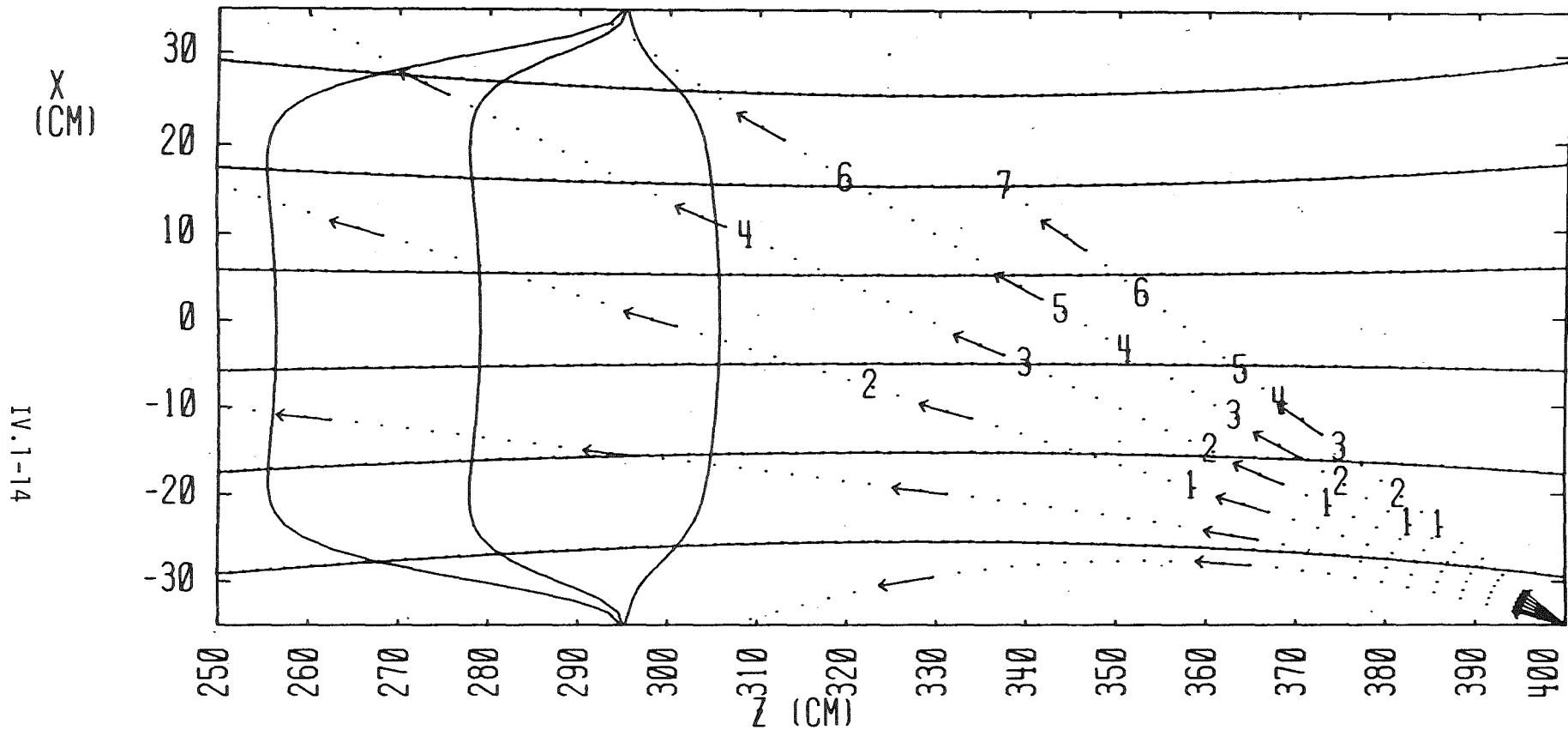
ORDINARY MODE
 FREQUENCY 56. GHZ
 B FIELD AT (0.0,300.0) 1.9698E+04 GAUSS
 DENSITY AT (0.0,300.0) 1.0000E+13 1/CM³
 EL. TEMP AT (0.0,300.0) 20.00 KEV
 INCIDENCE : FROM -75. TO -50. DEGREES (5.)

Fig. IV.1-2c Ray trajectories and absorption profiles for the 0-mode at 20 keV.



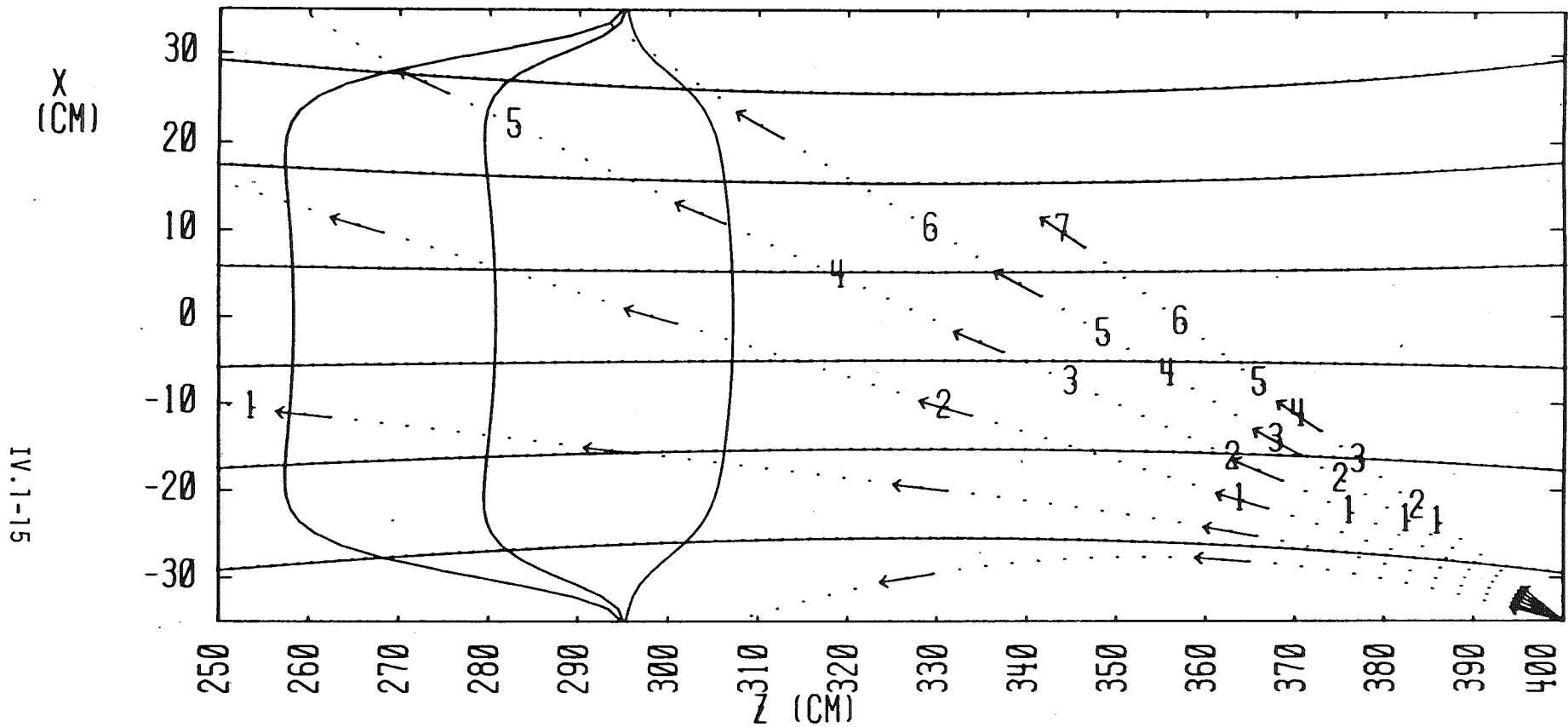
ORDINARY MODE
 FREQUENCY 56. GHZ
 B FIELD AT (0.0,300.0) 1.9545E+04 GAUSS
 DENSITY AT (0.0,300.0) 1.0000E+13 1/CM³
 EL. TEMP AT (0.0,300.0) 30.00 KEV
 INCIDENCE : FROM -75. TO -50. DEGREES (5.)

Fig. IV.1-2d Ray trajectories and absorption profiles for the 0-mode at 30 keV.



ORDINARY MODE
 FREQUENCY 56. GHZ
 B FIELD AT (0.0,300.0) 1.9391E+04 GAUSS
 DENSITY AT (0.0,300.0) 1.0000E+13 1/CM³
 EL. TEMP AT (0.0,300.0) 40.00 KEV
 INCIDENCE : FROM -75. TO -50. DEGREES (5.)

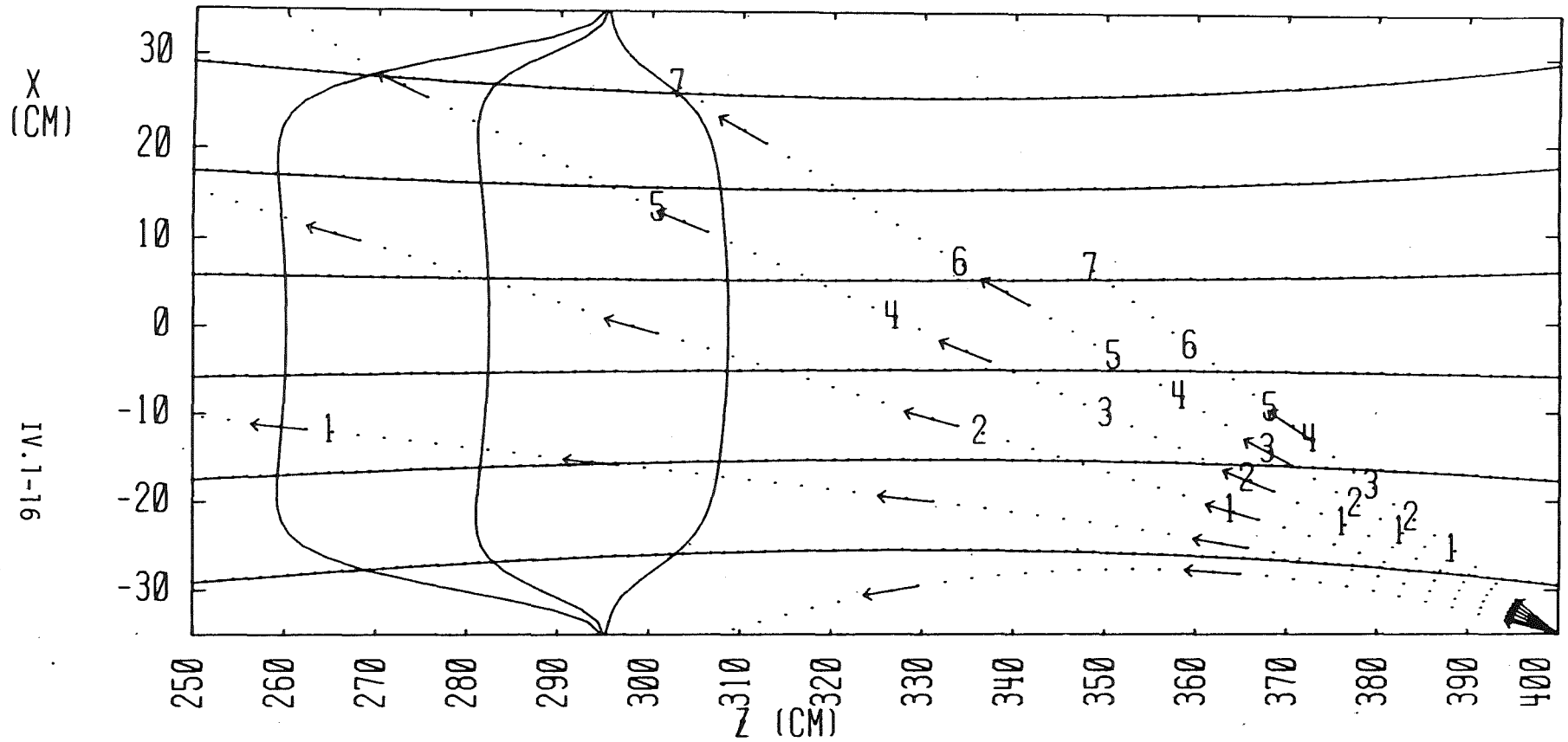
Fig. IV.1-2e Ray trajectories and absorption profiles for the 0-mode at 40 keV.



IV.1-15

ORDINARY MODE
 FREQUENCY 56. GHZ
 B FIELD AT (0,0,300.0) 1.9235E+04 GAUSS
 DENSITY AT (0,0,300.0) 1.0000E+13 1/CM³
 EL. TEMP AT (0,0,300.0) 50.00 KEV
 INCIDENCE : FROM -75. TO -50. DEGREES (5.)

Fig. IV.1-2f Ray trajectories and absorption profiles for the 0-mode at 50 keV.



ORDINARY MODE
 FREQUENCY 56. GHZ
 B FIELD AT (0.0,300.0) 1.9079E+04 GAUSS
 DENSITY AT (0.0,300.0) 1.0000E+13 1/CM³
 EL. TEMP AT (0.0,300.0) 60.00 KEV
 INCIDENCE : FROM -75. TO -50. DEGREES (5.)

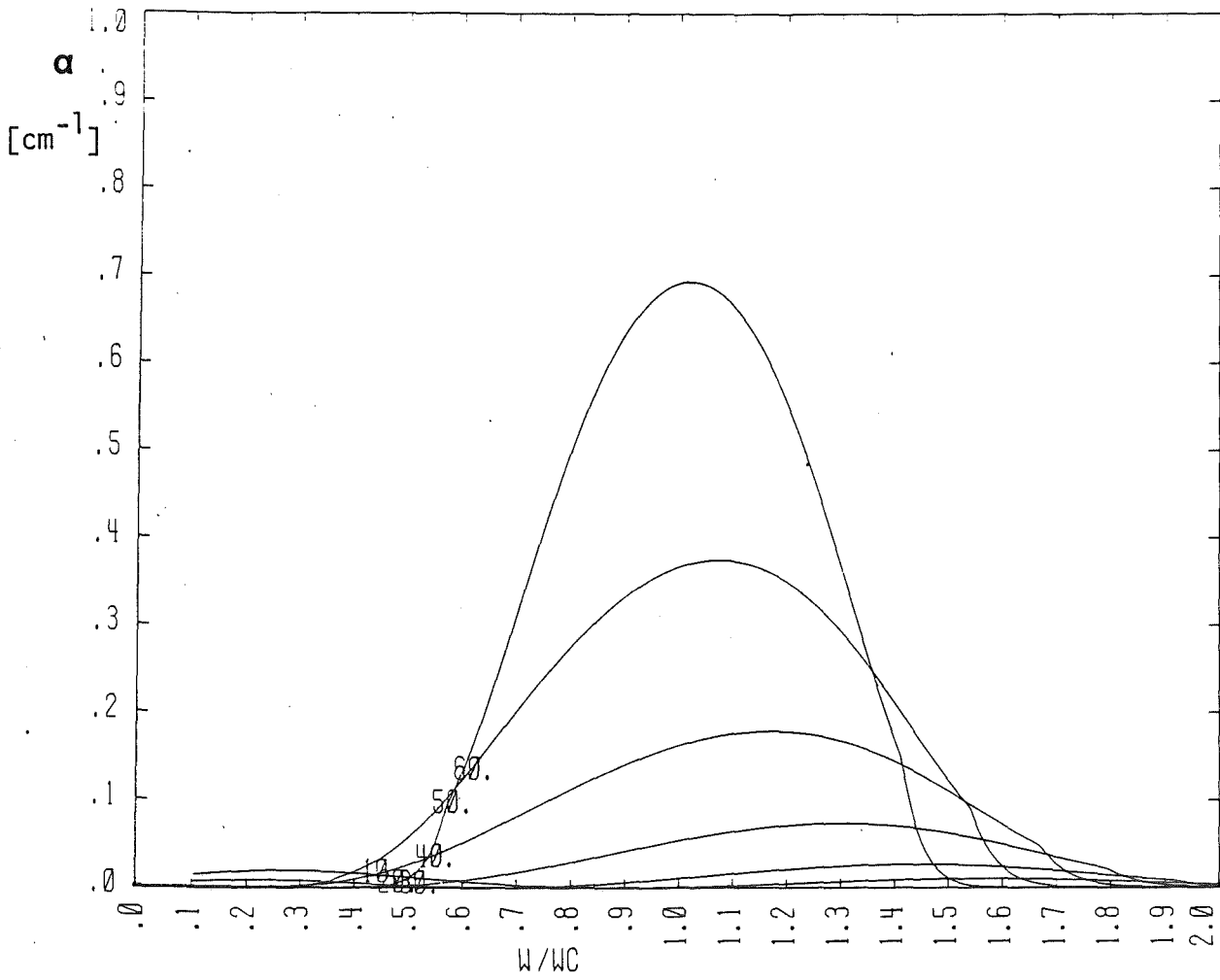
Fig. IV.1-2g Ray trajectories and absorption profiles for the 0-mode at 60 keV.

95. Within the accuracy of the model this probably means that total absorption of the ordinary mode can be expected for electron temperatures from ca. 10 keV on. For higher temperatures all rays in the 50°-60° range yield good absorption and penetration, with the 55°-60° launching direction giving the best centering around the plasma axis.

Careful examination reveals that the absorption is not symmetric about the cyclotron resonance surface. This is explained by cold plasma dispersion effects which vary quite strongly in that frequency range, especially when the angle θ between the wave propagation vector \bar{k} and the confining magnetic field \bar{B}_0 becomes small. This effect is clearly illustrated in Fig. IV.1-3 which represents the absorption coefficient α as a function of ω_c/ω with θ varying from 10° to 60° with 10° intervals. At 30 keV the dominant absorption mechanism is Doppler broadening for these directions, and the absorption profile is obviously asymmetric for the lower values of θ .

Very recently, the ray tracing and absorption code has been coupled to a one-dimensional time dependent transport code. Only preliminary results were obtained, but they contribute very positively to our understanding of the heating during the initial startup phase.⁽⁸⁾

At a temperature of 2.8 keV a 56 GHz wave was launched at 60° with respect to the normal. The cumulative absorption was 86% when the ray left the plasma which means that an unexpectedly low fraction of the energy will be reflected at the wall and, in all likelihood, be absorbed somewhere in or close to the central cell. The transport code results show that (Fig. IV.1-4) energy deposition is strongly peaked in the plasma core. Figure IV.1-4 shows the absorbed energy as it is distributed over annuli of constant width and



ORDINARY MODE
PARAMETER : THETA
VTH/C = .350 TE = 31.3 KEV
CYCLOTRON FREQUENCY : 56. GHZ
PLASMA FREQUENCY : 30. GHZ

Fig. IV.1-3 Absorption coefficient vs. frequency.

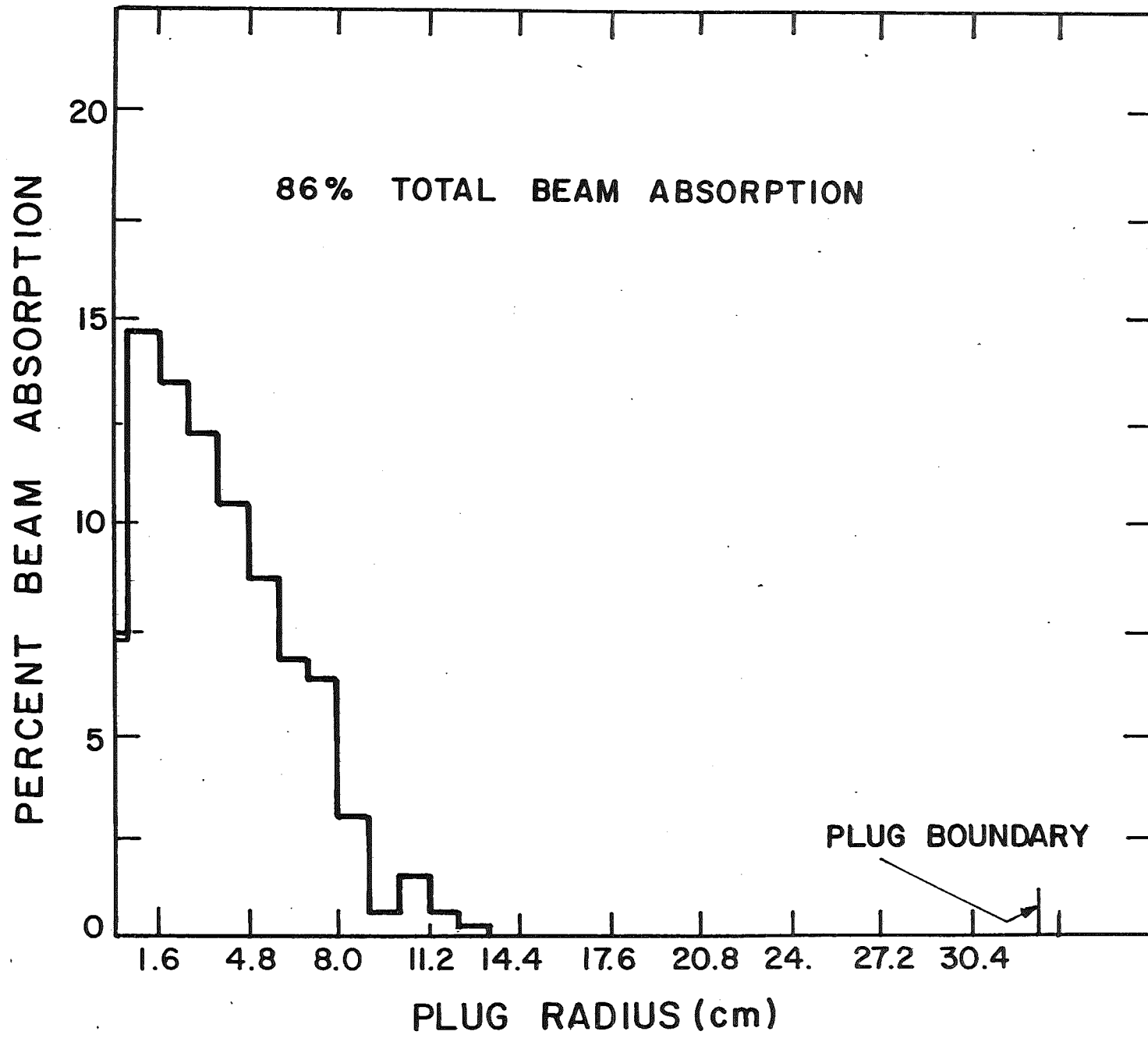


Fig. IV.1-4 Radial energy deposition profile.

hence the distribution per unit volume is even more peaked than suggested by the figure.

Concluding, it can be stated that a wave

- launched with ordinary polarization
- at 56 GHz
- at 55° with respect to the normal

will be totally absorbed in the electron temperature range between 5 and 60 keV, while contributing strongly to the plasma electron heating during the early startup phase.

IV.1.3 The Gyrotron Microwave Power Source

For the RF power source we chose a 56 GHz gyrotron because a suitable tube in that frequency range will be commercially available from at least two companies (Hughes Aircraft Co. and Varian Associates, Inc.) at power levels from 200 to 250 kW. It is expected that power levels between 350 kW and 1 MW^(9,10) for continuous wave (CW) operation will become available by 1988. We opted for a conservative extrapolation of present-day technology to the 350 kW level.

The wave produced by these tubes has a circular (azimuthal) electric field. This can be converted to a linear polarization by using a stepped reflector of which one-half of the surface is displaced half a wavelength with respect to the other half. The desired polarization direction can be obtained by rotating the reflector.

Both Varian and Hughes have 28 GHz, 200 kW CW tubes available and expect to produce CW, 200 kW tubes at 56/60 GHz within the next two years. Experts at both companies rate the cost of the tubes at \$1. to \$2. per watt of microwave output with another \$.50 to be added for the superconducting magnets.

The power supplies that are currently delivered for use with experimental gyrotrons are 80 kV, 8 A (i.e., 640 kW) devices costing $\$1.2 \times 10^6$ for 200 kW of RF output, or \$6. per watt.⁽¹¹⁾ This makes, however, a very inefficient use of some of the power supply equipment. The whole installation is typically to be fed from a 12 kV, 3 phase-grid and consists of a phase disconnecter, a step-start contactor, and a voltage regulator feeding a transformer-rectifier. The latter's cost scales as 1.3 times its KVA rating. The next and most costly device in the power supply is a series tetrode which is capable of feeding five gyrotrons in parallel. This, of course, would require upgrading the power rating of the transformer accordingly. It has been estimated that feeding five gyrotrons in parallel would reduce the cost of the power supply to about \$2.5 per watt RF power delivered. Therefore, it seems realistic to adopt a global figure of \$5/watt for a combined unit of gyrotrons, magnets and power supplies for TASKA.

IV.1.4 Beam Waveguide Launcher

Transport and energy balance studies have shown that about 7.5 MW of RF power for each plug at the electron cyclotron frequency are necessary to maintain the required electron temperature (59 keV) in the plug regions. As shown in section IV.1.2.2, a launching direction of 55° with respect to the normal ensures good absorption over a wide temperature range.

Since gyrotron sources at present are limited to power levels of about 350 kW, and it is not anticipated that the output of individual tubes is likely to rise above 500 kW to 1 MW in the future, power combining of several individual sources will be necessary. If delivering the total required power to the plasma is accomplished by multiple antennas, each feeding a separate region, then many ports and considerable space will be needed. This may very

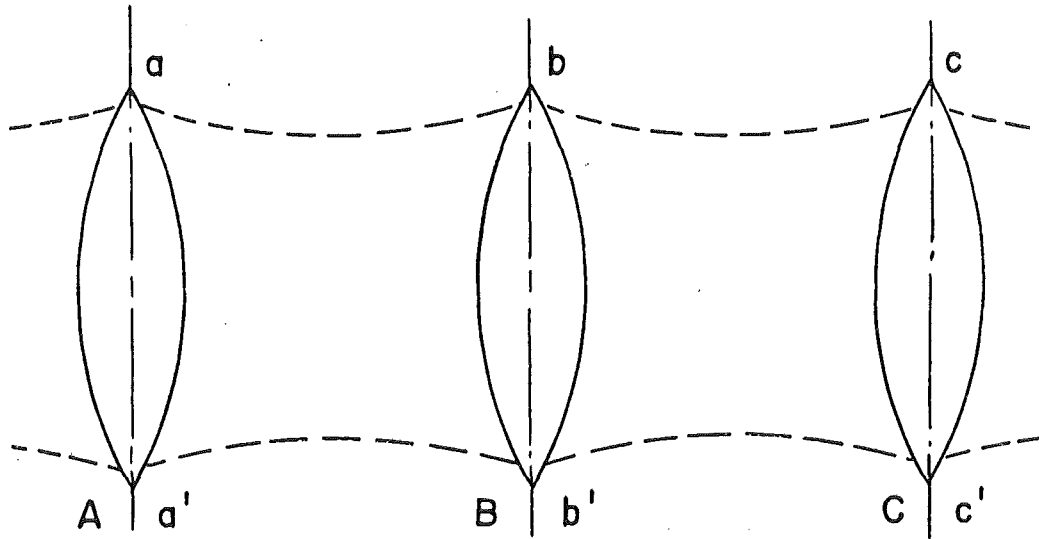
well conflict with magnet requirements. Passive combining results in an intolerable 3 dB loss and nonreciprocal combiners are also impractical at high power levels as well as in the presence of high magnetic fields.

To overcome these difficulties it is proposed to utilize a quasi-optical beam waveguide system. Such a system not only affords low loss spatial combining of gyrotron sources to multimegawatt levels but also directs the radiation onto the plasma region from specific angles.

The beam waveguide shown in Fig. IV.1-5 is an open (non-metallic) waveguide composed of periodically spaced phase transformers (lenses or conducting reflectors in the optical sense) which redirect the beam and thus maintain high energy concentration along its axis. Such phase correction can be obtained on reflection from parabolic mirrors as will be seen shortly. The lowest loss beam waveguide mode designated TEM_{00} is characterized by a Gaussian radial amplitude distribution and linear polarization. Beam modes in general are characterized by the product of a Gaussian and the generalized Laguerre polynomials.⁽¹²⁾ The lowest order Laguerre polynomial, L_0^0 , is simply equal to one, however, and hence the TEM_{00} mode transverse fields are given by

$$E_{\text{trans}} = A_{00} e^{-a^2 r^2 / R^2} \quad (\text{IV.1-14})$$

where R = guide radius and $a = \sqrt{k_0 / 2z_0}$ plays the role of the Fresnel number of geometrical optics with $2z_0$ designating the phase transformer spacing. Diffraction loss on such a waveguide is shown in Fig. IV.1-6 vs. the dimensionless parameter "a". Suppose, for example, a diffraction loss of 0.01 dB/iteration (or 0.2%) is chosen, leading to an "a" value at 56 GHz of 2.3 from Fig. IV.1-6. This "a" yields a "lens" spacing of 2 meters and a radius



BEAM WAVEGUIDE

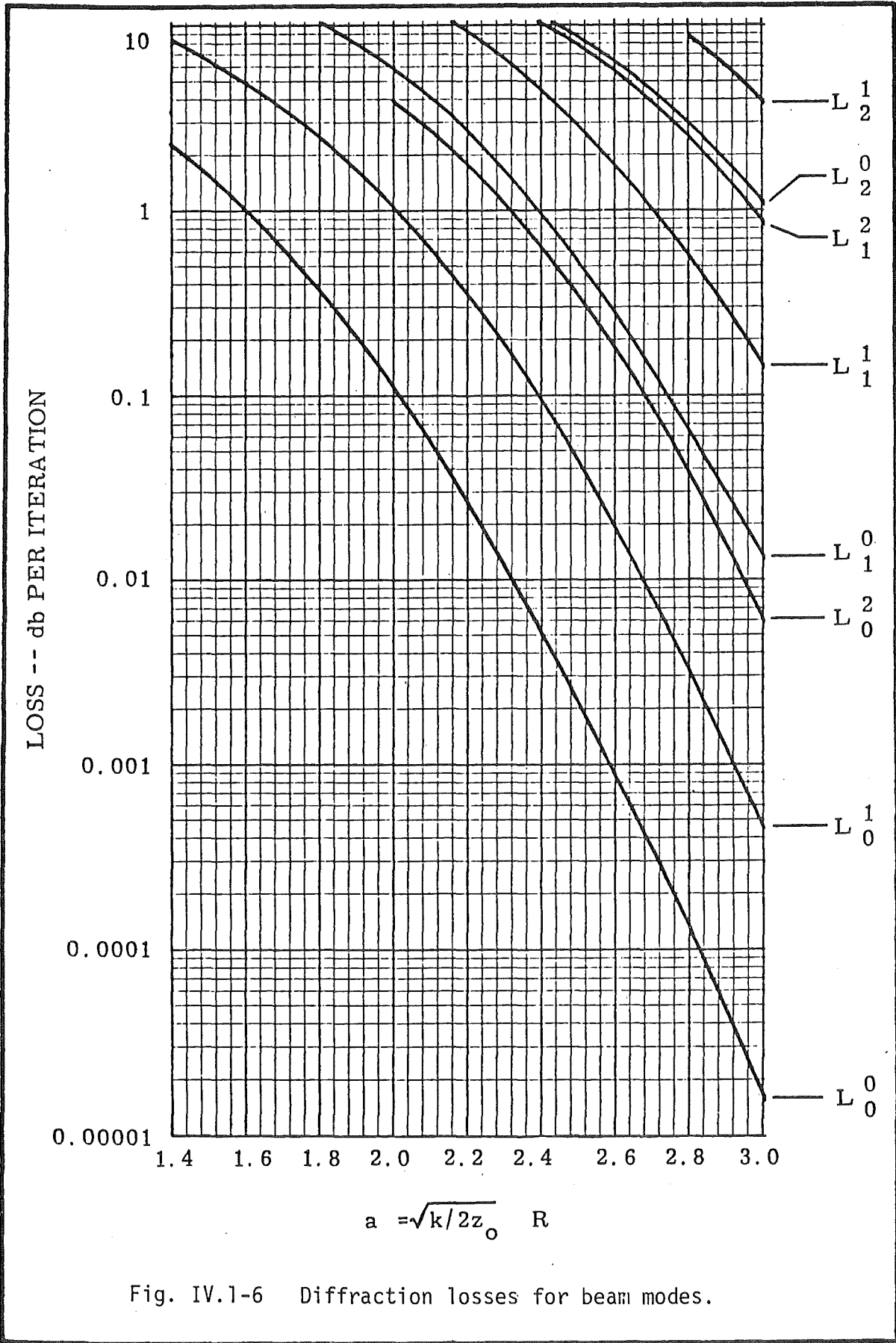
$$E_{trans} = A_{mn} L_n^m \left(\frac{a^2 \rho^2}{R^2} \right) e^{-\frac{a^2 \rho^2}{R^2}}$$

$$a = \sqrt{\frac{k_o}{2z_o}} R$$

R = guide radius

$2z_o$ = iteration length

Fig. IV.1-5 Beam waveguide.



of 9.5 cm. It is evident that at a given frequency it is possible to design the lens spacing and radius for any given diffraction loss.

It can be seen from Fig. IV.1-5 that the beam mode fields are reproduced at the centers of succeeding phase transformers, i.e. the fields of bb' equal the fields at aa' , etc. In addition, these fields must have uniform phase as must the fields midway between each transformer. In fact if a short circuiting metal plate were placed at the center of a phase transformer and another midway between two transformers a resonator would result. Such a resonator is also shown in Fig. IV.1-7 where the required phase correction is obtained by reflection from a parabolic mirror instead of from a half lens backed by a flat plate. That is, a Gaussian amplitude uniform phase beam mode at point "a" in Fig. IV.1-7 is exactly reproduced upon itself after reflection from the mirror.

Consider now the familiar Cassegrain system of geometrical optics shown in Fig. IV.1-8. In the absence of the hyperboloidal mirror, excitation at the focal point, a' , would result in parallel rays, i.e., a uniform phase front, at b . In the offset Cassegrain system shown, adding the hyperboloidal section merely switches the excitation point to "a" and aperture blocking is prevented by the offset. If now this system were excited at "a" by a beam mode (Gaussian amplitude, uniform phase) instead of a point source then that excitation would be exactly reproduced at "b" just as it was in Fig. IV.1-7 because the Cassegrainian tandem hyperboloid-paraboloid acts identically to a single paraboloid of focal length f .

Such an arrangement has considerable practical utility for plasma heating. If one imagines the plasma at point "b" and a proper beam mode excitation device at "a" then uniform phase radiation can be concentrated onto the

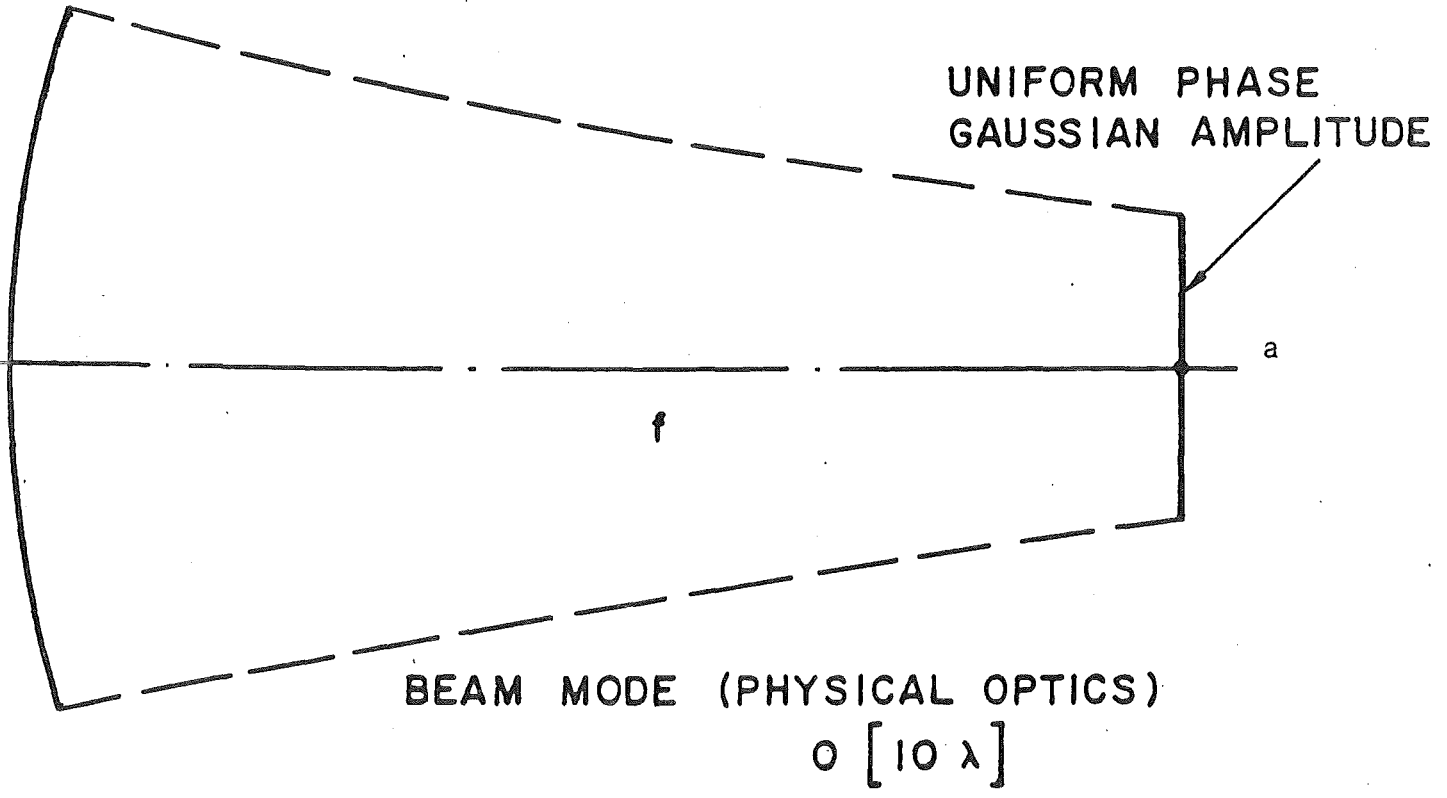


Fig. IV.1-7 Beam mode (physical optics)

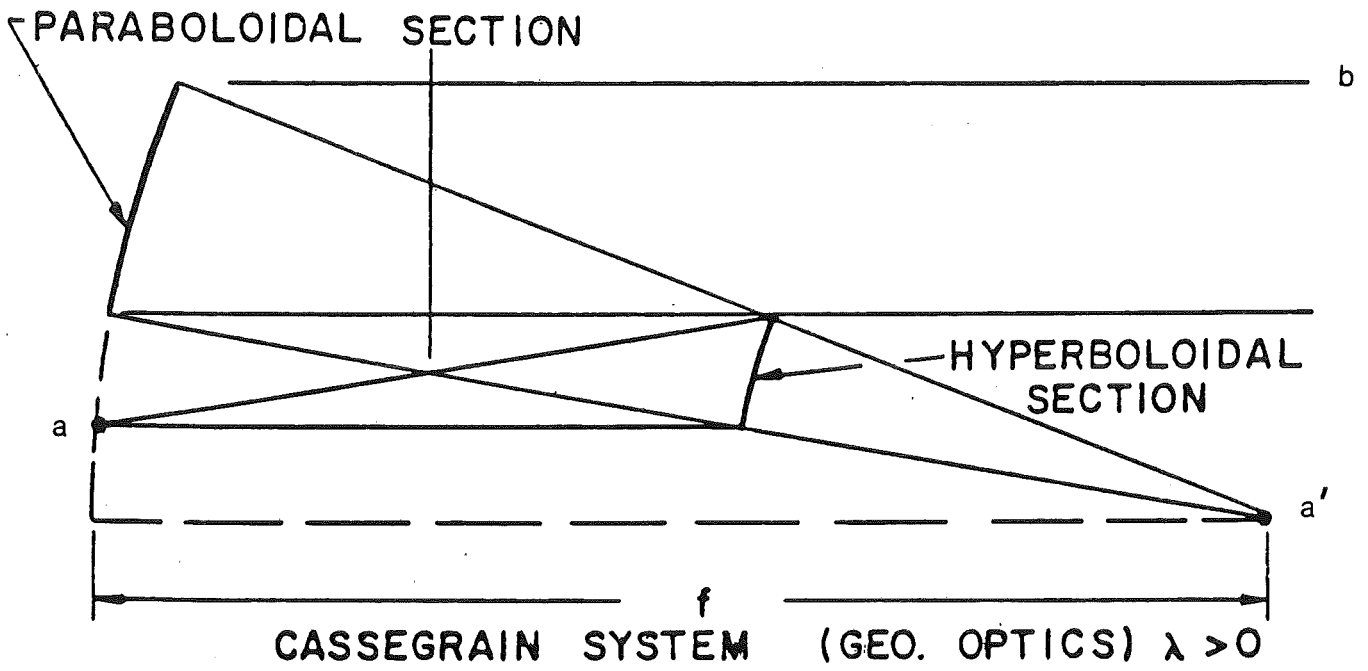


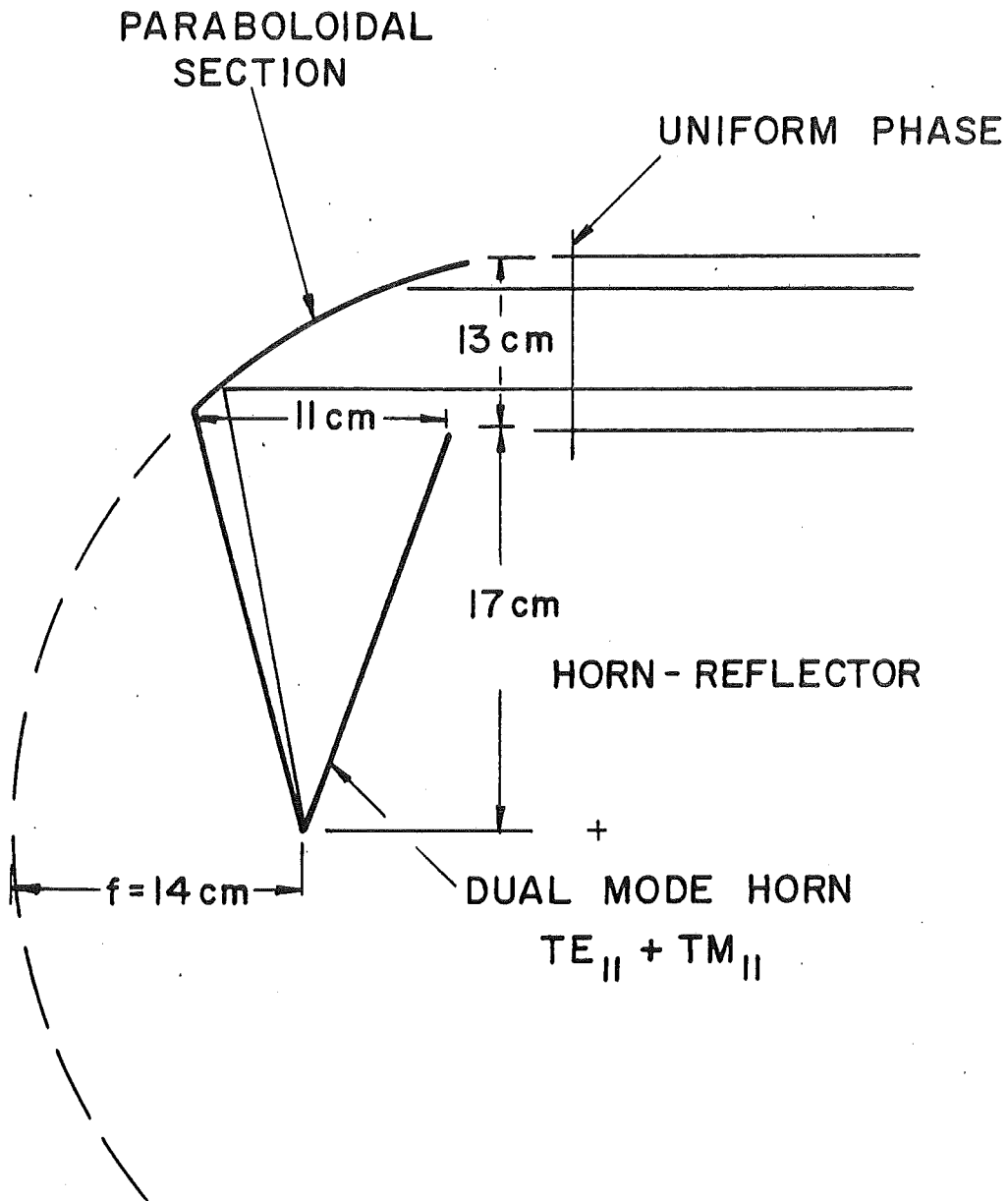
Fig. IV.1-8 Offset Cassegrain antenna

plasma from any desired angle and the source is shielded from the neutron radiation flux by the intervening hyperboloid which can be backed by neutron absorber. A suitable launcher for the fundamental beam waveguide mode is the familiar horn-reflector antenna.

Horn-reflector antennas have been employed for many years in communication systems.⁽¹³⁾ Such an antenna shown in Fig. IV.1-9 is also an offset paraboloid. Here, however, the apex of a cylindrical horn is placed at the focal point of the paraboloid. The horn has a mode converter in its throat which when fed with the TE_{11} mode of cylindrical waveguide produces both the TE_{11} and TM_{11} modes in the horn. These modes propagating together in the horn produce by interference a near Gaussian radial amplitude distribution at the horn mouth.⁽¹⁴⁾ Upon reflection from the paraboloid a uniform phase front is created and hence the resultant aperture field is just that required to launch a beam mode.

Since the dual mode horn must be fed with the TE_{11} cylindrical waveguide mode and because the gyrotron output is typically TE_{0n} an intervening mode transducer is required. Suppose, for example, a TE_{01} gyrotron is used. In that case a stepped twist-reflector will provide the necessary conversion to the TE_{11} mode. A quarter wave step over one half of the reflector converts the circular symmetric mode electric field into an anti-symmetric field. Now the quarter wave grating of the twist-reflector reverses the polarization of only one of the rectangular components of the electric field with the result that the fields now conform to those of the TE_{11} mode.

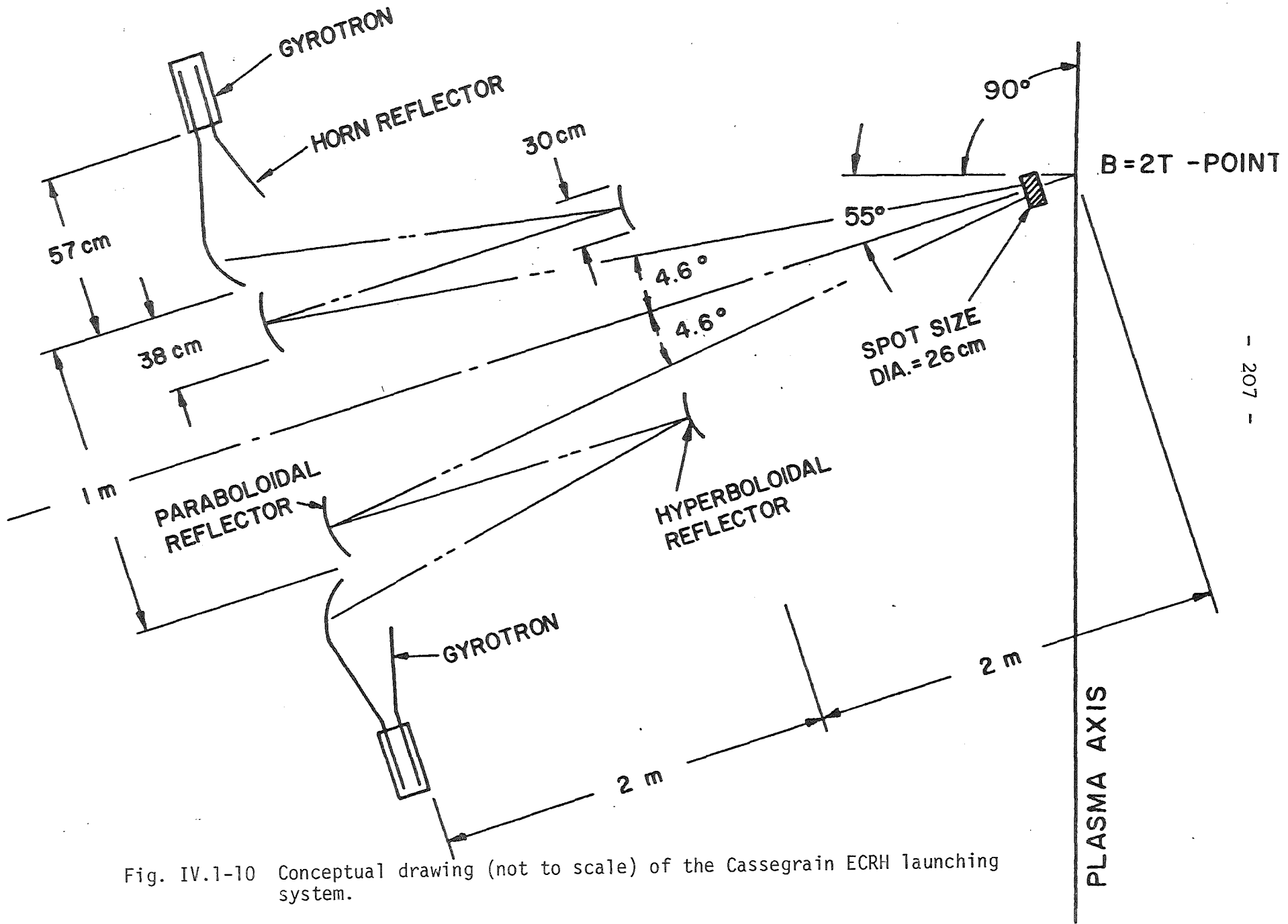
A complete delivery system incorporating each of the principles discussed above is shown in Fig. IV.1-10. This system designed for TASKA could consist of up to 13 gyrotrons distributed around an axis which in turn makes an angle



DIMENSIONS NOT TO SCALE

Fig. IV.1-9 Offset paraboloid launcher

IV.1-30



- 207 -

Fig. IV.1-10 Conceptual drawing (not to scale) of the Cassegrain ECRH launching system.

of 35° with the machine axis. For the design given, all beams incident on the plasma lie within an angle of 30° to 40° as required from our ray tracing calculations. Hence power levels per port of up to 4 megawatts are possible with this system if each individual gyrotron is limited to 350 kW. Each gyrotron feeds a stepped twist reflector mode converter which in turn excites the dual mode horn. Since individual sources are limited to 350 kW, breakdown fields in the metallic waveguides governed by

$$E_{\max}^2 = \frac{P_{\max}}{3.97 \times 10^{-3} \sqrt{1 - \left(\frac{\lambda}{3.41 r_0}\right)^2 r_0^2}}$$

are limited to about 4×10^6 V/m which pose no breakdown problems in the absence of plasma at $p_0 < 10^{-6}$ Torr. When the powers are combined, the Gaussian beam's maximum amplitude is dictated by

$$E_{\max}^2 = \frac{2z_0 P_{\text{avg}}}{\pi R^2} \left(\frac{4a^2}{1 - e^{-2a^2}} \right)$$

where "a" is the parameter of Fig. IV.1-6. This results in a field intensity of 113 kV/m for $P_{\text{avg}} = 4$ MW. This is a worst case calculation since it assumes all fields combining in phase, a highly unlikely event. Even in this worst case the field intensity is low because of the relatively large area over which the energy is distributed, and since no metal boundaries are in proximity to the fields there should be no breakdown problems.

It has been shown that a quasi-optical feed system for plasma heating in fusion reactors is totally compatible with the reactor constraints. Such a

system allows multiple medium power gyrotron sources to be combined into intense beams which can be focused onto the plasma in a well defined cone. The antenna system is derived from an offset Cassegrain and employs Gaussian beams which give good energy concentrations without breakdown and are characterized by an absence of side lobes. The antenna system also isolates the sources from neutron flux and allows the gyrotrons to be located well away from strong magnetic fields as well as providing for good vacuum pumping the intervening region.

References for Section IV.1

1. This report, section III.2.
2. LIBRIS, Physics Library, NMFEEC, Livermore, CA, Code P52.
3. D.B. Batchelor, R.C. Goldfinger, and H. Weitzner, IEEE PS-8 (1980), 78.
4. I. Fidone, G. Granata, G. Ramponi, and R.L. Meyer, Phys. Fluids 21 (1978), 645.
5. M. Bornatici, Proceedings of International Workshop on ECE and ECRH, Oxford, 1980.
6. M. Bornatici and F. Engelmann, Radio Science 14 (1979), 309.
7. I.P. Shkarofsky, Phys. Fluids 9 (1966), 561.
8. D. Braun (University of Wisconsin) private communication.
9. A. Stappens and H. Jory (Varian Associates), personal communication.
10. M. Heyne (Hughes Aircraft Co.), personal communication.
11. R.C. Black (Universal Voltronics), personal communication.
12. G. Goubau and F. Schwering, IRE-AP, May 1961, pp. 248-263.
13. Schelkunoff and Friis, Antennas Theory and Practice, John Wiley, 1952, pg. 569.
14. R.J. Chaffin and J.B. Beyer, IEEE MTT-12, Sept. 1964, p. 555.

IV.2 ICRF Heating in Central Cell

IV.2.1 Introduction

The overall power balance, heating system layout and heating efficiency of TASKA can be greatly improved by considering direct ion cyclotron frequency range (ICRF) heating of the central cell ions. As discussed in detail in Sections III.1-III.4, the potential use of direct central cell heating by an ICRF heating system provides an easier layout for access of high energy neutral beams in the plug and barrier regions with lower total power and energy requirements on them. In addition, the anticipated high heating efficiency of the ICRF system and relatively low cost per watt of RF power coupled to the ions make this an important design consideration. The central cell ICRF system will greatly improve the startup scenario and can add to the control of the plasma burn. The main concern of a central cell ICRF heating system is not in the heating efficiencies or cost factors which have been demonstrated at above the megawatt level in tokamaks such as PLT⁽¹⁾ and TFR,⁽²⁾ but in the viability of the antenna structure in the hot central cell region of the test reactor. Since very little work has been done on this subject, we will propose a design based on physics and machine requirements and give a preliminary evaluation of the antenna viability in a reactor environment.

IV.2.2 ICRF Physics and Design Considerations

The power balance calculations discussed in section III show that a central cell ion cyclotron heating requirement of 40 MW of power coupled to the central cell ions is required for the design operating point. The central cell operates at low magnetic field ($B_0 \approx 2.7$ T) and the relatively high $\beta = 50\%$ at full operating regime provides a fundamental deuterium ion cyclotron resonance frequency of $f_{cd} = 15$ MHz. In this frequency range and given

the radial constraint of the central cell reacting hot plasma edge at $r = 32$ cm, we are constrained to coil antenna coupling. The high density core plasma with $\bar{n} = 2 \times 10^{14}/\text{cm}^3$ will provide good coupling in the ICRF range.

In order to improve the antenna coupling to the plasma the second harmonic near $f = 2f_{cd} = 3f_{ct} = 30$ MHz is proposed as the frequency for the heating system.⁽³⁻⁵⁾ This will allow the wave evanescence in the plasma edge to be decreased and allow the wave mode, including the 14 cm thick plasma halo annulus, to be better coupled to the plasma core. Recent $f = 2f_{ch} = 42$ MHz heating experiments at above the megawatt level on the PLT tokamak have proven quite successful.⁽⁶⁾ It is expected that a detailed analysis of the scaling of this heating scheme to reactor parameters will also prove attractive. It also allows the possibility of minority fundamental hydrogen heating $f = 2f_{cd} = f_{ch}$ at lower ion temperatures as part of the startup scenario.

Another consideration for the ICRF system is its location to ensure heating of the central cell ions. The ideal location would be in the central region of the central cell with the magnetic field decreasing slightly towards the ends of the central cell where wave particle resonance and heating occurs. This would ensure that the wave would be fully absorbed in the central cell region and not allowed to propagate into the barrier regions where it could be absorbed and have a deleterious effect on the barrier performance. However, since the REGAT and blanket test modules are located in the central region of the central cell, we consider ICRF coupling regions towards the ends of the central cell.

To provide a directivity of radiated power, we first considered a phased array of four coil sets of two each on each end of the central cell. They would be excited in an $m = \pm 1$ configuration by 20.3 cm inner diameter coaxial

feeds which will accommodate the 5 MW/two coil set power coupled with a sufficient safety factor to eliminate RF arcing. To provide directivity towards the central part of the central cell a $\lambda_{\parallel}/4$ array with a $\phi = 90^{\circ}$ electrical phase advancement for each successive coil away from the central region could be employed to provide a maximum radiation towards the central region and a null towards the barrier region. However, the parallel wavelength values for the fast magnetosonic wave mode in the plasma region corresponding to $k_{\parallel} = 5-15 \text{ m}^{-1}$ require that $\lambda_{\parallel} = 1.26-0.42 \text{ m}$. At these lower frequencies, the substantial mutual inductance between the closely spaced adjacent coil sets in the vacuum region makes the RF circuit drive problem more difficult. It would be hard to achieve the 90° electrical phase difference required for directivity of the radiation pattern. The adjacent antennas are also very closely spaced (20 cm center to center) for this level of coupled RF power.

We then considered a $\lambda_{\parallel}/2$ spacing with a 180° electrical phase shift between adjacent coils. This provides a symmetric pattern of radiation in the axial direction but is easier to excite since the mutual inductance term is minimized due to the 180° electrical phase shift between adjacent coils. We must then invoke the property of reflection of the portion of coupled RF power propagating towards the barrier zone before it reaches the ion cyclotron resonant zone. This is feasible since the plasma density decreases drastically as one moves from the central cell to the barrier zone to $n_B = 6.8 \times 10^{12}/\text{cm}^3$. The plasma radius is also much smaller than in the central cell so that the na^2 criteria for fast mode propagation is not met and the mode can be localized in the central cell region.

Finally, to protect the antennas from the 3.5 MeV α particles resulting from the D-T fusions in the low field central cell region we have introduced a

14 cm thick plasma halo around the reacting plasma to allow the antenna to be located some distance from the fusion plasma. This allows the antenna to be located more than an α -particle gyroradius away to protect it from α -particle bombardment. The intervening region $32 \text{ cm} < r < 46 \text{ cm}$ cannot be made a vacuum region since the reduced plasma loading on the antennas would decrease the coupling efficiency and the wave fields would be evanescent from the antenna to the fusion plasma surface. Thus, the halo plasma with high density and lower temperature allows the fast wave to propagate while locating the antennas at a safer distance from the reacting fusion plasma.

Another consideration involves the launching and absorption of the RF power with the deuterium ions. An axial magnetic beach is proposed. This is desired since we wish to launch the RF power in a region where the wave frequency is well below ($\approx 10 - 15\%$) the second harmonic deuterium resonance and avoid local harmonic resonance of ions which could strike the antennas and interfere with an efficient coupling process. The wave then propagates from the ends of the central cell towards the central region where the magnetic field decreases by 10% and deuterium absorption occurs. For the 30 keV central cell ion temperatures and a dominant k_{\parallel} spectrum component of $k_{\parallel} = 7.85 \text{ m}^{-1}$, the $k_{\parallel} v_i$ Doppler width corresponds to 5% of the second harmonic resonance at $f = 30 \text{ MHz}$. At these higher densities, $n = 2 \times 10^{14}/\text{cm}^3$, the deuterium-tritium equilibrium and ion isotropization times will be sufficiently rapid so that both ion species will be heated to the same temperature and instabilities arising from a high degree of ion thermal anisotropy will not affect confinement. If additional flexibility is desired in determining the axial heating profile, the antennas can be driven at slightly different

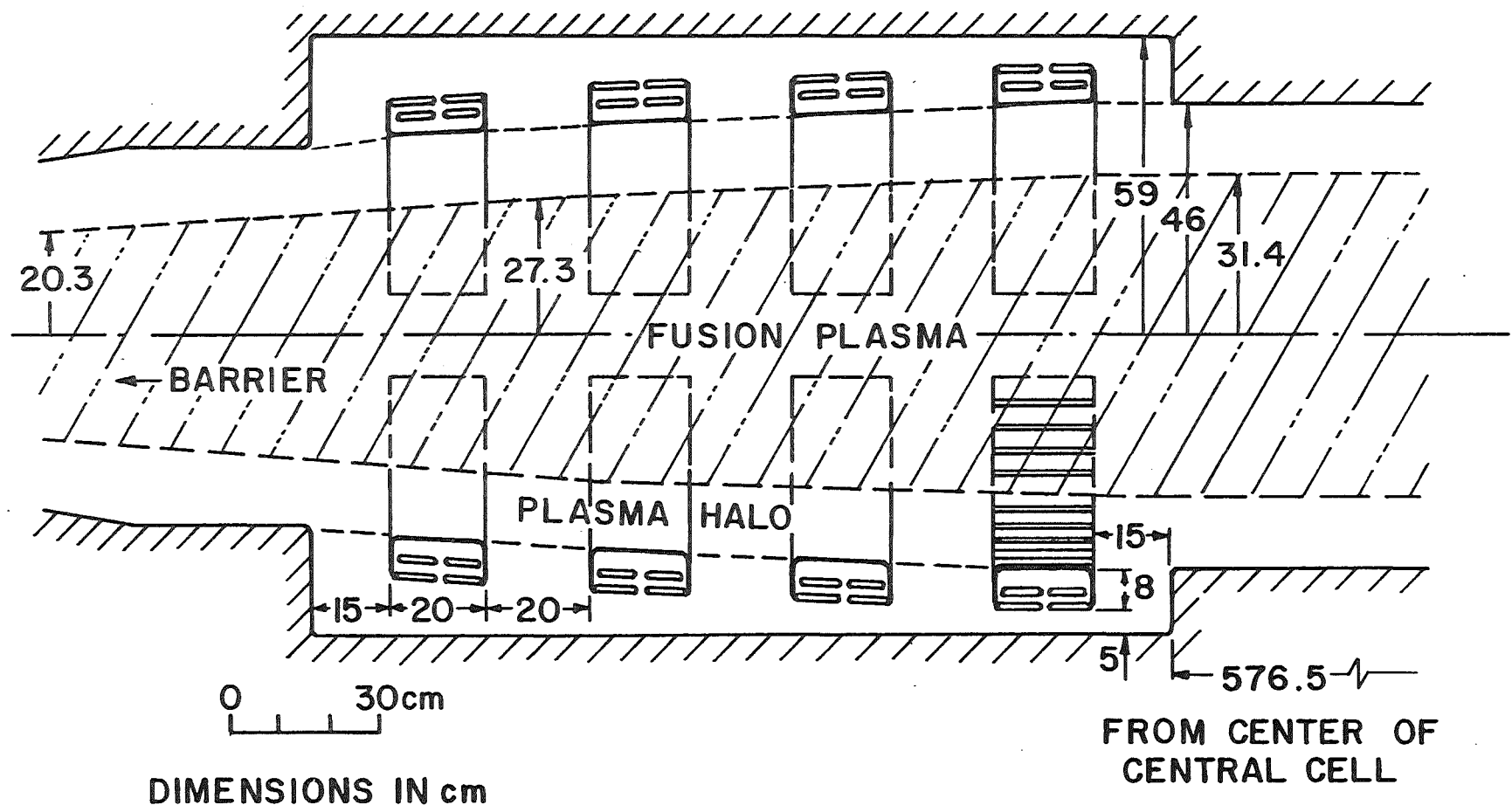
frequencies or a more broad band source excitation can be considered to tailor the axial power deposition.

IV.2.3 Antenna Layout

A more detailed drawing of the ICRF coil antenna launching region is shown in Fig. IV.2-1. The fusion reacting plasma producing α particles is given by $r \leq 32$ cm. A 14 cm halo plasma of sufficiently high density to allow fast wave coupling and propagation ($n > 8 \times 10^{12}/\text{cm}^3$) and sufficiently low temperature to minimize antenna Faraday shield erosion is produced between the core plasma and antenna. The antennas and Faraday shield are of 8 cm radial by 20 cm axial extent and are of an all conductor, no dielectric design scaled from recent designs used on TFR and PLT. Finally, a 5 cm gap between the back plate of the antenna Faraday shield and the first wall is required to minimize wall image currents affecting coupling efficiency.

Each antenna is of 20 cm axial extent with a 20 cm space between each Faraday shield. The electrical phase alternates by 180° between each antenna to minimize the mutual inductance term for the driving circuit and provide the dominant $k_{\parallel} = 7.85 \text{ m}^{-1}$ spectrum component. The total RF coil system (8-2 coil sets) then take up 2.8 m of axial extent of the central cell. The antennas can be end fed by a 20 cm diameter coax with 5 MW/two coil set power handling capacity. The 20 cm diameter coaxial feed through was scaled to provide an adequate breakdown protection based on current PLT experiments at 42 MHz. The two antenna set on PLT is fed by 10 cm diameter coax and has a coupled power capability to the plasma of 1.5 MW. The proposed 20 cm diameter coax should provide an adequate safety margin for the 5 MW/two coil set on TASKA. The Faraday shields surrounding the antenna coils will suppress axial electronic fields between the antennas. However, an RF test facility would be useful to

IV.2-6



- 215 -

CENTRAL CELL ICRF ANTENNA LAYOUT

Figure IV.2-1

test breakdown and material limitations for the high ICRF power density proposed for TASKA. At a frequency of 30 MHz and the wall diameter of 92 cm, a center fed resonant $\lambda/2$ antenna of 50 cm circumferential extent can also be considered to optimize the plasma load impedance to the RF drive and matching circuit to minimize high voltage breakdown. The feed system must be optimized for impedance matching and modular design for rapid replacement of antenna modules. By recessing the first wall to accommodate the antennas, the potential axial heat flux on the antenna array is eliminated.

IV.2.4 Materials Considerations

The antenna coils and Faraday shields must be made of good conductors which will withstand the neutron bombardment, radiation damage, plasma heat flux and surface erosion. If metallic material or copper clad stainless steel were used, cooling would be required. Water cooling is readily introduced to the central coaxial conductor by means of quarter-wave coaxial stubs outside the reactor vessel. The higher operating temperatures can anneal the neutron induced loss of high conductivity in these materials, keeping conductor RF power losses to an acceptable level. Another material which was considered is pyrolytic graphite. It has a high conductivity, high temperature capability, and could be considered to radiatively cool without the need for water cooling. It is also a low Z material and would help to lessen the impurity radiation problem. Its structural integrity and resistance to cracking and fracture will have to be further evaluated for use in fusion plasmas.

Furthermore, graphite is known to be very susceptible to neutron radiation damage. It is subject to large dimensional changes⁽⁷⁾ which are accompanied by the formation of microcracks throughout the material. As a

result, it is expected that the electrical conductivity of pyrolytic graphite will rapidly degrade with neutron irradiation damage.

It is, therefore, proposed to employ metallic materials for the antenna coils and the Faraday shields. In order to obtain good electrical conductivity, the antenna coils are made of austenitic stainless steels plated with high-conductivity copper. As demonstrated by Haubenberger⁽⁸⁾ the plating of copper on austenitic steels can be accomplished by electrolytic or explosive methods. The advantage of this composite metal is that the high-conductivity copper is needed only where the RF current is carried, namely in the skin depth layer. The surface temperature for the copper layer is chosen to be in the range from 270°C to 330°C where most of the neutron damage does not significantly contribute to a degradation of electrical conductivity. On the other hand, the temperature is sufficiently low for austenitic stainless steel so that swelling poses no severe problem.

The Faraday shields are made of molybdenum sections, which are loosely attached by appropriately machined tongues and grooves to the rear antennas. In contrast to the antennas which are cooled by water, the Faraday shields are cooled by radiation. Therefore, they reach temperatures estimated to be above 700°C. These temperatures are sufficiently high for molybdenum to avoid the radiation-induced embrittlement and a large shift of the DBTT.

The Faraday shield acts to ensure the coupling of the fast magnetosonic mode, minimizes electrostatic mode coupling and protects the coil conductors from particle bombardment and plasma flux which could cause internal arcing. As such, some erosion of the outer Faraday shield surface will not cause RF power loss in the antenna and will protect it. Further materials testing and

an RF test facility are required to develop materials for antenna coils for fusion reactor plasmas.

References for Section IV.2

1. J. Hosea and PLT Group, 8th Conf. Plasma Physics and Controlled Fusion Research, IAEA-CN-38/D-5-1, Brussels (1980).
2. Equipe TFR, 8th Conf. Plasma Physics and Controlled Fusion Research, IAEA-CN-38/D3, IAEA-CN-38/N5, Brussels (1980).
3. J.E. Scharer, J.B. Beyer, D.T. Blackfield, and T.K. Mau, Nucl. Fusion 19, 1171 (1979).
4. J.E. Scharer, B.D. McVey, and T.K. Mau, Nucl. Fusion 17, 297 (1977).
5. D.T. Blackfield and J.E. Scharer, to be published in Nucl. Fusion (1982).
6. P. Colestock, private communication.
7. R.D. Watson and W.G. Wolfer, "Mechanical Constitutive Laws for irradiation Behavior of Graphite", J. Nucl. Matls. 85&86 (1979), 159-164.
8. W.D. Haubenberger, "Ein Kupfer-Austenit-Verbundleiter für hohe mechanische Beanspruchung", Metall. 34 (1980), 999-1002.

IV.3 Neutral Beam Injection

IV.3.1 General

Neutral beam injection is the primary means for initial hot ion buildup in the plug, plasma heating, plasma fueling, and selective charge exchange barrier pumping in the TASKA tandem mirror device. The overall neutral beam injection requirement is generally divided into convenient modular (practical sized) neutral beam injector (NBI) units each producing an output atom current at a designated energy suitable for injection into the appropriate region of the plasma. The steady state NBI system for TASKA includes a pair of very high energy plug neutral beams (plug NBI) to help buildup and to maintain the plasma in the high potential end plugs, a pair of high energy pump beams (HE-NBI) to pump trapped ions out of the barrier minima, a set of six medium energy pump beams (ME-NBI) arranged for both barrier cell pumping and central cell fueling, and finally a pair of low energy neutral beams (LE-NBI) located to inject into a region of the thermal barriers where the plasma potential is such as to allow a low energy NBI's to pump out the higher energy trapped ions. The general layout of these NBI on the TASKA confinement vessel is shown in Fig. IV.3-1. The specific NBI equivalent current and energy requirements for each region and each function in TASKA are the result of a set of parametric code studies of plasma equilibrium needed for the neutron wall loading goal of 1.5 MW/m^2 (described in Section III.3). The specific NBI parameters needed to produce the specified incident (on plasma) neutral beam current and power for TASKA are given in Table IV.3-1, including the estimated ion source high voltage power supply current requirements (with a 20% margin).

For simplicity in initial wide ranging parameter studies, the equilibrium code calculations and the resultant NBI parameter listing in Table IV.3-1 are

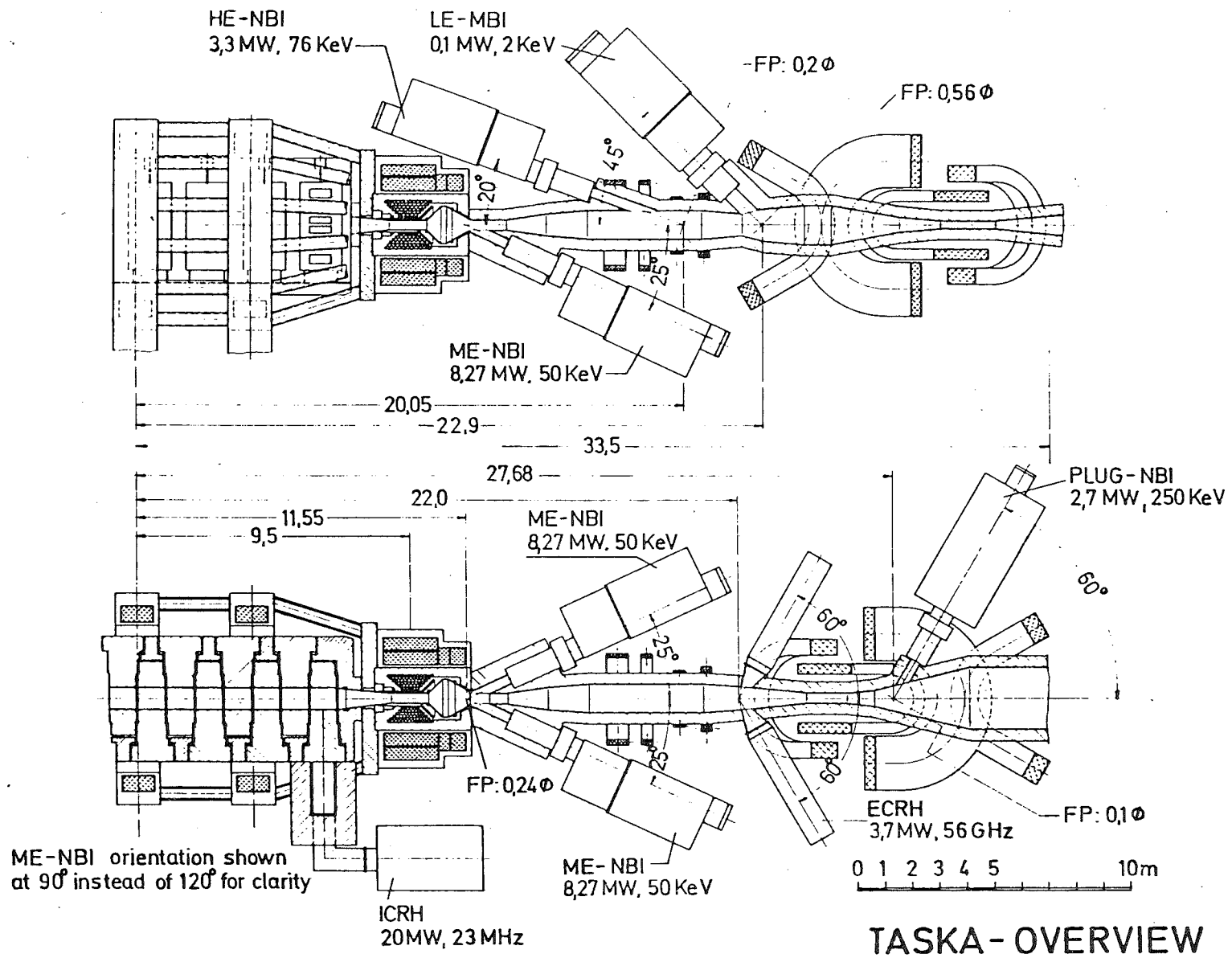


Fig. IV.3-1

Table IV.3-1. TASKA Neutral Beam Injector Requirements

	<u>Units</u>	<u>Plug Nb</u>	<u>HE-NBI</u>	<u>ME-NBI</u>	<u>LE-NBI</u>
Location		Plugs	Barriers	Barriers	Barriers
Injection angle	Degrees	60	20	25	45
V_0	kV	250	76	50	2 to 5
I_0 /NBI	A	10.8 (H^0)	43.4 (D^0)	3 x 55 ($D^0 + T^0$)	50 (D^0)
P_0 /NBI	MW	2.7	3.3	8.3	.1 to .25
# Ion sources per NBI		1 est.	1	3	1
Total # NBI		2	2	6	2
I^\pm estimate (for I_0 w/ 20% margin)	A	23 (H^-)	108.8 (D^+)	3 x 121 ($D^+ + T^+$)	97.5 (D^+)
j (s.c.l.)	A/cm ²	.05	.27	.3	.25
Extraction area ($f_t = .45$)	cm ²	~ 20 x 50	20 x 45	20 x 45	20 x 45
Beam focal length	m	7.5	12	7.5	6.3
Beam divergence	Degrees	< .3*	.5*	.7*	3.5* to 2.2*
Collimation (at TASKA wall; single source)	cm ²	~ 16 x 21	38 x 47	34 x 39	81 x 110 (5 kV un-focused)
Min. footprint (radius)	cm	8**	12	9.3	~ 38 (5 kV)
Gas flow (total)	Torr-l/s	~ 20	15	50	13

*Divergences quoted are conservative 1/e values with reduction of up to a factor of two likely within the planning time for construction.

**Minimum footprint quoted for slightly defocused beam to reduce beam loading on the remnant neutral beam dump.

both based upon only a single full energy species output (e.g., D^0 at an energy eV_0) from each NBI. Therefore, some revisions are to be expected in the NBI requirements of Table IV.3-1 when more refined equilibrium and self-consistent NBI calculations are made using the actual detailed output species composition from the ion sources. The best present D_2 fed ion sources yield an ion beam of 80% D^+ , ~ 15% D_2^+ , and ~ 5% D_3^+ (instead of 100% D^+), with the resultant neutral beam output including a mixture of full energy (eV_0), one-half energy, and one-third energy D^0 components after dissociation and charge exchange in the neutralizer cell. The result for this typical species mix is effectively 1.25 A atomic (D^+) current per A of electrical current, but with an average D^+ energy = .8 eV_0 .

The NBI's listed in Table IV.3-1 and their associated electrical power supplies and gas pumping vacuum system represent a significant portion of both the capital facility and operating costs of the machine. The machine performance (neutron wall loading) is predicted by code studies to be strongly dependent on the maximum performance of the NBI system (and also of the required ECRH and ICRH systems). Therefore part of the NBI task is to get the maximum reliable performance from the NBI system.

This chapter will therefore augment the simple NBI parameter listing of Table IV.3-1 by including a brief discussion of a typical positive-ion source neutral beam lines in Section IV.3.2 (to illustrate the factors limiting NBI performance), then describing a specific TASKA NBI prototype design selection in Section IV.3.3, and adding a few ion source details for ion source design selection in Section IV.3.4 for reference purposes. A negative ion source based NBI appears essential for efficient high energy NB production (e.g., for the 250 kV H^0 plug NBI), but is described only briefly in Section IV.3.5 due to

uncertainty as to which type of negative ion source will be found most practical and most efficient for high energy neutral beam formation.⁽¹⁾ Note, however, that the hot ion heating function of the 250 kV H⁰ plug NBI can also be attained through use of a heavier mass 375 kV He⁰ NBI using existing positive ion technology, if H⁻ source technology does not develop as rapidly as expected. Helium gas, however, is difficult to vacuum pump, and therefore this less desirable approach was not used for the TASKA reference design.

IV.3.2 Typical Positive Ion Source/Beam Line System

Each NBI unit includes one or more close coupled ion source, neutralizer cell and remnant ion sweep set(s) (as listed in Table IV.3-1), plus associated gas pumping panels, beam collimation apertures, and provision for beam diagnostics. The ion source tank section containing this equipment is in turn connected via a bellows (with provision for adjusting the ion source tank orientation for beam steering), a vacuum isolation valve, and ducting to the appropriate position on the TASKA confinement vessel. Extensive magnetic shielding and appropriate neutron shielding are required for the ion source, neutralizer cell and remnant ion sweep set(s). Finally, each NBI line requires a remnant neutral beam power (and gas) dump on the far wall of the confinement chamber. A sketch of a typical NBI system is shown in Fig. IV.3-2.

The ion sources, neutralizer cells, and associated gas pumping system are expected to largely determine the limits on the NBI performance. In particular, each ion source requires a relatively high amount of support technology for operation and represents a very high power instrument. As such, the ion source designs and power supply specifications are required to be within conservative specifications to allow long-lived and relatively trouble free service. The beam heat loads incident upon the ion sweep dump, collimation

IV.3-6

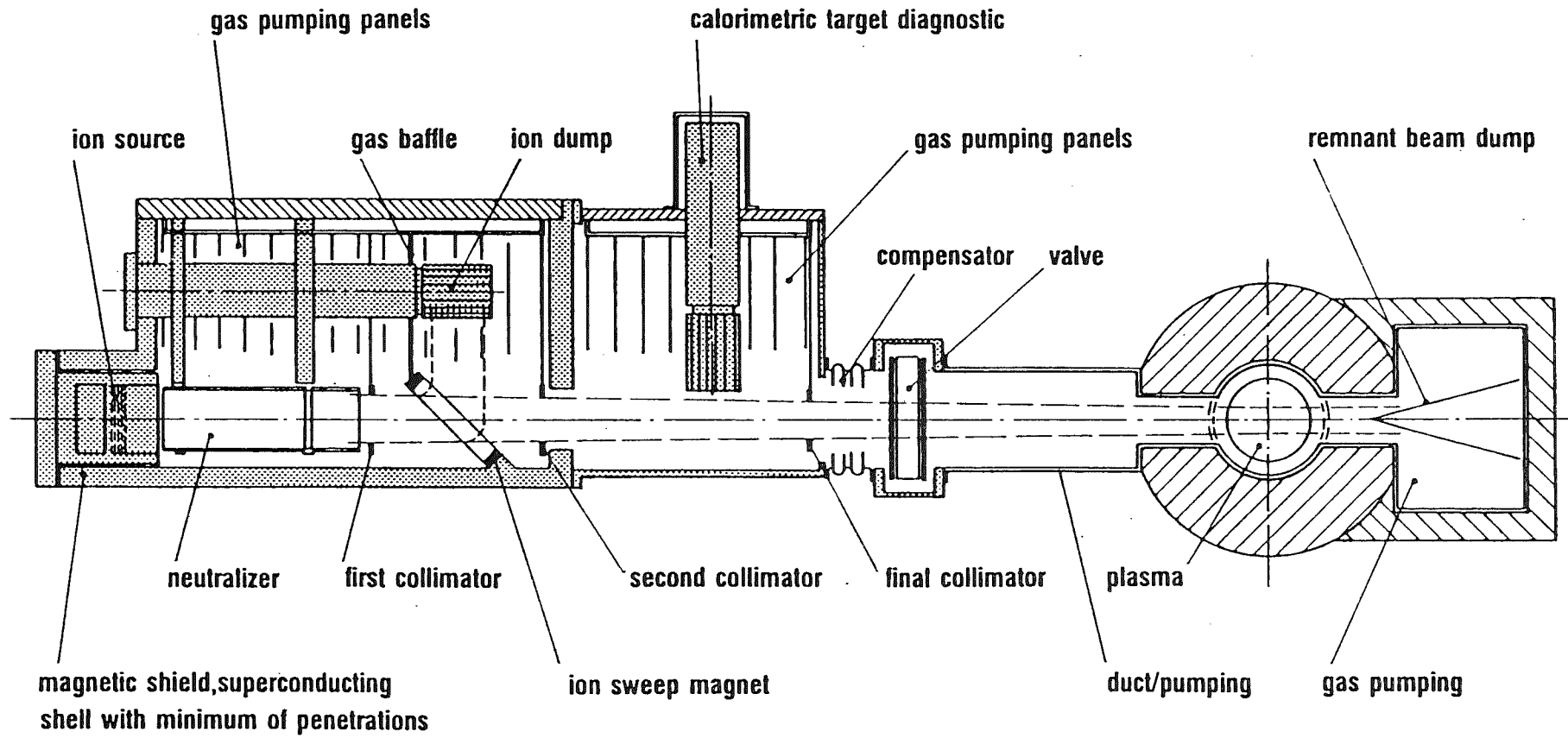


Fig. IV.3-2 Neutral beam injector

apertures, diagnostic calorimeter (when inserted into the beam), and the remnant neutral beam dump are often $> 2 \text{ kW/cm}^2$, so special design is required for adequate cooling and long lifetime. The LBL/IPP conceptual design study for the Zephyr NBI system is a good reference base for NBI details.⁽²⁾

IV.3.2.1 Primary Limitation to Ion Source Output

The primary limitations to the ion source output result from (1) the space charge limit on the extracted ion density, (2) the limited transparency of the electrode set needed to form the ion extraction and acceleration field, (3) the need for a reasonably small sized electrode area to allow for cooling and to maintain accurate inter-electrode gap and extraction aperture set alignment (between electrodes), and (4) the intrinsic divergence of the ion beam. A typical ion source⁽³⁾ is shown in Fig. IV.3-3.

IV.3.2.1.1 Space Charge Limited Current Density $j(\text{s.c.l.})$

The fundamental limit to the maximum extracted ion current density arises through the Childs-Langmuir equation for the space charge limited current density. The generalized⁽⁴⁾ form for a mixed ion species beam is:

$$\sum_i j_i M_i = \frac{1.72 V^{3/2}}{d^2}$$

where: $j_i \equiv$ current density of i^{th} species (mA/cm^2),

$M_i \equiv$ mass of i^{th} species (a.m.u.),

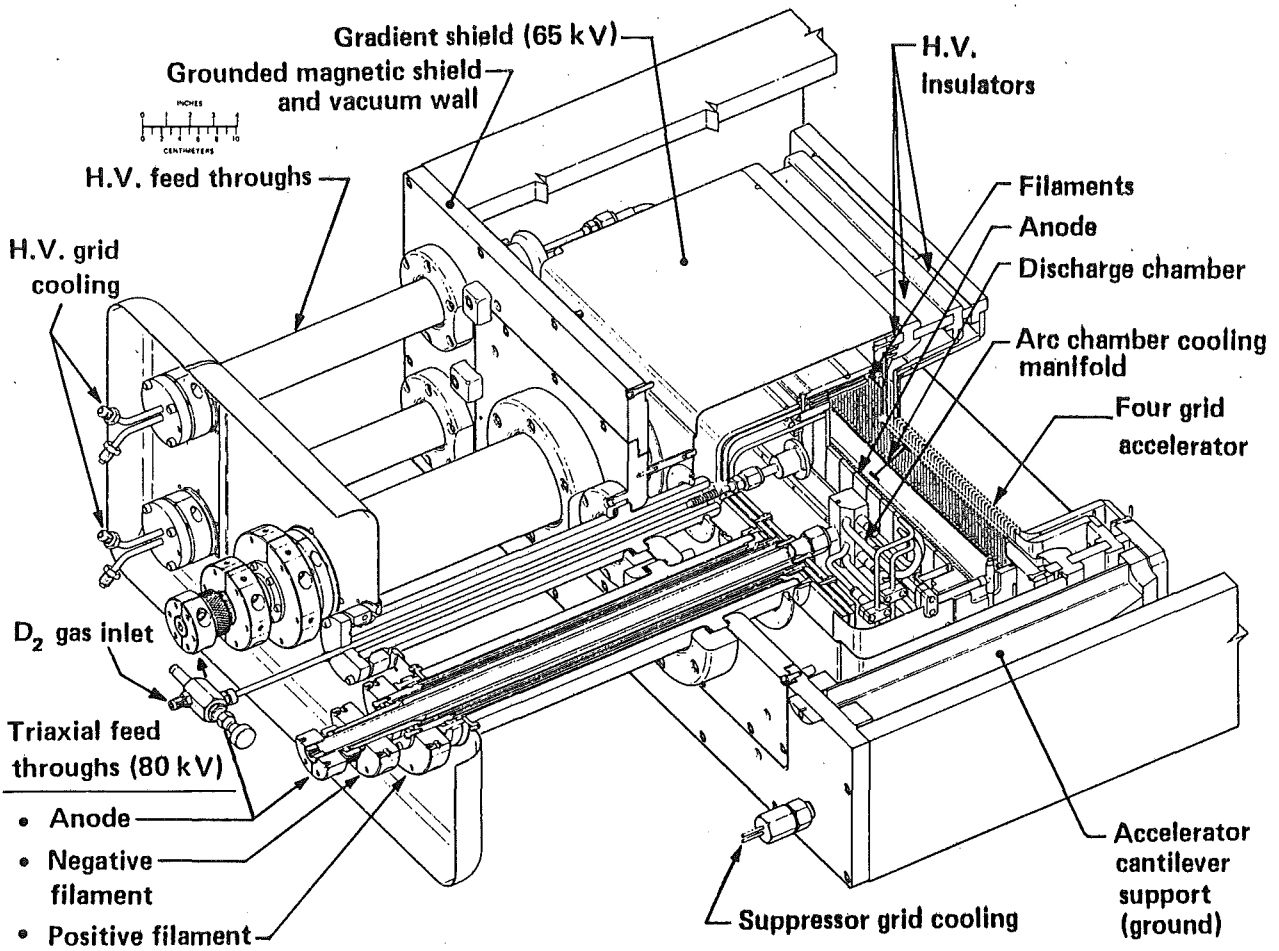
$V \equiv$ total voltage applied across the extraction gap (kV),

$d \equiv$ effective extraction gap (cm).

For a three electrode system $V = V_0 + |V_S|$, where eV_0 is the beam ion energy of interest and V_S is the (negative) electron suppressor electrode voltage. For good optics V_S is generally kept to the minimum needed (a few kV) to suppress

Fig. IV.3-3

MFTF 80 keV -- 80 "AMP" NEUTRAL BEAM



electron backstreaming (from the neutralizer cell region back into the ion source), so generally $V \sim V_0$. The extraction gap is limited by the need for a sufficient inter-electrode gap to avoid voltage breakdown. In general, the effective gap d is equal to the physical electrode gap plus a fraction of the characteristic aperture dimension. For a typical polished set of plane electrodes, the limiting breakdown voltage⁽⁵⁾ over a physical gap d is $V_{BD}(kV) \sim 60 \sqrt{d}$ (cm). The above space charge considerations form an upper limit on the total $j(\text{s.c.l.}) < 0.5 \text{ A/cm}^2$ (typical).

IV.3.2.1.2 Extraction Electrode Transparency f_t

Formation of a multi-ampere total ion beam then requires extraction from a substantial plasma area. Maintaining the required electrostatic field gradient (for a short gap over a large area) and shaping the plasma meniscus boundary for ion trajectories that balance the defocusing space charge forces against the focusing field from the aperture for minimum angular divergence output requires use of a set of multi-aperture electrodes for extraction. The first electrode of such a grid set reduces the effective plasma area available by a transparency factor f_t ; typically $f_t < 0.45$ for circular apertures and $f_t < 0.6$ for slot apertures. The average space charge limited current density for apertures then is $\sim f_t \times j(\text{s.c.l.})$.

IV.3.2.1.3 Extraction Electrode Area

The extraction electrodes for steady state multi-aperture ion sources are generally water cooled by flow through many capillary tubes. The required cooling flow through the small capillary tubes tends to limit the extractor grid dimension in the corresponding flow ("height") direction to < 20 cm. The need for highly accurate dimensional stability in both the extraction gap and aperture alignment similarly limits the orthogonal ("width") dimension. Dimen-

sions of up to approximately 20 cm x 50 cm appear feasible, though from an ion source failure standpoint even smaller modular units would be desirable if they can be packed closely together. Electrode cooling limitations, the need for a long electrode lifetime (minimum erosion loss from sputtering), and wall cooling requirements in the plasma source section of the ion sources combine to further limit extraction power densities. Therefore, average extraction current densities for high voltage steady state ion sources are expected to range from 0.1 to 0.3 A/cm², with total extraction areas < 10³ cm².

IV.3.2.1.4 Intrinsic Ion Beam Divergence $\theta(\text{div.})$

Another basic factor limiting ion source performance is the intrinsic angular divergence $\theta(\text{div.})$ of the ion beam resulting from a combination of initial transverse ion motion in the plasma chamber, plus any unbalanced transverse ion beam motion from distortions in the plasma meniscus formed for each aperture at the beam forming extraction electrode, or from any aperture grid to grid misalignment. The value of $\theta(\text{div.}) \approx \tan^{-1}(v_{\perp}/v_z)$ where v_{\perp} is the total transverse ion velocity and v_z is the final z component of the velocity after acceleration along the z axis. In practice $\theta(\text{div.})$ is experimentally measured for the total ion beam resulting from the merging of an array of beamlets, while code studies involve minimizing the divergence of a single typical beamlet for the selected operating parameters.

For scaling and planning purposes in this study a conservative empirical fit for much of the multiple circular aperture 1/e divergence data⁽⁴⁾ is adopted:

$$\theta(\text{div.}) \approx \frac{5}{\sqrt{V_0(\text{kV})}} \text{ degrees} .$$

A similar approximate scaling can be used for slot apertures, with θ (div.) parallel to the slots having a slightly lower coefficient and the divergence perpendicular to the slots higher by at least $\sqrt{2}$. Recent data for ion sources now under test show this empirical divergence reduced by ~ 0.7 . The initial ion transverse motion implied for these improved sources is still relatively large ($T_{i\perp} \sim 3.7$ eV if thermal) so it likely represents an intermediate limit with a lower $T_{i\perp} < 1$ eV possible with expected further plasma source development. However the D^+ ions from D_2 or D_2^+ dissociation in the plasma sources have \sim Frank-Condon energies of a few eV, so additional ion-wall accommodation is needed for cooling $T_{i\perp}$ (without again leading to molecular recombination).

IV.3.2.2 Ion Source Output Composition

Positive ion sources operating on a molecular gas such as D_2 (etc.) generally yield a mixture of primary atomic ions (D^+), diatomic ions (D_2^+), and triatomic ions (D_3^+). The exact mixture depends largely upon details of the arc operation, and upon the plasma chamber walls. For most applications, a 100% D^+ beam would be most desirable but present large sources appear to be limited to $\sim 80\%$ D^+ , $\sim 15\%$ D_2^+ , and $\sim 5\%$ D_3^+ .

IV.3.2.3 Impurity Limitation

Tandem mirror machines with substantial electrostatic potential end plugs or barriers, and closed magnetic field (e.g., tokamak type) confinement configurations are sensitive to accumulation of high Z impurities because of the expected relatively long radial diffusion loss times. Initial estimates for impurity plasma buildup in a tandem barrier indicate an ion source limitation of $< 0.1\%$ high Z ($Z > 2$) impurities is required.⁽⁶⁾ Several means of selectively ejecting impurities appear possible if necessary.

IV.3.2.4 Ion Current Loss During Extraction

In operation, the extraction electrode set (three or four electrode systems) contributes to an accelerated ion current loss and excess power supply drain. The major portion of this loss appears due to the ion beam ionizing some of the background gas flowing through the electrode apertures. The resultant ion and electron trajectories then impinge upon an electrode or wall and contribute to the electrical power supply current drain. The primary ion can also be lost through charge exchange on this gas, impact one of the electrodes, and possibly eject secondary electrons and thereby increase further the electrical current drain. The total acceleration power supply current loss for an early LBL 20 kV ion source design has been measured by Berkner⁽⁷⁾ to be ~ 20%; this yields an effective acceleration efficiency $\eta_{acc} \approx 80\%$. A higher η_{acc} is expected for the higher gas efficiency ion source design adopted for the TASKA NBI due to lower gas flow and density.

IV.3.2.5 Neutralization Efficiency

The beam line charge exchange neutralizer efficiency for conversion of a positive ion beam to a neutral beam is limited because the rate of electron pickup by the ion (cross section σ_{10}) can come into equilibrium with the rate for electron loss (cross section σ_{01}). The equilibrium fraction $F_{\infty}^0 = \sigma_{10}/(\sigma_{10} + \sigma_{01})$ is a rapidly decreasing function of energy, limiting reasonable positive ion beam conversion to ion beams with energies < 100 keV/nucleon. In practice, gas scattering and excess gas flow and pumping problems limit the gas cell to a thickness $\int n dl \sim 3/(\sigma_{10} + \sigma_{01}) \sim 10^{16}/\text{cm}^2$ for a conversion value ~ 0.95 of the infinitely thick value. The neutralizer efficiency for molecular ions is similar (for a sufficient cell thickness for nearly complete dissociation), except the cross sections are evaluated at the

reduced fragment energy (1/2 or 1/3 energy). However, the molecular ion dissociation process also adds approximately the Frank-Condon energy to the resultant fractional energy neutral components increasing their angular divergence (over that of the incident ion beam). In principle the neutralizer gas need not be the same as that of the ion source, but in practice it generally is, because the cell must be closely coupled to the ion source (ion beam transport without good space charge neutralization is impractical) and the need to avoid high Z impurities (that would be expected from any higher Z neutralizer gas back flow into the ion source though carefully designed metallic vapor curtain designs might be considered). The only useful exceptions are that H₂ or D₂ could be used as the charge exchange mediums for a T⁺ NBI. The best low gas flow designs for the required $\int n dl \sim 10^{16}/\text{cm}^2$ thickness neutralizer cell appear to use cooled (77°K) neutralizer walls for the main length and warm walls near the beam exit. Any additional neutralizer gas beyond that required with the minimum gas flow from the ion source should be added in the neutralizer cold wall section to reduce the neutralizer gas temperature (and flow velocity).

IV.3.2.6 Ion Sweep and Dump

The removal of the remaining ion equilibrium fraction of the beam at the exit of the neutralizer cell requires an ion sweep system, a high power density beam dump (or a direct energy collector), and appropriate gas pumping. The reason for this requirement is that the ions in the beam path beyond the end of the magnetic shielding would be bent by any transverse magnetic fringe field to strike the wall and possibly cause undesirable intense local heating and gas desorption. The ion sweep section is intended to remove these ions at a selected location with appropriate cooling design capability. The ion sweep

can be either magnetic or electrostatic in action with a $\sim 90^\circ$ deflection magnetic geometry being the most straightforward. The presence of fractional energy ions after molecular ion dissociation in the charge exchange neutralizer cell must also be considered in the magnetic ion beam dump (or direct energy recovery unit) design.

IV.3.2.7 Neutral Beam Line Transport Efficiency

The neutral beam line transport efficiency η_t involves two general types of losses. The first fundamental one being from the finite "Gaussian" beam density distribution $j = j_0 \exp[-(\theta/\theta_{div})^2]$ for a beam with an angular divergence θ_{div} (from the ion source or added in the neutralizer from scattering and molecular ion dissociation) contributing to beam losses on the beam line defining collimation. The second loss process is due to neutral beam ionization on any background gas with a beam attenuation $\propto e^{-\int \sigma_T n dl}$. An energetic ion formed from neutral beam ionization beyond the magnetic shielding would be deflected in any magnetic fringe field and likely impinge upon a wall and be lost. A total transport efficiency $\eta_{transp.} \sim 0.9$ is typical,⁽⁸⁾ but improvement is possible with a lower beam divergence and better gas pumping for a lower gas density ($\int n dl$) from the ion sweep to the TASKA plasma. Use of a focused ion beam input to the neutralizer can allow smaller collimation aperture dimensions (and hence reduce gas flow beyond the ion sweep section), and reduce the NBI footprint size on the plasma.

IV.3.2.8 Neutral Beam Support System

IV.3.2.8.1 Electrical Power Supplies

For operation, each ion source requires several types of programmed power. Each ion source involves a plasma source requiring substantial cathode and arc power (at high voltage if in the standard positive ion source configura-

ration, or near ground if the neutralizer sweep sections are arranged at negative high voltage - see Section IV.3.4.3). The main ion source power required is the high voltage acceleration supply, with associated current limiting controls in case of ion source sparking or breakdown. An intermediate voltage tap is also required for the gradient electrode if used with a four electrode system (desirable for $V_0 \gtrsim 50$ kV). Finally, a smaller few kV negative power supply is required to maintain the electron suppressor grid negative to prevent electron acceleration from the neutralizer back into the ion source.

IV.3.2.8.2 Gas Pumping System

Each ion source unit requires a minimum gas flow into the arc chamber for plasma formation and to support the extracted ion beam flow. In addition, sufficient gas must be added in the neutralizer for a total $\int n dl \gtrsim 3/(\sigma_{10} + \sigma_{01}) \sim 10^{16}/\text{cm}^2$. A high gas efficiency nominally 50 A (atomic ion equivalent current yield) 50 kV NBI is expected to require a total D_2 (or T_2) gas flow of ~ 15 torr-l/s. Preliminary calculations indicate that at least three pumping stages are desirable for a duct pressure $< 2 \times 10^{-5}$ torr and that the final duct must be short ($< \text{few m}$), well cooled, and shielded from any direct energetic beam impingement to avoid thermal "Stewart" desorption and possible duct choking.(9,10)

The computer code studies require a 44% D_2 and 56% T_2 fueling mixture of the ME-NBI beam, which can be obtained either through the use of separate T^0 and D^0 beam lines or by using a mixed D_2 , T_2 and DT input in each of the ME-NBI. The mixed gas approach appears the most desirable, as it would allow most of the ME-NBI gas effluent to simply be purified and recompressed for recycling, with just enough makeup gas added from the cryo-distillation facility to maintain the needed flow and gas composition. A relatively smaller cryo-

distillation plant could then be used to separate the H₂, D₂ and T₂ fractions from the vessel end wall pumps for use with the appropriate NBI as well as remove the accumulated fusion product He.

IV.3.2.8.3 Magnetic Shielding

Operation of the NBI with short ducts and small injection angles in the relatively intense fringe magnetic field of a few tesla from TASKA will require extensive magnetic shielding. The ion source is the most sensitive portion of a NBI with a perpendicular field requirement of $< .0001$ T. The beam path through the neutralizer section to the low particle density sweep region must also have $\int B_{\perp} dl$ fields $\ll 1.50 \times 10^{-2}$ T-cm to avoid excessive ion beam deflection prior to charge exchange conversion from an ion to a neutral. The task appears to require either superconducting shielding, or an extensive set of bucking coils to reduce the fields to a range handled by Fe and μ -metal. Details of the magnetic shielding for the TASKA NBI are described in Section V.6.

IV.3.2.8.4 Remnant Neutral Beam Dump

A remnant neutral beam power dump and associated gas pumping system is required at the far vessel wall for each of the high power NBI's (all except the LE-NBI). The specific arrangement for TASKA is given in Section VIII.3. During TASKA startup these dumps must be capable of handling a major fraction of the NBI power (typically just beyond the design beam focus waist and therefore over a relatively small footprint area) with power levels often > 2 kW/cm² for short periods ($\lesssim 20$ msec) and a small fraction of the NBI power during steady state equilibrium operation, with minimal evolved gas return to the hot plasma region.

IV.3.3 Specific NBI Design Parameters for TASKA

The specific NBI design choices indicated in Table IV.3-1 for TASKA represent a compromise between high output performance and a reduced current density conservative design for reliable long lived operation. The prototype ion source design adopted for this study was based upon the Jülich (KFA) version of the Culham/JET ion source.⁽¹¹⁾ The Culham type ion source uses a multipole cusp wall arc chamber to achieve up to ~ 50% gas efficiency, a plasma source power requirement of $\lesssim 2$ kW/A extracted beam, an atomic ion fraction (e.g., D⁺) $\gtrsim 80\%$, and a plasma ion temperature $\lesssim 0.4$ eV for a minimum contribution to the ion beam divergence.⁽¹²⁾ The prototype ion source design is also based upon use of a set of four water cooled electrodes, with shaped circular apertures for extraction. A focused ion beam can be achieved either by using spherically shaped electrodes, programmed aperture offset,⁽¹³⁾ or subdividing the extraction area into a set of tilted subsections (as will be used with JET⁽¹⁴⁾). The resultant NBI design parameters for the TASKA beam lines are listed in Table IV.3-1. Note that the gas flow requirements are the total flow for the ion source and neutralizer cell to attain $0.95 F_{\infty}^0$ conversion of the primary (full energy) ions to neutrals. The beam collimation dimensions listed at 8 m as an example are scaled to allow $2\theta(\text{div.})$ clearance around both the height and width of the focused beam from the rectangular source extraction area indicated. The scaling for $2\theta(\text{div.})$ beam clearance "width" for collimation has the form $W = |W_0 - 2Z\theta_f| + 4Z\theta_D$ for small angles where W_0 = the initial ion beam width, $\theta_f = W_0/2L$ where L is the beam focal length, and θ_D is the divergence angle in radians. A similar expression applies for the beam height, with appropriate substitution of the initial beam height H_0 . The beam footprint including the beam edge out only to θ_D has a minimum "radius" at the

beam focus $Z = L$ of $L\theta_D$ (or \sim elliptical axis $L\theta_{Dx}$ and $L\theta_{Dy}$ if from a bi-gaussian distribution with different θ_{Dx} and θ_{Dy} divergences along the beam x and y axis).

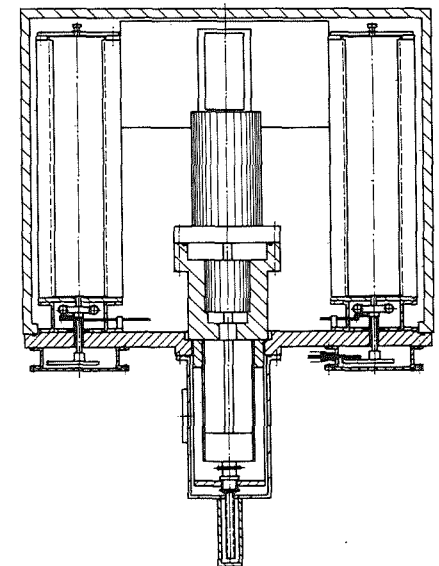
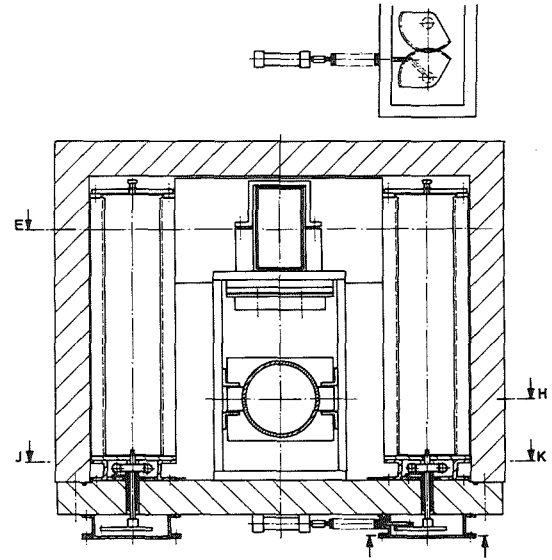
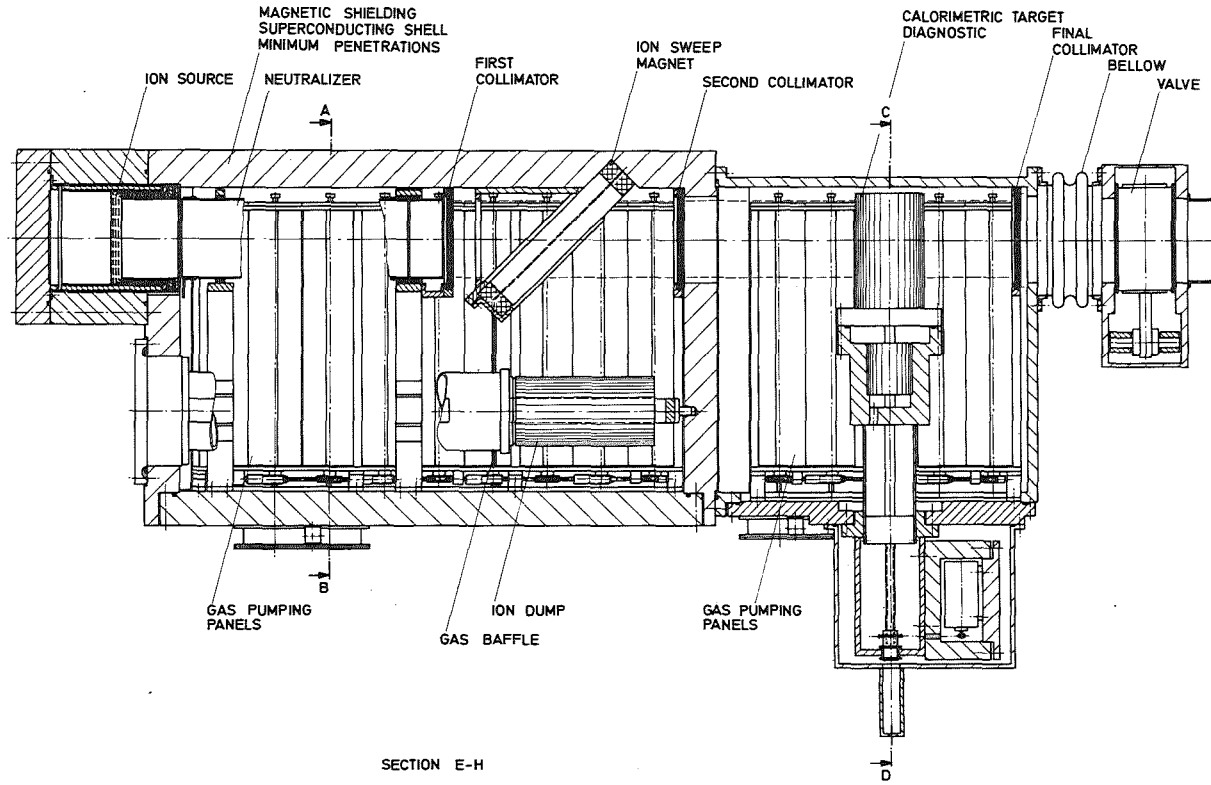
A prototype ion source tank section for the HE-NBI is shown in Fig. IV.3-4. Steady state high speed gas pumping is attained using an articulated "two position" folded wall system of getter pumping panels as described in Section IV.4. The ion sweep beam dump and the insertable beam calorimeter shown are of the water cooled (high speed) rotating design developed by Hemmerich and Kupschuss⁽¹¹⁾ at KFA Jülich. Detailed optical Doppler shift measurements of the line spectra from the neutral beam at the neutralizer exit are expected to be the main on-line beam diagnostic for measuring the beam current density distribution, divergence, and species composition.⁽¹⁵⁾

The power supplies for a typical 50 kV 50 A equivalent NBI (e.g., one of the ion source-neutralizer-ion sweep sets of the ME-NBI) are listed in Table IV.3-2. NBI operation will also require fast automated power supply control and an extensive interlock system. Diagnostic sensors will be required to assure proper cooling, proper beam aiming, presence of a suitable target plasma, and a suitable ion sweep field before the NBI can be turned on to prevent possible damage to some wall section (without adequate power handling capability). Further considerations on this are given in Section VIII.3.3.

The use of T_2 gas, the high neutron fluences during operation, induced radioactivity in components, and the high fringe-field magnetic shielding problem with the TASKA coils energized combine to prohibit short term NBI maintenance. This study therefore envisions continued research and development on NBI components and a conservative design to result in NBI with mean time before failure > 1 year. The ion source tank design shown in Fig. IV.3-4

Fig. IV.3-4 TASKA - HIGH ENERGY NEUTRAL BEAM INJECTOR

IV.3-19



SECTION A-B

SECTION J-K

SECTION C-D

Table IV.3-2. Typical Ion Source Power Supply Requirements

(e.g., for Ion Source for 50 kV 50 A Equivalent D⁰ NBI)

Filaments	15 V	2,000 A
Arc power supply	50 to 150 V	to 4,000 A
Accel. power supply	50 kV	to 110 A (with 20% margin)
Gradient grid	~ 40 kV	< 5 A
Suppressor grid	-1 to -5 kV	< 10 A

includes planned access during major maintenance shutdown periods for remote maintenance to the ion source components from the rear of the tank and access to the pumping panels from the top of the tank. An excess current output capacity of 20% is included with the parameter listing of Table IV.3-1, to cover expected degradation of performance and losses from component failures over the operating period before required major maintenance. If possible this excess NBI capacity should be in the form of "spare" installed ion source, neutralizer, and ion sweep units, since equipment failures in an ion source beam line tend to disable the entire unit and not just fractionally degrade performance.

IV.3.4 Design Considerations for a Positive Ion Source (Options)

An ion source is generally considered to consist of two distinct units, (1) a plasma source of appropriate plasma density and area, and (2) a multi-apertured extraction system.

IV.3.4.1 The Plasma Source (Arc Chamber)

The plasma source for the present large area ion source designs is generally either of the $B \approx 0$ type (developed at LBL)⁽¹⁶⁾ or of the magnetic multipole wall ($B(\text{central}) \approx 0$) type in use at Culham,⁽¹⁷⁾ ORNL,⁽¹⁸⁾ and under test at LBL,⁽¹⁹⁾ or of the periplasmatron design by Fontenay-aux-Roses.⁽²⁰⁾ In any case, the primary need is for a source of uniform density ($\delta n/n < 0.05$) plasma with adjustable density ($n \lesssim 5 \times 10^{12}/\text{cm}^3$) to match the extraction current density $j(\text{s.c.l.})$ over the needed area (up to 20 cm x 50 cm). The multipole cusp magnetic wall type of plasma source is quoted as having the highest gas efficiency, highest power efficiency, and highest primary ion fraction (D^+ , D_2^+ , D_3^+ fractions of at least $\sim 80\%$, 15%, 5%).⁽¹²⁾

IV.3.4.1.1 Plasma Source Cathode

Cathode electrode construction is now generally based upon use of a large number of pure tungsten hairpin filaments arranged as a window frame or fence around the outside edge of the extraction area of interest, with a typical filament lifetime of about 100 hr.⁽²⁾ Future designs should consider larger area, lower temperature tungsten operation (to reduce tungsten evaporation and give longer lifetime) or use of a hollow thoriaated tungsten or sintered LaO/Mo cathode for long lived good emission.⁽²¹⁾ The usual cathode design requires a total emission electron current larger than the expected arc current. Cathode lifetime is a limiting maintenance problem, but one year lifetime appears a reasonable goal. Filament circuits are generally designed in parallel with one leg common (to avoid large electric field differences in the plasma) and with a stabilizing arc voltage dropping resistor connection to each hairpin circuit to help distribute the arc current. The orientation of the hairpin filament and input leads are generally arranged for a minimum resultant B field. Cathode temperatures are found to be arc current dependent and must be readjustable for maximum filament lifetime.

IV.3.4.1.2 Plasma Source Anode

The outer walls of the plasma chamber are generally arranged to function as a large area anode surface for electron collection. However, in the multi-pole field ion source the wall is built to include narrow strips of high field permanent magnets so the walls appear as a set of line cusps with strong local (short range) magnetic fields tending to reduce the electron mobility and increase their ionizing efficiency. This feature appears to improve gas efficiency, power efficiency and the atomic ion fraction.⁽¹²⁾ Wall anode heating by the arc discharge electrons is concentrated along these strips; this

requires careful cooling design for steady state operation. Normally the chamber walls are of copper for good conductivity and quite thin walled at the line cusp magnets for maximum magnetic field utilization. This suggests use of special thin capillary cooled wall construction designed such that the walls do not experience the vacuum load and a thin protective covering layer of chrome or molybdenum to reduce metallic sputtering or evaporation.

IV.3.4.1.3 Ion Source Gas Feed

The back wall of the arc chamber is generally used as a gas manifold or gas distribution system. If thermionic dissociation of D_2 appears useful in increasing the source output D^+ fraction the ion source feed gas can be arranged to enter through a heated tungsten diffuser. The gas flow directly into the ion source should be the minimum required for arc operation (with extraction). The remainder of the gas required to produce a neutralizer thickness $\int n \, dl \sim 10^{16}/\text{cm}^2$ should be fed directly into the neutralizer (colder gas to reduce the gas flow).

IV.3.4.1.4 Arc Associated Electrode Feedthrough Insulator

Ceramic to metal bonded vacuum tight feed-throughs are required for each cathode lead into the arc chamber (relatively high temperature environment service). Ceramic standoff of the first extraction electrode from the anode wall is also desirable, though pulsed ion sources in a low neutron fluence environment have used simple Kapton plastic sheets for needed insulation. The cathode back wall plate should be designed to be readily removable for cathode replacement (the item with the shortest expected lifetime). All ceramic seals and cooling circuits should include flexible (e.g., bellows) connections to avoid mechanical stress on ceramic insulators under varying temperature conditions.

IV.3.4.2 Extraction Electrode System

The multi-aperture ion extraction electrode system must serve the functions of defining the shape and location of the plasma meniscus for each aperture, forming the extraction field to achieve optimum ion beamlet extraction optics and acceleration, and orienting the total array of beamlets for the desired total beam focal length. The first "accel" or beam forming electrode serves as an interface between the plasma chamber and the first acceleration gap, and defines the location and area of each extraction meniscus surface. The auxiliary gradient or second electrode (in a four electrode system - not present in a three electrode system) allows optimum field gradient control near each plasma meniscus surface, somewhat independent of the main extraction voltage V_0 . The next electrode is the negative voltage "decel" electron suppression grid; this is made relatively thick to reduce field penetration through each of its aperture openings. Finally, the last electrode of the extraction set is used to establish the ground plane for each beamlet of the neutralizer ion beam system. The extraction electrode system is best designed for a specific voltage and current density. Design optimization involves a parameter study of the ion optics of an individual beamlet to minimize its beam divergence. Several ion extraction system codes are available including "WOLF" at LBL,⁽²²⁾ a version of the "BATE" code at Culham,⁽¹²⁾ and the "SNOW" at LASL.⁽²³⁾ The choices in extraction system include:

- Number of electrodes: three is simpler, four allows wider range of current adjustment and likely is best for good beam optics for $V_0 \gtrsim 50$ kV.
- Multi-aperture type: circular apertures appear to have slightly lower average divergence, lower acceleration losses and heat load, but also lower

transparency; slot electrodes have the best 1-D divergence, are easier to fabricate and align, but appear more susceptible to plasma variations causing electrical (accel) breakdown.

- Shaped aperture rims: a semi-Pierce shaped⁽²⁴⁾ edge is required for the apertures in the first beam forming electrode to obtain the best optics. Simpler aperture forms are often used for higher transparency or for easier machining, cooling and alignment. The design (appropriate to either circular apertures or the cylindrical symmetry of slots) should be chosen from code optimization studies.
- Electrode materials: choose for needed cooling and structural stability. Water cooled copper or molybdenum is the most common, but one could consider composites such as stainless steel covered with electrodeposited copper with milled channels and a copper covering (with a thin chrome or molybdenum surface film to reduce sputtering).

IV.3.4.3 Electrical Configuration

The standard power supply arrangement for powering a positive ion source is to run the plasma source at the positive high voltage V_0 , the gradient grid at a slightly reduced positive high voltage, the electron suppressor grid a few kV negative and the final grid and neutralizer at ground potential. This configuration involves the minimum volume at high voltage potential, though power supplies for the ion source arc chamber are then at high voltage, and are quite susceptible to problems from high voltage sparking. Direct energy recovery of the remnant ion sweep portion would require use of another neutralizer exit electron suppression grid or transverse magnetic field at the entrance to the ion collector region to prevent unwanted electron acceleration to the positive ion collector plate.

An attractive alternate configuration would place the ion source at or near ground potential, the gradient grid at a slight negative voltage, the electron suppressor at the maximum negative high voltage and the neutralizer cell at negative high voltage, $-V_0$. This configuration also requires a second electron suppressor grid or transverse magnetic field at the exit of the neutralizer to prevent unwanted electron acceleration from the plasma produced by ionization occurring within the neutralizer gas. However, the use of a sweep magnetic field and direct energy recovery of the swept ion flux fulfill this requirement.

IV.3.5 Negative Ion Source Based NBI

Negative ion beams appear essential for efficient production of neutral beams with an energy > 100 keV/nucleon, because of the decrease of F_{∞}^0 with energy. In the case of the plug NBI, the equilibrium fraction of H^+ conversion to H^0 at 250 keV has fallen so $F_{\infty}^0 \sim 0.01$, while conversion of H^- to H^0 remains a high 0.8 (for the plasma stripping cell) and is almost independent of energy. The factor limiting wide use of negative ions for all high energy NBI systems is the present lack of good, high current, steady state negative ion sources. However, recent progress appears promising at least for the following two types of negative ion sources: (1) using double charge exchange of a low energy ion beam in a suitable alkali metal vapor, or (2) using direct negative ion extraction from a volume or surface negative ion production source.

- (1) The characteristics of double charge exchange sources are largely determined by requirements for maximum positive ion to negative ion (two stage) conversion; cesium or strontium have conversion efficiencies of 0.25 to 0.5 for H^- energies $\lesssim 1$ kV. Typical system requirements include:

- A low energy, high current source of positive ions; limited by $j(\text{s.c.l.}) \propto v^{3/2}/d^2$, with the minimum gap d limited by mechanical tolerances, and the $\theta(\text{div.}) \propto 1/\sqrt{V}$ is poor. Use of a source of molecular ions at higher energies may be desirable. A suitable source of charged pellets, with acceleration to the required velocity range, is also a possible alternative.⁽²⁵⁾
- A double charge exchange cell filled with a suitable alkali metal vapor such as cesium or strontium. This must be designed for the specific application in order to minimize high Z impurity flow into the ion source or down the beam line; this will likely require a special vapor jet curtain design.
- A large area (or large array of small areas) accelerator section is required to accelerate the negative ions to the final desired energy. The use of grids is a problem for high beam current densities, and optics of large area short gap accelerators tend to be difficult without grids. Pumping must be good enough to achieve a low enough vacuum pressure to prevent excessive beam drain and negative ion loss, but not so low as to prevent production of positive ions for needed space charge neutralization during beam transit from the double charge exchange cell to the accelerator section. Use of time averaged current from an electrostatically focused RF acceleration system (array)⁽²⁶⁾ has some attractive features.
- A stripping cell is required to remove the loosely bound electron. Gas cells have H^- to H^0 conversion efficiencies of ~ 0.65 , plasma filled cells an efficiency of ~ 0.83 , and photostripping with an intense laser beam can have an even higher efficiency.

- The beam line also requires a remnant ion sweep, appropriate gas pumping (gas efficiency is relatively poor as only part of the low energy positive beam can be used), and other hardware standard to an NBI.
- (2) The characteristics of a direct extraction negative ion source depend upon details of the volume or surface source. Typical system requirements include:
- The Ehlers⁽²⁷⁾ surface source uses H⁺ arc plasma bombardment of a shaped cesium covered tungsten negatively biased surface to yield a suitable flux of "backscattered" H⁻ ions available for direct extraction. A major problem of this approach is separation of the plasma electrons from the H⁻ before extraction and acceleration to a significant energy.
 - A version of the Bacal⁽²⁸⁾ type of volume source is under study by Holmes.⁽¹²⁾ A standard multipole arc chamber is operated in a lower arc current density range favoring molecular ion and negative ion production. The major problem is again the means for separating out the electron portion of the current before extraction or acceleration to a significant energy. This source requires no cesium, but the current density is expected to be limited to $\leq 0.05 \text{ A/cm}^2$.
 - The two above approaches will likely be arranged for two stage acceleration - first extraction of a suitable H⁻ rich beam and then the major accelerator stage (only negative ions) to a full energy eV_0 . Acceleration requirements are similar to (1) above.
 - A stripping cell is required as in (1) above.

- The beam line also requires a remnant ion sweep, appropriate pumping, and other hardware appropriate for a standard NBI.

Recent results with both of these negative ion approaches appear sufficiently promising to incorporate this approach in the plug - NBI. Pulsed yields of over one ampere have been achieved from both the surface source and double charge exchange sources. The general characteristics of the volume sources without cesium appear very desirable if the output current can be increased.

References for Section IV.3

1. J.H. Fink, "Neutral Beam Injectors for 1990 and 2005," UCRL-53112, Lawrence Livermore Laboratory (1981).
2. W.S. Cooper, V.P. Elischer, D.A. Goldberg, D.B. Hopkins, V.L. Jacobson, K.H. Lou, and J.T. Tanabe, "A Conceptual Design for the Zephyr Neutral Beam Injection System," Lawrence Berkeley Laboratory LBL-12383 (1981).
3. A. Molvik et al., "A Compact 80 keV Neutral Beam Module," (A.W. Molvik, E.D. Baird, K.H. Berkener, W.S. Cooper, T.J. Duffy, K.W. Ehlers, J. Fink, D. Gardner, and C. Wilder), Proc. Seventh Symposium on Engineering Problems in Fusion Research, Knoxville, TN, Vol. 1, p. 295 (1977).
4. J.E. Osher, "A Review of the Production of Intense Ion and Neutral Beams with Energies Below 10 keV," First Symposium on Ion Sources and Formation of Ion Beams, Brookhaven National Laboratory (1971).
5. H. Heard, "Electron Loading and High Voltage Sparking of Metals in Vacuum," UCRL-2252 (1953).
6. J.E. Osher, "Energetic Impurity Considerations for MFTF-B," Magnetic Fusion Energy Quarterly Report, Oct.-Dec. 1979, UCRL-50051-79-4, p. 20 (1980).
7. K.H. Berkner, Lawrence Berkeley Laboratory, private communication (1978).
8. G.D. Porter, F.H. Coensgen, R.S. Devoto, A.W. Molvik, J.E. Osher, J.W. Shearer, and K.I. Thomassen, "Review of the Neutral-Beam Current Requirements for the Mirror Fusion Test Facility (MFTF)," Lawrence Livermore Laboratory UCRL-52517 (1978).

9. J.H. Feist, "A Computer Program for Parameter Studies of a Neutral Injection Beam Line," Proc. of the Seventh Symposium on Engineering Problems of Fusion Research, Knoxville, TN, Vol. 2, p. 1554 (1977).
10. L.D. Stewart, "Studies of Neutral Beam Power Loss in Stray Magnetic Fields," IEEE Trans. on Nuclear Science NS-28, 1323 (1981).
11. J. Hemmerich and P. Kupschuss, KFA Jülich, private communication (1981).
12. A. Holmes, Culham, U.K., private communication (1981).
13. A.J.T. Holmes and E. Thompson, "Beam Steering in Tetrode Extraction Systems," RSI 52, 172 (1981).
14. E. Thompson, JET, U.K., private communication (1981).
15. G.A. Cottrell, "Optical Profilometry of Intense Neutral Beams," CLM-P634, Culham Laboratory (1981).
16. K.H. Ehlers, W.R. Baker, K.H. Berkner, W.S. Cooper, W.B. Kunkel, R.V. Pyle, and J.W. Stearns, "Design and Operation of an Intense Neutral Beam Source," J. Vac. Sci. Technol. 10, 922 (1973).
17. A.P.H. Goede and T.S. Green, "Stability Limits on Ion Source Operation," Culham Report CLM, 522 (1978).
18. C.C. Tsai, H.H. Haselton, M.M. Menow, N.S. Ponte, P.M. Ryan, D.E. Schechter, and W.L. Stirling, "Study on a Rectangular Plasma Generator for Extracting 30A/10 Sec Ion Beam," Engr. Problems of Fusion Research, Vol. 8, 665 (1979).
19. J.A. Patterson, G.W. Koehler, R.P. Wells, and L.A. Biagi, "The Mechanical Design and Fabrication of a Convectively Cooled Ion Accelerator for Continuously Operating Neutral Beam Systems," Engineering Problems of Fusion Research, Vol. 8, (1979); also K.W. Ehlers and K.N. Leung "Characteristics of the Berkeley Multi-Cusp Ion Source," Lawrence Berkeley Laboratory Report LBL-9107 (1979).
20. A. Bariaud, B. Becker, M. Desmons, M. Fumelli, P. Raimbault, F.P.G. Valckx, "Intense Neutral Beam Development at FAR for JET," Engr. Problems for Fusion Research, Vol. 8, 685 (1979).
21. D.M. Goebel, J.T. Crow, and A.T. Forrester, "Lanthanum Hexaboride Hollow Cathode for Dense Plasma Production," RSI 49, 469 (1978).
22. W.S. Cooper, K. Halbach, and S.B. Magyary, "Computer-Aided Extractor Design," Proc. of Second Symposium on Ion Sources and Ion Beams, II-1 Berkeley, Lawrence Berkeley Laboratory Report LBL-3399 (1974).
23. R. Hamm, Los Alamos Scientific Laboratory, private communication (1980).

24. L.R. Grisham, C.C. Tsai, J.H. Whealton, and W. Stirling, "Effect of Emission Aperture Shape Upon Ion Optics," RSI 48, (1977).
25. O.F. Hagen, P.R.W. Henkes, R. Klingelhöfer, B. Krevet, H.O. Mosher, "Negative Ion Production by Charge Exchange of Hydrogen Clusters with Cesium Vapor Target - Status Report," Proc. of the Second International Symposium on the Production and Neutralization of Negative Hydrogen Ions and Beams," Brookhaven National Laboratory Report BNL-51304 (1980).
26. A.W. Maschke, Brookhaven National Laboratory, private communication (1979).
27. K.W. Ehlers and K.N. Leung, "Characteristics of a Self-Extracting Negative Ion Source," Proc. of the Second International Symposium on the Production and Neutralization of Negative Hydrogen Ions and Beams, Brookhaven National Laboratory Report BNL-51309 (1980).
28. M. Bacal, A.M. Bruneteua, H.V. Doucet, W.C. Graham, and G.W. Hamilton, "H⁻ and D⁻ Production in Plasma," Proc. of the Second International Symposium on the Production and Neutralization of Negative Ions and Beams, Brookhaven National Laboratory Report BNL-51304 (1980).

IV.4 Vacuum System

IV.4.1 Introduction

The vacuum pumping system for TASKA has been designed to meet the following requirements:

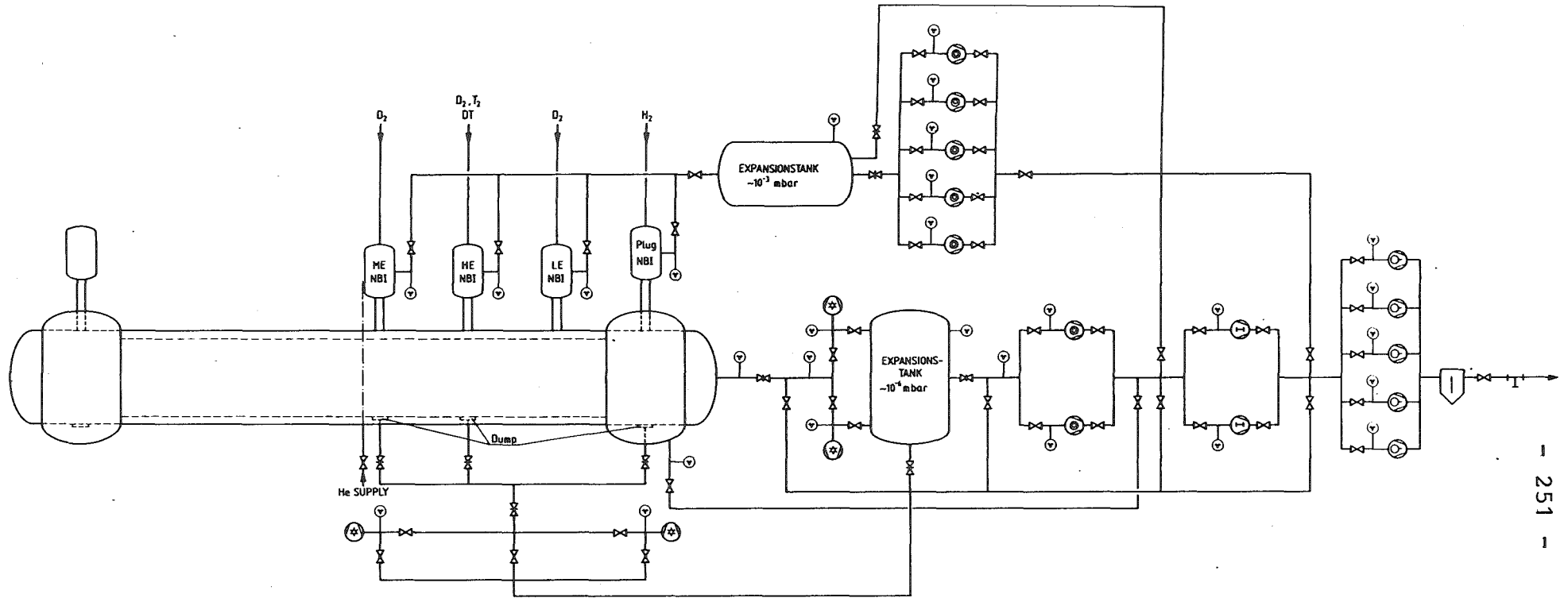
- Pumping hydrogen, hydrogen deuteride (HD), deuterium, tritium, hydrogen tritride (HT), deuterium tritride (DT), and helium from the vacuum vessel to a total pressure of 10^{-5} torr between experimental shots.
- Pumping hydrogen, hydrogen deuteride, deuterium, tritium, hydrogen tritride, deuterium tritride, and helium from the vacuum vessel and regeneration of cryopanel.
- Largely oil-free and contamination-free pumping system.
- Backfilling the vacuum vessel with He to 20 torr.
- The pumping system should be attached to the vacuum vessel to form a compact modular unit. It must not occupy too much space for pumping leads and pipe connections.
- Regeneration of the volume getter panels in the neutral beam injectors.

The consideration of these requirements led to the design of two pumping units, one of which is shown schematically in Fig. IV.4-1. Cryopumps, combined with turbomolecular pumps and backed by roughing pumps (at some distance from the vacuum vessel), offer an optimum solution to evacuate the vacuum vessel and the neutral injection beam dumps.

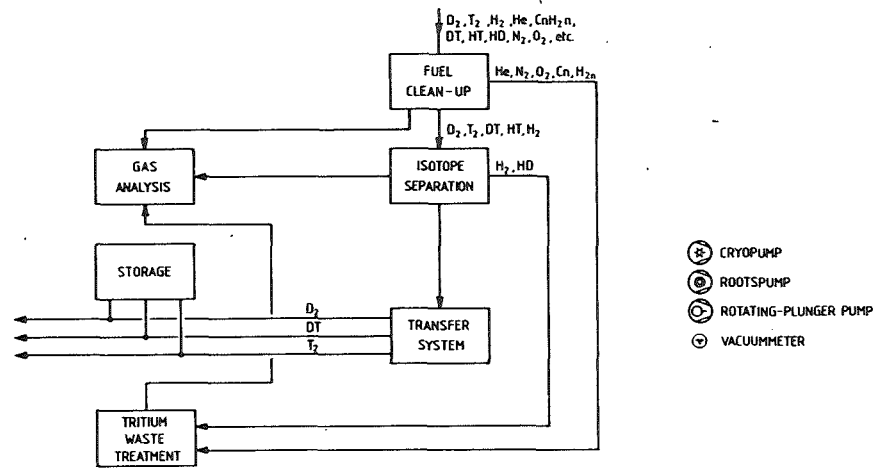
IV.4.2 Vacuum Pumping of the Discharge Chamber

The vacuum system for the discharge chamber must provide for evacuation from atmospheric pressure and maintaining the chamber at 10^{-5} mbar at the operating temperature of the wall. In order to achieve this low pressure, we anticipate performing a series of operations to clean and degas the chamber

IV.4-2



- 251 -



- ⊗ CRYOPUMP
- ⊙ ROOTSPUMP
- ⊕ ROTATING-PLUNGER PUMP
- ⊖ VACUUMMETER

Fig. IV.4-1 Vacuum system.

wall. During the construction of the chamber, the components must be electro-polished and cleaned ultrasonically. Lowering the specific outgassing rate from the chamber wall to 10^{-11} torr- μ /cm²-s at room temperature and to 10^{-9} torr- μ /cm²-s at the operating temperature⁽¹⁾ will be accomplished by conditioning the chamber wall by means of a discharge through inert gases. To obtain the design pressure in the degassed chamber, an effective pumping speed of 2×10^3 μ /s will be required.

For evacuation in the range between 10^{-3} and 10^{-6} torr under conditions which exclude a large inventory of tritium, cryopumps are used. The cryopumps are backed by turbomolecular pumps needed for the pumping of helium and for cleaning the cryopumps. As a primary evacuating system, a scheme consisting of two pumping stations, both at the ends of the vacuum chamber, is used. These stations will have cryopumps each with a pumping speed of 12×10^6 μ /s for H₂. This will provide an oil free vacuum which is needed in this pressure range.

The pumping lines will have gate valves which close on the order of one second and seal hermetically in 10 seconds.

An inert gas (He) is admitted into the discharge chamber at the end of a burn cycle to reduce the possibility of localized overheating of the chamber wall.

IV.4.2.1 Calculations

Gas load with consideration of:

- leaks
- permeation
- outgassing
- vapor pressure of the materials

- particle flow from the central cell.

The total gas load pumped from the end cell is about 100 torr-ℓ/sec, of which 55 torr-ℓ/sec is the gas load from the direct convertor.

Pressure in the vacuum vessel $p < 10^{-5}$ torr.

$$S = \frac{100 \text{ torr } \ell}{s \times 10^{-5} \text{ torr}} \sim 1.0 \times 10^7 \frac{\ell}{s}$$

Pumping speed

$$S_{\text{eff}} \sim 15 \times 10^6 \frac{\ell}{s} .$$

Pumping speed of the cryopanel $S \sim 1.2 \times 10^5 \ell/s \cdot m^2$.

Cryo-area $\sim 125 \text{ m}^2$.

Maximum cycle time: $t_c = \frac{\rho A_K RT_n}{SM \times p} \times d$

$$R : 8314 \text{ J/K kmol}$$

$$\rho : \sim 80 \text{ kg/m}^3$$

$$S/A_K : 120 \text{ m}^3/s \cdot \text{m}^2$$

$$p : 10^{-3}/s \cdot \text{m}^2$$

$$T_n : 293 \text{ K}$$

$d : 0.025 \text{ mm}$ thickness of the condensate

$$t_c \sim 25 \text{ h} .$$

Regeneration system for the cryopumps.

Maximum gas load from the cryopumps 2 h regeneration time ~ 400 torr- ℓ /s.

In order to keep the tritium inventory low the cycle time should also be 2 h.

Maximum pressure in the expansion tank by using a turbopump with a pumping speed of 50000 ℓ /s.

$$p \sim \frac{400 \text{ torr-}\ell/\text{s}}{50000 \ell/\text{s}} = 8 \times 10^{-3} \text{ torr} .$$

IV.4.3 Evacuation System for the Dumps

The purpose of the evacuation system for the dumps is to avoid the diffusion of the scattered and sputtered particles from the dumps. The pumping load is determined by the particle flux from the neutral beam injectors. In the outline design, it is proposed to use 4 cryopumps with a pumping speed of 1.0×10^6 ℓ /s (for H_2). Each cryopump needs a cryopanel area of ~ 95 m^2 .

IV.4.3.1 Calculations

Gas load $Q \sim 6$ torr- ℓ /s (all dumps in the right or left part), pressure in the dumps $p \sim 10^{-5}$ torr.

$$S \sim \frac{6 \text{ torr-}\ell}{s \times 10^{-5} \text{ torr}} \sim 6 \times 10^5 \frac{\ell}{s}$$

Pumping speed

$$S_{\text{eff}} \sim 1.0 \times 10^6 \frac{\ell}{s} .$$

Pumping speed of cryopanel(s)(1)

$$S \sim 120000 \frac{\ell}{s \cdot m^2} .$$

Cryo-area ~ 9 m^2 .

The cycle time should be 2 hrs.

IV.4.4 Evacuation System for the Neutral Beam Injectors

One of the main characteristics for the design of the neutral beam injectors is the need of DC-operation (see Section IV.3). This condition can be realized by large volume getter panels inside the boxes of the neutral beam injectors. Using this pumping system, one has a weak dependence of the pumping speed on the gas load.⁽²⁾

Since H₂ isotopes form a solid solution with the getter material the amount of gas which can be adsorbed depends on the temperature of the getter material and on the acceptable equilibrium pressure in the gas phase established by H₂ isotopes at a given concentration of the getter material.

Regeneration of the volume getter panels, saturated with hydrogen isotopes, may be obtained by raising its temperature and by removing the evolved hydrogen isotopes by means of turbomolecular pumps.

IV.4.4.1 Calculations

IV.4.4.1.1 He Neutral Beam Injection System

Within the practical geometry (see Section IV.3) of the beamline we have a gas flow of 7.1 torr-ℓ/s into the first stage of the box, ~ 2 torr-ℓ/s in the second stage of the box.

Each of the rotating flat getter panels is about 875 x 1200 mm and has a D₂ pumping speed of 18000 ℓ/s (at 400-200°C). The reversible sorbtion capacity at constant pumping speed (at 200°C and 10⁻⁵ torr) is 21000 torr-ℓ for each panel.

The power required for activation or regeneration of each getter panel at 700°C is about 7500 watt (760 A). The duration of the treatment is 45 minutes. Operation at 400°C and 200°C would require about 24% and 4.5% of the activation power.⁽³⁾

First stage: 12 panels

Gas load $Q \sim 7.1 \text{ torr-}\ell/\text{s}$

Attainable pressure

$$p \sim \frac{7.1 \text{ torr-}\ell/\text{s}}{\text{s} \cdot 120 \times 18000 \ell} \sim 3.2 \times 10^{-5} \text{ torr}$$

Maximum cycle time

$$t_c = \frac{21000 \text{ torr-}\ell \cdot 12 \text{ s h}}{7.1 \text{ torr-}\ell \cdot 3600 \text{ s}} \sim 9.9 \text{ h}$$

Sweep: 6 panels

Gas load $Q \sim 2 \text{ torr-}\ell/\text{s}$

Attainable pressure $p \sim 1.9 \times 10^{-5} \text{ torr}$

Maximum cycle time $t_c \sim 18 \text{ h}$

Second stage: 10 panels

Gas load $Q \sim 2 \text{ torr-}\ell/\text{s}$

Attainable pressure $p \sim 1.2 \times 10^{-5} \text{ torr}$

Maximum cycle time $t_c \sim 28 \text{ h}$.

IV.4.4.1.2 ME Neutral Beam Injection Systems

The gas flow in the beam line is (see Section IV.3) 27 torr- ℓ /s into the first stage of the box, 5 torr- ℓ /s into the sweep, and 3 torr- ℓ /s into the second stage.

The panel geometry is 875 x 2300 mm. The pumping speed for the D_2 , T_2 mixture is about 24000 ℓ /s and the reversible sorbtion capacity is 28000 torr- ℓ .

First stage: 14 panels

Gas load $Q \sim 27 \text{ torr-l/s}$

Attainable pressure

$$p \sim \frac{27 \text{ torr-l s}}{\text{s } 14 \times 24000 \text{ l}} \sim 8 \times 10^{-5} \text{ torr}$$

Maximum cycle time

$$t_c \sim \frac{28000 \text{ torr-l } 14 \text{ s h}}{27 \text{ torr-l } 3600 \text{ s}} \sim 4 \text{ h}$$

Sweep: 10 panels

Gas load $Q \sim 5 \text{ torr-l/s}$

Attainable pressure $p \sim 2.1 \times 10^{-5} \text{ torr}$

Maximum cycle time $t_c \sim 15.6 \text{ h}$

Second stage: 14 panels

Gas load $Q \sim 3 \text{ torr-l/s}$

Attainable pressure $p \sim 8 \times 10^{-6} \text{ torr}$

Maximum cycle time $t_c \sim 37 \text{ h}$.

Since the ME Neutral Beam injects deuterium and tritium, the cycle time should be minimized in order to keep the tritium inventory low. The minimum cycle time is equal to the regeneration time which is 45 minutes.

IV.4.4.1.3 Regeneration System for the Volume Getter Panels

When the pumping speed for the hydrogen isotopes has decreased to an unacceptable limit due to the increased isotope concentration in the getter

material, a regeneration process is carried out. More frequent regenerations are performed when pumping tritium. An indefinite number of pumping cycles are possible.

For regeneration of the volume getter panels within the neutral beam boxes we assumed an average gas load of $Q \sim 200 \text{ torr}\cdot\ell/\text{s}$. The total pumping speed for the expansion tank must be in the order of $2 \times 10^5 \ell/\text{s}$ and we will maintain a pressure of 10^{-3} torr :

$$p \sim \frac{200 \text{ torr } \ell \text{ s}}{\text{s } 2 \times 10^5 \ell} \sim 10^{-3} \text{ torr} .$$

The pumping system consists of five turbomolecular pumps; four in action, one for reserve.

IV.4.5 Roughing Pump System

For evacuation in the range $760\text{-}10^{-1} \text{ torr}$ a combination between roots pumps and rotating-plunger pumps are used.

IV.4.4.5.1 Calculations

Roots pumps

Maximum gas load $Q \sim 400 \text{ torr}\cdot\ell/\text{s}$

Pressure after the turbomolecular pumps $< 0.1 \text{ torr}$

Pumping speed of the roots pumps

$$S \sim \frac{400 \text{ torr } \ell}{\text{s } 0.1 \text{ torr}} \sim 4000 \ell/\text{s}$$

$$S_{\text{eff}} \sim 2000 \text{ m}^3/\text{h} .$$

We need two roots pumps in the evacuating system; one in action, one for reserve.

Rotating plunger pumps

Pressure after the roots pump < 1 torr

Pumping speed of the rotating plunger pumps

$$S \sim \frac{400 \text{ torr } \ell}{\text{s } 1 \text{ torr}} \sim 400 \ell/\text{s}$$

$$S_{\text{eff}} \sim 2000 \text{ m}^3/\text{h} .$$

We need five rotating plunger pumps; four in action, one for reserve.

IV.4.6 Control of Vacuum Parameters

For measuring the neutral gas pressure in the chamber during a burn cycle, a pulsed noise free ionization gauge will be used, which will make pressure measurements of the neutral gas in the vicinity of the plasma in the range 5×10^{-3} torr - 1×10^{-9} torr.

Controlling the background gases during a burn cycle will be done by a mass spectrometer capable of operating in a radiation environment.

The pressure and partial pressure of the background gases in the range $1-10^{-8}$ torr in the discharge chamber, in the neutral beam boxes, in the pumps, vacuum lines and other elements of the vacuum system will be measured with commercial vacuum gauges and mass spectrometers with analog outputs.

References for Section IV.4

1. R.A. Haefer, Kryo-Vakuumtechnik, Springer-Verlag Berlin-Heidelberg-New York, (1981) pp. 124-144.
2. B. Ferrario and L. Rossi, "New Types of Volume Gettering Panels for Vacuum Problems in Plasma Machines," Proc. 7th Intern. Vac. Congr. and 3rd Intern. Conf. Solid Surfaces, Vienna, 1977.
3. Standard Plane Panel Type 15 WP 875/2, SAES Getters S.p.A., Milano, Italy.

IV.5 Tritium Fuel Cycle

IV.5.1 Overview

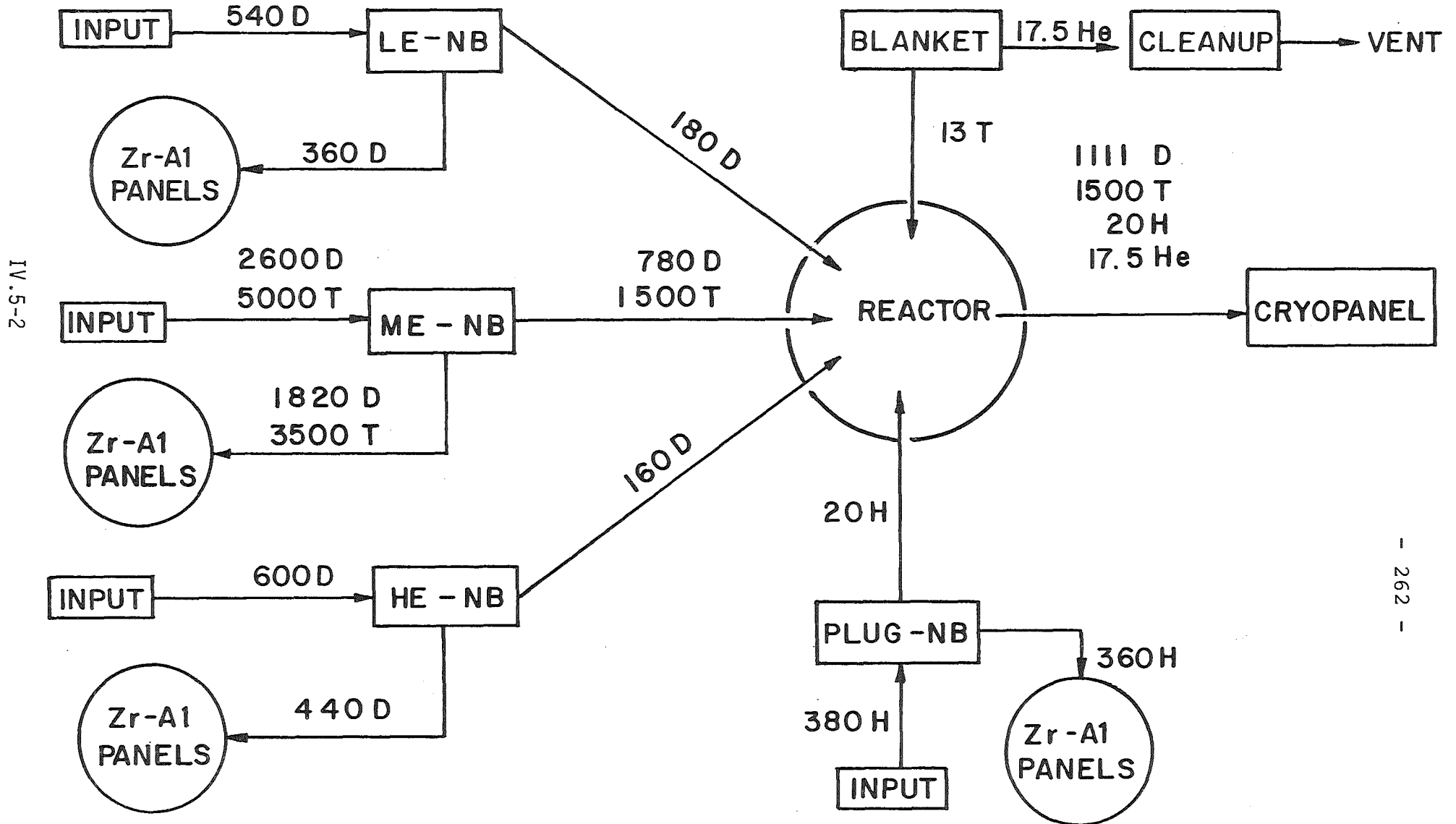
This section describes the hydrogen isotope pathways in the fueling of TASKA and discusses the tritium handling, containment and inventory associated with the fuel cycle. (The tritium inventory and extraction from the breeding blanket and the fuel purification systems are described in Section VI.5.) Three specific areas associated with the tritium fuel cycle are discussed: (1) In TASKA the tritium fueling is accomplished by injection of a mixed deuterium-tritium neutral beam. The inefficiency of the neutral beam injection (NBI) system requires large amounts of fuel to be pumped, purified and recycled. (2) The use of Zr-Al getter panels to pump uninjected tritium from the neutral beam lines. (3) The requirement of tritium barriers in the beam, ion and thermal dumps to prevent tritium diffusion into the water coolant cycle. The tritium fueling and exhaust flow is summarized in Fig. IV.5-1 and the tritium inventories associated with the fuel cycle are given in Table IV.5-1.

IV.5.1.1 Neutral Beam Fueling

In TASKA the primary fueling beam injects 49.7 MW of a DT mixture (44% D and 56% T) at an energy of 50 keV. There are 6 total DT NBI guns; three are located in the barrier region at each end of the central cell. Additional deuterium fueling (and heating) is provided by two low energy (2 keV) and two high energy (76 keV) deuterium neutral beams that deliver 0.2 MW and 6.6 MW respectively into the barrier region. In the plug at both ends of the machine, a 250 keV beam injects 5.4 MW of hydrogen. The NBI parameters are given in Tables IV.5-2 and IV.5-3.

Fig. IV.5-1

TASKA FUEL AND EXHAUST CYCLE
FLOW RATES IN g/d



IV.5-2

Fig. IV.5-1

Table IV.5-1. Tritium Inventory in TASKA Fuel and Exhaust Cycle

		<u>Subtotals (g)</u>
NBI Getter Panels (g):		259
LE-NBI	2.6	
ME-NBI	256	
HE-NBI	0.5	
PLUG-NBI	0.09	
Cryopanel (g):		125
Beam Dump	6	
End Cell	119	
Dump Areas (g):		0.52
DT-Beam Dump	0.50	
DT-Ion Dump	?	
Thermal Dumps	0.02	
Fueling and Exhaust Subtotal (g):		385
Storage (g):		5,000

Table IV.5-2. Injection Parameters for TASKA Neutral Beams

<u>Beam Designation</u>	<u>Energy (keV)</u>	<u>Power (MW)</u>	<u>Species</u>	<u>Number of NBI</u>	<u>Location</u>
LE-NB	2	0.2	D	2	Barrier
ME-NB	50	49.7	.44 D .56 T	6	Barrier
HE-NB	76	6.6	D	2	Barrier
PLUG-NB	250	5.4	H	2	Plug

Table IV.5-3. Injection Rates for TASKA Neutral Beams

<u>Beam Designation</u>	<u>Species</u>	<u>Particles/sec per NBI</u>	<u>g/d Total</u>
LE-NB	D	3.1×10^{20}	180
ME-NB	D	4.5×10^{20}	780
	T	5.8×10^{20}	1,500
HE-NB	D	2.7×10^{20}	160
PLUG	H	6.7×10^{19}	20

A disadvantage of using neutral beams to fuel fusion devices is the fact that NBI is an inefficient method; the amount of fuel circulated in the beam lines is usually much greater than the amount injected into the reactor chamber.⁽¹⁾ The gas injection efficiency (ϵ) for a neutral beam injector can be defined as:

$$\epsilon = \frac{\text{gas injected into the reactor chamber}^* / \text{NB}}{\text{total gas input/NB}}$$

[The total gas flow into a beam line is approximated as

$$\tau = 15 \times \frac{I^0(A)}{50(A)} \times \frac{.8}{f_{00}^0}$$

where τ is the gas flow ($\frac{\text{torr}\cdot\text{l}}{\text{sec}}$) for a 150 cm neutralizer of efficiency f_{00}^0 injecting I^0 amps⁽²⁾.] The gas injection efficiencies are approximately 30% (Table IV.5-4) for the D and DT beams. The plug-NB is of much higher energy (requiring negative ion technology) and has a gas efficiency of about 5%. The overall mass balance for the NBI system is given in Table IV.5-5.

For tritium NBI, low gas efficiencies result in large quantities of tritium that must be handled by the NB vacuum system, which typically uses cryopanel or getter panels for pumping. The inventory in the pumping panels as a function of the gas injection efficiency (based on 1500 g T/d injected) is shown in Fig. IV.5-2 for a 0.75 hr and a 2 hr pump on-line time. Low injection efficiencies can result in intolerably high inventories. In TASKA tritium is injected at a rate of 1500 g/d. The gas efficiency is about 30%

* includes gas not trapped by plasma.

Table IV.5-4. Approximate Gas Efficiencies for TASKA Neutral Beams

<u>Beam Designation</u>	<u>Gas Injected/NBI* (torr·ℓ/sec)</u>	<u>Gas Efficiency (%)</u>	<u>Total Gas Input/NBI (torr·ℓ/sec)</u>
LE-NB	4.4 (50 A)	33	13
ME-NB	15. (165 A)	30	50
HE-NB	3.9 (44 A)	26	15
PLUG-NB	0.98 (11 A)	5	20

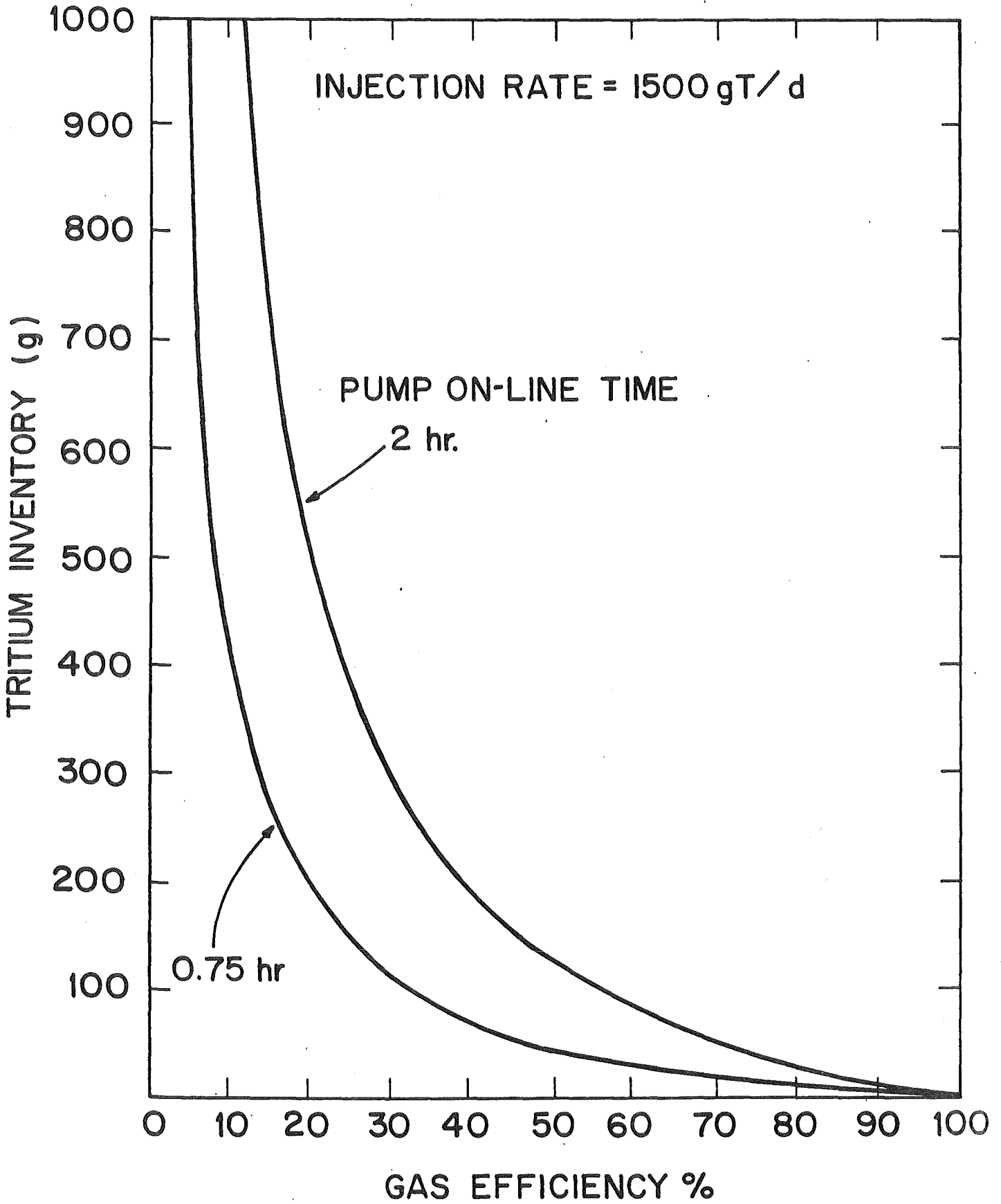
Table IV.5-5. Mass Balance for Neutral Beams

<u>Species</u>	<u>Source</u>	<u>Total (g/d)</u>	<u>Recycled (g/d)</u>	<u>Injected (g/d)</u>
T	ME-NB	5,000	3,500	1,500
D	LE-NB	540	360	180
	ME-NB	2,600	1,820	780
	<u>HE-NB</u>	<u>600</u>	<u>440</u>	<u>160</u>
	TOTAL D	3,740	2,620	1,120
H	PLUG	380	360	20

*Based on 11.28 amps atomic = 1 torr·ℓ/sec molecular gas flow.

Fig. IV.5-2

TRITIUM INVENTORY IN NEUTRAL BEAM PUMPING SYSTEM



resulting in 5000 g T/d being supplied to the injection system and 3500 g T/d must be pumped by the NB vacuum system and recycled. The tritium inventory in the NB vacuum system (45 min on-line time) is 259 g, a large component of the total active tritium inventory.

IV.5.1.2 Tritium Inventory in Zr-Al Getter Panels

The NB gases are pumped by Zr-Al getter panels⁽³⁾ with turbomolecular backing pumps. The getter material⁽⁴⁾ is capable of pumping hydrogen and its isotopes as well as other active gases, such as O₂, CO and N₂. The hydrogen isotopes are absorbed reversibly while the active gases react chemically to form stable products and are permanently fixed into the getter.⁽⁵⁾ The recommended operation temperature is 200-400°C when impurities are present, whereas pure hydrogen (\leq 10 ppm impurities) can be pumped even at room temperature.⁽⁶⁾ Inert gases are not pumped by the getters. This may be important where tritium is concerned, because of the unavoidable presence of the ³He decay product. Compared to hydrogen, water and methane are pumped slowly at the higher temperature (\sim 400°C) by a mechanism which involves dissociations or cracking at the surface followed by absorption of the subsequent components.⁽⁷⁾ The use of Zr-Al alloys as getters has been proposed to control plasma density and impurities in tokamak chambers such as TFTR⁽⁸⁾ and divertor channels.⁽⁹⁾

For NB pumping, both cryopanel and getter panels can provide the necessary vacuum requirements. Getter panels are thought to be more suitable for tritium pumping in NB lines than cryopanel for the following reasons:

- (1) The thermal loading from condensation and gas conduction is a more severe problem for cryopanel (4°K) than getter panels (\sim 673°K).⁽¹⁰⁾
- (2) Similarly, the tritium beta decay heat is more critical in the case of cryopanel.⁽¹¹⁾
- (3) Operating costs are higher (\sim 40X) for cryopanel due mainly to liquid

helium consumption.⁽¹²⁾ (4) The getter surface holds gases chemically at room temperature and thus, an accident causing large releases of gas is less likely.⁽¹¹⁾ Also, the manufacturer of Zr-Al getters states that the danger of fire in the pumping system caused by an air leak is only possible at or above 500°C.⁽¹³⁾ The advantages of Zr-Al alloys over Ti as a getter material has been reviewed elsewhere.⁽⁸⁾

There is some actual experience in the pumping of tritium with Zr-Al getters. Research at Lawrence Livermore National Laboratories (LLNL) was conducted to evaluate the pumping speed and holdup capabilities of commercially available getter pumps for tritium handling in TFTR.^(13,14) Results of the study indicated that the ratio of pumping speeds of deuterium to tritium follows the square root mass ratio. The pumps were shown to be satisfactory getters for tritium at temperatures between 250-400°C and on a short term basis tritium decay did not appear to adversely affect the pumps.⁽¹³⁾ Additional research was performed to measure the amount and chemical form of tritium released when a commercial getter cartridge was loaded with tritium and then exposed to moist air at ambient temperatures. Pumps loaded with 750 Ci of tritium released 0.04 Ci after 66 min and a total of 0.1 Ci (~ 0.01%) was released after 1200 hrs. The majority of gas is released upon initial exposure (> 72% in 4 min) and the rate decreases rapidly with time. Of the total released gas 80% was in the form of tritiated water.⁽¹⁴⁾ Recommended areas for further research include investigation of the effects of radiolysis and ³He production on the holdup and pumping capabilities of the getters over a time scale representative of what would be experienced in future fusion reactors and evaluation of tritium holdup under normal and off-normal conditions after a number of recycles have been performed.⁽¹⁵⁾

An important parameter in determining the tritium inventory in the getter material is the amount of time the panels are on-line pumping (Fig. IV.5-3). In TASKA, the getter panels are arranged so that one surface is absorbing gas, while the back surface is being degassed. With this arrangement the panels can be periodically rotated to control the tritium inventory. The minimum pump on-line time is equal to the time required to regenerate the pump surface. The pump regeneration time can be estimated from Eq. (IV.5-1):⁽¹⁶⁾

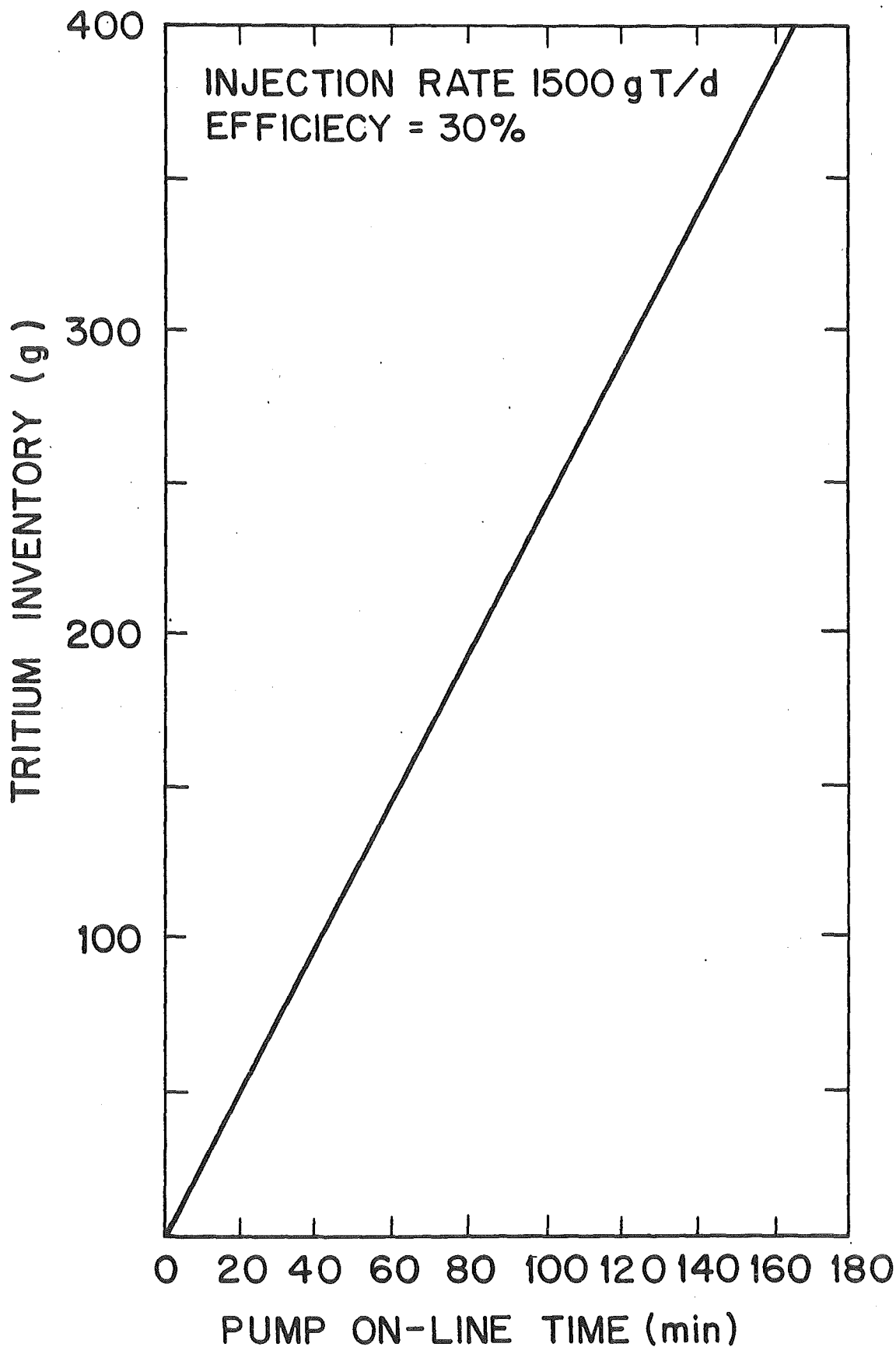
$$t = \frac{M}{F} \left(\frac{1}{q_F} - \frac{1}{q_0} \right) 10^{-\left(4.4 - \frac{7000}{T}\right)} \quad (\text{IV.5-1})$$

where: t = regeneration time (sec)
 M = mass of Zr-Al getter (g)
 F = back-pumping speed (ℓ/s)
 q_F, q_0 = final and initial concentration (torr· $\ell/g(\text{Zr-Al})$)
 T = regeneration temperature (K)

and the exponential term is the solubility constant for hydrogen in Zr-Al in terms of torr· $\ell^2/g(\text{Zr-Al})^2$. The following assumptions were made in evaluating Eq. (IV.5-1):

- The entire gas load is absorbed onto the getter panels.
- The panels pump uniformly at a constant rate.
- The temperature is constant during regeneration.
- The hydrogen pumping rate is 1-10 $\ell s^{-1} \text{cm}^{-2}$ depending on activation and operating conditions.⁽⁶⁾ Correcting for isotope effects, the getter pumping speed for DT is approximated as 3 $\ell s^{-1} \text{cm}^{-2}$.
- Average required pressure $\sim 5 \times 10^{-5}$ torr.
- Total Zr-Al mass $\sim 5 \times 10^4$ g.

TRITIUM INVENTORY IN NEUTRAL BEAM PUMPING SYSTEM



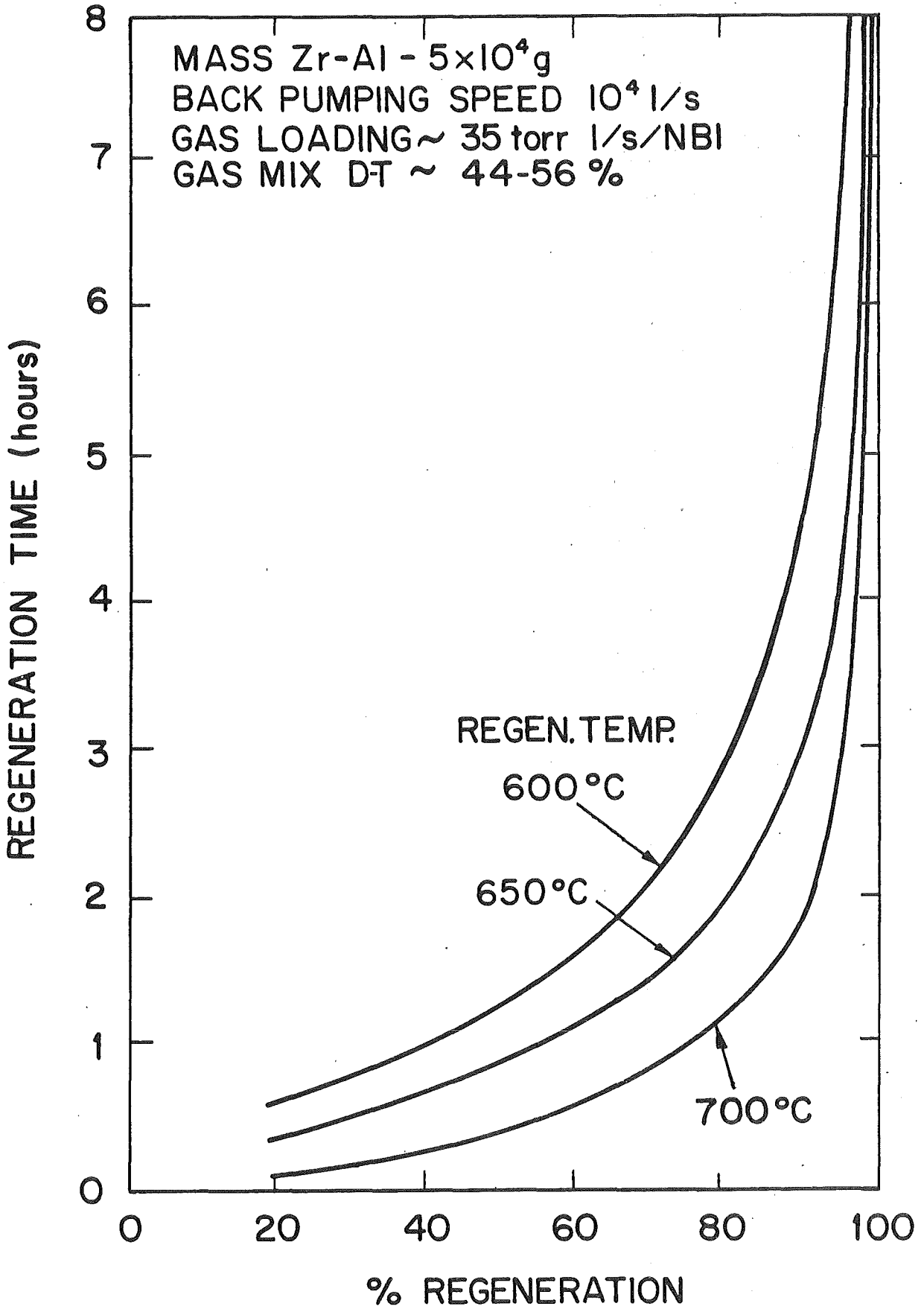
For a DT gas loading of 35 torr·ℓ/sec, the regeneration profiles at 600, 650, and 700°C are shown in Fig. IV.5-4. The regeneration temperature is kept below 750°C to avoid any adverse effects of copper evaporation from amagnetic constantan (Cu-45% Ni) backing plates.⁽¹⁶⁾ It is desirable to choose a minimum regeneration time at the maximum allowable temperature. The thermal effects of continuous frequent recycling may be critical;⁽¹⁷⁾ however, the getter panel lifetime is usually limited by impurity absorption.⁽⁹⁾ For 700°C regeneration, values as short as 30-45 min^(18,10) have been reported. The maximum value is determined by the H₂ embrittlement limit of 20 torr·ℓ/g⁽¹⁶⁾ which corresponds to ~ 8 hrs for the given gas loading. For TASKA a 45 min regeneration time was chosen at 700°C. This results in regenerating about 60% of the absorbed gases. The pump inventory after 45 min on-line is 110 g T (18.3 g T/NBI) and the initial tritium hold-up after degassing is 44 g T (7.3 g T/NBI).

At steady state the hold up will be 73 g (44 g T/0.6). This gives a tritium inventory of 183 g on the pumping face and 73 g on the degassing face resulting in a 256 g T total inventory in the Zr/Al getter panels in the DT beam lines.

It is noted that the above analysis is preliminary and contains many approximations and assumptions that can be evaluated only when the complete details of the vacuum system are available. The general principles illustrated, however, are important and lay the ground work for a more in-depth future study.

For the neutral beams which inject pure deuterium, the regeneration time is much less critical. The major source of tritium contamination into the deuterium NB is particle backstreaming from the reactor vessel. The

REGENERATION PROFILES



backstreaming rate depends on the gas pressure near the reactor wall, the local particle loss rate from the reactor plasma, and the area of the duct opening connecting the beam line to the reactor vessel.⁽¹¹⁾ The tritium backstreaming is approximated in a simple fashion from Eq. (IV.5-2) by assuming random molecular flow onto a unit area (Eq. IV.5-2):

$$F = \frac{NP}{(2\pi MRT)^{1/2}} \quad (\text{IV.5-2})$$

where: $F = \text{molecules cm}^{-2}\text{sec}^{-1}$

$N = 6.02 \times 10^{23} \text{ mole}^{-1}$

$R = 8.314 \times 10^7 \text{ erg } ^\circ\text{K}^{-1}\text{mole}^{-1}$

$M = \text{molecular weight (g mole}^{-1}\text{)}$

$P = \text{gas pressure at the wall (dyne cm}^{-2}\text{)}$

$T = \text{wall temperature (}^\circ\text{K)}.$

Assuming a pressure of $\sim 10^{-6}$ torr of gas (50% D_2 and 50% T_2) and a wall temperature of 400°C results in a flow rate of $3 \times 10^{14} T_2 \text{ cm}^{-2}\text{sec}^{-1}$. This is probably a maximum value as the neutral gas pressure at the wall is estimated to be in the range of 10^{-7} to 10^{-8} torr. However, gases from the beam dumps may contribute to the equilibrium gas pressure. Therefore, 10^{-6} torr is taken as an upper limit. For one LE-NB with duct size 81 cm x 110 cm the backstreaming rate is $3 \times 10^{18} T_2 \text{ sec}^{-1}$, which is $\sim 2\%$ of the injection rate. A similar calculation for the HE-NB and PLUG-NB results in tritium backstreaming of $5 \times 10^{17} T_2 \text{ sec}^{-1}$ (0.4% injection rate) and $1 \times 10^{17} T_2 \text{ sec}^{-1}$ (0.3% injection rate) respectively. The actual backstreaming rate is unknown and will have to be investigated by experiment and in-depth calculations.

The tritium pump inventory in the pure deuterium and proton NB lines is determined by the tritium impurity level that is allowed to build up from backstreaming. The estimated backstreaming is small and thus the getter panels can be regenerated more slowly than the minimum 45 min time used for the DT beam line. For a 12 hr regeneration time, the following total inventories are obtained: LE-NB ~ 2.6 g T, HE-NB ~ 0.5 g T, and PLUG-NB ~ 0.09 g T.

The recycled gases from the pure deuterium and proton beams are continuously sent to the isotopic separation unit (Section VI.5) so that tritium impurities are not allowed to build up in the beams. This minimizes the pump tritium inventory and also reduces tritium losses in the beam and ion dumps of the mono-isotopic neutral beams.

IV.5.1.3 Reactor Exhaust

The DT fusion power in TASKA is 86 MW. At a particle energy of 17.6 MeV, this corresponds to a burn rate of 3.05×10^{19} particles/sec. The tritium fractional burnup in TASKA can be defined in two ways:

1. Overall burn fraction (f_o):

$$\% f_o = \frac{T_{\text{burned}}}{T_{\text{total input to beam lines}}} = \frac{13 \text{ g/d}}{5000 \text{ g/d}} \times 100 = .26\%$$

2. Injected burn fraction (f_I):

$$\% f_I = \frac{T_{\text{burned}}}{T_{\text{injected into the reactor chamber}}} = \frac{13 \text{ g/d}}{1500 \text{ g/d}} \times 100 = .87\%$$

The low burn fraction has a negative impact on the tritium inventory and recycling (Fig. IV.5-5).

TRITIUM INVENTORY IN EXHAUST PUMPS

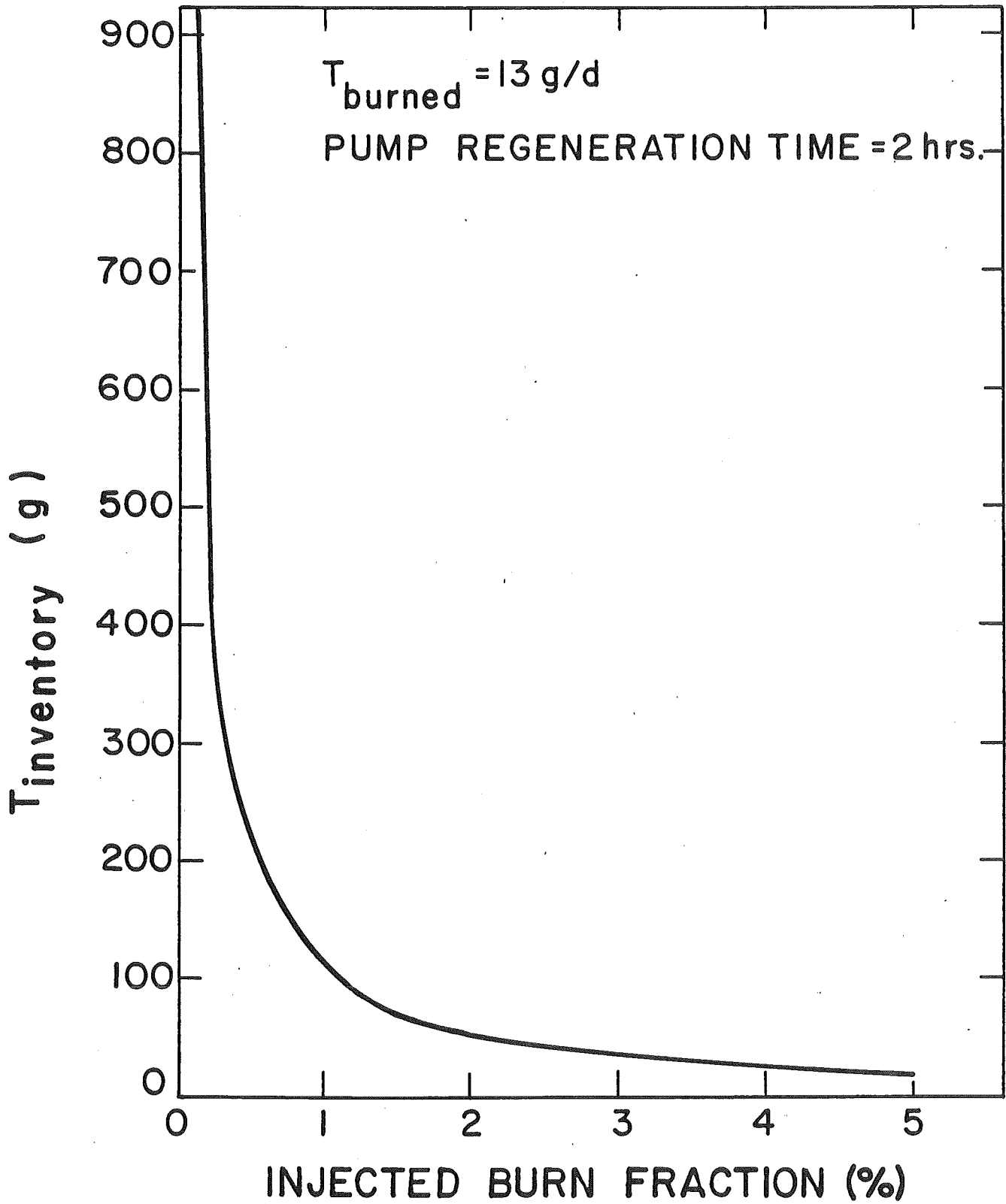


Table IV.5-6. Reactor Exhaust Characteristics

	<u>T</u>	<u>D</u>	<u>H</u>	<u>He</u>
Fuel Injected (g/d)	1,500	1,120	20	--
Fuel Burned (g/d)	13	9	--	--
Fusion Ash (g/d)	--	--	--	17.5
Breeding (g/d)	13	--	--	17.5
Exhaust Pumped (g/d)	1,500	1,111	20	17.5

The components in the exhaust are given in Table IV.5-6. Note that the tritium from the breeding blanket is included as it will be allowed to permeate through the blanket coolant tubes into the central cell (Section VI.5) and will be pumped with the exhaust gases. The helium ash must also be evacuated with the exhaust.

Of the 1500 g T/d that is injected into the central cell, 5% of this gas load (75 g T/d) is not absorbed by the plasma and is incident on a beam dump. The majority of this gas is pumped by cryopanel located in the beam dump area. For an on-line time of 2 hrs the inventory in the beam dump cryopanel is 6 g.

The remaining 95% of the injected tritium will flow axially through the end cells and be deposited in a thermal dump. It is assumed that all of the ions and half of the alphas flow to one end of the central cell and the electrons and remaining alphas flow to the opposite end. Periodically, an area of the thermal dump will be used to test a direct convertor module. For the tritium analysis we will assume only a thermal dump at both ends of the reactor. Particles will impact on the thermal dump and then be pumped by the

end cell cryopanel. For a 2 hr on-line time the inventory in the end cell cryopanel is 119 g T.

IV.5.1.4 Tritium Considerations in Beam, Ion, and Thermal Dump Areas

In TASKA there are three main areas where high energy tritium particles impact metal surfaces; the beam and ion dumps associated with the DT-NBI and the thermal dump in the end cells. In these areas tritium particles implant at a certain depth and then diffuse in both directions. Since the implantation depth is small with respect to the thickness of the dump and the front face temperature is much higher than the back face, the majority of particles will diffuse out the front face into the vacuum and only a small fraction diffuses out the back into the dump coolant.

A simplified method of estimating the flow of tritium into the coolant assumes that the front and back diffusion rates are equal; then, the ratio of the tritium flux to the water is related to the flux to the vacuum by the ratio δ/t where δ is the implantation depth and t is the plate thickness.⁽¹⁹⁾ For the DT beam dump a flux of 37.5 g T/d hits a 6 mm thick molybdenum surface and implants at a depth of 5.4×10^{-5} cm. This results in a loss of about 34 Ci/d per dump using the simple model.

A more sophisticated model which takes the temperature dependence of the diffusion process into account is outlined in Section VIII.5. This model gives much lower values for the diffusion of tritium into the coolant as the temperature on the back face is much lower. The estimated losses to the dump coolant using the temperature dependent model are summarized in Table IV.5-7. These estimates appear more realistic than those obtained from the simplified method. For example, a value of 16 Ci/d is calculated for the diffusion into the DT beam dump coolant (Section VIII.3). Tritium barriers can also be used

Table IV.5-7. Tritium Implantation Parameters

	End Cell	
	<u>DT Beam Dump*</u>	<u>Thermal Dump</u>
Material	Mo	Stainless Steel
Area (cm ²)	1.2 x 10 ⁴	5.4 x 10 ⁵
Thickness (cm)	0.6	0.4
Temperature (°C)		
Front Face	277	546
Back Face	190	200
Tritium Flux (g/cm ² /sec)	7 x 10 ⁻⁸	1.6 x 10 ⁻⁸
T Implantation Depth (cm)	5.4 x 10 ⁻⁵	4 x 10 ⁻⁵
C _{max} (g T/cm ³)	6.6 x 10 ⁻⁵	1 x 10 ⁻⁷
T _{inventory} (g)	0.50	0.02
T _{loss-to-coolant} (Ci/d) (no barrier)	16	7

*Totals for all DT beam dumps

to minimize the permeation even further (< 1 Ci/day). The maximum tritium inventory (Table IV.5-7) in the dumps is calculated by multiplying the maximum concentration at the implantation depth by the total dump volume. (There is insufficient data to do a similar calculation for the DT ion dump at this time.)

IV.5.1.5 Storage

A certain quantity of tritium must be maintained in storage in the event of a temporary malfunction of any of the tritium handling equipment. Typical-

ly the storage supply is equivalent to a one day's fuel supply. For TASKA this corresponds to 5000 g T stored on uranium beds.

IV.5.1.6 Comments on the Tritium Fuel Cycle

The tritium fuel cycle has been described with particular emphasis on the use of tritium neutral beams, Zr-Al pumping and losses through dump areas. The tritium inventory has also been estimated.

The following areas need further work in the TASKA tritium fuel cycle:

- Integration of the analysis of tritium in the Zr-Al getter panels with the overall vacuum system designed by FRG.
- Reassessment of the regeneration profiles with the vacuum system data obtained from FRG.
- Indepth calculations or experiments are needed to assess the problem of backstreaming.
- Effects of tritium decay and the formation of ^3He in the neutral beam pumping system.
- Assessment of total impurities in NB recycle gases.
- Incorporation of tritium barriers into beam, ion, and thermal dump areas.
- Further details about the ion dump are needed to calculate the tritium losses.
- More detailed examination of loss mechanisms from the fuel cycle.

It is difficult to compare the tritium aspects of neutral beam fueling with other proposed methods of fueling magnetic confinement devices such as pellet injection or gas puffing. Improvements in neutral beam technology may increase the efficiency reducing the tritium inventory and recycling. The efficiencies and inventories associated with the formation of simple, solid DT fuel pellets are difficult to assess. However, based on the TASKA analysis,

pellet fueling would decrease the large amount of fuel recycling, eliminate the problems associated with tritium losses in the DT ion and beam dumps and reduce the tritium storage inventory. Finally, the tritium aspects cannot be compared without also comparing the plasma physics fueling considerations.

References for Section IV.5

1. M.S. Ortman, E.M. Larsen, S.I. Abdel-Khalik, "A Study of the Tritium Handling Systems in Magnetic and Inertial Confinement Fusion Reactors With and Without Tritium Breeding," Nuclear Tech./Fusion 1, (April 1981) 255-274.
2. J. Osher, personal communication (see Section IV.3).
3. Zr-Al Getter Panels (86% Zr, 14% Al); trade name St 101, manufactured by S.A.E.S. Getters S.p.A. Via Gallarate 215, 20151 Milan, Italy.
4. B. Kindl, "Investigations on the Structure and Gettering Properties of Zirconium-Aluminum Alloys," Supplemento Al Nuovo Cimento 1(2), (1963) 647-662.
5. A. Barosi, T.A. Giorgi, L. Rosai, "Characteristics of SORB-AL Nonevaporable Getter Cartridges and Their Potential Use in Fusion Reactors," Proc. Int. Conf. Radiation Effects & Tritium Technology for Fusion Reactors, Gatlinburg, TN, 1-3 October 1975, Vol. IV, CONF 750989, (US-ERDA, 1975) 203-225.
6. B. Ferrario and L. Rosai, "New Types of Volume Gettering Panels for Vacuum Problems in Plasma Machines," Proc. 7th Intern. Vac. Congr. and 3rd Intern. Conf. Solid Surfaces, (Vienna, 1977) 359-362.
7. J. Vaumoron, G. Gasparia, and G. Bertoli, "Possibilities and Limitations of a Nonevaporable Getter Pump," J. Vac. Sci. Technol. 9(2), (1972) 982-986.
8. J.J. Sredniawski, "A Surface Pumping System for TFTR Impurity and Density Control," 4th ANS Topical Mtg. on Technology of Controlled Nuclear Fusion, King of Prussia, PA (1980).
9. M. Borghi and B. Ferrario, "Use of Nonevaporable Getter Pumps in Experimental Fusion Reactors," J. Vac. Sci. Technol. 14(1), (Jan./Feb. 1977).
10. L. Rosai, B. Ferrario, and P. della-Porta, "Behavior of Sorb-AC Wafer Pumps in Plasma Machines," J. Vac. Sci. Technol. 15(2), (March/April 1978), 746-750.

11. J. Kim and L.D. Stewart, "Implications of Tritium in Neutral Beam Injectors," Proc. Tritium Technology in Fission, Fusion and Isotopic Applications, Dayton, Ohio, April 29-May 1, 1980, CONF-800427, American Nuclear Society (1980), 132-136.
12. S.W. Schwenterly, "Development of Vacuum Components for Neutral Beam Injection Applications," Proc. 7th Symposium on Engineering Problems in Fusion Research, Knoxville, TN, October 1977, Vol. II (IEEE, 1977), 1793-1795.
13. M.F. Singleton and C.M. Griffith, "Evaluation of a Nonevaporable Getter Pump for Tritium Handling in the Tokamak Fusion Test Reactor," Lawrence Livermore Laboratory, UCRL-52584, Sept. 1978.
14. T.J. Biel, A.E. Sherwood, M.F. Singleton, and R.M. Aline, "Tritium Release from a Nonevaporable Getter Pump Cartridge Exposed to Air at Ambient Temperature," Lawrence Livermore Laboratory, UCRL-52801, July 1979.
15. K.E. Lind, J.J. Mauro, H.J. Howe, Jr., et al., "Safety Related Research Required to Support Future Fusion Research Reactors," Proc. Engineering Problems in Fusion, 1979, San Francisco, (IEEE, 1979), 2198-2203.
16. B. Ferrario, A. Barosi, M. Borghi, and T.A. Giorgi, "H₂, D₂ and T₂ Pumping and Handling in Fusion Experiments Using SORB-AC Nonevaporable Getter Cartridges," Proc. Symposium on Fusion Technology (SOFT), 14-18 June 1976, Garmisch, 51-56.
17. J. Stredniawski, "In Torus Surface Pumping for the TFTR Flexibility Modification," Proc. Symposium on Engineering Problems of Fusion Research, San Francisco, CA, 13 Nov. 1979, CONF-791102, 505-512.
18. L. Bromberg and D.L. Jassby, "In Torus Zirconium-Aluminum Getter Pumping for Beam Driven Tokamaks," Proc. 7th Symposium on Engineering Problems in Fusion, Knoxville, TN, (IEEE, 1977) Vol II, 971-975.
19. Conceptual Design of a Mirror Reactor for a Fusion Engineering Research Facility (FERF), Lawrence Livermore Laboratory, 23 August 1974, UCRL-51617, 104-106.

V. The TASKA Magnet System

V.1 Introduction

V.1.1 Magnet Design Philosophy

The objective of the TASKA study is the conceptual design of a mirror-based fusion engineering test facility using technologies that should be available in a few years. In the field of magnet technology, axisymmetric coils of 15 T peak field (Nb_3Sn -conductors) and 8 T peak field in C-shaped coils (NbTi -conductors) at 4.2 K can probably be provided in the near future. These data must be taken as constraints for the plasma physics model of TASKA. On the other hand, the basic geometry of the magnet system is determined by both the plasma physics requirements and space requirements for heating and handling.

Firstly, the field magnitude on the machine axis is important, as well as the ripple in the central cell region. Special field shapes have to be taken into account, e.g. the minimum B field configuration in the end plug or multipole components. The shape of the magnetic field lines must not incorporate any large excursions or runaways.

The second requirement is to provide space for the plasma, the blanket and the radiation shield. The neutral beam injectors must be oriented with the correct injection angles. Space for microwave heating waveguides and vacuum pumps has to be provided. The coil supports and the reinforcement also need space as well as the supply lines for current and coolant. Diagnostic devices for plasma measurement and control need space in low field regions.

The reaction of the electromagnetic forces in the structure must be compatible with other space requirements as mentioned above. In particular, the reaction of a pulsed load, e.g. in case of failure, has to be taken into account. However, in TASKA fatigue problems are of minor importance compared with Tokamaks. Additional structural requirements are the maximum allowable strain and stress in the windings and the arrangement and size of cooling channels.

Conductor-related requirements taken into account are the design current density in the superconducting material at the designed magnetic field strength and the operating temperature. These parameters, together with the filling

factor and the amount of stabilization and structural material, give the overall current density in the winding bloc. For the stabilization material, the magnetoresistance has to be known, especially for high magnetic fields. The cooling mode and the arrangement (radial or axial or both) have to be chosen. An absolute limitation is the maximum field at superconductor, which is of the order of 8 T for NbTi and 15 T for Nb₃Sn, at 4.2 K. Conductor movement must be largely restrained. For pulsed operation the AC losses must be accommodated.

Other requirements for the magnet system are low costs and a reliable safe discharge. Magnetic pollution has to be as small as possible and, in certain critical areas, magnetic shielding is necessary, e.g. for neutral beam sources.

V.1.2 General Description of the Magnet System

The magnet system of TASKA consist of:

- 3 solenoids in the central cell to give the required central cell field and ripple (CC1, CC2, CC3),
- 2 sets of hybrid solenoids to provide the magnetic mirror field between central cell and barrier (BC1, BC2),
- 2 transition coils for plasma cross section shaping (RCN1, RCN2),
- 2 Yin-Yang systems to provide gross MHD-stability with a minimum B region (CEEN1 and CEEP1, CEEN2 and CEEP2),
- 2 recircularizing coils for plasma cross section shaping (RCP1, RCP2) and
- 8 coils for field shaping in the thermal barrier region (FSC1, ..., FSC8).

The arrangement and the winding cross sections of the magnets are shown in Fig. V.1-1; the names are also indicated. Only the right half of the machine is shown, the left half being a mirror image but rotated by 90° around the z-axis. Fig. V.1-2 shows a computer drawing of the TASKA magnet system and Fig. V.1-3 shows the types and specifications of the coils.

Table V.1-1 gives the z-positions of the magnet centers, where the center of the barrier coil is defined as the center of the normalconducting insert coil. The main magnetic characteristics are given in Table V.1-2. Fig. V.1-3 shows

the magnetic field on axis, while Fig. V.1-1 shows also the field lines in the x-plane (upper half) and y-plane (lower half).

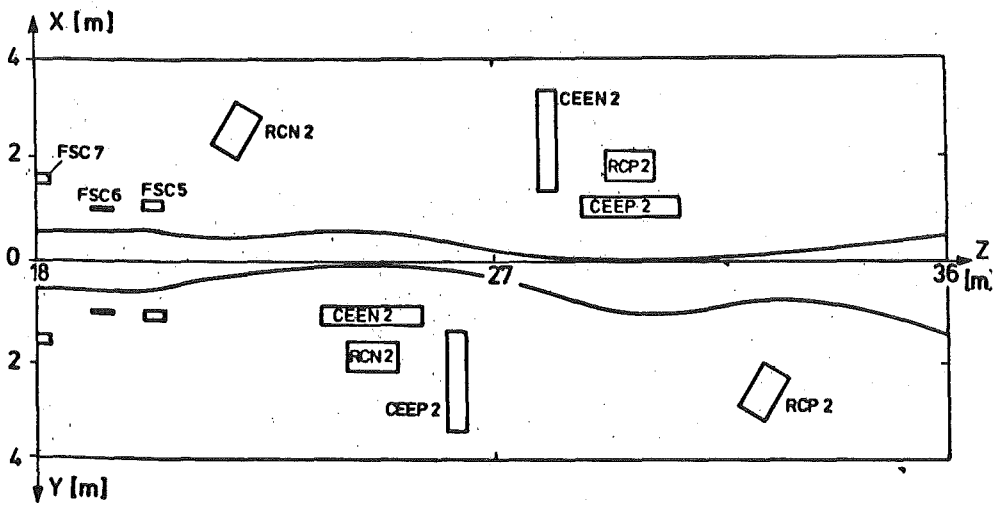
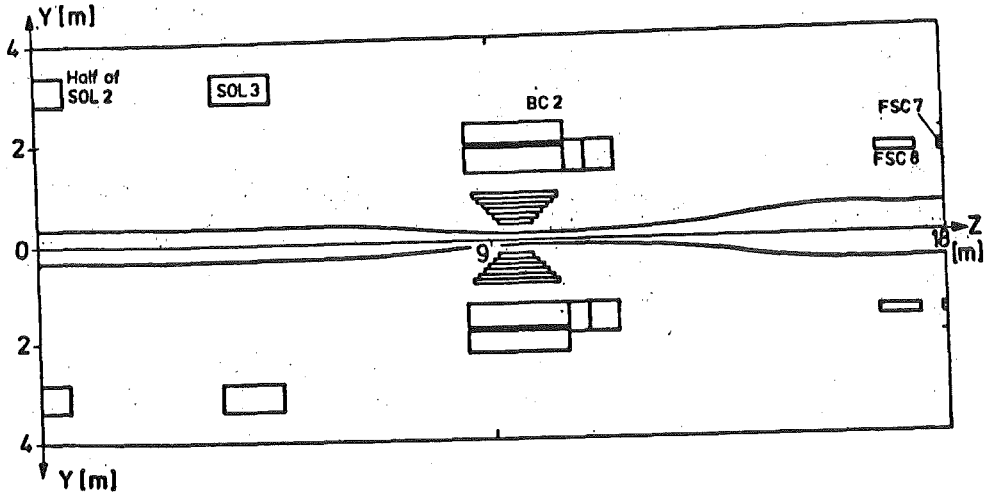


Fig. V.1-1 Winding cross section of the TASKA magnets in x- and y-plane. The right half of the machine is shown.

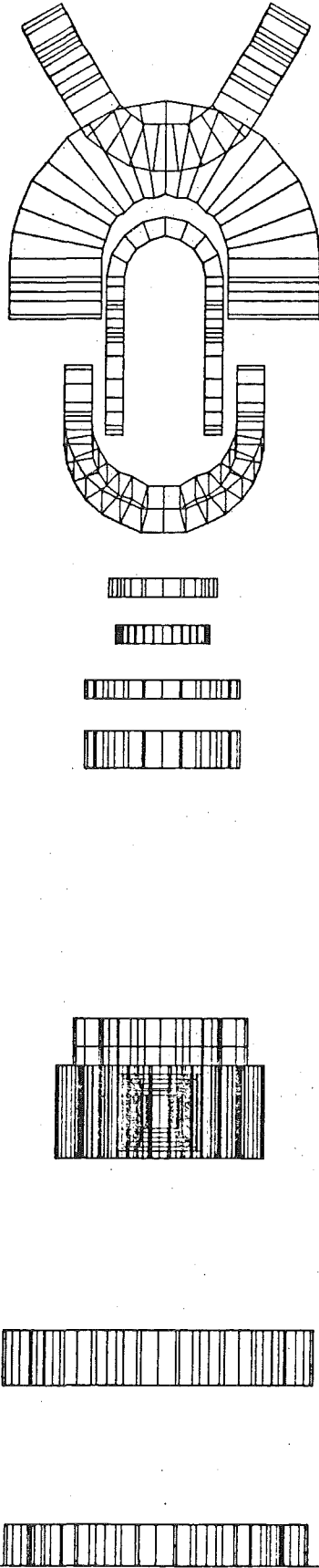


Fig. V.1-2 Computer drawing of the TASKA-magnet system (right half)

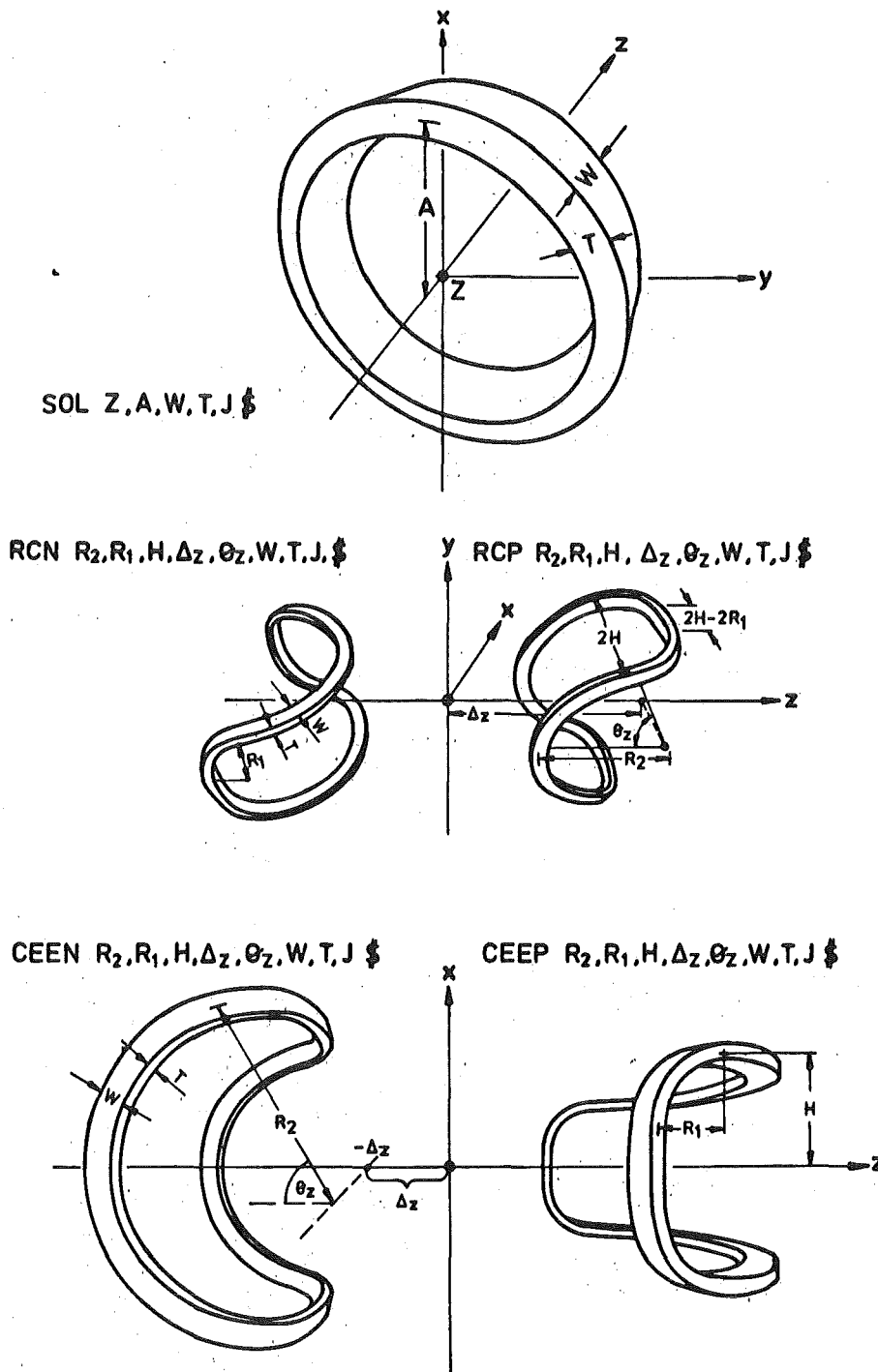


Fig. V.1-3 Magnet types in TASKA, together with the necessary input parameter set to specify each coil in the computer code EFFI(1)

Table V.1-1 Z-positions of the magnet centers

	m
RCN1	- 32.16
CEEN1	- 27.86
CEEP1	- 27.50
RCP1	- 23.20
FSC1	- 20.80
FSC2	- 19.80
FSC3	- 18.60
FSC4	- 17.35
BC1	- 9.5
SOL1 (CC1)	- 4.2
SOL2 (CC2)	0.0
SOL3 (CC3)	+ 4.2
BC2	+ 9.5
FSC8	17.35
FSC7	18.60
FSC6	19.80
FSC5	20.80
RCN2	23.20
CEEN2	27.50
CEEP2	27.86
RCP2	32.16

Table V.1-2 Main magnetic characteristics of TASKA

Magnetic field in central cell	2.7 T
Maximum field in barrier coil	20 T at $z = \pm 9.6$ m
Minimum barrier field	0.8 T at $z = \pm 19.8$ m
First maximum in plug	6.25 T at $z = \pm 24.70$ m
Minimum in plug	4 T at $z = \pm 27.20$ m
Second maximum in plug	6.25 T at $z = \pm 29.70$ m

All quoted fields are vacuum fields.

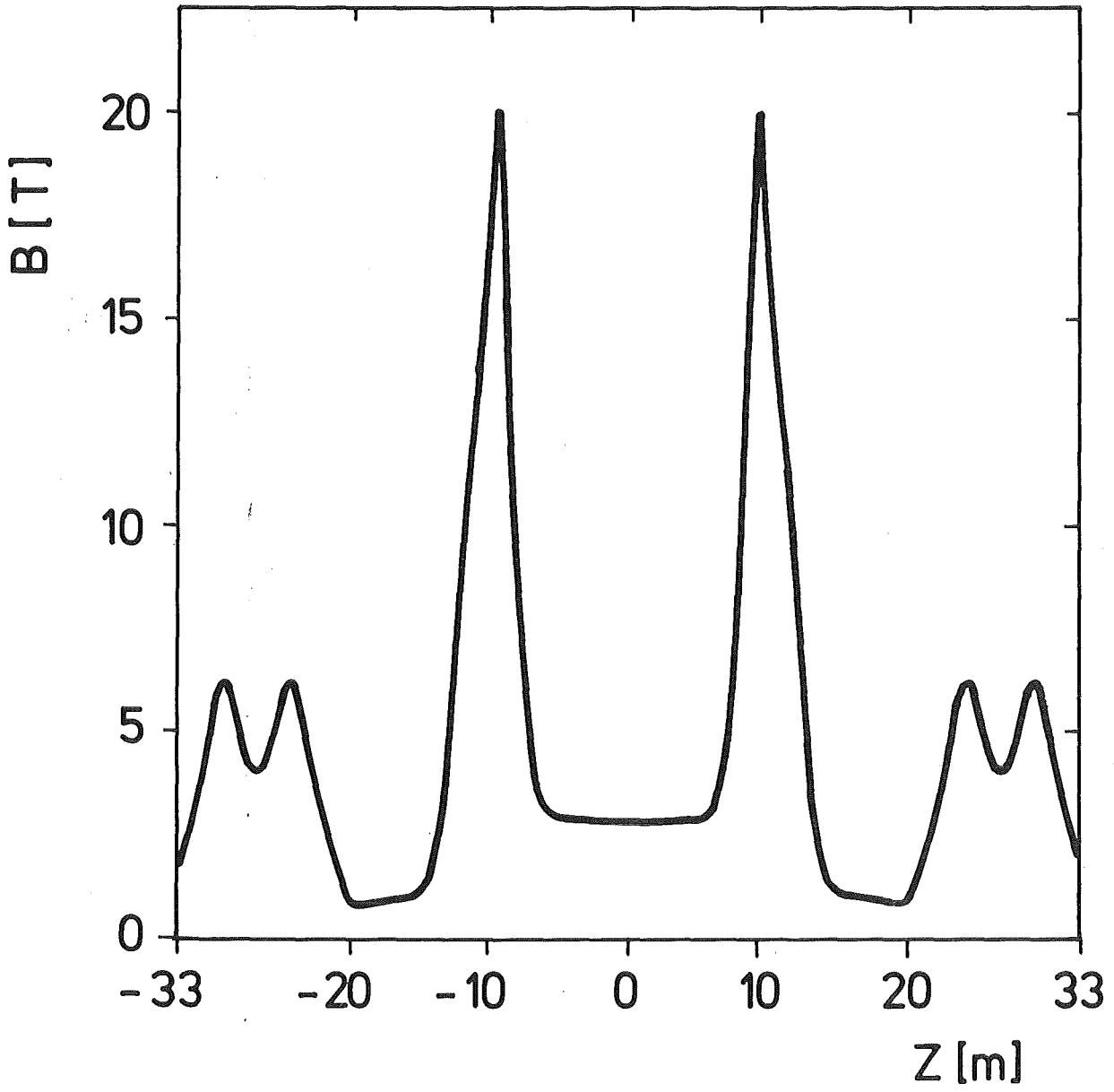


Fig. V.1-4 Magnetic field on axis

The magnet system parameters are the result of a trade-off between plasma physics requirements, magnet engineering limitation and access requirements for neutral beam injection and blanket handling.

For the central cell, a four solenoid design was compared with a three solenoid design. With the three solenoid design, the field ripple requirement along the axis $\Delta B/\bar{B}$ (\bar{B} =average magnetic field in the central cell) of <5% could be fulfilled with a coil length of 1.2 m. Additionally, access for shield and blanket handling was sufficient and better than in the four-solenoid-design.

The barrier coil shape takes into account the low injection angle of 20° of the high energy neutral beam injector. This coil is built up by a set of superconducting solenoids consisting of four winding packages with different current densities and different thicknesses of the winding cross sections to provide space for the neutral beam injector. In order to obtain a B-field as high as possible and to provide space for the neutral beam dumps, a normalconducting insert coil is placed concentrically within the superconducting coil set and located axially with respect to the center of largest radial thickness of the superconducting packages. The injection field region is defined by the plasma physics requirements and in particular by the footprint of the medium energy neutral beam. The field shape in the injection region was adjusted by using different current densities in the smaller parts of the barrier coil.

The positioning of the high energy neutral beam injector required an increase of the barrier length over the value defined by physics and magnet technology considerations. It was achieved by an axial translation of the end plug magnets outside. However, as a result, the minimum field in the thermal barrier region is lower than the 0.8 T required in the plasma model. Therefore field shaping coils (in this case normal conducting) on each side are used to enhance the field to the required level; these coils will be integrated into the shield. The boundary position of these coils is dictated again by the beam ducts of the high energy, medium energy and low energy neutral beam injectors.

The C-shaped end plug magnets are more compact than the end plug magnets in WITAMIR-I (2,3) and are comparable to the MFTF-B end plug magnets. (4) This is because of a smaller plasma radius and less shield thickness.

Note that the maximum field in the plug is 6.25 T and the minimum field is 4 T, while the maximum conductor field is less than 8 T. Unique to this design in the end plug is that the Yin and the Yang magnets have no common center; in fact the centers of the magnets are separated by 0.36 m. The reason is that for a given minimum plug field (4 T), the maximum plug field can be increased without raising the conductor field. Thus, a plug mirror ratio as high as possible can be provided.

References for section V.1

1. S.J. Sackett, EFFI, A Code for Calculating the Electromagnetic Field, Force and Inductance in Coil Systems of Arbitrary Geometry, Lawrence Livermore National Laboratory, Livermore, CA, UCRL-52402 (1978)
2. B. Badger et al.: WITAMIR-I, A University of Wisconsin Tandem Mirror Reactor Design, University Wisconsin Report, UWFD-400 (1980) and
3. W. Maurer, D.C. Larbalestier, I.N. Sviatoslavsky: Magnets for the Tandem Mirror Fusion Power Reactor WITAMIR-I, MT-7, IEEE Transactions on Magnetics, p. 1927, 1981
4. K.I. Thomassen, Program Leader, and V.N. Karpenko, Project Manager, Tandem Mirror Fusion Test Facility-MFTF-B Conceptual Design Report and Project Proposal, Lawrence Livermore Laboratory, Rept. LLL-Prop-163, Rev. 1. (January 23, 1980); this document updates LLL-Prop-163, dated August 1, 1979.

V.2 Central Cell Magnets

The three central cell magnets have an inner diameter of 5.6 m and winding cross sections of 1.2 m x 0.5 m (central solenoid CC2) and 1.2 m x 0.58 m (outer solenoids CC1 and CC3), respectively. These magnets are comparable to big bubble chamber magnets already existing, e.g., at ANL⁽¹⁾ and CERN⁽²⁾. Therefore the technology for the central cell magnets is currently available and is based on the experience with these large coils.

The axial spacing of the three magnets allows sufficient access to the interior of the central cell for exchange of blanket modules or portions of the shield. In table V.2-1 the main parameters of the central cell magnets are given. The current density of the center coil is 1160 A/cm², while the outside coils have 1350 A/cm² to fulfil the ICRH requirements. The maximum field at the conductor is less than 6 T.

Fig. V.2-1 shows a cross section of the center coil and one of the outside coils with the B-field contours of 5 T, 4 T, 3 T and 2 T. It turns out that the current density could be graded for a most cost-effective design.

The conductor for these coils consists of NbTi with copper and/or aluminium stabilizer and stainless steel reinforcement. The conductor is described in section V.7.

References for section V.2

1. R.E. Jones et al.: Advances in Cryogenic Engineering, 15
141 (1970)
2. F. Wittgenstein: Rev. Industries Atomique 5/6, 23 (1970)

Table V.2-1: Main Central Cell Magnet Parameters

Name		CC1	/	CC2	/	CC3
<u>geometric features</u>						
center of magnet: z-position	m	-4.2		0.		4.2
minor radius	m	2.8		2.8		2.8
major radius	m	3.38		3.3		3.38
average radius	m	3.09		3.05		3.09
bundle cross section	mxm	1.2x0.58		1.2x0.50		1.2x0.58
mean turn length	m	19.42		19.17		19.42
volume of winding	m ³	13.5		11.5		13.5
mean density	t/m ³	~ 6.3		~ 6.3		~ 6.3
weight of winding	t	~86		~72.5		~86
<u>electromagnetic features</u>						
bloc current density	A/cm ²	1350		1160		1350
Ampère-turns	10 ⁶ A-turns	9.4		6.96		9.4
self-inductance per N ²	10 ⁻⁶ H/N ²	8.325		8.343		8.325
stored self-energy	MJ	368		202		368
max. conductor field	T	<6.0		<6.0		<6.0
<u>operating features</u>						
operating temperature	K	4.2		4.2		4.2
max. working strain	%	< 0,25		<0,25		<0.25
max. " stress	MPa	< 500		<500		<500
<u>conductor properties</u>						
superconductor				NbTi		
stabilizing material				Al		
structure material				SS		

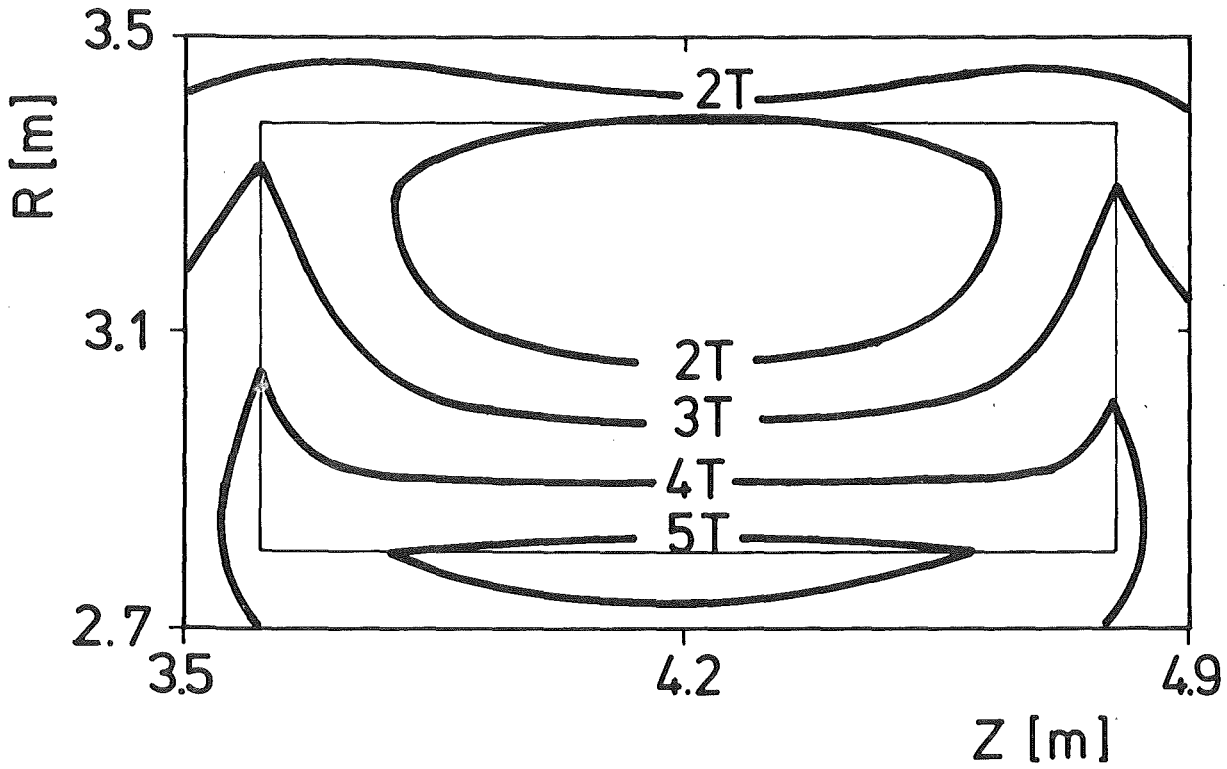
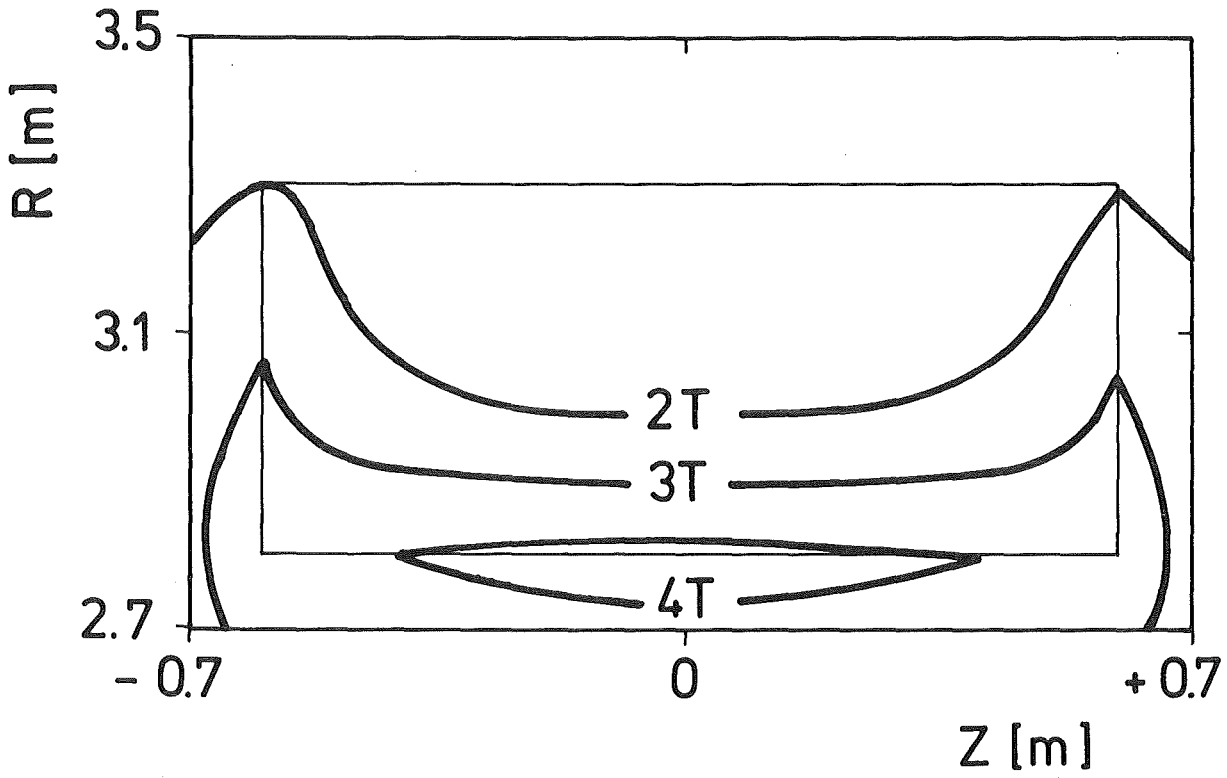


Fig. V.2-1: Cross section of central cell coils with 2T, 3T, 4T and 5 T B-contours (Top:center coil in central cell; bottom: neighbour coil).

V.3 The Barrier Mirror Coil

The barrier mirror magnet is a hybrid consisting of a superconducting outer solenoid set and a normalconducting insert coil. The aim of this magnet is to produce a field in the mirror throat as high as possible. A maximum field of 20 T on axis is achieved with this design. The superconducting coil gives 13.7 T on axis, - the rest is delivered by the normal conducting insert coil. The thickness of the superconducting coil varies axially; the reason is to provide access for one of the barrier pump beams as discussed previously in chapter V.1.

V.3.1 The Superconducting Solenoid Set

The superconducting part consists of four winding packages; a cross section is seen in Fig. V.3-1. Some field lines are given to show the region where NbTi (up to 8 T on conductor) and Nb₃Sn (up to 15 T) can be used. Fig. V.3-2 and Fig. V.3-3 give additional information about the radial and axial field variation in the barrier coil. The radial variation shows that the maximum field at the superconductor is 15 T. The radial variation is calculated at the z-position, where the maximum on axis field occurs. Fig. V.3-3 shows that the field at the superconductor (R=1.3 m) varies from about 10 T to 14 T.

In Table V.3-1 the main parameters of the superconducting coils are given with Fig. V.3-4 showing the locations and names of the various coils. The design of this coil set approaches the limits of the technology which can be expected in the near future: Nb₃Sn superconductor with about 15 T at the conductor and a stored energy of about 2.6 GJ in the coil set.

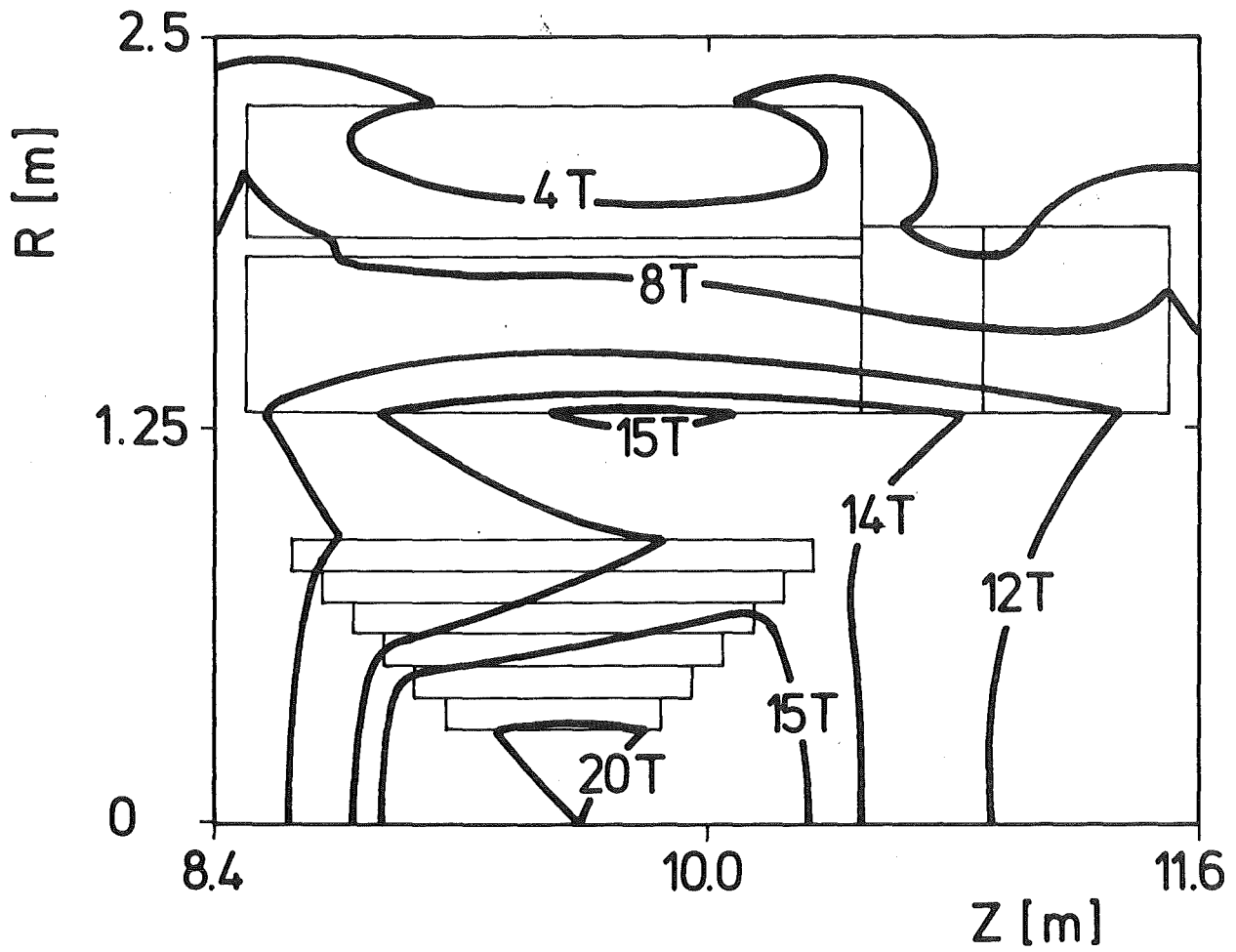


Fig. V.3-1: Cross Section of the Barrier Coil
with 4 T, 8 T, 12 T, 14 T, 15 T, 20 T
B-contours

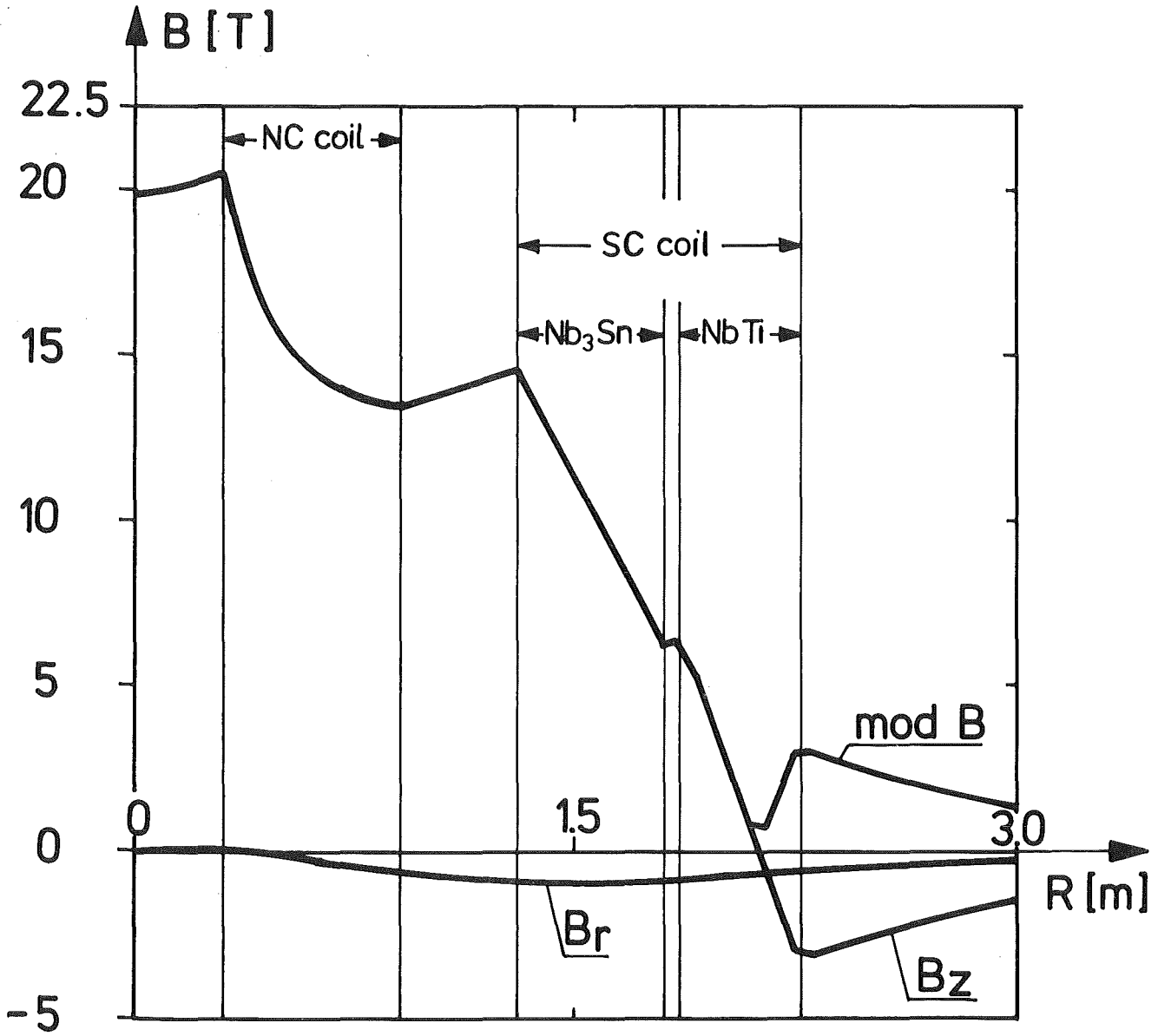


Fig. V.3-2: Radial variation of magnetic field in the barrier coil at $z = 9.6$ m (maximum field point on axis).

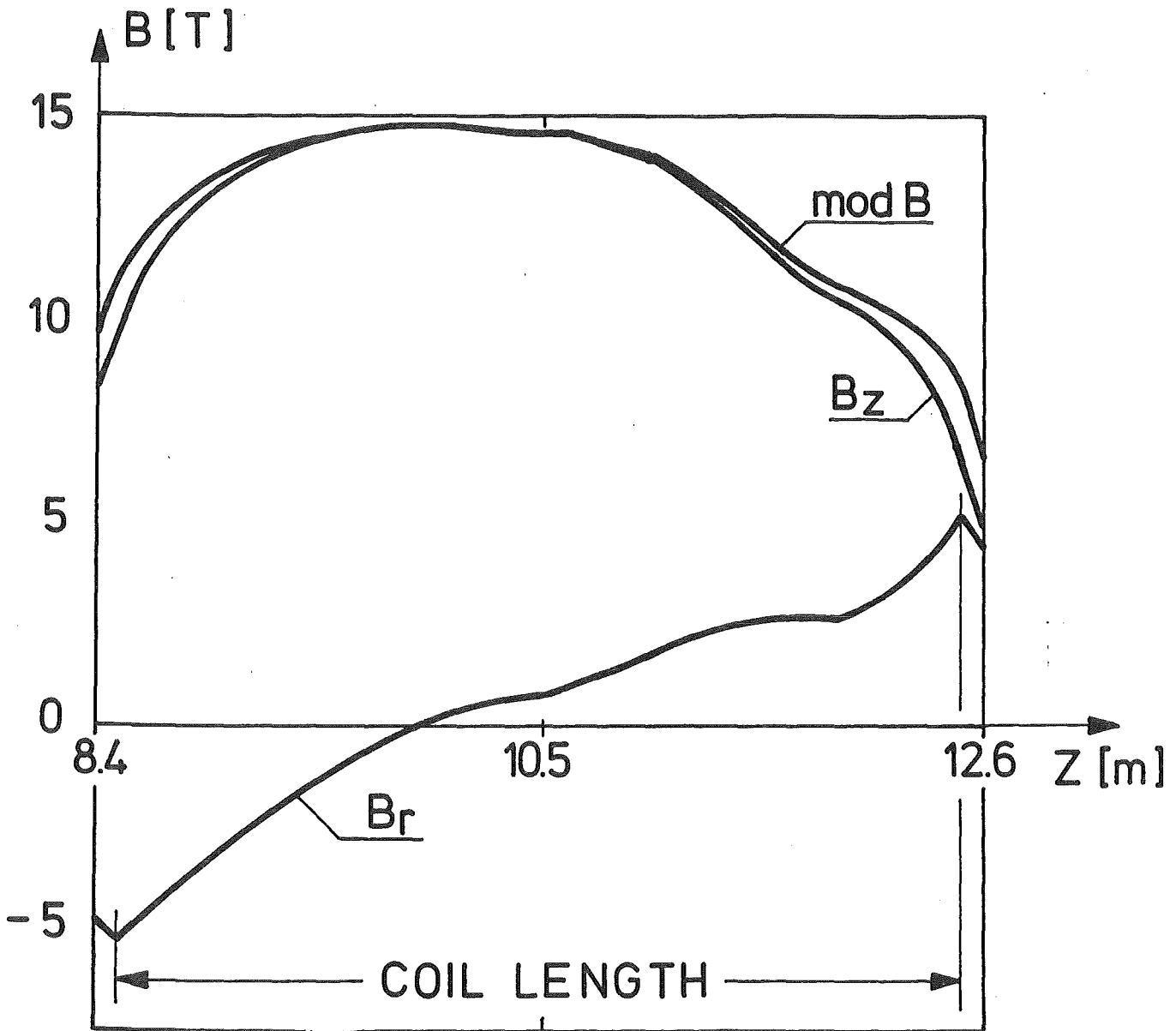


Fig. V.3-3: Axial variation of magnetic field in the barrier coil at $r=1.3$ m (along the inner edge of the superconducting winding bloc).

Table V.3-1: Main magnet parameters of the superconducting solenoid set of the barrier coil

		LI	LO	ML	MR	total
center of the magnet:						
z-position (m) relative to center cell plane of symmetry		± 9.5	± 9.5	± 10.7	± 11.2	
<u>geometric features</u>						
	<u>unit</u>					
minor radius	m	1.3	1.86	1.3	1.3	
major radius	m	1.8	2.28	1.9	1.9	
average radius	m	1.55	2.07	1.6	1.6	
bundle cross section	mxm	0.5x2.0	0.42x2.0	0.6x0.4	0.6x0.6	
mean turn length	m	9.74	13.0	10.05	10.05	
volume of winding	m ³	9.74	10.93	2.413	3.62	
mean density	t/m ³	~ 6.3	~ 7	~ 6.3	~ 6.3	
weight of winding	t	62	77	15.2	22.8	177
<u>electromagnetic features</u>						
bloc current density	A/cm ²	1600	2400	2000	2200	
Ampère-turns	10 ⁶ A-turns	16	20.16	4.8	7.92	49
self-inductance per N ²	10 ⁻⁶ H/N ²	2.354	3.876	4.145	3.792	
stored self-energy	MJ	301	788	48	119	
max. conductor field	T	< 15	< 8.6	< 15	< 14.5	
<u>operating features</u>						
operating temperatures	K	4.2	4.2	4.2	4.2	
max. working strain	%	0.24	0.24	0.24	0.24	
max. " stress	MPa	500	500	500	500	
<u>conductor properties</u>						
superconductor		Nb ₃ Sn	NbTi	Nb ₃ Sn	Nb ₃ Sn	
stabilizing material		Al	Cu	Al	Al	
structure material		SS	SS	SS	SS	

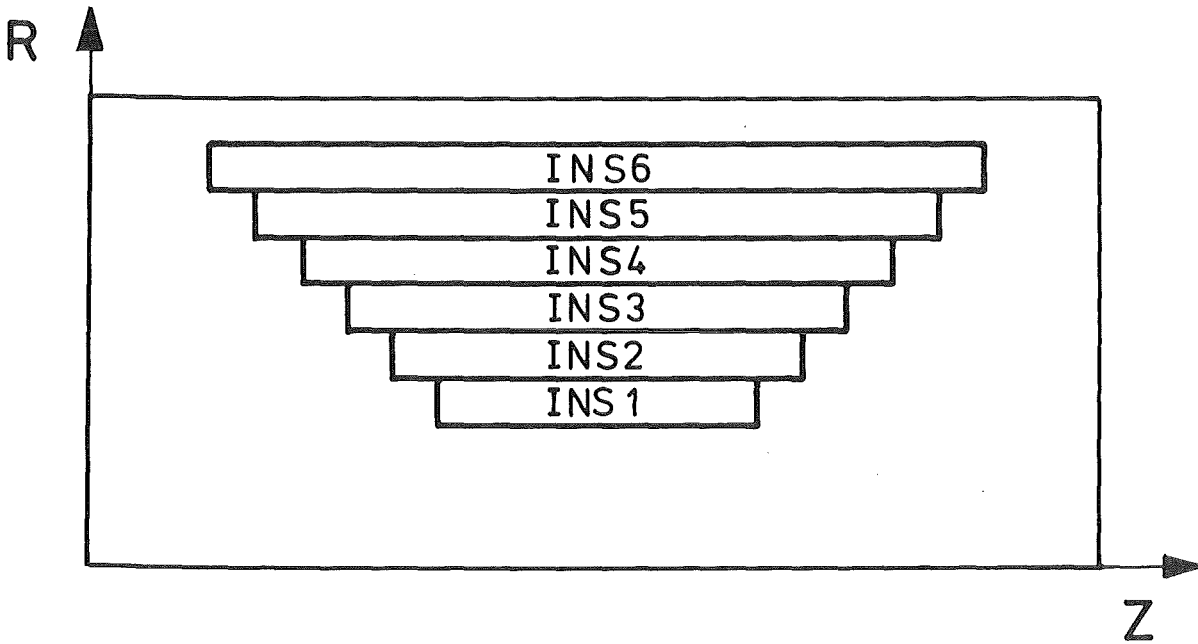
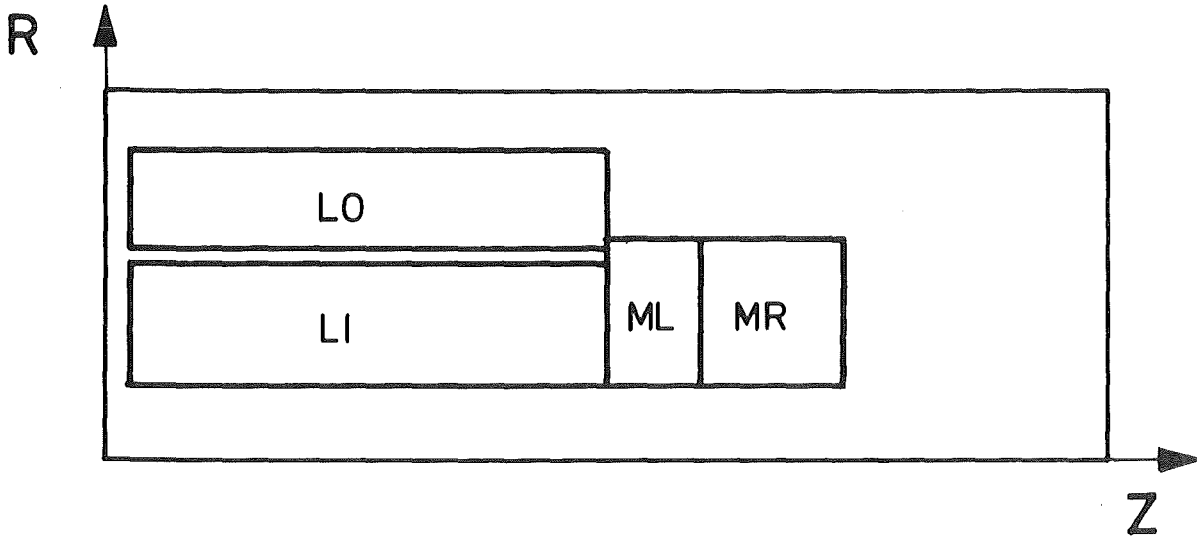


Fig. V.3-4: Names of the magnet parts

V.3.2 The Normalconducting Insert Coil

The primary objective of the high field barrier coil in TASKA is to establish a magnetic mirror for particles in the central cell. Increasing the barrier field reduces the particle current passing into the barrier region and consequently the requirements for pumping in the barrier. As pumping is done by power-consuming neutral beams into the barrier, a power-trade-off was studied (see Chapter III.3) between pumping requirements and enhancement of the barrier field with normalconducting coils inserted into the radiation shield of the superconducting coils. The sample case chosen for the study showed a decrease in neutral beam power from 200 MW to 150 MW when the peak field on axis in the barrier coil was increased from 13.7 T to 20 T [1]. The power needed for operation of the insert coils is less than the 50 MW of beam power saved, and it can be provided more economically via rectifiers. Without further refined optimization studies it was decided to design the barrier coil set for a peak field of 20 T in which 6.7 T are provided by the insert, 13.3 T by the superconducting coil.

The design of the insert coil is governed by the following aspects which are discussed in the following paragraphs:

- Geometric constraints,
- Minimization of dissipated power,
- Stress and heat transfer limits,
- Conductor design and insulation.

Geometric constraints limit the radial region in which a normalconducting insert can be positioned. The radius of the vacuum chamber at the 20 T point is 0.15 m, increasing along the axis towards lower field values. At the central cell side of the peak field point, the fusion power density in the plasma is about the same as in the central cell, subjecting the normalconducting insert to neutron and gamma radiation. As long as little operational experience with magnet coils in high radiation fields is available, conservative assumptions with respect to the lifetime of conductor and insulation, and to the operating features at high fluxes must be taken. It was therefore decided to allow radial space for a radiation shield of 0.15 m which is sufficient to reduce the radiation flux by one order of magnitude. The inner radius of the insert is thus fixed at 0.3 m.

The outside radius of 0.9 m is governed by the position and radiation shielding requirements of the superconducting coil. With an inner coil radius of 1.3 m and 0.1 m of radial space needed for coil case, superinsulation and vacuum tank, 0.3 m are available for a final effective radiation shield in addition to the shielding established by the normal-conducting insert. 30 cm of additional shielding is certainly on the safe side and may appear overconservative but a detailed neutronics analysis must consider voids in the shielding for hydraulic and power leads to operate the insert. Should the detailed analysis show that the amount of shielding can be reduced, decrease of the inner radius of the superconducting coil will be far more economical than increase of the insert outer radius. Finally, the axial length of the insert can be made as long as the superconducting coil if desired.

In a solenoidal magnet, the least power is dissipated for generation of a given central field B_0 if the current density in the cross section varies as the "Kelvin"-distribution [2]:

$j_k \sim r (r^2+z^2)^{-3/2}$. In a real magnet, it is of course impractical to realize this distribution but it should be approached if possible. With the radial variation being most important, it was decided to subdivide the insert coil set into 6 nested cylinders of 0.1 m thickness each. The length of each cylinder is determined by power optimization for axially constant current density. Let $\alpha_k = r_{out,k}/r_{in,k}$ and $\beta_k = l_k/2r_{in,k}$ denote the geometry parameters of the k-th cylinder, then according to [2] we have

$$B_{0,k} \sim j_k \cdot F(\alpha_k, \beta_k) \text{ and } P_k \sim j_k^2 \cdot \beta_k \cdot (\alpha_k^2 - 1)$$

for field contribution and power dissipation, with $F(\alpha, \beta) = \beta(\sinh^{-1} \frac{\alpha}{\beta} - \sinh^{-1} \frac{1}{\beta})$. The parameter α_k is fixed for each coil by its thickness of 0.1 m, giving

$$P_k \sim \frac{\beta_k}{F^2(\alpha_k, \beta_k)} \quad \text{From } dP_k/d\beta_k = 0 \text{ we have}$$

$F(\alpha, \beta) = 2\beta \cdot \frac{dF(\alpha, \beta)}{d\beta}$ as a condition for β of a solenoid of constant current density, fixed α , and minimum power dissipation. Evaluation of this condition shows that optimum β is very accurately approximated if the length of the solenoid equals its average diameter (see Table V. 3.2-1).

Table V.3.2-1: Main Parameters of the normalconducting insert coils of the barrier coil

		INS1	INS2	INS3	INS4	INS5	INS6	Total
<u>Geometric Features</u>								
	<u>Unit</u>							
Center of the magnet: z-position +)	m	± 9.5	± 9.5	± 9.5	± 9.5	± 9.5	± 9.5	
Minor radius	m	0.3	0.4	0.5	0.6	0.7	0.8	
Major radius	m	0.4	0.5	0.6	0.7	0.8	0.9	
Average radius	m	0.35	0.45	0.55	0.65	0.75	0.85	
Bundle cross section	mxm	0.1x0.7	0.1x0.9	0.1x1.1	0.1x1.3	0.1x1.5	0.1x1.7	
Mean turn length	m ₃	2.2	2.83	3.46	4.084	4.712	5.341	
Volume of winding	m ³	0.15	0.26	0.38	0.53	0.71	0.91	2.9
Weight of winding ₃ (Mean density 7t/m ³)	t	1.1	1.8	2.7	3.7	4.9	6.3	20.5
<u>Electromagnetic Features</u>								
Blot current density	A/cm ²	2800	1683	1137	814	613	480	
Ampère turns	10 ⁶ A-turns	1.96	1.51	1.25	1.06	0.92	0.82	7.52
Self-inductance per N ²	10 ⁻⁶ H/N ²	0.4169	0.5508	0.6877	0.8249	0.9597	1.096	
Stored self-energy	MJ	0.97	0.64	0.48	0.4	0.32	0.28	12.0
Loss Power	MW	4.3	2.6	1.8	1.3	0.9	0.7	11.6
<u>Conductor Properties</u>								
Conductor	Hardened copper with $\bar{\rho} = 2.5 \times 10^{-8} \Omega \text{m}$ at average operating temperature and 300 MPa tensile strength, Height ≥ 3.3 cm, Width ≥ 10.7 cm, Current ≤ 100 kA, Pressure drop in Water ≤ 15 bar, $\Delta T = 60^\circ \text{C}$							

+) ± 9.5 means, one is at 9.5 m on the positive side of the z-axis and
 one is at -9.5 m on the negative " " " "

A similar power minimization is possible for adjustment of current density in the radially nested coils (for a general procedure, see Chapter 4 of Ref. [2]). For two concentric solenoids which have to generate a central B_0 , one has $B_0 = c_k \cdot j_k + c_l \cdot j_l$ and $P = d_k \cdot j_k^2 + d_l \cdot j_l^2$ with $c = \mu_0 \cdot r_{in} \cdot F(\alpha, \beta)$ and $d = \rho \cdot 2\pi\beta \cdot (\alpha^2 - 1) \cdot r_{in}^3$, ρ material resistivity. Loss power P is minimized if current densities j are graded such that

$$j_l/j_k = (c_l \cdot d_k) / (c_k \cdot d_l) .$$

The procedure just described offers a straightforward method for the design of a set of nested solenoids with constant current density each. However, experience with small insert coils in high field hybrid magnets [3] shows that two additional technical constraints must be considered: The upper limit of stress $\sigma = j \cdot r \cdot B$ in the coil of the order of 200 to 500 MPa depending on the conductor alloy chosen, and the upper limit on heat removal from the conductor which limits the current density in copper to about 25 kA/cm². While this latter limit is of no concern for large radius magnets, the stress limit will become essential for mirror fusion applications. The TASKA-insert is not yet governed by the stress limit if a copper alloy is chosen that can operate up to 300 MPa (e.g. SE-Cu with temper F 30 as offered by Kabelmetal, Osnabrück/W. Germany).

Heavily radiation loaded magnets were operated in the past mainly in accelerator centers, e.g. LAMPF and SIN [4]. The difference to conventional magnets is that a ceramic insulation must be used if doses of more than 10^9 rad are expected. MgO and Al₂O₃ as compacted powders will withstand doses in excess of 10^{12} rad, making resistivity-increasing transmutations in the conductor material the prime life-time limiting effect. Recently, a detailed analysis [5] was published in which an MgO-insulated copper conductor, jacketed by a steel sheet for chemical and mechanical protection of the insulation, was optimized for use in an unshielded bundle divertor magnet for a Tokamak-based FED. The analysis concluded that even with conservative assumptions, the required magnet can be built and operated.

In TASKA, coil INS 1 is simultaneously subjected to the highest Ohmic power dissipation and radiation load. Several key parameters are therefore given and justified for this coil; they may be applied to the other insert coils as well. An average resistivity in the copper at the average operating temperature, $\rho = 2.5 \times 10^{-8} \Omega m$, is taken, even considering transmutations after 10^{12} rad.

(1) Conductor cross section

The conductor must be bent at a radius of 0.3 m. Combining LANL-experience of ratios: radius of bending to height of 6 and US-manufacturer recommendations of a factor of 12 for ceramically insulated conductors into a factor of 9, a conductor height of $h = 3.33$ cm results, giving three layers for the coil thickness of 10 cm. Contrary to bundle diverter coils or Yin-Yang-coils, the solenoidal conductor is bent only in one plane, allowing an almost arbitrary width of the conductor. Operational safety and desire for thin insulators call for low voltage, the water cooling system calls for large hydraulic diameters of cooling channels and short channel lengths. Both requirements favor a wide conductor which should be limited only by practical considerations on the operating current. If a reasonably manageable peak current of $I_0 = 100$ kA is assumed (bus bar dimensions, losses and cooling), the conductor width as given by $w = I_0 / (h \cdot \bar{j})$, \bar{j} being the average current density in the conductor bloc of 2800 A/cm² for INS 1, becomes $w = 10.7$ cm.

(2) Layout of conductor

According to table V.3.2-1, a power of 4.3 MW is Ohmically dissipated in INS 1 for a copper filling factor of $\lambda = 0.7$. Additional 0.2 MW of nuclear heating must be considered if a peak power deposition of 2 MW/m³ is used, as indicated by the neutronics calculations. Power dissipation in the MgO-insulation [5], the resistivity of which decreases significantly in an radiation environment, is negligible in INS 1 due to the low terminal voltages and to the 0.15 m shield between plasma and coil. The water cooling system must finally handle a heat load of 4.5 MW, mainly caused by Ohmic heating. 30 % of the conductor cross section are available for steel jacket, insulator, and cooling channels. Using a steel jacket \varnothing of 0.6 mm and an MgO thickness of 1.4 mm, about 3.6 cm² of cross section area (~10 %) remain for cooling channels. In order to have a hydraulic diameter as large as possible and at the same time a large surface area of the channels for good heat-transfer, three parallel channels of 1.2 cm diameter each are proposed, spaced along the width of the conductor. Hollow copper conductors with 2 or more parallel channels are produced by Kabelmetal, Osnabrück. With this design and hydraulic operation of the three layers of INS 1 in parallel, the cooling system will require 1.5 MPa of (ideal) pressure

drop and 15 m/s of water velocity. If these values are too high for reliable operation or in view of pumping power needed, a reduction of current density in INS 1 and an increase in INS 2 may be considered (Minimization of the sum of pump power and Ohmic power).

In summary, the normal conducting insert coils of TASKA appear feasible even with conservative assumptions. With the remote handling scheme designed for their exchange, an operating failure can be tolerated. Some development-needs for construction of the insert are:

- Ceramic insulation and jacketing of large rectangular conductors,
- economic provision of a cladding of cooling channels which is corrosion-resistant against radiolysis products of water,
- Design of electrical (100 kA) and hydraulic (15 bar) manifolds.

References for Chapter V.3

- [1] R.P. Drake : private communication, Aug. 1981
- [2] D.B. Montgomery: Solenoid Magnet Design. New York: Wiley Interscience 1969
- [3] G. Landwehr: Problems connected with the generation of continuous magnetic fields above 15 T, IEEE Trans. Magn. 1981/17/5, p. 1768
- [4] A. Harvey: High Current-Density Coils for High-Radiation Environments, IEEE Trans. Magn. 1981/17/5, p. 1717
- [5] J.H. Schultz: A Costing and Sizing Code for Highly Irradiated Normal Magnets. M.I.T. Res. Rep. PFC/RR-81-13, Cambridge, Mass.

V.4 The End Plug Coils

Each end plug is formed by a Yin-Yang pair and two transition coils. The main features of these coils are given in Table V.4-1 with Fig. V.4-1 showing the locations and names of the end plug magnets. The current densities of these C-shaped coils are less than 2000 A/cm^2 . Their design is straightforward, because they are similar in geometry and electrical parameters to those of the MFTF-B machine. Characteristic dimensions are an overall height of about 7 m for the Yin-Yang system and about 5 m for a transition coil. These are comparable to the MFTF-B dimensions of about 6 m overall height for the Yin-Yang and about 12 m for the outside A-cell coil. The successful test of a MFTF-B Yin-Yang in February of 1982 encourages us to state that the C-shaped end plug magnets of TASKA can be built with current technology ⁽¹⁾.

Fig. V.4-2 shows B-contours for the region of closest approach between a transition coil and a Yin coil. Fig. V.4-3 demonstrates the magnetic well of the Yin-Yang.

References for section V.4

1. T.K. Fowler, private communication

Table V.4-1: Main Parameters of the end plug Magnets.

		TC/RC	Yin/Yang
<u>geometric features</u>			
center of the magnets	unit m	$\pm 22.7/\pm 31.66$	$\pm 27.0/\pm 27.36$
"Minor" radius A 1	m	1.6	0.9
"major" radius A 2	m	1.4	1.4
average "major" radius R2	m	1.9	2.4
average "minor" radius R2	m	1.9	1.09
sweep angle	degree	60	90
bundle cross section	mxm	1.0x0.6	2.0x0.38
mean turn length	m	19.90	21.93
volume of winding	m ³	11.94	16.67
mean density	t/m ³	~7	~7
weight of winding	t	~84	~117
<u>electromagnetic features</u>			
bloc current density	A/cm ²	1900	1630
Ampère-turns	10 ⁶ A-turns	11.4	12.4
self-inductance per N ²	10 ⁻⁶ H/N ²	7.497	5.349
stored self-energy	MJ	487	411
max. conductor field	T	< 7	< 7.9
<u>operating features</u>			
operating temperature	K	4.2	4.2
max. working strain	%	0.25	0.25
max. " stress	MPa	500	500
<u>conductor properties</u>			
superconductor		NbTi	NbTi
stabilizing material			Cu(3/4 hard)
structure material			

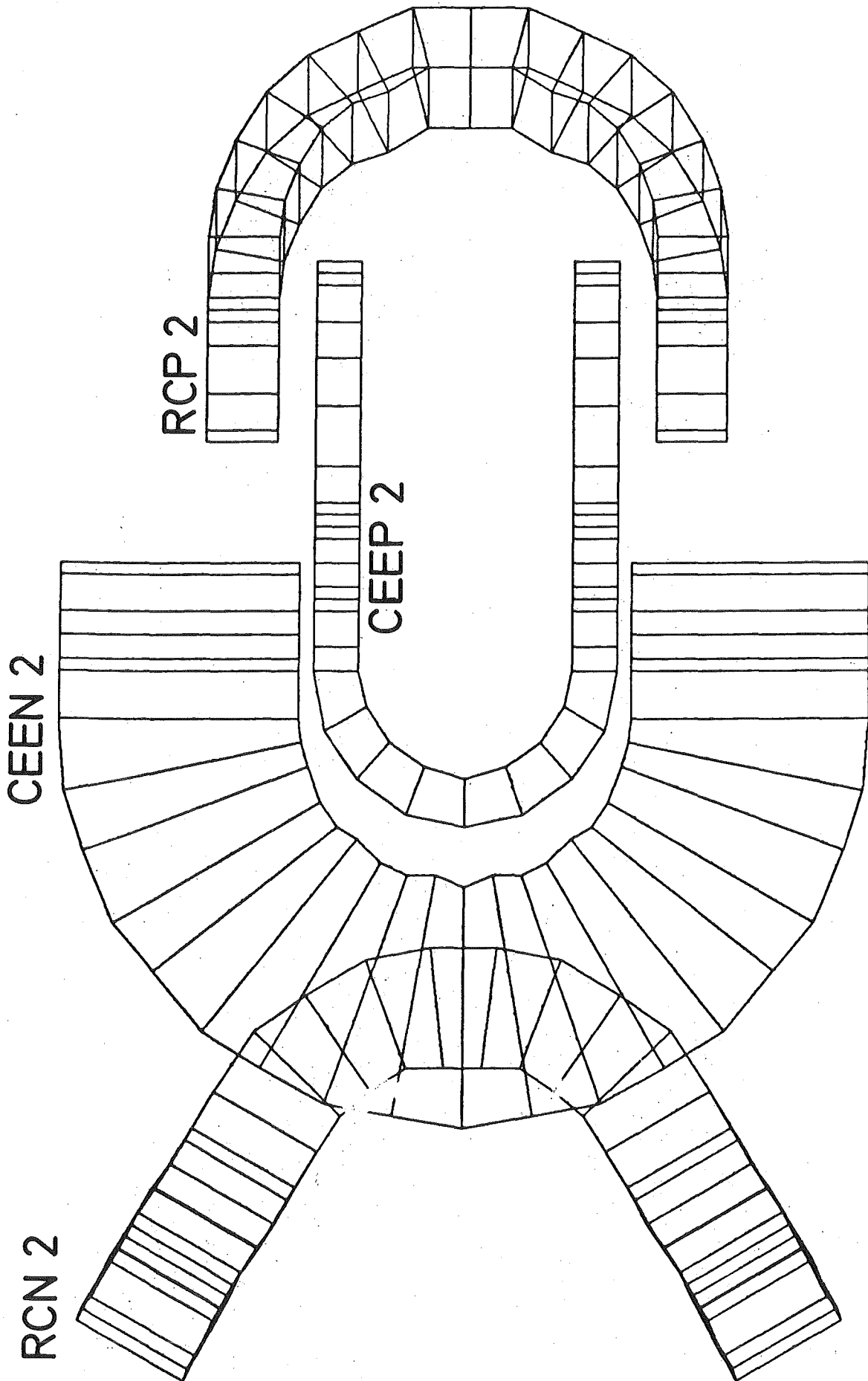


Fig. V.4-1: Identification of end plug magnets

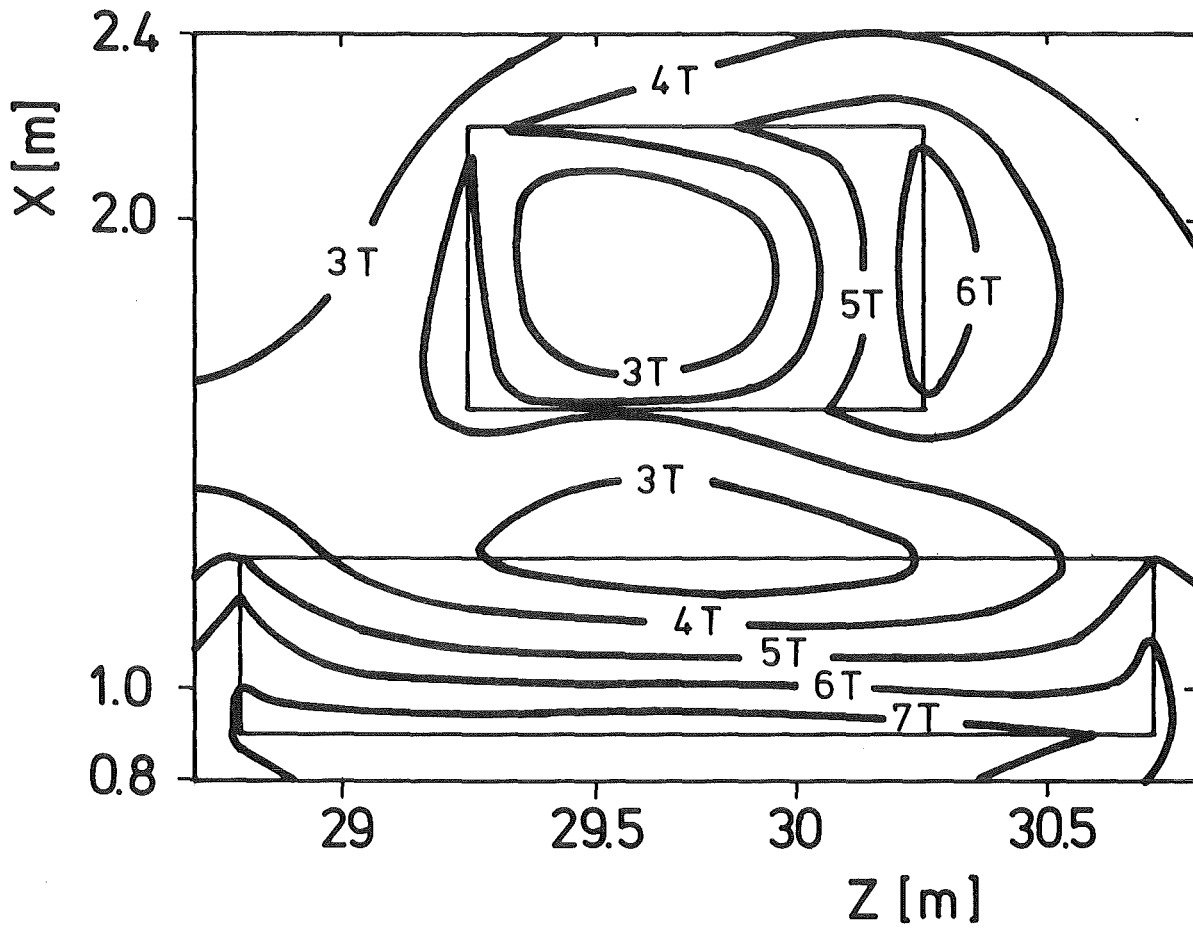


Fig. V.4-2: Field at conductor for the region of closest approach between a transition and Yin coil.

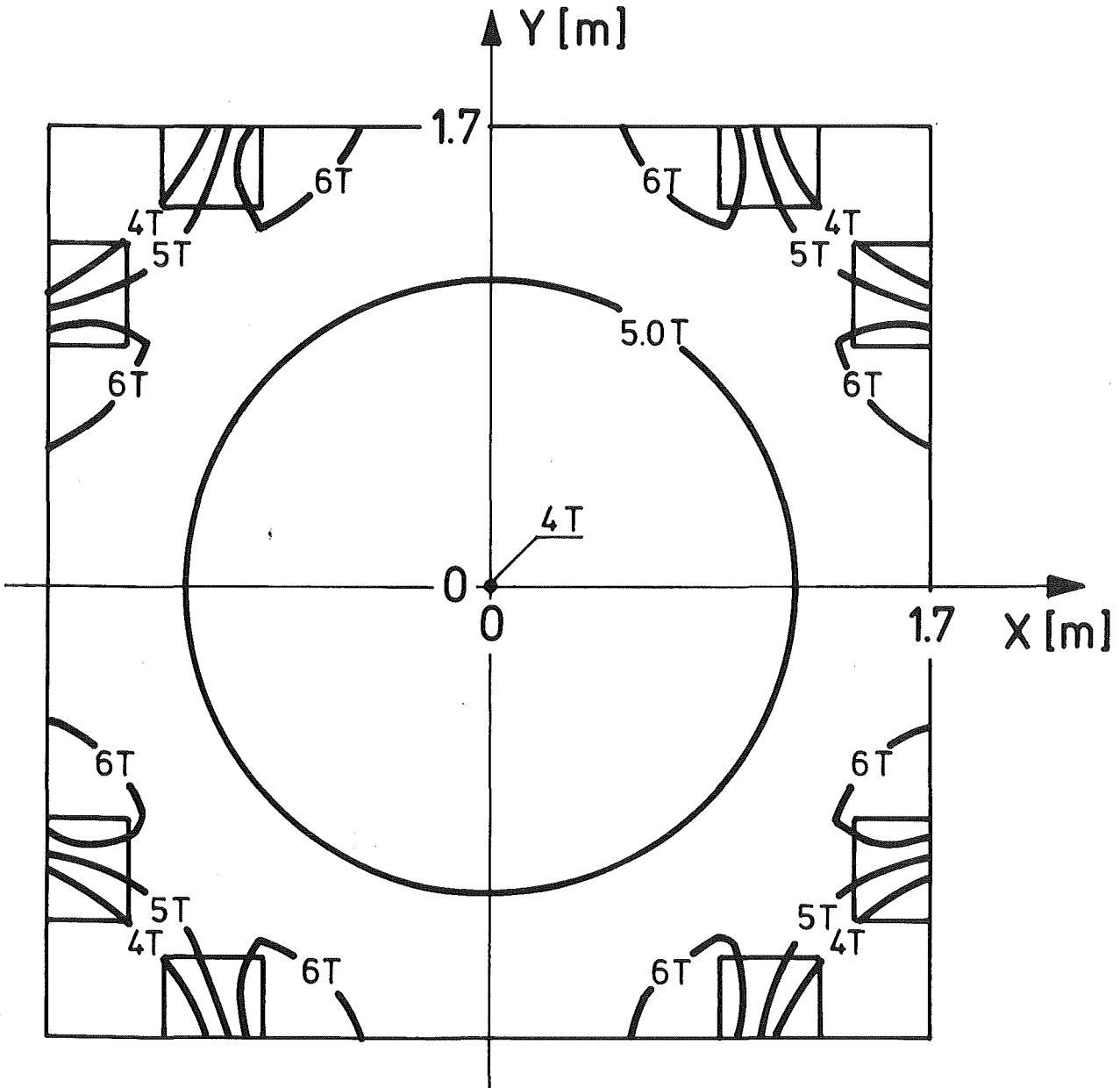


Fig. V.4-3: Demonstration of the magnetic well in the Yin-Yang coil set ($z=27.18$ m corresponds to the center of the coil set).

V.5 Field Shaping Coils

As explained in section V.1, field shaping coils had to be introduced in the barrier region to shape the field such that the high energy pump beam can be injected at the point of minimum barrier field. These coils are partly integrated with the shield. They are normalconducting and will be built with the same hardened copper material as the barrier insert coil. Table V.5-1 gives the main parameters of these coils with Fig. V.5-1 showing their locations and names. The ohmic losses of the eight field shaping coils are 9 MW.

Table V.5-1: Main Parameters of the Field Shaping Coils

<u>Magnet:</u>		FSC8	/	FSC7	/	FSC6	/	FSC5
<u>geometric features</u>		<u>unit</u>						
center of magnet: z-position ^{+))}	m	±17.35		±18.6		±19.8		±20.8
minor radius	m	1.5		1.5		1.0		1.0
major radius	m	1.7		1.7		1.05		1.2
average radius	m	1.6		1.6		1.025		1.1
bundle cross section	mxm	0.8x0.2		0.4x0.2		0.4x0.05		0.4x0.2
mean turn length	m	10.06		10.06		6.44		6.92
volume of winding	m ³	1.61		0.81		0.13		0.553
mean density	t/m ³	~8		~8		~8		~8
weight of winding	t	~12.87		~6.44		~1.03		~4.43
<u>electromagnetic features</u>								
bloc current density	A/cm ²	650		480		450		-795 *)
Ampère-turns	10 ⁶ A-turns	1.04		0.384		0.09		0.636
self-inductance per N ²	10 ⁻⁶ H/N ²	4.161		5.154		3.111		3.037
stored self-energy	MJ	2.25		0.38		0.013		0.614
consumed power	MW	2.43		0.666		0.094		1.25
<u>operating features</u>								
operating temperature	K	room		room		room		room
max. working strain	%							
max. " stress	MPa	<210		<210		<210		<210
<u>conductor properties</u>								
conductor		hardened copper						
structure material		with						
		$\rho \sim 2.5 \times 10^{-8} \Omega m$						

*) inverse current direction

+) ± means; one on the positive z-axis and one on the negative side

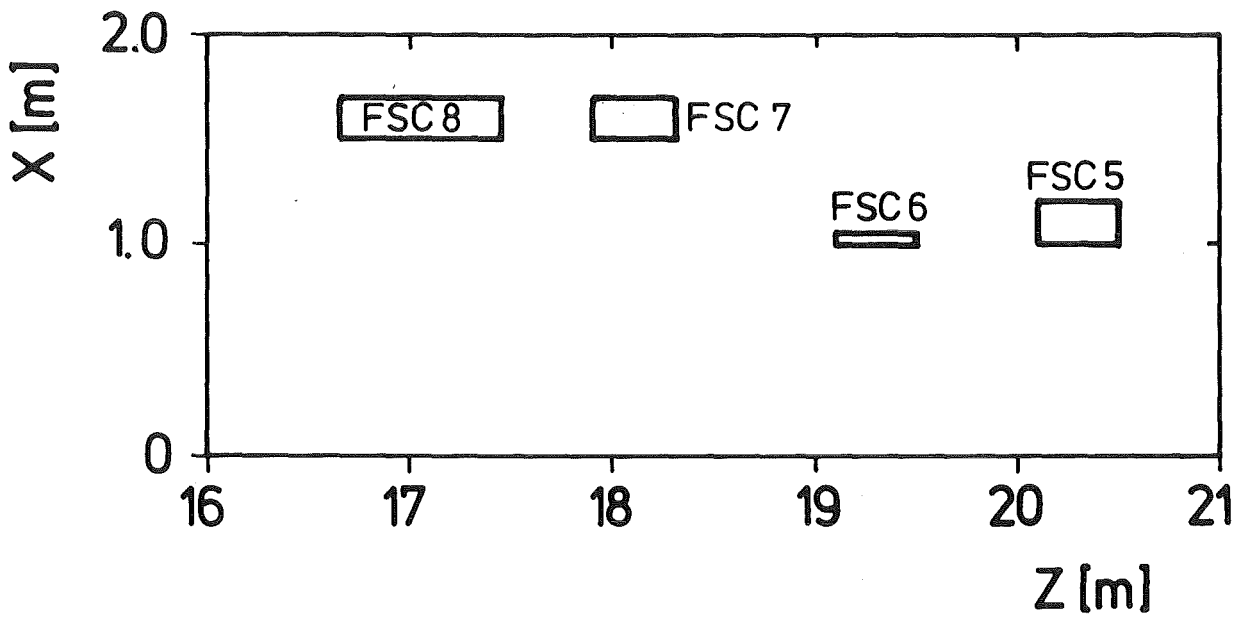


Fig. V.5-1: Position of field shaping coils

V.6 Magnetic Shielding

Shielding of the intense magnetic fields in TASKA must be considered in view of a reduction of magnetic pollution of the environment and in view of provision of regions of reduced magnetic field for the operation of machine components, in particular of ion sources and ion beam paths in the neutral beam generators (see Section IV.3.2.8). Reduction of magnetic pollution, a problem common to all devices of magnetic fusion [1], is not considered here because no conclusive information on exposure levels is available and means for exposure reduction (distance, bucking coils, ferromagnetic shields) are known and developed.

Magnetic shielding of vital TASKA-components in intense stray fields is exemplified by the source for the high energy pump beams, situated just outside the 20 T-barrier coils. As shown in Fig. V.3-1, fields in excess of 2 T must be shielded from a volume of about 10 m^3 . The beam sources are designed to allow a thickness of 0,2 m around for shielding. Ferromagnetic materials of saturation flux densities of the order of 2 T are not sufficient for this task, although they may be used around the most sensitive parts, i.e. ion source and beam line to the neutralizer, if the field intensity is reduced of these points by bulk shielding. The only conceivable method at present appears bulk shielding by superconductors, using their perfect diamagnetic properties. Some experimental evidence ([2],[3]) with shielding tubes of about 2 m length and several cm bore is available, indicating that fields of about 2 T can be shielded by stacks of superconductors and stabilizing normalconductors of about 1 cm thickness. In order to permit a free flow of the shielding currents, wide superconductor foils are generally used. This technique is also proposed for superconducting magnetic shields studied in the field of magnetic levitation [4]. In experiments on the inverse problem, i.e. trapping of magnetic fields by superconductors [5], good results were also achieved with helically wound Nb_3Sn ribbons. However, homogeneous fields were trapped in this case, and the results may not be transferable to the inhomogeneous shielding problem in TASKA. Several computer programs, based on iteration and the definition of current elements in a superconducting shield, were developed to predict the shielding capability

and current distribution in conjunction with the critical current properties of the superconductor [6],[7].

In summary, available results on shielding properties of superconductors suggest their applicability for shielding the neutral beam sources in TASKA. However, experiments are needed to demonstrate efficient large volume shielding in dependence on superconductor thickness. Field leakage into the source region will depend on the width of foils of superconductors that can be manufactured. However, the leakage fields will be shieldable conventionally at the most sensitive places.

Local shielding of neutral beam generators will distort the overall magnetic flux pattern. Again, the region of the barrier coils with the high energy pump beam generators is most sensitive because the shielding level is high and the axisymmetry of the vacuum magnetic field on axis is distorted in a plasma region in which the central cell particles are reflected. A plasma physics analysis is needed to find out the level of non-axisymmetry tolerable in this region. One cure to this problem might be provision of axisymmetric, ferromagnetic material around the barrier coil. It would reduce the flux density at the neutral beam generator and, conversely, shield the plasma from flux distortions due to the neutral beam shield. Magnetic pollution from TASKA would be reduced. Accurate magnetostatic calculations are complicated by the high level of saturation at which the iron would operate.

At present, no final solution to the shielding problem for the high energy pump beam can be given with the spatial limitations assumed. If experimental results can be scaled-up from small dimensions, stacked superconducting foils will be used. If no solution appears at hand, the spatial limitations must be relaxed, e.g. by extending the barrier length to remove the neutral beam generator further from the barrier coil, thus decreasing the stray fields. Even now, the design barrier length of TASKA with the need for bucking coils and the two-stage pumping scheme proposed for the barrier are consequences of a credible design for the high energy pump beam with short duct length.

References for Chapter V.6

- |1| INTOR-Report, Conceptual Design Phase I, Chapter XVI.5.3,
July 1981, IAEA Vienna

- |2| F. Martin and S.J.St. Lorant, J. Appl. Phys. 44 (1973), 460

- |3| E.U. Haebel and W. Witzeling, Proc. 6th Int. Conf. Magn. Technol.,
Bratislava Aug. 30 - Sept. 2, 1977, Vol. II, p. 349

- |4| H. Joyce et al., IEEE Trans. Magn. 17 (1981), 2154

- |5| M. Rabinowitz et al., Appl. Phys. Lett. 30 (1977), 607

- |6| W. Witzeling, Cryogenics 16 (1976), 29

- |7| J.T. Williams, IEEE Trans. Magn. 17 (1981), 2150

V.7 Superconductors for TASKA

V.7.1 Introduction

To guarantee reliable and safe operation of the TASKA-magnets, a number of design criteria for the conductors have to be met:

- The conductor must sustain the mechanical stresses due to magnetic forces. Each turn should sustain its hoop stresses by suitable addition of reinforcing material.
- The conductor must recover from small disturbances like conductor movement, plastic deformation of material etc., i.e. cryogenic stabilisation is essential for magnets of this size.
- In the case of a nondisappearing normal zone, the magnet has to be discharged safely without irreversible damage by excess voltage or temperatures.

These requirements have been combined to a design procedure which is outlined in Fig. V.7-1. The components of this procedure are now described.

V.7.2 Stresses

The hoop stresses in a self supporting winding of a solenoid are given by

$$\sigma_r = \frac{I_o (B \cdot r)_{\max}}{A_r} \quad (V.7-1)$$

where

A_r : cross sectional area of reinforcement

σ_r : stress in reinforcing material

B : Magnetic field in axial direction

I_o : Operating current

r : Radius

$(B \cdot r)_{\max}$: The maximum value in the coil. In the TASKA-solenoids the maximum is attained with the field B_{\max} at the inner turn with radius r_{\min} .

With stainless steel chosen as reinforcing material and a maximum allowable

strain of .24 % in accordance with the strain capability of Nb₃Sn, a stress

$$\sigma_{\max} = 500 \text{ MPa}$$

is used as a design parameter.

V.7.3 Fast Discharge

The maximum hot spot definition temperature is fixed to

$$T_{\max} = 200 \text{ K}$$

It is given by the hot spot integral

$$A_s \int_{4.2\text{K}}^{T_{\max}} \frac{\gamma_s C_{ps}}{\rho_s} dT + A_r \int_{4.2\text{K}}^{T_{\max}} \frac{\gamma_r C_{pr}}{\rho_s} dT = \frac{Q_o}{U_o} \cdot \frac{I_o}{A_s} \quad (\text{V.7-2})$$

- Q_o : Stored energy
- U_o : Maximum discharge voltage
- I_o : Operating current
- γ : Density of material
- C_p : Specific heat
- ρ : Specific resistivity
- A_s : Cross sectional area of stabilizer
- A_r : Cross sectional area of reinforcing material

In this treatment the amount of stabilizing material is primarily determined by the hot spot temperature. The enthalpy of the reinforcing steel is utilized. This requires good thermal contact between these two components, but gives a higher mean current density. Aluminum is well suited because of its high electric conductivity in high magnetic fields.

The hot spot integrals $\int \gamma_s (C_p/\rho) dT$ for the combinations stainless steel-aluminum, aluminum - aluminum and copper - copper have been calculated:

$$J (200 \text{ K}) = 6.5 \cdot 10^{16} \frac{\text{A}^2\text{s}}{\text{m}^4} \quad \text{for Al-Al}$$

$$J (200 \text{ K}) = 13.3 \cdot 10^{16} \frac{\text{A}^2 \text{s}}{\text{m}^4} \quad \text{for Al-SS}$$

$$J (200 \text{ K}) = 9.7 \cdot 10^{16} \frac{\text{A}^2 \text{s}}{\text{m}^4} \quad \text{for Cu-Cu.}$$

The maximum discharge voltage U_0 is set to 2.5 kV in the barrier coil and to 1 kV in the other coils. After a quench is detected in one coil, a fast discharge is initiated in this coil alone while the others are discharged slowly or remain at the nominal current.

V.7.4 Cryogenic Stability

With the amount of stabilizer fixed by coil protection requirements, the condition of cryogenic stability must be fulfilled by a proper choice of cooled surface and cooling mode.

Pool boiling at 4.2 K is chosen as it combines simple cryogenics (no pumps and pumping losses) with relatively high heat transfer.

For the cold end recovery heat flux from the conductor to helium, the measured value for samples of the MFTF-Yin-Yang conductor was chosen

$$q_{\text{rec}} = 2000 \text{ W/m}^2.$$

The resistivity of high purity aluminum is

$$\rho = 10^{-10} \text{ } \Omega\text{m},$$

which takes account of magneto-resistivity, strain and radiation induced resistivity up to 10^{17} n/cm^2 .

For copper at 8 T, $\rho = 5,3 \cdot 10^{-10} \text{ } \Omega\text{m}$ was used.

The cooled perimeter p is then determined by

$$\frac{I_0^2 \rho}{A_s} \lesssim p \cdot q_{\text{rec}} \quad (\text{V 7-3})$$

V.7.5 Design Procedure

Equations (V.8-1,2,3) constitute a system to determine in a unique manner the parameters A_s , A_r and p as a function of the nominal current I_0 : This dependence is shown in Fig. V.7-2 for the conductor employed for the central cell solenoids.

The overall current density in the conductor is only weakly dependent on the current level as the main fraction of the cross section in coils of this size is occupied by steel.

The proper choice of I_0 is finally determined by an iterative procedure with the constraint that the required values of A_r , A_s and p are compatible with requirements of fabrication, winding and insulation of the conductor.

A number of features have served as guidelines in the choice of a conductor concept for the solenoids in TASKA. These are listed below:

- Cooling on the sides of conductor
 - heat transfer rate independent of position in the coil
 - radial interturn forces easily transmitted
- No interturn forces transmitted to superconductor or stabilizer
 - source of degradation eliminated
 - no plastic deformation in stabilizer
- Metallurgical bond (solder) between superconductor, stabilizer and steel
 - source of frictional heating eliminated
 - enthalpy of steel utilized in hot spot protection (essential for large coils)
- Standard NbTi- or Nb₃Sn multifilamentary conductors as the basic unit.
- Margin for critical current $j_{sc} = \frac{2}{3} j_c (B_{max})$

V.7.6 Conductor Parameters

This design procedure had led to the conductor principle shown in Fig. V.7-3. This is of the 10 kA conductor for the central cell solenoid. The design parameters for the solenoids are listed in table V.7-1 and table V.7-2.

The same conductor scheme is applied for all solenoids. Aluminum stabilizer turns out to be essential in the barrier coil (copper would require a cooled perimeter ten times larger, a requirement not compatible with a simple compact conductor). The technology of Al-stabilization is also used with profit in the NbTi-coils.

For the recircularizing coils and Yin-Yang-coils, the principle of the MFTF-B conductor was adopted due to lower stress levels and the necessity to bend the conductor on two axes. Stabilization and reinforcement is here combined in the conductor jacket of 3/4 hard copper.

To increase the overall current density and to lower costs, a twofold graded conductor is used in the Nb₃Sn- as well as NbTi-part of the barrier coil. Grading of the CC-coils has only a minor impact on the overall current density according to table V.7-1. Using the grade 1 conductor throughout will save splices in the coil so this simpler version is recommended.

The overall current densities in table V.7-1 and -2 are obtained with a filling factor of 0.8 to allow for insulation and helium passages.

In order to manufacture the TASKA magnets development is still required in two areas:

- Aluminum stabilization; soldering to SS and superconducting strands
- Nb₃Sn-technology for large coils and high fields.

Table V.7-1: Conductor parameters of central cell solenoids

Coil		CC/Grade 1	CC/Grade 2
Maximum field	(T)	6.0	4.0
Minimum radius	(m)	2.8	3.1
Stored energy	(GJ)	0.37(0.2)	
Discharge voltage	(kV)	1.0	
Reinforcer/stabilizer		SS/Al	
Superconductor		NbTi	
Critical current density in sc	(A/cm ²)	1.2 x 10 ⁵	1.8 x 10 ⁵
Filament diameter	(μm)	30 - 60	
Operational current	(A)	10 000 (8600 for center coil CC2)	
Overall j _c in coil	(A/cm ²)	1350 (1160)	1600
Helium + Insulation	(%)	32	32
Cross sectional areas			
- Steel	(cm ²)	3.4	2.50
- Aluminum	(cm ²)	1.5	1.6
- Superconductor	(cm ²)	0.125	0.08
Total	(cm ²)	5.025	4.18
Cooled perimeter	(cm)	4.0	4.0

Table V.7-2: Conductor parameters of barrier coil

Coil/Grade		LI1 ML1	LI2 ML2	L01	L02
Maximum field	(T)	15	12.5	8.5	5.0
Minimum radius	(m)	1.3	1.50	1.86	2.0
Stored energy	(GJ)		2.0		
Discharge voltage	(kV)			2.5	
Reinforcer/stabilizer		SS/Al		SS/Al	
Superconductor		Nb ₃ Sn		NbTi	
Critical current density in sc	(A/cm ²)	1.5 x 10 ⁴	5 x 10 ⁴	0.6 x 10 ⁵	1.5 x 10 ⁵
Filament diameter	(μm)		1 - 3 (sc + bronze)	30 - 60	
Operational current	(A)			10 000	
Overall j _c in coil	(A/cm ²)	1200	1400	1600	2000
Helium + Insulation	(%)	20	20	20	20
Cross sectional areas					
- Steel	(cm ²)	3.9	3.9	3.2	2.0
- Aluminum	(cm ²)	1.70	1.7	1.8	2.0
- Superconductor	(cm ²)	1.0	0.3 (sc + bronze)	0.25	0.1
Total	(cm ²)	6.6	5.9	5.25	4.1
Cooled perimeter	(cm)	4.0	4.0	3.0	3.0

Table V.7-3: Yin-Yang and recircularizing coils

Coil		CEEN/CEEP (Yin/Yang)	RCN/RCP (TC/RC)
Maximum field	(T)	7.9	7.0
Minimum radius	(m)	0.9	1.6
Stored energy	(GJ)	0.411	0.487
Discharge voltage	(kV)		1.0
Reinforcer/stabilizer			Cu (3/4 hard)
Superconductor			NbTi
Critical current density	(A/cm ²)		5 x 10 ⁴
Filament diameter	(μ m)		\approx 200
Operational current	(A)		4000
Overall j_c in coil	(A/cm ²)	1630	1900
Cross sectional areas:			
- Steel	(cm ²)		-
- Copper	(cm ²)	2.0	2.0
- Superconductor	(cm ²)	0.12	0.12
Total	(cm ²)	2.12	2.12
Max. hoop stress	(MPa)	142	220
Cooled perimeter	(cm)	2.3	2.3

CONDUCTORS FOR TASKA

DESIGN PROCEDURE

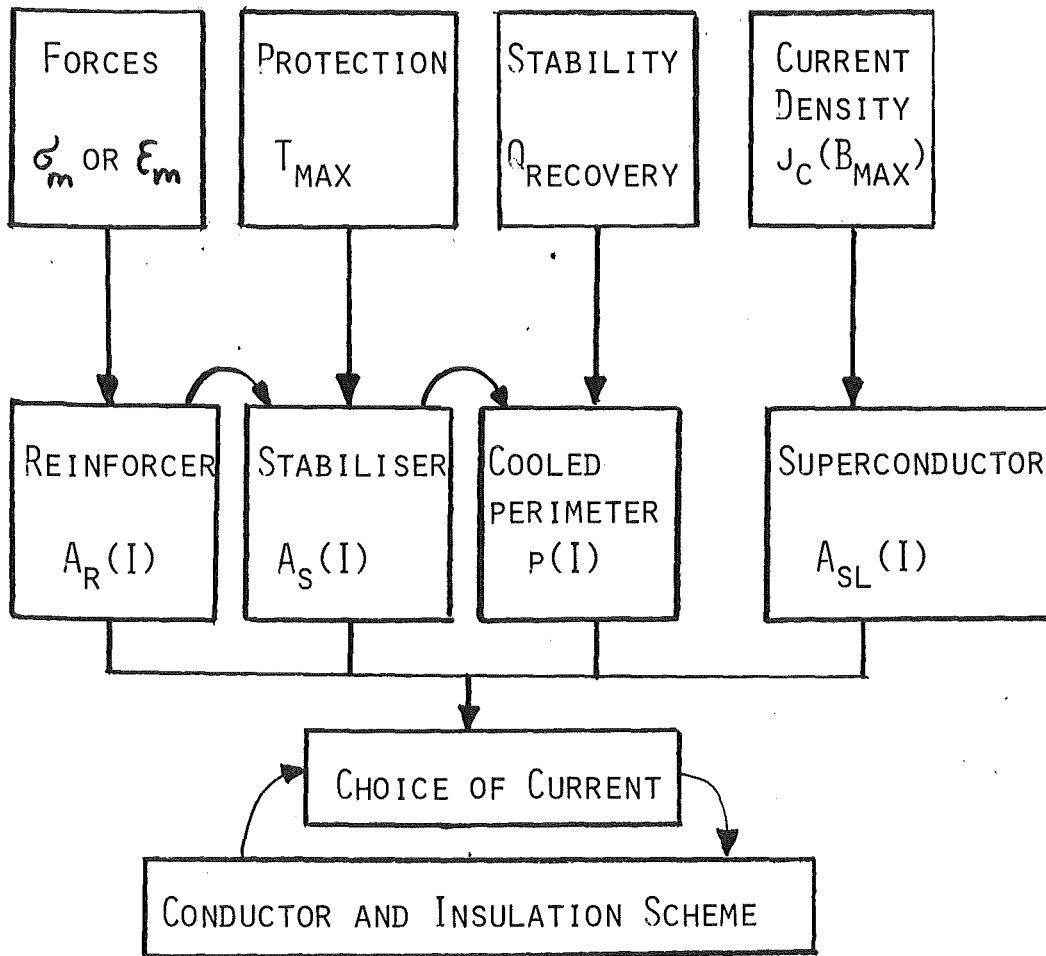


FIG. V.7-1 DESIGN PROCEDURE FOR TASKA-CONDUCTORS

CC - CONDUCTOR GRADE I

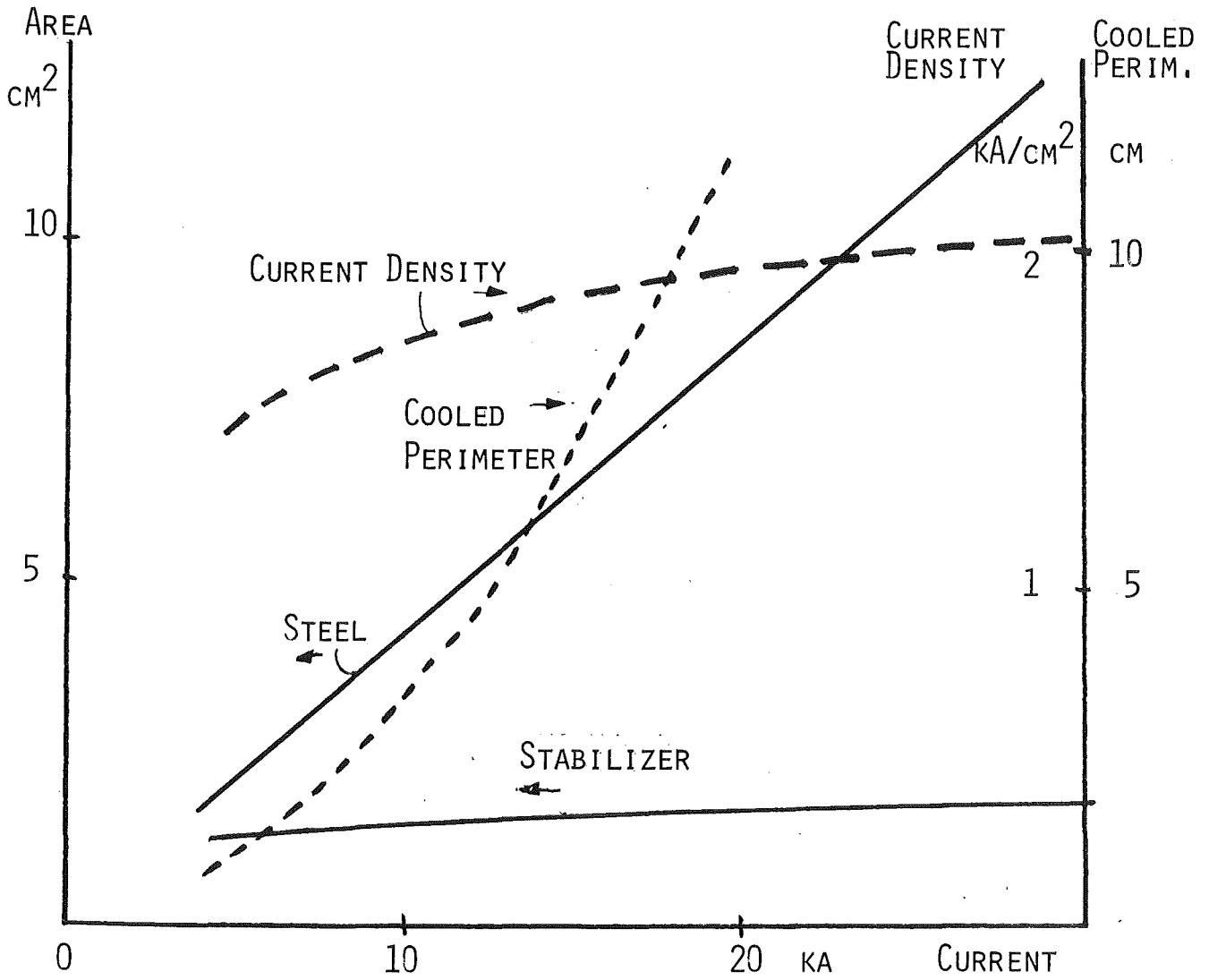


FIG. V.7-2 CONDUCTOR PARAMETERS AS FUNCTION OF CURRENT

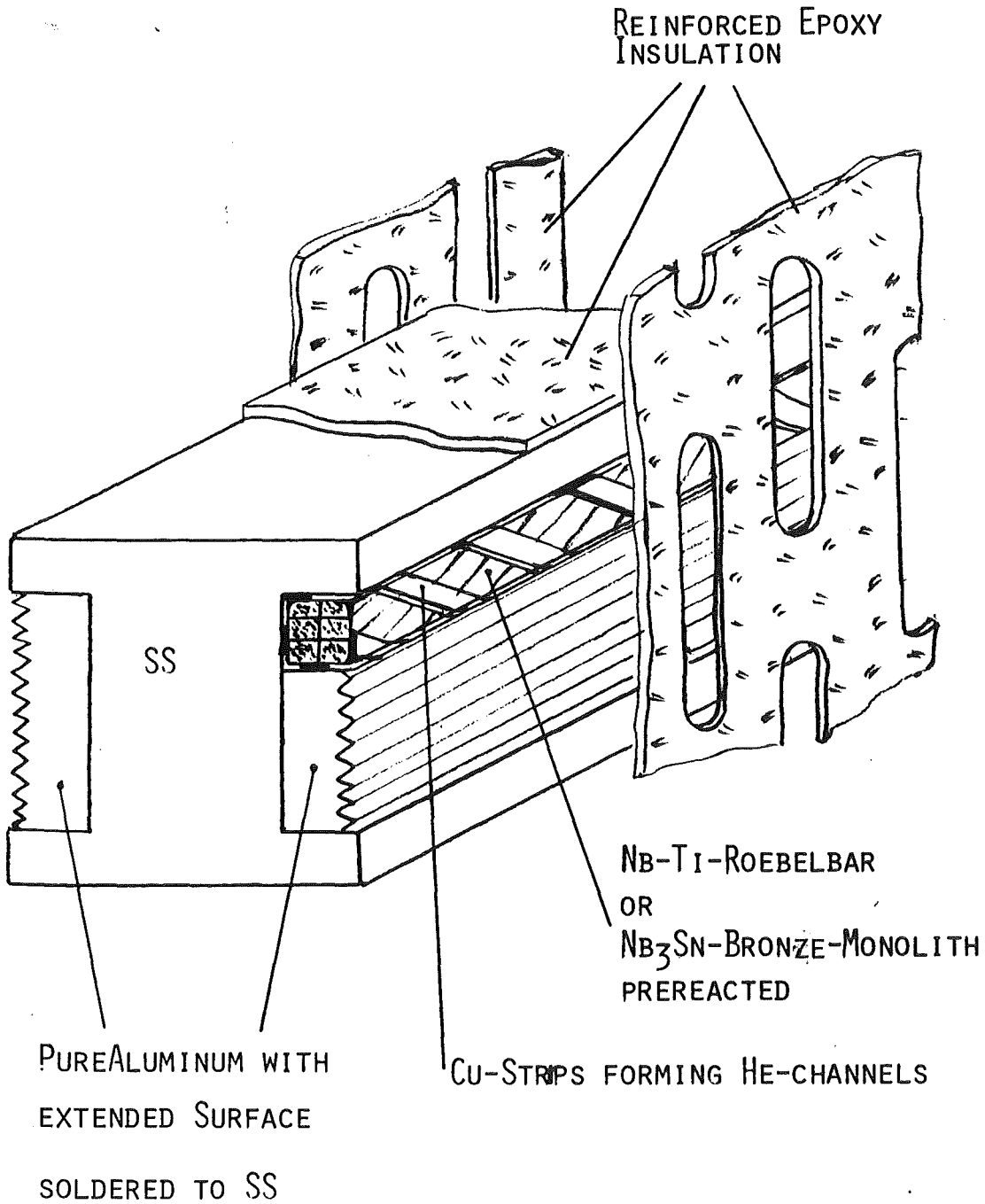


FIG. V.7-3 SCHEME OF AL-STABILIZED CONDUCTOR FOR SOLENOIDS

V.8 Coil Support

With regard to magnetic forces, the TASKA coil-system can be divided into three independent regions: the central cell (including the barrier coils) and the two plug regions. The forces between these regions are negligible compared to those which appear within each one. Therefore each region can be considered as an isolated system. The forces which act on the field-shaping coils located between the plug region and the central cell are relatively small. These coils can be supported by the shielding structure and don't need a special support system.

V.8.1 Central Cell

As all coils of the central cell and barrier are solenoids with a common axis - the Z-axis - the body forces acting on each coil are axisymmetric to the Z-axis and the resulting intercoil forces lie on the Z-axis. Under normal operation, this means that, if all coils are completely energized, the resulting forces are also symmetrical to the center of the central cell. Fig. V.8-1 shows the resulting forces in MN acting on the coils under normal working conditions. Because of the symmetry, the resulting force on the central coil is zero. The maximum forces which have to be supported are between the barriers and the outer central cell coils; these forces are 51 MN each. As the support structure must be laid out for the maximum forces likely to be encountered, abnormal operation must be investigated, i.e. one or more coil(s) are not energized. The maximum force between the coil in the center and one of the outer central cell coils appears when the other outer central cell coil is not energized. Then the resulting force is 45 MN. This is shown in Fig. V.8-2. All these forces have been calculated with the "HEDO" code⁽¹⁾.

Fig. V.8-3 shows the main parts of the coil support structure. They consist of:

- the annular elements A which bear the load from the whole barrier region,
- twelve inclined supporting struts B between each barrier and the outer central cell coils,

- twelve horizontal supporting struts D between each outer central cell coil and the coil in the center,
- the casing C for the three central cell coils. The reverse of each casing consists of thick cylindrical rings which protects the conductor of the coil against the load exerted by the struts from both sides.

The supporting struts are exposed only to compressive load. The maximum compressive stress is only 36 MPa. This is a very low value which guarantees a good stiffness of the whole supporting structure.

V.8.2 Plug Region

Fig. V.8-4 shows the plug region which consists of the two outer transition coils and the two yin-yang coils. The whole plug region has mirror-symmetry to the x-z-plane and to the y-z-plane. It has also axisymmetry to the axis w which is normal to the z-axis and has an angle of 45 degrees with respect to the x- or y-axis.

The forces which appear are all mirror-symmetrical to the x-z-plane and to the y-z-plane. That means that the arcs which are notated in Fig. V.8-4 with index "2" are mirror-symmetrically loaded to those which are signed with index "1". Thus there are no resulting moments on the coils and the resulting forces lie on the z-axis. If all coils are completely energized then the forces are also symmetric about the w-axis. That means that the arcs which are notated in Fig. V.8-4 with capital letters have the same mechanical load as the arcs notated with small letters.

Fig. V.8-4 shows also the resulting forces (calculated) with the "EFFI"-code⁽²⁾ for each coil under normal operation. The maximum force which must be supported is between the two yin-yang coils with an amount of 99 MN; this is about a factor of two higher than in the central cell. The forces are nearly symmetrical to the w-axis. Only a small resulting force of 3 MN, due to the influence of the central cell coils and the field shaping coils on the plug region, makes a small distortion of symmetry with a maximum of 5 %. Therefore for further investigations the plug region can be treated as symmetrically mechanically loaded.

Figs. V.8-5 to V.8-8 show the body forces calculated by the "EFFI"-code for each arc under normal working conditions. Each arc had been divided every 10 degrees into 12 to 18 sections and for any section the resulting force has been calculated. These forces are drawn as histograms over the angle of the arcs in Figs. V.8-5 to V.8-8. The highest force on one element is 22 MN, which results in a load of 52 MN per m along the mean length of the arc.

The support structure of the end plug coils is shown in Fig. V.8-9. In order to obtain a high stiffness the coil casings are supplied with a large number of ribs. All the coils are supported by each other. The two yin-yang coils are fixed together by their outer ribs (A). Each transition coil is fixed to both yin-yang coils by many cover plates (B). The large arcs of the yin-yang coils are held together by 6 large tie rods (C) at each coil. Two of them (D) are also fixed to the transition coils. These tie rods bear the main part of the forces which try to bend apart the coil arcs.

References for section V.8

1. H. Preis, Calculation of the Magnetic Field, Magnetic Forces and Behaviour of Large Coil Systems for Fusion Experiments IPP III/24
2. S.J. Sackett, EFFI, A Code for Calculating the Electromagnetic Field, Force and Inductance in Coil Systems of Arbitrary Geometry, Lawrence Livermore Laboratory, Livermore, CA, UCRL-52402 (1978)

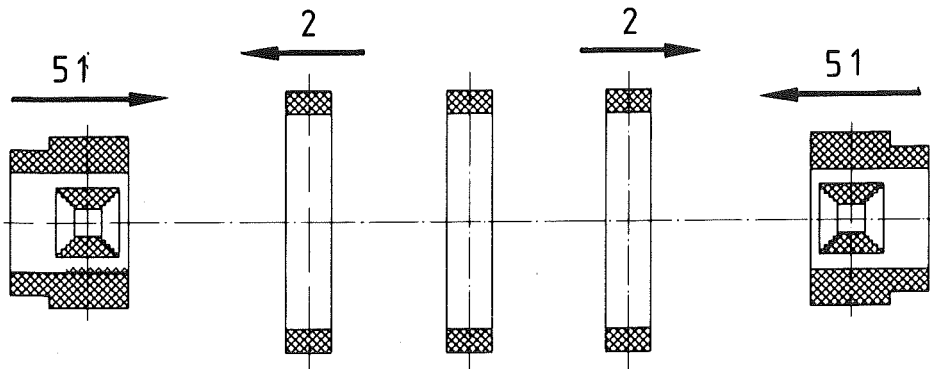


Fig. V.8-1: Forces on central cell coils and barrier coil under normal working conditions (Units: MN)

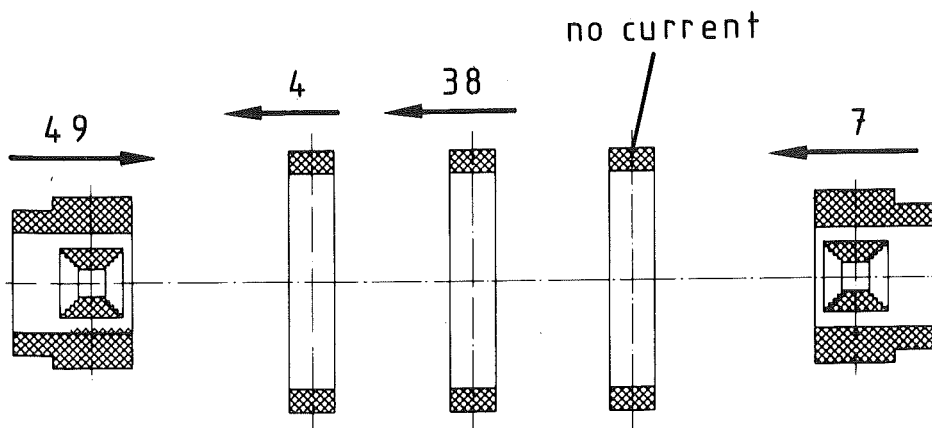


Fig. V.8-2: Forces on central cell coils and barrier coil with one coil not energized (Units: MN)

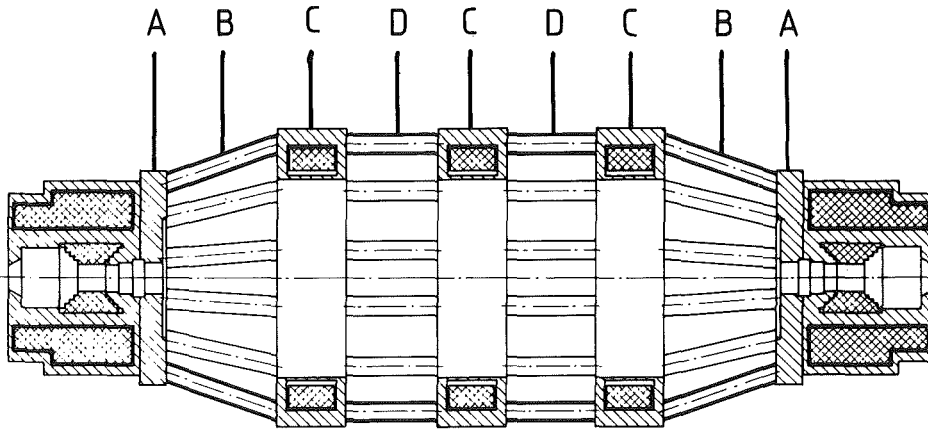


Fig. V.8- 3: Main components of Central-Cell support structure

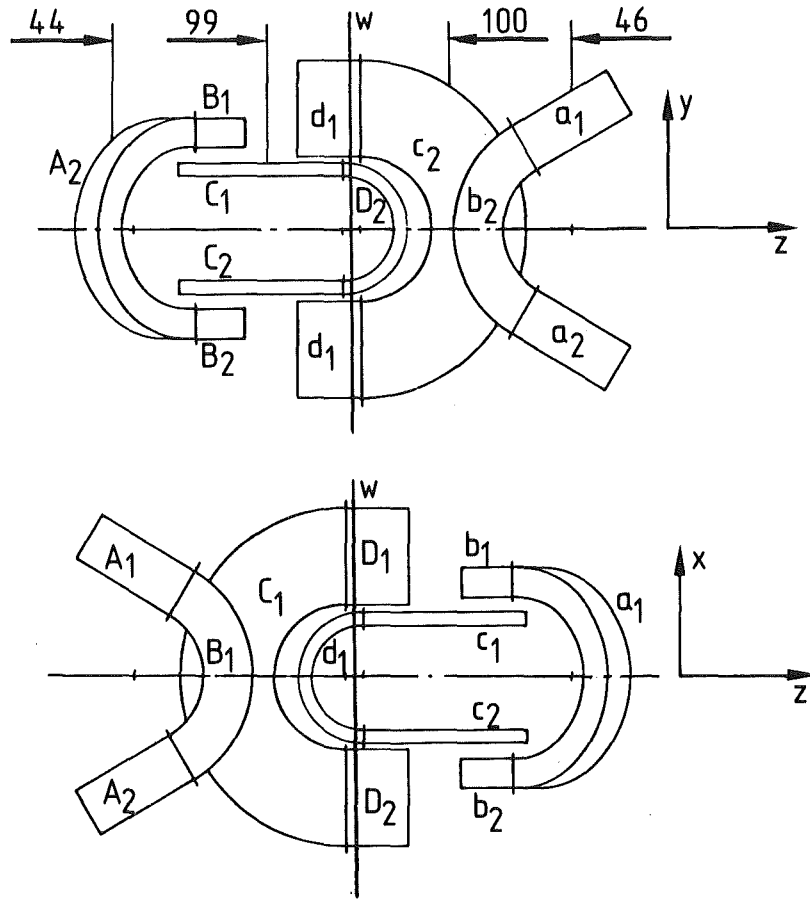


Fig. V.8-4: Subdivision of Plug coils into single arcs and resulting forces on the coils under normal operation

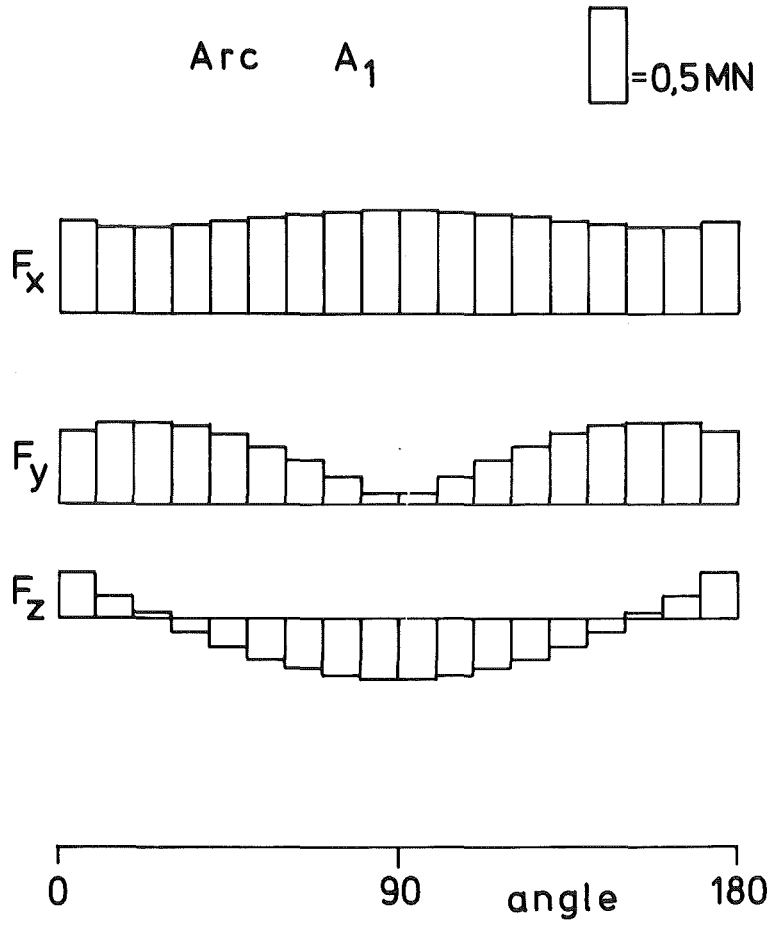


Fig. V.8-5: Forces on arc No. A₁

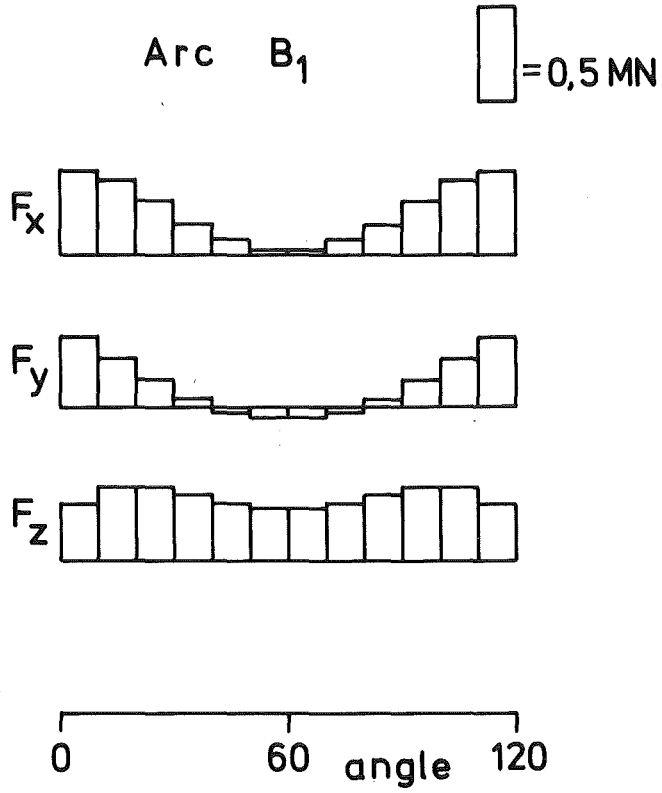


Fig. V.8-6: Forces on arc No. B_1

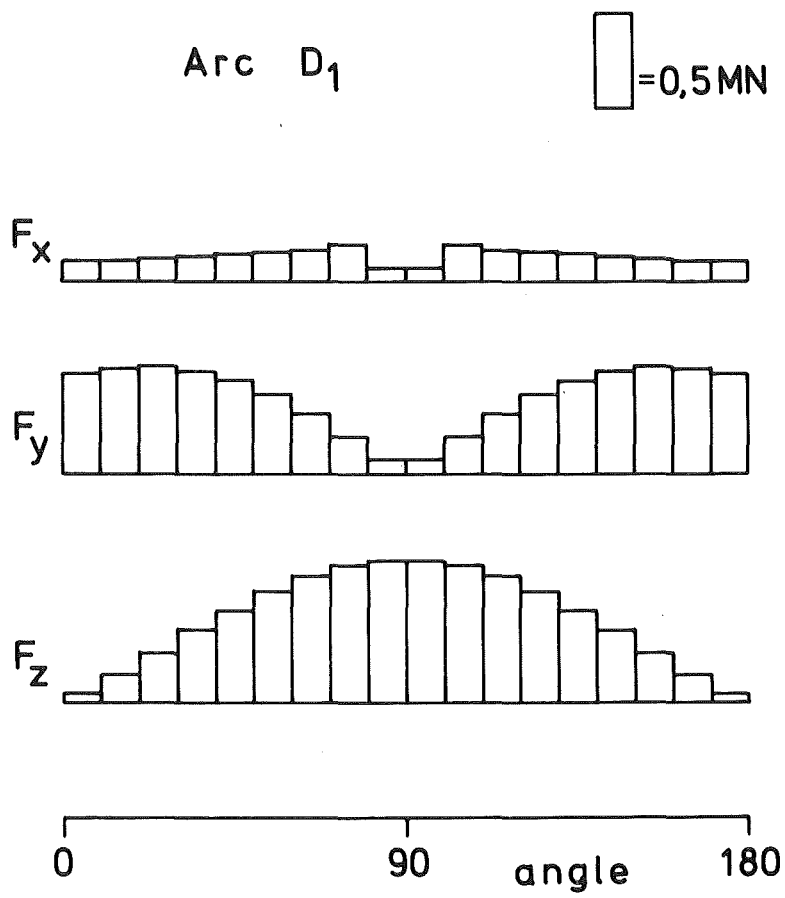


Fig. V.8-8: Forces on arc No. D_1

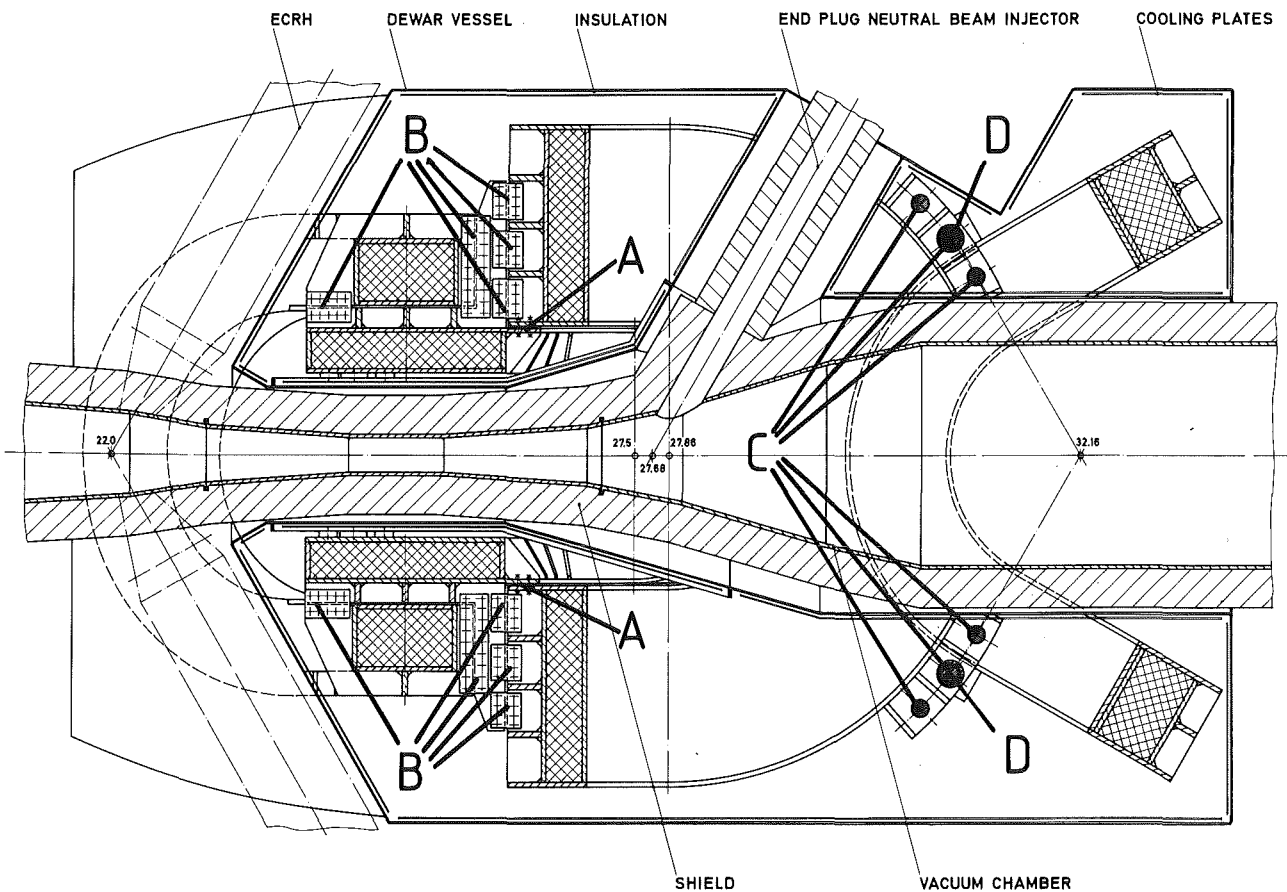
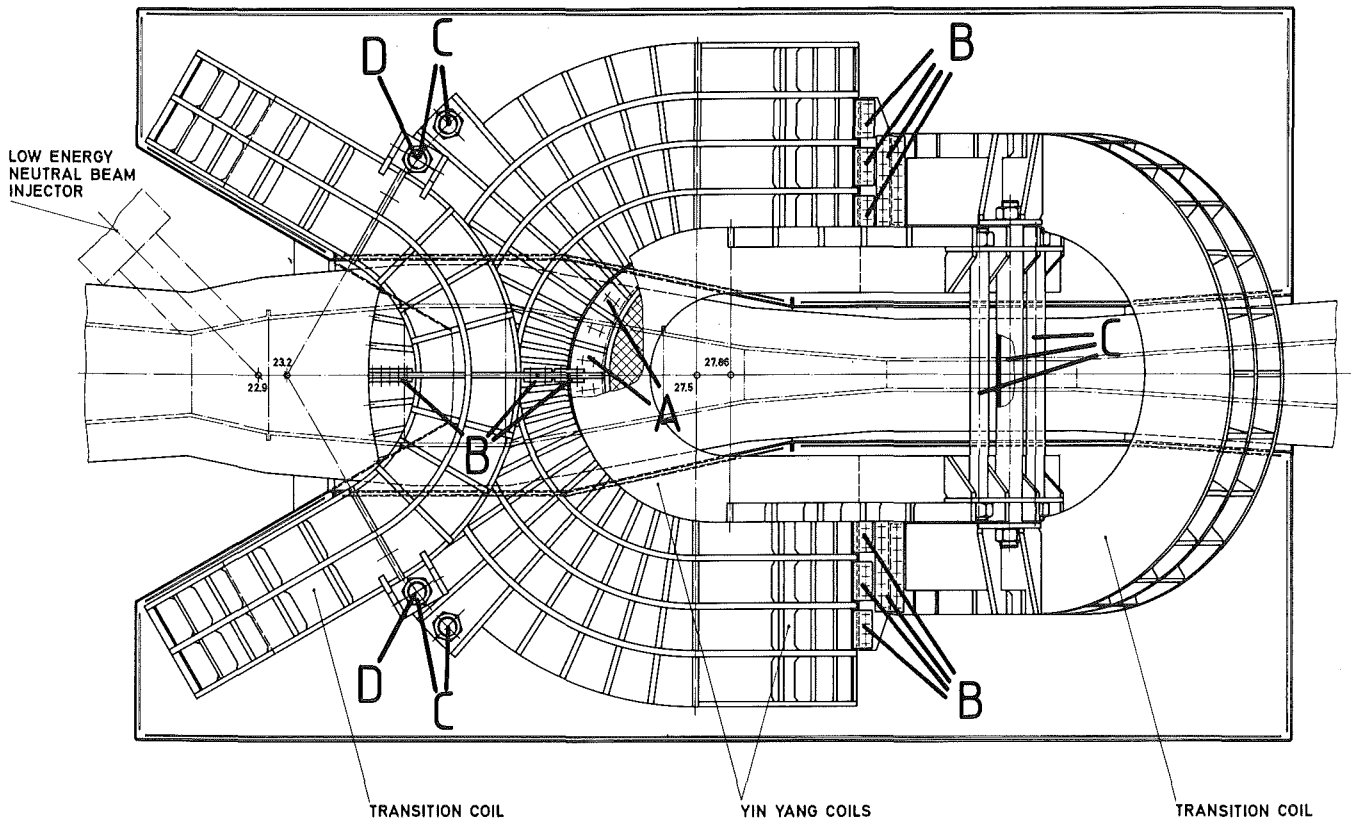


Fig. V.8-9: Support structure of the end plug coils

V.9 The Impact of the Magnetic Properties of Ferritic Steels.

The use of the martensitic HT-9 stainless steel in the central cell blanket modules has considerable advantages because of its high resistance to radiation damage (see materials section). However, because of the fact that HT-9 is a ferromagnetic material, its magnetic aspects should be considered carefully in the magnet design and in the blanket design of TASKA. In the appendix the complete analysis is given.

Here we give the conclusions of the detailed analysis of the magnetic field perturbations by various blanket configurations:

- the perturbation and reduction for a magnetically saturated structure is significant only near the ends, and over an axial region of the order of the outer blanket diameter or width.
- if the length is of the order of the outer diameter or width, then the two end zones overlap and the perturbation extends over the entire length of the blanket.
- the use of a homogenized magnetization is indeed justified.
- the temperature dependence of the saturation magnetization can be accounted for by using an average magnetization.
- the field perturbation near the ends of the blanket depends however strongly on the configuration, the symmetry, and the material distribution of the blanket cross section.

V.10 Conclusions

The magnet configuration of TASKA allows the following conclusions:

- The DC nature of tandem mirror magnets is a big advantage compared with pulsed magnets or DC magnets with pulse load as in Tokamaks. So fatigue is no limitation.
- The technology of the central cell magnets and the endplug magnets is available today. This is proven by big bubble chamber magnets and the successful Yin Yang test in Livermore.
- The technology of the barrier coils needs further development with respect to Nb_3Sn conductor technology in conjunction with hybrid coil inserts.
- Further investigations are required for radiation-resistant insulation materials as needed in the normal-conducting insert of the barrier coil.

Appendix:

V.9 The Impact of the Magnetic Properties of Ferritic Steels

V.9.1 Introduction

The use of the martensitic HT-9 stainless steel in the central cell blanket modules has considerable advantages because of its high resistance to radiation damage (see materials section). However, because of the fact that HT-9 is a ferromagnetic material, its magnetic aspects should be considered carefully in the magnet design and in the blanket design of TASKA. In the following we will discuss the magnetostatic forces in the blanket and the magnetic field asymmetry which exists in the central cell as a result of the presence of the ferromagnetic blanket, and which may have an effect on the plasma confinement.

The 3-D computer program GFUN3D⁽¹⁾ has been used in the following study. First we will consider a necessary model used in GFUN to carry out this study.

V.9.2 Homogenization Model

The computer code GFUN solves for the magnetization in the iron which must be divided into small elements. These elements can be prisms and/or tetrahedra. To achieve accuracy the aspect ratio of any element should not exceed 5:1. A maximum of 400 elements was allowed in the original version of the program. If n is the number of elements, then $(3n)$ linear equations are solved by the program. The computer storage needed for such a problem is slightly larger than $(3n)^2$ computer words.

If one tries to simulate the very fine details of the blanket, tube by tube, one would exceed, very quickly, the allowable computer storage. Consider, for example, a hypothetical case of a tube of l cm length, d cm inner diameter, and t cm thickness. This tube can be simulated by hexahedra fitting its wall. Each hexahedron will be divided into a minimum of five tetrahedra.

Abiding by the maximum aspect ratio allowed, the minimum number of hexahedra is estimated as $\sim \frac{\pi d}{(5t)} \times \frac{\ell}{(5t)} = \frac{\pi}{25} \frac{d\ell}{t^2}$, and the minimum number of tetrahedra (elements) as $\frac{\pi}{5} \frac{d\ell}{t^2}$. If $d = 10$, $\ell = 100$, and $t = .7$ cm, then the minimum number of elements is 1283.

Although GFUN has been modified to make use of the large computer storage of some modern computers, to accept a greater number of elements, the computer time needed to solve such a problem would neither be reasonable nor acceptable.

To avoid this problem a homogenization model has been used in which the iron is homogenized throughout the blanket. This means that the magnetization, the magnetic dipole density, \bar{M} , of the iron within a region of the blanket is distributed uniformly within that region, and this region is considered as a section of a ferromagnetic material with magnetization \bar{M}_b equal to M multiplied by the volume concentration of the iron in it. For example, if the B-H curve of the iron is as in Fig. V.9-1, then the B-H curve of a homogenized region containing 44% iron (volume ratio) will be as in Fig. V.9-2.

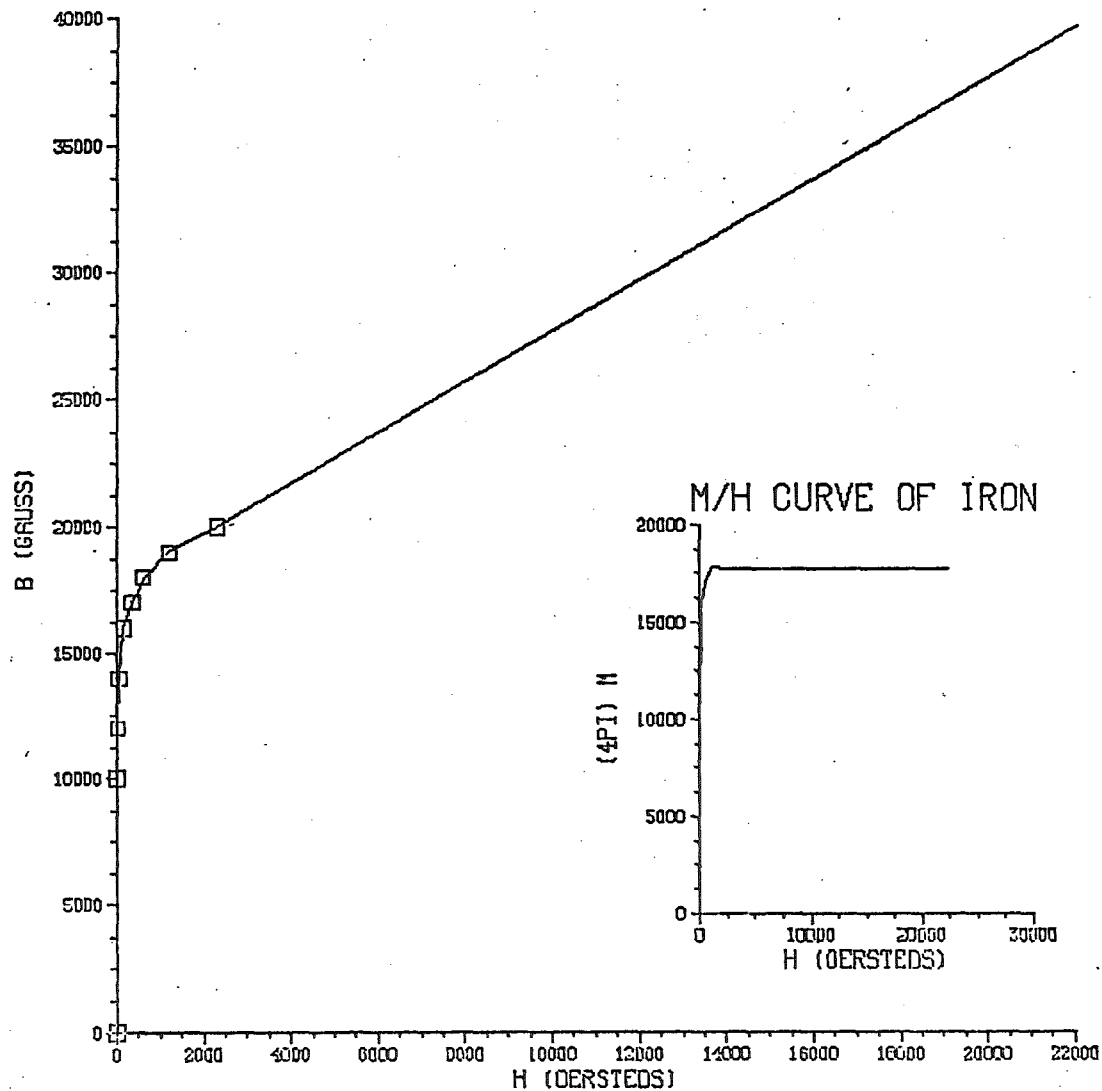
One would expect that the magnetic field calculated using this scheme to be precise everywhere except within the blanket itself, and especially when the iron is saturated, which will be the case in the central cell.

To check the validity of this model we present the magnetic field mapping for two cases. In both cases a 10 meter long solenoid with inner radius of 2.5 m, outer radius of 3 m, and current density of 400 A/cm^2 is used to generate the magnetic field. In the first case, the iron region consists of three rows of circular rings. The width of each ring is 6 cm, and the axial distance between the rings (edge to edge) is also 6 cm.

B H MATERIAL CODE- 3

- 1)	0.0	0.0
- 2)	10000.0	10.0
- 3)	12000.0	20.0
- 4)	14000.0	60.0
- 5)	16000.0	160.0
- 6)	17000.0	350.0
- 7)	18000.0	600.0
- 8)	19000.0	1200.0
- 9)	20000.0	2300.0
- 10)	40000.0	22300.0

B/H CURVE OF IRON



V.9-3

- 345 -

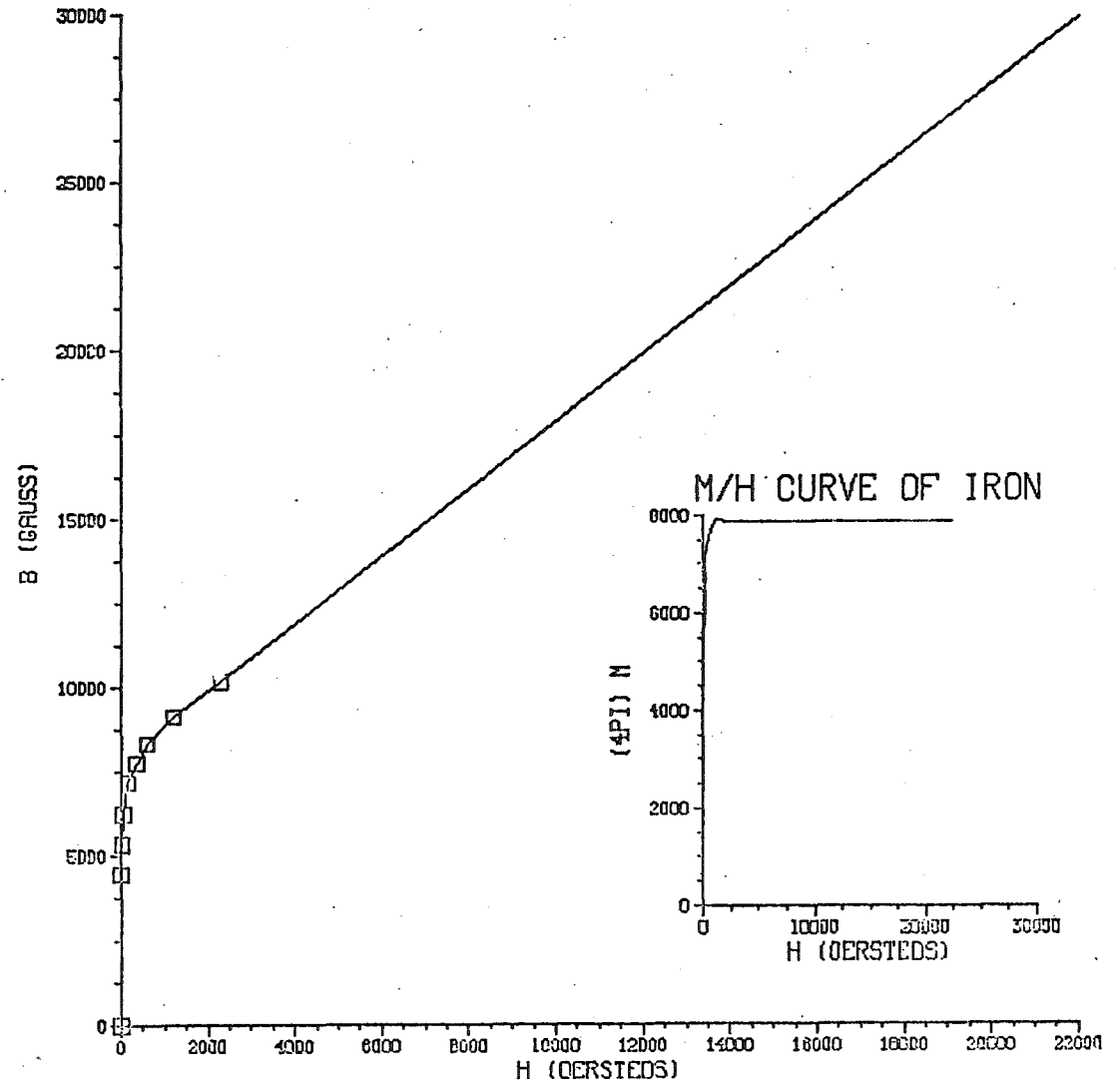
Fig. V.9-1 A typical B-H curve for iron.

FRAME 4, GFUN LOSN1 DATE 11/30/81 TIME 00:21:08

B H MATERIAL CODE- 3 VOL. (%) - 44.48

- 1)	0.0	0.0
- 2)	4453.2	10.0
- 3)	5348.3	20.0
- 4)	6260.0	60.0
- 5)	7205.1	160.0
- 6)	7755.3	350.0
- 7)	8338.9	600.0
- 8)	9116.8	1200.0
- 9)	10172.3	2300.0
- 10)	30172.3	22300.0

B/H CURVE OF IRON



- 346 -

V.9-4

Fig. V.9-2 The B-H curve modified for homogenized material containing 44.5% iron.

The starting point of each row, the inner and outer diameters of its rings in cm are as follows: -123, 40, 45; -117, 46, 51; and -123, 52, 57, for the first, the second and the third row, respectively. In the second case, the homogenized case, the iron of the first case is assumed to uniformly fill a cylinder of 40 cm inner diameter and 57 cm outer diameter, and to extend axially from -123 to 123 cm. The volumetric ratio of the iron in this cylinder is .44, which was multiplied by the magnetization of the iron of the first case to produce new M-H and B-H curves for this homogenized case (Figs. V.9-1 and V.9-2).

The magnetic fields calculated in both cases are mapped and shown in Figs. V.9-3 and V.9-4 for the first and the second case, respectively. Note the fields are in kilogauss and are due only to the iron in both cases, i.e., the field of the solenoid is not included. One can see that the homogenized case has produced an almost identical field everywhere except near the iron region.

V.9.3 The Magnetostatic Forces

V.9.3.1 One-Dimensional Estimate of the Magnetostatic Forces

The total magnetostatic force exerted on a magnetized body by sources of external origin has been expressed in various forms⁽²⁾ which are all equivalent, although confused in some references. If a body has a volume V and magnetic moment \bar{M} , and is subjected to external magnetic field \bar{H}_0 , the total force is given by⁽²⁾

$$F = \int_V \bar{M} \cdot \nabla \bar{H}_0 d\tau . \quad (V.9-1)$$

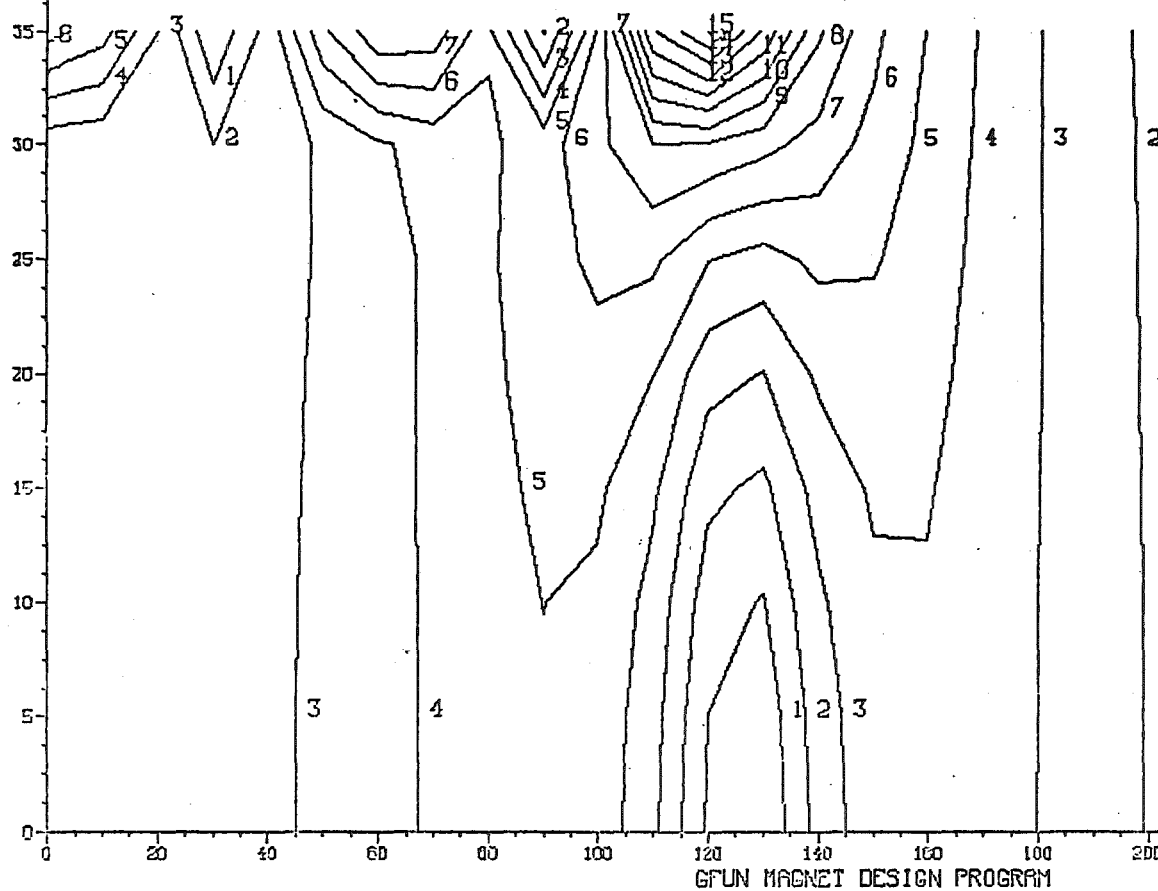
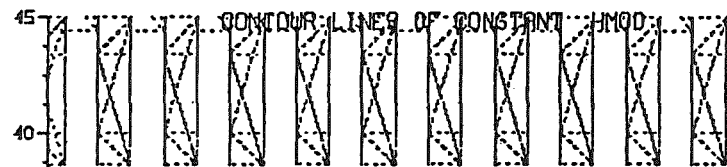
There exists also a couple

FRAME 7, GFUN LOSN1 DATE 11/30/81 TIME 00:04:34

1 CONDUCTOR ELEMENTS 160 IRON ELEMENTS

Z-X PLANE

Y- 0.000

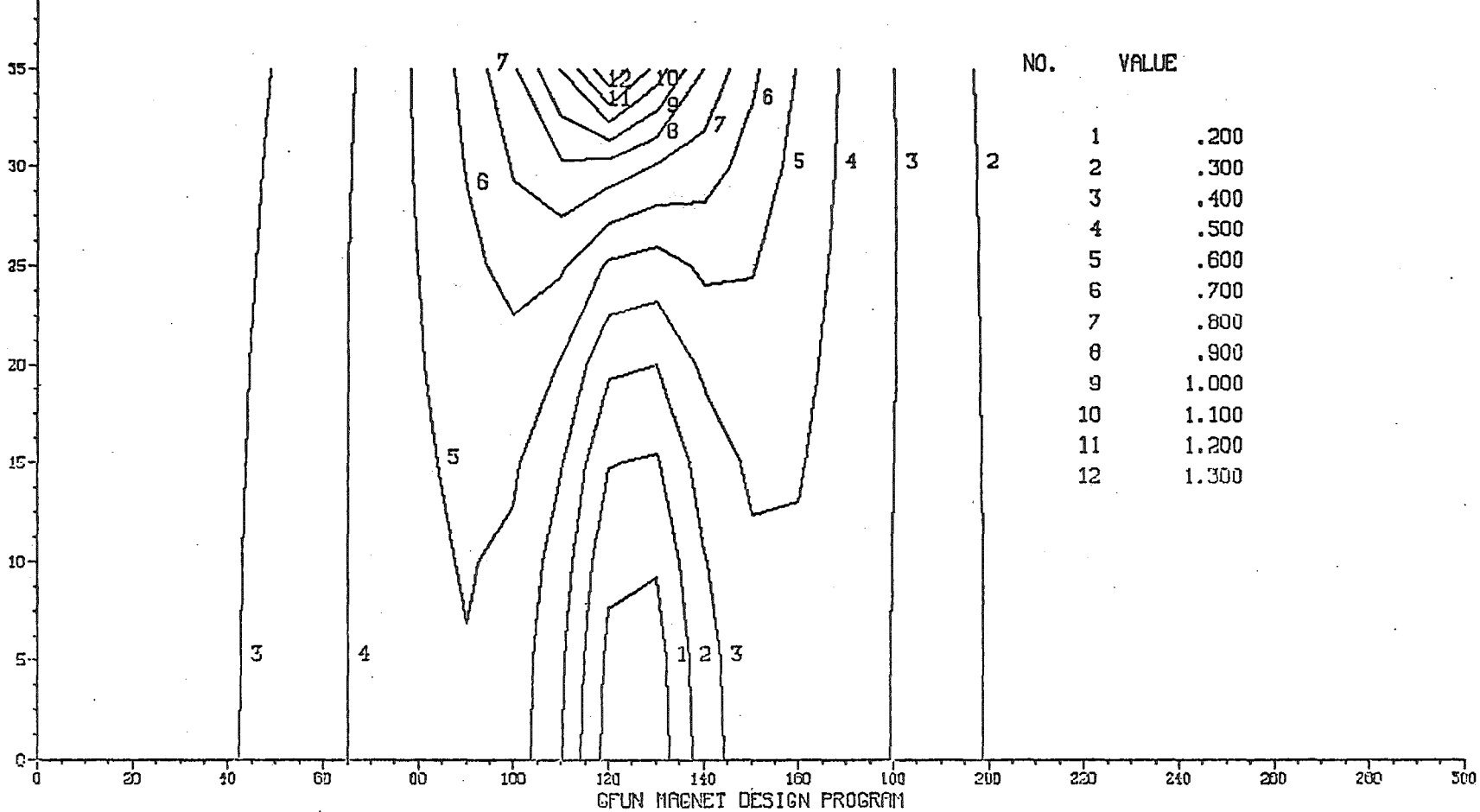
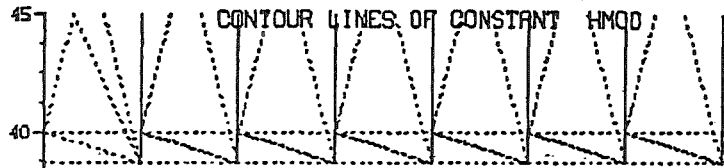


NO.	VALUE
1	.200
2	.300
3	.400
4	.500
5	.600
6	.700
7	.800
8	.900
9	1.000
10	1.100
11	1.200
12	1.300
13	1.400
14	1.500
15	1.600

V.9-6

348

Fig. V.9-3 The magnetic field map for case 1.



V.9-7

- 349 -

Fig. V.9-4 The magnetic field map for case 2, the homogenized case.

$$\bar{C} = \int_V \bar{M} \times \bar{H}_0 d\tau, \quad (V.9-2)$$

such that the torque about an arbitrary origin O, with respect to which the position vector of the centroid of the volume element $d\tau$ is \bar{r} , is given by

$$L = \int \bar{r} \times (\bar{M} \cdot \nabla \bar{H}_0) d\tau + \int \bar{M} \times \bar{H}_0 d\tau. \quad (V.9-3)$$

A simple one-dimensional estimate of the magnitude of \bar{F} can be made as follows. Assume the iron is saturated, and $4\pi\bar{M}$ is on the order of 18000 gauss (see Fig. V.9-1). Also assume the gradient of the field $\nabla \bar{H}_0 = 10^3$ gauss/cm, then the maximum magnetostatic force \bar{F} the body is subjected to, is

$$\bar{F} = \frac{18000}{2\pi} \times 10^3 \times V \text{ dyne}$$

$$\bar{F}/V = 1433 \times 10^3 \text{ dyne/cm}^3$$

$$= 14.33 \text{ newton/cm}^3. \quad (V.9-4)$$

The weight per unit volume, assuming the density of the iron is 7.81 g/cm^3 is,

$$\frac{\bar{W}}{V} = 7.81 \times 981 \times 10^{-5} \text{ newton/cm}^3$$

$$(V.9-5)$$

$$= .077 \text{ newton/cm}^3.$$

The magnetostatic force is about 187 times the weight of the ferromagnetic body.

V.9.3.2 GFUN3D Force Calculations

We have modeled the force calculations in GFUN3D, using only the field of the coils, i.e., neglecting any contribution of other existing ferromagnetic bodies which may contribute to the field on the body whose force is calculated. If included, this would have a small effect when the iron is saturated which is the case in the central cell. The gradient of the field $\nabla \overline{H}_0$ is evaluated at the centroid of each iron element and assumed constant within it.

A section of a blanket module has been modeled as shown in Fig. V.9-5 in a cross section view of the blanket in the x-y plane, and in Fig. V.9-6 a cross section view in the z-y plane; note that the blanket starts at the center of the reactor and extends for only 20 cm.

The magnitude of the total magnetostatic force on this short section of the blanket was found to be 17076 newtons. The magnitude of each component of the total force and the total torque around the origin are shown in Figs. V.9-5 and V.9-6. The resulting force is about .2 the weight of the blanket. The field gradient in this part of the reactor is very small, and one would expect a larger force if the gradient is changed due to, for example, a loss of power in one of the central cell solenoids. Consequently, the design of the supports for the blanket should take that into account.

The obtained force distribution was used to calculate the stresses in the central pipe in the blanket using SAP4 code.⁽⁴⁾ The maximum effective stress due to the magnetic force alone is about 0.1 MPa. This is negligible compared to the thermal stresses, which if included, would result in a maximum effective stress of 125.0 MPa.

FRAME 2, UW-GFUN LOSN1 DATE:02/02/82 TIME:11:13:52 NC:34, NI: 575
34 CONDUCTOR ELEMENTS 575 IRON ELEMENTS
X-Y PLANE
ELEMENT 1 TO 575 DISPLAYED MATE- 3

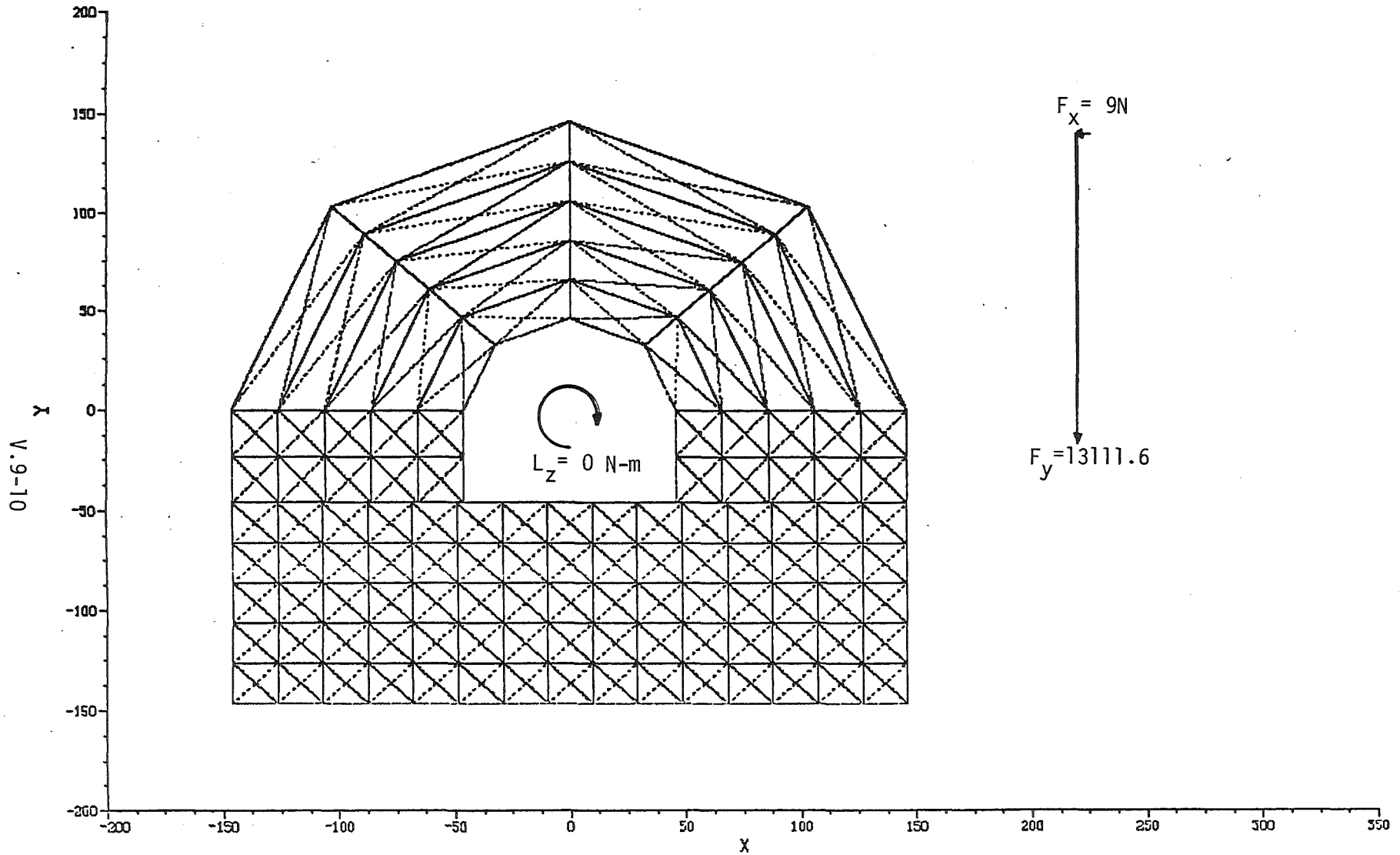


Fig. V.9-5 View of the blanket in x-y plane showing the components of the total magnetostatic force and torque.

34 CONDUCTOR ELEMENTS 575 IRON ELEMENTS

Z-Y PLANE

ELEMENT 1 TO 575 DISPLAYED MATE- 3

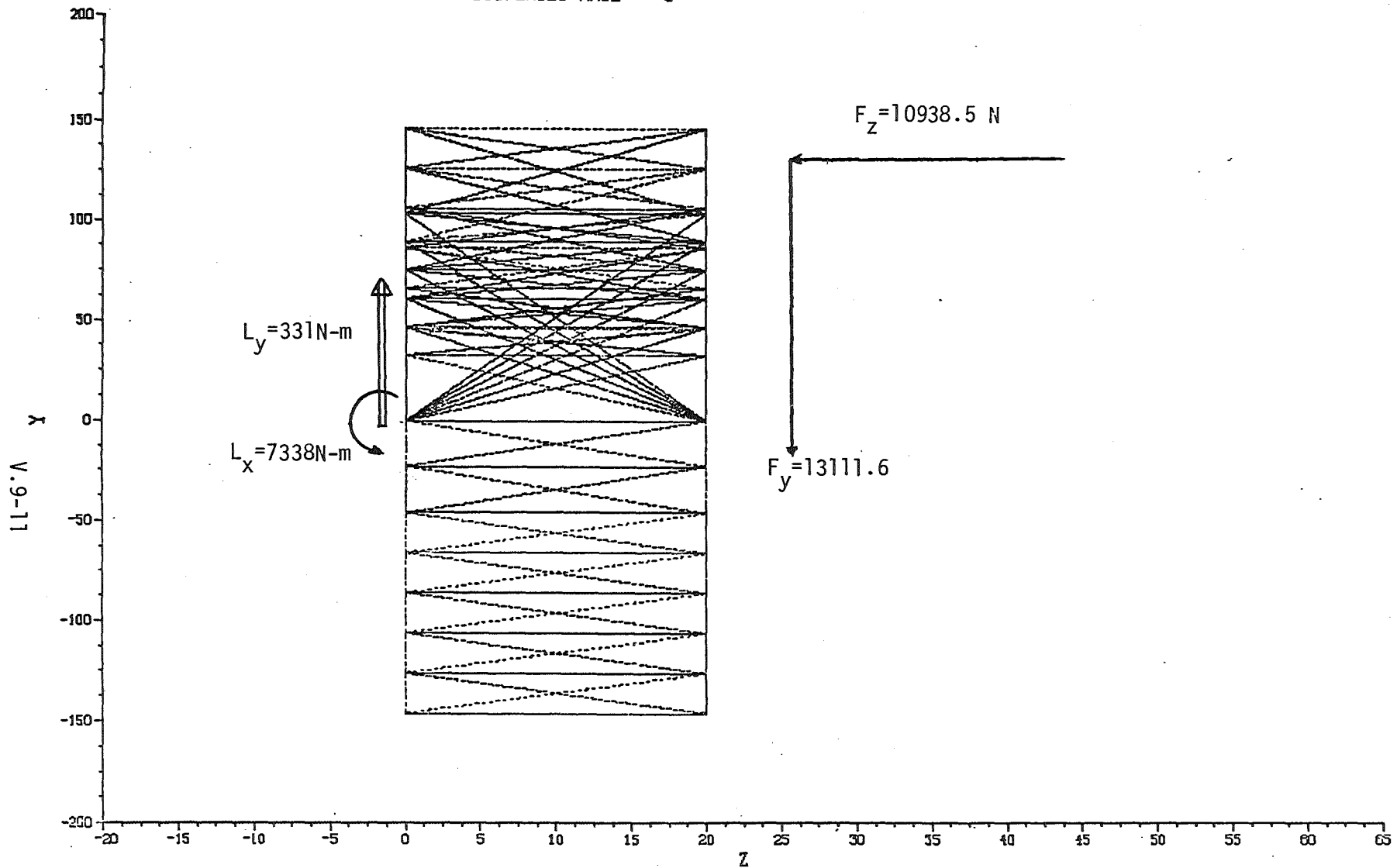


Fig. V.9-6 The view of the blanket in the z-y plane showing the components of the total magnetostatic force and torque.

V.9.4 Field Shielding and Field Asymmetry

The presence of the ferromagnetic HT-9 stainless steel in the blanket will partially shield the magnetic field in the central cell seen by the plasma. In addition, it will also reshape the central cell field configuration and possibly destroy its symmetry. However, both effects will vanish if the blanket is made long enough. In this case, the effects will appear only at the ends of the blanket.

Consider an infinite blanket which has any arbitrary shape. The magnetization \vec{M} can be replaced by two currents flowing on the inner and the outer surface of the blanket, and each is equal to $\vec{n} \times \vec{M}$, where \vec{n} is the outward normal of the surface. The currents are opposite in direction, and each will cancel the effect of the other inside the plasma region. This is a direct result of applying Ampere's law: $\int_C \vec{H} \cdot d\vec{\ell} = \Sigma I = 0$. The field inside the plasma region will be exactly the same as if there is no iron.

For short blankets the end effects start to appear, and both field shielding and field shaping will occur. The shielding of the magnetic field depends on the permeability of the iron. For saturated iron, the shielding will be a minimum. For the blanket considered before, the field on the axis of the reactor with and without the blanket is shown in Figs. V.9-7 and V.9-8, respectively, and from $z = -100$ cm to $z = +100$ cm. The average reduction of the field over the 200 cm is about .01 tesla, as can be estimated from the field integrals shown in the figures, and the maximum reduction of the field is about .02 tesla and occurs at about the center of the blanket.

Figure V.9-9 shows the contours of $\sqrt{B_x^2 + B_y^2}$ at $z = 0$. Figure V.9-10 shows the contours of the magnitude of the field at $z = 10$, i.e. at the center of the blanket section. Apparently the presence of the blanket has destroyed

FRAME 4, UM-GFUN LOSN1 DATE:02/07/82 TIME:21:08:25 NC:34, NI: 0
 34 CONDUCTOR ELEMENTS 0 IRON ELEMENTS
 Z-Y PLANE
 FIELD INTEGRAL- 5825.1 (SINP) H-AVE- 2.91

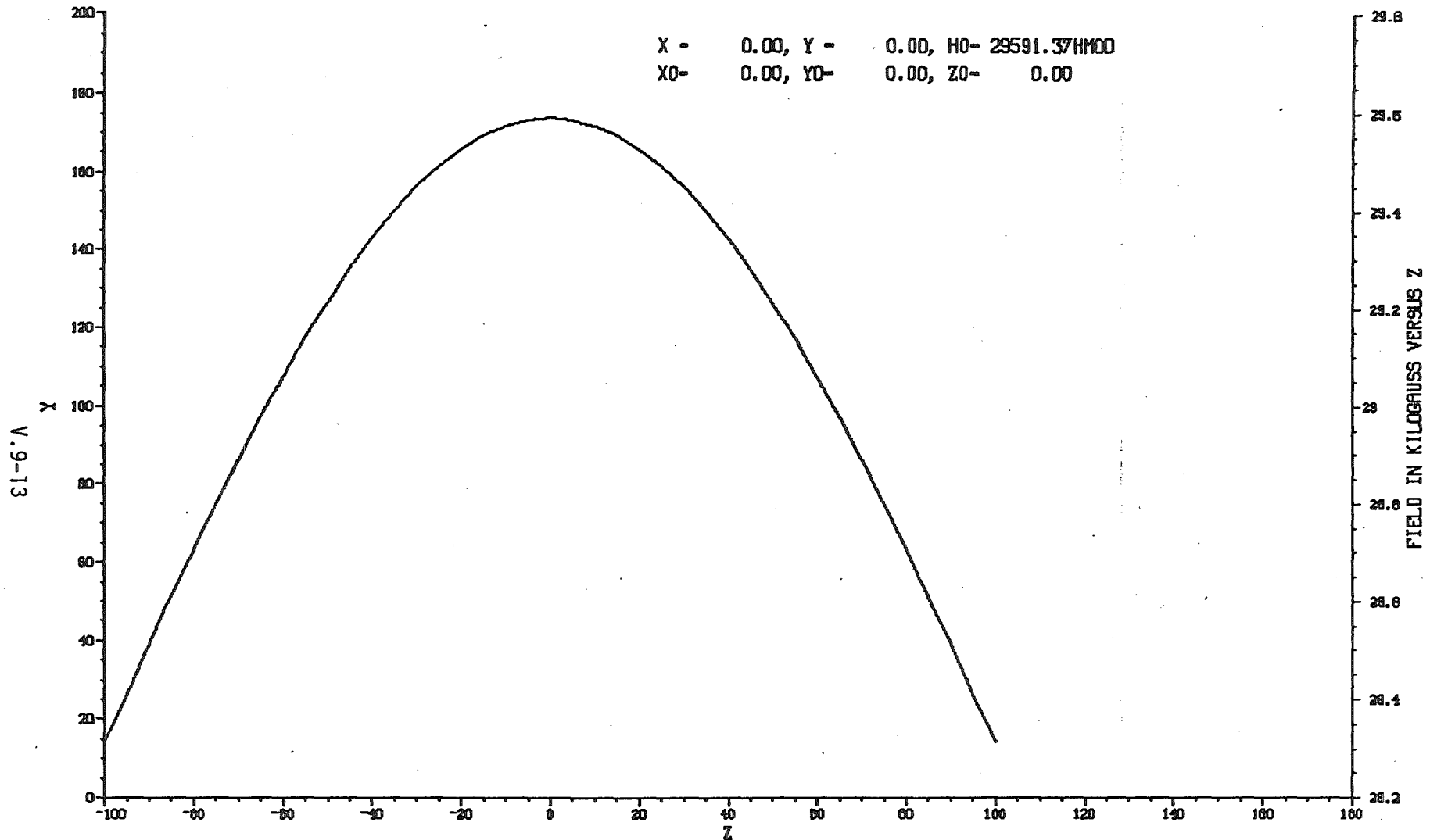


Fig. V.9-7 The magnetic field on the axis of the central cell without the ferromagnetic blanket.

FRAME 6, UH-GFUN LOSN1 DATE:02/07/82 TIME:21:13:01 NC:34, NI: 575
 34 CONDUCTOR ELEMENTS 575 IRON ELEMENTS
 Z-Y PLANE
 FIELD INTEGRAL- 5812.9 (SIMP) H-AVE- 2.91

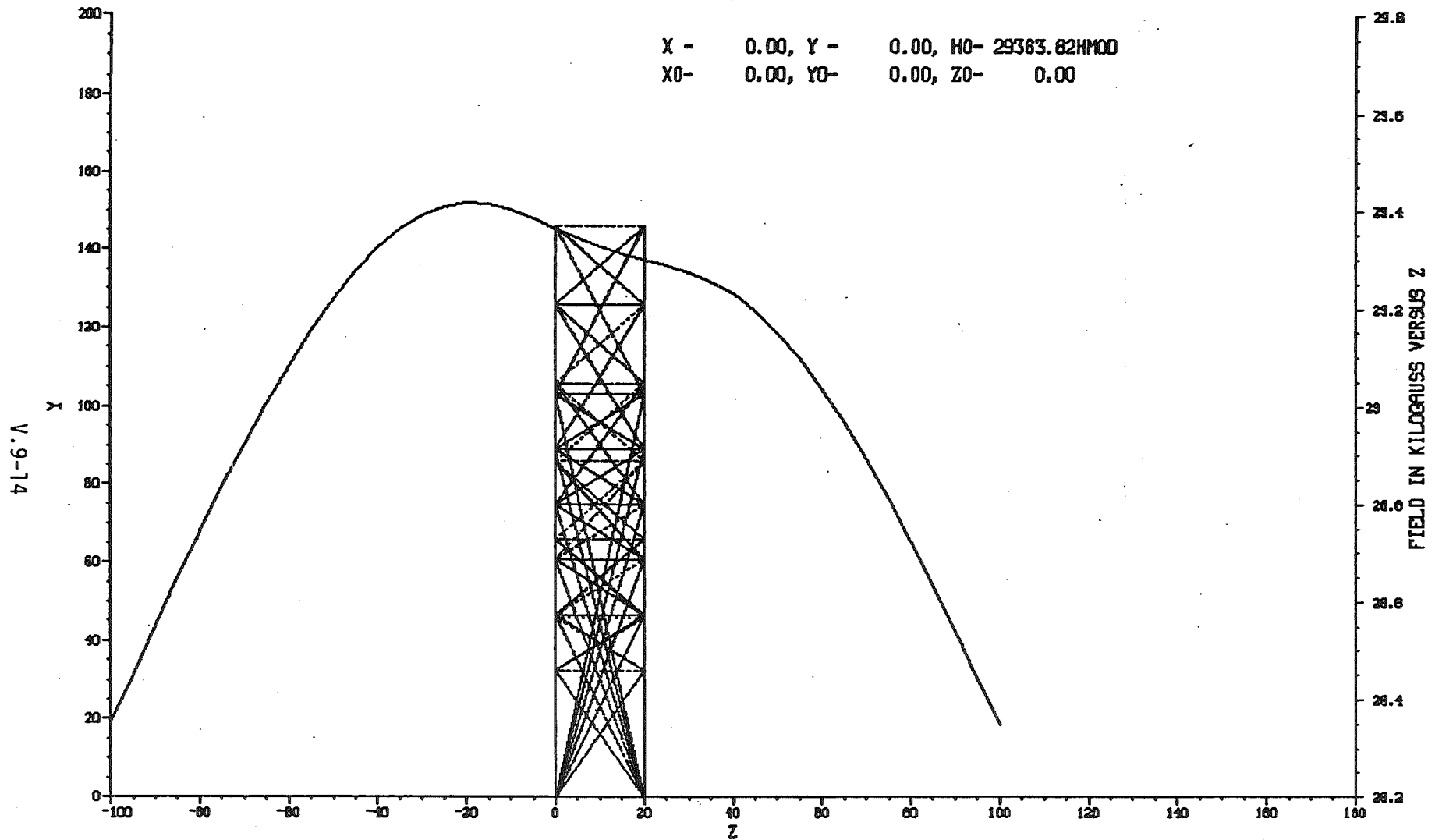


Fig. V.9-8 The magnetic field on the axis of the central cell, with the presence of the short section of the blanket.

34 CONDUCTOR ELEMENTS 575 IRON ELEMENTS

X-Y PLANE

ELEMENT 9 TO 9 DISPLAYED MATE- 0

Z- 0.000

CONTOUR LINES OF CONSTANT MODX

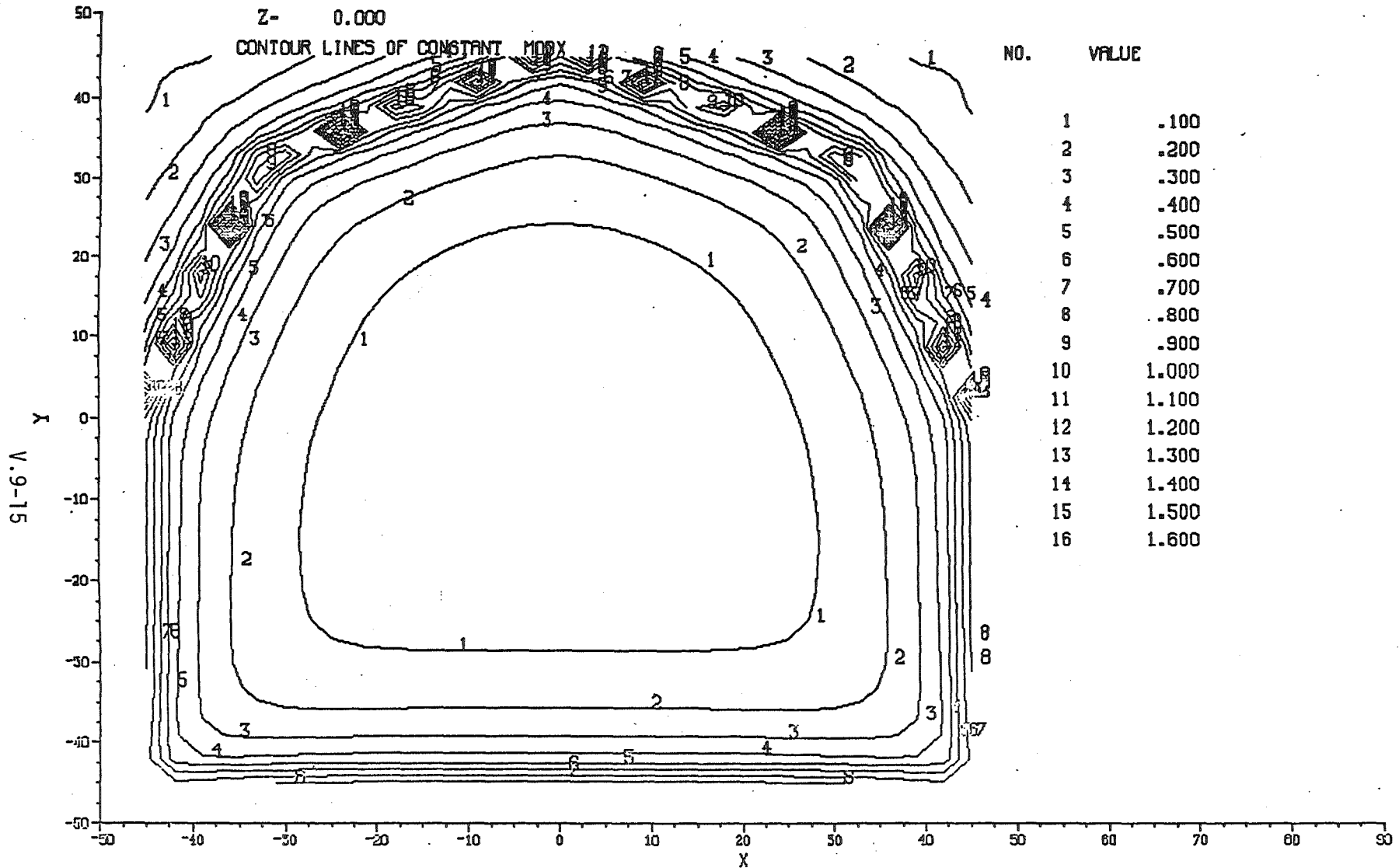


Fig. V.9-9 Map of the magnetic field; $\sqrt{B_x^2 + B_y^2}$ at the left end of the blanket.

FRAME 9, UW-GFUN L0SN1 DATE:01/28/82 TIME:10:12:25 NC:34, NI: 575
 34 CONDUCTOR ELEMENTS 575 IRON ELEMENTS
 X-Y PLANE
 ELEMENT 9 TO 9 DISPLAYED MATE- 0
 Z- 10.000

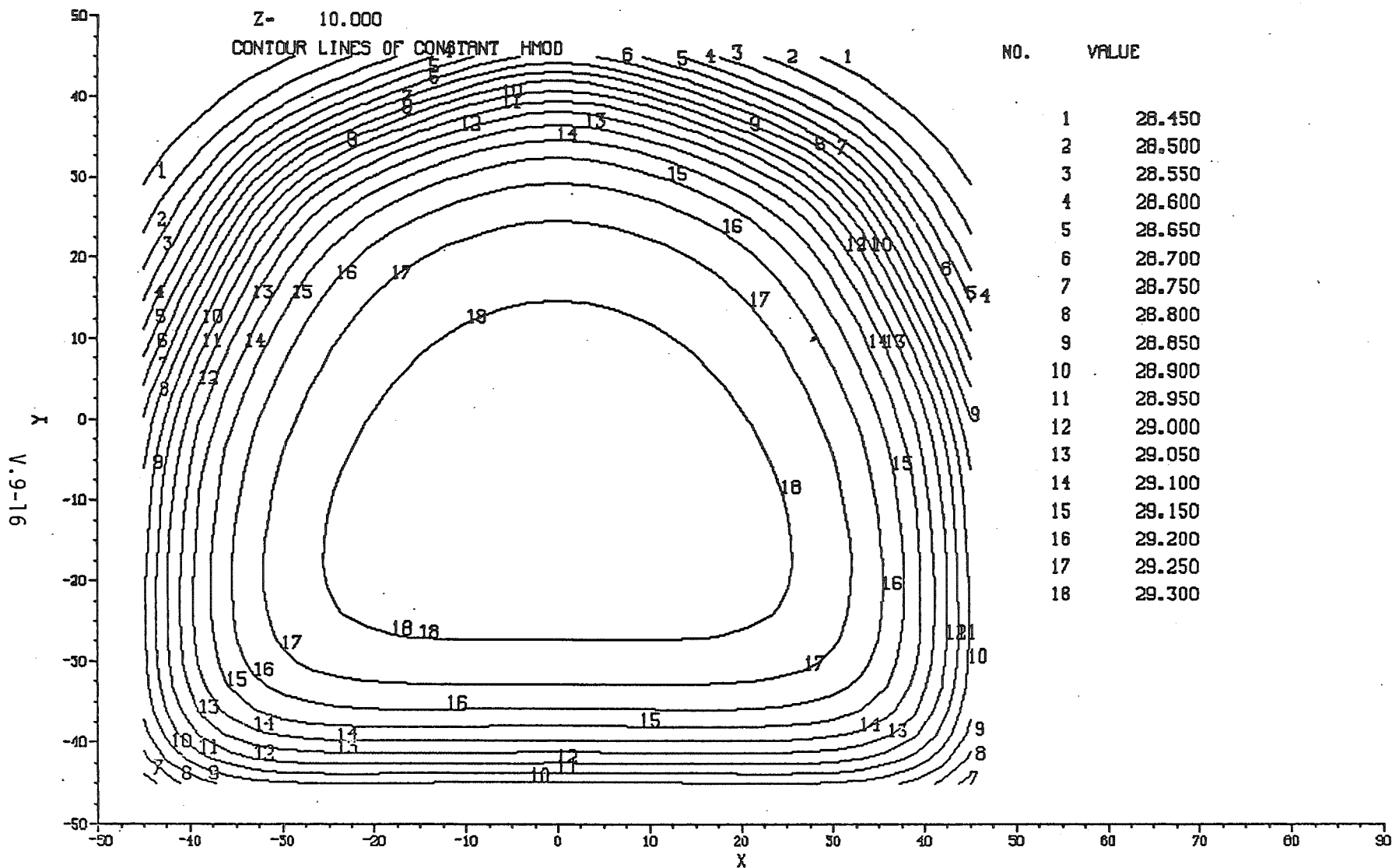


Fig. V.9-10 Map of the magnetic field; mod(B) at the center of the blanket section.

the symmetry of the field, and the field contours take almost the same shape as that of the blanket. The perturbation was initially thought to create radial diffusion of the plasma and hence destroys the confinement of the plasma.

To examine this problem further we have calculated the gradient of the field in cylindrical coordinates to evaluate the term $\frac{\bar{B}_x \nabla |B|}{B^3}$ which can be readily used to estimate the drift in any direction.⁽³⁾ The field, the gradient of the field, and the $\frac{\bar{B}_x \nabla |B|}{B^3}$ components are shown in Figs. V.9-11a, V.9-11b, and V.9-11c, respectively, at $z = 0$ and a radius of 30 cm, i.e., near the edge of the plasma. For further discussion and for the conclusions with respect to this problem refer to the plasma section.

V.9.5 Field Shielding and Perturbation in Case of Long Ferromagnetic Blankets

The magnetic field perturbation, and in particular the reduction in the magnetic field in the plasma, will also depend on the length of the blanket. In the previous section, the computations were done for a short section of the blanket because it was desired to model as accurately as possible the azimuthal distribution and configuration of the ferromagnetic blanket. The number of elements required is large so that the entire blanket could not be modeled in detail.

In order to study the effect of the length of the blanket on the magnetic field distribution, two different blanket configurations were examined in more detail.

One blanket model had the shape of a cylindrical annulus, and one the shape of a rectangular prism with a rectangular hole. The former model was treated analytically, whereas the latter was evaluated numerically with GFUN.

FRAME 20, UN-GFUN LDSN1 DATE:01/28/82 TIME:12:50:42 NC:34, NI: 575
X-Y PLANE Z- 0.0, R- 30.0, PHI- 0.0
FIELD COMPONENTS IN K-GAUSS

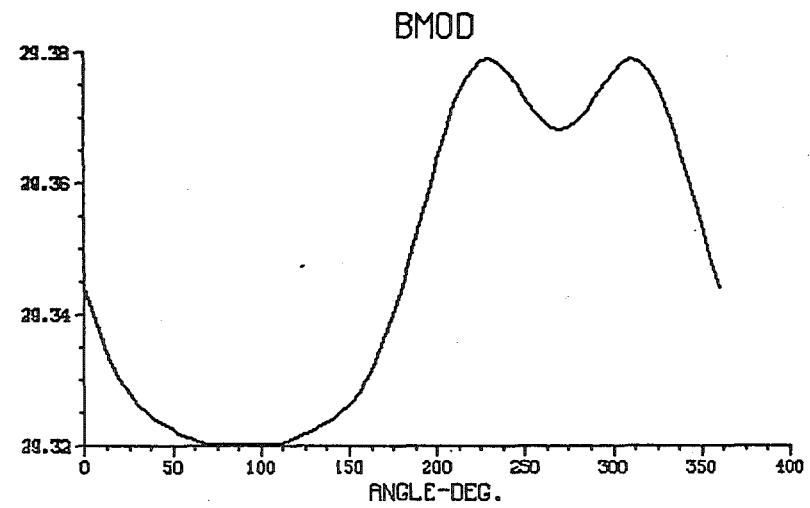
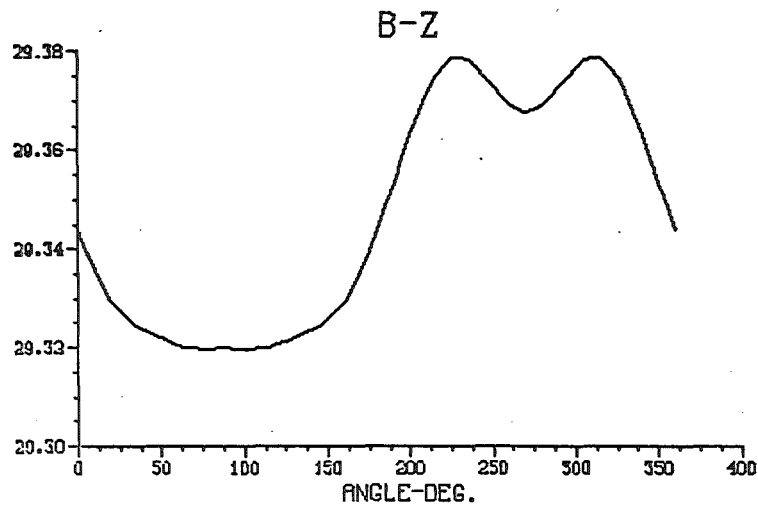
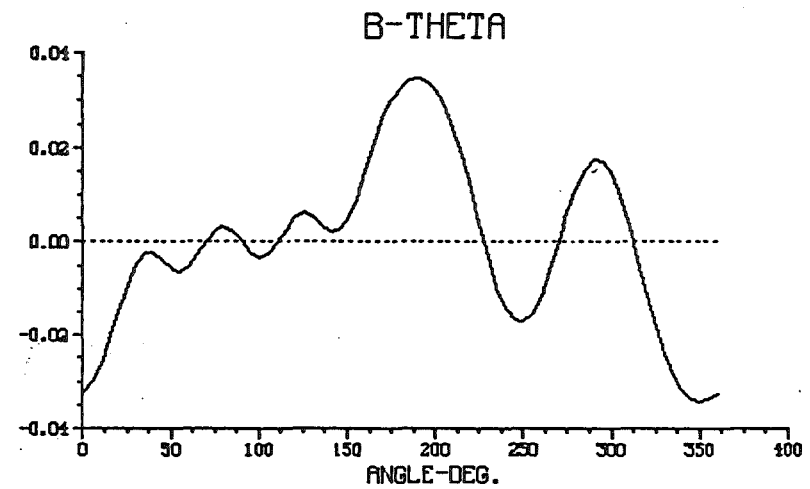
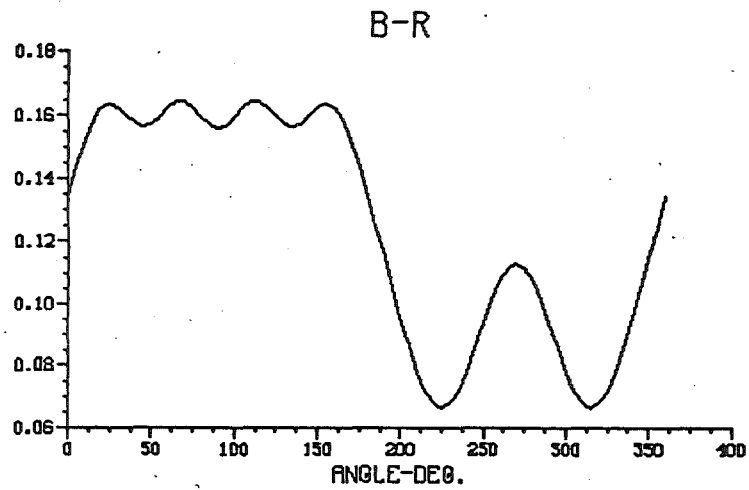


Fig. V.9-11a The azimuthal distribution of the magnetic field components at 30 cm radius and at the center of the central cell with the presence of the blanket included.

V.9-18

360

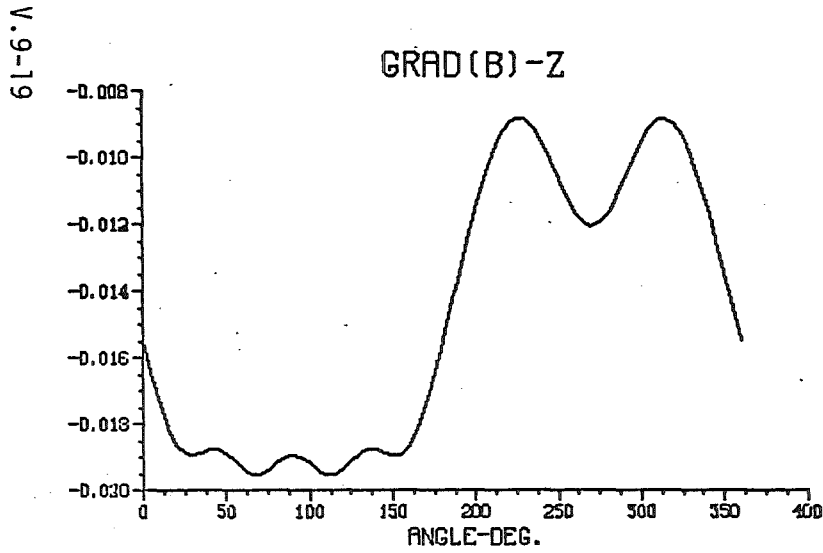
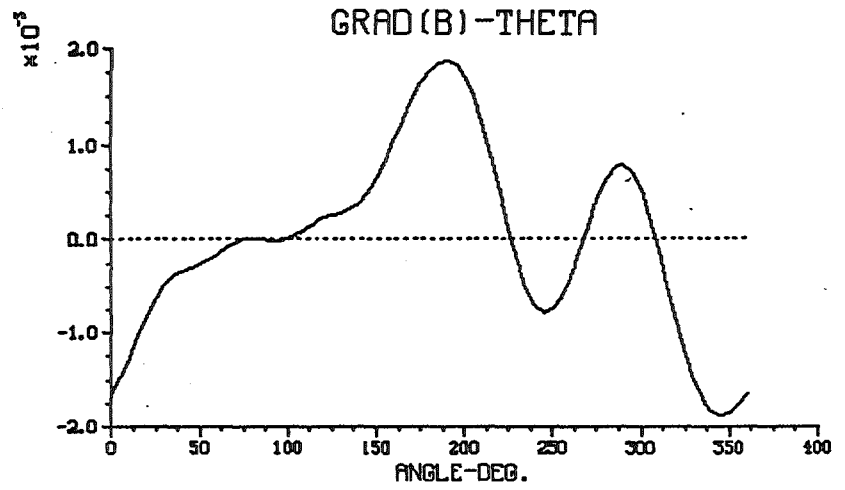
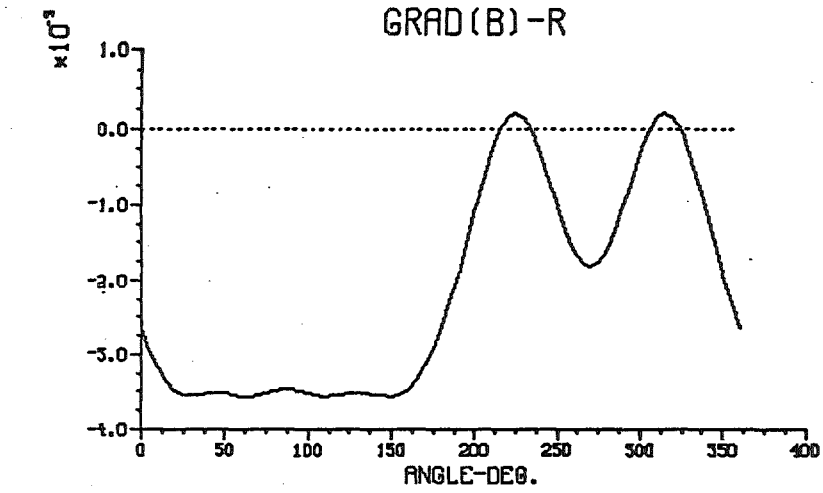
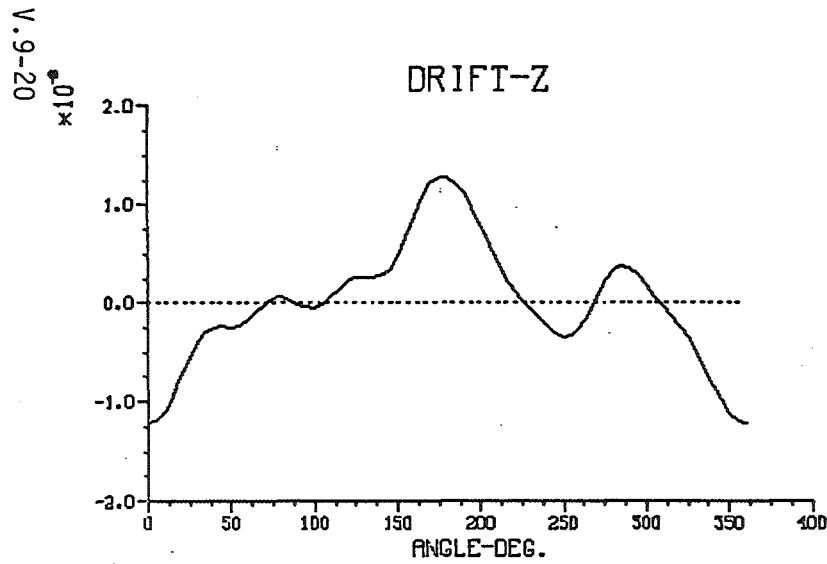
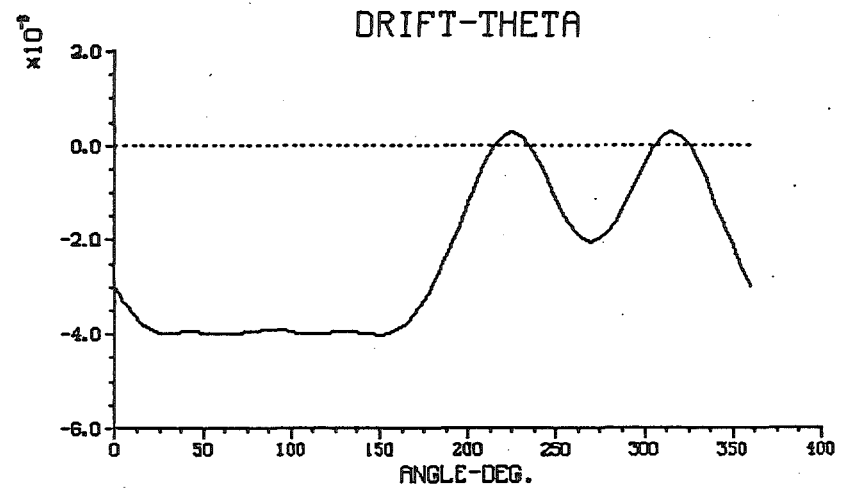
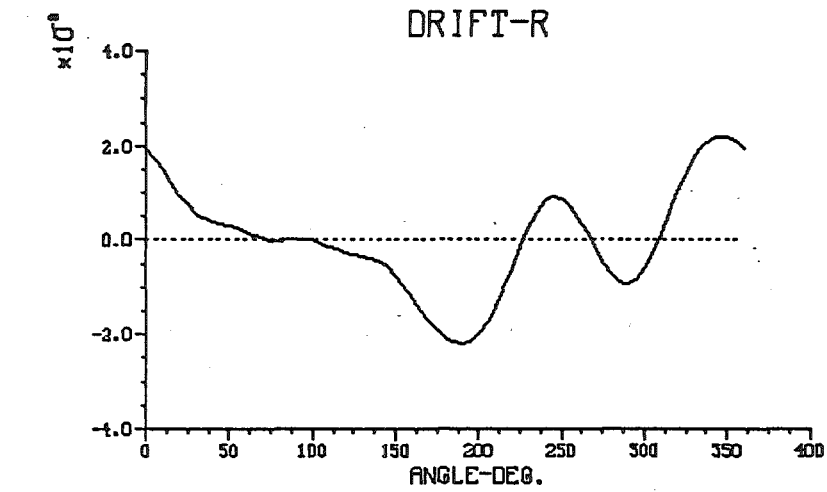


Fig. V.9-11b Azimuthal distributions of $\bar{V}B$.

FRAME 22, UW-GFUN LOSN1 DATE:01/28/82 TIME:12:50:45 NC:34, NI: 575
 X-Y PLANE Z- 0.0, R- 30.0, PHI- 0.0
 DRIFT COMPONENTS (B X GRAD(B)/B**3) IN 1/(CM-KG)



V.9-20

362

Fig. V.9-11c Azimuthal distributions of $\frac{\bar{B} \times \nabla \bar{B}}{B^3}$, the drift term.

For the circular blanket, the inner and outer radii are designated a and b, respectively, whereas the total length is $L = 2\ell$. If it is assumed that the ferromagnetic blanket structure is magnetized to saturation, and if this saturation magnetization $\mu_0 M$ is constant everywhere and parallel to the axial direction, then the field perturbation $\Delta \vec{B}$ can be computed analytically. The total field is then the sum of the vacuum field \vec{B}_0 and the field perturbation $\Delta \vec{B}$, i.e. $\vec{B} = \vec{B}_0 + \Delta \vec{B}$. The field perturbation can be computed from

$$\Delta \vec{B}(\vec{r}) = \frac{\mu_0}{4\pi} \oint \frac{(\vec{r} - \vec{r}') \times \vec{M} \times \vec{n}'}{|\vec{r} - \vec{r}'|^3} dS' - \frac{\mu_0}{4\pi} \int \frac{(\vec{r} - \vec{r}') \times \nabla' \times \vec{M}'}{|\vec{r} - \vec{r}'|^3} dV' . \quad (V.9-6)$$

For a constant magnetization the second term vanishes and the field $\Delta \vec{B}$ is given by the surface integral. Since \vec{M} was assumed to be axial, $\vec{M} \times \vec{n}$ vanishes on the end faces of the annulus, and contributions arise only from the cylindrical surfaces. In fact, the field $\Delta \vec{B}$ is identical to the one produced by two concentric solenoids of equal length with equal but opposite currents. The axial field on axis is found to be given by

$$\begin{aligned} \frac{2\Delta B_z(z)}{\mu_0 M} &= \frac{(\ell + z)}{\sqrt{a^2 + (\ell + z)^2}} + \frac{(\ell - z)}{\sqrt{a^2 + (\ell - z)^2}} \\ &\quad - \frac{(\ell + z)}{\sqrt{b^2 + (\ell + z)^2}} - \frac{(\ell - z)}{\sqrt{b^2 + (\ell - z)^2}} \end{aligned} \quad (V.9-7)$$

where z is the distance from the midplane. The variation of the axial field on axis is shown in Fig. V.9-12 for differential lengths as a function of the reduced axial position z/ℓ . It is seen that the field reduction on axis is due to end effects. For sufficiently long blankets, i.e. when $L/2b \gg 1$, then the field reduction on axis at the midplane becomes very small. The end

FIELD REDUCTION AS A FUNCTION OF BLANKET LENGTH

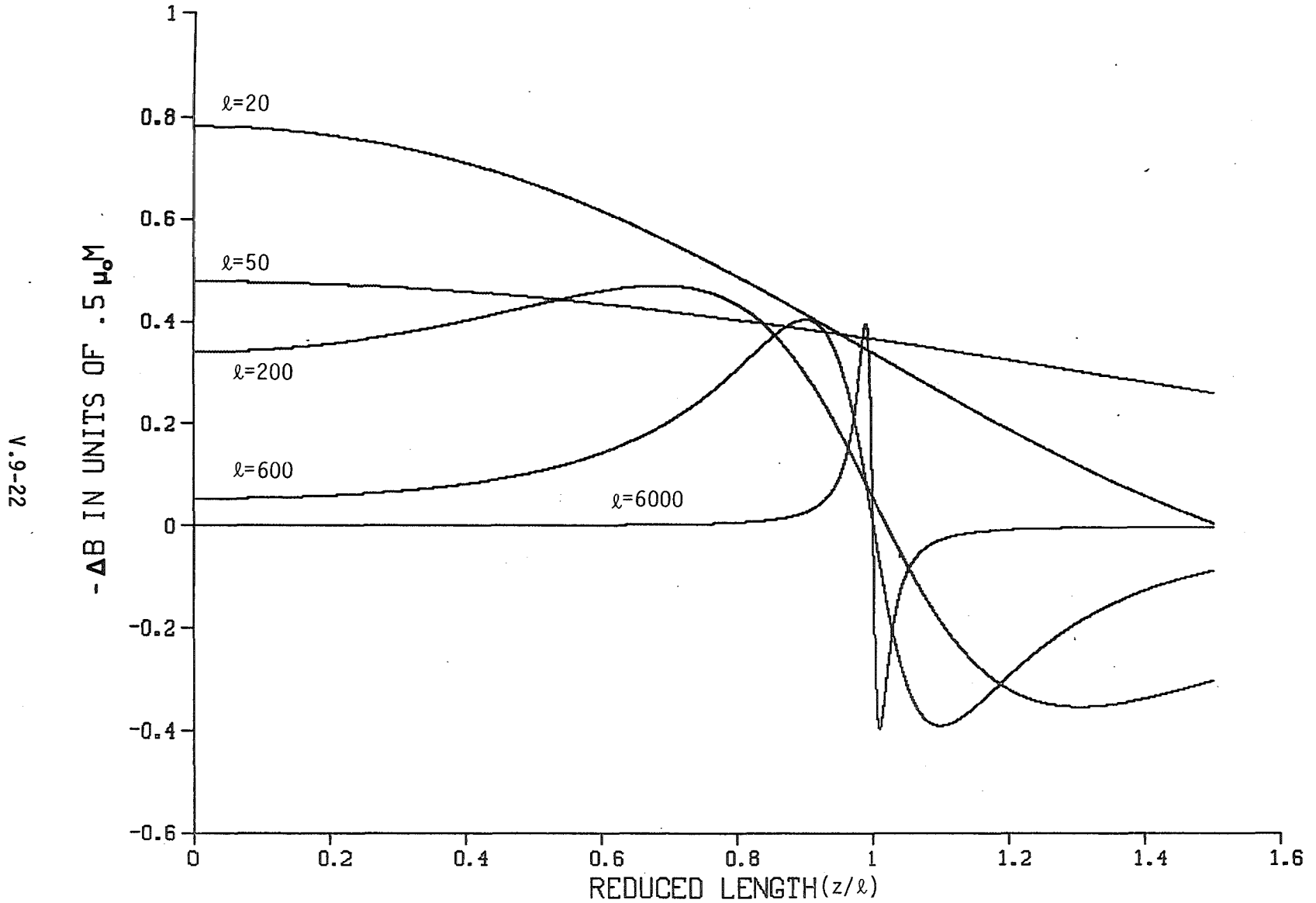


Fig. V.9-12. Axial field reduction on axis as a function of the reduced axial distance z/l ; for different half-lengths l of the blanket with 50 cm inner radius and 150 cm outer radius.

effects for large aspect ratios $L/2b$ consists of an axial region inside the blanket where the field is reduced ($-\Delta B$ is positive) and an outside region where the field is enhanced ($-\Delta B$ is negative). Both regions have an axial extension of the order of the outer diameter of the blanket. As the blanket gets shorter, the two end effects overlap, reinforcing each other inside the blanket region.

To elucidate this point further, the field on axis at the midplane,

$$\frac{\Delta B_z(0)}{\mu_0 M} = \frac{1}{\sqrt{1 + a^2/\ell^2}} - \frac{1}{\sqrt{1 + b^2/\ell^2}} \quad (\text{V.9-8})$$

and the average field on axis

$$\frac{1}{\mu_0 M L} \int_{-\ell}^{+\ell} \Delta B_z(z) dz = \frac{\Delta \bar{B}_z}{\mu_0 M} = \sqrt{1 + \frac{a^2}{L^2}} - \frac{a}{L} - \sqrt{1 + \frac{b^2}{L^2}} + \frac{b}{L} \quad (\text{V.9-10})$$

were computed for various configurations. Figure V.9-13 shows that both the field reduction at the midplane and the average field reduction show a maximum when the aspect ratio $L/2b$ is between 0.1 and 1. As this aspect ratio increases, the field reduction drops again at a rate proportional to $2b/L$.

So far, we modeled the blanket as a homogenized medium. Therefore, if M_0 is the value of the magnetization in the ferromagnetic steel and f is the metal fraction in the blanket, then $M = M_0 f$.

In order to test the validity of this homogenization procedure, the field reduction was computed for a blanket model consisting of a number of concentric annuli of various thicknesses and various separation distances. For each individual annulus, the field reduction was computed according to the above equation, the contributions from all annuli added, and the result divided by

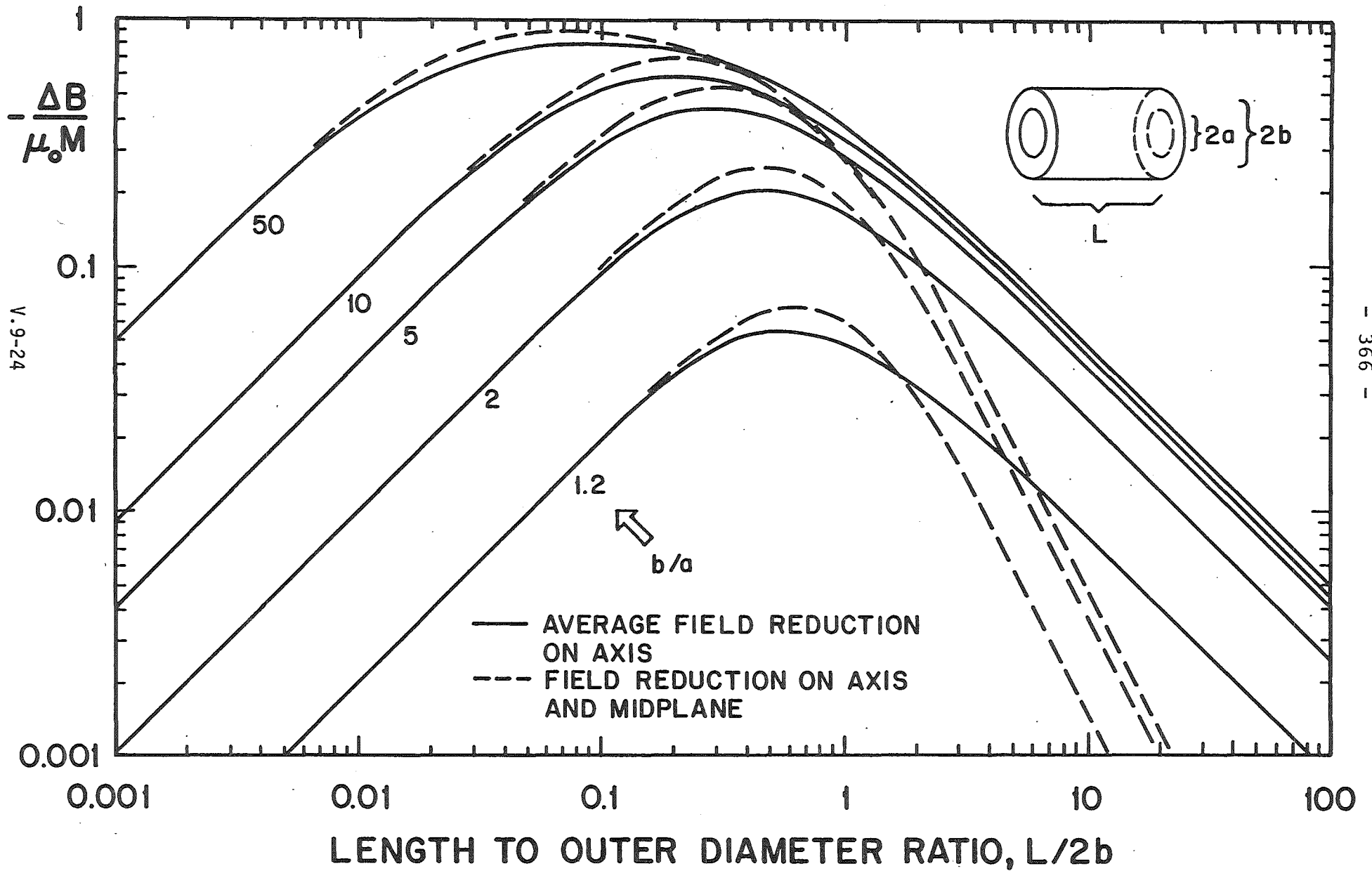


Fig. V.9-13. Effect of radial and axial dimensions on the field reduction on axis.

the average magnetization $\mu_0 M_0 f$. Some results are shown in Fig. V.9-14. It is found that the homogenization approach is indeed justified and gives very accurate results when the aspect ratio $L/2b > 0.1$. Furthermore, as the number of annuli is increased, the agreement with the homogenized result improves.

We also examined the effect of a radial variation of the magnetization. Since the saturation magnetization M_0 is a function of the temperature of the ferromagnetic steel, temperature variations through the blanket are of concern.

For a constant magnetization gradient

$$\frac{dM}{dr} = \frac{[M(b) - M(a)]}{(b - a)}$$

the field reduction on axis and at the midplane is given by

$$\frac{\Delta B_z(0)}{\mu_0} = \frac{M(a)}{\sqrt{1 + a^2/\ell^2}} - \frac{M(b)}{\sqrt{1 + b^2/\ell^2}} + \frac{\ell[M(b) - M(a)]}{b - a} \ln \left[\frac{b + \sqrt{b^2 + \ell^2}}{a + \sqrt{a^2 + \ell^2}} \right] \quad (V.9-11)$$

Although a closed-form solution was found for $\Delta B_z(z)$, an analytical expression for $\Delta \bar{B}_z$ could not be obtained. Therefore, we only show the results for $\Delta B_z(0)/\mu_0 \bar{M}$ in Fig. V.9-15. \bar{M} is the volume-average of the magnetization. It is seen again that for large aspect ratios $L/2b$, the field reduction decreases, and that the detailed distribution of the magnetization has little effect. The effect of temperature on the magnetization can therefore be

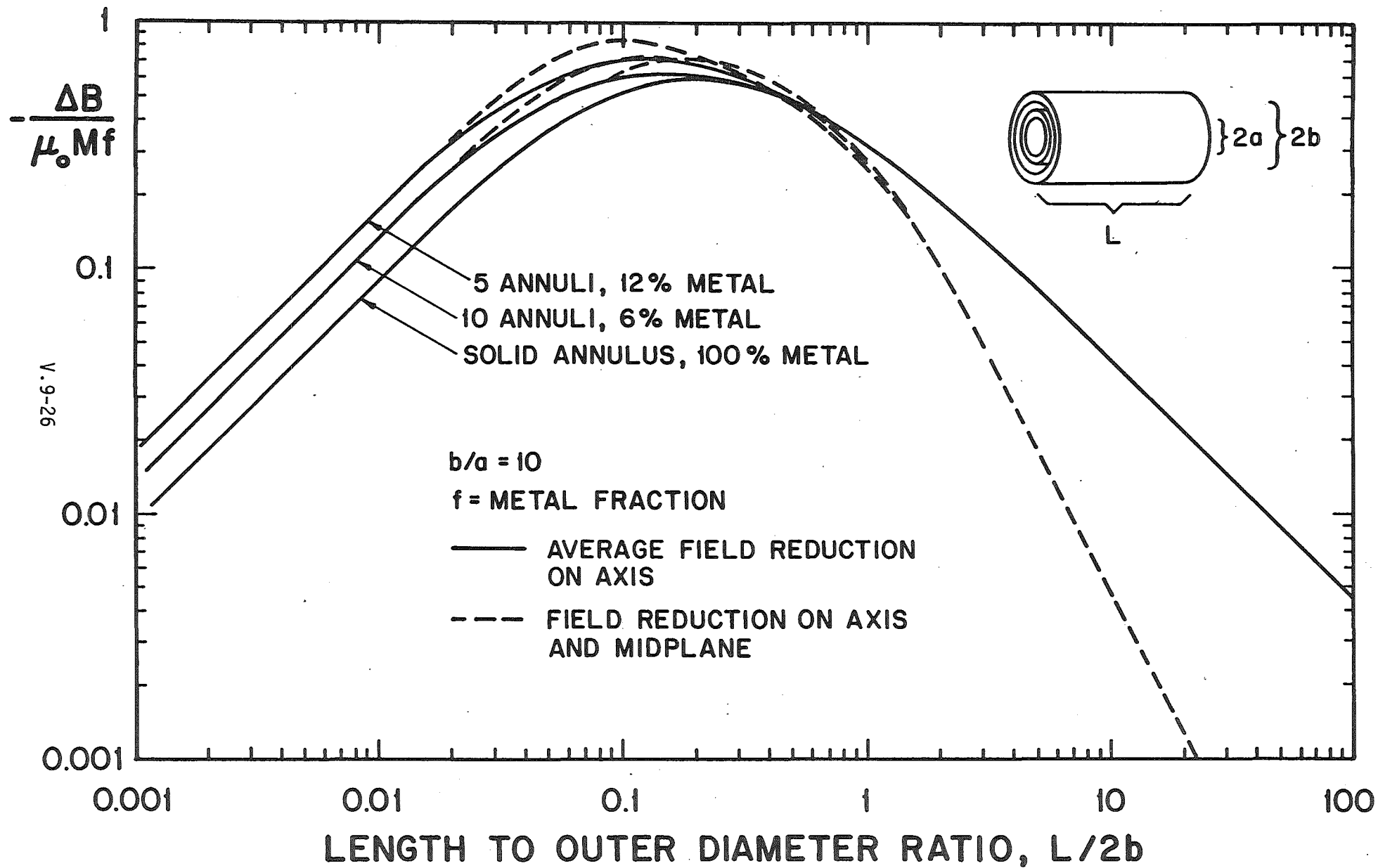


Fig. V.9-14. Effect of material distribution on the field reduction on axis.

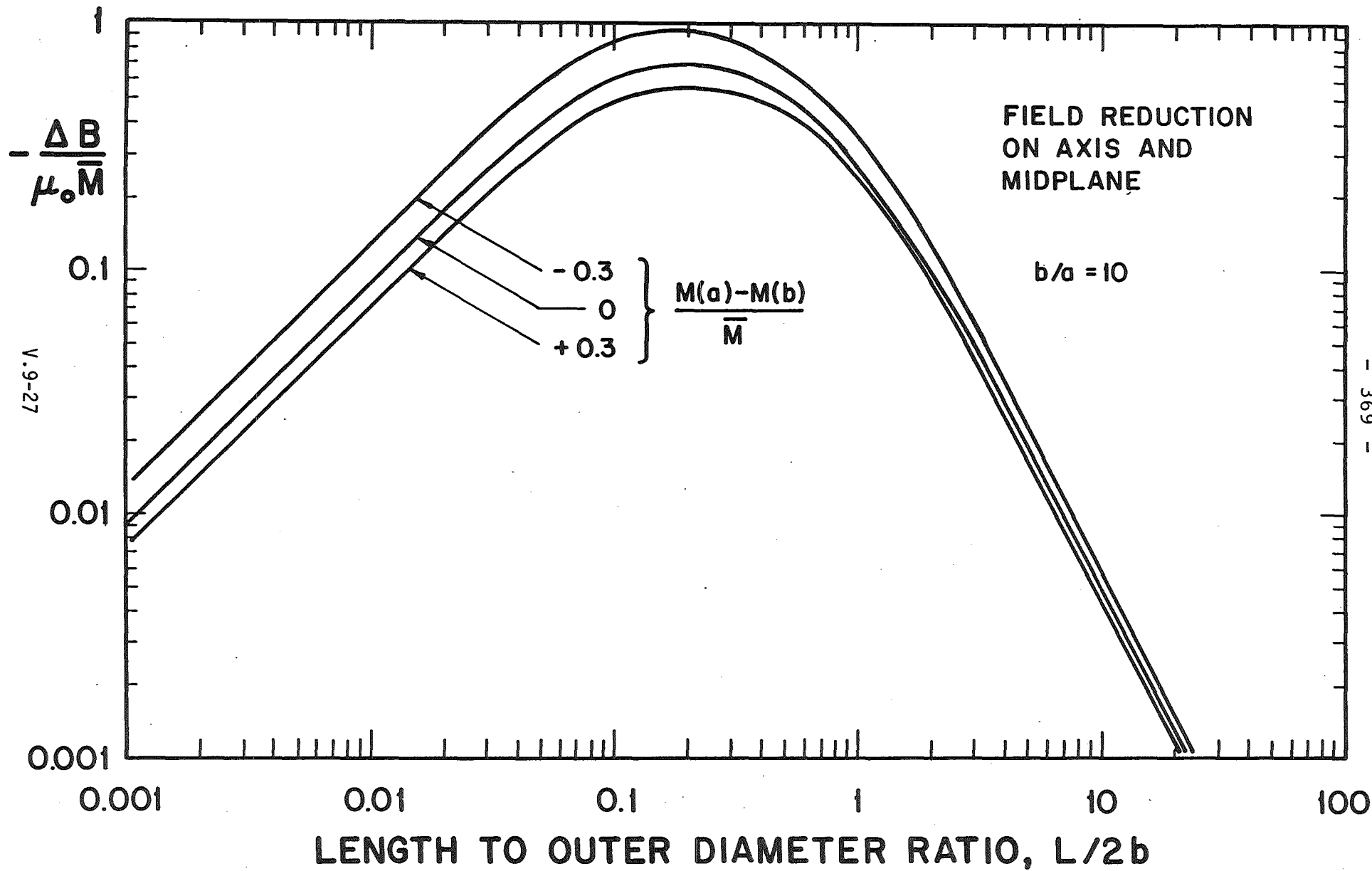


Fig. V.9-15. Effect of radial variations in the magnetization on the field reduction.

accounted for in an approximate manner if one employs the magnetization averaged over the entire blanket region.

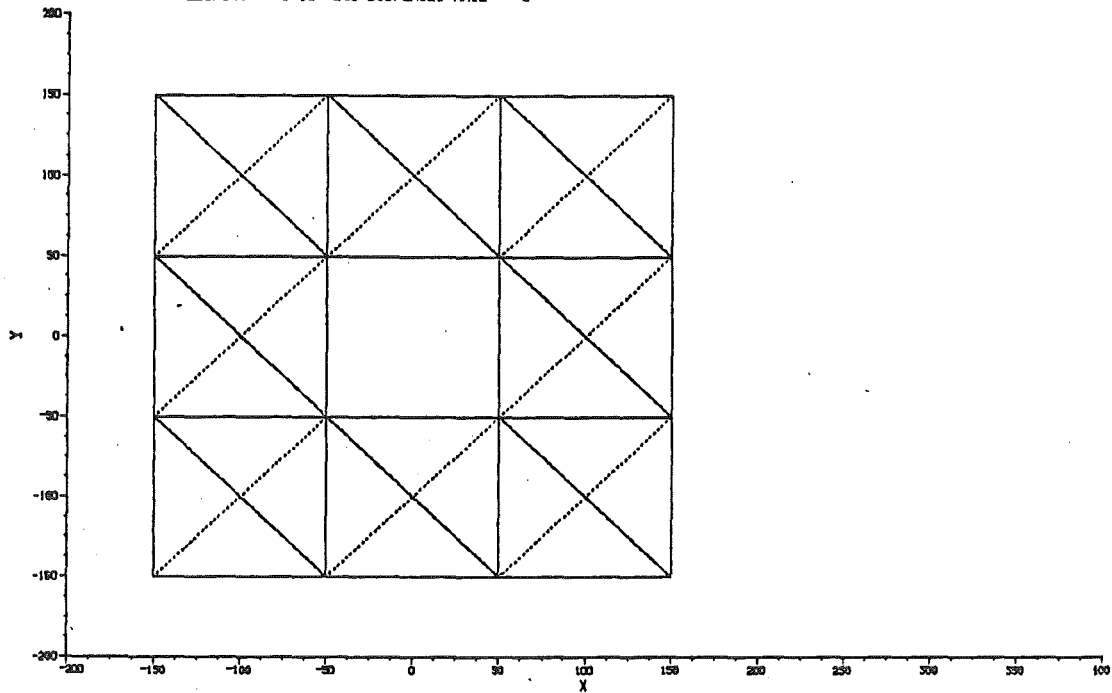
As mentioned in the beginning of this section we have studied the effect of long blankets with GFUN. Two blankets are considered which are shown in Figs. V.9-16 and V.9-17. The two blankets have the same length (12 m), but have different cross sections as shown in the figures. The magnetic field on the axis was calculated and is shown in Fig. V.9-18. The two blankets produced exactly the same field. The field with no blanket present in the central cell is also shown in the same figure with the dashed line. The maximum reduction in the field on the axis was about 500 gauss, and occurs at $z = 550$ cm, near the end of the blanket. This is in agreement with the previous analytical results.

The shape of the blanket as discussed in the previous section should have an effect on the field especially near the blanket (i.e. at the plasma edge). Figures V.9-19-V.9-21 show the field components in cylindrical coordinates at radius = 20 cm and at the location $z = 600$ cm with no blanket, with the square blanket, and with the rectangular blanket (note the fine scale on these figures), respectively. It is seen that the two different blanket cross sections affect the field in different ways which depends on the shape and symmetry properties of the blanket cross sections.

In summary, the detailed analysis of the magnetic field perturbation by various blanket configurations has shown that:

- a. the perturbation and reduction for a magnetically saturated structure is significant only near the ends, and over an axial region of the order of the outer blanket diameter or width;

FRAME 10, UN-GFLN L09N1 DATE:03/01/82 TIME:09:10:25 NC:32, NI: 240
32 CONDUCTOR ELEMENTS 240 IRON ELEMENTS
X-Y PLANE
ELEMENT 1 TO 240 DISPLAYED RATE- 3



FRAME 11, UN-GFLN L09N1 DATE:03/01/82 TIME:09:12:54 NC:32, NI: 240
32 CONDUCTOR ELEMENTS 240 IRON ELEMENTS
Z-Y PLANE

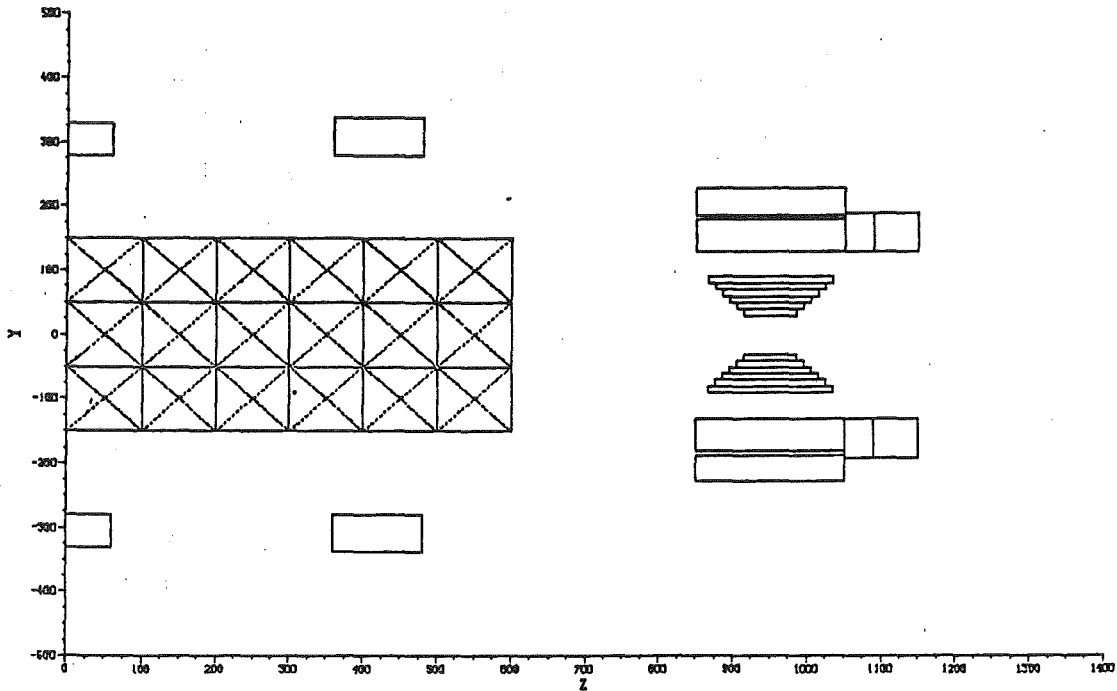
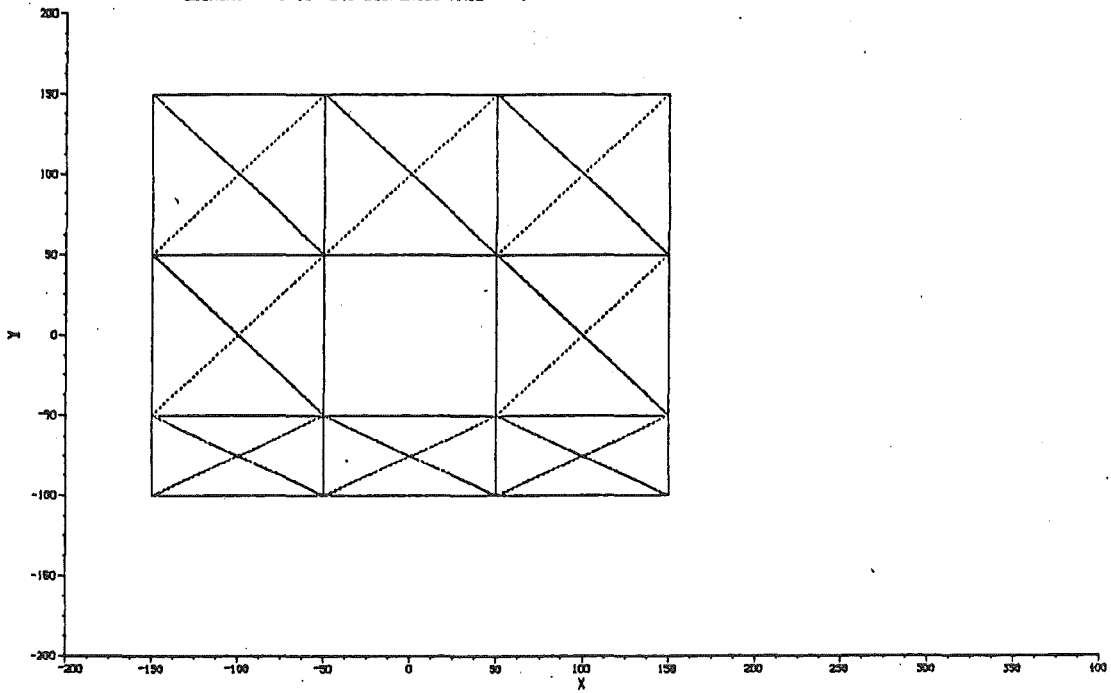


Fig. V.9-16. Two cross section views of the symmetric square cross section blanket.

FRAME 5, UN-GFUN LOSN1 DATE:03/03/82 TIME:13:41:08 NC:32, NI: 240
32 CONDUCTOR ELEMENTS 240 IRON ELEMENTS
X-Y PLANE
ELEMENT 1 TO 240 DISPLAYED RATE- 3



FRAME 6, UN-GFUN LOSN1 DATE:03/03/82 TIME:13:42:10 NC:32, NI: 240
32 CONDUCTOR ELEMENTS 240 IRON ELEMENTS
Z-Y PLANE

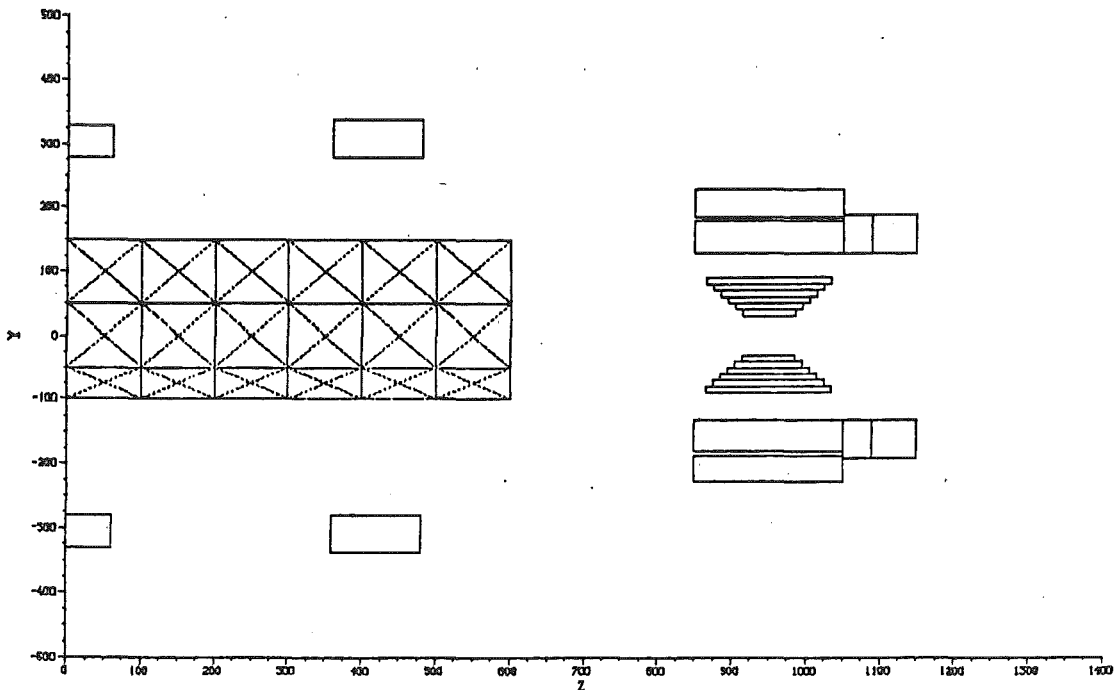


Fig. V.9-17. Two cross section views of the asymmetric rectangular blanket.

FRAME 6, UH-9FUN L0SN1 DATE:03/03/82 TIME:08:36:38 NC:32, NI: 240
 32 CONDUCTOR ELEMENTS 240 IRON ELEMENTS
 Z-Y PLANE
 FIELD INTEGRAL- 34160. (SIMP) H-AVE- 2.63

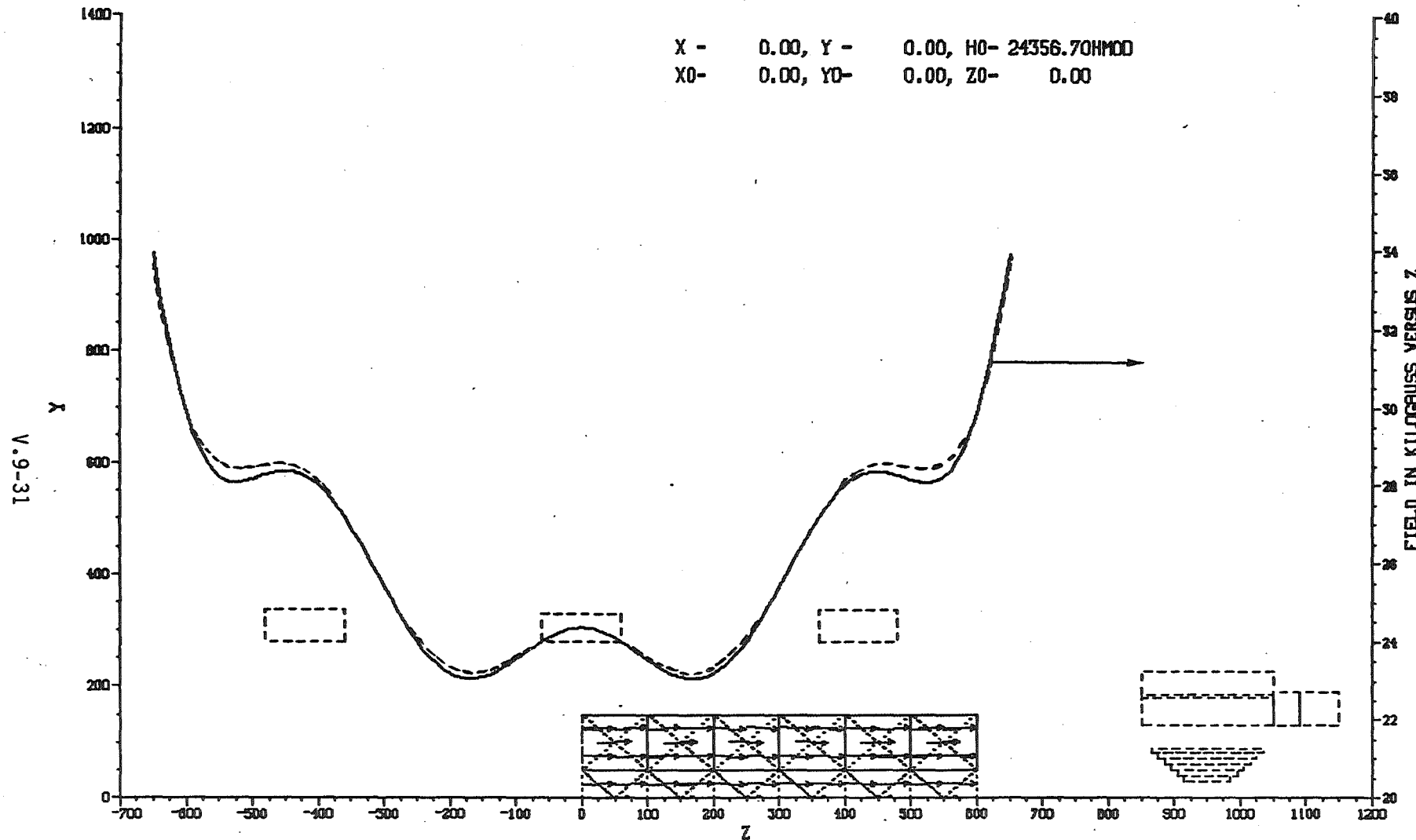
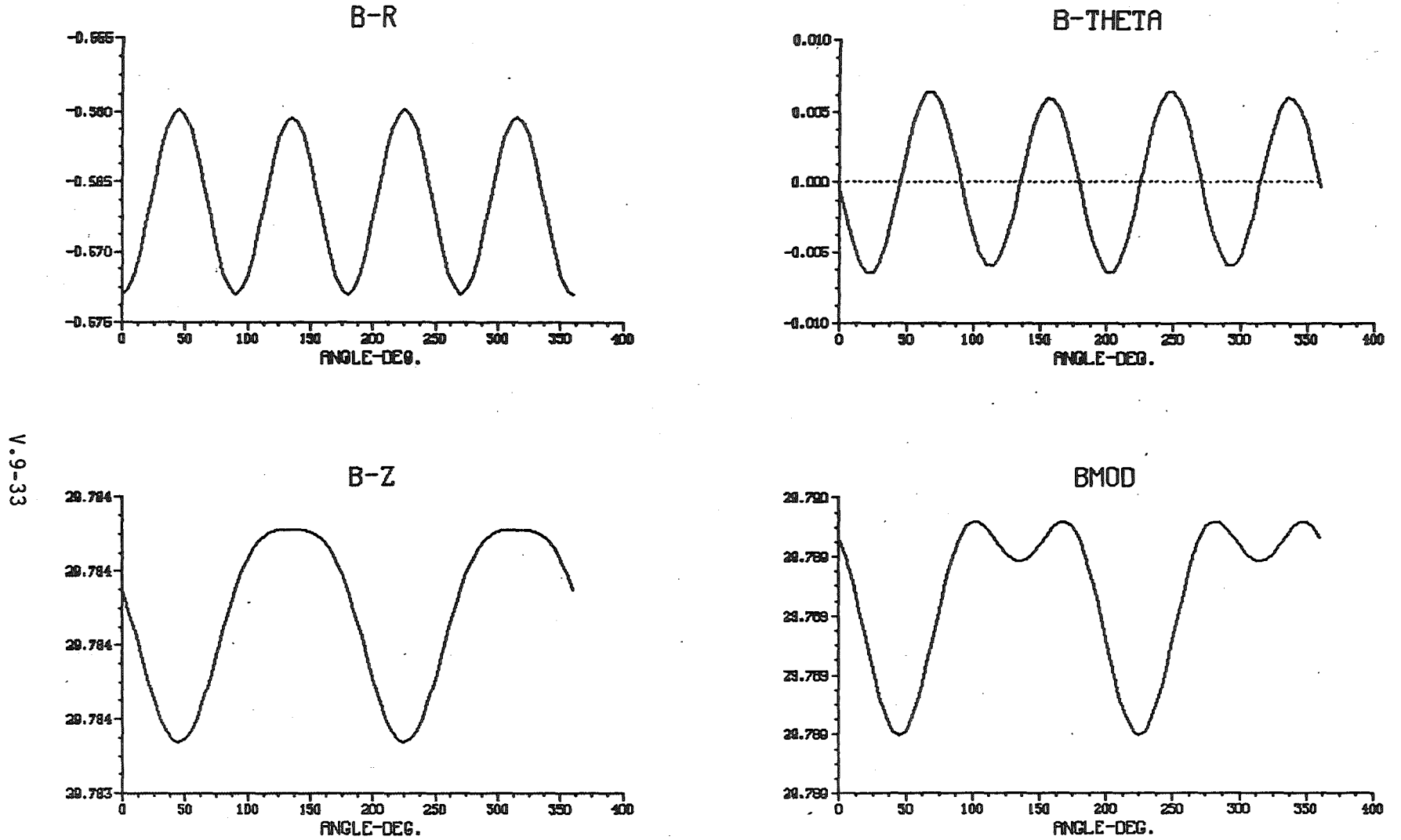


Fig. V.9-18. The magnetic field on the axis without the blanket (dashed line), and with the blanket (solid line).

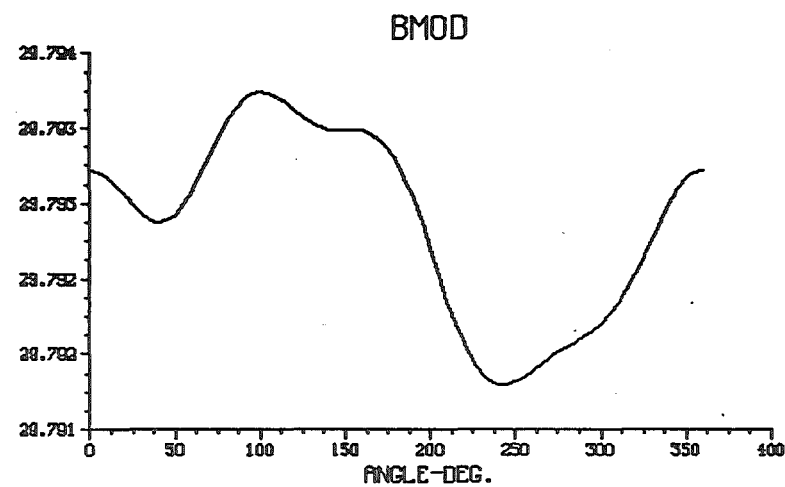
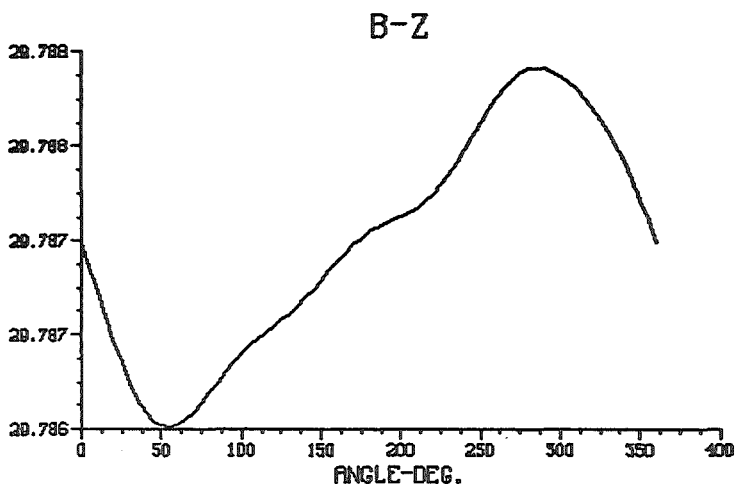
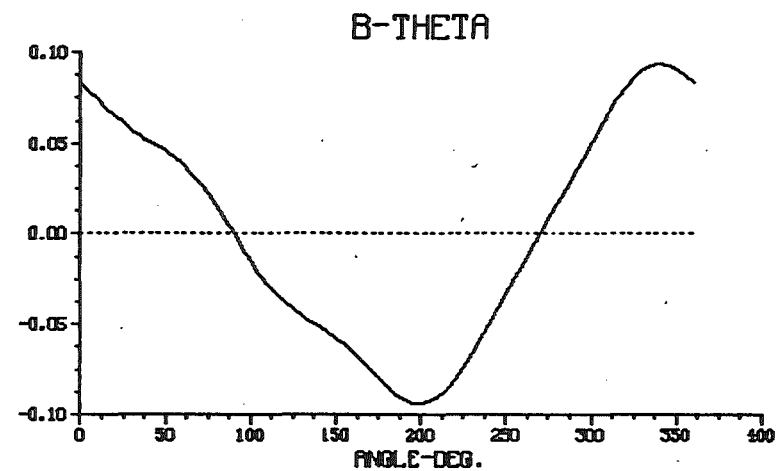
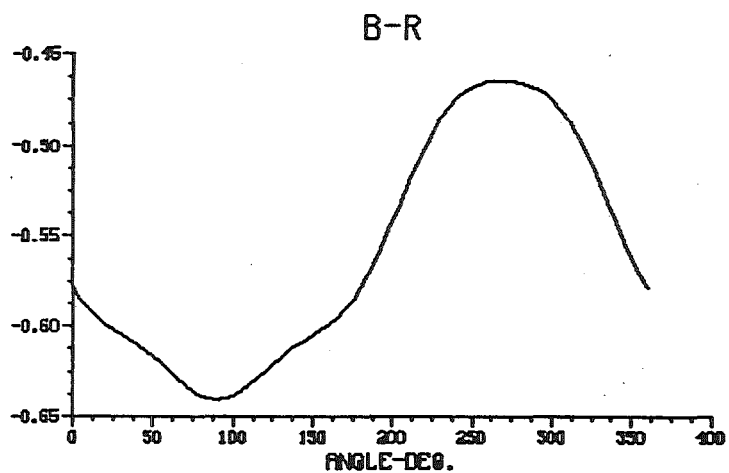


V.9-33

- 375 -

Fig. V.9-20. Field components as in Fig. V.9-19, but with the presence of the symmetrical square blanket (Fig. V.9-16).

FRAME 28, LW-GFUN LOSN1 DATE:03/03/ TIME:14:45:04 NC:32, NI: 240
X-Y PLANE Z=600.0, R= 20.0, PHI= 0.0
FIELD COMPONENTS IN K-GAUSS



V.9-34

- 376 -

Fig. V.9-21. Field components as in Fig. V.9-19, but with the presence of the asymmetric rectangular blanket (Fig. V.9-17).

- b. if the length is of the order of the outer diameter or width, then the two end zones overlap and the perturbation extends over the entire length of the blanket;
- c. the use of a homogenized magnetization is indeed justified;
- d. the temperature dependence of the saturation magnetization can be accounted for by using an average magnetization;
- e. the field perturbation near the ends of the blanket depends however strongly on the configuration, the symmetry, and the material distribution of the blanket cross section.

References for Section V.9

1. H.G. Armstrong, et al., "GFUN3D User Guide", Rutherford Laboratory, United Kingdom, RL-76-029, 1979.
2. W.F. Brown, Jr., "Magnetoelastic Interactions", Springer-Verlag, NY, 1966.
3. W.M. Stacey, Jr., "Fusion Plasma Analysis", John Wiley & Sons, NY, 1981.
4. S.J. Sackett, "User Manual of SAP4," Lawrence Livermore Laboratory, UCID-18226, 1979.

VI Central Cell

VI.1 General Design

VI.1.1 Introduction

The central cell in a tandem mirror can be regarded as the heart of the system, that is, where the useful energy is produced. Most of the fusion reactions take place in the central cell and thus it is here that fuel can be bred, thermal energy extracted and materials radiation damage tests performed. Although the end plugs are indispensable to the operation of the tandem mirror, they really play a supporting role by insuring the proper conditions within the central cell for fusion reactions to take place.

VI.1.2 Description of Central Cell

The central cell in TASKA consists of a long cylindrical structure which surrounds the plasma and is made up of a blanket, vacuum chamber, reflector and shield. This cylindrical structure fits inside three superconducting solenoids which provide the confining field within the central cell. On either end of the central cell there is an ICRF heating section, each consisting of four launching antennae. These antennae are recessed within the first wall and, therefore, do not intersect the path of charged particles streaming out toward the end plugs. The central cell coils are supported independently of the blanket/shield and are capable of being translated axially on tracks, to provide access for blanket modules located within the bore of the coils. Coolant inlet and outlet tubes, and cables are routed down into the reactor basement to free the space above for remote handling machines and the overhead crane.

An important mission of TASKA is to provide a test bed for materials and blanket system components. In order for it to be self sufficient with respect

to tritium, the blanket must have a breeding ratio greater than unity. Thus, the primary function of the central cell is to generate neutrons for the test bed. The blanket is provided for the purpose of breeding enough tritium as to make the reactor self sufficient. In a power reactor, the blanket energy is used to generate electricity. However, in TASKA, a small fraction of the blanket energy will be used to generate electricity for demonstration purposes only. The remaining energy will be disposed of.

Figure VI.1-1a shows a layout of the TASKA central cell with the blanket modules numbered 1-11 and Fig. VI.1-1b is another view of the central cell showing the intercoil structure. It can be seen that there are modules of several different shapes and lengths. The modules adjacent to the ICRF zones (1 and 11) are oversized whereas those adjacent to the REGAT module (7 and 9) are undersized. Blanket modules 2, 5, 6, and 10 have the same axial length, whereas modules 3 and 4, designated as blanket test modules, are somewhat shorter. Fig. VI.1-1b shows also that it is possible to integrate the launching antennae of the ICRF in modules of the same length as the modules 1 and 11.

The inner surfaces of blanket modules 6, 7, 9 and 10 are tapered. This was done in order to enhance and more uniformly distribute the neutron flux to the REGAT module (see Chap. VII for details). Table VI.1-1a gives the room temperature dimensions and the locations of each module. Axial distance is measured from the center of the central cell and negative numbers indicate locations to the left of the centerline. The spaces between blanket modules are also indicated on the table. It will be noted that the spaces between blanket modules 1 and 2, and 10 and 11 are 1.5 cm. The spacer between the modules 2, 3, 4 and 5 are 3 cm whereas all the other spaces are 1.0 cm. This allowance is made to account for the greater expansion of the oversized modules and with regard to the different materials of test blanket modules. Additional parameters and facts about the blanket modules are given in table VI. 1-1b.

TASKA CENTRAL CELL LAYOUT

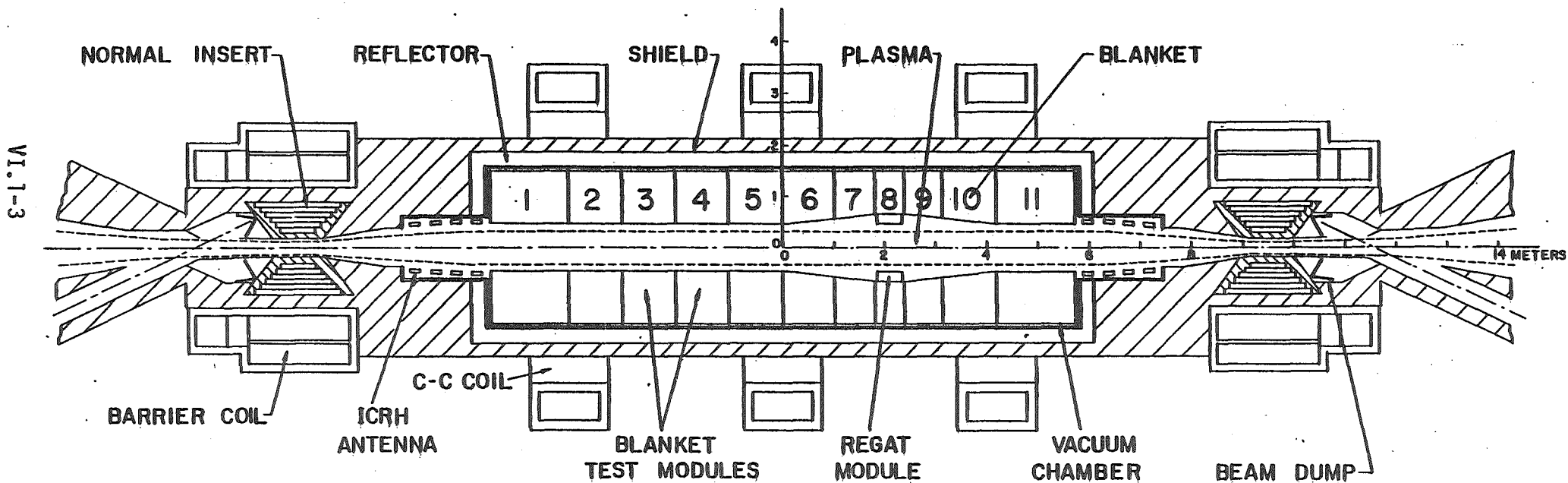
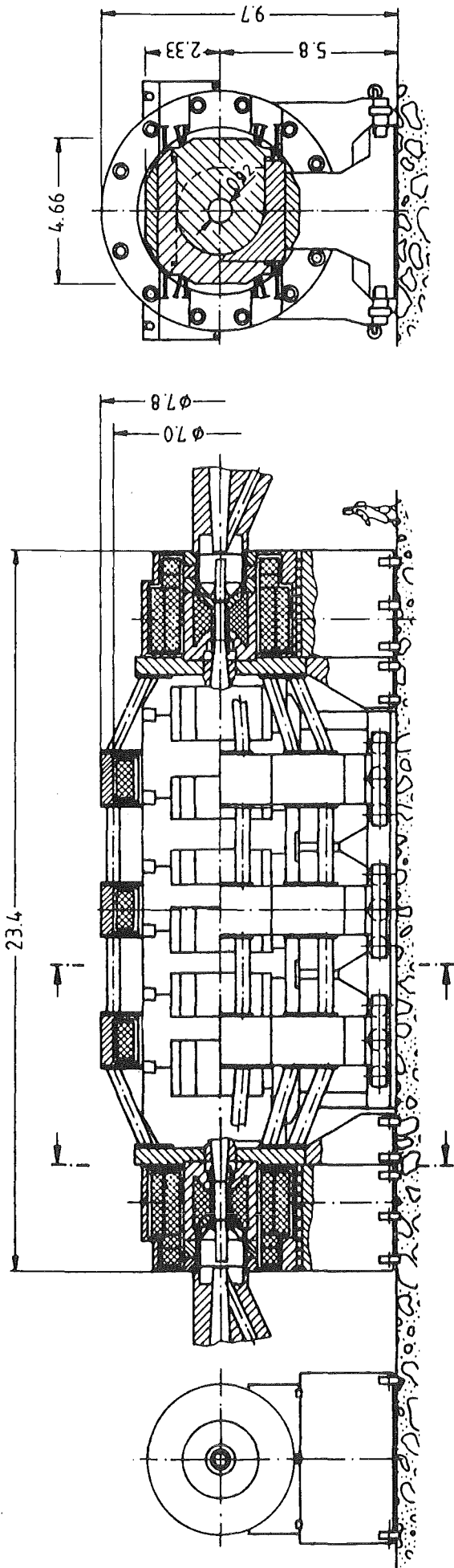
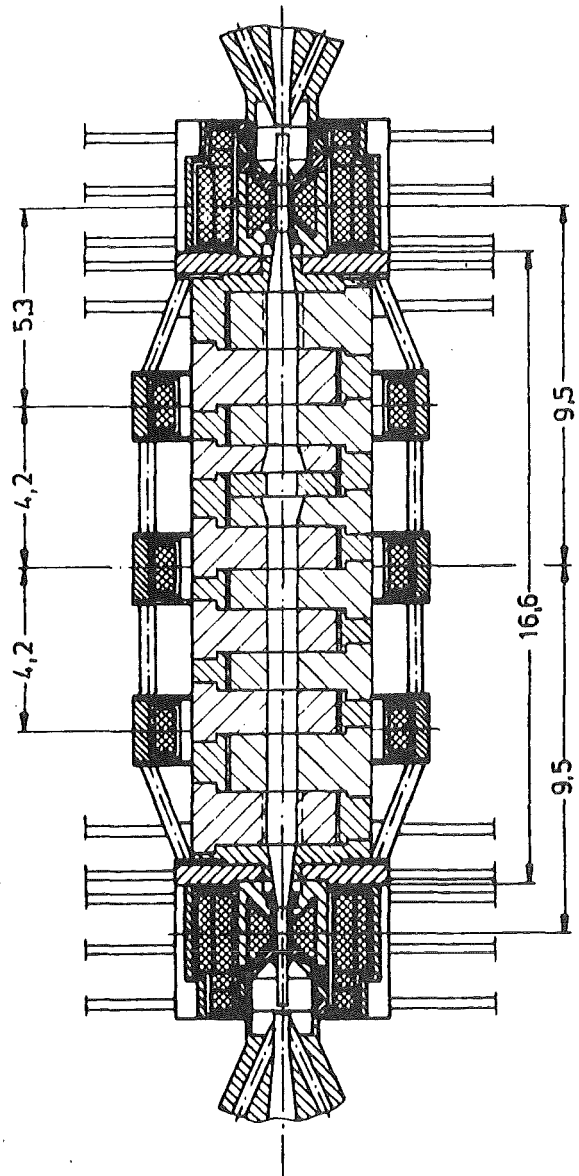


Fig. VI.1-1a Numbered blanket modules to correspond with Table VI.1-1.



VI.1-4



0 1 2 3 4 5 6 7 8 9 10m

Fig. VI.1-1.b. Central cell

Table VI.1-1a

Blanket Module Dimensions and Locations
in the Central Cell

Blanket Module Number	Location of Module Center Line (cm)	Axial Length (cm)	Inner Min. (cm)	Radius Max. (cm)	Outer Radius (cm)
1	-499.25	156.5	46		146
Space		1.5			
2	-367.50	104.0	46		146
Space		3.0			
3	-262.00	101.0	46		146
Space		3.0			
4	-158.00	101.0	46		146
Space		3.0			
5	-52.50	104.0	46		146
Space		1.0			
6	52.50	104.0	46	64	146
Space		1.0			
7	142.25	73.5	64	73.5	146
Space		1.0			
8	210.00	60.0	66		146
Space		1.0			
9	277.75	73.5	64	73.5	146
Space		1.0			
10	367.50	104.0	46	64	146
Space		1.5			
11	499.25	156.5	46		146

Table VI.1-1b

Blanket Overview

	Permanent breeding blanket A	Permanent breeding blanket B	Permanent breeding blanket C	Breeding test blanket	Material test blanket	ICRF module	
Length [m]	1,04	1,565	0,735	1,01	0,60	1,535	
Number	4	2	2	2	1	2	
Breeder material	$\text{Li}_{17}\text{Pb}_{83}$	$\text{Li}_{17}\text{Pb}_{83}$	$\text{Li}_{17}\text{Pb}_{83}$	liquid Li	—	—	
Coolant medium	$\text{Li}_{17}\text{Pb}_{83}$	$\text{Li}_{17}\text{Pb}_{83}$	$\text{Li}_{17}\text{Pb}_{83}$	liquid Li	GAS	H_2O	
Coolant	Max. pressure [MPa]	2,1	2,1	2,1	0,5 *	3,5	~ 10
	Inlet temperature [°C]	300	300	300	300	~ 100	
	Outlet temperature [°C]	400	400	400	450	~ 150	

* without MHD-losses

Blanket No. 8 is the one which backs up the REGAT module. This is a non-breeding blanket and will contain the same material composition as the shield.

The blanket modules are surrounded by a vacuum chamber made of 4 cm thick 316 stainless steel. There is a 5 cm gap between the blanket and the vacuum chamber. Rectangular flanges attached to the vacuum chamber provide the closures for the blanket modules. Adjacent blanket modules have flanges on opposite sides of the vacuum chamber such that the flanges do not overlap each other. Thus, adjacent blanket modules are inserted and removed from the vacuum chamber from opposite sides. Since blanket module removal from the vacuum chamber is in the horizontal direction, the flange surface is always oriented vertically. The only exception is in the REGAT module (No. 8) which is designed for vertical removal. The flange surface for this module is oriented horizontally at the top of the vacuum chamber.

The vacuum chamber is followed by a 28 cm thick reflector zone consisting of water cooled 316 stainless steel. The function of the reflector is to reflect neutrons back into the blanket. Each blanket module has the vacuum chamber wall combined with the reflector as the module closure which seals against the flange. This portion of the reflector is attached to and is a permanent part of the blanket module as can be seen in Fig. VI.1-2.

The last element in the central cell is the biological shield which is needed to protect the central cell solenoids and personnel during hands on operations at the fusion device, which might be possible at shut down periods. The shield is 25 cm thick and is composed of ferritic steel structure, B_4C , Pb and water cooling. The shield part adjacent to the blanket module closure is also attached to the module as shown in Fig. VI.1-2. Table VI.1-2 gives the central cell engineering parameters.

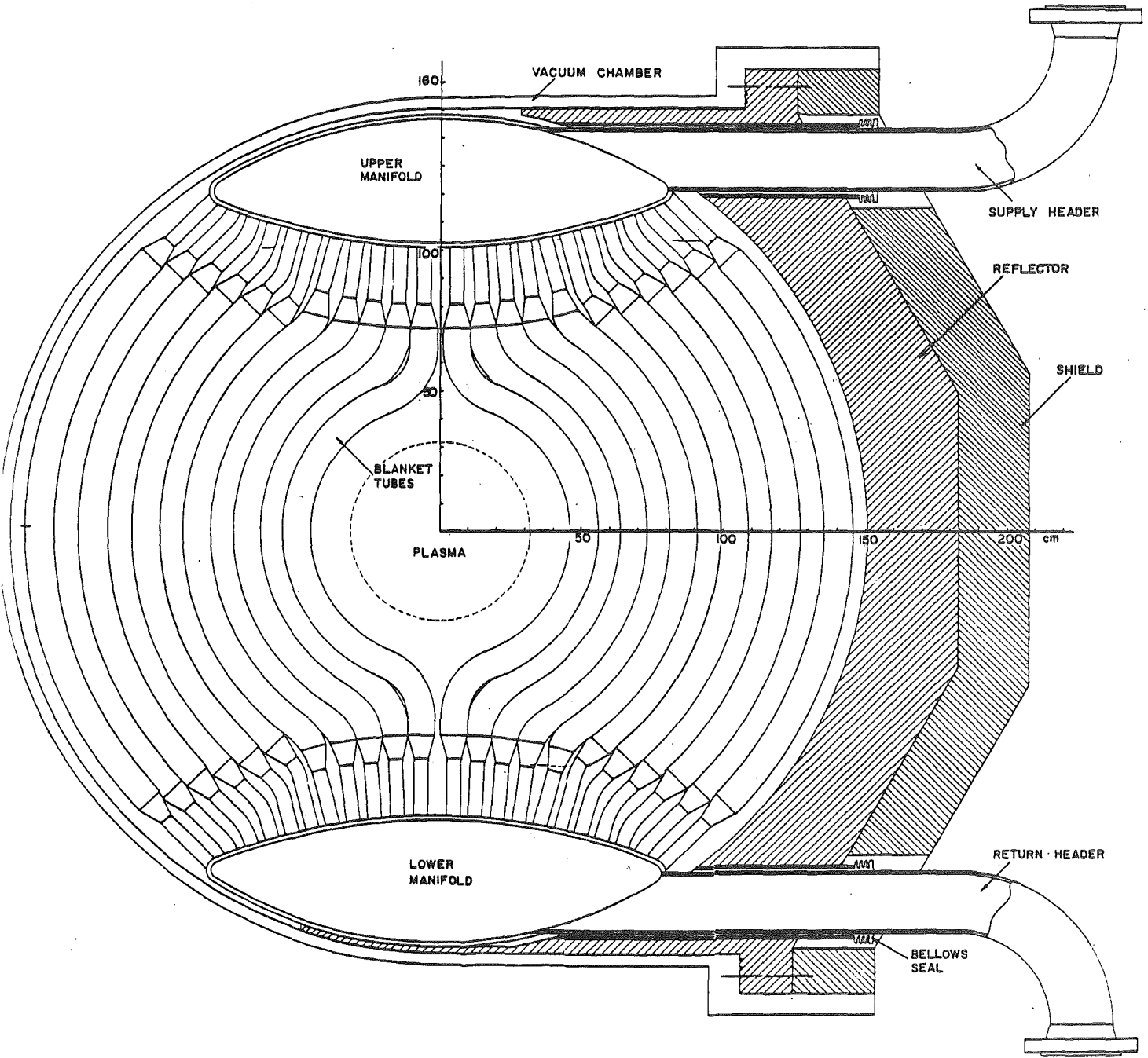


Fig. VI.1-2. Vertical section of TASKA blanket

Table VI.1-2. Central Cell Engineering Parameters

*Central cell length (Physics definition) (m)	19.2
**Central cell length (Engineering definition) (m)	16.7
Blanket inner diameter (m)	0.92
Permanent breeding zone length (m)	8.76
ICRH zone length (m)	3.07
Blanket test module length (m)	2.02
Material test module length (m)	0.60
Breeding blanket first wall area (m ²)	25.32
ICRH launching area (m ²)	8.49
Blanket test module first wall area (m ²)	5.84
Material test module first wall area (m ²)	1.44
Blanket thickness (m)	1.0
Vacuum chamber inner diameter (m)	3.02
Vacuum chamber wall thickness (m)	0.04
Reflector thickness (m)	0.28
Shield thickness (m)	0.25

*Distance between magnetic peaks.

**Distance between inner edges of superconducting barrier coils.

VI.1.3 Evolution of TASKA Blanket Design

The TASKA blanket design has undergone several iterations. Although there have been minor modifications along the way, there have been four major design changes since the first proposed blanket. These changes are shown graphically in Fig. VI.1-3 and are designated A-E. Heavy arrows indicate the direction of blanket module removal from the central cell. The reasons for the design changes are given in capsule form on Fig. VI.1-3 and will be further discussed in the following sections.

The blanket initially proposed for TASKA (designated "A" in Fig. VI.1-3) was similar to that used in WITAMIR,⁽¹⁾ a tandem mirror power reactor conceptual design completed at the University of Wisconsin in 1980. In this blanket, the breeding material came into a manifold at the top, then flowed down through tubes on both sides of the plasma, finally collecting in the bottom manifold where upon it was pumped to a steam generator. The removal scheme for these blanket modules was from the top. This was practical in WITAMIR because both shield enclosure and the reactor building were evacuated. There was no separate vacuum chamber. Blanket modules were removed in designated locations along the central cell and were translated axially to these locations within the shield.

Such a scheme did not seem practical for a materials test reactor, where frequent access to the plasma chamber will be needed. For this reason it was decided to provide TASKA with a separate vacuum chamber, and because it would be difficult to design overlapping closures for top removal of all the modules, it was proposed that alternating sideways removal be adopted instead. This led to the design designated "B" in Fig. VI.1-3.

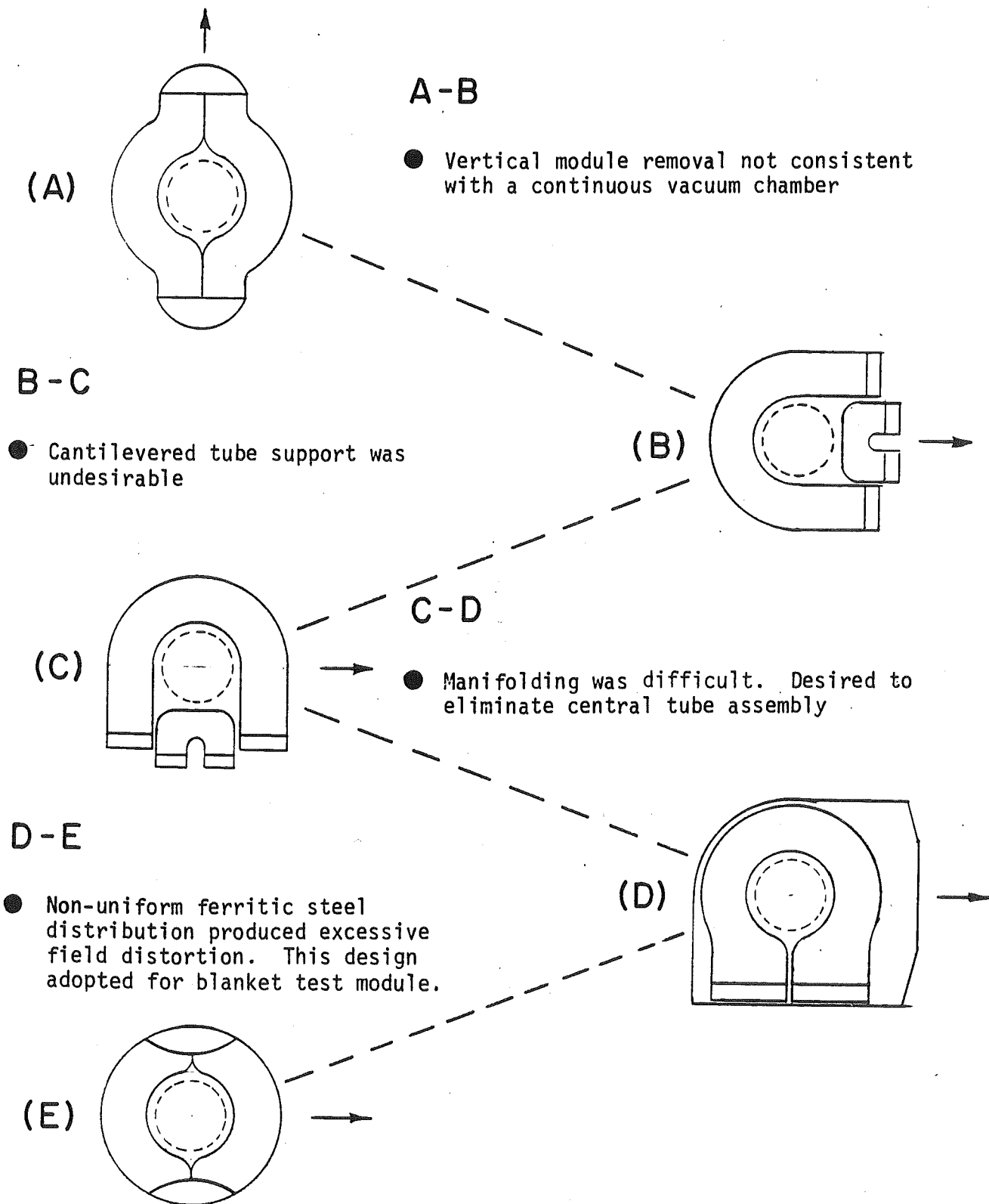


Fig. VI.1-3. Evolution of TASKA breeding blanket design

The new design retained the tubular structure but in a U-shaped configuration oriented sideways. The coolant thus flowed around the plasma on three sides and a separate segment of tubes was needed to fill the void in the U and cover the fourth side. The undesirable feature of this design was the unsupported tubes which were essentially cantilevered. It was also recognized that the MHD pressure drop would be somewhat higher in this design, although the effect was not that great. A solution to the unsupported tubes problem was proposed in which essentially all the features of the "B" design were retained but the blanket was rotated 90°, such that the U shape was oriented vertically with the open space on the bottom. This design is designated "C" in Fig.

VI.1-3.

The "C" design was carried along in the course of the study for a long time and it will be noticed that many of the analyses in the TASKA report are predicated on it. The transition to "D" came in the final detailed blanket design version. In the detailed design it was concluded that it was difficult to manifold the additional segment of tubes needed to close the U. The new design "D" has tubes circumventing the plasma completely such that the additional segment of tubes was no longer needed. Furthermore, the new design had a casing which completely enclosed the blanket tubes on all sides. The casing was stepped on all sides in such a way as to prevent primary neutron streaming and was designed to match the steps in the adjacent blanket modules inserted from the opposite direction.

Design "D" appeared to be destined for final adoption except for one flaw. Since the material proposed for the blanket was the ferritic steel HT-9, the magnetic field code for ferritic steels, GFUN, (which became operational late in the study) predicted major field distortions in the plasma envelope due to

the grossly uneven distribution of steel in the "D" design. One other problem with the "D" design was the potential for neutron streaming through the space between manifolds, however, appropriately placed shield material can circumvent this problem. This design was adopted for the blanket test module (see Section VII.3).

Another design of the blanket subject to a near uniform distribution of ferritic steel and the constraints of a fixed blanket material composition resulted in the "E" design. This design comes as close as possible to a near uniform distribution of ferritic steel while still retaining the good features of the "C" and "D" designs. Although the casing has been eliminated, the tube and manifolds are stepped in such a way as to prevent streaming. A detailed design has been performed and will be discussed in the next section.

VI.1.4 Mechanical Description of Central Cell Components

VI.1.4.1. Blanket Design

The breeding blanket design for TASKA is shown in Fig. VI.1-2 and Fig. VI.1-4.

Figure VI.1-2 is a vertical cross section through the center of a module showing eleven rows of tubes on either side of the plasma. The end of each tube is attached to a smaller diameter tube by means of a conical transition section. The small diameter tube is then attached to the manifold.

The innermost tubes face the plasma on one side and are, thus, an effective first wall. The sharp bend radius toward the manifold is equal to four times the tube radius which is consistent with the minimum bend radius that can be produced without buckling the tube wall. All the other tubes have bend radii which are larger.

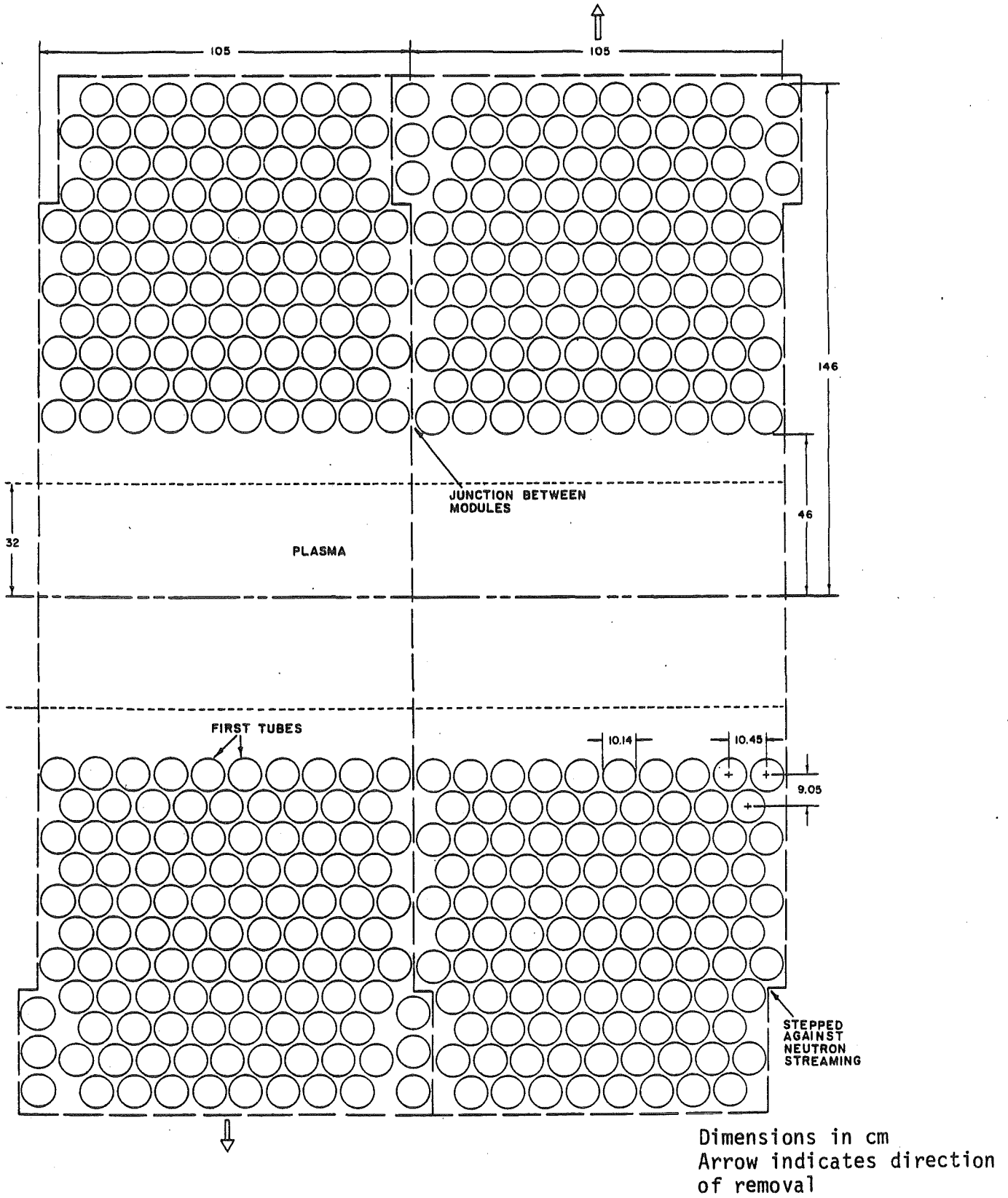


Fig. VI.1-4 Horizontal section through two blanket modules.

The outer diameter of the tubes is 10.14 cm and the wall thickness is 0.227 cm. The transition tubes are 5 cm OD and have a wall thickness of .175 cm. The axial centerline distance between tubes is 10.45 cm and the radial centerline distance is 9.05 cm.

Figure VI.1-4 is a horizontal cross section through two adjacent modules showing the stepping in the tubes where the modules interface. It also shows the staggering of tubes needed to allow the two modules to slide relative to each other at this interface. The missing tubes add to the void fraction within the blanket. The actual volumetric fractions in the blanket were based on a segment extending from one module centerline to the other, thus covering the interface between them. These fractions are 73% breeding material, 7% HT-9 structure and 20% void. The same proportions were also maintained in the blanket quadrant covering the manifold.

The modules shown in Fig. VI.1-4 have 104 cm axial length and have a blanket thickness of 1 m. The radius to the front surface of the first tube is 46 cm. There are ten tubes in the front row and a total of 208 tubes in each module. A separation of 1 cm per meter was allowed between modules at room temperature. At operating temperature the gaps close to ~ 0.4 cm. Modules will be keyed in the center such that they will expand equally in both directions axially. From Fig. VI.1-1 it can be seen that there are three different axial lengths of blanket modules. For example, modules 1 and 11 are 156.5 cm long and have 15 tubes in the front row, whereas modules 7 and 9 are 73.5 cm long, and, if they were not conical, would have had seven front tubes.

This brings up the question of how a tapered effect can be produced with the proposed tubular construction. It will be recalled that the tapered blanket shape is needed to enhance and more uniformly distribute the neutron

flux to the REGAT module. Figure VI.1-5 shows how tubes can be eliminated in progressive rows in order to achieve this effect. A smooth tapered wall is not necessary to achieve the enhancement effect, rather a more extensive view of the plasma is needed, with reflection from the bulk of the blanket behind the tapered surfaces.

The manifolds in each module consist of two arcs joined at the points of intersection. The manifold walls are 1.7 cm thick. It is necessary to step the top half of the manifolds in order to prevent neutron streaming in the vertical direction. This is illustrated in Fig. VI.1-6. Table VI.1-3 gives all the pertinent mechanical parameters of the TASKA blanket.

A few words must be said about the question of whether or not casings are needed for the blanket modules. The only argument in favor of a casing for the blanket modules is the vacuum argument. This is a very important issue which cannot be ignored or deemphasized. Arguments against providing a casing are many, not the least of which is the design complication created by the need for cooling the casing. Thus, it appears that the need for a casing can only be justified on the basis of the vacuum requirement.

As far as vacuum requirements go, the casing performs two functions:

1. It reduces the exposed surface area which may be a source of impurities.
2. It isolates the long narrow channel between the tubes from the plasma chamber.
3. It simplifies leak detection and reduces consequences of leaks at tubes and manifolds which might occur after a certain time of operation.

It is clear that in fabricating the blanket good high vacuum system practices have to be followed. This implies that weldments must be full penetration, leaving no reentrant cracks which can be sources of impurities. Furthermore, the blanket module must undergo a series of cleaning operations such as degreasing and pickling. After this, the blanket module must be baked

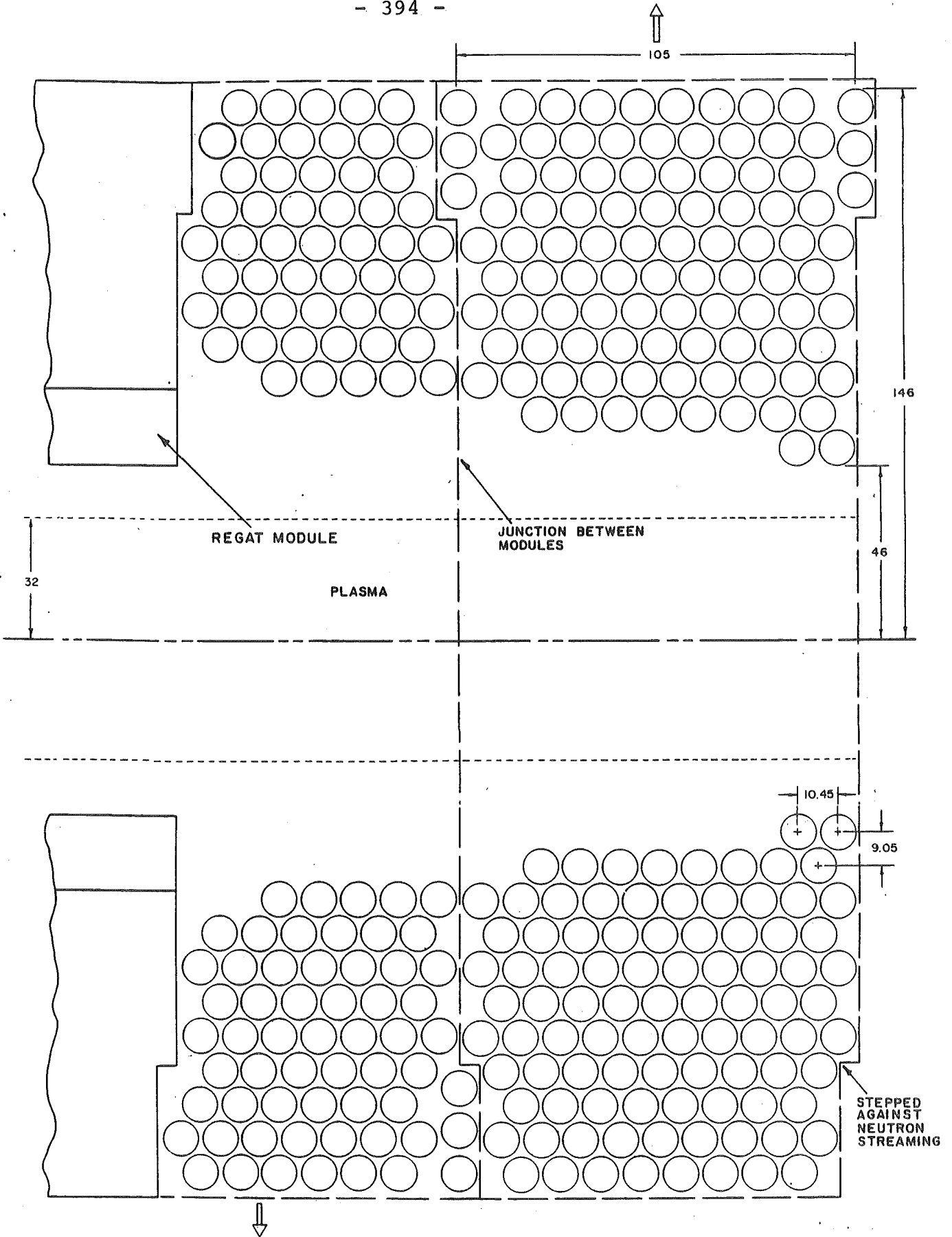


Fig. VI.1-5 Blanket shaping near REGAT modules.

STEP IN ADJACENT BLANKET
MODULE MANIFOLDS

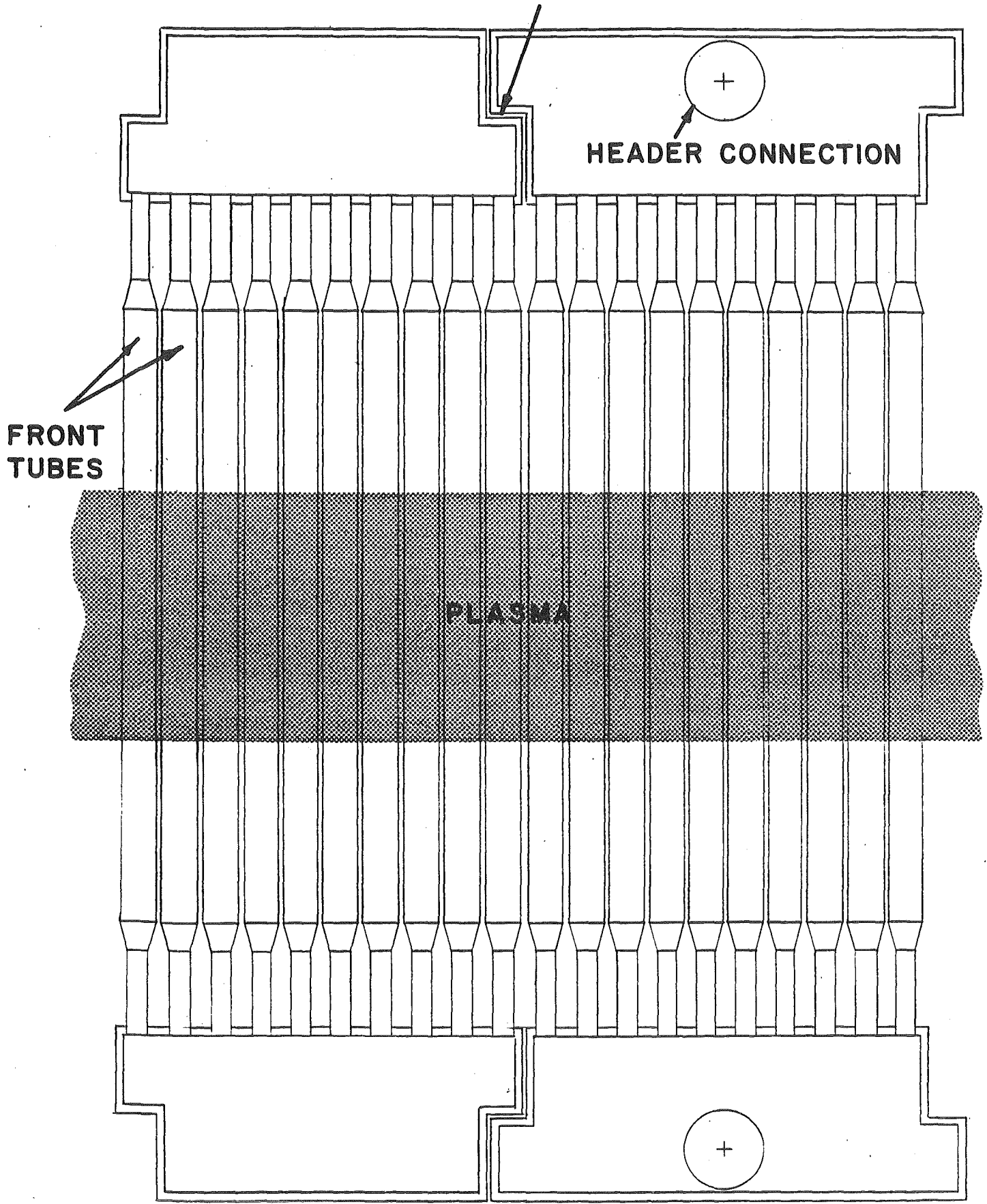


Fig. VI.1-6 Vertical section in the axial direction showing manifold stepping.

Table VI.1-3. Pertinent Mechanical Blanket Parameters

Blanket material	HT-9
Tube outer diameter (cm)	10.14
Tube wall thickness (cm)	0.227
Axial tube centerline distance (cm)	10.45
Radial tube centerline distance (cm)	9.05
Transition tube outer diameter (cm)	5.0
Transition tube wall thickness (cm)	0.175
Number of tubes per module	208
Manifold wall thickness (cm)	1.7
Tube surface area/m of cc (m ² /m)	140
Volume of Li ₁₇ Pb ₈₃ /m of cc (m ³ /m)	4.45
Mass of structure/m of cc (kg/m)	3293

in a special oven at a temperature of $\sim 600^{\circ}\text{C}$ for 10-20 hours. Transfer of the module to the reactor must be under conditions which will insure cleanliness. In situ backing of the blanket modules while the chamber is evacuated will also be necessary. With such preparation, the outgassing rate of mild steel can be reduced to $\sim 10^{-9}$ Pa $\text{m}^3/\text{sec m}^2$.(2)

The total tube surface area in TASKA is $\sim 1600 \text{ m}^2$. Using this outgassing rate the total gas throughput from the exposed surface is 1.3×10^{-5} torr ℓ/s . The total vacuum throughput of TASKA will be on the order of 10-100 torr ℓ/s . It is evident that the level of impurities from the wall will be no more than $1 \times 10^{-3}\%$ of the throughput. Furthermore, the bulk of the contaminants will be CO or CO_2 which will dissociate at 100 eV and will travel within the plasma halo out of the reactor.

The second area of concern is the evacuation of the spaces between the tubes. In the case of the TASKA design, the space is equivalent to a 2 cm diameter tube, with the longest path being 1 m long. This $\frac{L}{R}$ ratio of 100 gives a transmission probability of $\sim .03$ if the sticking coefficient is assumed to be zero.(3) This effectively means that if the bulk of the chamber is evacuated to 10^{-7} torr, the innermost recesses of the spaces between the tubes will only reach a pressure of 3×10^{-6} torr as long as there is a source of molecules present. Since at these pressures there will be several monolayers of molecules on the surface, a sticking coefficient of zero is reasonable to assume.

The initial baking and evacuation of the chamber after it had been exposed to atmospheric pressure will, therefore, require a long time, perhaps as long as 24-48 hours. However, once the reactor is in operation, the surfaces will be covered with hydrogenous species and helium. It would not be

detrimental to the operation of the reactor if the hydrogenous species pressure within the spaces between the blanket tubes was somewhat higher than in the plasma scrapeoff zone.

It is significant to note that experience on TMX has shown that only surfaces in close proximity to the plasma are sources of impurities whereas surfaces further removed do not seem to contribute. If this is true, then a casing will only be marginally helpful or not at all.

Although a casing can be incorporated into the present design, for the present we feel that it will not be needed. This brings up the question of how a leak can be determined in a blanket system without casings. Obviously, each module inlet and outlet coolant headers will require shut-off valves to provide the capability of isolating any one module from the rest of the system. Further, a capability must be provided for pressurizing each individual blanket with a suitable gas which can be detected with a mass spectrometer. After the breeding material is drained out of the modules, they can be individually pressurized and the leak isolated.

As in the previous designs, the blanket modules will be supported on the bottom, with the load path being through the vacuum chamber wall to the reflector and shield. Finally, the load is transferred to the structure attached to the floor of the reactor hall. Because of the substantial load which must be transferred through the bottom manifold, it will require some internal reinforcing. This reinforcing will be in the form of plates oriented perpendicular to the axis of the reactor. Care must be exercised to insure that the plates will not impede the flow of breeding material or add substantially to the overall system pressure drop.

Just looking at a normal blanket module of 104 cm axial length, it is interesting to note that the mass of the breeding material will be ~ 43.6 tonnes and the structure ~ 3.4 tonnes. These values do not include the masses of reflector and shield which will be part of the module. Nevertheless, once the breeding material is drained out of the module, there will be a substantial reduction in mass.

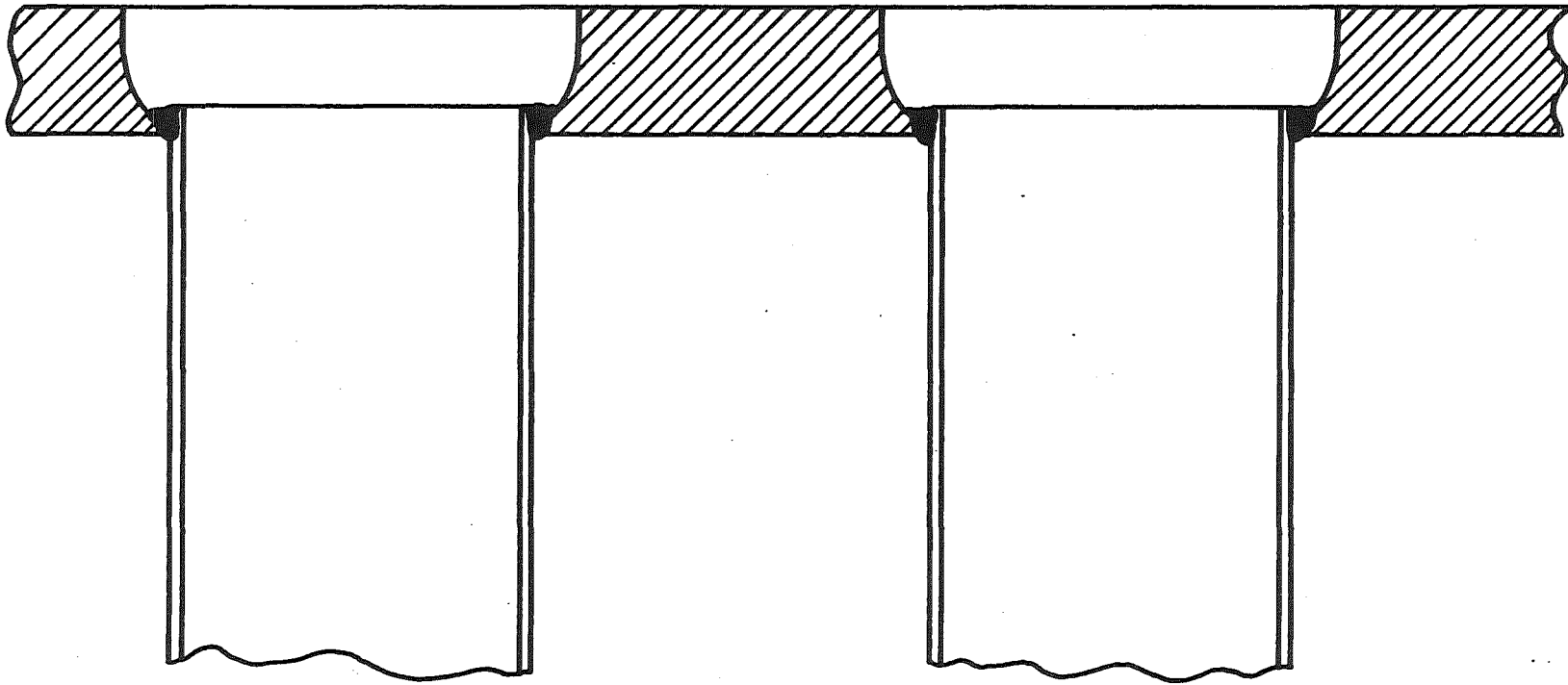
A few words must be said about the fabrication of such a blanket. We feel that the fabrication is relatively simple and well within present day technology.

The design calls for only 13 shapes of tubes. Fabrication of the tubes themselves will be fairly simple and can be made on a production line basis. The conical connectors are identical for all the tubes; however, the lengths and bends in each of the 13 shapes are different. A common method for bending tubes of this nature is to fill them with a soft material such as indium or woods metal, and then put them through dies which progressively bend them until the desired shape is achieved. The woods metal is then melted out and the tube cleaned in preparation for welding.

Joining sections of tubes together is performed with external welding. However, joining the tubes to the manifold plate will be done from the back side. Fig. VI.1-7 is a full scale drawing of how this can be accomplished. Notice that there are no reentrant gaps on the side where the tube is attached to the manifold. It is absolutely essential that there be no reentrant gaps at the points of attachment which can become sources of trapped gas.

It will also be noticed that the penetration into the manifold is always perpendicular to the tangent at that point. This will facilitate the assembly of the modules. The holes into the manifold plate are relieved as shown in Fig. VI.1-7, with

Welding is done from this side



VI.1-22

- 400 -

Fig. VI.1-7 Full scale drawing of how blanket tubes are welded to the bottom manifold plate.

the tube penetrating only part of the way. This will make it possible to insert the tubes individually rather than trying to assemble the whole module all at once.

When the tubes are all welded, the back side of the manifold is assembled and welded. The final step in the blanket assembly is the attachment of the header to the manifold. This is accomplished by welding from the outside. Finally, the assembly will be heat treated.

VI.1.4.2 Vacuum Chamber Design

The vacuum chamber in TASKA is a water cooled 4 cm thick walled cylinder of 151 cm internal radius. It is made of 316 stainless steel and surrounds the blanket. In this way the vacuum chamber wall is effectively protected from radiation damage. The chamber has rectangular flanged openings which alternate from one side to the other along the length of the central cell (see Fig. VI.1-8a). These openings allow the blanket modules to be inserted and removed from the vacuum chamber. The part of the reflector which is attached to the blanket module makes a seal with the vacuum chamber flange as shown in Fig. VI.1-2.

In the vicinity of the ICRH antennae, the chamber necks down to a radius of 59 cm at a distance of 582.5 cm from the center of the reactor. This radius is maintained for 165 cm after which another necking down to a radius of 37 cm occurs. At this point the chamber is attached to the transition section leading to the barrier coil.

VI.1.4.3 Reflector Design

The reflector in TASKA is a 28 cm thick water cooled slab of 316 stainless steel. Actually there are three segments to the reflector as shown in Fig. VI.1-8b:

1. The segment which constitutes the closure in each module.
2. The bottom segment which is part of the support path for the blanket.

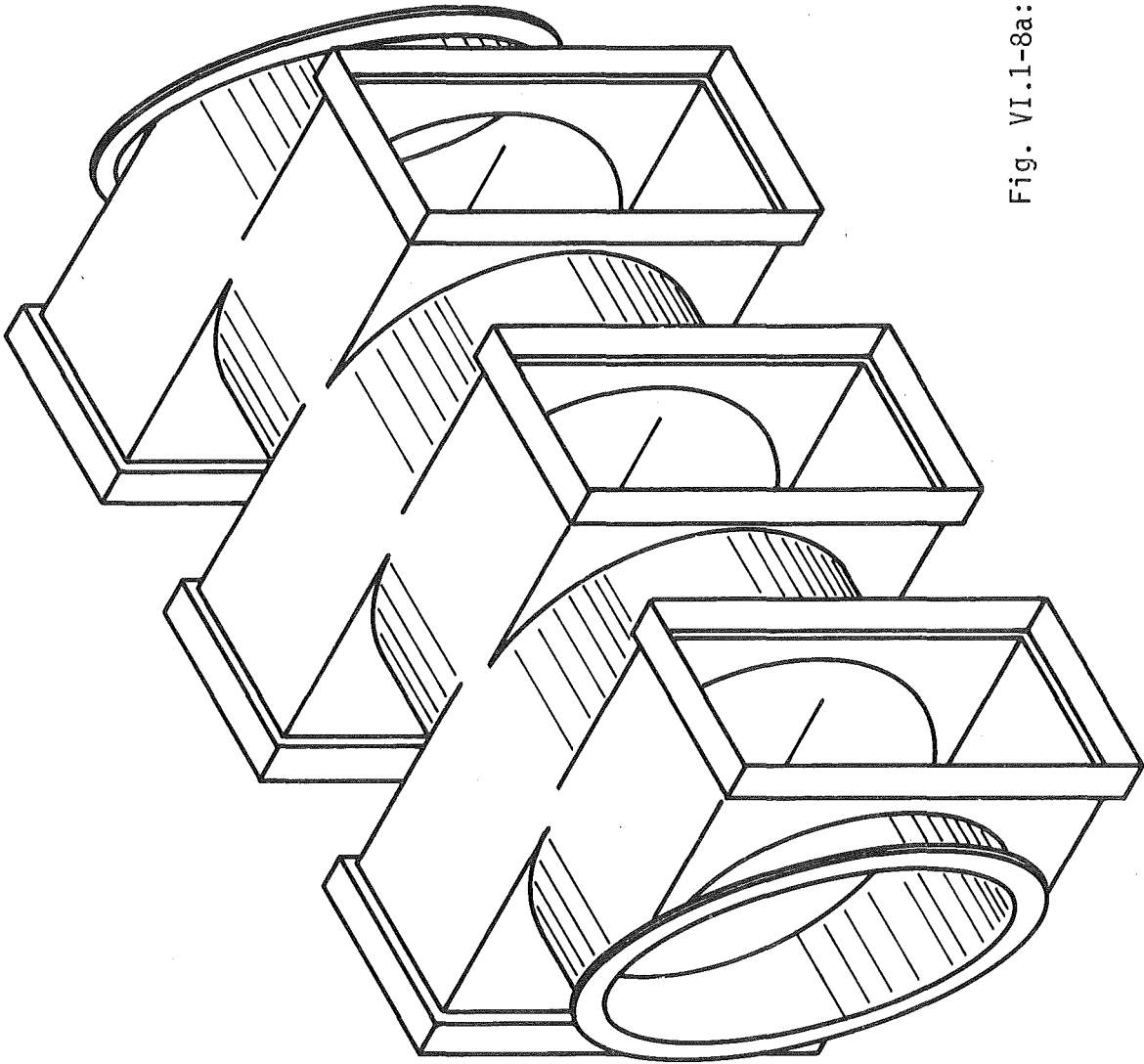
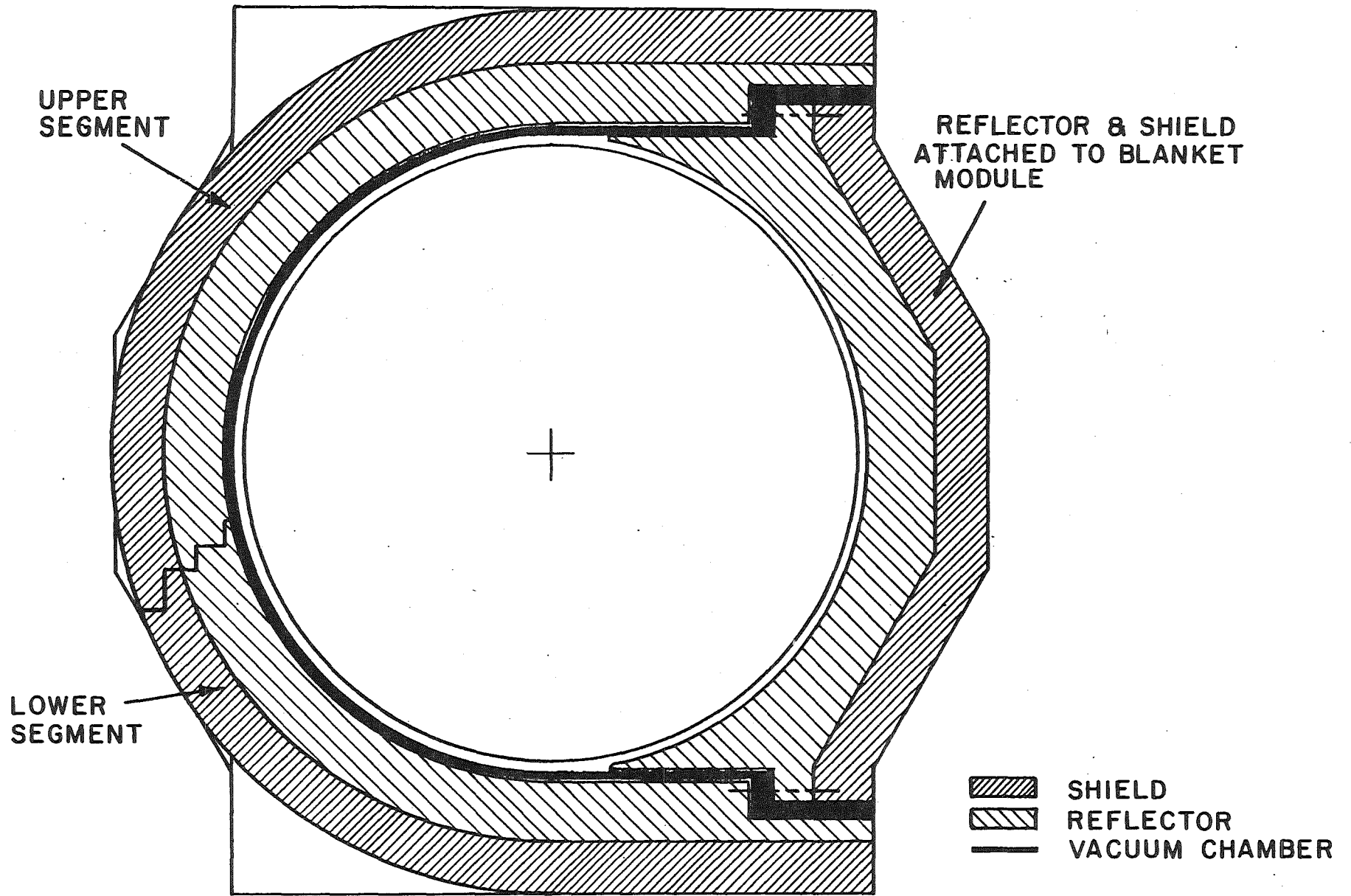


Fig. VI.1-8a: Vacuum chamber

VI.1-24



- 403 -

Fig. VI.1-8b Reflector and shield segmentation.

3. The top and side segment. This segment is designed to be removable to make it consistent with the central cell maintenance scheme.

Figure VI.1-9 shows how the reflector can be fabricated. It essentially consists of 20 cm thick sections of stainless steel that have cooling passages machined in the sides. Holes drilled through tube sections at either extremities will allow the cooling water to traverse the assembly from one end to the other. The assembly is then bolted together and the junctions between the slabs welded shut. The bolt head and nut penetrations are also welded shut. The number of cooling water traverses depends on the size of the segment. Large pieces may have several supply and return connections.

One complication arises in the area where the blanket header has to penetrate the reflector. Here the coolant must traverse the slab above (or below) the penetration and a sleeve is used to seal off the penetration as shown in Fig. VI.1-10. A bellows is then used to seal the header to the sleeve in the reflector.

The shape of the reflector which is part of the blanket module is shown in Fig. VI.1-3. It will be noticed that it is thicker than the specified 25 cm thickness. The reason for that is the fact that the 4 cm thick vacuum wall is included in the reflector. This segment of the reflector also constitutes the closure for the blanket module, for it is the seal in the flanges between the reflector and the vacuum chamber which is the vacuum barrier. It is envisaged that this will be a double metal seal with an evacuated space in between.

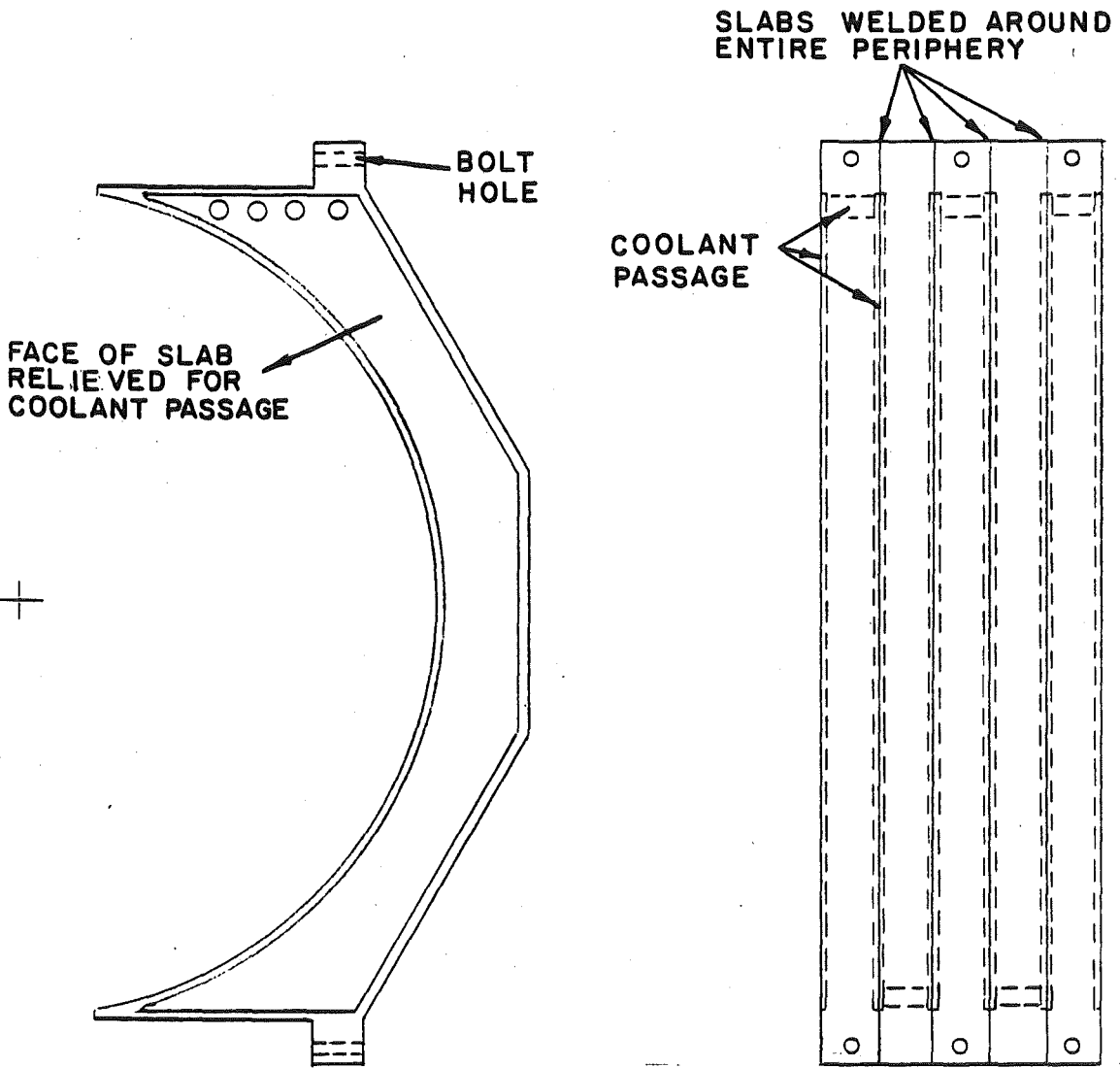


Fig. VI.1-9 Reflector fabrication

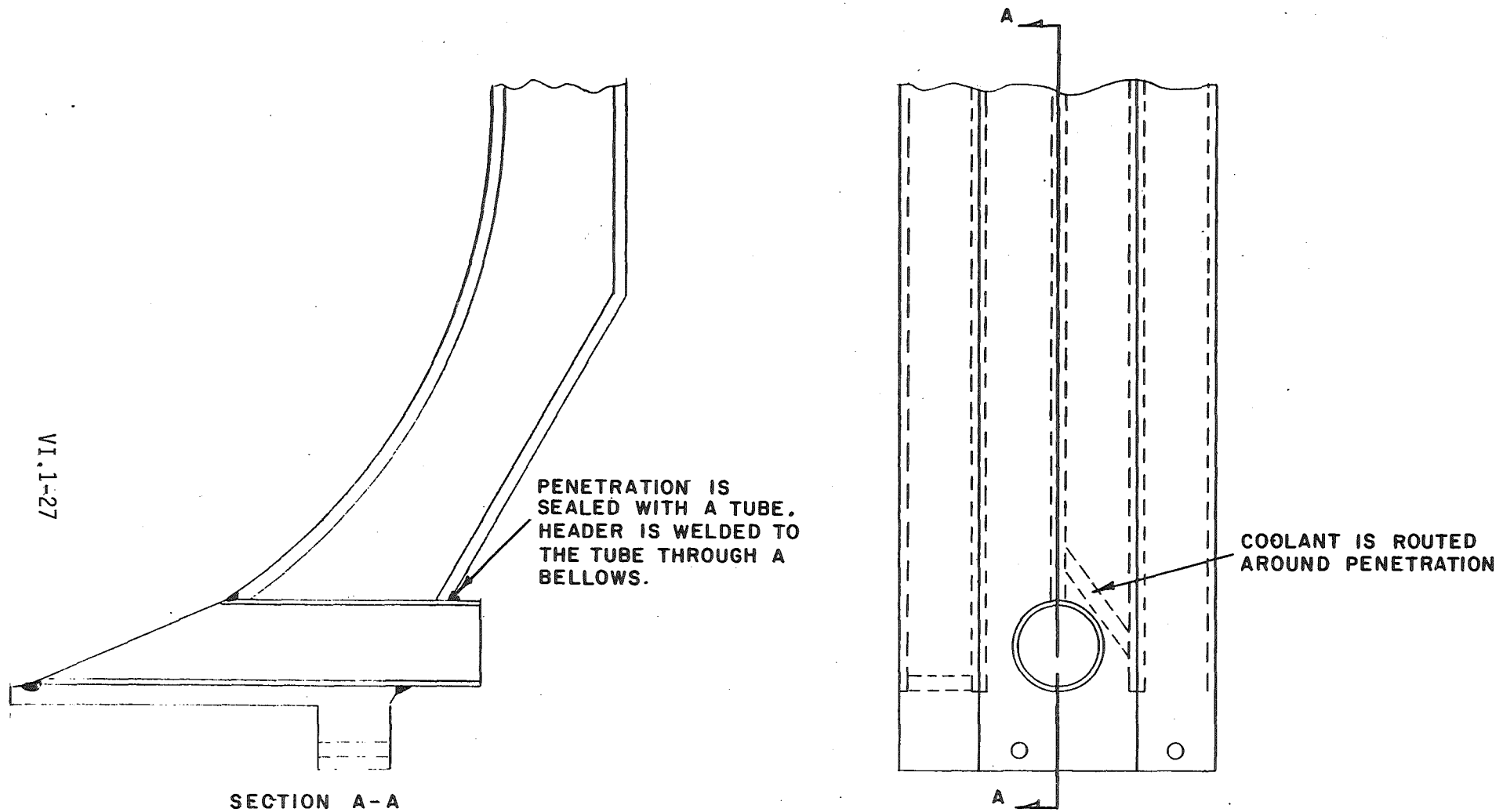


Fig. VI.1-10 Design of penetration through reflector closure for the blanket module.

VI.1.4.4 Shield

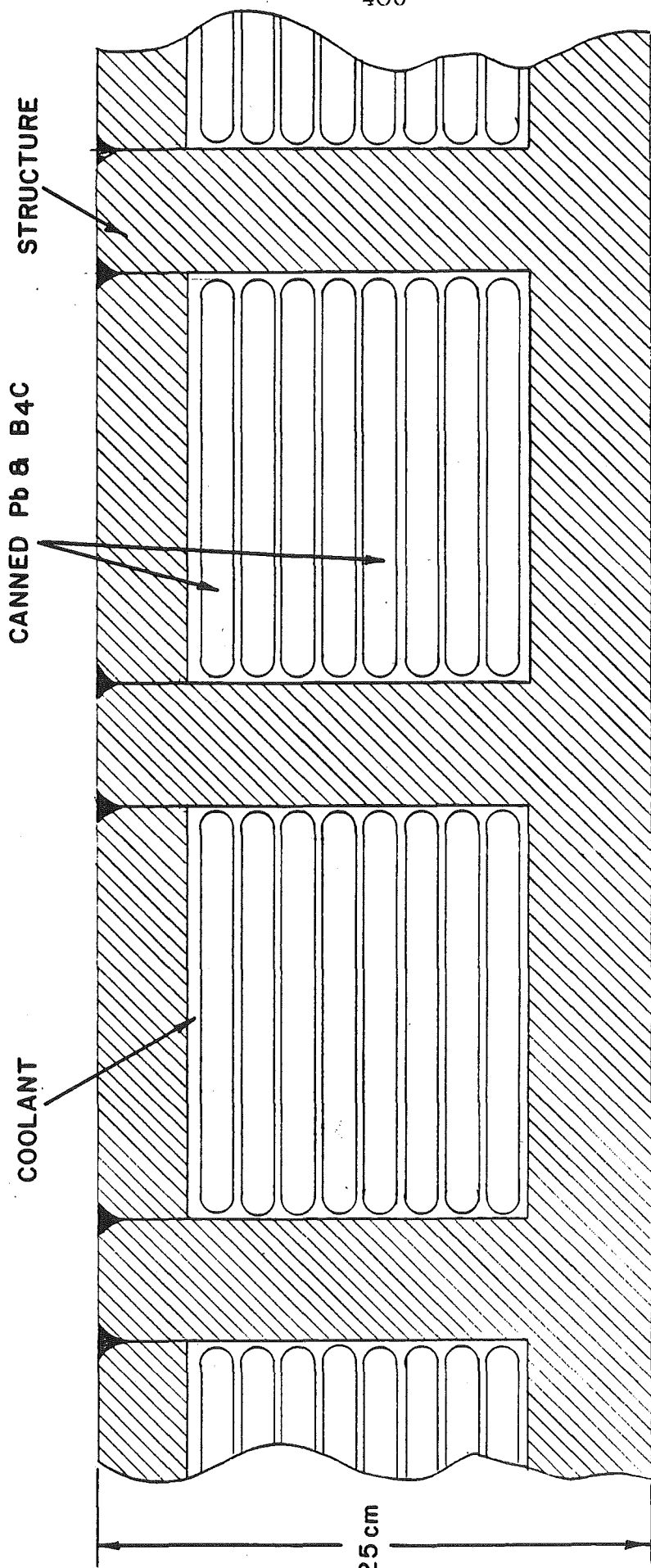
The shield in the central cell is 25 cm thick and is composed of 56% 1422 ferritic steel, 26% B_4C , 14% Pb and 4% cooling water. One possible shield geometry is shown in Fig. VI.1-11. The heavily ribbed structure can be oriented parallel to the chamber axis. The pockets will be filled with canned slabs of B_4C and Pb in the appropriate proportion with spaces in between for cooling water. The pockets are then capped off and welded shut.

Nuclear heating in the shield will be low enough to allow low velocity and low pressure water cooling. Thus, water traversing one shield pocket from one end to the other will be routed onto the next, snaking its way around the shield. In this way a minimum amount of coolant connections will be necessary.

The shield will also be divided into three segments, the same as the reflector (see Fig. VI.1-8). One segment will be permanently attached to the blanket module closure. The bottom segment constitutes some of the support structure for the central cell. The upper and the side opposite the blanket closure will be made into a continuous shield segment. An important aspect of the shield is to prevent neutron streaming, and to that end, the shield must have overlapping steps between adjacent shield segments.

The shield has to be self supporting, since the vacuum chamber is not strong enough to support it. Thus, the segments must be bolted together and must form a continuous self supporting structure.

Elsewhere in the reactor, the shield will vary in thickness from one place to another. With some variation, the same type of shield construction can be used in these areas as well.



25 cm

VI.1-29

Fig. VI.1.11 Possible shield design.

References for Section VI.1

1. B. Badger, et al., "WITAMIR-I, A Tandem Mirror Reactor Study", University of Wisconsin Fusion Engineering Program UWFDM-400 (Sept. 1980).
2. L. Holland, W. Steckelmacher, and J. Yarwood, "Vacuum Manual", E&FN Spon, London.
3. C.G. Smith and G. Lewin, "Free Molecular Conductance of a Cylindrical Tube With Wall Sorption", PPPL, Oct. 1965, Vol. 3, No. 3, Journal of Vacuum Science & Technology.

VI.2 Neutronics

VI.2.1 Design Goals

The neutronics design goals include adequate volumes and neutron fluences for the requirements of the materials and engineering test zones, tritium breeding, magnet and penetration shielding, and acceptable access to the building following shutdown. Energy production is given a low priority as achieving the other goals will ensure adequate heating for testing power conversion modules. The test zones are discussed in other sections of this report. The permanent blanket and shield are assessed in Section VI.2.2 with both one- and three-dimensional calculations. The special problems connected with shielding in the barrier and plug regions are taken up in Section VI.2.3. Radioactivity produced during operation is described in Section VI.2.4. A natural lithium test blanket design is discussed in Section VI.2.5.

VI.2.2 Central Cell Permanent Blanket

It was felt that even though the power level of TASKA is modest and purchase of tritium from outside sources would be possible without an unmanageable economic impact, it would nevertheless be much more impressive if breeding was also achieved. This could easily be accomplished by a larger power rating where the test zones were a smaller perturbation on the central cell. As the reactor is made smaller while meeting the demands of the test zones, adequate breeding becomes difficult. The good breeding performance achieved with $\text{Li}_{17}\text{Pb}_{83}$ in earlier studies made in connection with the WITAMIR⁽¹⁾ design led us to choose this material as the breeding material in TASKA. HT-9 was chosen as the structural material. As little HT-9 was used as possible while meeting structural demands in order to enhance breeding. A schematic of the central cell is shown in Fig. VI.1-1. The permanent blanket and its associ-

ated shield can be represented approximately by the one-dimensional schematic, Fig. VI.2-1. The general composition of the various regions are given in Table VI.2-1, including some that refer to a three-dimensional model of the entire central cell. The relatively large void fractions in the blanket are due to the tube configurations for the coolant-breeding material as shown in Fig. VI.1-4. The neutron and gamma fluxes for the one-dimensional model were calculated using the ONEDANT⁽²⁾ discrete ordinates code on the MFE computer at LLNL. The data base is XSLIBA⁽³⁾ (a 30 neutron - 12 gamma energy group cross section library⁽⁴⁾) and the problems were run in the S_4 - P_3 approximation.

Key results from these calculations include the heating and radiation damage results for thermal hydraulic and materials design. The power density as a function of radius is shown on Fig. VI.2-2. The peak power density is 11 W/cm^3 and falls rapidly into the blanket. The radiation damage as measured by the displacements per atom per full power year (dpa/FPY) as a function of the radius is shown in Fig. VI.2-3. It should be noted that the result is normalized to correspond to a wall loading of one megawatt per square meter. Thus if the time to reach a particular dpa is required, the result at a given radius using the dpa/FPY from the figure must then be divided by the actual wall loading in MW/m^2 (1.52 in the present case) and multiplied by the capacity factor. The peak dpa rate in the first wall is 14.8 dpa per full power year. On the basis of this model, the tritium production as a function of position is given on Fig. VI.2-4.

Prior to this final calculation with the above model, several calculations were carried out to determine the shield thickness based on protection of the superconducting magnets. The magnet limits are set by several criteria: deterioration of insulation such as mylar and epoxy with dose, the

Fig. VI.2-1
Central Cell

	Radius (cm)
	0

Plasma	
-----	32
Vacuum	
-----	46
F.W.	46.3

Blanket	
-----	146
Vacuum	151

Vacuum Tank	155

Reflector	183

Shield-A	196.95

Shield-B	204.5

Shield-C	208

Void	270

Mylar	280

Magnet	338

Void	1550

Concrete Shield	1700

Table VI.2-1

Region	Thickness (cm)	Composition
First Wall	0.3	100 v/o HT-9
Breeding Blanket	100	73 v/o $\text{Li}_{17}\text{Pb}_{83}$ 7 v/o HT-9 20 v/o void
Blanket Test Modules	100	73 v/o Li (nat.) 7 v/o AS 1.4970 20 v/o void
REGAT Module	20	20 v/o NaK 40 v/o 316 SS 15 v/o H_2O 25 v/o void
Vacuum Tank	4	100 v/o 316 SS
Reflector	28	90 v/o 316 SS 10 v/o H_2O
Shield-A	13.95	95 v/o Fe 1422 5 v/o H_2O
Shield-B	7.55	86 v/o B_4C 10 v/o Fe 1422 4 v/o H_2O
Shield-C	3.5	100 v/o Pb
Concrete Shield	200	87 v/o Ordinary Concrete 8 v/o Steel Reinforcement 5 v/o H_2O

Fig. VI.2-2

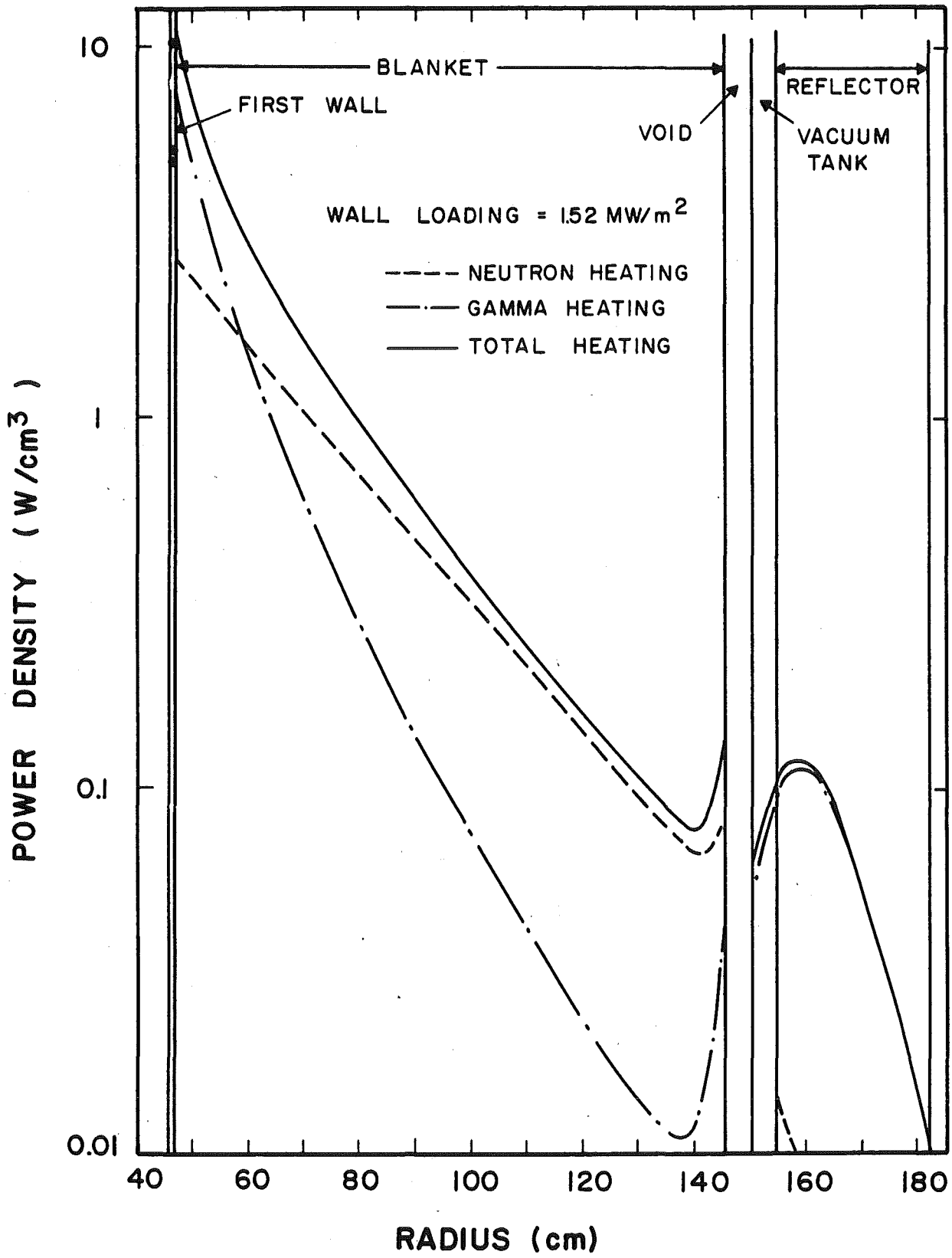


Fig. VI.2-3

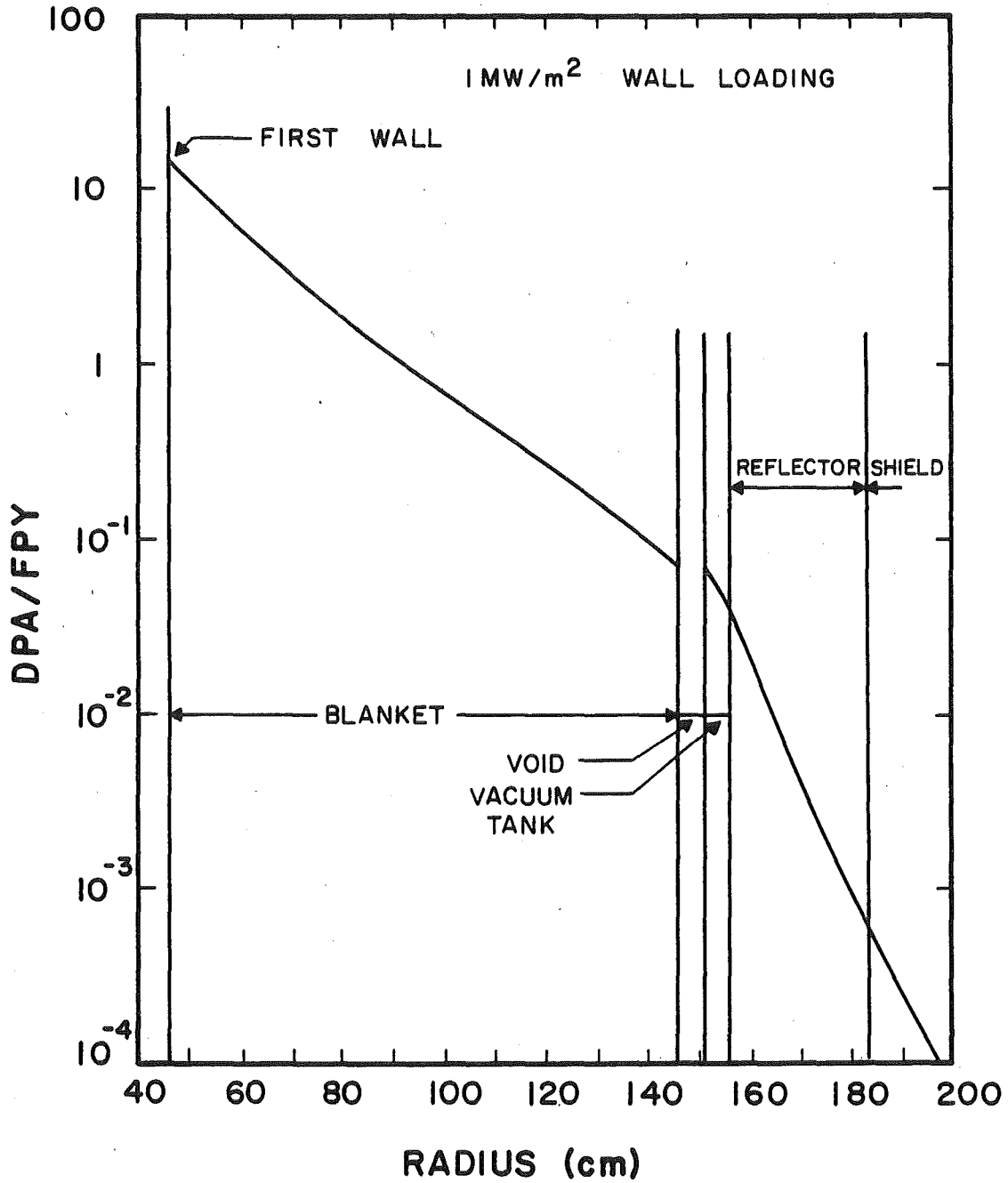
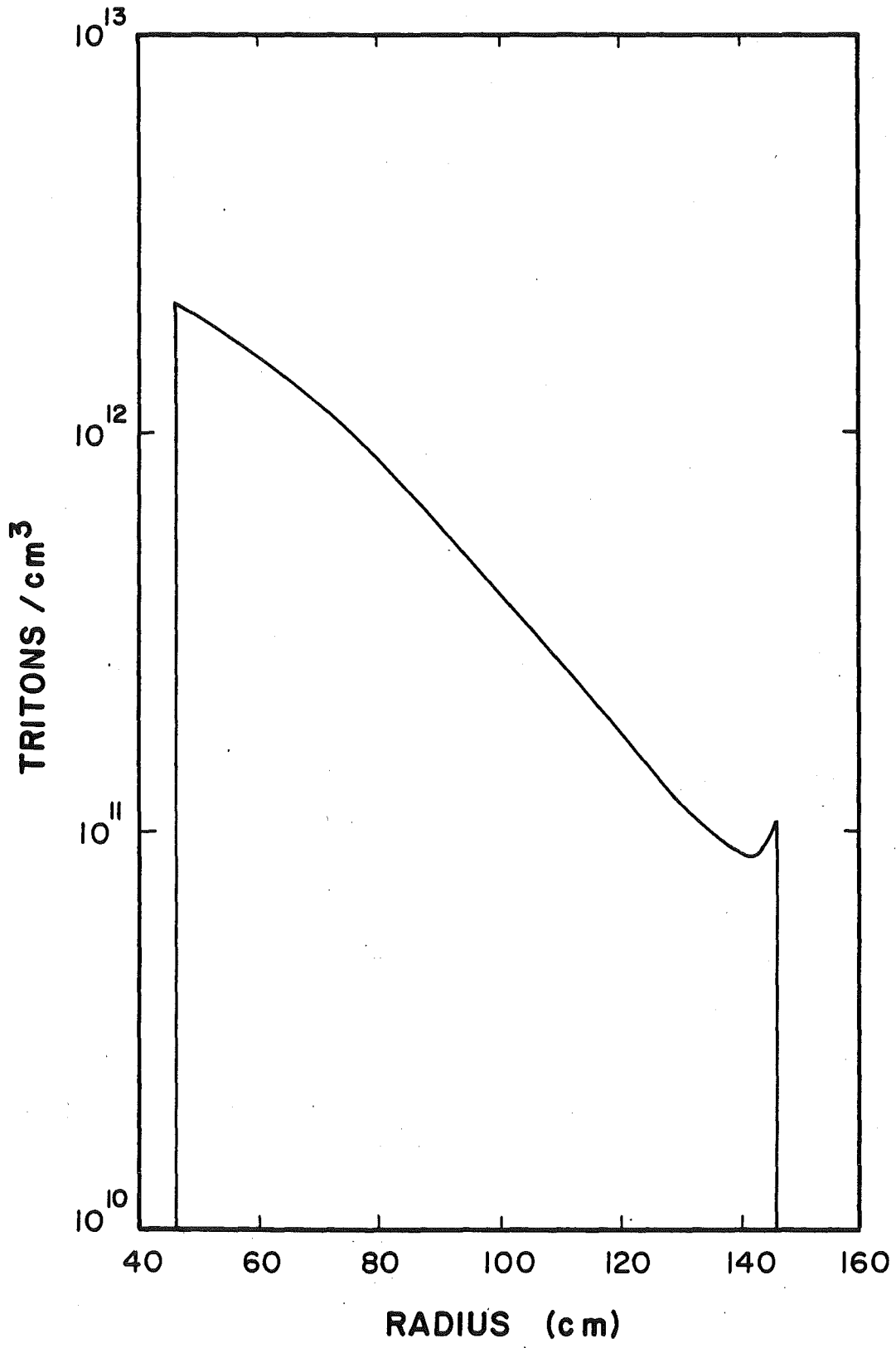


Fig. VI.2-4



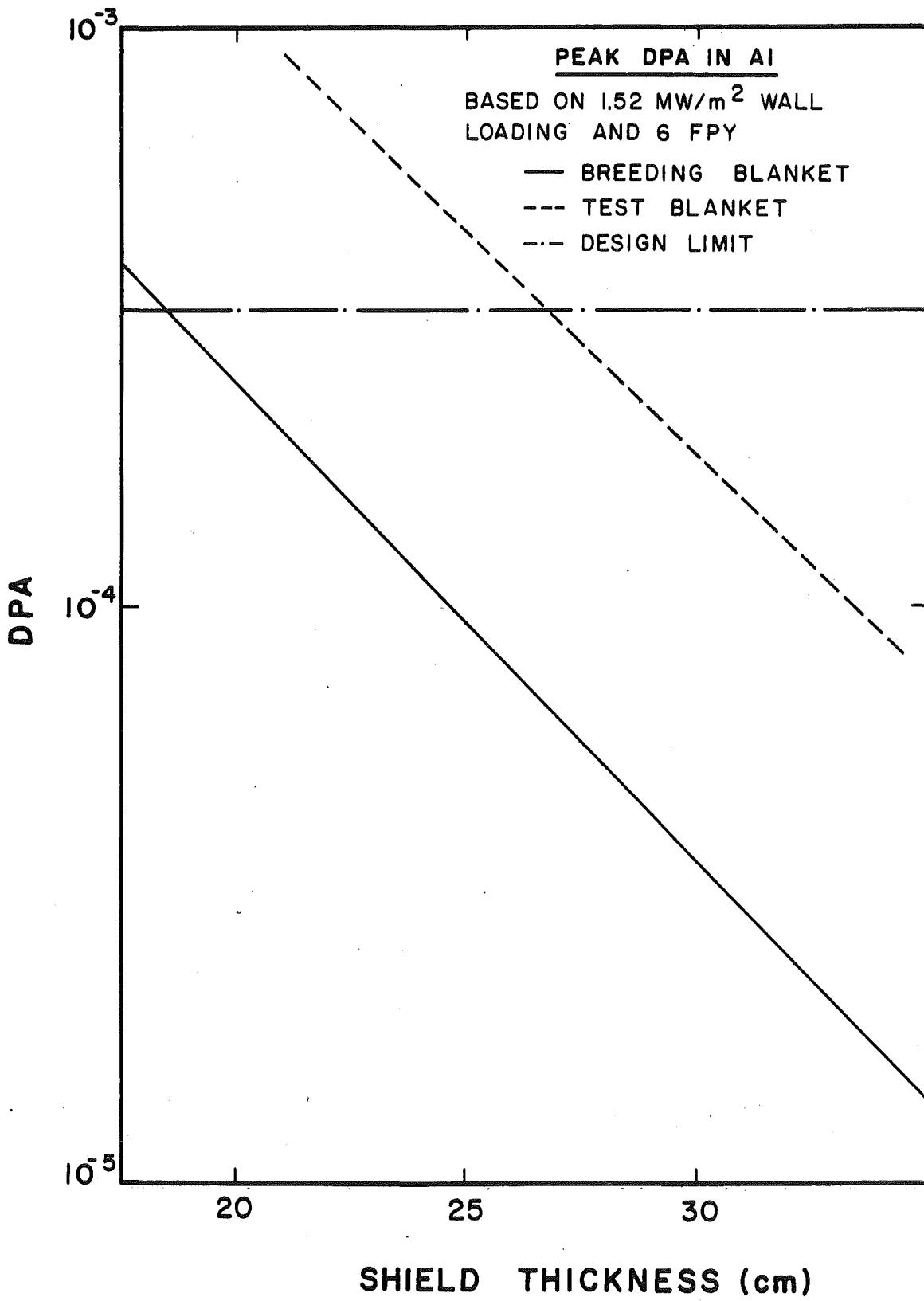
cryogenic heat load, and resistivity increases in the stabilizer for the superconductor. Dose limits for mylar and epoxy are taken as 10^{10} and 5×10^9 Rad, respectively. The coil design is based on the resistivity of the aluminum stabilizer not exceeding $10^{-7} \Omega \text{ cm}$. Since the resistivity of high purity aluminum is $10^{-8} \Omega \text{ cm}$, the induced resistivity (ρ_r) due to irradiation should not exceed $9 \times 10^{-8} \Omega \text{ cm}$. For aluminum⁽⁵⁾ the induced resistivity is given by

$$\rho_r = 8 \times 10^{-7} [1 - \exp(-366 d)] \Omega \text{ cm}$$

where d is the displacements per atom. With this set equal to $9 \times 10^{-8} \Omega \text{ cm}$, the value of d is $3.26 \times 10^{-4} \text{ dpa}$. Once this value of d is reached, the magnet must be annealed to ensure proper performance. Calculation for several shield thicknesses yields the dpa results shown on Fig. VI.2-5. On the basis of this, the shield thickness was set at 0.25 m which yields $9.4 \times 10^{-5} \text{ dpa}$ in 6 FPY for the permanent blanket. Since TASKA is only expected to operate for 5.3 FPY this is more than adequate. The second curve representing the shield behind a test blanket corresponds to $4.5 \times 10^{-4} \text{ dpa}$ on the same basis. This would imply annealing before starting the last year of operation. However, the latest designs do not call for magnets behind the test modules. The dose values in the mylar and epoxy are $1.85 \times 10^7 \text{ Rad/FPY}$ and $1.61 \times 10^7 \text{ Rad/FPY}$, well below the design limits. Other data of interest are the peak helium and hydrogen production rates in the iron of the first wall. These are 107.1 and 347.6 appm/FPY, respectively. Finally based on this model, the peak biological dose outside the concrete shield is 1.12 mR/hr.

The tritium production and total heating in the central cell are based on three-dimensional continuous energy calculations. These were performed using

Fig. VI.2-5



the Monte Carlo code MCNP⁽⁶⁾, and the Recommended Monte Carlo Cross Section (RMCCS) library⁽⁷⁾ on the MFE computer at LLNL. The coupled neutron and gamma ray model was used and results are based on 4,000 histories giving relative errors of less than 5%. As the plasma density varies in the central cell, barrier, and plug regions, so does the neutron source density. The radius of the plasma also varies. Assuming a flat profile, the source is uniform to the plasma boundary. Weighting the source density by the area of the cross section leads to the linear source density shown on Fig. VI.2-6. This can be approximated as constant in the central cell, but is fortunately much weaker in the barrier and plug zones. The Monte Carlo modeling of the central cell and nearby barrier regions has been carried out. A view emphasizing the central cell is shown on Fig. VI.2-7. This model and the related calculations give a tritium breeding ratio of 1.04. The region-wise details of the tritium production are shown in Table VI.2-2. With the same region-wise description the energy deposition in MeV/fusion neutron is given on Table VI.2-3. This results in the rather low blanket energy multiplication of 1.06. However, as pointed out earlier, this was not a design issue.

In summary, the central cell blanket and shield meet all the goals stated at the beginning of this section. The breeding margin is not great, but is probably adequate and relatively modest design changes could increase the breeding if necessary. Other performance goals have substantial margins for error.

VI.2.3 Barrier Region

The barrier region contains the narrow throat area at the end of the central cell as shown in Fig. VI.2-8. The constriction is caused by the very high (20 T) magnetic field. This field is produced by a system of coils

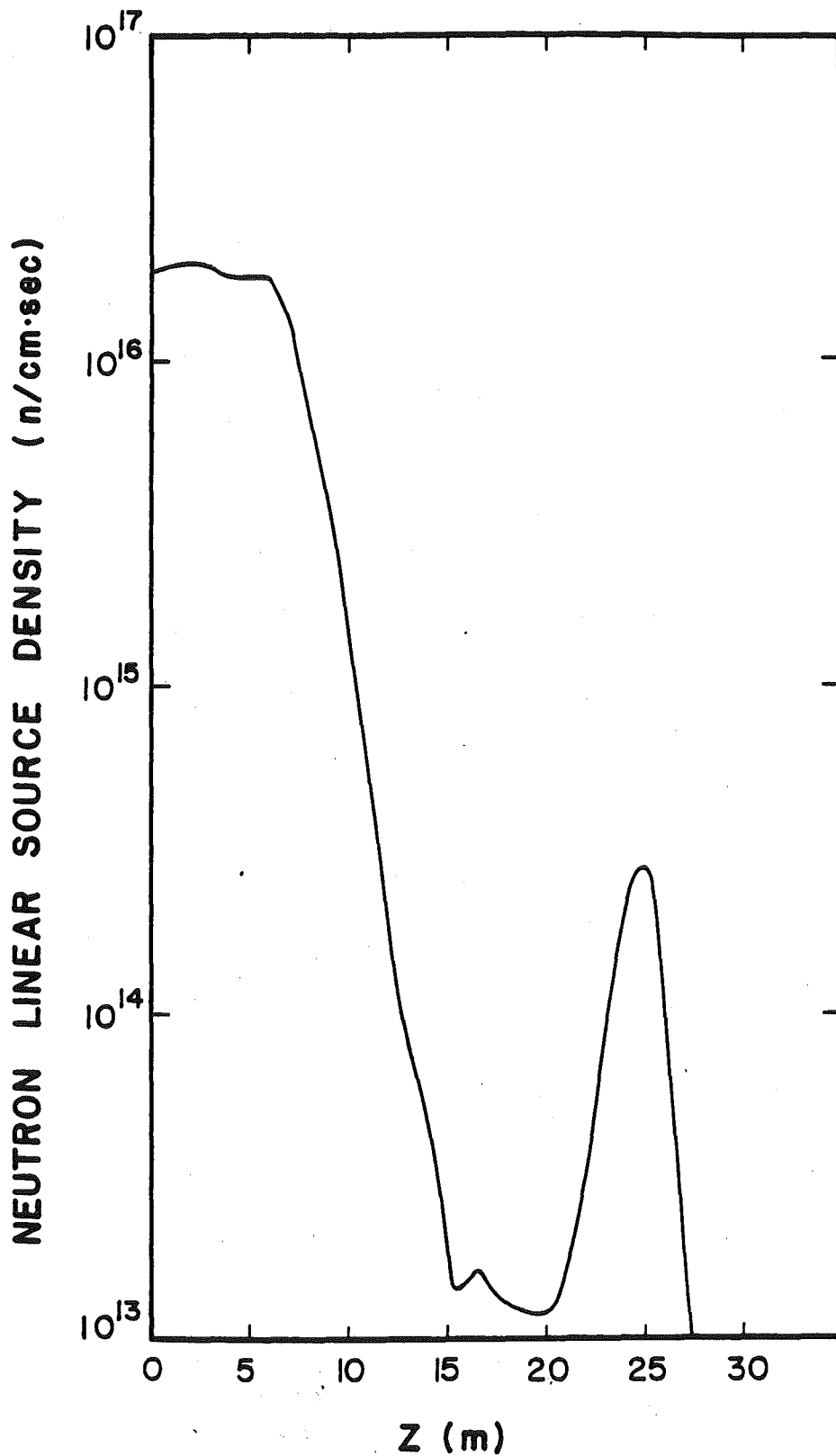


Figure VI.2-6 Variation of the neutron linear source density along the z axis.

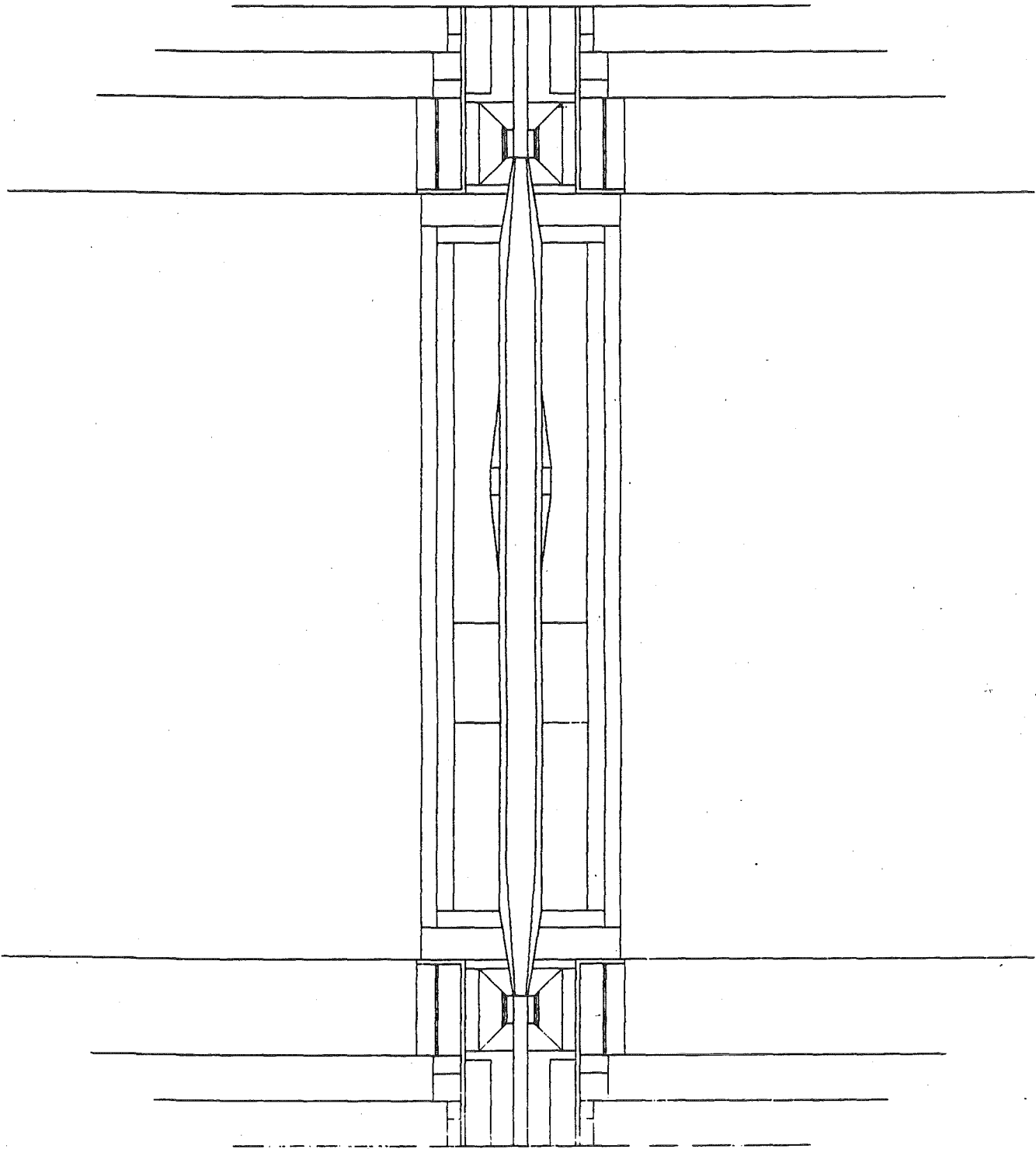


Fig. VI.2-7 Monte Carlo model of central cell and barrier region.

Table VI.2-2. Tritium Production

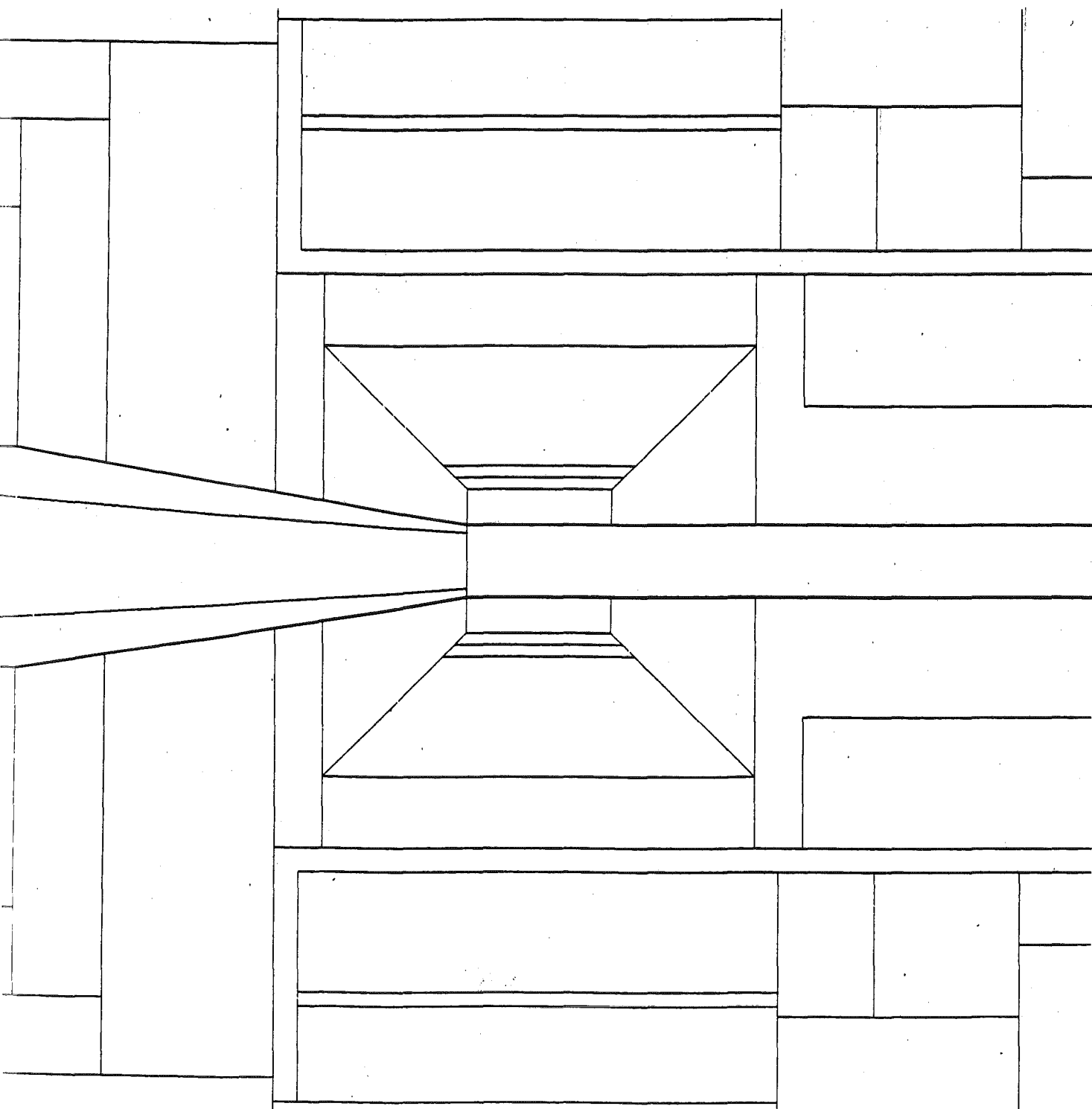
Region			T per Fusion		
			⁶ Li	⁷ Li	Total
Breeding Blanket		Width (m)			
	1	1.565	0.15463	0.00027	0.15490
	2	1.80	0.16316	0.00027	0.16343
	3	1.80	0.16240	0.00027	0.16267
	4	1.05	0.10933	0.00021	0.10954
	7	1.05	0.09919	0.00018	0.09937
	8	1.565	0.13854	0.00023	0.13877
	Total	8.83	0.82725	0.00143	0.82868
Blanket Test Modules	5	1.05	0.07144	0.03144	0.10288
	6	1.05	0.07754	0.03186	0.10940
	Total	2.10	0.14898	0.06330	0.21228
System Total		10.93	0.97623	0.06473	1.04096

Table VI.2-3. Nuclear Heating in Central Cell (MeV/fusion)

Region	Neutron Heating	Gamma Heating	Total Nuclear Heating
First Wall	0.0955	0.1197	0.2152
Breeding Blanket	4.9139	3.7665	8.6804
Blanket Test Modules	1.6579	0.5287	2.1866
REGAT Modules	0.1854	0.3489	0.5343
Reflector	0.1344	0.9054	1.0398
Shield	1.2649	1.0985	2.3634
Total	8.2520	6.7677	15.0197

Energy multiplication = 1.06

Fig.. VI.2-8 Barrier and adjacent regions.



including Cu insert coils with only a thin shield in front. For this reason, a primarily tungsten shield is used to obtain maximum attenuation. A one-dimensional model described by the schematic shown on Fig. VI.2-9 is used as a basis for determining shield performance. The calculations are based on a linear source density of 2.677×10^{15} neutrons/cm·sec which with a wall radius of 17 cm gives a neutron wall loading of 0.566 MW/m^2 . The resulting dose rate to the MgO insulation used in the normal coil is 4.35×10^{11} Rad/FPY. With a design limit of 10^{12} Rad this implies a replacement of this coil every 2.3 FPY of operation. For TASKA's expected life and capacity factor only two replacements are required during its total operation.

There are other coils in the barrier region referred to as field shaping coils. These are also normal coils. Further one-dimensional calculations were used in choosing the required shielding. At 16.5 m from the midplane, the wall radius is 80 cm and the linear neutron source density is 1.62×10^{13} /cm sec leading to a $7.28 \times 10^{-4} \text{ MW/m}^2$ maximum wall loading. With 20 and 30 cm shields, the peak dose rate in MgO is 3.87×10^8 Rad/FPY which with a 10^{12} Rad limit is more than adequate. During the operation the peak biological dose rate outside a surrounding concrete shield is determined to be 1.23 mR/hr easily meeting the upper bound of 10 mR/hr deemed acceptable.

A series of one-dimensional calculations were carried out to assess the shield needed to protect the yin-yang and the recircularizing coils which are both superconducting systems. The results are based on the linear source density of 2.8×10^{14} /cm sec corresponding to the peak at 25 m and using a wall radius of 18 cm leading to a 0.056 MW/m^2 maximum neutron wall loading in this zone. Calculations for several shield thicknesses enable us to plot the peak dpa in the copper stabilizer versus shield thickness (Fig. VI.2-10), and

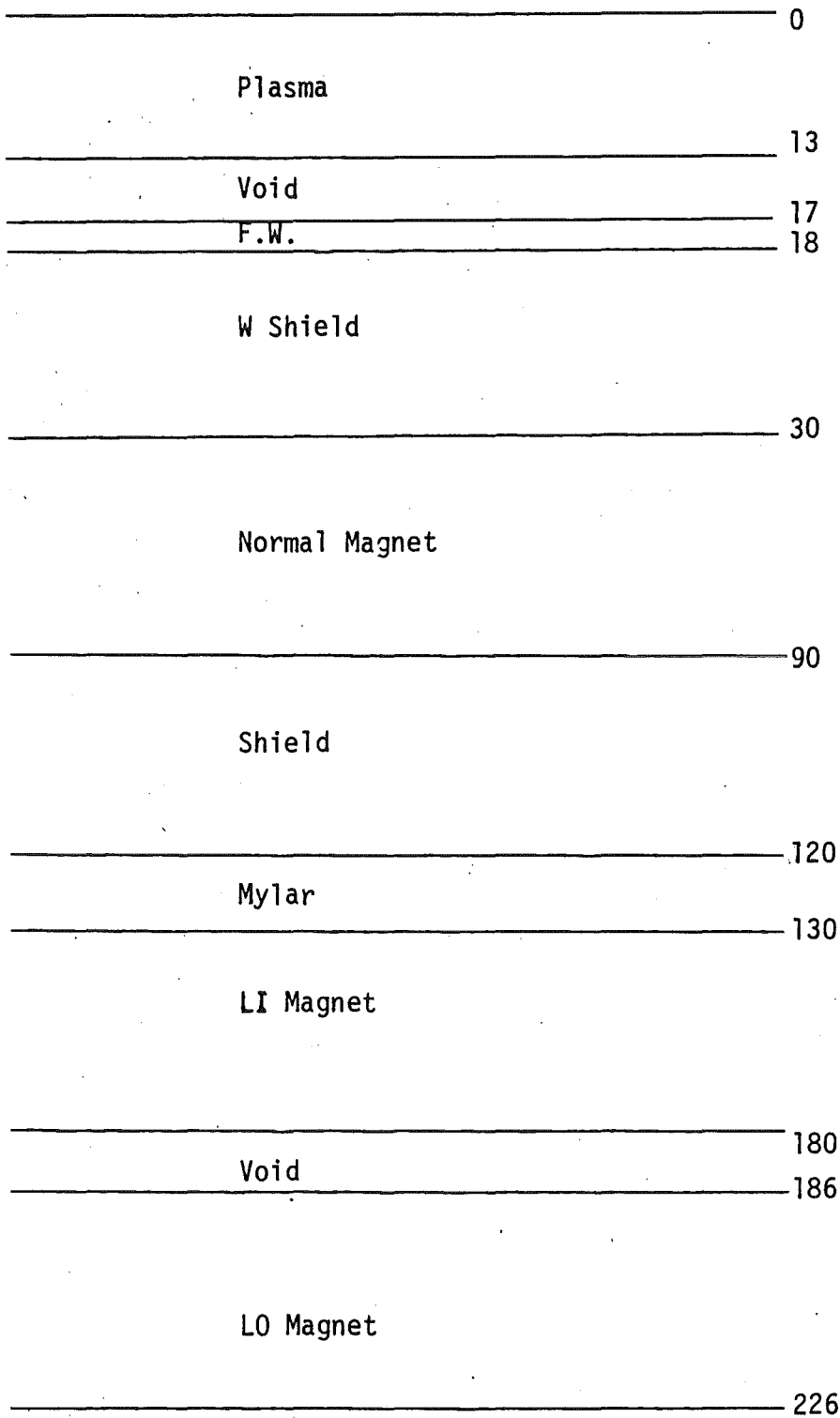
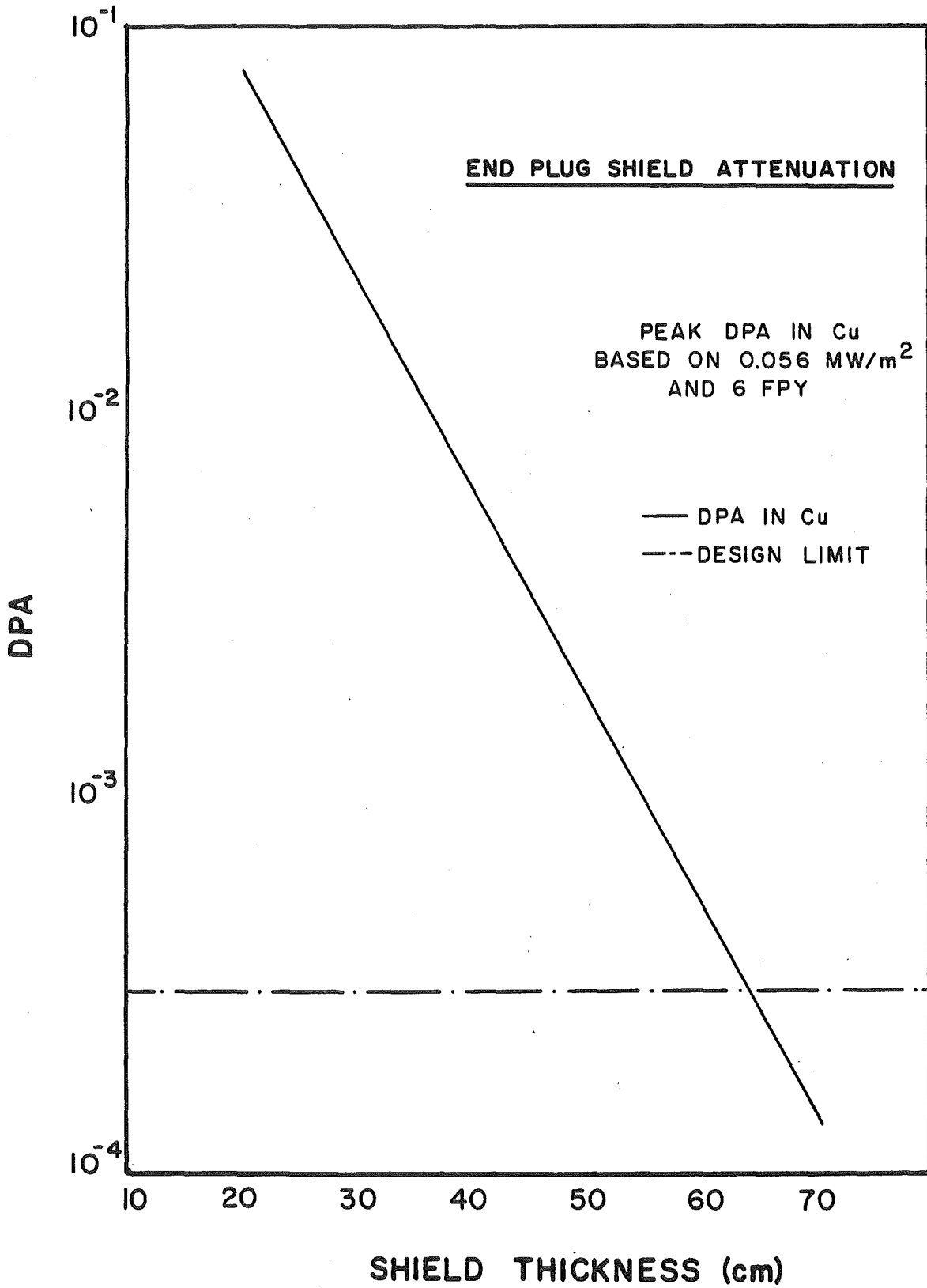


Fig. VI.2-9. Barrier midplane section.

Fig. VI.2-10



the peak dose in mylar and epoxy based on 6 FPY, Figs. VI.2-11 and VI.2-12. The copper resistivity should not exceed 10^{-7} Ω cm to meet stabilization requirements, but in a magnetic field of 8 T its resistivity is 5.3×10^{-8} Ω cm without induced resistivity (ρ_r). Thus, the induced resistivity should not exceed 4.7×10^{-8} Ω cm. For copper⁽⁵⁾ the induced resistivity is

$$\rho_r = 3 \times 10^{-7} [1 - \exp(-563 d)] \Omega \text{ cm}$$

where d is the dpa, limiting d without anneal to 3×10^{-4} dpa.

The choice of a 60 cm shield then gives 8.47×10^{-5} dpa/FPY and a single anneal during TASKA's lifetime. The peak doses in mylar and epoxy under these conditions is 2×10^8 and 1.9×10^8 Rad/FPY respectively. With limits of 10^{10} and 5×10^9 Rad in the mylar and epoxy, this shield is adequate for our needs. The peak biological dose rate outside the surrounding concrete shield is found to be 0.62 mR/hr, again well below the 10 mR/hr limit.

VI.2.4 Radioactivity

The radioactivity for the TASKA study was calculated using the compositions and zones shown in Fig. VI.2-13. Cylindrical geometry was chosen and the flux was taken from the midplane of the reactor. The flux was calculated using the ANISN⁽⁸⁾ code with a P_3S_8 approximation. The transport cross sections were taken from a coupled 25 neutron - 21 gamma group data library.⁽⁹⁾

Since these calculations were performed the thickness of the first wall of the blanket has been reduced to an equivalent of 0.3 cm. This will have the effect of reducing the activity in the first wall by about a factor of three and increasing the activity of the blanket near the first wall slightly. However, since the principal contribution to the dose after shutdown outside the shield comes from the regions near the edge of the shield, the change in the first wall thickness is expected to result in a negligible change in this quantity.

Fig. VI.2-11

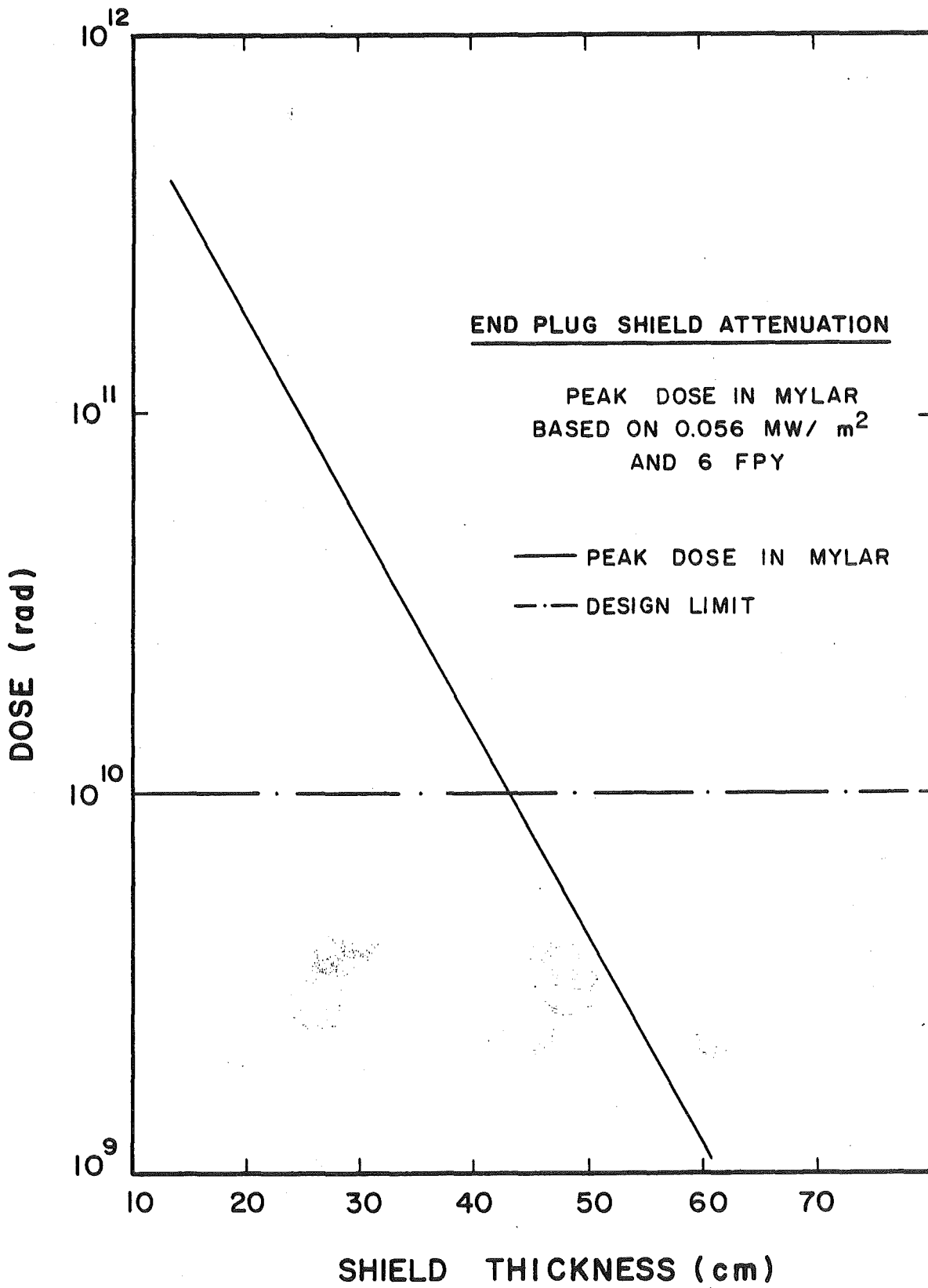


Fig. VI.2-12

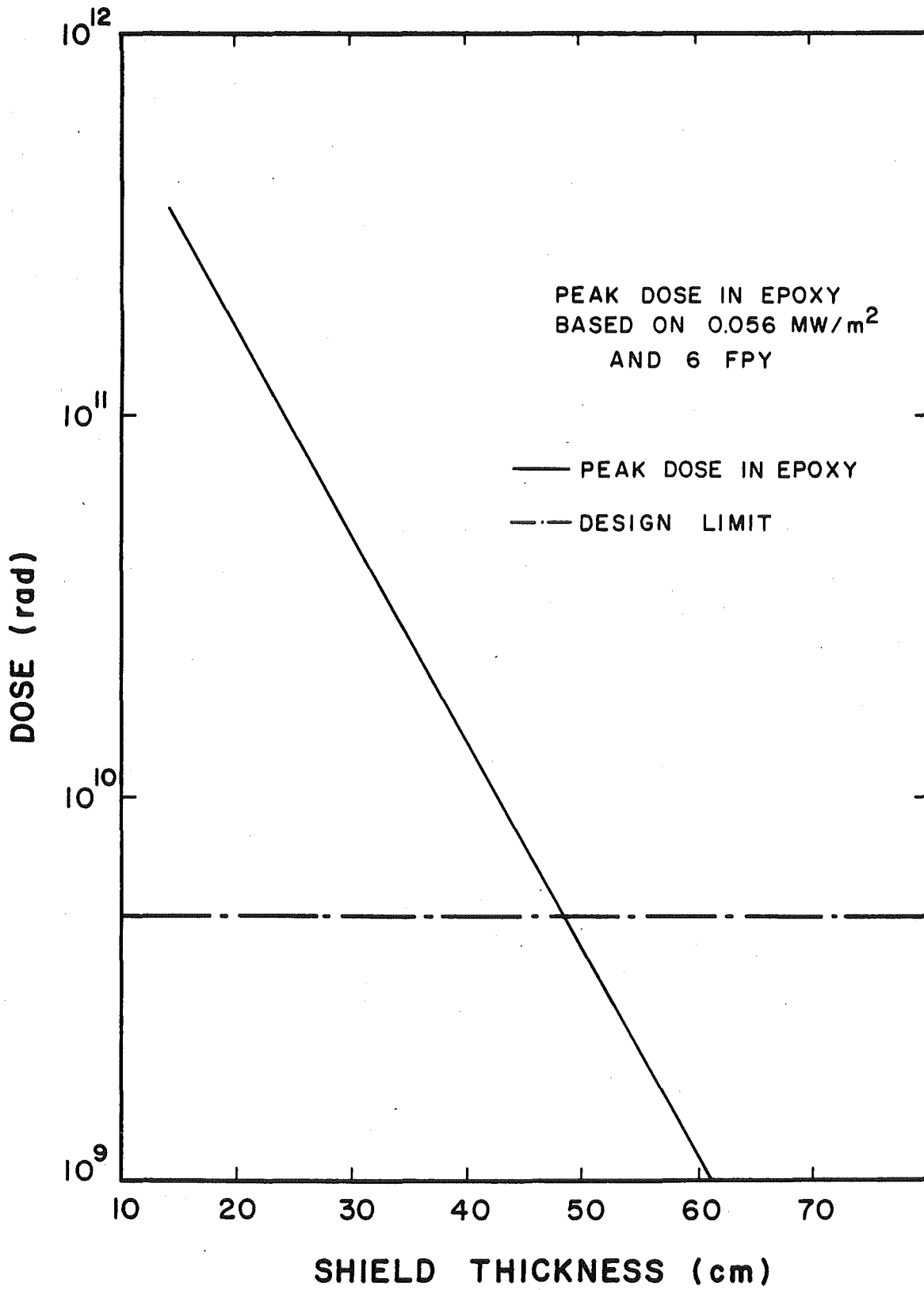
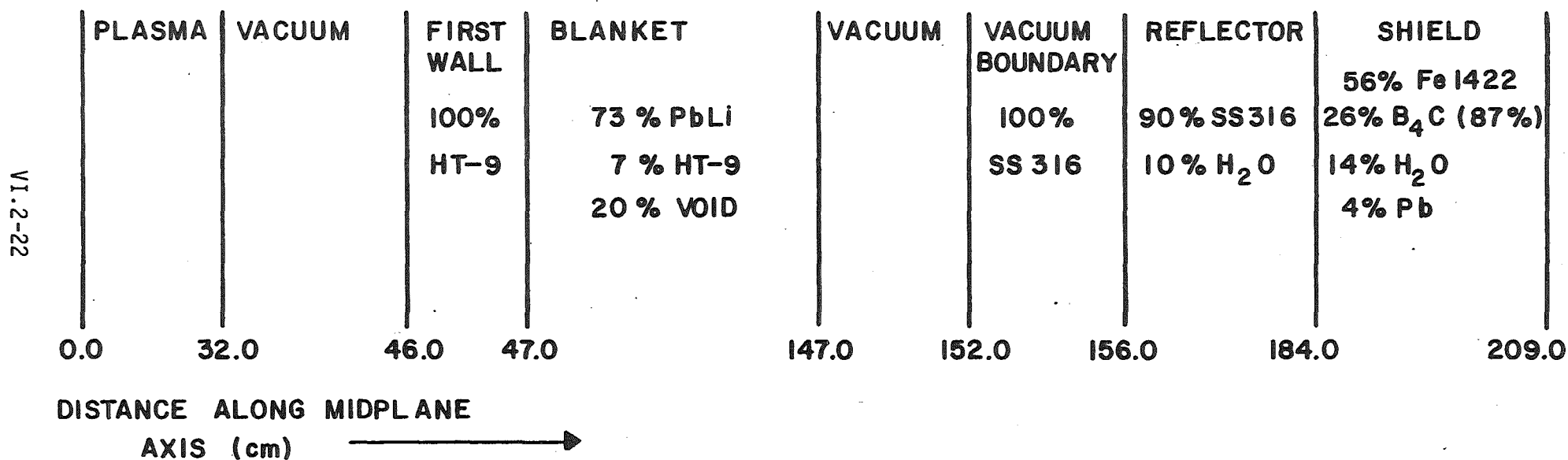


Fig. VI.2-13

DIAGRAM OF MODEL USED IN CALCULATING
ACTIVATION PARAMETERS FOR TASKA



The flux was then used as the input to the DKR code.⁽¹⁰⁾ The results of this calculation are shown in Figs. VI.2-14- VI.2-19. The calculations were done for an operating time of 2 years and the diagrams indicate the respective magnitudes of the quantities of interest for the combined reflector and shield and the combined blanket and first wall. The levels of the specific activity, biological hazard potential, and percent afterheat are all of the same order of magnitude as those of previous studies (see WITAMIR-I)⁽¹⁾, i.e., the activity at shutdown is about 1 curie per watt, the biological hazard potential for air is about 100 km³ per kilowatt and the afterheat is about .7% of the total operating power. The highest volumetric activity is found in the first wall but the inner part of the blanket is highly activated as well. In the reflector and shield, the induced activities are respectively 3.41×10^{-2} curies/cm³ and 6.69×10^{-6} curies/cm³ one day after shutdown.

The time dependence of the activity is basically the same as in most other steel reactors. After shutdown, Fe-55, Mn-56, Cr-51, and Pb-203 are the isotopes which contribute the most to the radioactivity. The relative contribution of Fe-55 is higher than in previous studies because of the relative thickness of the first wall (1 cm vs. 0.3 cm in earlier studies) and the choice of material (HT-9). The Mn-56 and Pb-203 both decay rapidly, diminishing the activity by a factor of two after one day. After this, the decay is influenced by the Fe-55 until about 50 years when the Ni-63 found in the 316 SS takes over. At this time the graphs show that the reflector and shield are the dominant sources of radioactivity. This is due to the compositions of the zones (see Fig. VI.2-13), i.e., the reflector has a very high concentration of nickel from the 316 SS. The long term decay is governed by Mo-93 and Nb-93m.

Fig. VI.2-14

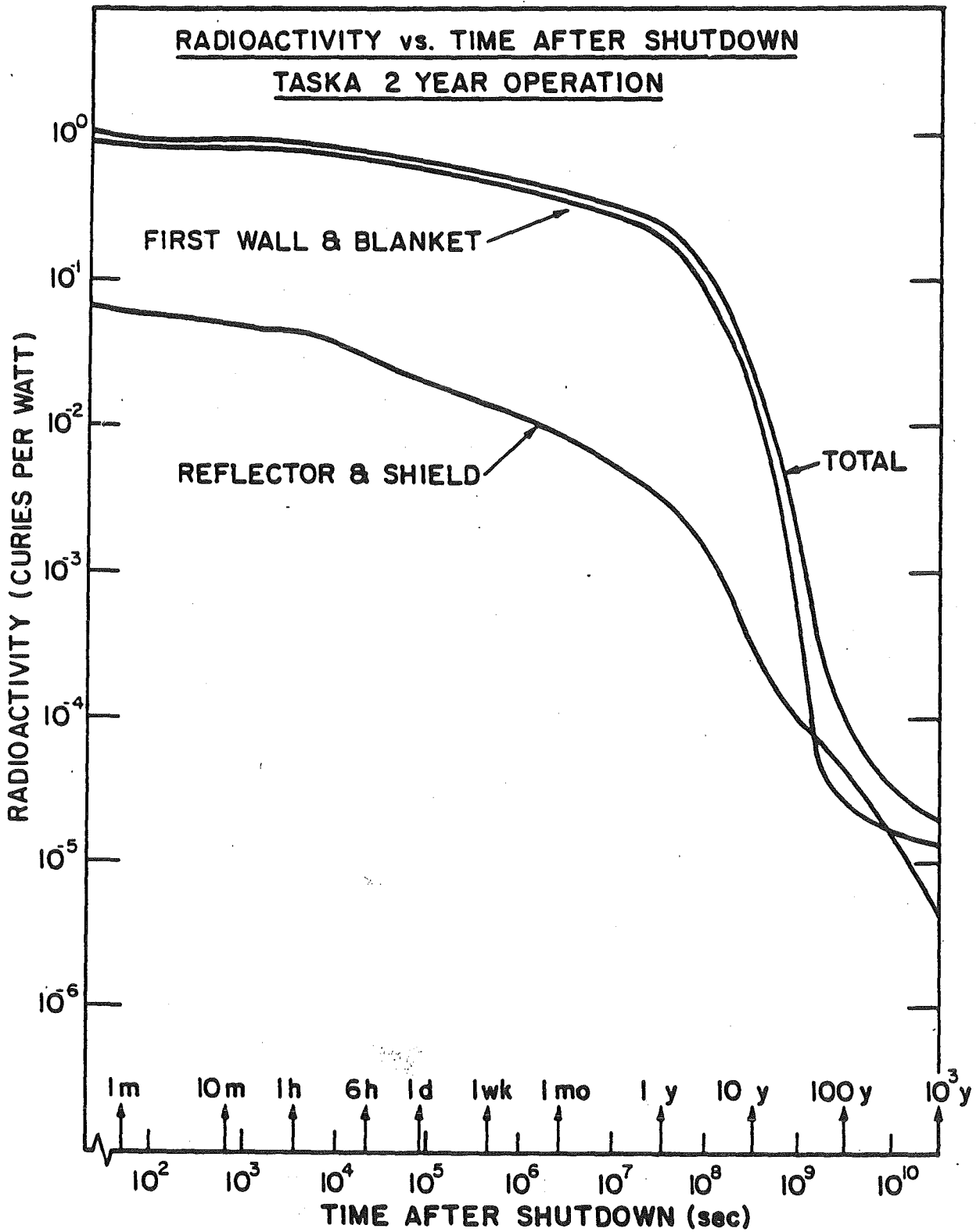


Fig. VI.2-15

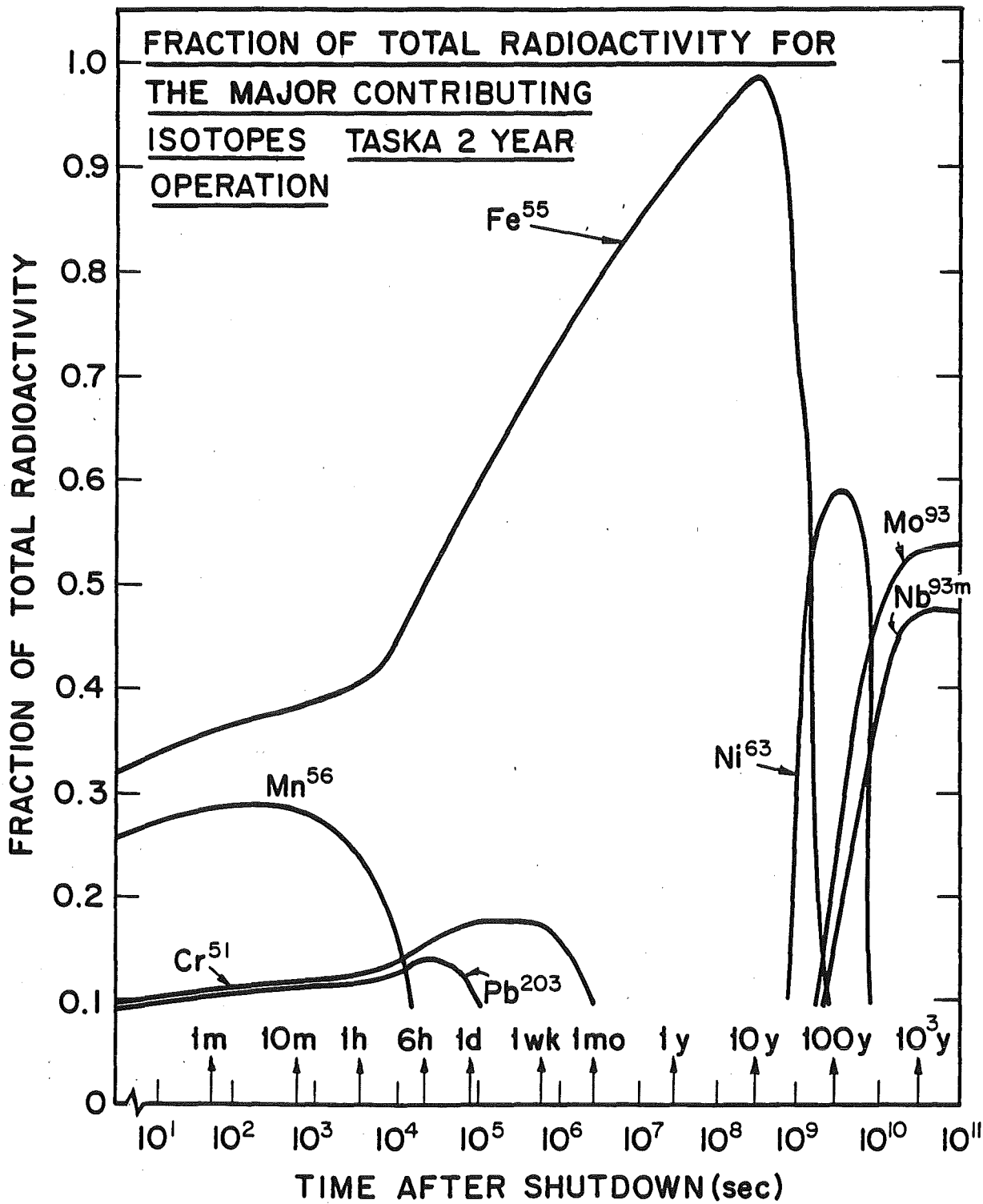


Fig. VI.2-16

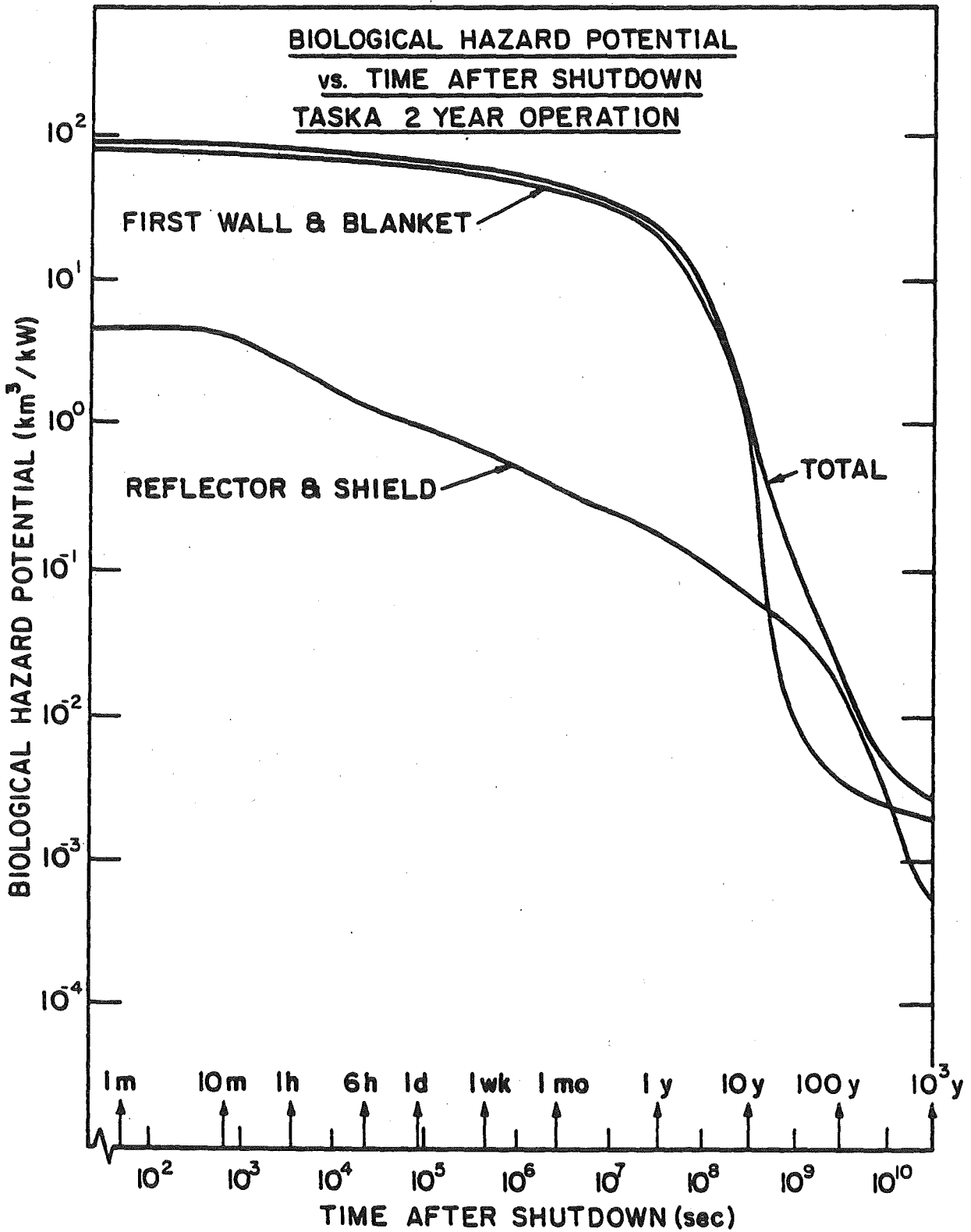


Fig. VI.2-17

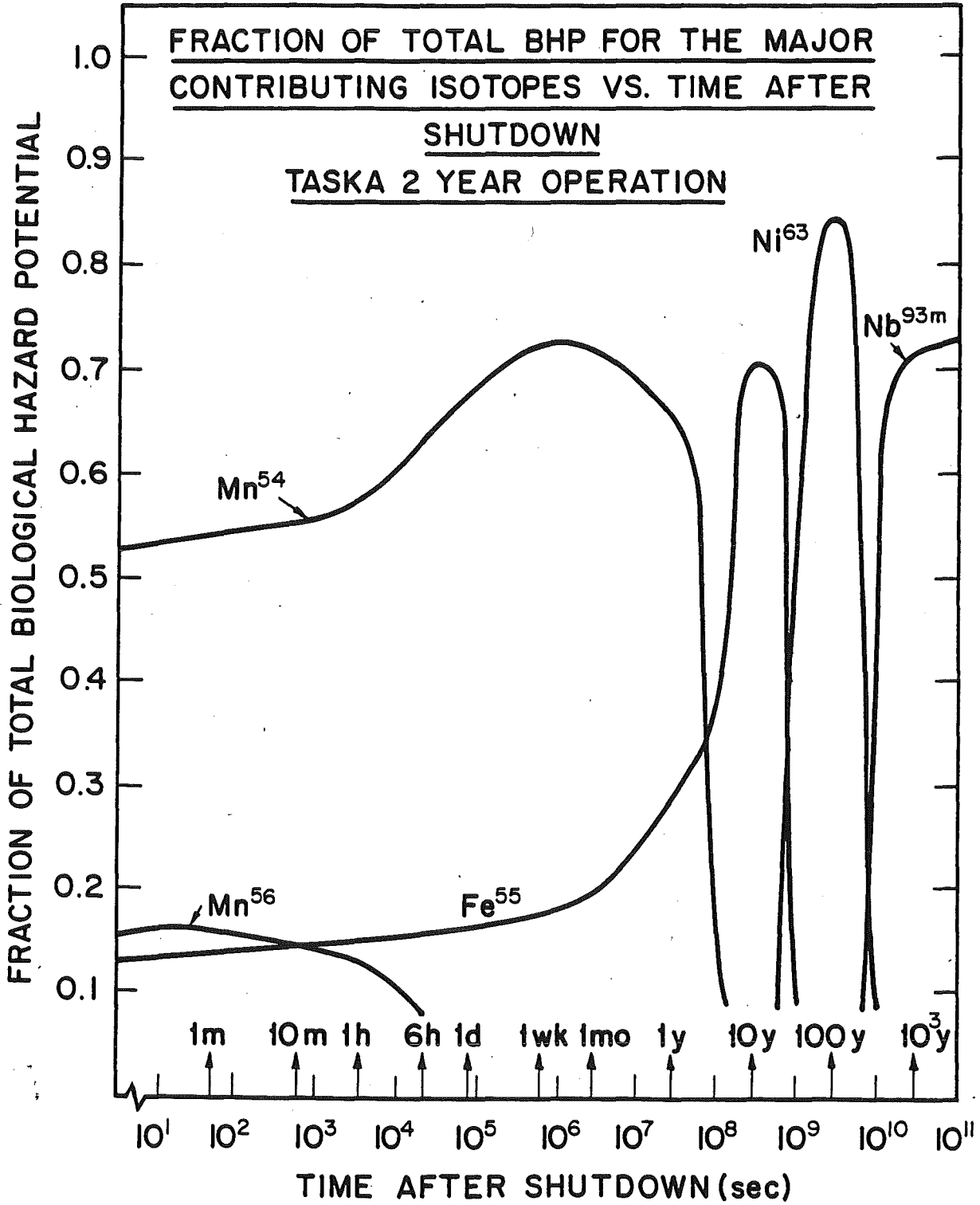


Fig. VI.2-18

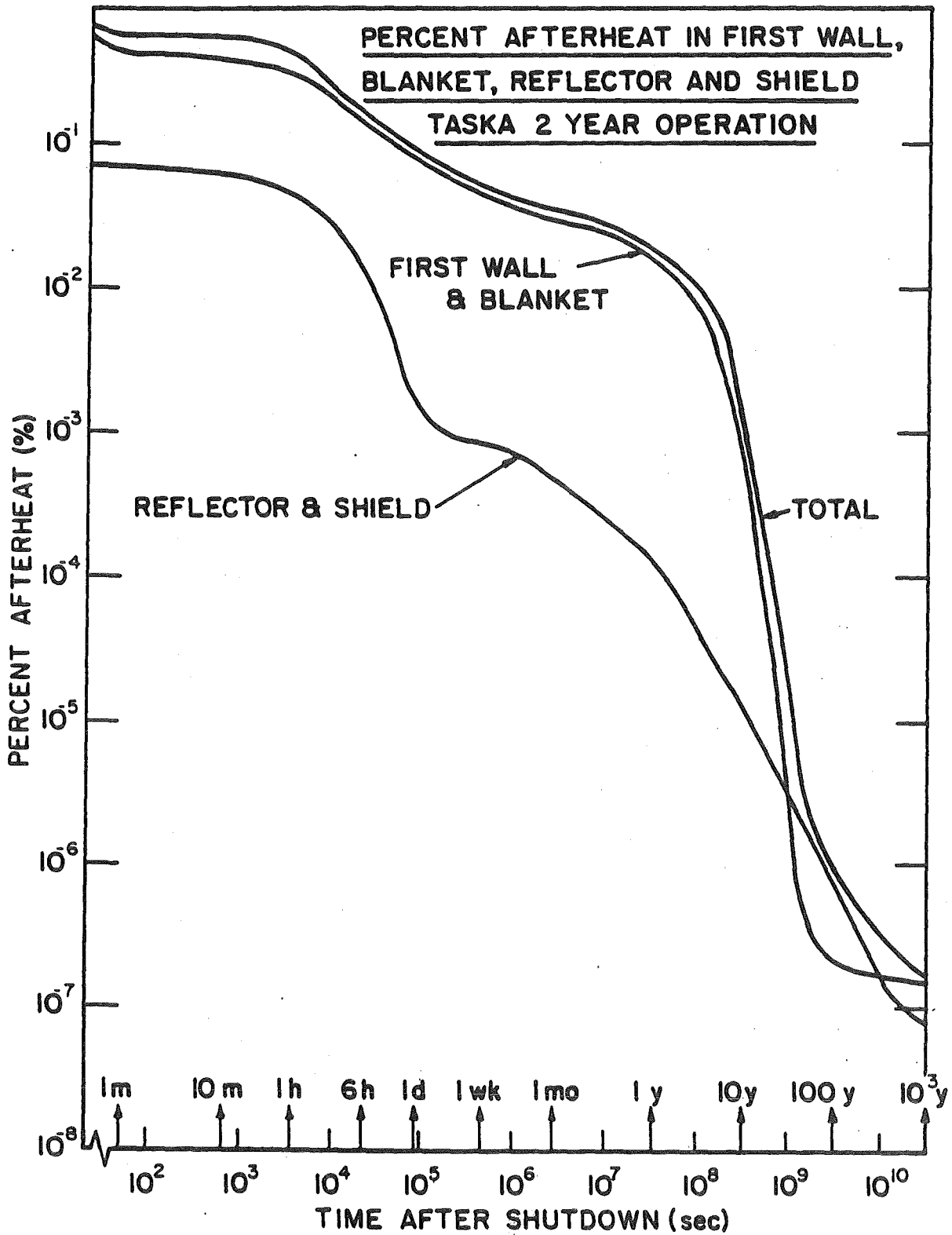
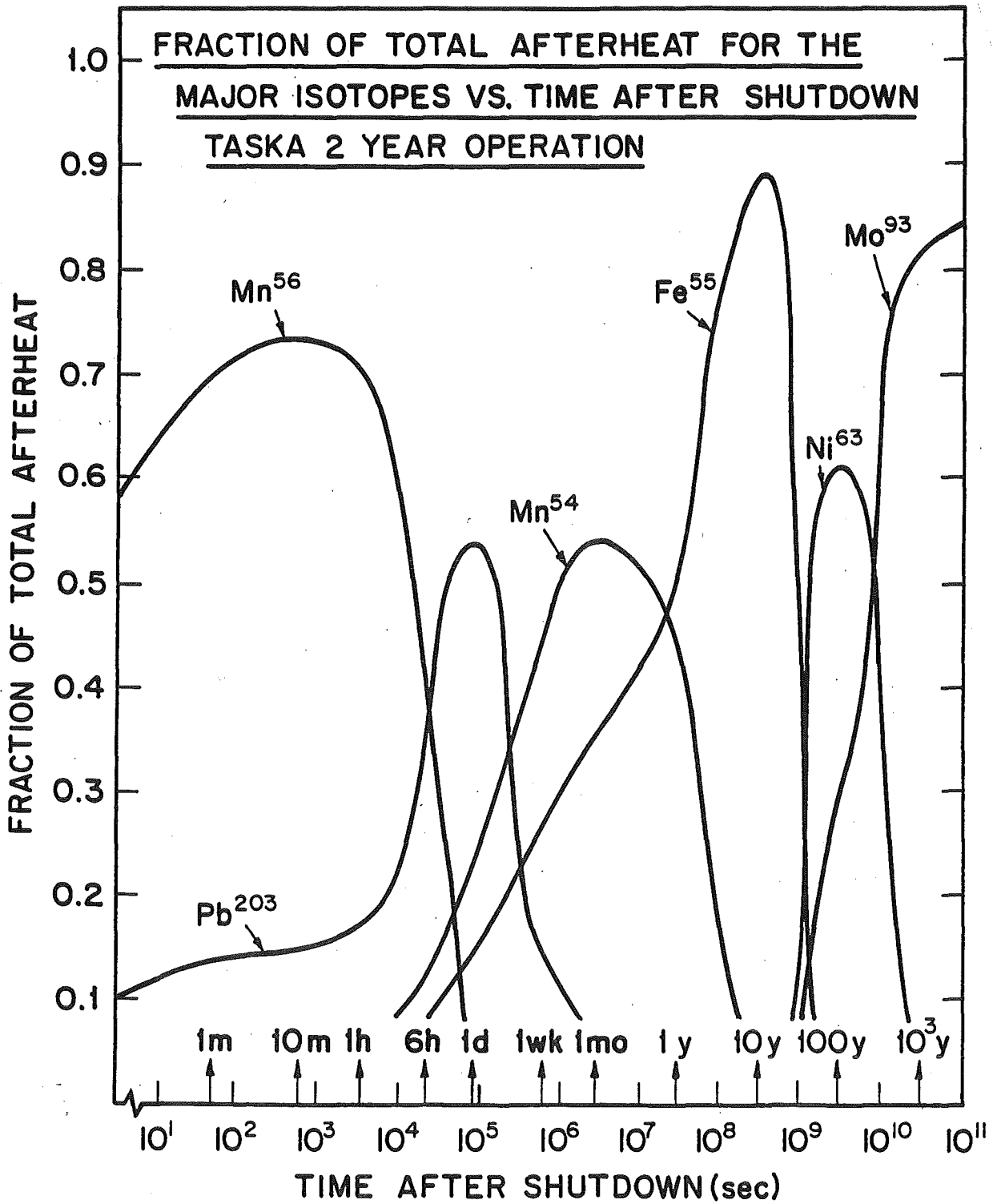


Fig. VI.2-19

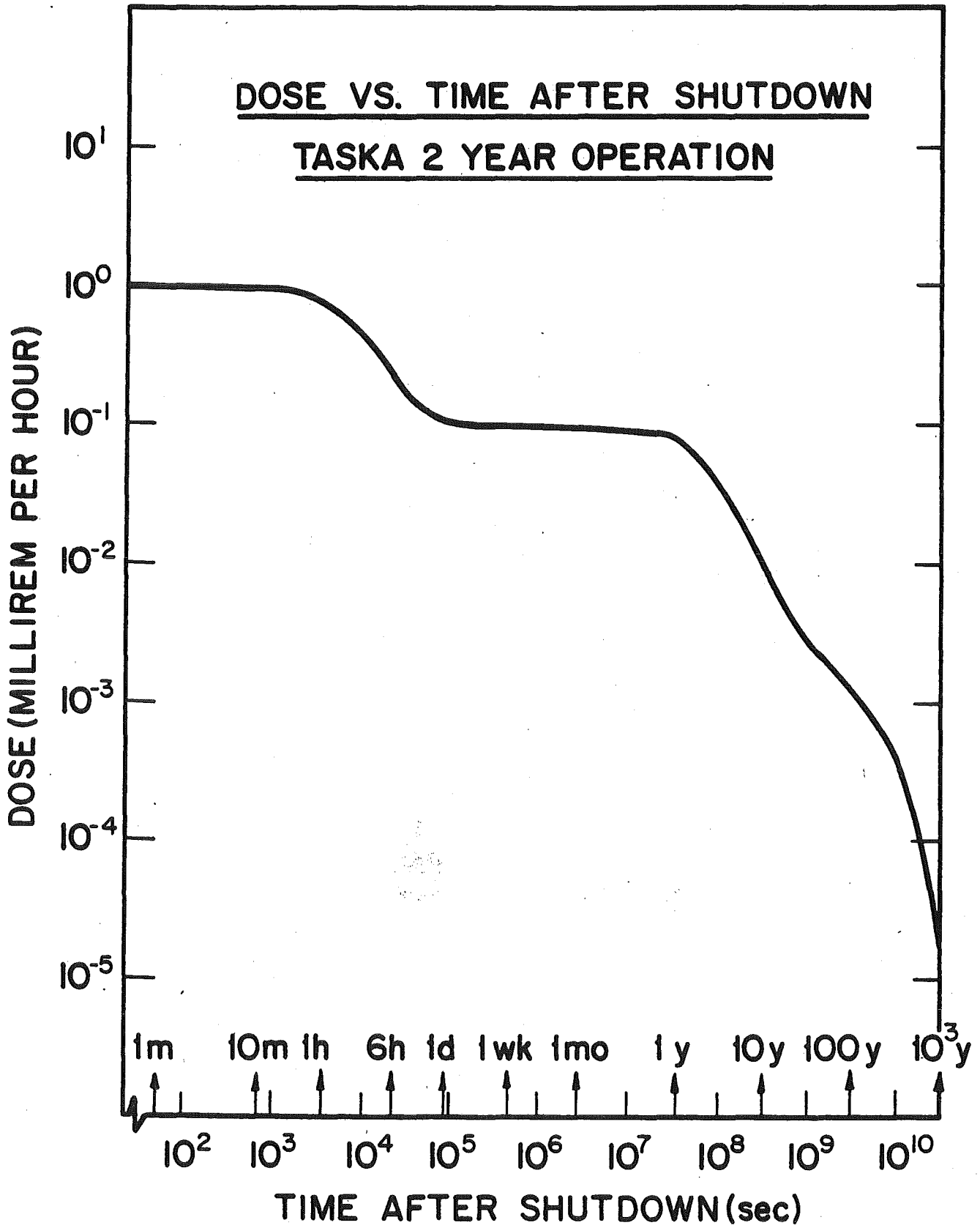


The time dependence of the afterheat differs from that of the activity because of the small decay heat of Fe-55. The isotopes Mn-56, Mn-54, and Pb-203 dominate the afterheat at shutdown. Because of the rapid decay of both of these isotopes, the afterheat drops by a factor of two in about two hours, and by a factor of ten in under a week. After these isotopes decay, Fe-55 dominates (from 1 y to 20 y) because of its abundance. The long term afterheat is governed by Ni-63 (20 y - > 300 y) and Mo-93 (300 y). The BHP follows essentially the same curve as the radioactivity. The dominant isotope here, however, is Mn-54 ($t_{1/2} = .82$ years). Also giving significant contributions are Mn-56 and Fe-55. The Fe-55 eventually dominates until it decays and Ni-63 and Nb-93m take over. The BHP takes about one year to drop by a factor of two and 20 years to drop by a factor of 100.

As shown in the WITAMIR calculation, the activity, BHP, and afterheat in the magnets are very low and decay rapidly after shutdown (3-5 orders of magnitude in one day).

The dose rate after shutdown was calculated using two methods which yielded similar results. First, a forward calculation was done using the gamma source from the DKR code (this produces a spatially dependent case). Second, an adjoint calculation was performed using tissue kerma factors as a source in the last zone of the shield. The results of the dose calculation are shown in Fig. VI.2-20. At shutdown the dose rate outside the shield is about 1 mR/hr and is low enough to allow hands-on maintenance. It drops by one order of magnitude in about one day and by two orders of magnitude in under ten years. Since the blanket of TASKA has no major penetration and the flux falls off rapidly toward the ends of the machine, the dose calculated

Fig. VI.2-20



here (that of the midplane of the machine) should be an upper limit for the entire system and should allow immediate after shutdown hands-on maintenance.

VI.2.5 Test Blanket

For the TASKA central cell, a natural lithium blanket has been studied. This will allow testing of a blanket concept that is a prominent candidate for a power reactor and one which differs appreciably from the proposed permanent blanket of TASKA. Neutronic calculations were performed to determine:

- the tritium breeding.
- the conversion of the fusion neutron related energy into heat.
- the attenuation of the neutron and gamma fluxes in connection with magnet and equipment protection.
- the resistance to radiation damage.

VI.2.5.1 Codes and Data Libraries

The neutronic and photonic calculations were made with the one-dimensional code ONETRA.⁽¹¹⁾ A P_3 - S_8 approximation in cylindrical geometry was used in the transport calculations. The fusion cross section library has been taken from the University of Wisconsin (UW) which is a combined P_3 , VITAMIN-C,⁽¹²⁾ MACKLIB-IV,⁽¹³⁾ coupled 25 neutron-21 gamma group library. It contains data blocks for 48 isotopes with 4 data blocks for each isotope corresponding to a P_3 Legendre expansion of the scattering cross section.

From these libraries one can generate the so-called response functions. Some important response functions for this study are:

- neutron and gamma kerma factors,
- displacement cross sections,
- $(n,2n)$, $(n,3n)$ cross sections,
- hydrogen and helium production cross sections,

- ${}^6\text{Li}(n,\alpha)t$, ${}^7\text{Li}$ inelastic continuous cross sections (for tritium breeding),
- absorption and total cross sections.

At KfK a special KfK-UW-library can be used immediately in ONETRA calculations as cross section blocks have the standard Los Alamos structure acceptable to the code.

The KfK cross section data set KfK INR⁽¹³⁾ (26 neutron groups) was also used for some calculations.

VI.2.5.2 Calculations and Results

The calculational model of the blanket, reflector and shield together with the compositions in these zones is shown in Fig. VI.2-21. Note that TASKA, because it is basically a long cylinder, lends itself well to one-dimensional cylindrical modeling.

For simplifying the calculations the blanket region had to be considered as a homogeneous zone, consisting of breeding and structural materials.

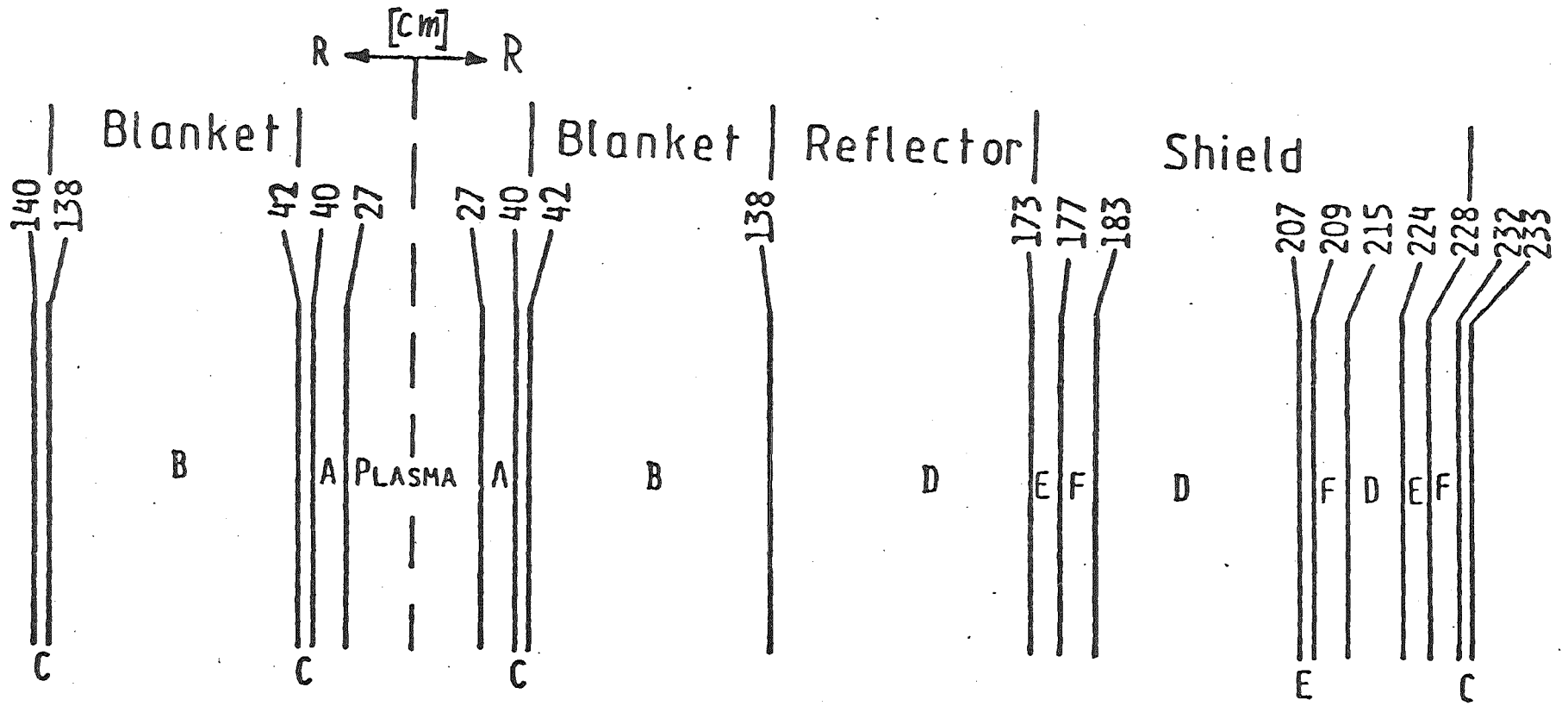
Due to the P_3 - S_8 approximation, the 46 energy groups, and the high number of fine mesh steps (about 160) in the calculations, the IBM-3033 computer at KfK needed about 6000 K-bytes of main storage.

Therefore, it was necessary to reduce the configuration to the outer radius of the reflector ($r = 177$ cm). However, this fact does not have much influence on tritium breeding, heating rate distribution and some other parameters.

The results of the neutronic calculations are given in Table VI.2-4. These values are normalized to a wall load of 1 MW/m^2 .

For a homogeneous blanket composition, consisting of 73 vol.% Li_{nat} , 7 vol.% SS 1.4970, 20 vol.% void, a total tritium breeding ratio of 1.32 T-atoms/source neutron was obtained.

VI.2-34



- A = VACUUM
- B = 73% Li_{NAT} ; 7% SS 1.4970; 20% VOID
- C = 100% SS 1.4970
- D = 95% SS 1.4970; 5% H_2O
- E = 95% Pb
- F = 87% B_4C

Fig. VI.2-21 TASKA blanket, reflector and shield composition.

Table VI.2-4. TASKA Neutronics Parameters
(Based on 1 MW/m² Wall Load)

General

1. Breeding Ratio	
⁶ Li	0.921
⁷ Li	0.401
Total	1.322
2. Energy Deposition per 14.1 MeV Neutron	
Neutron	12.429 MeV
Gamma	5.572 MeV
Total	18.001 MeV
3. Energy Multiplication (total)	1.28

First Wall

1. Radius*	40.0 cm
2. Volume/Unit Length	515.2 cm ³ /cm
3. Thickness	1.0 cm
4. Power Density	
Neutron	2.98 W/cm ³
Gamma	5.04 W/cm ³
Total	8.02 W/cm ³
5. DPA per yr/MW/m ²	8.61
6. H Production ppm/yr	364.0
7. He Production ppm/yr	88.0
8. Energy Deposition per 14.1 MeV Neutron	
Neutron	0.860 MeV
Gamma	1.457 MeV
Total	2.317 MeV

Breeding Blanket

1. Radius	42.0 cm
2. Volume/Unit Length	54287 cm ³ /cm
3. Thickness	96.0 cm

*The main design has changed to a new radius; however, the results are so insensitive that the calculations were not repeated.

Table VI.2-4. (continued)

4. Power Density	
Neutron	0.377 W/cm ³
Gamma	0.093 W/cm ³
Total	0.470 W/cm ³
5. Energy Deposition per 14.1 MeV Neutron	
Neutron	11.472 MeV
Gamma	2.840 MeV
Total	14.312 MeV
<u>Reflector</u>	
1. Radius	138.0 cm
2. Volume/Unit Length	38594 cm ³ /cm
3. Thickness	39.0 cm
4. Power Density	
Neutron	0.0045 W/cm ³
Gamma	0.059 W/cm ³
Total	0.063 W/cm ³
5. Energy Deposition per 14.1 MeV Neutron	
Neutron	0.097 MeV
Gamma	1.275 MeV
Total	1.372 MeV

Although natural Li (92.5 at.% ${}^7\text{Li}$, 7.5 at.% ${}^6\text{Li}$) was used as breeding material, the main contribution to the tritium breeding comes from ${}^6\text{Li}$ (0.92 T-atoms/source neutron).

In Fig. VI.2-22 the radial breeding rate distribution is plotted for a 100 cm thick blanket.

The radial power density distribution is given in Fig. VI.2-23.

In the first wall and the reflector the gamma heating rate predominates whereas the contribution from neutrons to the heating rate is much higher in the blanket.

Hydrogen and helium production and the average dpa per year were considered for the first wall only (see Table VI.2-4).

Further neutronics parameter information is given in Section VII.3.2 (blanket modules) of this TASKA study.

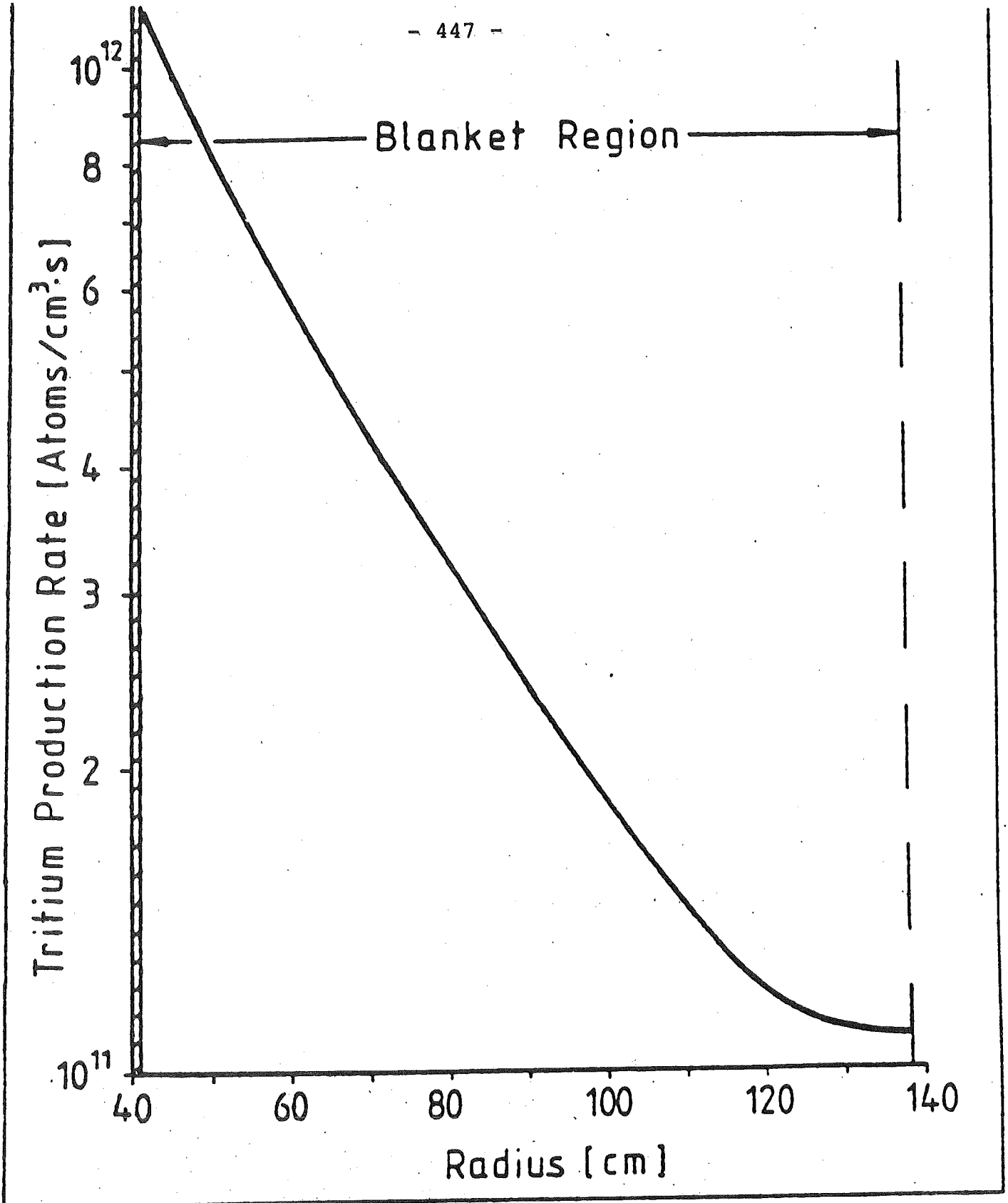


Fig. VI.2-22 Radial breeding rate distribution at 1 MW/m² neutron wall loading.

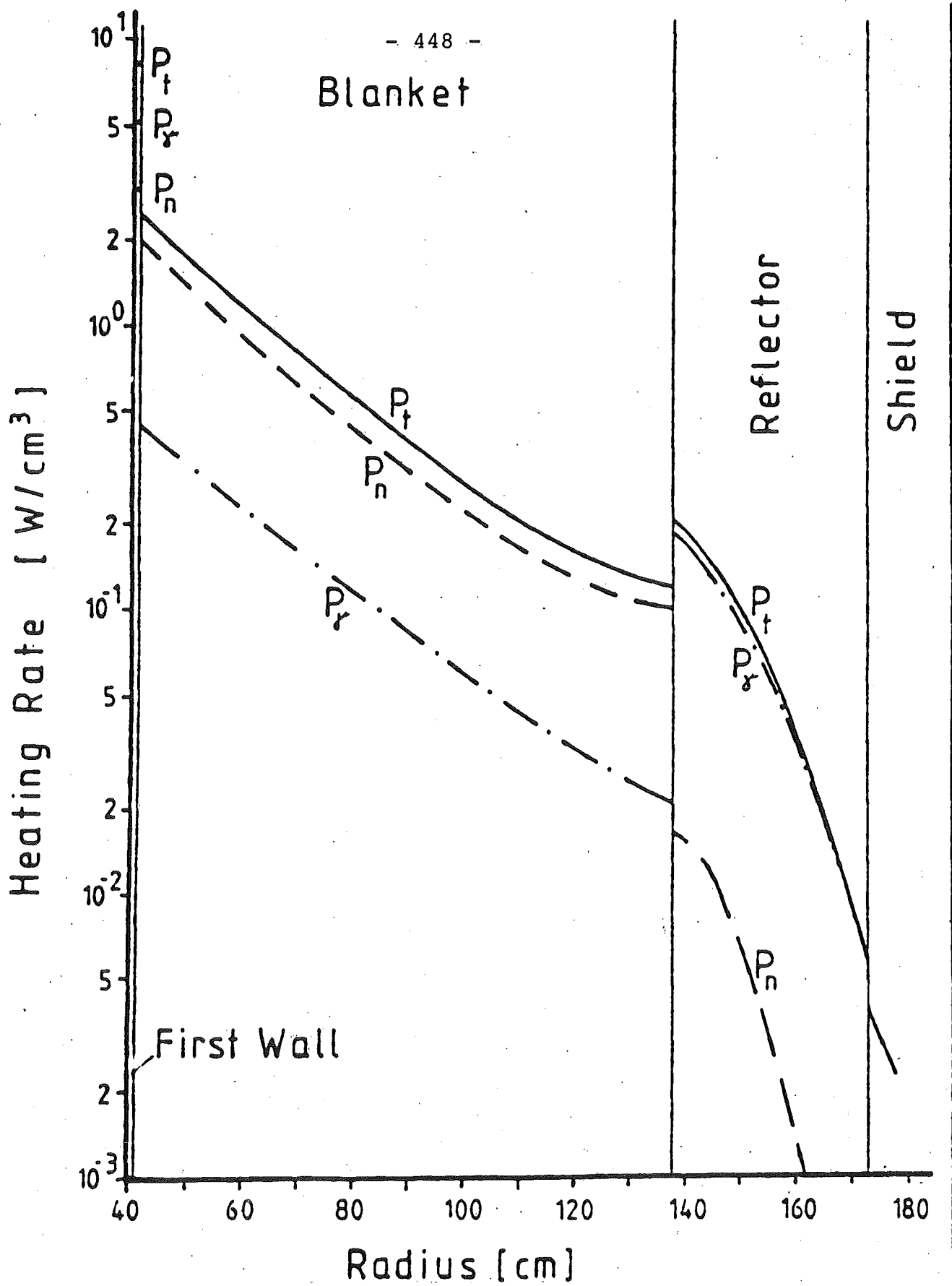


Fig. VI.2-23 Radial heating rate distribution at 1 MW/m² neutron wall loading.

References for Section VI.2

1. B. Badger et al., "WITAMIR-I, A University of Wisconsin Tandem Mirror Reactor Design," University of Wisconsin Fusion Engineering Program Report UWFD-400 (Sept. 1980).
2. R.D. O'Dell, F.W. Brinkley, Jr., and P.R. Marr, "User's Manual for ONEDANT: A Code Package for One-Dimensional, Diffusion-Accelerated, Neutral-Particle Transport," Los Alamos National Laboratory Report (to be issued).
3. W.T. Urban, Private Communication. This is a coupled neutron-photon library based on ENDFB-V.
4. D.J. Dudziak, R.D. O'Dell, and R.E. Alcouff, "Transport and Reactor Theory," October 1 - December 31, 1980, Program Report, LA-8771-PR, (March 1981) p. 14.
5. M. Abdou, J. Nucl. Mat. 72, (1978) 147.
6. Los Alamos National Laboratory Group X-6, "MCNP - A General Monte Carlo Code for Neutron and Photon Transport, Version 2B," Los Alamos National Laboratory Report LA-7397-M, Revised (April 13, 1981).
7. P.D. Soran and R.E. Seamon, "Graphs of the Cross Sections in the Recommended Monte Carlo Cross-Section Library at the Los Alamos Scientific Laboratory" Los Alamos National Laboratory Report LA-5137, (February 1974).
8. W.W. Engle, Jr., "ANISN, A 1-D Discrete Ordinates Code With Anisotropic Scattering", ORNL-K 1693 (1973).
9. R.T. Perry and G.A. Moses, "A Coupled P3 Vitamin-C MACK-IV, Coupled 25 Neutron - 21 Gamma Group Cross Section Library", UWFD-390, University of Wisconsin.
10. T.Y. Sung and W.F. Vogelsang, "DKR, A Radioactivity Calculation Code for Fusion Reactors", UWFD-170, University of Wisconsin, 1976.
11. V. Brandl, "User Manual for the KAPROS-Model ONETRA," (based on "ONETRAN, A One-Dimensional S_N Code" by T.R. Hill, LASL, USA) unpublished.
12. RSIC Data Library Collection, DLC-41, ORNL.
13. RSIC Data Library Collection, DLC-60, ORNL.
14. E. Kiefhaber, "The KFKINR Set of Group Constants," KfK-Bericht 1572.

VI.3 Thermal Hydraulics

VI.3.1 MHD Effects

The dominant force on a conducting fluid across the magnetic field lines is the MHD force. The effect of the MHD force is to increase the pressure drop and retard heat transfer by suppressing turbulence. In a D-T fusion reactor blanket, with the breeding material serving also as the coolant, the only severe heat transfer problem occurs at the first wall. For a TMR, the first wall surface heat load is only 2 W/cm². The effects of MHD on heat transfer are, therefore, not critical and the heat transfer calculations can be carried out by assuming no turbulence. The MHD pressure drop will increase the stress in the blanket and also increase pumping power. The lower magnetic field in TASKA compared to a tokamak will reduce the MHD pressure drop. Its magnitude and effects, however, still have to be assessed.

It is well known that whenever an electrically conducting fluid flows across field lines, eddy currents will appear wherever curl [v x B] is non-zero. This produces a retarding force which causes extra pressure drops in the fluid. These pressure drops will be classified here into two categories⁽¹⁾, the Hartmann and end-of-loop effects.

The Hartmann pressure gradient arises in fully-developed laminar flow with a uniform transverse magnetic field. For such a flow between parallel plates, in a uniform magnetic field normal to the plates, the pressure gradient is given by the following equation:⁽²⁾

$$-\frac{dP}{dx} = \frac{\mu v}{a^2} \left[\frac{H_{\perp}^2 \tanh H_{\perp}}{H_{\perp} - \tanh H_{\perp}} + \frac{H_{\perp}^2 C}{1+C} \right] \quad (\text{VI.3-1})$$

where μ = viscosity

v = coolant velocity

C = wall conductance ratio, $\sigma_w t_w / \sigma a$

a = channel half-width

H = Hartmann number

σ_w = electrical conductivity of the wall material

σ = electrical conductivity of the coolant

t_w = wall thickness.

When the fluid is in a channel with a conducting wall and under large magnetic fields ($H \gg 1 + 1/C$), the last term of Equation VI.3-1 dominates, giving

$$-\frac{dP}{dx} = \frac{v B_{\perp}^2 \sigma_w t_w}{a(1 + c)} \quad (\text{VI.3-2})$$

If the wall is strong enough to withstand the pressure and the corrosion of the lithium, the value of C is usually on the order of 10^{-2} or larger; hence, Equation VI.3-2 is an excellent approximation in the present range of Hartmann numbers ($H \sim 10^5$).

The end-of-loop effects are caused by gradients of $[\underline{v} \times \underline{B}]$ in the flow direction. The resulting pressure drops are given approximately by the following equation⁽²⁾

$$\Delta P = K_{PIE} \frac{\sigma b_{av}}{v_{av}} \Delta(v^2 B_{\perp}^2) \quad (\text{VI.3-3})$$

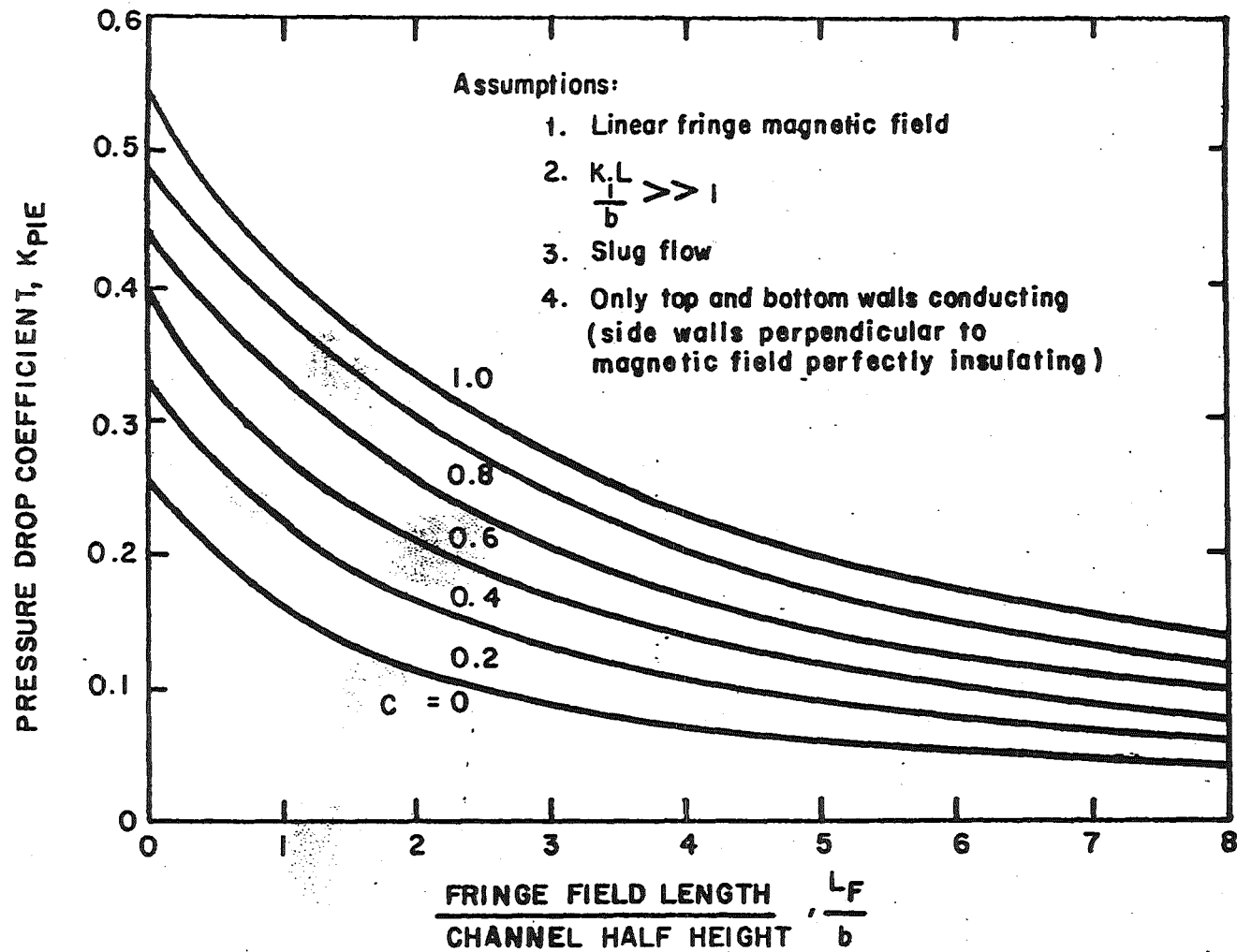


Fig. VI.3-1 - PRESSURE DROPS DUE TO ENTRANCE AND EXIT EDDY CURRENT FOR LINEAR FRINGE MAGNETIC FIELDS SEPARATED BY A LONG REGION OF UNIFORM MAGNETIC FIELD.

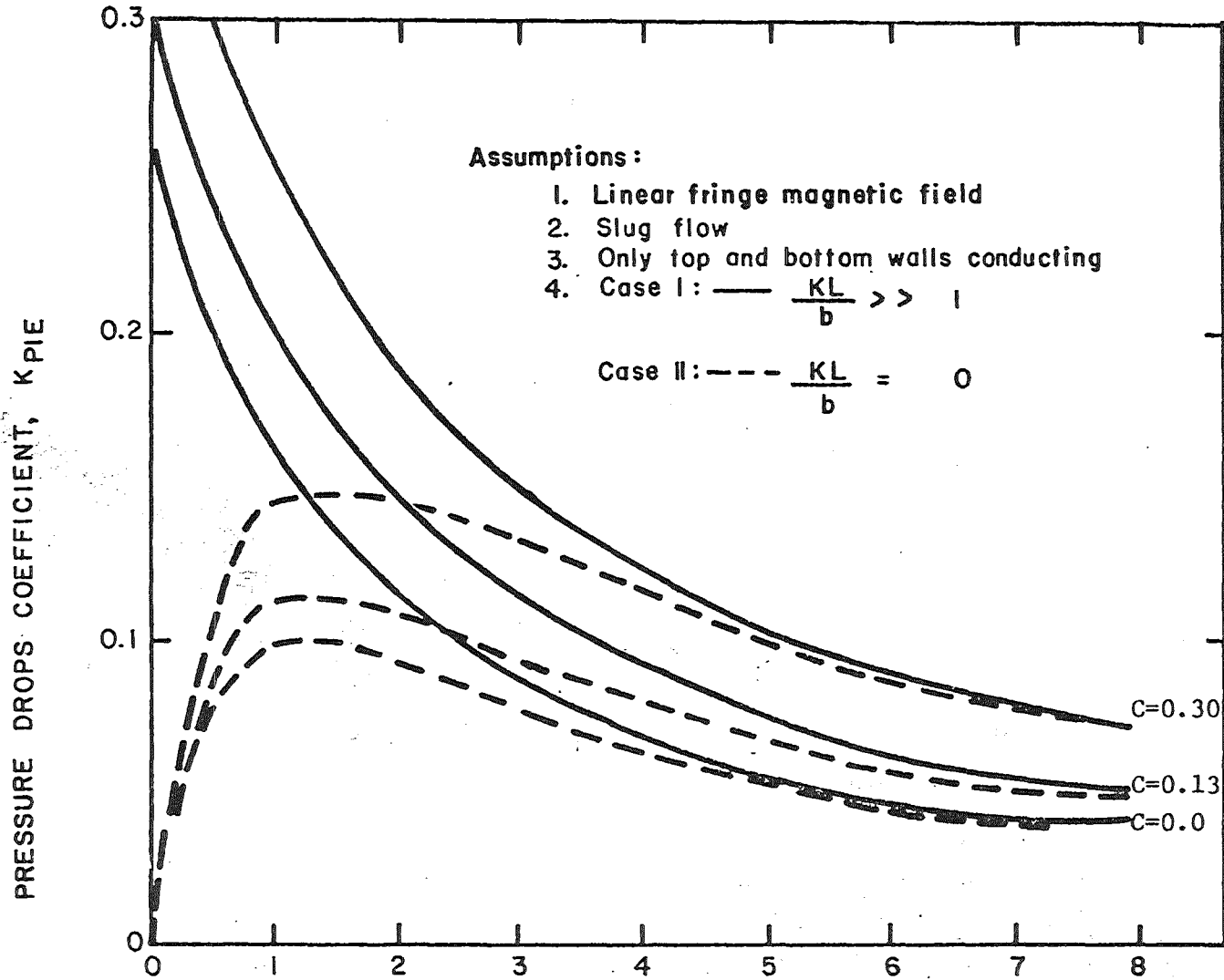


Fig. VI.3-2 PRESSURE DROP DUE TO ENTRANCE OR EXIT EDDY CURRENTS.

Here b = mean half-width of the local cross section in the direction normal to B_{\perp}

\bar{a}_v = arithmetic mean of values for initial and final cross sections.

The coefficient K_{pIE} has been presented by Hoffman and Carlson⁽¹⁾ for flows in tubes and ducts with varying B_{\perp} ; the results are summarized in Figures VI.3-1 and VI.3-2. We will use the same plots here to estimate K_{pIE} for changes of velocity and channel width; in this estimation L_F is taken as the downstream length of the region of varying vB_{\perp} .

The MHD pressure drop calculations for $Li_{17}Pb_{83}$ coolant are calculated from Eq. VI.3-2 and VI.3-3. The results are summarized in Table VI.3-1. The calculations are based on local magnetic field = 2.7 tesla. The resulting pressures are shown in Fig. VI.3-3. The largest pressure drop occurs in the feed and discharge tubes due to the high local velocity. This pressure drop has been reduced by using a laminated tube structure, with a sleeve 1 mm thick, which is insulated from the main structural tube. The thin inner wall reduces the Hartmann pressure drop as can be seen from Eq. VI.3-2. The total MHD pressure drop in the reactor is 1.08 MPa, which corresponds to a pumping power requirement of 500 kW. The maximum blanket pressure is 1.02 MPa. The important blanket parameters are summarized in Table VI.3-2.

VI.3.2 Heat Transfer Calculations

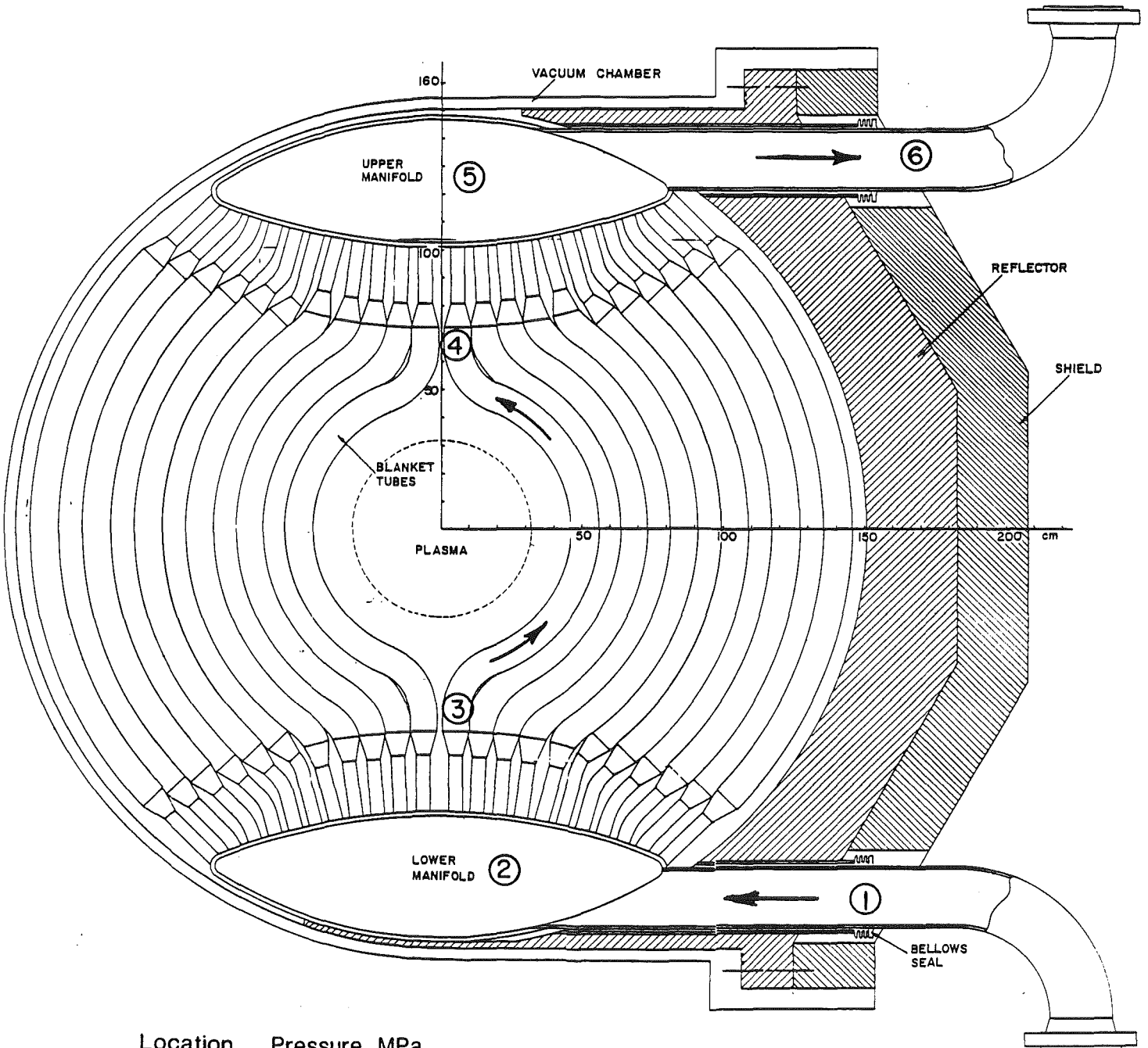
The temperature profile in the coolant tube can be calculated by assuming only conduction. This can be justified due to the MHD effects on suppressing of turbulence. The most severe heat transfer problems occur in the first row of tubes. The energy deposited in the first row of tubes consists of a volumetric component due to nuclear heating and a surface heating load from the plasma. The effects of these two components can be decoupled. The

Table VI.3-1 Summary of MHD Pressure Drop Calculations

	v, m/sec	r, cm	L _F /b	K _{PIE}	t _w , mm	L, m	ΔP _E	ΔP _M	ΣΔP
Feed pipe (discharge pipe)	1.75	10	10	.1	1.0*	3	.08	.36	.44(x2)
Connecting tube	.42	2.325	2	.15	1.75	.2	.02	.05	.07(x2)
Blanket tube	.097	4.843			2.27	1.45		.06	<u>.06</u>
Total									1.08 MPa

*Thickness of the inner sleeve of the pipe.

Fig. VI.3-3 Blanket Pressure Distribution



Location Pressure, MPa

1	1.46
2	1.02
3	.95
4	.61
5	.54
6	.10

Table VI.3-2 TASKA Blanket Parameters

Total blanket power	45 MW
Coolant inlet temperature	300°C
Coolant outlet temperature	400°C
Maximum blanket structural temperature	440°C
Minimum blanket structural temperature	300°C
Blanket coolant flow rate	2.9×10^3 kg/sec
Maximum power per module	8 MW
Maximum coolant flow rate per module	5.2×10^2 kg/sec
I.D. of feed (discharge) tube	20 cm
Coolant velocity in feed (discharge) tube	175 cm/sec
Maximum coolant velocity in connecting tube	42 cm/sec
Maximum coolant velocity in blanket tube	9.7 cm/sec
Maximum blanket pressure	1.02 MPa
Total MHD pressure drop	1.08 MPa
Pumping power required	500 kW

volumetric heating load increases the bulk temperature in the coolant, while the surface heating load generates a temperature gradient. The results of these two effects can then be superimposed to obtain a complete temperature profile.

The coolant temperature range is chosen between 300 and 400°C. The maximum volumetric heating is 11.24 W/cm³. The total coolant passage length is 145 cm. Therefore, the required coolant velocity is 9.7 cm/sec. The minimum coolant residence time in the blanket is 15 seconds.

The neutronic calculations are carried out for a homogenized cylindrical blanket. However, the curvature of the first wall is not a major factor in the model developed here and the first bank of tubes is assumed to be an infinite plate with a thickness of 10 cm. The mathematical problem then is conduction heat transfer to an infinite plate moving at a constant velocity with a uniform surface heating load, as shown in Fig. VI.3-4. If the heat conduction in the y direction is small in comparison to the x direction, the solution for the temperature can be obtained from the solution of T(t,x) from stationary systems with a constant heat input. The solution for an infinite plate with a constant heat input is:⁽³⁾

$$[T(t,x) - T_0] = \frac{2q}{k} (\alpha t)^{1/2} \sum_{n=1}^{\infty} \left[\text{ierfc} \frac{(2n-1)R-x}{2(\alpha t)^{1/2}} + \text{ierfc} \frac{(2n-1)R+x}{2(\alpha t)^{1/2}} \right]$$

in which T(t,x) temperature in a stationary system at time t and
 distance x from surface

T₀ initial temperature

q surface heat flux

k thermal conductivity

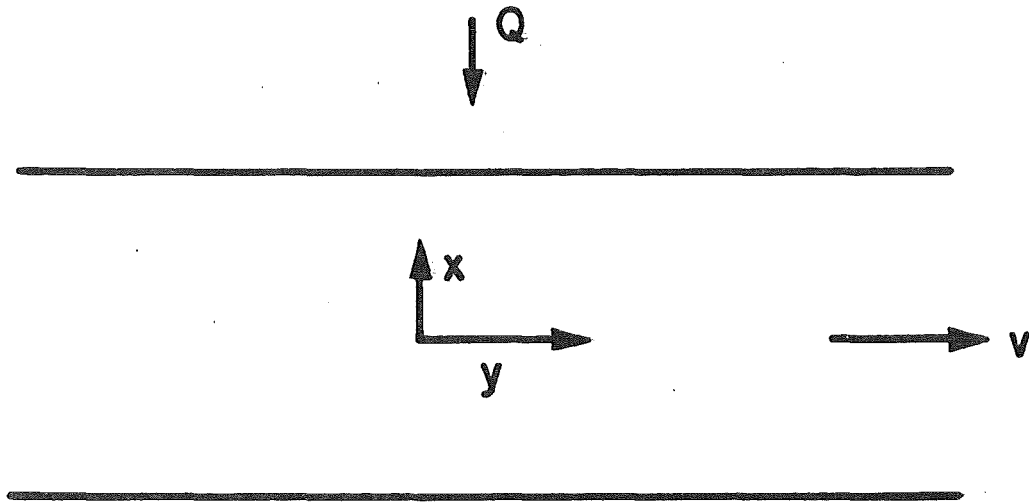


Fig. VI-3-4 GEOMETRY OF THE
HEAT TRANSFER CALCULATIONS

- α thermal diffusivity
- R thickness of the plate.

The required solution can then be obtained by

$$\theta_1(y,x) = T \left(\frac{y}{v}, x \right) - T_0. \quad (\text{VI.3-5})$$

- in which $\theta(y,x)$ temperature rise
- v coolant velocity.

The bulk temperature rise due to nuclear heating is

$$\theta_2(y) = 100 \times \frac{y}{L}. \quad (\text{VI.3-6})$$

in which L is the length of coolant passage. The superimposed temperature in the entire coolant passage is then

$$T(y,x) = \theta_1(y,x) + \theta_2(y) + T_0. \quad (\text{VI.3-7})$$

The temperature distribution of the blanket is calculated by this technique. A finite difference calculation was also performed to confirm the results of this calculation and the difference is less than 5°C. Fig. VI.3-5 shows the maximum temperature of the first wall as a function of distance from the entrance. The temperature difference across the first wall is 4°C. Figure VI.3-6 shows the temperature across the coolant tube at the coolant exit. The maximum blanket temperature is 440°C. This is considerably higher

Fig. VI-3-5 FIRST WALL TEMPERATURE AS A FUNCTION OF DISTANCE FROM COOLANT INLET

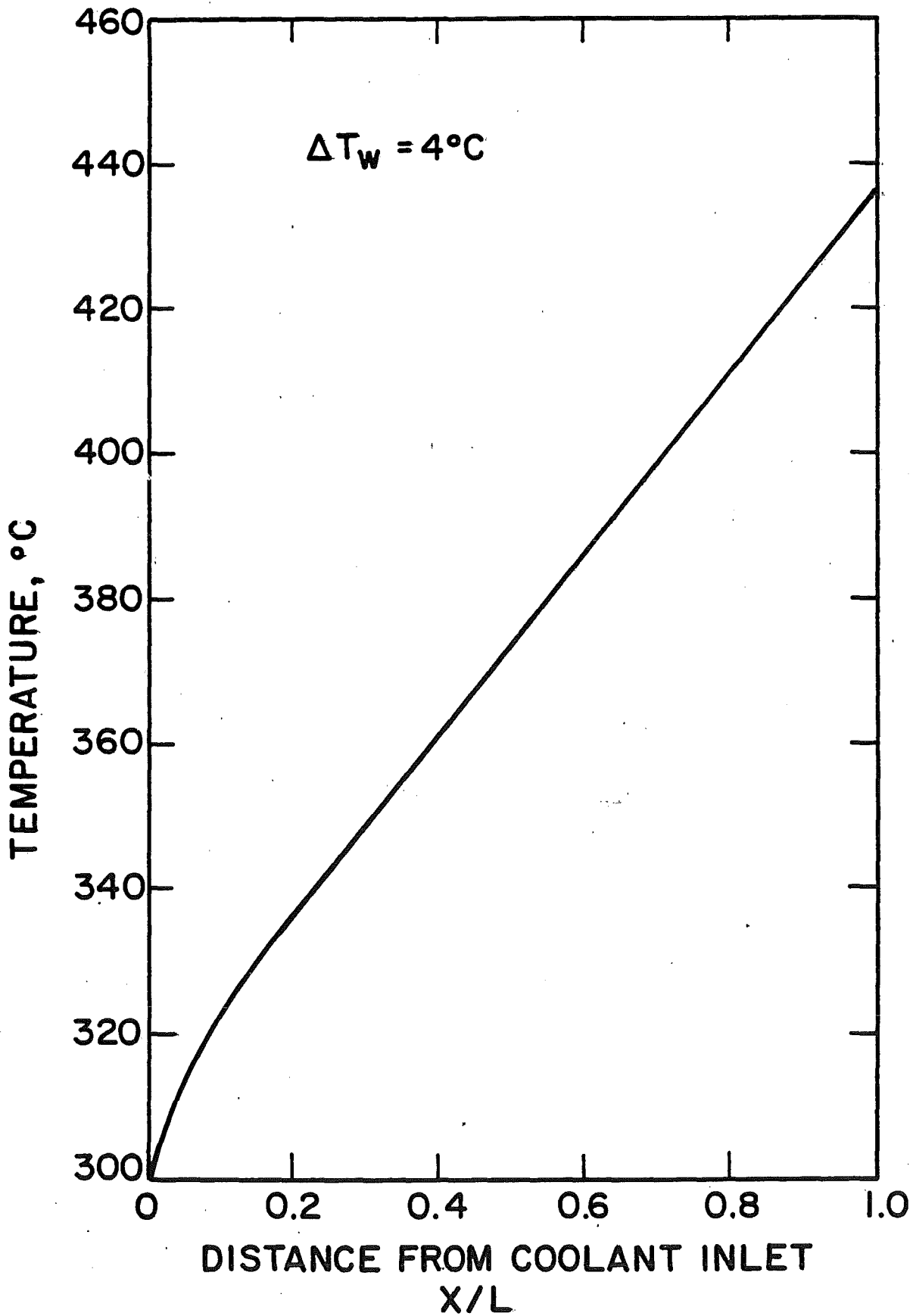
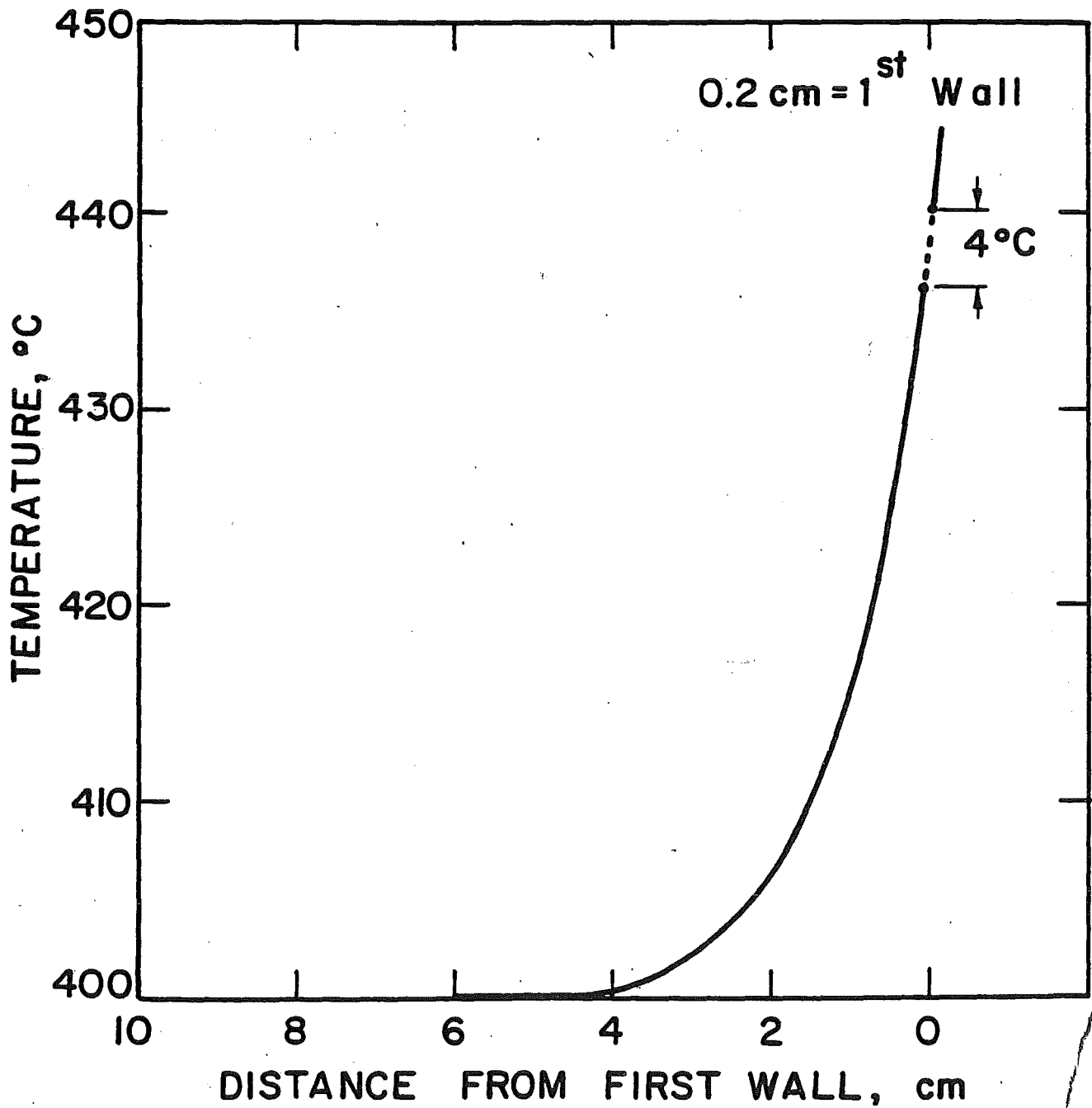


Fig. VI-3-6 COOLANT TEMPERATURE AT THE EXIT



from the plasma and nuclear heating from the first wall structure.

The large temperature difference from the coolant due to the bulk of the coolant is caused by MHD effects. The calculation assumes the absence of turbulence and heat transfer by conduction only. The total surface heating load on the coolant is 4 watt/cm^2 which, with $\Delta T = 36^\circ\text{C}$, corresponds to a very small heat transfer coefficient of $.11 \text{ watt cm}^2\text{-}^\circ\text{C}$. This heat transfer coefficient is consistent with a pure conduction system with $hD/k = 7$. Therefore, a first wall design of this type is only applicable to a power system with a very small surface heat flux.

VI.3.3 Cooling of the Reflector and the Shield

The coolant tube arrangement in the reflector is shown in Fig. VI.3-7. The distance between two coolant channels is 20 cm. The maximum volumetric energy deposition is $.1 \text{ W/cm}^3$. Therefore, the maximum temperature difference between two coolant channels is less than 30°C . The maximum heat flux to the coolant wall is $.1 \text{ W/cm}^2$ which can easily be removed by either helium or water. For this design, water will be used as the coolant. The inlet or outlet water temperatures are 80 and 140°C , respectively. The total power in the reflector is 5.08 MW , which corresponds to a coolant flow rate of 20 kg/sec . Since there is no need for good heat transfer, the maximum velocity needed can be less than 1 m/sec . The pressure drop is $.01 \text{ MPa}$. The pumping power required is less than 1 kW .

The shield is also cooled by forced convection water. For simplicity of the design, the water condition is chosen to be the same as the reflector. The shield design includes the two end modules of the central cell. The total energy deposited of 11.3 MW in the shield is, therefore, large compared to a conventional shield. The maximum energy flux to the coolant is $\sim 10 \text{ W/cm}^2$

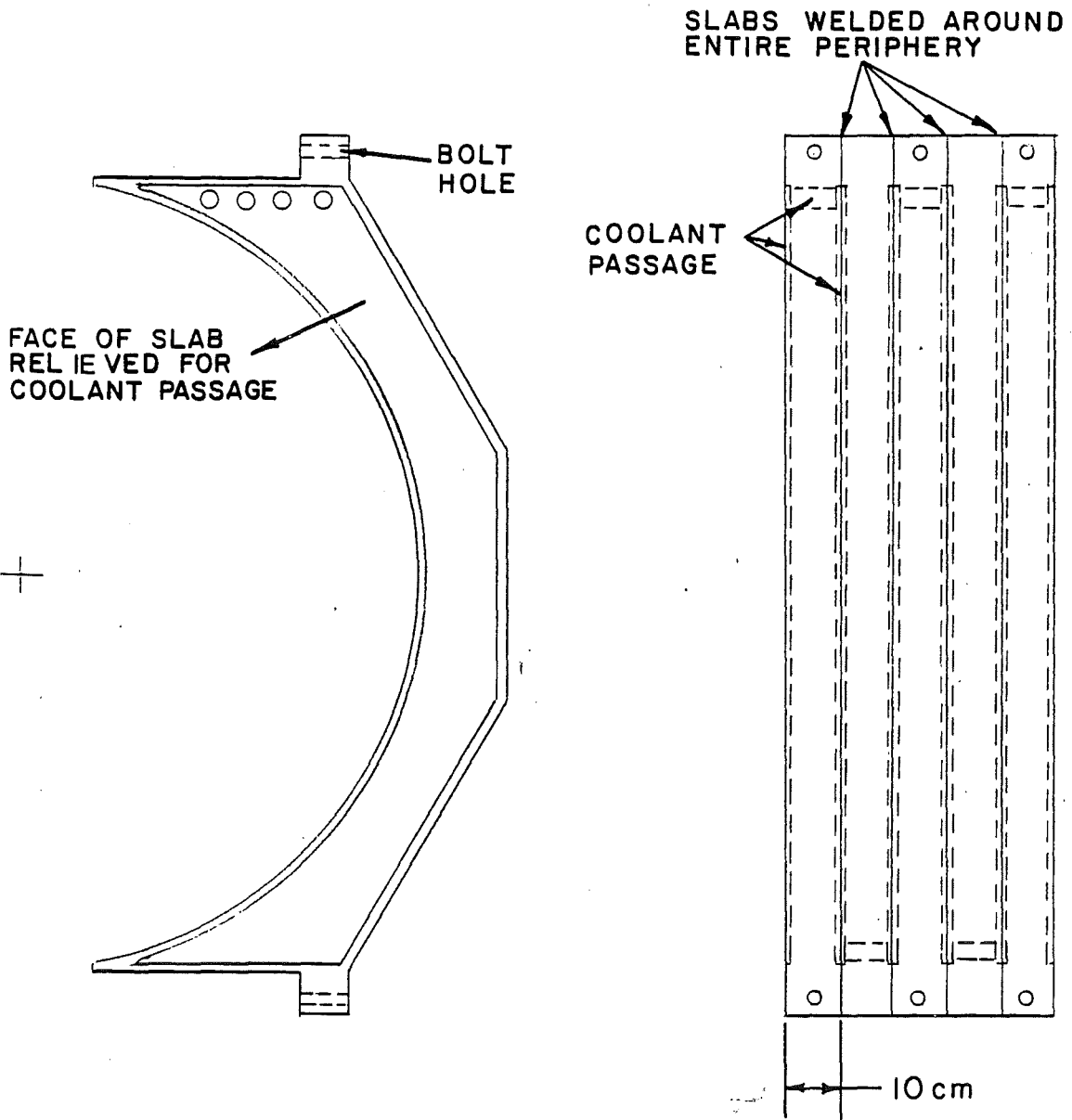


Fig. VI.3-7 Reflector Coolant Passage

conventional shield. The maximum energy flux to the coolant is $\sim 10 \text{ W/cm}^2$ which can also be handled easily by forced convection water. With a water velocity of 1 m/sec in a 1 cm ID coolant tube, a heat transfer coefficient of $1 \text{ W/cm}^2\text{-}^\circ\text{C}$ can be obtained, which corresponds to a film temperature drop of only 10°C . This is readily acceptable. The total coolant flow rate is 45 kg/sec. With a pressure drop of .01 MPa, the pumping power required is 2 kW.

The parameters of the reflector and the shield are summarized in Table VI.3-3.

Table VI.3-3 Parameters of the Shield and the Reflector

Coolant inlet temperature	80°C
Coolant outlet temperature	140°C
Total reflector power	5.08 MW
Maximum reflector energy deposition	.1 W/cm ³
Maximum heat flux to reflector coolant	.5 W/cm ²
Maximum reflector structural temperature	170°C
Minimum reflector structural temperature	80°C
Total shield power	11.3 MW
Maximum shield energy deposition	7.5 W/cm ³
Maximum heat flux to reflector coolant	10 W/cm ²
Maximum shield structural temperature	165°C
Minimum shield structural temperature	80°C
Coolant velocity	1 m/sec
Total coolant flow	65 kg/sec
Total pumping power	3 kW

References for Section VI.3

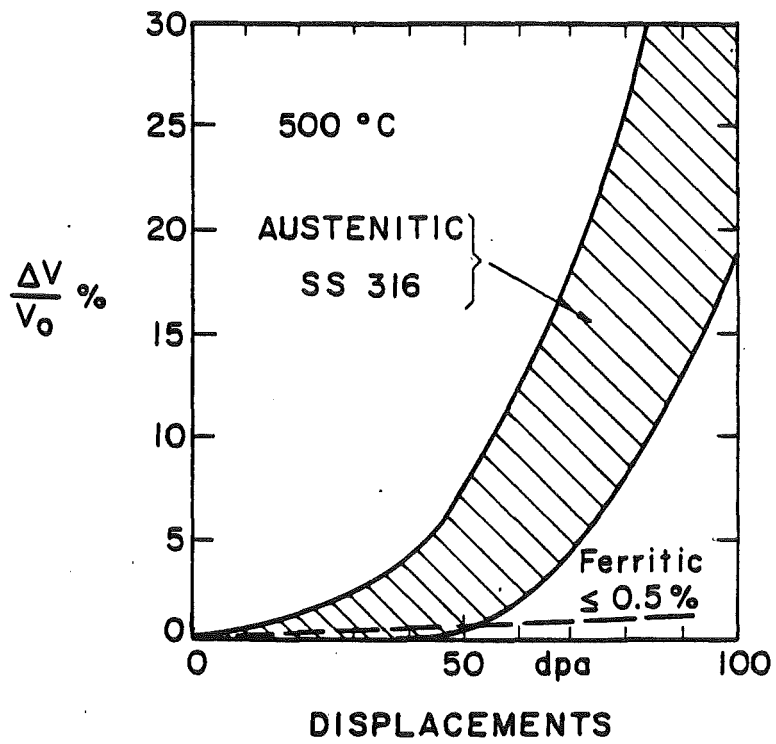
1. M.A. Hoffman and G.A. Carlson, "Calculation Techniques for Estimating the Pressure Losses for Conducting Flows in Magnetic Fields", USAEC Report UCRL-51010, 1971.
2. G.W. Sutton, and A. Sherman, "Engineering Magnetohydrodynamics", McGraw Hill, New York, 1956.
3. H.S. Carslaw and J.C. Jaeger, "Conduction of Heat in Solids", Oxford University Press, 1959.

VI.4 Structural Materials for TASKA

VI.4.1 General Considerations

Since TASKA is to be considered as one of the first fusion materials test facilities, structural materials to be used for its design must be those for which there exist a sufficiently broad data base in high radiation fields and in high temperature environments. Accordingly, the two alloy classes considered as potential candidates were the austenitic stainless steels and the ferritic (or martensitic) steels. Both materials classes were judged to be suitable structural materials for the blanket and the vacuum boundary. The major disadvantage of the austenitic stainless steels is their large propensity for swelling. This is clearly demonstrated by considering the swelling behavior of both austenitic type 316 stainless steel and ferritic steels as based on breeder reactor irradiation at about 500°C. As seen in Fig. VI.4-1, austenitic steels exhibit a rapid rate of swelling after an incubation dose varying between 30 and 60 dpa, depending on the particular heat treatment. In contrast, ferritic steels have not exhibited more than 0.5% swelling in similar irradiation experiments.⁽¹⁾ Based on the breeder reactor experience and the review given below, it appears that the blanket components exposed to the highest neutron fluence in TASKA would swell about 15% to 20% if made of 20% CW type 316 stainless steel. Although a linear expansion of 5% to 7% due to swelling can be accommodated with the blanket designs contemplated for TASKA, it is doubtful that a significantly larger expansion could be accommodated in a power producing tandem mirror fusion reactor. Therefore, although the austenitic stainless steels were judged suitable for TASKA they do not seem to be the answer for future fusion reactors.

Fig. VI.4-1. Swelling behavior of austenitic and ferritic steels irradiated in EBR-II.



In order to gain fusion reactor relevant experience with a structural material, it was decided to select ferritic steels as the prime candidates for TASKA. However, in the course of this design study, it was discovered that ferritic steels used as structural materials for the blankets may significantly perturb and lower the magnetic field and its distribution in the central cell region, particularly at either end of the central cell. The amount of field perturbation and reduction that can be tolerated in a mirror reactor is, at the present time, not known. It appears, however, that these issues can be resolved by appropriate designs of the blanket modules and by a modest increase of the magnetic field in the central cell region.

It will be evident from the discussions below that ferritic steels are to be preferred over austenitic steels for the following reasons:

- A) Much greater resistance to neutron induced void formation and metal swelling.
- B) A greater resistance to in-reactor creep below 600°C.
- C) Better ductility retained after high temperature fission neutron irradiation.
- D) Better thermal stress resistance, at least by a factor of two.
- E) Better compatibility with the $Pb_{83}Li_{17}$ breeder/coolant material.
- F) Considerably more experience in heat exchanger design and aqueous environments.
- G) Lower material cost per unit weight.
- H) Less demand on Cr (12 vs. 18%) and Ni (0.5 vs. ~ 8%) resources which generally have to be imported.

The specific choice of HT-9 over other ferritic steels should not be taken too seriously. This alloy system has been identified as one particularly attractive to the fast breeder and, as such, gives us a convenient data base from which to extrapolate its performance in a fusion environment. It is quite possible that other ferritic steels might be developed to give even better properties in a fusion environment and future studies ought to be open to new ideas in this area.

VI.4.2 Physical and Thermal Properties of HT-9

The general class of alloys that we considered are the ferromagnetic steels which contain roughly 9 to 13% Cr with some small addition of various strengthening and stabilizing elements such as Mo. These steels are conventionally used in the normalized and tempered condition for high temperature applications. Although the heat treatment can result in either a tempered martensite or bainite structure, depending on the alloy and thermal treatment parameters, this class of materials is usually referred to as "martensitic" stainless steels for simplicity.

Because of the encouraging and rapidly expanding data base from the U.S. Fast Breeder Reactor Program and the significant operational history in Europe, the alloy Sandvik HT-9 (DIMX20CrMoWV121) was selected for TASKA. The normal composition of this alloy is given in Table VI.4-1 and Fig. VI.4-2⁽²⁾ gives the binary section of the Fe-Cr-C phase diagram at 12%. For high temperatures and extended time service, the alloy is usually heat treated at 1050°C for 0.5 hours in the austenite zone (Fig. VI.4-3), air cooled and then tempered at 780°C.

The thermal properties of the 9 Cr-1 Mo system, which should be close to HT-9 are given in Table VI.4-2.⁽³⁾

Table VI.4-1. Nominal Composition of HT-9 Alloy

<u>Element</u>	<u>Wt%</u>
Fe	Balance
Cr	11.5
Mo	1.0
Ni	0.5
W	0.5
Mn	0.5
V	0.3
Si	0.25
C	0.20

Fig. VI.4-2
(Reference 2)

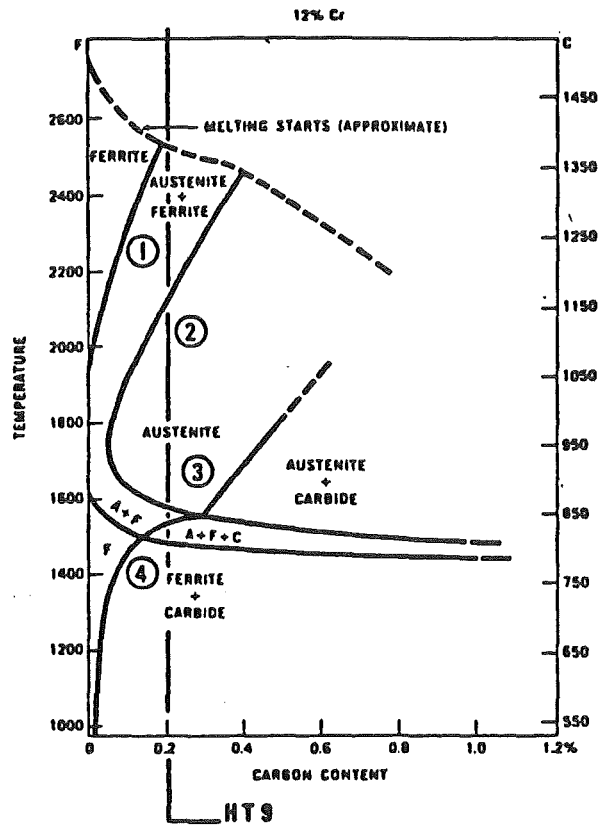


Fig. VI.4-3
(Ref. 2)

TYPICAL HEAT TREATMENT PROFILE FOR A MARTENSITIC STAINLESS STEEL

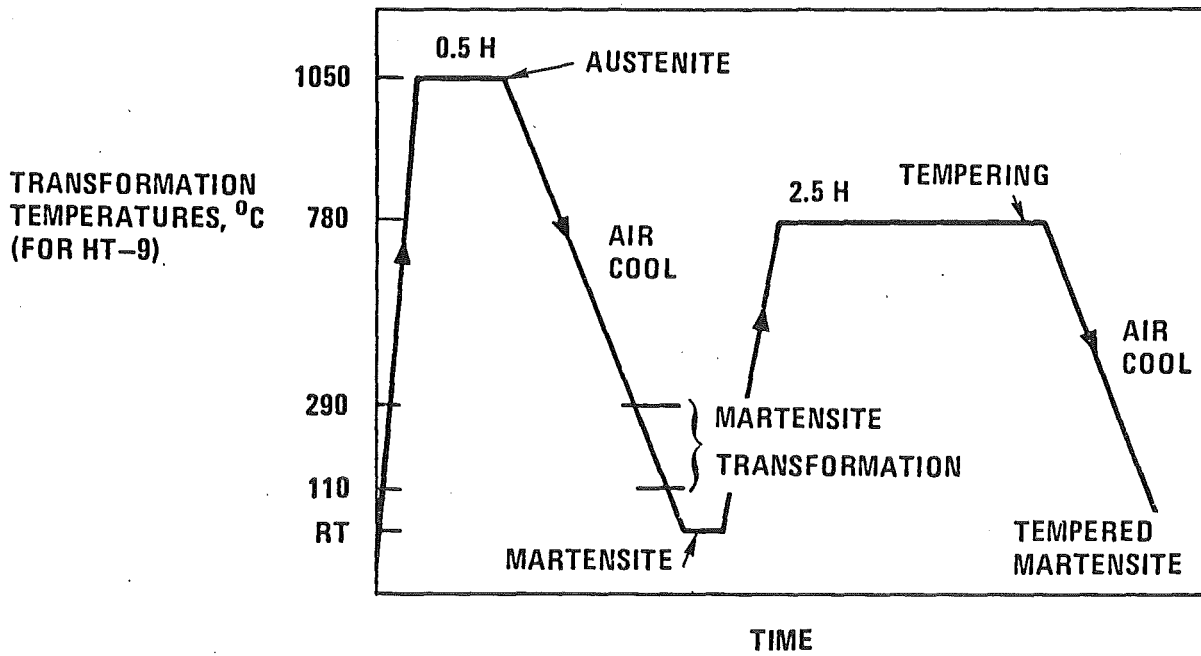


Table VI.4-2. Selected Thermal Properties of the 9 Cr-1 Mo Steel(20)

Temperature		Thermal Conductivity	Thermal Diffusivity	Specific Heat	Instantaneous Coefficient of Thermal Expansion	Mean Coefficient of Thermal Linear Expansion
°F	°C	W cm ⁻¹ C ⁻¹	cm ² s ⁻¹	cal g ⁻¹ C ⁻¹ x 10 ³	10 ⁻⁶ C ⁻¹	10 ⁻⁶ C ⁻¹
70	21	.222	.066	.105	3.23	
100	38	.227	.067	.106	3.28	3.25
150	66	.235	.067	.109	3.35	3.29
200	93	.242	.067	.112	3.42	3.34
250	121	.249	.068	.114	3.49	3.39
300	149	.254	.068	.117	3.56	3.42
350	177	.260	.067	.120	3.63	3.46
400	204	.263	.067	.123	3.69	3.49
450	232	.267	.066	.126	3.75	3.52
500	260	.270	.065	.129	3.82	3.56
550	288	.273	.064	.133	3.87	3.59
600	316	.275	.063	.136	3.93	3.62
650	343	.277	.062	.140	3.98	3.65
700	371	.277	.061	.144	4.04	3.68
750	399	.279	.059	.147	4.09	3.70
800	427	.279	.057	.152	4.13	3.73
850	454	.280	.055	.157	4.18	3.76
900	482	.279	.053	.163	4.23	3.79
950	510	.279	.051	.169	4.27	3.81
1000	538	.279	.050	.175	4.31	3.83
1050	566	.277	.047	.183	4.35	3.86
1100	593	.277	.045	.191	4.39	3.89
1150	621	.275	.043	.201	4.43	3.92
1200	649	.273	.040	.213	4.46	3.93
1250	677	.272	.037	.229	4.49	3.96
1300	704	.270	.034	.250	4.52	3.98
1350	732	.268	.030	.276	4.55	4.00
1375	746		.028	.295*		
1400	760	.263	.038	.216	4.57	4.02
1450	788	.260	.043	.190	4.60	4.04
1500	816	.260	.046	.178	4.62	4.06

* Extrapolated value

The electrical conductivity of the ferritic steels is in the range of 0.002 to 0.005 Ω^{-1} depending on the composition and heat treatments. No specific value was found for HT-9.

VI.4.3 Use of Martensitic Steels

It is fortunate that there are so many applications for martensitic steels throughout the U.S. and the world. A recent summary by scientists at General Atomic revealed that there are major applications for high temperature martensitic stainless steels in the following areas:⁽⁴⁾

- Fossil Power Plants

 - Superheaters

 - Reheaters

 - Evaporators

 - Steam piping

- Nuclear Power Plants

 - Superheaters, reheaters, U.K. Hinkley Point "B" AGR

 - Steam generator: U.K. PFR

 - He compressors, circulators: U.S. Fort St. Vraains HTGR

- Other Applications

 - Gas and steam turbine components

 - Aircraft and missile thin wall pressure vessels

 - Petroleum industry pressure vessel linings

It was found that the 9-12 Cr steels were used in foreign fossil power plants under the following conditions:

<u>Location</u>	<u>Usage</u>	<u>Alloy</u>	<u>Temp °C</u>	<u>Service Status</u>
U. K.	13 plants	9 CrMo(V)	450-660	< 110,000 hrs.
	12 plants	12 CrMo	430-850	< 45,000 hrs.
Austria] 96 Tons	9 CrMo	< 610	< 110,000 hrs.
Belgium				
Czechoslovakia				
Germany				
Switzerland				
Turkey] > 250 Tons	12 CrMo(V,W)	< 610	< 130,000 hrs.
Yugoslavia				

In addition to past and current usage, several future areas of use are being considered.

<u>System</u>	<u>Application</u>	<u>Alloys</u>
US-LMFBR	Ducts (cladding)	HT-9
	Steam generator	MOD 9 Cr-1 Mo
US-GCFR	Ducts, cladding, steam generator, shielding	HT-9/MOD 9 Cr-1 Mo
French Super	Ducts	9-17 Cr
Phenix	Steam generator	9 Cr-1 Mo
Japanese FBR	Steam generator	9 Cr-2 Mo
US-HTGR	Steam generator & pumping, He-He heat exchangers He circulators	HT-9/MOD 9 Cr-1 Mo
US-LWR	Steam generator	HT-9/MOD 9 Cr-1 Mo

It is from this extensive experience that one can often obtain a great deal of mechanical property data which is summarized in the next section.

VI.4.4 Mechanical Properties of HT-9

The tensile strength of HT-9 is compared to that for several other candidate CTR materials in Fig. VI.4-4. This figure shows that HT-9 is superior to annealed 316 SS up to $\sim 600^{\circ}\text{C}$ and it compares favorably to Ti-6Al-4V in the 400-600 $^{\circ}\text{C}$ range. However, above 500 $^{\circ}\text{C}$ the yield strength begins to drop, and it is best to limit its operating range to below 500-550 $^{\circ}\text{C}$.

The effect of long term exposure at 600 $^{\circ}\text{C}$ on the tensile properties of HT-9 is shown in Fig. VI.4-5.⁽³⁾ It can be seen that exposure to 600 $^{\circ}\text{C}$ temperatures for 80,000 hours (~ 10 years) reveals that there is very little degradation of ultimate or 0.2% yield strength. The percentage elongation also stays between a comfortable 10 and 30% even after long term exposure. A recent study⁽⁶⁾ also reports that HT-9 specimens subjected to 1 atm of hydrogen gas during testing at 200-400 $^{\circ}\text{C}$ had no effect on ductility.

The ductility of HT-9 is compared to other CTR alloys in Fig. VI.4-6⁽⁵⁾ and reveals that HT-9 retains a factor of 2 better ductility in the 400 $^{\circ}\text{C}$ -600 $^{\circ}\text{C}$ range compared to 316 SS.

Long term stress rupture data for HT-9 and other alloys at 500 $^{\circ}\text{C}$ is shown in Fig. VI.4-7. This information reveals that for up to 10 years of exposure, HT-9 can withstand stresses up to ~ 200 MPa.

The effect of 80,000 hour-600 $^{\circ}\text{C}$ service exposure on HT-9 stress-rupture properties is shown in Fig. VI.4-8. There is a slight degradation of the properties but it appears that stresses of 20 ksi (~ 130 MPa) or more are quite reasonable for 100,000 hour exposures.

Fig. VI.4-4a

Ultimate tensile strength versus temperature for candidate CTR alloys. (5)

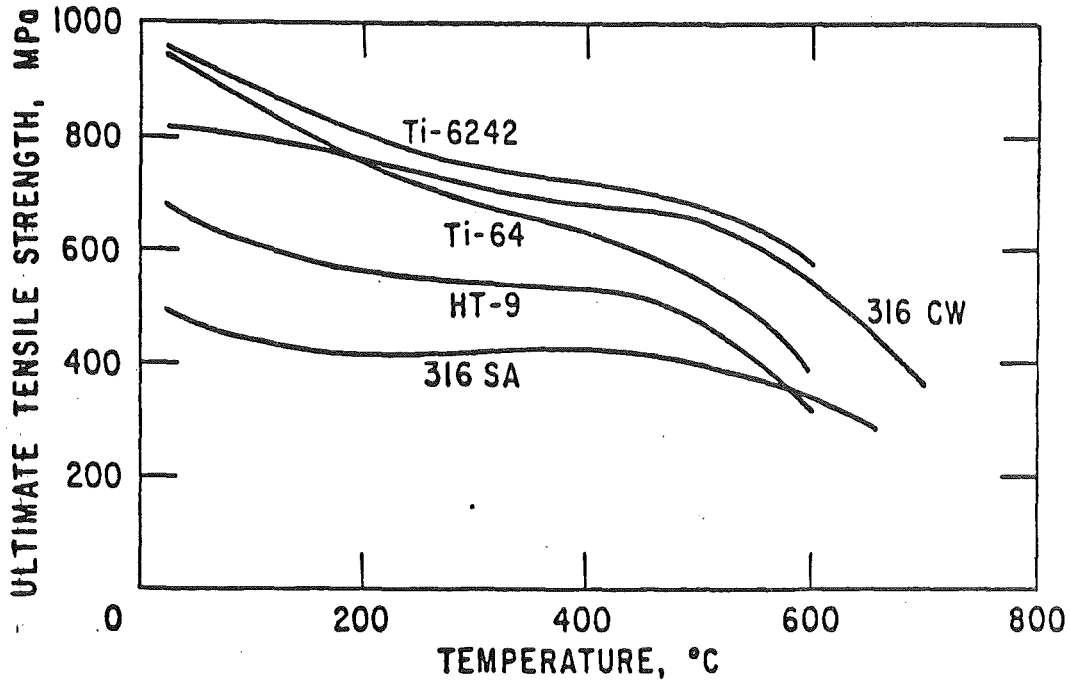


Fig. VI.4-4b

Tensile yield strength versus temperature for candidate CTR alloys. (5)

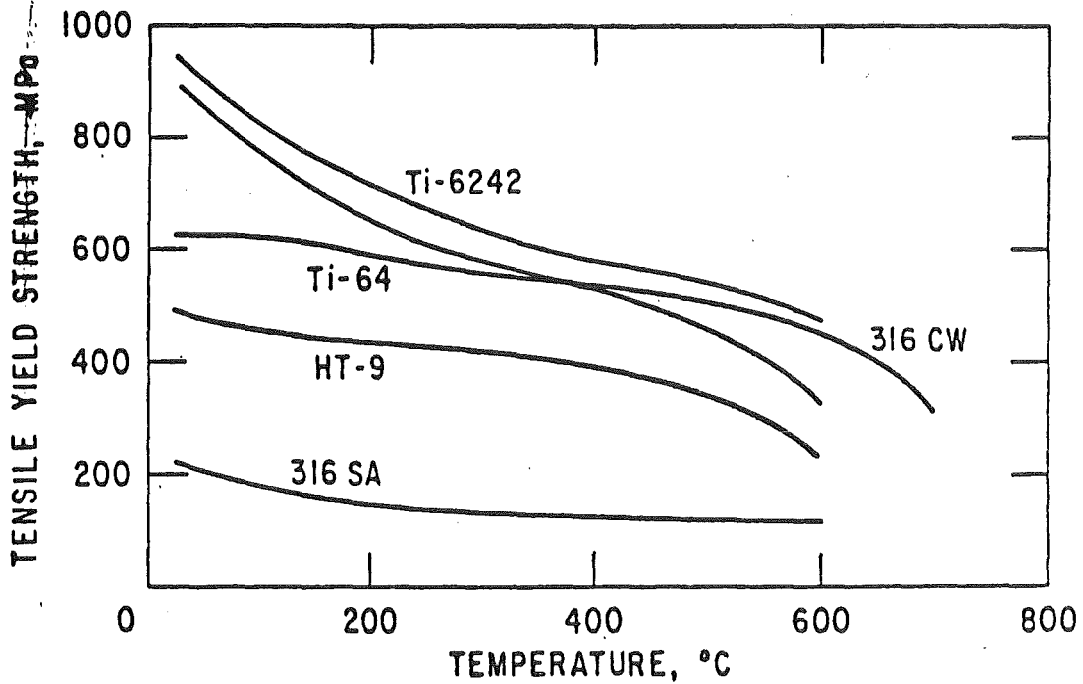


Fig. VI.4-5
(Reference 3)

EFFECT OF 80,000 HOUR, 600°C SERVICE EXPOSURE ON HT-9 TENSILE PROPERTIES

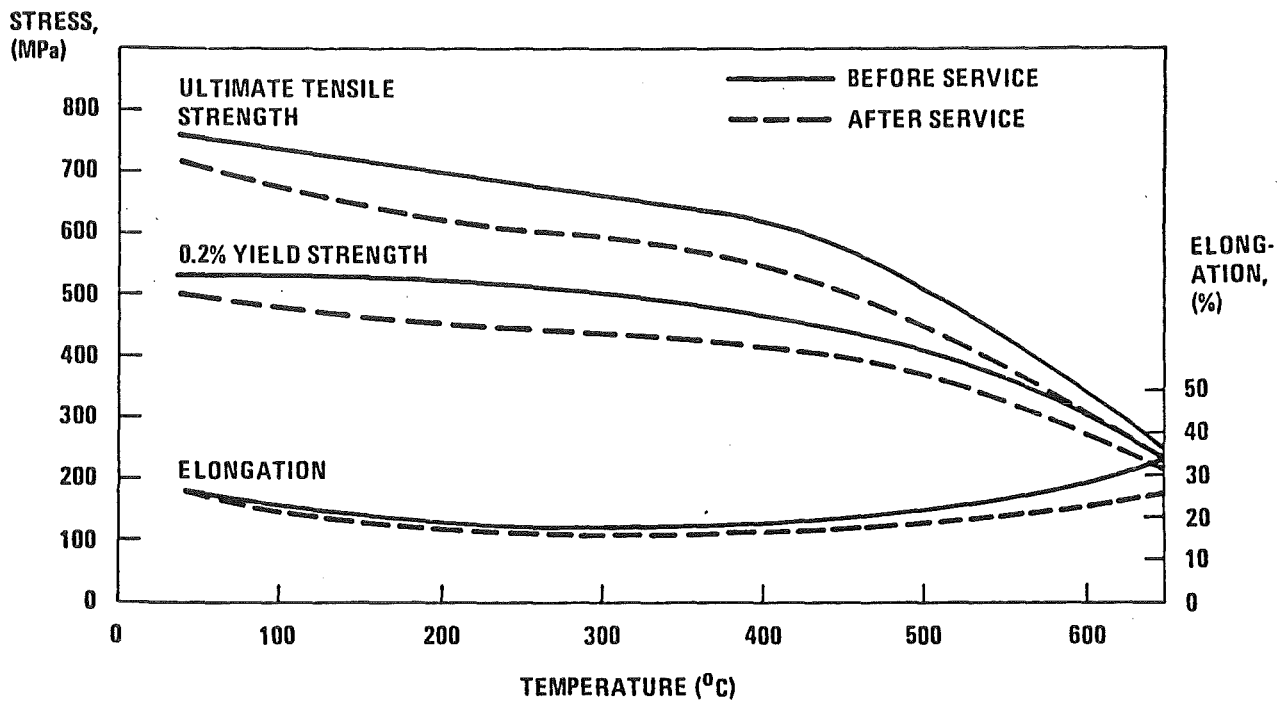
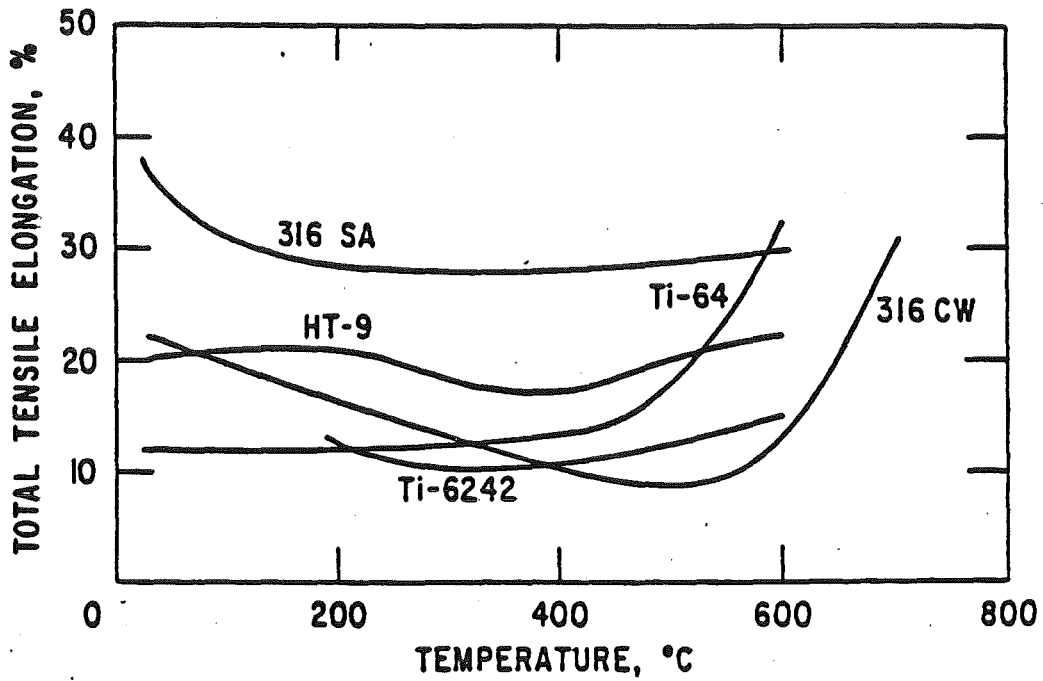
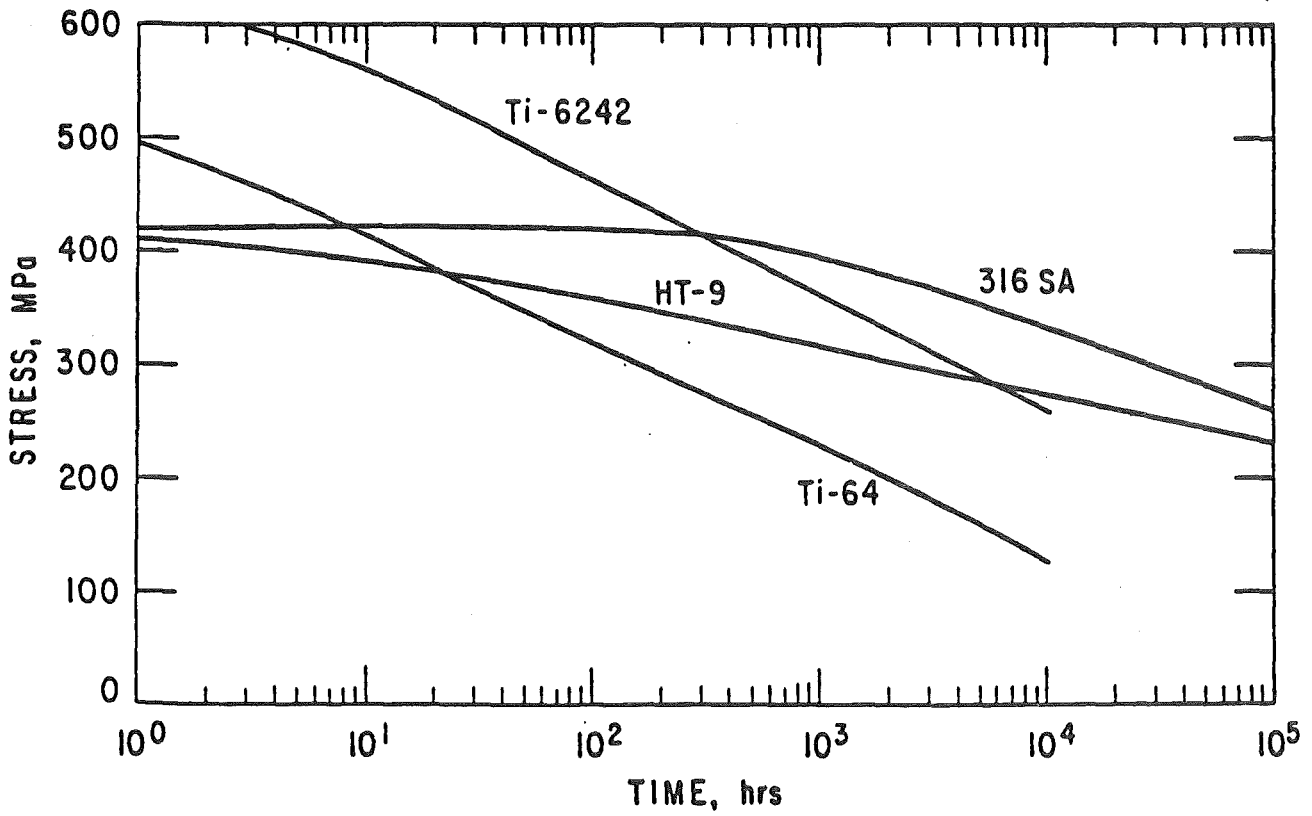


Fig. VI.4-6



Total tensile elongation versus test temperature for candidate CTR alloys. (22)

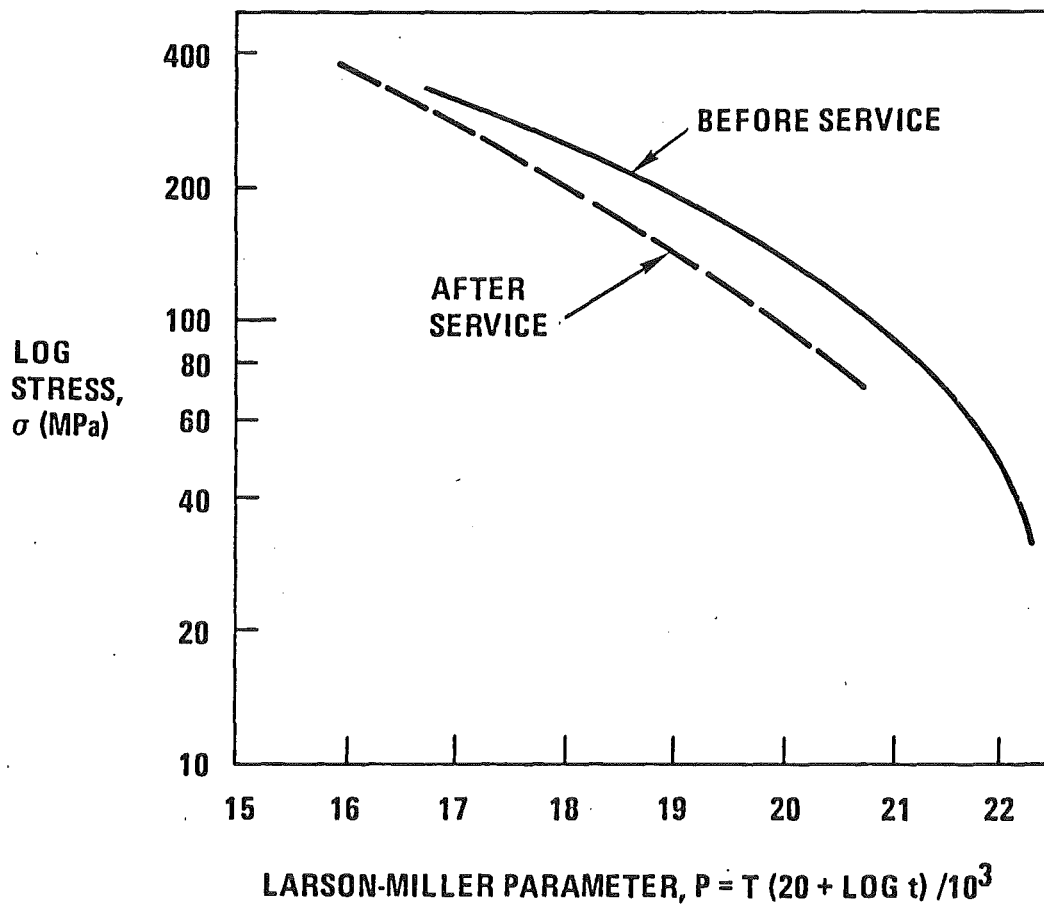
Fig. VI.4-7



Stress rupture data at 500°C for candidate CTR alloys.(22)

Fig. VI.4-8
(Reference 4)

EFFECT OF 80,000 HOUR, 600°C SERVICE EXPOSURE ON HT-9 STRESS-RUPTURE PROPERTIES



Even though TASKA is a steady state device, there will be numerous startups and shutdowns that will impose large stresses on the structure. Therefore, information on crack growth rates is important. Such information is given in Fig. VI.4-9 for helium environments and reveals that even under the most severe conditions the crack growth rates of unirradiated HT-9 are less than 10^{-4} mm per cycle at 530°C operating temperatures. If the HT-9 is tested in air, a much more aggressive environment, the crack growth rates are increased, even at 425°C (Fig. VI.4-10). However, the growth rates are still roughly 4 times lower than found in 20% CW 316 SS or 9 Cr-1 Mo alloys.

VI.4.5 Thermal Stress Factor

When rigidly held plates are subjected to high heat fluxes, the resulting differential thermal expansion generates large stresses and in extreme circumstances can even cause failure. This can be a particularly difficult problem for tokamaks.

A typical figure of merit which has been used to indicate the resistance of metals to failure is the ratio of the yield stress to the thermally induced stress. If we assume equal thickness and nuclear heat generation rates, then the figure of merit, M (a high value is desired), is:

$$M = \frac{2\sigma_y K(1 - \nu)}{\alpha E}$$

where: σ_y is the yield strength;

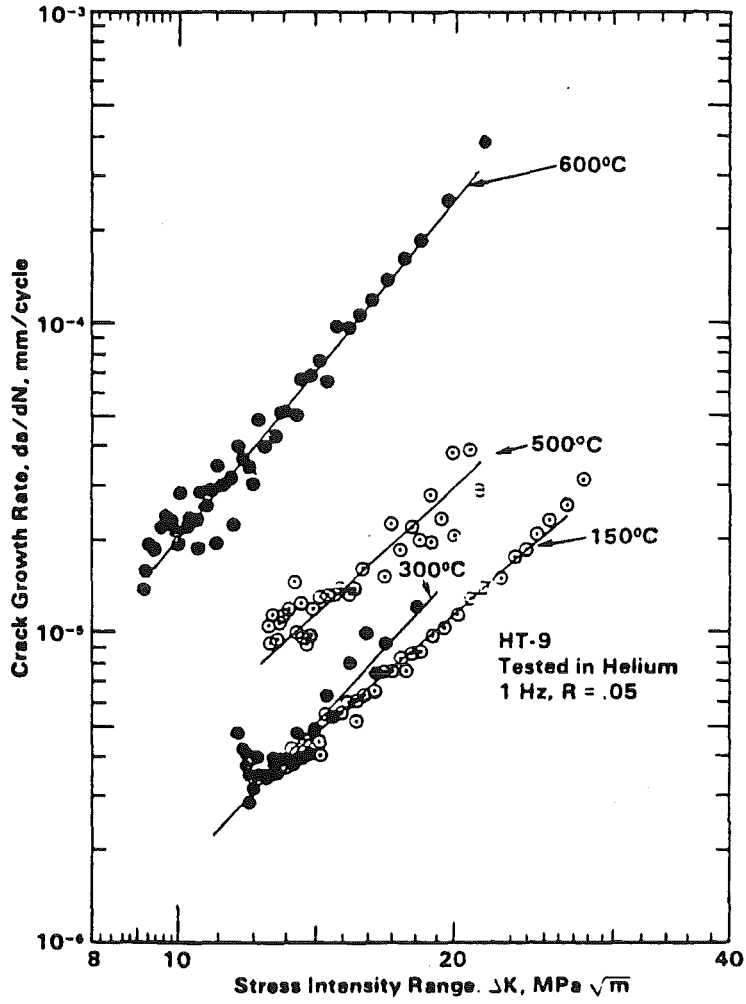
K is the thermal conductivity;

ν is Poisson's ratio;

α is the thermal expansion coefficient;

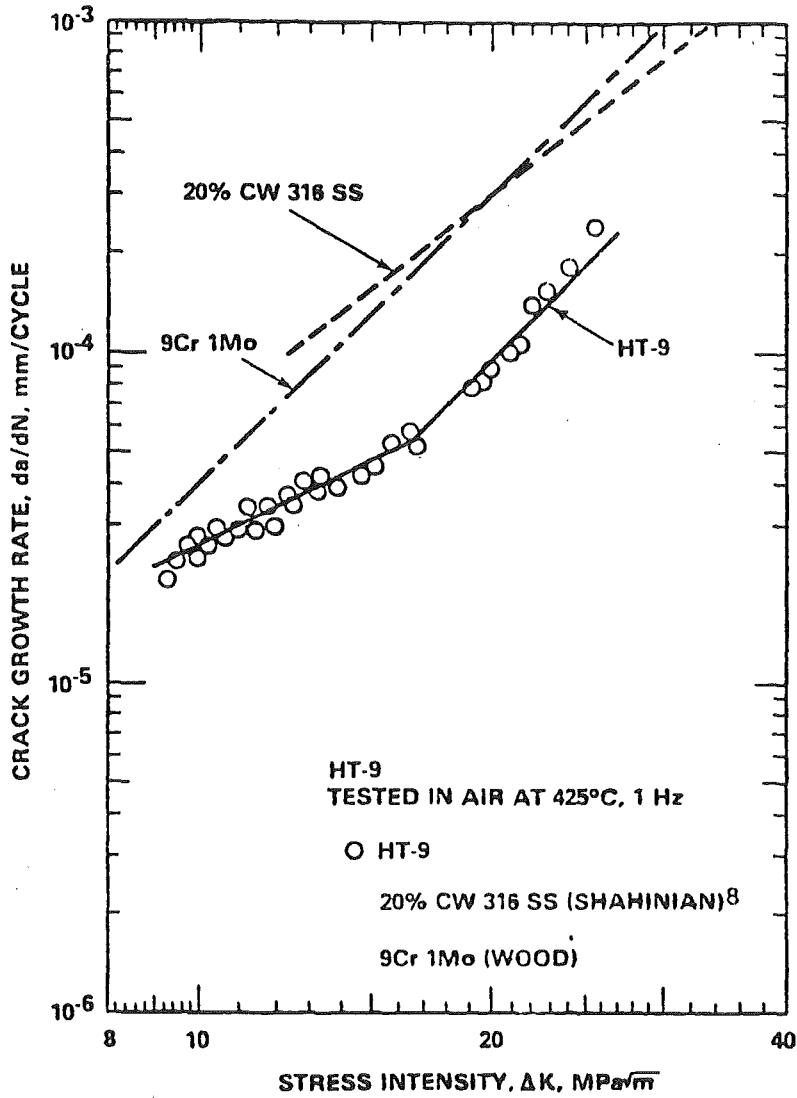
E is Young's modulus.

Fig. VI.4-9



Comparison of Crack Growth Between 150 and 600°C.

Fig. VI.4-10



HT-9 crack growth compared with 9 Cr-1 Mo and 20% CW 316 SS. Reference -- D. A. Mervyn et al., p. 132 in DOE/ER-0045/2, March 31, 1980.

Typical values of M have been calculated for 316 SS, HT-9, Ti alloys, Inconel 718, and V-20 Ti, at 500°C. These values are given in Table VI.4-3.

It can be seen that the HT-9 alloy has a figure of merit of at least twice that of cold worked 316 SS and slightly less than Ti and Mo alloys at 500°C. HT-9 is clearly inferior to refractory metals but, for lack of extensive irradiative experience we will not consider those systems in TASKA.

VI.4.6 Compatibility of HT-9 with Pb-Li Alloys

As might be expected, there is little data concerning the $Pb_{83}Li_{17}$ eutectic alloy on HT-9 at temperatures of 350-550°C. There is a small amount of information on low alloy, high strength steels in pure lead,^(7-9,11,14) and some data on 2-1/4 Cr-1 Mo alloys with a $Li_{99}Pb_1$ system at 500°C.⁽¹⁰⁾ The only information on liquid metals and HT-9 is a recent study at ANL in pure lithium and lithium contaminated with nitrogen at 482°C⁽¹²⁾ and a recent ORNL investigation with $Pb_{83}Li_{17}$.⁽¹³⁾

Despite claims in earlier studies that low alloy steels were not embrittled by pure lead, recent results showed embrittlement could occur near the melting point of the lead (327°C).^(11,14) The embrittlement of the high strength 4100 series steels (see composition in Table VI.4-4) started at ~ 200°C and reached a maximum (lowest ductility) at ~ 320°C. Above ~ 370°C there was degradation in the ductility (see Fig. VI.4-11). The addition of Sn increased the width of the embrittling zone.

At higher temperatures, 700°C, 2-1/4 Cr-1 Mo alloy suffered a severe attack after 300 hours of exposure to lead.⁽⁹⁾ However, the addition of Ti to the Pb completely eliminated the corrosion under the same conditions. It has been known for a long time that the addition of Ti or Zr to Pb would inhibit corrosion by forming tightly adhering TiC and ZrC films on the steel surface.

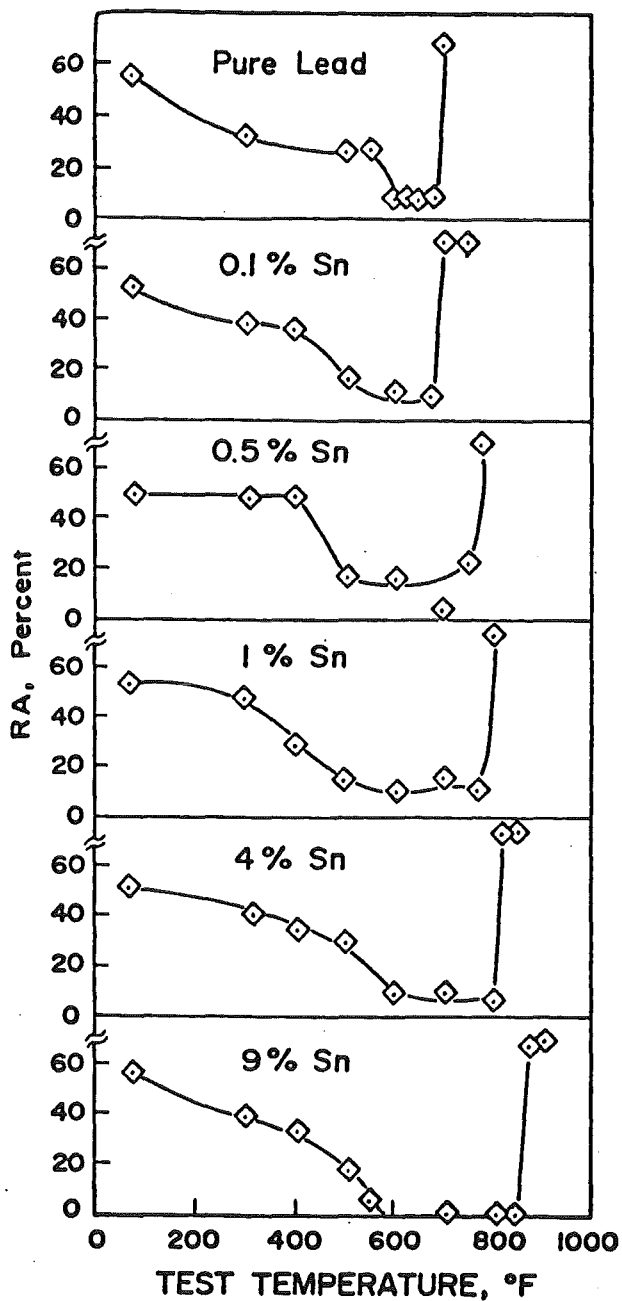
Table VI.4-3. Thermal Stress Resistance of
Potential Fusion Materials at 500°C

<u>Alloy</u>	<u>Thermal Stress Resistance (W/m) x 10⁻³</u>
Annealed 316 SS	1.3
20% CW 316 SS	4.9
HT-9	8.5
Ti-6Al-4V	10.2
Ti-6Al-2Sn-4Zr-2Mo	10.4
Inconel-718	10.7
V-20 Ti	12.2

Table VI.4-4. Comparison of Some Alloy Steels Which Have Been Tested
in Pb, Li or Pb-Li Alloys

<u>Alloy</u>	<u>Element - wt% (Bal. Fe)</u>				
	<u>Cr</u>	<u>Mn</u>	<u>Mo</u>	<u>C</u>	<u>Si</u>
4140	0.96	0.87	0.18	0.41	0.23
4145	1.00	0.88	---	0.47	0.33
Croloy	2.25	0.5	1.0	0.12	---
HT-9	11.5	0.5	1.0	0.2	0.25

Fig. VI.4-11



Reduction of area, RA, for 200-ksi (1379-MPa) 4145 steel, surface wetted with various Pb-Sn alloys as a function of test temperature. (30)

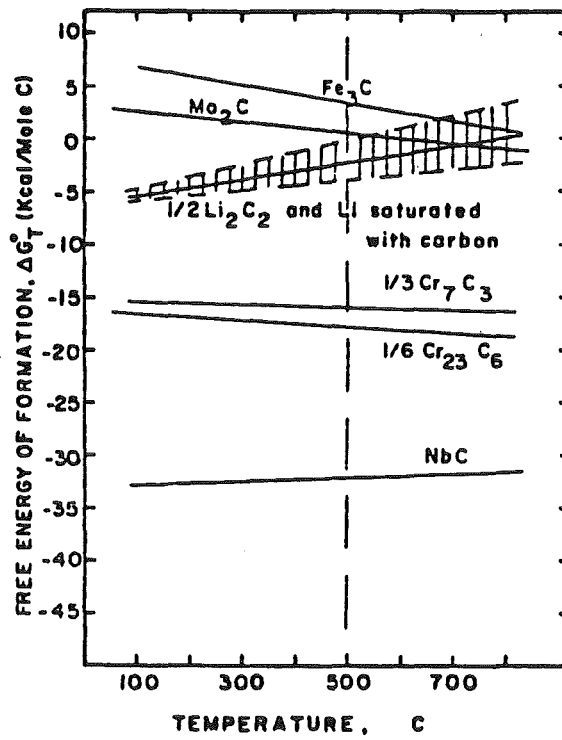
On the other end of the spectrum, a $\text{Li}_{99}\text{Pb}_1$ alloy was shown to attack Fe_3C and Mo_2C in the welded zones of a 2-1/4 Cr-1 Mo alloy at 500°C after exposure up to 1600 hours. Figure VI.4-12, from the paper by Anderson et al.⁽¹⁰⁾, shows that the cementite and Mo_2C are unstable with respect to Li below 500°C while the chromium carbides are stable over a wide range.

Work at Harwell⁽¹⁵⁾ has shown that low alloy steels can be significantly decarburized by exposure to Li even at ~ 200°C. However, higher Cr containing steels such as 2-1/2 Cr-1 Mo, or the 9 Cr-1 Mo alloys showed much greater resistance.⁽¹⁶⁾ Presumably, the higher Cr content of HT-9 would help to protect that alloy from decarburization and hence embrittlement.

A recent study by Chopra and Smith⁽¹²⁾ has shown that nitrogen can have a large effect on the fatigue life of HT-9 in flowing Li at 482°C. They found that in short term fatigue tests, where the nitrogen level was between 80 and 130 ppm, the fatigue life in Li was the same as that obtained in Na. However, when the nitrogen level reached > 1000 ppm of nitrogen, there was a dramatic drop in the fatigue life (Fig. VI.4-13) by as much as a factor of 5. This strongly suggests that close control of the nitrogen level in the TASKA coolant will be necessary.

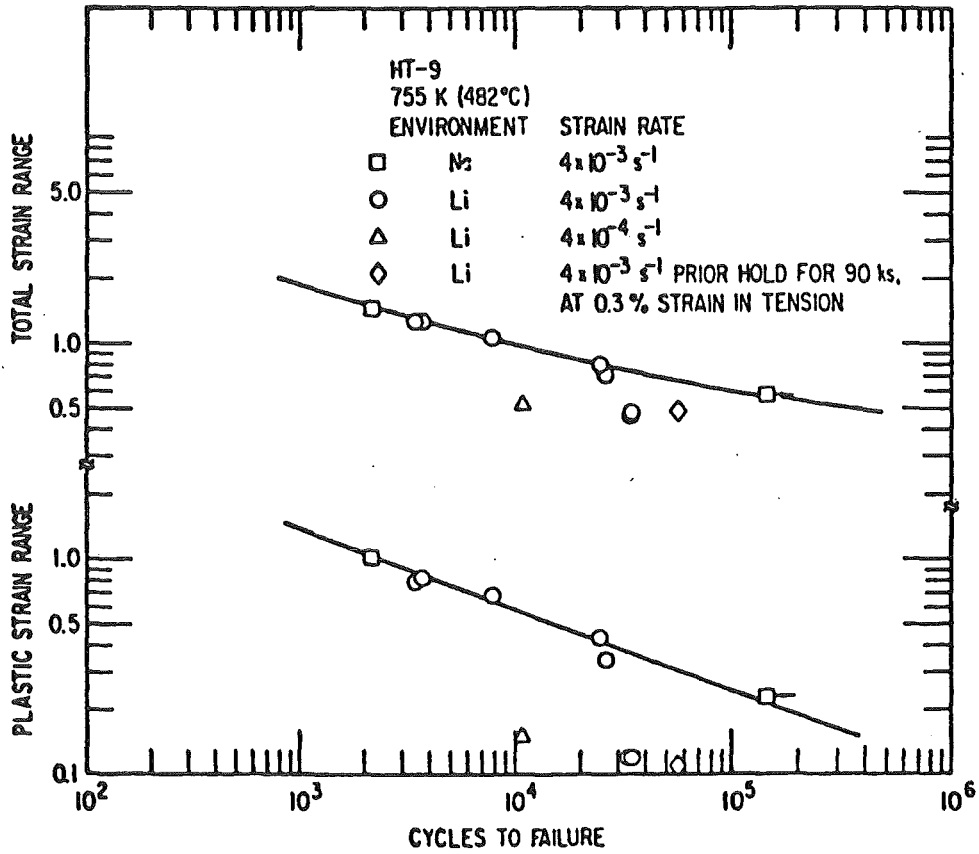
Tortorelli and DeVan have most recently studied the compatibility of type 316 stainless steel and HT-9 with static Pb-17 at.% Li in the temperature range from 300 to 500°C. The effects of corrosion were characterized by changes in specimen weight and tensile properties after exposure. Figure VI.4-14 shows the weight change as a function of exposure at a temperature of 500°C. Less weight change was obtained at lower temperatures, as seen from the results in Table VI.4-5.

Fig. VI.4-12



Relative thermodynamic stability of several carbides in carbon saturated lithium.

Fig. VI.4-13



Total and plastic strain range vs. cycles to failure for HT-9 alloy tested in lithium at 755 K.

Fig. VI.4-14
Weight loss in liquid Li and $\text{Li}_{17}\text{Pb}_{83}$

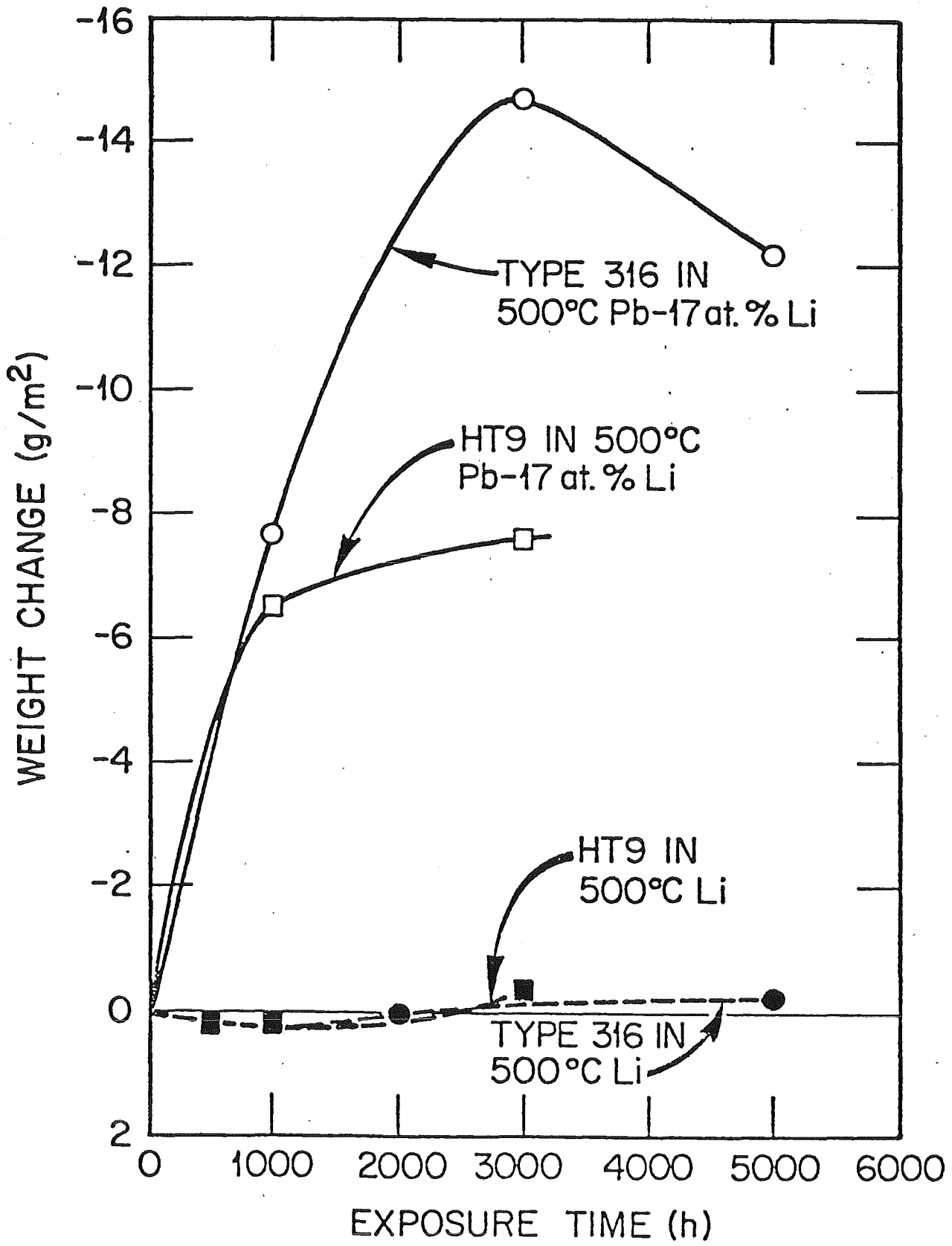


Table VI.4-5. Weight Changes of Type 316 Stainless Steel and Sandvik HT-9(a)
Exposed to Static Argon and Pb-17 at.% Li

Exposure Temperature (°C)	Exposure Time (h)	Weight Change ^(b) (g/m ²)			
		Type 316 in Pb-Li	Type 316 in Ar	HT-9 in Pb-Li	HT-9 in Ar
300	1000	-0.4	-0.1	-2.3	
	3000	-0.4	0.0	-6.6	
	5000	-1.0	0.0	-6.6	
400	1000	-0.9	-0.1	-3.2	
	3000	-1.2	0.0	-5.6	
	5000	-3.2	0.0	-5.6	
500	1000	-7.6	+0.1	-6.5	+0.2
	3000	-14.7	0.0	-7.6	0.0
	5000	-12.2	+0.1		
900	20	-11.9 ^(c)	+0.1		

(a) Normalized and tempered.

(b) Average of measurements from two specimens unless otherwise noted.

(c) Average of measurements from six specimens.

Although both type 316 stainless steel and HT-9 show significant weight losses when exposed to static Pb-17 at.% Li at 500°C, no significant changes in room temperature tensile properties could be detected, as demonstrated by the results in Table VI.4-6.

In summary, it appears that Pb₈₃Li₁₇ can have a corrosive effect on HT-9 at temperatures of 500°C and presumably higher temperatures. The application of molten Pb₈₃Li₁₇ as a breeding and coolant material together with ferrous alloys may therefore be limited to temperatures below 500°C.

Table VI.4-6. Tensile Results^(a) for Type 316 Stainless Steel

Exposed to Static Argon and Pb-17 at.% Li

Exposure Temperature (°C)	Exposure Time (h)	Strength (MPa)				Elongation ^(c) (%)	
		Yield ^(b)		Ultimate Tensile			
		Pb-Li	Ar	Pb-Li	Ar	Pb-Li	Ar
300	1000	242	229	577	574	84	86
	3000		248		583	85	88
	5000	238	246	582	584	88	86
400	1000	235	237	574	568	88	88
	3000	242	243	584	582	85	88
	5000	245	245	589	580	85	84
500	1000	240	240 ^(d)	570	576 ^(d)	88	87
	3000	250	251	575	592	84	89
	5000	246	253	570	594	89	87
900	20	248 ^(e)	215	593	518 ^(e)	86	89

(a) Average of measurements from two specimens unless otherwise noted (scatter within ±10%).

(b) 0.2% offset.

(c) In 12.7 mm.

(d) One specimen measurement.

(e) Average of measurements from six specimens.

VI.4.7 Magnetic Properties of HT-9

Figure VI.4-15 shows the hysteresis loops for 9 and 12% Cr steels. HT-9 exhibits a similar hysteresis loop as shown in Fig. VI.4-16.⁽⁴⁾ It is found that the area of the hysteresis loop is reduced at the operating temperature goes up and the value of B_{sat} is reduced from ~ 1.4 T at 25° to 1.1 T at

Fig. VI.4-15
(Reference 4)

COMPARISON OF MAGNETIC PROPERTIES OF TWO CANDIDATE MAGNETIC MATERIALS

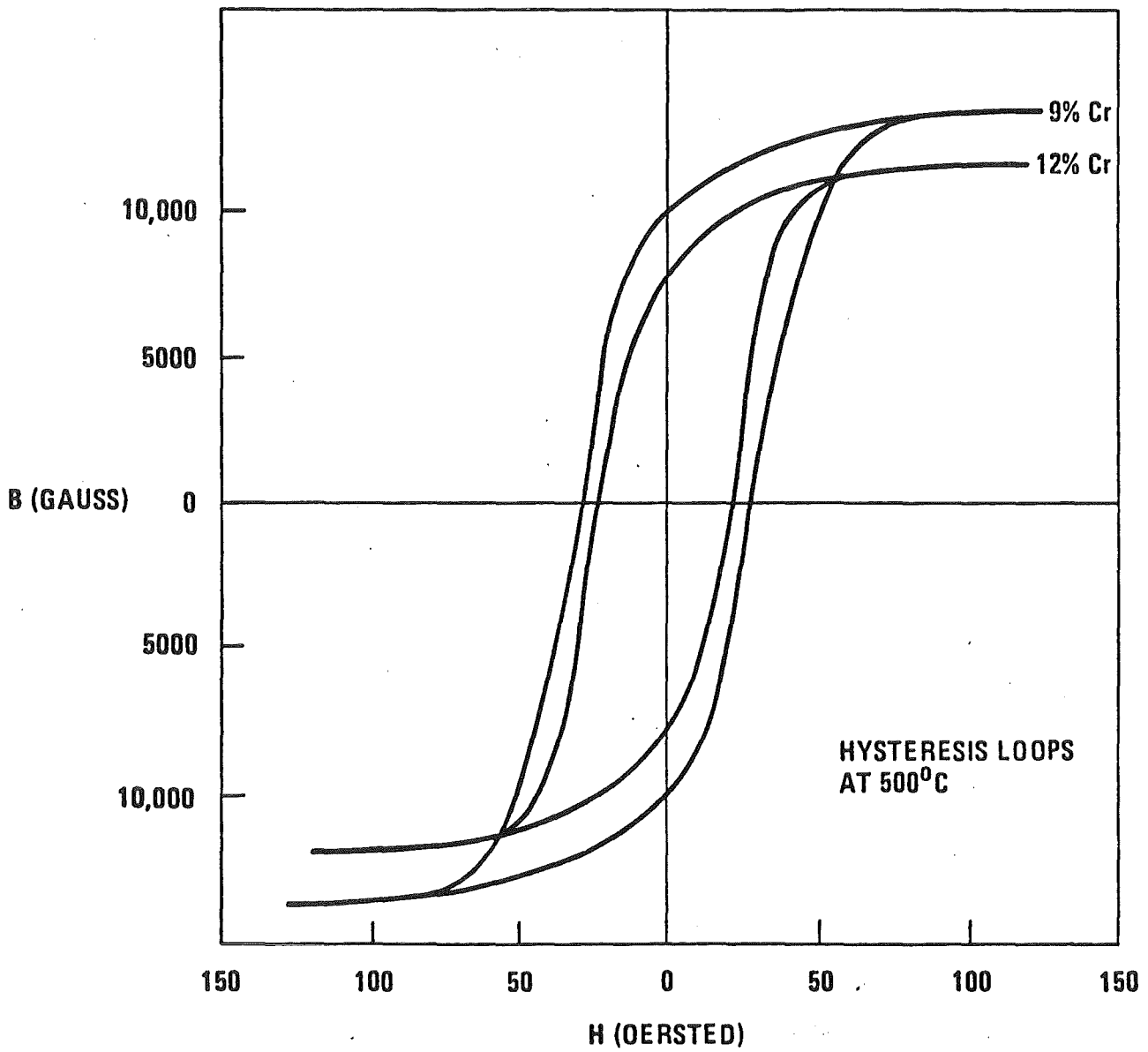
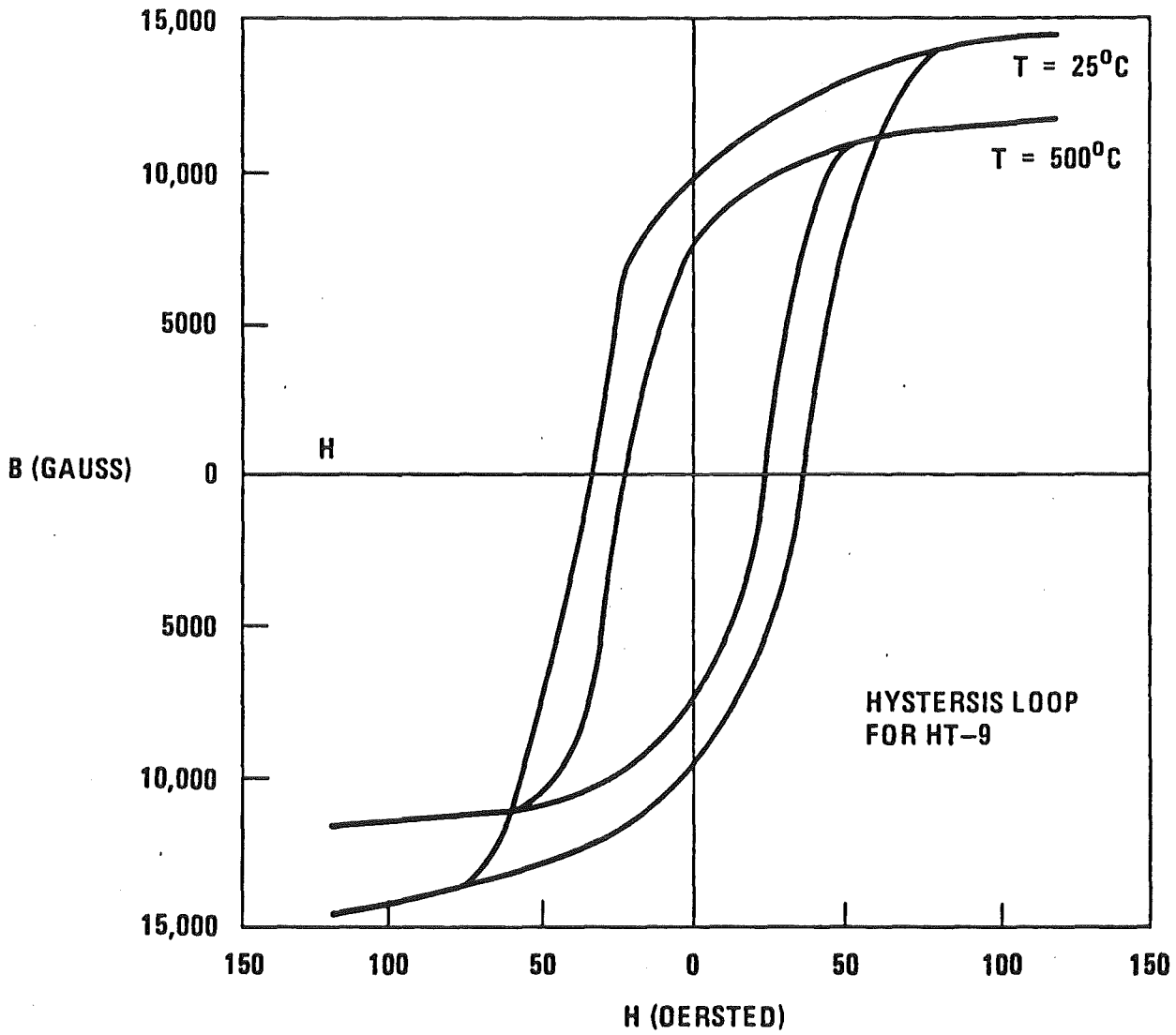


Fig. VI.4-16

MAGNETIC MATERIALS IN MAGNETIC FUSION DEVICES ARE IN SATURATION



500°C. Since the magnetic field at the blanket from the central cell coils is roughly 3 tesla, it is clear that the blanket material will be saturated during the operation of TASKA. Another way of stating the above is that the permeability as defined,

$$B = \mu H$$

is very close to one under TASKA conditions.

Since the saturation magnetization is a substantial fraction of the magnetic field produced by the central coil, in contrast to tokamaks where it is a small fraction, it is expected that the ferromagnetic blanket structure will perturb and reduce the central cell magnetic field. This is discussed further in Section V.9.

VI.4.8 Effects of Irradiation on HT-9 Type Alloys

VI.4.8.1 Introduction

It was previously pointed out there is a considerable data base for low temperature, relatively low fluence, irradiation of ferritic steels. More recently, because of interest in the applications of ferritic steels in the core structures of LMFBR's, some information about the high temperature behavior of ferritic steels irradiated to moderately high fission neutron fluences has begun to appear.⁽¹⁷⁾ Unfortunately, the data is not as extensive as that for the austenitic system but a great deal of information should be available in the next year or two. It must also be pointed out that there is no data on HT-9 (or any other ferritic steel) irradiated with D-T neutrons. Therefore, all of the results quoted here from fission neutron, heavy ion, and electron irradiation will have to be extrapolated to typical TASKA conditions.

VI.4.8.2. Survey of Irradiated Ferritic Steel Information Pertinent to TASKA

There are four sources of data which may be used for our study.

- 1) Fast neutron data from EBR-II.
- 2) Thermal neutron data from test reactors and commercial power plants.
- 3) Heavy ion data.
- 4) High voltage electron microscopy data.

It is not the purpose of this section to present a complete literature survey, but only to highlight those papers which might have a direct bearing on the performance of HT-9 in TASKA. A summary of the work of interest to this study is given in Table VI.4-7.

There are four areas in which measurements have been made on irradiated ferritic steel:

- A) swelling due to voids;
- B) tensile properties;
- C) in-reactor creep;
- D) shift in ductile to brittle transition temperature (DBTT).

VI.4.8.3 Void Swelling in Ferritic Steel

The void swelling problem, which has plagued the austenitic steels in the LMFBR program and has presented some serious problems for the design of first walls in fusion reactors, seems to be greatly reduced in the ferritic steel system. Smidt et al.⁽²⁶⁾ showed in 1976 that the ferritic steels (including HT-9) were very resistant to the production of voids during heavy ion bombardment. In fact, he found that the maximum swelling rate was ~ 0.01-0.02% per dpa compared to values at least 10 times higher for the 316 stainless steel systems. One MeV electron irradiation experiments also revealed that ferritic

Table VI.4-7. Summary of Pertinent Irradiation Data for HT-9 in WITAMIR-I

<u>Type of Irradiation (Reference)</u>	<u>Material</u>	<u>T_{irr}</u> <u>°C</u>	<u>Fluence</u> <u>x 10²² n/cm²</u>	<u>Type of Test</u>	<u>Comments</u>
fast n(17)	HT-9	419	1.1	DBTT, σ_y	100°C shift
fast n(18)	405 SS	400-405	2.3	ΔV , σ_y , duct.	---
fast n(19)	HT-9	540-565	4.0	ϵ_{irr}	---
fast n(20)	FV-448	380, 420, 460, 615	(30 dpa)	ΔV	---
fast n(21)	HT-9	605 625-635	2 4	ϵ_{irr}	---
fast n(22)	2-1/4 Cr 1 Mo	371-427	0.29	FCP, DBTT	No effect of irradiation
fast n(23)	15% Cr-Fe FV-448	380-615	30	ΔV	No ΔV change
fast n(24)	HT-9	440-600	1.1		---
fast n(25)	HT-9	550	7.5	duct., ΔV	---
Heavy Ion(26)	HT-9, EM-12	450-650	(250 dpa)	ΔV	No He
1 MeV Elec.(27)	S4	395-550	(20 dpa)	ΔV	10 ppm He
LWR n(25)	HT-9, 9 Cr 1 Mo, 2-1/4 Cr	50	1.3 (9.3 dpa)	σ_y , duct.	10-80 ppm He
fast n(29)	430 F, 416, EM-12, H11	400-650	17.6	ΔV	$\Delta V < 0.57\%$
fast n(30)	2-1/4 Cr-1 Mo 430 F, 416, EM-12, H11, 2-1/4 Cr-1 Mo	425	5.05	TEM	

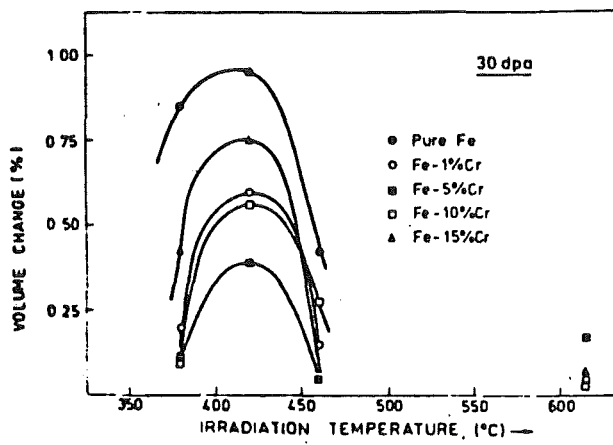
steels were quite resistant to the formation of voids, even after predoping the specimens with 10 appm of He. (32)

Neutron irradiation of Fe-10 Cr and FV-448 (11% Cr, 1 Mn, 0.6 Mo, 0.65 Ni) alloys showed very little swelling up to 30 dpa in the temperature range of 375°C-460°C. (23) Figures VI.4-17 and VI.4-18 show that the addition of up to 5% Cr reduces the swelling compared to pure iron. Further additions of Cr have less effect but still reduce the swelling to ~ 0.02% per dpa level. Other fission neutron irradiations of FV-448 to ~ 30 dpa in the 380°C-615°C temperature range show that < 0.1% swelling was observed. Similarly irradiation of 405 SS (15 Cr, 0.3 Ni, 0.6 C, 0.15 Al) to 400°C with 2.3×10^{22} n/cm² (E > 0.1 MeV) revealed no swelling at all. (18) Recent results from EBR-II irradiations (30) on various ferritic steels whose composition and structure is given in Table VI.4-8 has further confirmed the expectation that the swelling resistance of the ferritic class of steels is generic rather than dependent on one particular composition or heat treatment. As shown in Fig. VI.4-19, swelling is less than 1% for displacement doses between 70 and 90 dpa.

Table VI.4-8. Comparison of the Nominal Major Element Compositions and Microstructures of the Ferritic Alloys Examined

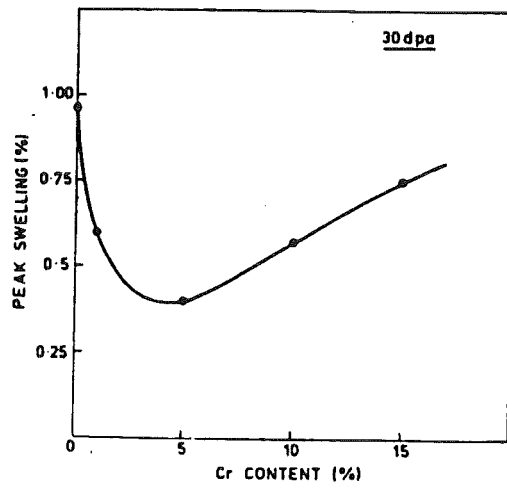
<u>Alloy</u>	<u>Cr</u>	<u>Mo</u>	<u>C</u>	<u>Structure</u>
AISI 430F	18	0.04	0.05	Duplex - Ferrite/Martensite
AISI 416	13	0.2	0.1	Ferritic
EM-12	10	2.0	0.06	Duplex - Ferrite/Martensite
H-11	5	1.4	0.4	Martensitic
2-1/4 Cr-1 Mo	2.2	1.0	0.1	Martensitic

Fig. VI.4-17



Swelling as a function of temperature for binary iron-chromium alloys compared with pure iron.

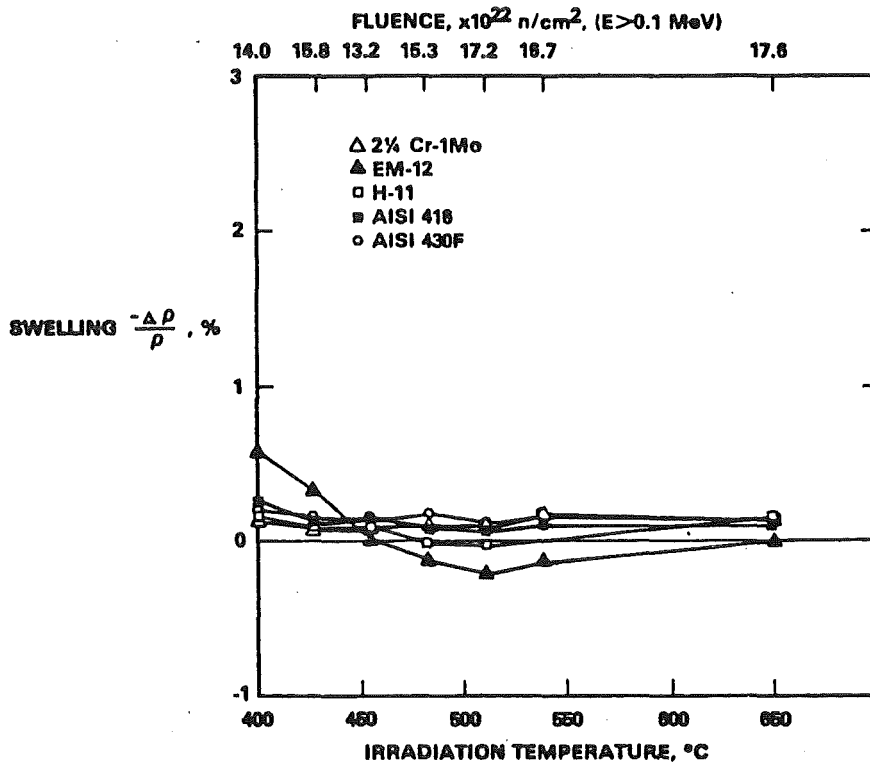
Fig. VI.4-18



Magnitude of peak swelling as a function of chromium content for binary iron-chromium alloys.

Fig. VI.4-19
Swelling in the ferritic alloys.

**SWELLING IN COMMERCIAL ALLOYS:
FERRITIC ALLOYS (PATH E)**



Irradiation of HT-9 to 1.1×10^{23} n/cm² (48 dpa) over the range of temperature from 400°C-600°C reveals that the swelling rate is less than 0.01% per dpa compared to a value of 0.35% per dpa for 316 SS (Fig. VI.4-20).⁽²⁵⁾ Such studies do not simulate the helium production in HT-9 correctly, but HT-9 doped with 1% Ni is now being inserted into thermal fission reactors to obtain the necessary higher helium concentrations. However, only tensile properties on doped HT-9 have so far been measured.

VI.4.8.4 Effects of Neutron Irradiation on the Tensile, Creep, and Stress-Rupture Properties of Ferritic Steel

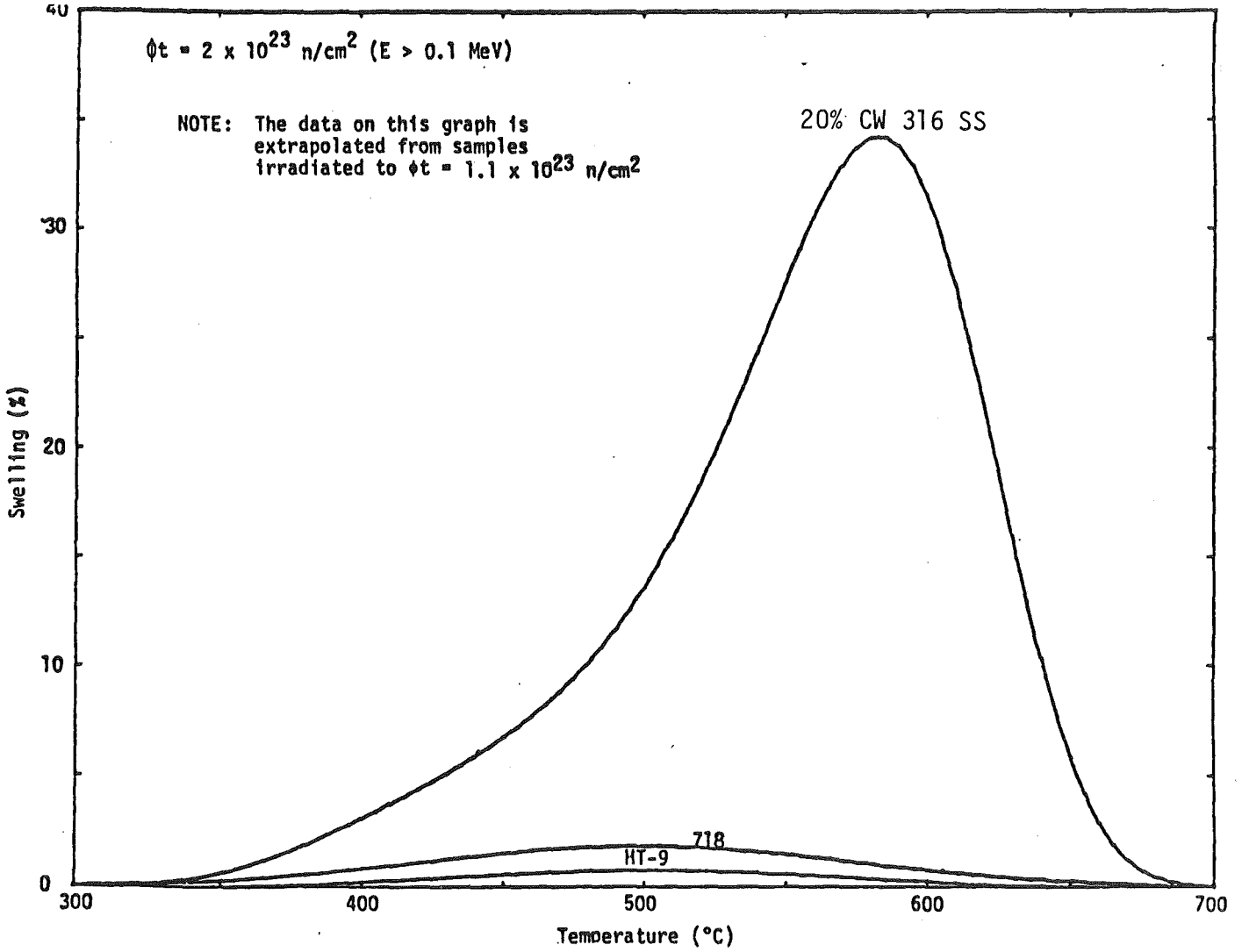
There are three results reported in the literature that are pertinent to the use of HT-9 in TASKA. An early study by Garr et al.⁽¹⁸⁾ showed that 405 SS, which was given a 1 hour anneal at 980°C before irradiation, suffered relatively little loss in ductility after being irradiated to 2.3×10^{22} n/cm² (10 dpa) at 400°C-425°C (see Table VI.4-9). The total elongation remained at 11.2% at 500°C while the uniform elongation dropped from 9.4% to 4.0%.

In another study⁽²⁵⁾ where HT-9 was irradiated to 1.1×10^{23} n/cm² (48 dpa) at 550°C the total elongation remained above 10% when tested at 550°C and 670°C.

Smidt et al.⁽¹⁷⁾ found that irradiation to ~ 5 dpa at 419°C resulted in very little reduction of ductility during post-irradiation room temperature tests. They found that after such an irradiation, there was still 6.3% uniform elongation and 13.9% total elongation remaining.

More recently, Klueh and Vitek⁽³⁰⁾ irradiated tensile specimens of various ferritic steels with the compositions as given in Table VI.4-10. The HFIR irradiations were carried out at 50°C to doses between 6.5 and 9.5 dpa and to helium concentrations ranging between 10 to 80 appm He. The low helium

Fig. VI.4-20



Swelling of candidate CTR materials during neutron irradiation (25).

Table VI.4-9. Pertinent Data of Irradiation Effects on
Tensile Properties of Ferritic Steel

<u>Material</u>	<u>T_{irr}/Test</u>	<u>dpa (a)</u>	<u>Appm He (b)</u>	<u>Yield Stress-MPa</u>	<u>Tensile Stress-MPa</u>	<u>Uniform Strain-%</u>	<u>Total Strain-%</u>
405 SS	---/500	Control	---	346	712	9.4	11.2
(18)	425/500	10	3.9	461	516	4.0	11.2
HT-9	550/550	48	19	N.R.	N.R.	N.R.	14.
(25)	550/670	48	19	N.R.	N.R.	N.R.	> 10
HT-9	---/253	Control	---	653	823	7.5	16.4
(17)	419/25	5	2	971	1037	6.3	13.9

N.R. = Not Reported

(a) use 4.4 dpa per 10^{22} n/cm² (E > 0.1 Mev)
 (b) use 0.39 appm He/dpa

Table VI.4-10. Composition of Ferritic Steels Irradiated in HFIR at 50°C.

Element	Alloy Content, ^a wt %				
	HT9 Breeder (91354)	HT9 (XAA-3587)	HT9 + 1% Ni (XAA-3588)	HT9 + 2% Ni (XAA-3589)	HT9 + 2% Ni Adjusted (XAA-3592)
C	0.20	0.21	0.20	0.20	0.15
Mn	0.47	0.50	0.47	0.49	0.32
P	0.004	0.011	0.010	0.011	0.008
S		0.004	0.004	0.004	0.004
Si	0.31	0.18	0.13	0.14	0.07
Ni	0.54	0.43	1.14	2.27	2.30
Cr	11.2	11.99	11.97	11.71	13.60
Mo	0.96	0.93	1.04	1.02	1.59
V	0.31	0.27	0.31	0.31	0.30
Nb		0.018	0.015	0.015	0.016
Ti		0.003	0.003	0.003	0.002
Co	0.02	0.017	0.015	0.021	0.018
Cu	0.04	0.05	0.05	0.05	0.05
Al	0.03	0.030	0.017	0.028	0.018
B	0.0007	<0.001	<0.001	<0.001	<0.001
W	0.5	0.54	0.53	0.54	0.64
As	0.01	<0.001	0.002	<0.002	<0.002
Sn	0.01	0.002	0.001	0.002	0.002
Zr		<0.001	<0.001	<0.001	<0.001
N		0.020	0.016	0.017	0.014
O		0.005	0.007	0.007	0.007

^aBalance iron.

Element	Concentration, ^a wt %		
	9 Cr-1 Mo (XA-3590)	9 Cr-1 Mo + 2% Ni (XA-3591)	9 Cr-1 Mo + 2% Ni Adjusted (XA-3593)
C	0.09	0.064	0.067
Mn	0.36	0.36	0.36
P	0.008	0.008	0.008
S	0.004	0.004	0.004
Si	0.08	0.08	0.10
Ni	0.11	2.17	2.24
Cr	8.62	8.57	12.30
Mo	0.98	0.98	1.70
V	0.209	0.222	0.29
Nb	0.063	0.066	0.074
Ti	0.002	0.002	0.002
Co	0.013	0.015	0.017
Cu	0.03	0.04	0.03
Al	0.013	0.015	0.016
B	<0.001	<0.001	<0.001
W	0.01	0.01	0.01
As	<0.001	<0.001	<0.001
Sn	0.003	0.003	0.003
Zr	<0.001	<0.001	<0.001
N	0.050	0.053	0.059
O	0.007	0.006	0.007

^aBalance iron.

concentration range corresponds to alloy compositions with the lowest nickel concentration, whereas the high helium concentrations were achieved with the alloys containing about 2% nickel. Post-irradiation tensile tests were performed at room temperature (25°C) and at elevated temperature (300°C), and the results are listed in Tables VI.4-11 and VI.4-12.

As can be seen from Figs. VI.4-21 and VI.4-22, both the yield and the ultimate strength increased after irradiation. However, the uniform and total elongation were reduced by irradiation as shown in Figs. VI.4-23(a) and VI.4-23(b).

In particular, the uniform elongation dropped to values less than 0.5% for the room temperature post-irradiation tests, whereas the total elongation remained above about 2%. This behavior is indicative of localized plastic flow, a phenomenon also observed in highly irradiated austenitic steels.

By comparing the ratios of irradiated to unirradiated tensile properties among the alloys with different nickel concentration, Klueh and Vitek concluded that helium (at least in the range from 10 to 85 appm He) has no effect on either the increase in yield and ultimate strength, or on the reduction in uniform and total elongation. Hence, the observed changes in tensile properties are entirely due to the displacement damage. It should be noted, however, that this conclusion may not be applicable for irradiations at elevated temperature and to higher doses. Nevertheless, all the results so far on the tensile properties of irradiated ferritic steels look very promising. Recent investigations by Wassilev⁽²⁸⁾ on post-irradiation rupture life of the martensitic steel 1.4914 (whose composition is similar to HT-9 but contains additionally 0.25% Nb as a carbon-stabilizing element) showed modest reduction in the rupture life after an irradiation dose of about 5 dpa and a helium

Table VI.4-11

Tensile properties of unirradiated and irradiated normalized-and-tempered^a
12 Cr-1 MoVW Steels

Fluence, >0.1 MeV, (neutrons/m ²)	Displace- ment Level (dpa)	Helium Concentration ^b (at. ppm)	Test Temperature (°C)	Strength (MPa)		Strength Ratios ^c		Elongation (%)	
				Yield	Ultimate	R _y	R _u	Uniform	Total
× 10 ²⁵									
<u>12 Cr-1 MoVW (91354)</u>									
0			25	549	716			6.64	9.91
1.3	9.3	26	25	983	987	1.79	1.38	0.31	2.12
0			300	490	647			5.53	8.63
1.2	9.1	20	300	784	800	1.60	1.24	1.36	4.49
<u>12 Cr-1 MoVW (XXA-3587)</u>									
0			25	553	759			8.06	11.15
1.3	9.3	22	25	980	992	1.77	1.31	0.39	2.89
0			300	483	652			5.10	7.98
1.2	9.1	18	300	783	815	1.62	1.25	1.80	5.08
<u>12 Cr-1 MoVW-1 Ni (XXA-3588)</u>									
0			25	576	800			7.09	10.64
1.3	9.3	45	25	1115	1134	1.94	1.42	0.56	2.96
0			300	519	761			5.94	9.04
1.2	9.1	41	300	899	931	1.73	1.22	1.11	3.78
<u>12 Cr-1 MoVW-2 Ni (XXA 3589)</u>									
0			25	719	899			4.63	7.81
1.2	9.1	74	25	1227	1249	1.71	1.39	0.51	2.19
0			300	646	827			3.49	6.18
0.89	8.5	50	300	1019	1128	1.58	1.36	0.83	3.02
<u>12 Cr-1 MoVW-2 Ni (adjusted) (XAA-3592)</u>									
0			25	769	938			4.76	7.65
1.3	9.3	83	25	1310	1338	1.70	1.43	0.57	2.78
0			300	696	894			3.21	6.29
1.2	9.1	63	300	1056	1094	1.52	1.22	0.65	3.07

^aAll heats were normalized by heating 0.5 h at 1050°C, then rapidly cooled in flowing helium. Heats 91354, XXA-3587, and XXA-3588 were tempered 2.5 h at 780°C; heats XXA-3589 and XXA-3592 were tempered at 700°C for 5 and 8 h, respectively.

^bCalculated level of helium from ⁵⁸Ni and ¹⁰B. [Each alloy was assumed to contain 0.007 wt % B (total)].

^cR_y = ratio of irradiated-to-unirradiated yield strengths; R_u = ratio of irradiated to unirradiated ultimate tensile strengths.

Table VI.4-12

Tensile properties of unirradiated and irradiated^a normalized-and-tempered^b
9 Cr-1 MoVNb Steels

Fluence, >0.1 MeV (neutrons/m ²)	Displace- ment Level (dpa)	Helium Concentration ^c (at. ppm)	Test Temperature (°C)	Strength (MPa)		Strength Ratio ^d		Elongation (%)	
				Yield	Ultimate	R _y	R _U	Uniform	Total
<u>9 Cr-1 MoVNb (XA-3590)</u>									
0			25	541	656			5.11	9.61
1.3 × 10 ²⁶	9.3	11	25	878	878	1.62	1.34	0.23	3.23
0			300	483	581			3.59	7.13
1.1	7.6	10	300	716	716	1.48	1.23	0.22	3.70
<u>9 Cr-1 MoVNb-2 Ni (XA-3591)</u>									
0			25	734	851			3.74	7.50
1.3	9.3	80	25	1289	1297	1.76	1.52	0.36	1.60
0			300	650	757			2.29	5.29
1.2	8.6	72	300	1088	1107	1.67	1.46	0.41	2.72
<u>9 Cr-1 MoVNb-2 Ni (adjusted) (XA-3593)</u>									
0			25	817	927			3.44	7.46
1.3	9.3	82	25	1286	1298	1.57	1.40	0.48	2.63
0			300	766	878			3.57	6.59
1.1	7.7	63	300	1093	1114	1.43	1.27	0.51	2.31

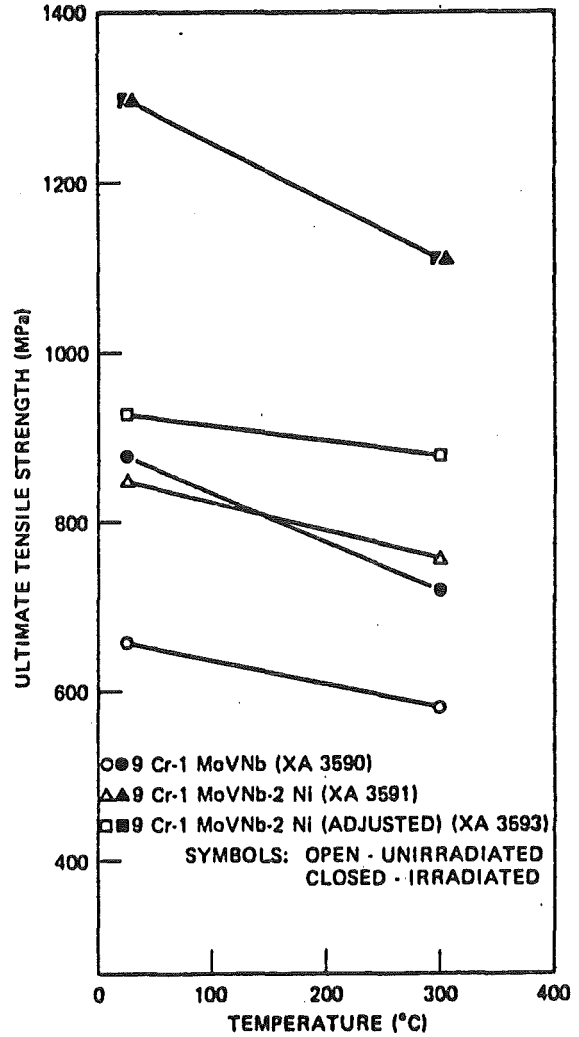
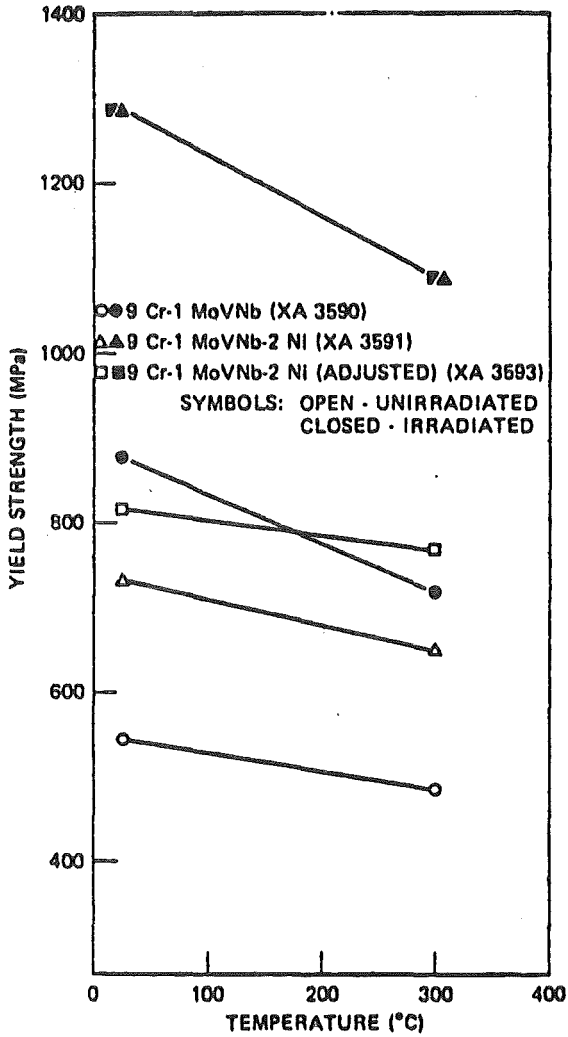
^aIrradiation was in HFIR at 50°C.

^bAll heats were normalized by heating 0.5 h at 1040°C, then rapidly cooled in flowing helium. Heat XA-3590 was tempered 1 h at 760°C; heats XA-3591 and XA-3593 were tempered at 700°C for 5 and 8 h, respectively.

^cCalculated level of helium from ⁵⁸Ni and ¹⁰B. [Each alloy was assumed to contain 0.0007 wt % B (total)].

^dR_y = ratio of irradiated-to-unirradiated yield strengths; R_U = ratio of irradiated-to-unirradiated ultimate tensile strengths.

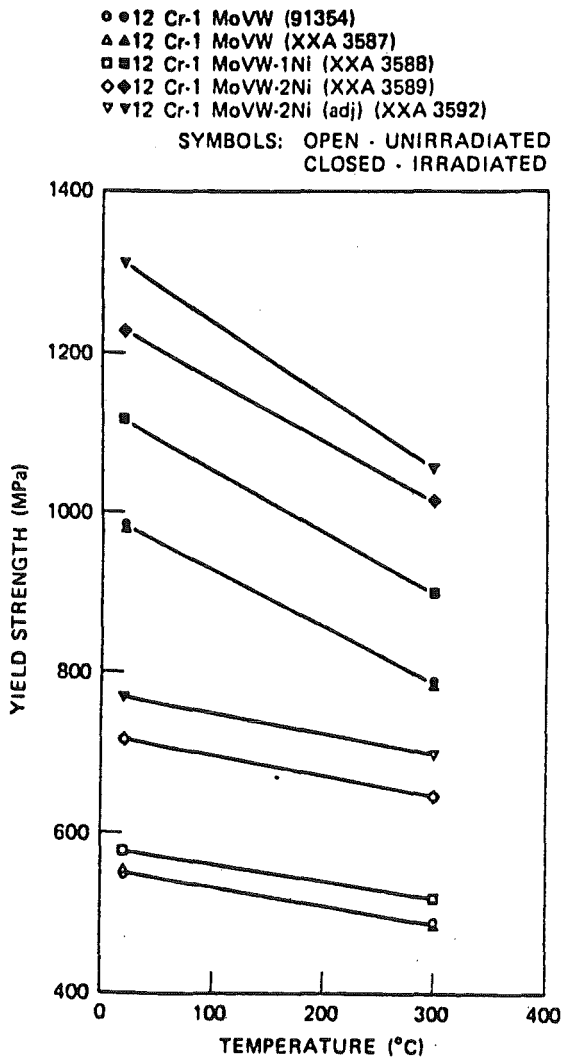
Fig. VI.4-21



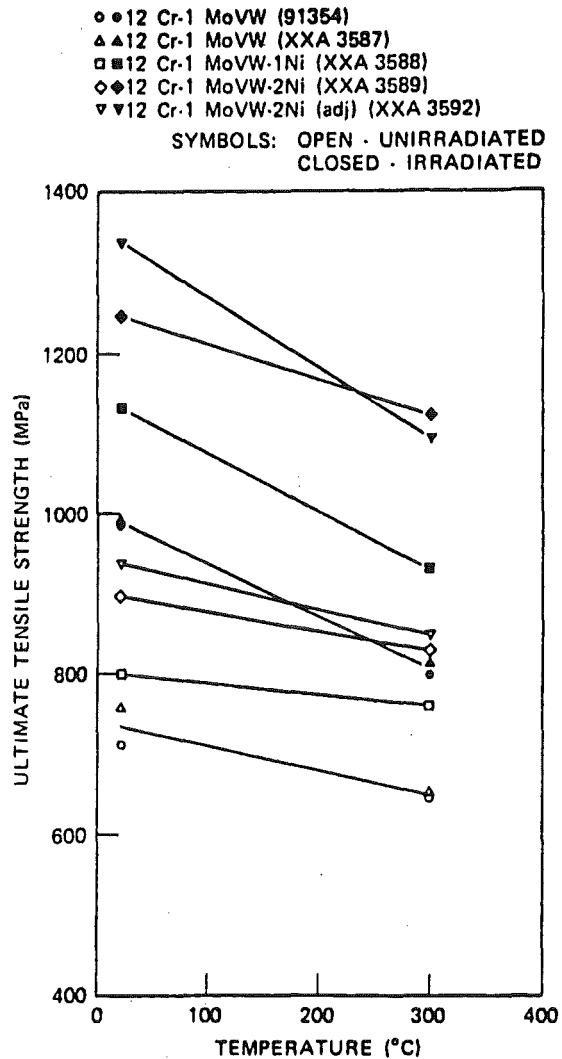
a) The 0.2% yield strengths of 9 Cr-1 MoVNb steels unirradiated and after HFIR irradiation to produce up to 9.3 dpa and 10 to 80 at. ppm He.

b) The ultimate tensile strengths of 9 Cr-1 MoVNb steels.

Fig. VI.4-22

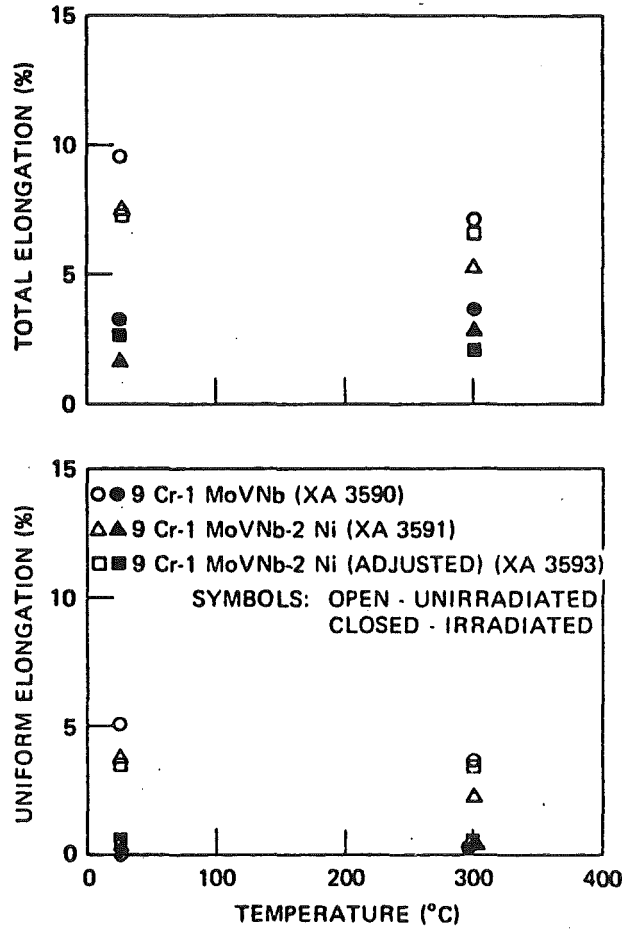


a) The 0.2% yield strengths of 12 Cr-1 MoVW steels unirradiated and after irradiation in HFIR to produce up to 9.3 dpa and 20 to 80 at. ppm He.



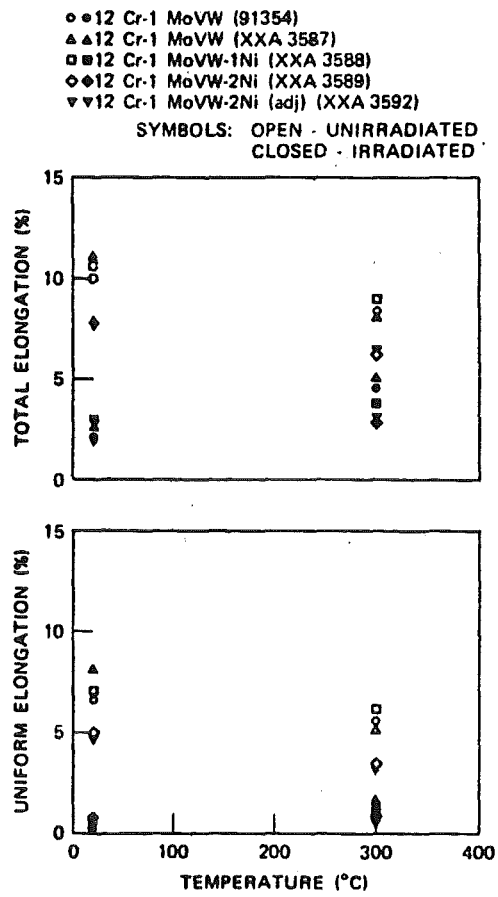
b) The ultimate tensile strength of 12 Cr-1 MoVW steels unirradiated and after irradiation in HFIR.

Fig. VI.4-23 a



(a) The uniform and total elongation of 9 Cr-1 MoVNb steel unirradiated and after irradiation in HFIR to produce up to 9.3 dpa and 10 to 80 at. ppm He.

Fig. VI.4-23b



(b) The uniform and total elongation of 12 Cr-1 MoVW steels unirradiated and after irradiation in HFIR to produce up to 9.3 dpa and 10 to 80 at. ppm He.

accumulation of 90 appm. The results are shown in Fig. VI.4-24(a). The reduction in rupture life can be explained by two simultaneous effects of radiation damage. First, there is an increase in post-irradiation thermal creep as shown in Fig. VI.4-24(b). Second, the ductility for the post-irradiation test is reduced as illustrated by the results of Fig. VI.4-24(c). It should be noted that the post-irradiation ductility loss of this martensitic steel is much less severe than for austenitic alloys. Figure VI.4-24(d) shows the strain to rupture versus rupture life for both the irradiated martensitic steel 1.4914 and the irradiated, and Ti-stabilized austenitic steel 1.4970. It is seen that the rupture strain decreases rapidly with increasing rupture life for the austenitic steel, but it remains nearly independent of the rupture life and at a more than adequate level of $\geq 5\%$ for the martensitic steel.

Microstructural evaluation showed that the dramatic loss in ductility is due to the well-known helium embrittlement of grain boundaries in the austenitic steel, leading to intergranular failure. In contrast, the fracture mode in the martensitic steel is characterized by ductile transgranular failure in spite of the fact that helium is found to promote also the grain boundary bubble formation. It appears that the martensitic steels have a much reduced susceptibility for helium embrittlement as compared to austenitic steels.

VI.4.8.5 In-Reactor Creep of HT-9

There are basically two sources of information in this area, both from Paxton et al. (19,24). They found that the in-reactor creep of HT-9 is superior to CW 316 SS, especially in the 550°C to 650°C range (much higher than we propose to use HT-9). Figure VI.4-25 shows that at stress levels of 70 MPa (~ 10 ksi) the total creep at 560°C after 1.5×10^{23} n/cm² (~ 75 dpa) is

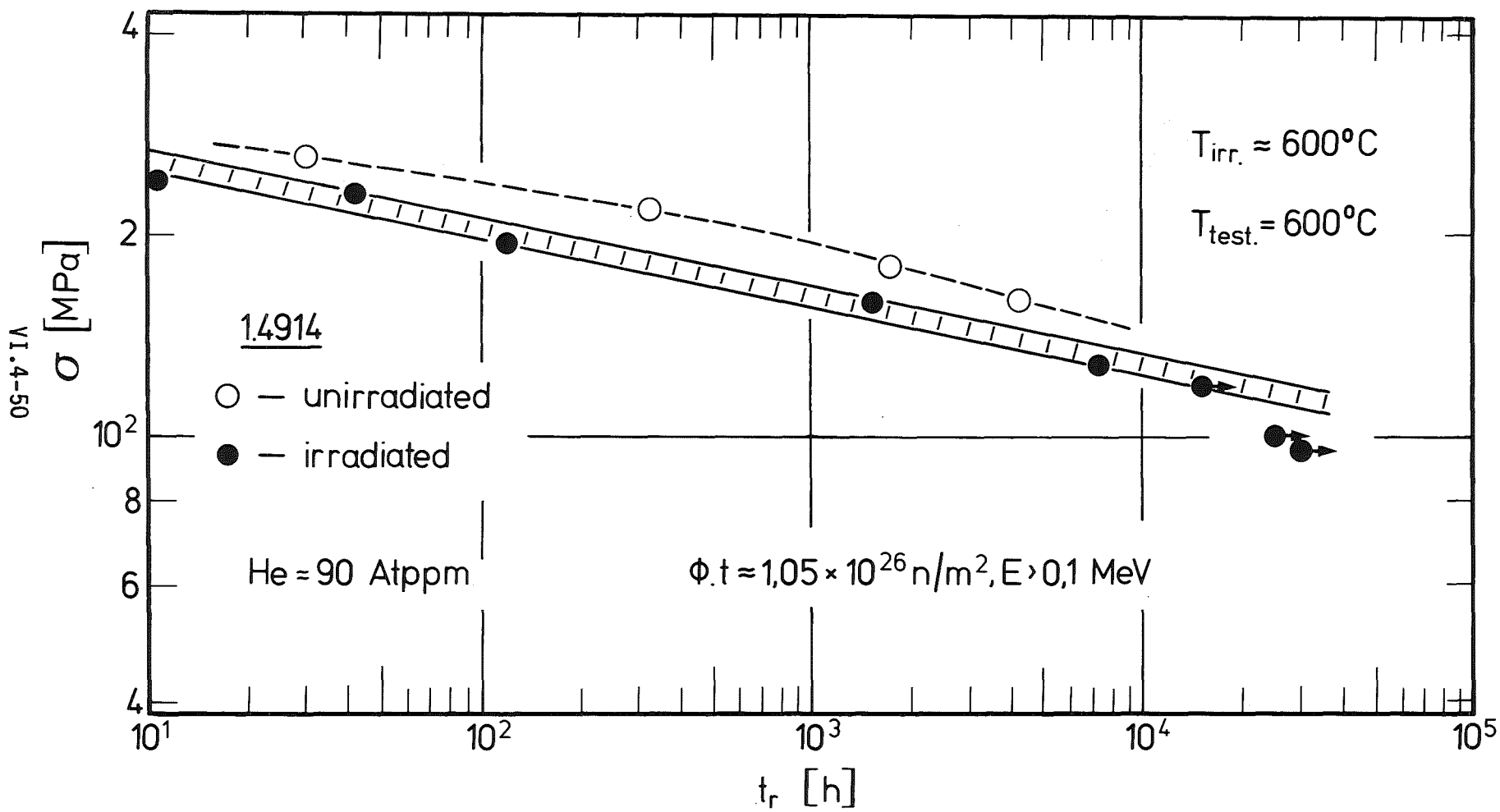
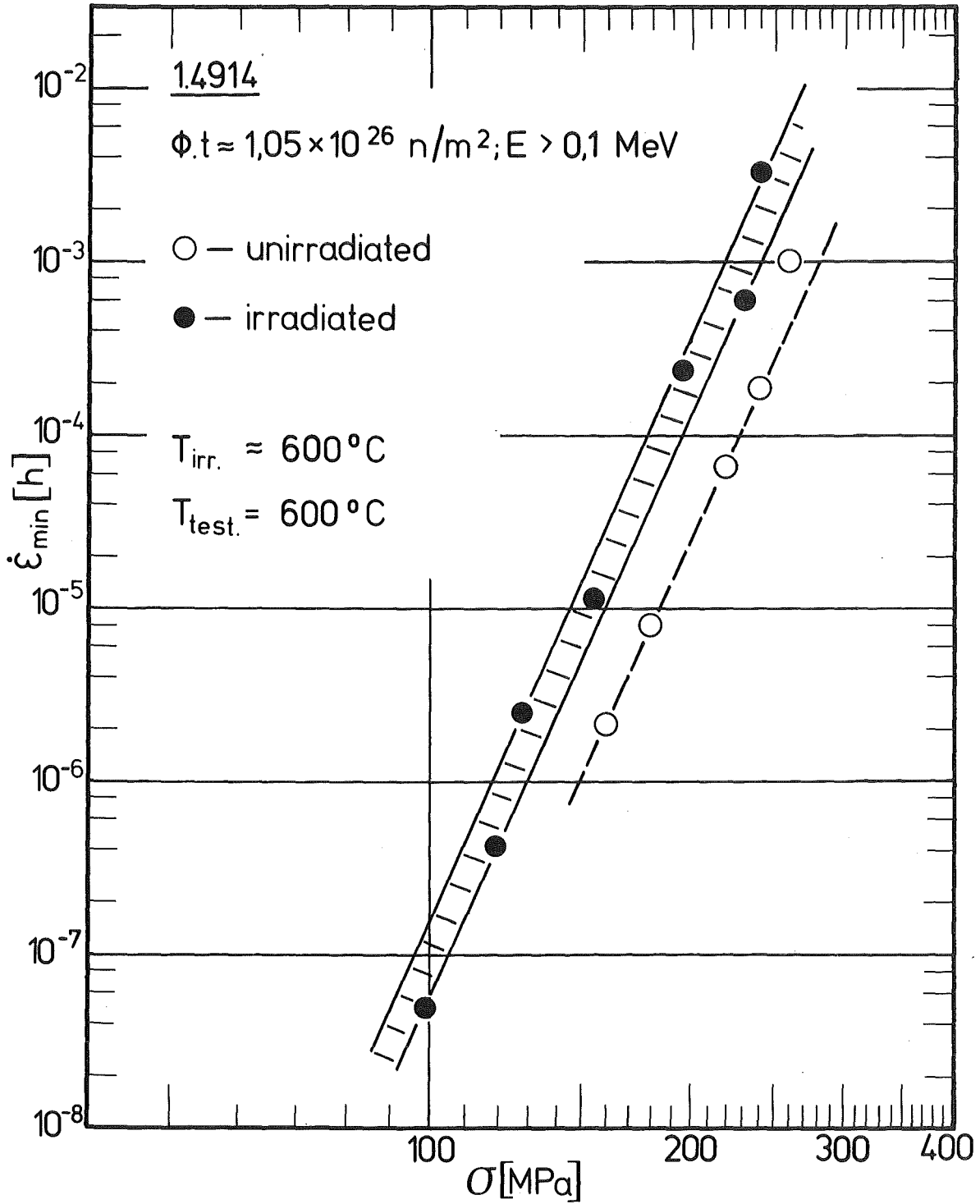


Fig. VI.4-24a Rupture life of the unirradiated and irradiated martensitic steel 1.4914.

Fig. VI.4-24(b)

Minimum creep rate of the unirradiated and irradiated martensitic steel 1.4914.



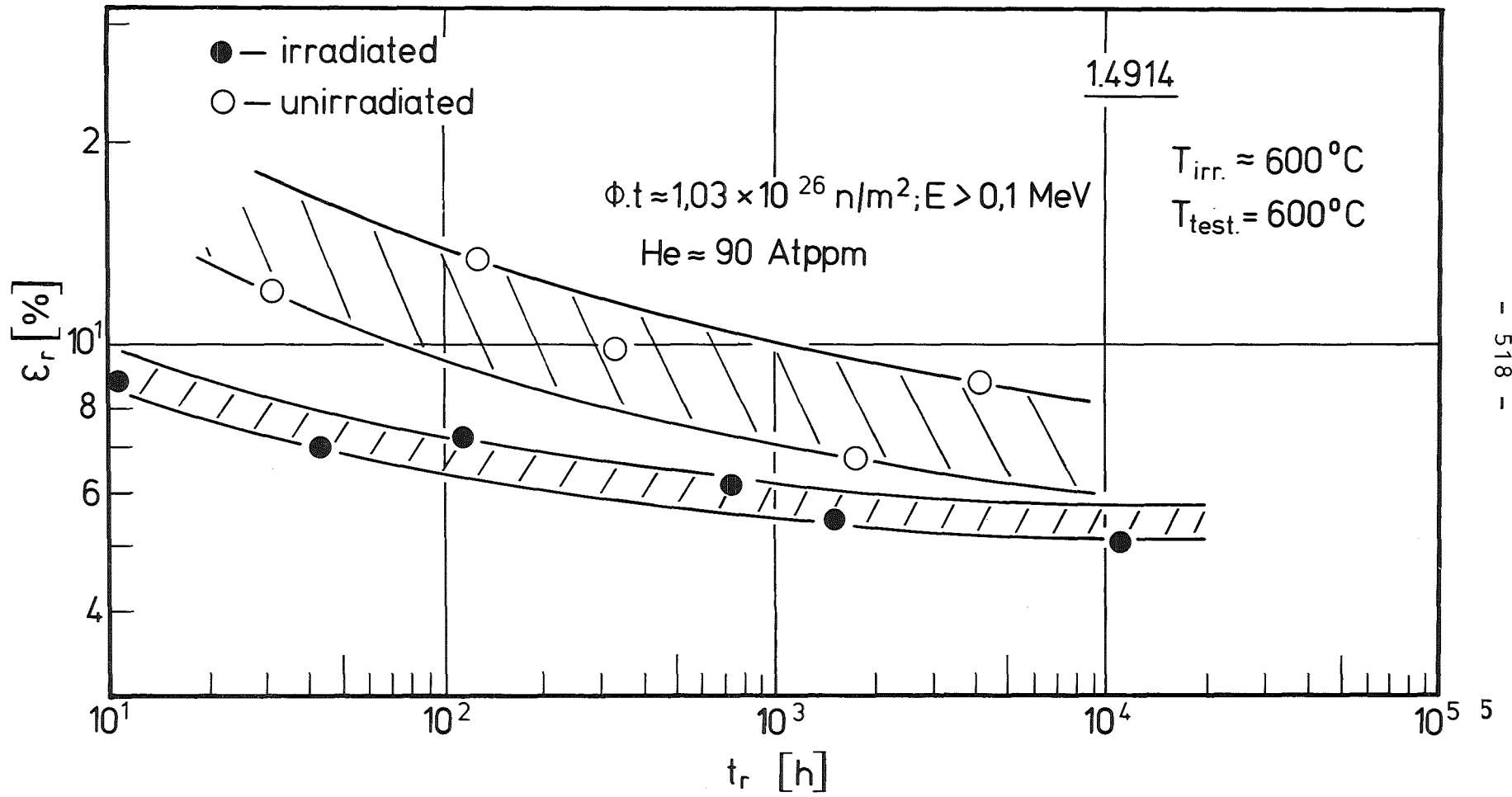


Fig. VI.4-24(c) Creep ductility of the unirradiated and irradiated martensitic steel 1.4914.

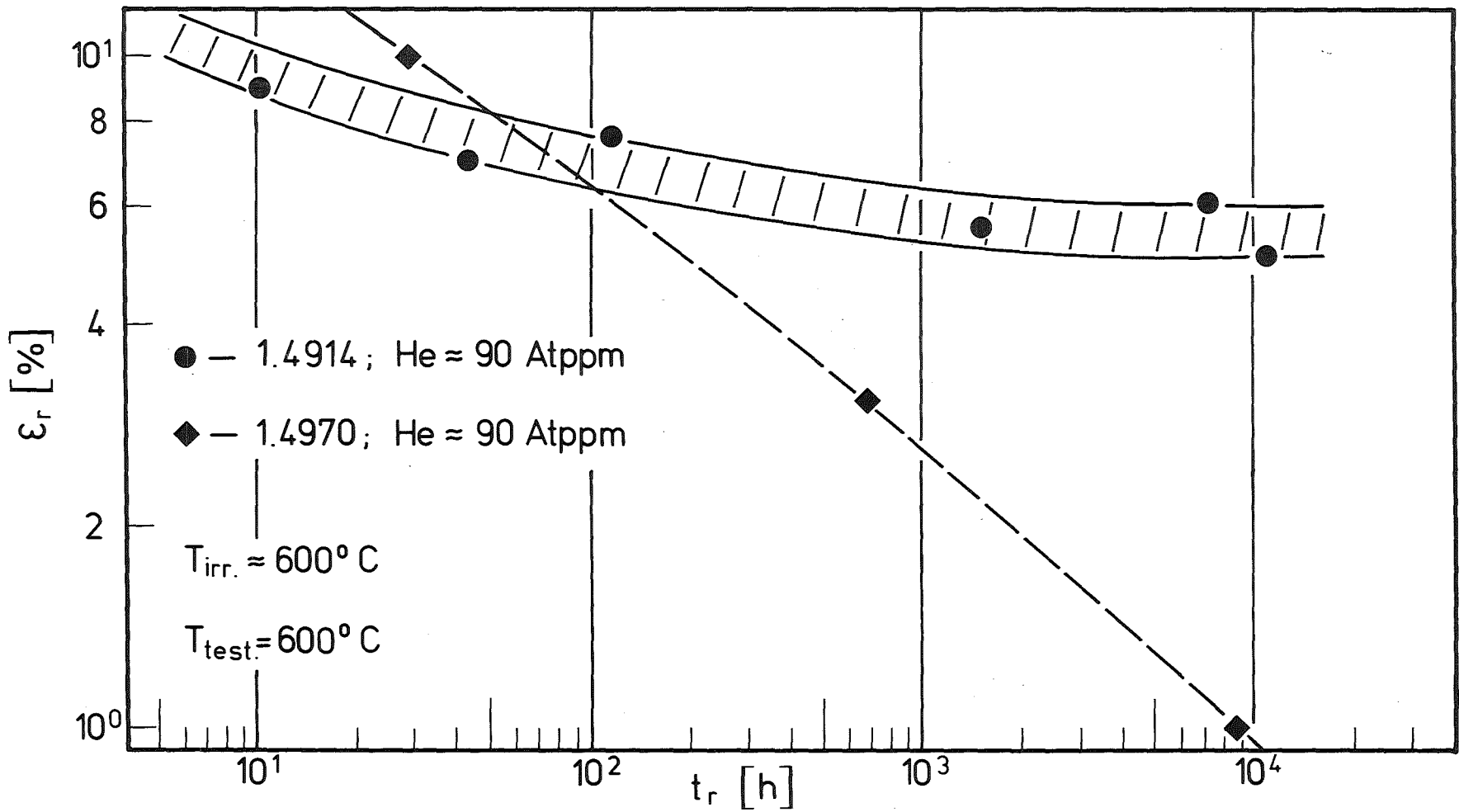
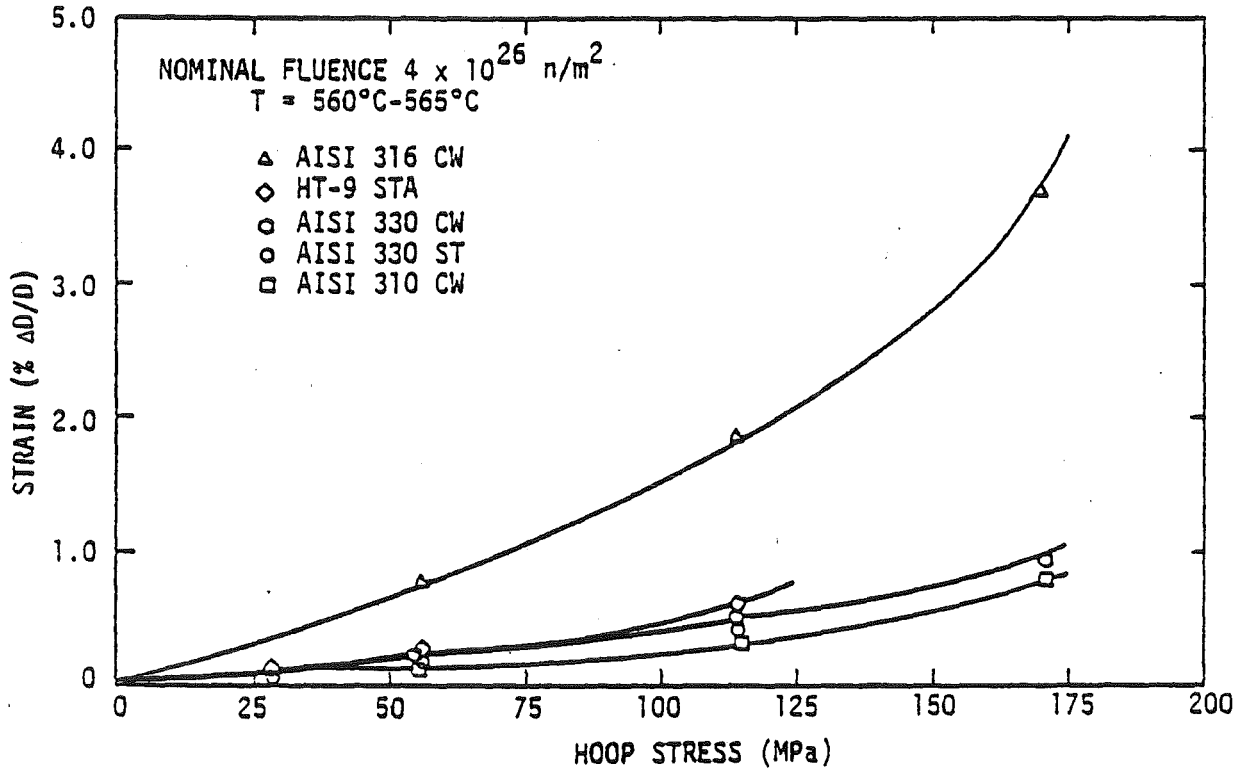


Fig. VI.4-24(d) Comparison of the ductility between the irradiated steels 1.4914 and 1.4970.

Fig. VI.4-25



In-reactor creep of HT-9 (12Cr-1Mo-0.3V) compared to 20% CW 316SS (ref. 19,24).

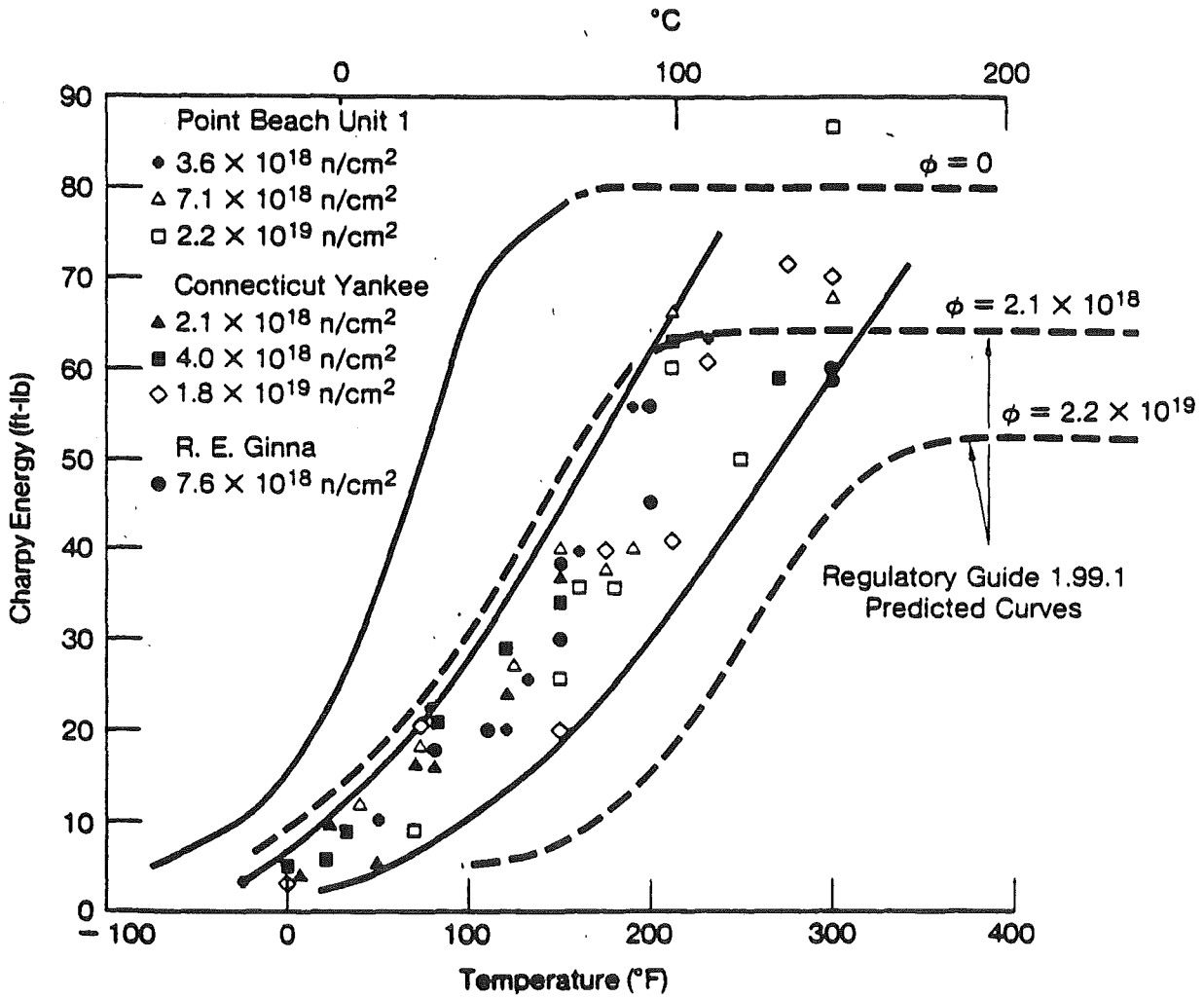
~ 1.3%. This is reduced to ~ 0.7% at 450°C. Paxton et al.^(19,24) show that at hoop stresses of 70 MPa and 2×10^{22} n/cm², diametral strains of only 0.4% are observed at 605°C. However, recent irradiation creep measurements by Herschback et al.⁽²⁹⁾ on 2-1/2 Cr-1 Mo steel did not show any radiation-enhanced creep at a temperature of 450°C and a tensile stress of 100 MPa. At higher temperatures there appears to be an enhancement of thermal creep. Similar trends have also been observed in a 12 Cr martensitic steel according to private communications with Herschback and Ehrlich.

VI.4.8.6 DBTT Shift During Neutron Irradiation

Practically all the information available on DBTT shifts for ferritic steels has been obtained through low temperature (< 300°C) and low fluence (< 10^{21} ncm⁻² or ~ 0.5 dpa) data. Past experience has shown that if ferritic steels are irradiated under these conditions, significant DBTT shifts can occur. Figure VI.4-26 gives data from seven different fluence levels on A 302B ferritic steel.⁽³³⁾ It can be seen that the DBTT is ~ 100°C at irradiation temperatures of 288°C up to 2.2×10^{19} n/cm² (0.01 dpa). This DBTT shift can be partially recovered and the 50% recovery time is 17 hr at 400°C or ~ 2 hr at 440°C.⁽²⁸⁾ Anderko⁽²¹⁾ has recently reviewed the known DBTT shift and given the tentative correlation with irradiation temperature as shown in Fig. VI.4-27.

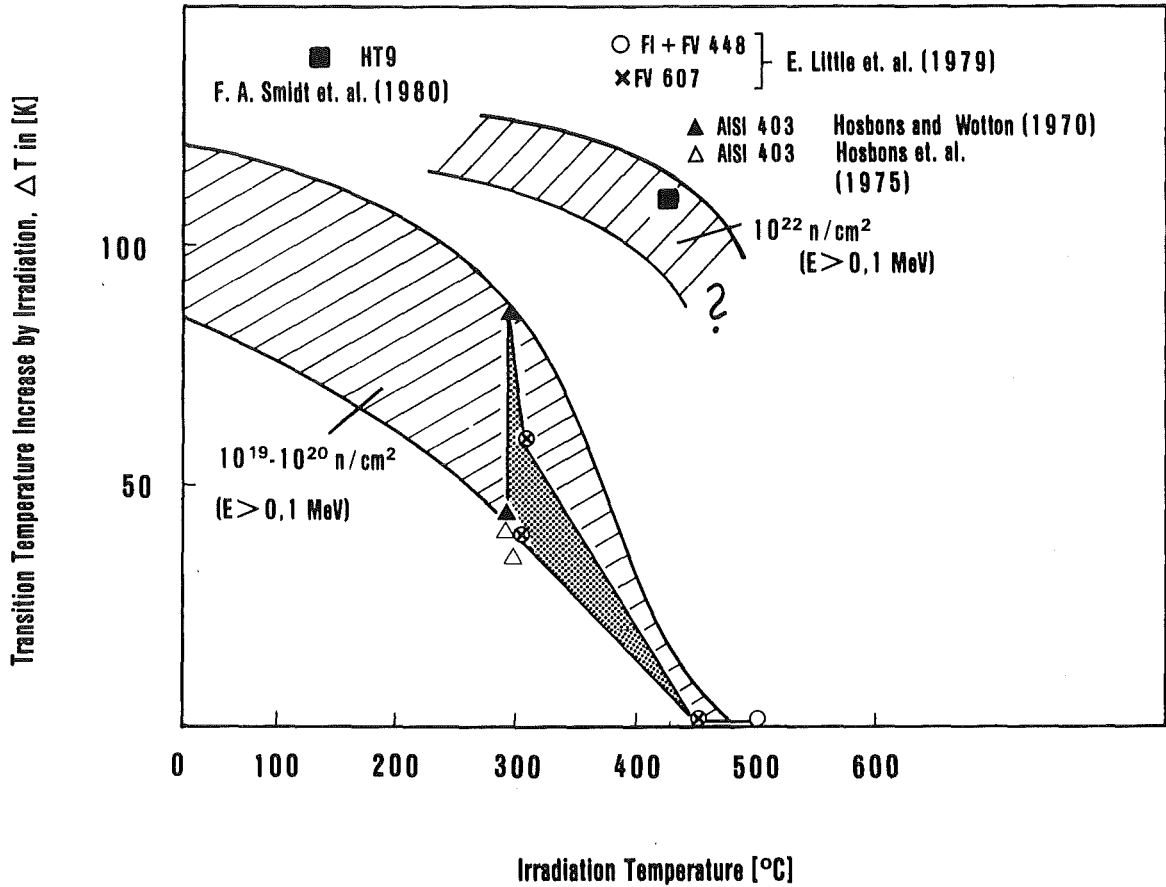
There is only one set of data on the HT-9 alloy at high temperatures and fluences. Smidt et al.⁽¹⁷⁾ found that the transition temperature shifted from ~ 0°C (as received) to ~ 100°C after a 5 dpa (1×10^{22} n/cm²) irradiation at 427°C (Fig. VI.4-28). Presumably this shift will drop rapidly at higher temperatures so operation up to 530°C may not be a problem. Indeed, British scientists have found there is no DBTT shift following neutron irradiation at

Fig. VI.4-26



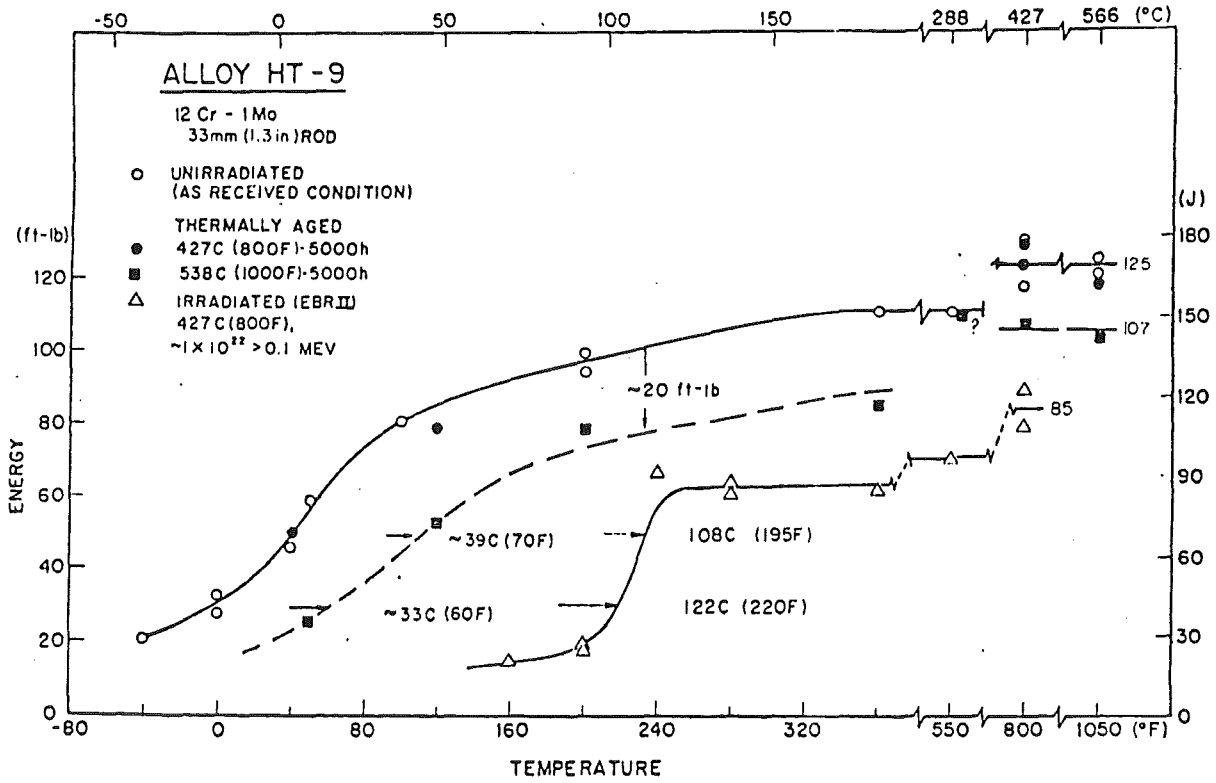
Low flux irradiation results for ASTM Reference A 302 B (0.20 weight percent Cu, 0.011 weight percent P) from three reactors. Charpy data for seven fluence levels with predicted Charpy curves (Regulatory Guide 1.99.1) for the lowest and highest levels.(28)

Fig. VI.4-27



Increase of impact transition temperature as a function of irradiation conditions (Charpy notch specimens).

Fig. VI.4-28



Charpy-V energy values as a function of test temperature for HT-9 in the as-received condition, after 5000 hr aging at 427°C, after 5000 hr aging at 538°C, and after irradiation to a neutron fluence of 1.1×10^{22} n/cm² ($E > 0.1$ MeV) at an irradiation temperature of $419^\circ\text{C} \pm 15^\circ\text{C}$ in the EBR-II reactor(17)

450°C.⁽³³⁾ However, it is not known how much the DBTT shift will be after irradiation in the low temperature region (~ 350°C), but it is expected to be a maximum of ~ 40°C per dpa. Damage accumulated in that temperature region may have to be removed by periodic annealing.

VI.4.9 Fabrication of TASKA Blanket Module

Several considerations should be discussed pertaining to the fabrication of an HT-9 TASKA blanket module. They consist of the fabrication and procurement of the proper product forms, manufacture of pieces into the component's configuration through welding, the post weld heat treatment (PWHT) of the weldments, and non-destructive examination to ensure a high reliability of the completed structure. These issues are discussed below.

VI.4.9.1 Manufacture of HT-9 TASKA Blanket Module Tubes

Table VI.4-13 lists the tube and pipe material specifications for use of 12 Cr-1 Mo steels including the alloy grade and designation and known producers. This is an indication of the common use of HT-9 in pipe and tubular products and their acceptance by industry and standards. Table VI.4-14 lists some specific applications in CEGB boilers for HT-9 (or the 12 Cr-1 Mo equivalent alloy) which use welded tubes on the same order of size as those of the TASKA plant blanket design. Also included are notations of failures and the reasons.

As is seen in Table VI.4-14, tubes of nearly the same dimensions as those for TASKA are used frequently and successfully. These tubes are placed into service in the fully tempered condition. The manufacturers' recommend an austenitization at 1050°C for 0.5-1.0 hrs with air-cool, followed by a tempering treatment at 760-780°C for 1.5-2.5 hrs, also followed by an air-cool. This is done to "normalize" the microstructure, which relieves stresses and

Table VI.4-13. Tube and Pipe Material Standards that Include 12 Cr-1 Mo Ferritic/Martensitic Steel Alloys^(a)

Country of Material Standard	Standard Number	Standard Titles	Alloy Grade and/or Designation	Alloy Composition (wt%)			Additions	Trade Names or Alloys
				Cr	Mo	C		
U.K.	BS 3604-78	Steel pipes and tubes for pressure purposes; ferritic alloy steel with specified elevated temperature properties	CFS 762 HFS 762	12	1	0.2	0.3V-0.5W-0.5Ni	(Equivalent to HT-9)
	None	This alloy has not been used in tube form; applications have been in bar and forgings	---	12	1.7	0.1	2.5Ni-0.35V	Jethete M152
FRG	DIN17175-79	Seamless steel tubes for elevated temperatures	Werkstoff No.	12	1	0.2	0.5Ni-0.3V	HT-91
	Votuev Werkstoffblatt 110		Werkstoff No. 1.4935; alloy X20CrMoVW121	12	1	0.2	0.5Ni-0.3V 0.5W-0.1Nb	
Russia	None	Product forms not known	20KH12WNMF	12	0.6	0.2	0.7Ni-0.3V-0.1Ti 0.9W-0.1Nb-0.2Cu	Unknown
			15KH12VNMF	12	0.6	0.15	0.6Ni-0.2V 0.9W	
			18KH12VMBFP	12	0.5	0.18	0.6Ni-0.2V 0.5W-0.3Nb-0.002B	
	5-2006-73	Steel heat exchanger and communication tubes (closest applicable standard which only includes the lower Cr-Mo alloy)						

(a) Manufacturing process: seamless tube and pipe, normalized and highly treated.

Table VI.4-14. Superheater and Reheater Applications of Martensitic/Ferritic Steels in CEGB Boilers

Material	Station	Position	Operating Temperature (°C)	Wall Dimensions			Life (h)	Failures (h)	Notes
				Dia. (mm)	Thickness (mm)	Total Length (m)			
12Cr-Mo-V	Aberthaw (2)	Radiant	430-460				16,900	6/17,000	Failures due to overheating
	"A" 1 4	superheater superheater	430-460				18,600	8 tubes	
	Aberthaw (2)	Division	600-650 but				3,700		Overheating Most of creep life used up
	"B" 7	wall pendant superheater	can reach 800				16,500	2,000 2 tubes	
	8 9	Superheater Superheater					11,000		
	High Marnham (1) 5	Final stage reheater	540-650	54	4.5	18	35,000	None	
	Staythorpe	Horizontal	550	58.5	4.5		4,000	None reported	
	Northfleet (6)	Radiant superheater	540-850		727	24,000	20,000	Numerous	Overheating
Bankside (6)	Secondary superheater	590			9	22,000	None	Loss of tube wall thickness	
12Cr-1Mo	Kingsnorth (6)	Downcomer tubes	Up to 622	49	6	10	8,400	None	

VI.4-61

Table VI.4-15. Typical Service Data for X20CrMoV(W)121 (Alloy HT-9 Type) Steam Piping

Plant Data		Main Steam					Reheat Steam				Start-up Year
Name	Location	Size (MW)	Press. (atm)	Temp (°C)	Pipe o.d. (in.)	Pipe Wall (in.)	Press. (atm)	Temp (°C)	Pipe o.d. (in.)	Pipe Wall (in.)	
Arzberg	FRG	300	220	540	11	1.4	55	540	17	0.5	1974
Neurath A, B, C	FRG	300	200	535	14	1.3	--	--	--	--	1972
Neurath D, E	FRG	600	195	535	20	1.8	--	--	--	--	1975
Weisweiler G, H	FRG	600	195	535	20	1.8	--	--	--	--	1974
Frimmersdorf Q	FRG	300	200	535	14	1.3	--	--	--	--	1970
Robert Frank IV	FRG	450	286	540	8.5	1.4	--	--	--	--	1973
Lausward	FRG	300	215	540	12	1.5	55	540	29	1.4	1976
Asnaesvaerket	Denmark	255	210	545	9	1.0	--	--	--	--	1968
Stignsnaevaerket	Denmark	250	210	560	9	1.3	--	--	--	--	1969
Skaerbackvaerket	Denmark	250	190	545	11	1.3	--	--	--	--	1969
IS Vestkraft	Denmark	250	193	545	12	1.2	--	--	--	--	1969
Studstrupvaerket	Denmark	250	174	545	13	1.4	--	--	--	--	1972
Fynsvaerket	Denmark	256	185	535	8	0.9	--	--	--	--	1974
NEFO	Denmark	300	199	535	13	1.6	--	--	--	--	1976
Kraftwerk											
Hanasaari	Finland	150	160	535	9	1.1	--	--	--	--	1973
KW Amer-Centrale	Holland	175	195	575	6	1.3	--	--	--	--	1960
Centrale-Velsen	Holland	460	181	535	18	2.0	--	--	--	--	1974
KW Maasvlakte	Holland	550	199	540	17	1.9	--	--	--	--	1974
KW Rovinari	Rumania	330	196	540	10	1.2	--	--	--	--	1974
KW Wolfersheim	FRG	65	210	550	7.5	0.9	--	--	--	--	1962
KW Standinger	FRG	250	260	545	9	1.3	--	--	--	--	1964
Robert Frank III	FRG	300	260	545	10	1.4	--	--	--	--	1967
KW Westfalen	FRG	320	226	550	12	2.0	--	--	--	--	1968
CKW Weser Veltheim	FRG	300	198	535	13	1.4	--	--	--	--	1969
KW Offleben C	FRG	325	181	525	10	1.0	--	--	--	--	1972
KW Certsheinwerk	FRG	?	181	530	13	1.4	--	--	--	--	1972
KW Franken I	FRG	300	225	540	14	1.8	--	--	--	--	1972
KW Neideraubein	FRG	600	175	530	18	1.5	--	--	--	--	1973
KW Lunen	FRG	?	136	525	10	0.7	--	--	--	--	1971
KW Moorberg	FRG	515	215	540	16	2.0	--	--	--	--	1973
KW Scholven	FRG	714	210	535	19	2.2	--	--	--	--	1974
KW Emsland	FRG	365	181	530	13	1.4	--	--	--	--	1974
KW Frauen	FRG	300	225	540	14	1.8	--	--	--	--	1975
KW Veltheim	FRG	450	235	540	12	1.8	--	--	--	--	1975
KW Huckingen	FRG	300	176	530	13	1.3	--	--	--	--	1975
HKW Niehler Hafen	FRG	300	178	540	13	1.6	--	--	--	--	1975

VI.4-63

Atomic has noted that only two failures related to welding are known to have occurred.

Commercial experience, therefore, has demonstrated that this alloy is readily weldable if proper precautions are taken regarding preheat and post weld heat treatment (PWHT). However, the as-welded joint is untempered martensite, which is prone to fracture if the weld is handled improperly and to hydrogen cracking if the weld is allowed to sit idle prior to the PWHT. The function of the preheat is to input sufficient heat to slow the cooling rate after welding, to drive off any moisture or hydrocarbons absorbed in the plate surface prior to welding, and to reduce the thermal shock to the weld region. In the case of multipass welds, interpass temperatures are sometimes specified to prevent the transformation to martensite, which occurs around 250°C. The PWHT is generally recommended immediately after welding to temper the joint, which lowers the strength considerably, but increases its toughness.

The conical section of each tube of the TASKA blanket will be welded to the manifold as shown in Fig. VI.1-7. As stated, the welds must be full penetration to insure that outgassing will not be a significant problem for the vacuum system. In order to insure this, non-destructive examinations by radiography would be needed on each row of tube-to-manifold weldment as they are completed. This could be done by applying film to the manifold side of the welds with a radiation source on the other. With that, and visual examination, it is felt the full penetration requirement could be met without re-welding on the underside which would be difficult and costly. In order to insure that each tube is completely sealed and no through-cracks are missed

during NDE, each tube could be lightly pressurized and leaks detected prior to welding the next row of tubes.

After the last row of tubes is welded to the manifold and the manifold top is welded to the bottom section, the structure may be subject to hydrogen attack. This is not uncommon in high strength, stressed materials exposed to moisture. A welded structure such as the TASKA blanket will also be subject to triaxial stresses in the as-welded joints. The first row of tubes might be in the non-stress relieved condition during welding and inspection of all others. A pretreatment to reduce the strength and increase the toughness could sufficiently slow the crack growth due to hydrogen. This pretreatment may be a low-temperature heat treatment ($< 400^{\circ}\text{C}$) for enough time to increase the ductility of the material significantly. The coolant tubes are placed fairly close to each other in the manifold (~ 4 cm) and therefore, the welding of the next row of tubes may provide sufficient heat input to lightly temper the previous row of weldments. This will also reduce the potential cracking before the final heat treatment.

After welding, care must be exercised in handling or transporting the blanket modules. A heat treatment is required to temper the welded joints which is traditionally a post-weld heat treatment (PWHT) of 760°C for 2.5 hrs. This can be performed by using insulated heating tapes wrapped around the weldments. However, this may be only one option. It will "fully" temper the weldment giving it superior thermal properties to the parent metal (as indicated by so few weldment failures in boiler service). Another choice is to post-weld heat treat the entire structure. This could be done using furnaces available in many steel processing plants, although heating and cooling rates would need to be carefully controlled.

There is some concern about the effect of neutron damage on weldments and heat affected zone (HAZ) microstructures which might still exist after the PWHT. The concern is primarily due to the lack of irradiated mechanical property data on weldments. Irradiated HAZ properties may not be different from the parent metal, but until that is shown by data, it is prudent to consider eliminating the weld zone by re-austenitizing the entire structure. This will have two primary benefits. The first is to eliminate the metallurgically different zones of a weld joint, while the second is to eliminate any potential problems caused by exacerbated irradiation damage in heat affected zones.

A weld joint is one which can be characterized as "as-cast", that is, the material in the fusion zone was cooled from a liquidous state such that chemical segregation will occur at dendrite structures. The "as-cast" material is not re-austenitized at 760°C, and so is retained even after the PWHT. Furthermore, delta ferrite tends to form at the dendritic boundaries (and also in the material not melted during welding immediately adjacent to the fusion line in the parent metal). The ferrite in a dual-phased structure such as this, will swell disproportionately from the martensite. This difference in swelling may promote cracking near the fusion line interface.

Other options which might be considered to avoid deleterious microstructures include re-austenitization followed by a full tempering treatment. This could be done using higher temperature heating tapes to attain the required 1050°C, but such a solution would require some development. Another approach would be to heat treat the entire structure in a large furnace typical of those in steel mills for high-temperature soaking of ingots. Large forgings have been heated to temperatures on the order of 1000°C with care-

fully controlled heating and cooling rates to minimize thermal stresses. In air, high temperatures would cause scale formation (which is tightly adherent on 12 Cr-1 Mo steel) so a protective atmosphere of argon or helium could be provided. After austenitization at 1050°C, the structure would be cooled sufficiently fast to prevent the formation of bainitic or perlitic decomposition products, yet slowly enough to minimize stresses due to the transformation to martensite.

Finally, the temperatures needed to austenitize the structure may lead to some distortion. The exact degree of this problem is not known, but manufacturers of heat treating furnaces suggest that development work on a prototype could answer the feasibility question fairly rapidly. The design of a true engineering structure will require strict tolerances to be built into the components. When these are known and when the thermal distortion is quantified, the engineering feasibility of this process will be established.

VI.4.10 Expected Irradiation Performance of HT-9 in TASKA

In this section we will attempt to extrapolate the data discussed in previous sections to TASKA conditions. The reader is certainly aware by now that the uncertainties in this extrapolation process are very large and certainly more experimental and theoretical data is required before one could confidently predict component lifetimes. Nevertheless, we will proceed with our projections based on what we now know.

It appears that the swelling rate in the HT-9 alloy will be in the range of 0.01% dpa⁻¹ or smaller over the 350°C-530°C operating range. At the maximum damage rate of 14.8 dpa per operating year, this amounts to a maximum swelling rate of ~ 0.15% per year. The effect of much higher helium

concentrations on this swelling is unknown and close attention should be paid to experiments currently in U.S. mixed-spectrum neutron fission reactors.

As the high temperature ($\sim 550^{\circ}\text{C}$) irradiations indicated; adequate total elongation ($> 10\%$) is retained for low He levels (~ 19 appm) and modest doses (~ 50 dpa). Higher levels of He are likely to reduce ductility at temperatures above 500°C , but not at lower temperatures. On the other hand, the low temperature irradiations ($\sim 50^{\circ}\text{C}$) in HFIR resulted in a more severe radiation-induced embrittlement with total elongations of the order of 5% or less, and uniform elongations around 0.5%. Fortunately, helium was not found to influence this reduction in ductility.

There is still no information on the radiation-induced embrittlement in the temperature range from 350 to 450°C .

The creep rates appear to be in the range of 0.2% per year and are not greatly affected by irradiation in the TASKA operating range. Since the creep rate depends on the damage rate, which is about the same in TASKA ($0.8 \times 10^{-6} \text{ s}^{-1}$) as in EBR-II ($\sim 1 \times 10^{-6} \text{ s}^{-1}$) where the data was taken, we feel somewhat more confident in predicting the 0.2% per year value.

The DBTT shift of ferritic steels is of concern for irradiation temperatures between 300 to 400°C , the temperature range for TASKA in the blanket region. The shift at the lowest irradiation temperature occurs rapidly over a few days, but then saturates at a temperature around 200°C . Saturation appears to be reached after about 0.05 to 0.1 dpa. The shift in DBTT decreases with increasing irradiation temperature. From post-irradiation annealing experiments on nuclear pressure vessel steels, irradiated at about 300°C and subsequently annealed at 400°C for 168 hours, it is found that the shift can

be reversed and the DBTT be restored to 55 to 75% of its initial value.

Figure VI.4-29 summarizes the annealing data.⁽³⁴⁾

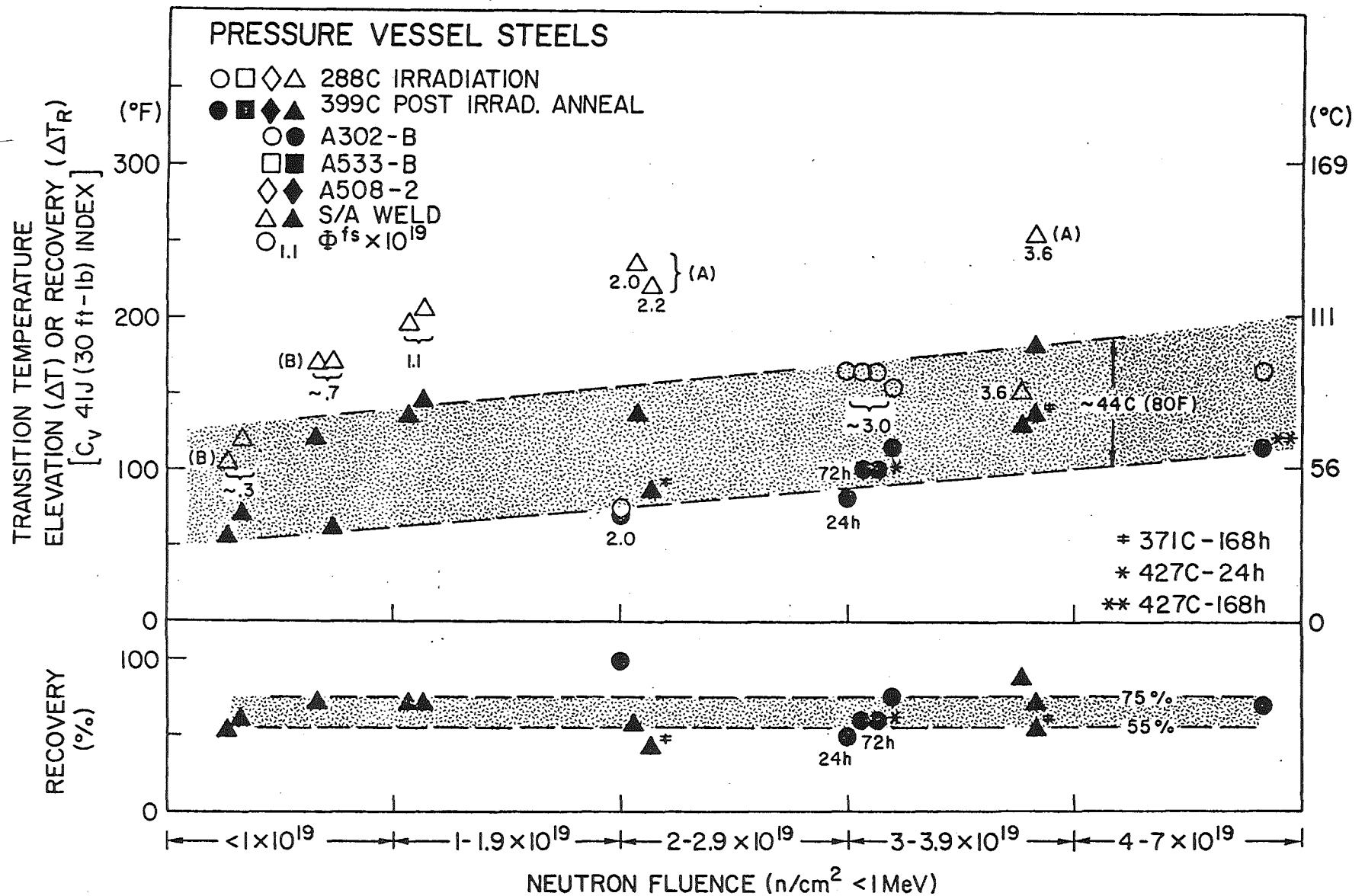
The implications of the DBTT shift for TASKA are the following. While the reactor is on power or the blanket coolant $Pb_{83}Li_{17}$ above its melting point ($\sim 280^{\circ}C$), the blanket structure remains everywhere above the DBTT. Above this temperature, the material is ductile and the fracture toughness is more than adequate.

When a blanket module is scheduled for removal, the coolant flow should be reversed for several days while the reactor remains on power. As a result of this operation, the parts of the blanket structure previously exposed to a low irradiation temperature will recover, while the parts previously exposed to the high temperature will experience now some shift in the DBTT. However, the overall effect on the entire blanket structure should be beneficial. Although the DBTT in thick section specimens will most likely remain above room temperature in spite of the annealing procedure, it is expected that the DBTT for the thin walled tubes used in the TASKA blankets will indeed be below room temperature.

Figure VI.4-30 shows the effect of the section thickness of fracture specimens on the DBTT for types 409, 437, and other proprietary ferritic steels.⁽³⁵⁾ It is seen that the DBTT is lower by about $100^{\circ}C$ for a thickness of 2.5 mm as compared to the conventionally thicker specimens of 1 cm or larger.

Since the wall thickness of the blanket coolant tubes is 2.77 mm, the DBTT for the blanket structure is expected to be at least $50^{\circ}C$ lower, if not more, than the present data indicates. Therefore, DBTT shift may not present

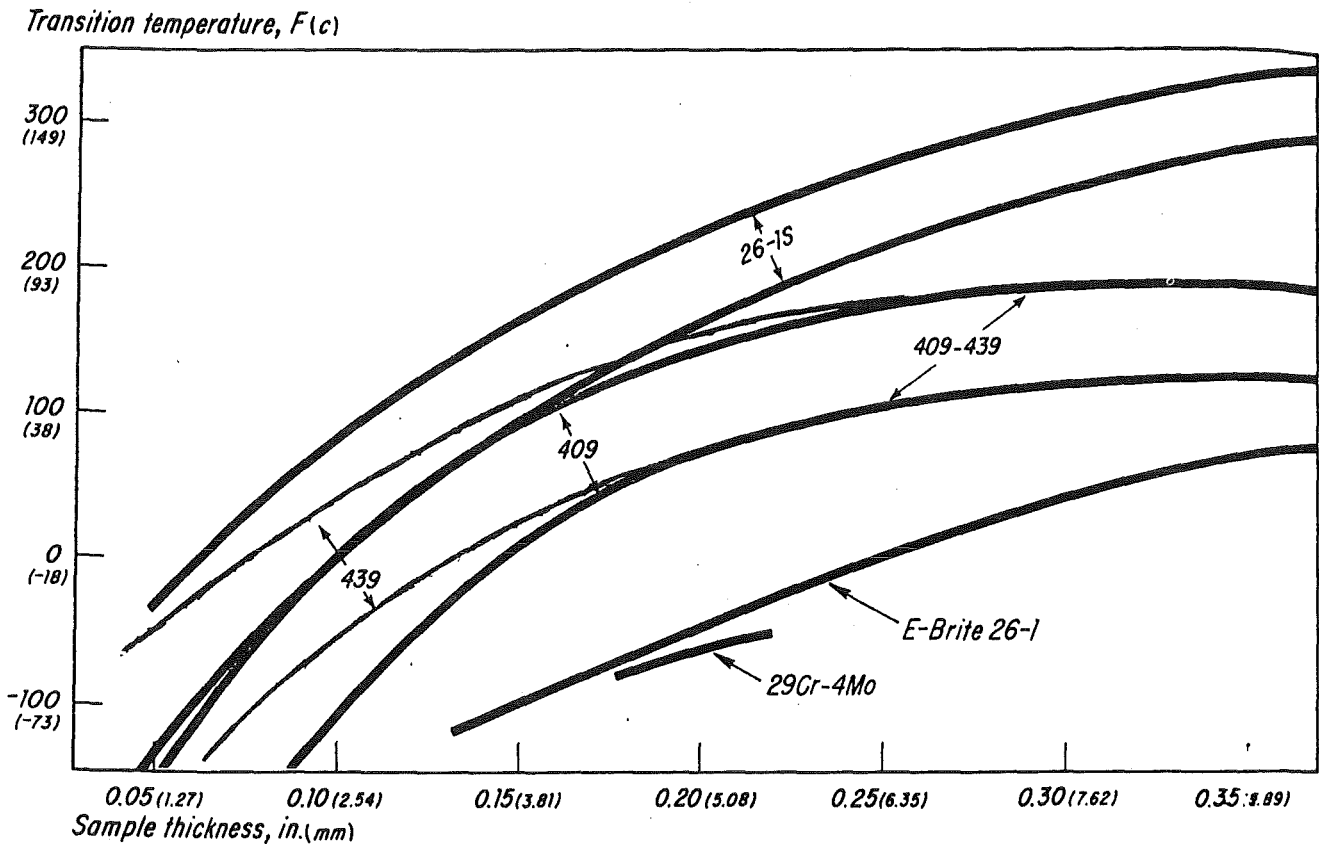
VI.4-70



- 534 -

Fig. VI.4-29 Summary of transition-temperature changes (41-J index) observed for several steels with 288 C (550 F) irradiation (open symbols) and with 399 C (750 F) postirradiation heat treatment (filled symbols). Limited data for 371 C (700 F) and 427 C (800 F) annealing are also shown.

Fig. VI.4-30



Ductile-to-brittle transition temperatures (DBTT) for ferritic stainless steels rise with section thickness. Bands for 26-1S, 409, and 439 indicate data scatter.

any restriction on the use of ferritic steels in fusion reactors, and TASKA in particular.

References for Section VI.4

1. Compilation of data taken from USDOE-DAFS and USDOE-ADIP Quarterly Progress Reports.
2. J.C. Lippold, "Weldability of HT-9: The Autogeneous GTA Process," p. 98 in DOE/ER-0045/2, March 31, 1980.
3. J. Chafey and L. Thompson, "Post-Service Evaluation of an HT-9 Superheater Tube in Service for 80,000 Hr. at 600°C," Proc. Materials-Environment Interactions in Structural and Pressure Vessel Containment Service Symposium, ASME, New York, NY (1980) 53.
4. J.M. Rawls et al., "Assessment of Martensitic Steels as Structural Materials in Magnetic Fusion Devices," GA-A15749, General Atomic Comp. (1980).
5. E.E. Bloom et al., private communication
6. R.F. Stoltz, "Mechanical Property Measurements of HT-9 in Hydrogen: 25 to 400°C," p. 88 in DOE/ER-0045/2.
7. W.R. Warke and M.M. Breyer, "Effect of Steel Composition on Lead Embrittlement," J. of the Iron and Steel Institute, (Oct. 1971) p. 779.
8. C.F. Old, "Liquid Metal Embrittlement of Nuclear Materials," J. Nuclear Materials 92, (1980) 2.
9. R.C. Asher, D. Davis, and S.A. Beethour, "Source Observations on the Compatibility of Structural Materials with Molten Lead," Corrosion Science 17, (1977) 545.
10. T.C. Anderson et al., "Intergranular Penetration of 2-1/4 Cr-1 Mo Weldments by a Lithium-Lead Liquid," to be published, 2nd Int. Conf. on Liquid Metal Technology in Energy Production, April 20, 1980, Richland, Washington.
11. J.C. Lynn, W.R. Warke, and P. Gordon, "Solid Metal-Induced Embrittlement of Steel," Mat. Sci. and Engr. 18, (1975) 51.
12. O. K. Chopra and D. L. Smith, to be published.
13. P.F. Tortorelli and J.H. DeVan, "Compatibility of Stainless Steel with Pb-17 at.% Li," Internat. Corrosion Forum, Houston, preprint.

14. M.M. Breyer and K.L. Johnson, "Liquid Metal Embrittlement of 4145 Steel by Lead-Tin and Lead-Antimony Alloys," *J. of Testing and Evaluation* 2, (1974) 471.
15. C.F. Olds and P. Trevena, AERE-R9505 (1979).
16. J.E. Cordwell, in: Proc. BMES Conf. on Liquid Alkali Metals, Nottingham, p. 177, 1973.
17. F.A. Smidt, Jr., "The Fracture Resistance of HT-9 After Irradiation at Elevated Temperature," p. 163 in DOE/ER-0045/2, March 31, 1980.
18. K.R. Garr, C.G. Rhodes, D. Kramer, "Effects of Microstructure on Swelling and Tensile Properties of Neutron-Irradiated Types 316 and 405 Stainless Steels," AI-AEC-13-31, June 15, 1972.
19. M.M. Paxton, B.A. Chim, and E.R. Gilbert, "The In-Reactor Creep of Selected Ferritic, Solid Solution Strengthened, and Precipitation Hardened Alloys," *J. Nucl. Mat.* 95, (1980) 185.
20. E.A. Little, R. Bullough, and M.H. Wood, "On the Swelling Resistance of Ferritic Steel," AERE-R9678, Feb. 1980.
21. K. Anderko, "Zur Eignung Warmfester Vergütungsstähle mit 9 bis 12% Chrom für Komponenten im Kern Schneller Reaktoren-Ein Überblick," *J. Nuclear Materials* 95, (1980) 31.
22. L.A. James, "Fatigue-Crack Growth Behavior in Fast-Neutron-Irradiated Ferritic Steels and Weldments," *J. Engr. Mat. and Tech.* 102, (1980) 187.
23. E.A. Little, "Void Swelling in Irons and Ferritic Steels: I. Mechanisms of Swelling Suppression," *J. Nuclear Materials* 87, (1979) 11. (See also *ibid.*, p. 25.)
24. M.M. Paxton, B.A. Chim, E.R. Gilbert, and R. E. Nygren, *J. Nuclear Materials* 80, (1979) 144.. See also E. R. Gilbert and B. A. Chim, "In-Reactor Creep Measurements," *Nucl. Tech.* 52, (1981) 273.
25. Data from General Atomic contained in summary by F. Coffman, Sept. 8, 1978.
26. F.A. Smidt et al., "Swelling Behavior of Commercial Ferritic Alloys, EM-12 and HT-9, as Assessed by Heavy Ion Bombardment," p. 227, in ASTM-STP-611, Amer. Soc. Testing and Materials, Philadelphia, 1976.
27. M. Snykers, "Void Swelling of an Oxide Dispersion Strengthened Ferritic Alloy in a High Voltage Electron Microscope," *J. Nuclear Materials* 89, (1980) 80.

28. C. Wassilew, "Vergleich der Zeitstand - und Kriecheigenschaften austenitischer Stähle mit dem des martensitischen Stahls 1.4914 nach Neutronenbestrahlung," Proc. Internat. Conf. Mech. Behavior in Nucl. applications of Stainless Steels at Elevated Temp., May 1981, Varese, Italy; to be published.
29. K. Herschbach, W. Schneider, and K. Ehrlich, "Bestrahlungsinduziertes Kriechen und Schwellen des Austenitischen Werkstoffes Nr. 1.4981 zwischen 400 und 500°C (RIPCExI)," J. Nucl. Materials 101, (1981) 326-335.
30. R.L. Klueh and J.M. Vitek, "Tensile Properties of Ferritic Steels After Low-Temperature HFIR Irradiations," Alloy Dev. for Irrad. Performance Quart. Prog. Rep. DOE/ER-0045/6, July 1981, p. 139.
31. M.K. Zimmerschied, D.T. Peteron, R.W. Powell, and J.F. Bates, "Immersion Density Analysis of Commercial Alloys Irradiated to a Very High Fluence," Alloy Dev. for Irrad. Performance Quart. Prog. Report DOE/ER-0045/5, April 1981, p. 226.
32. D.S. Gelles, "Microstructural Examination of a Series of Commercial Ferritic Alloys Irrad. to Moderate Fluence," Alloy Dev. for Irrad. Performance Quart. Prog. Report DOE/ER-0045/6, July 1981, p. 157.
33. E.A. Little, D.R. Arkell, D.R. Harries, G.R. Lewthwaite, and T.M. Williams, Conf. on Irradiation of Fuel and Structural Materials in Fast Reactors, Ajaccio, Corsica, 1979.
34. Resolution of the Reactor Vessel Materials Toughness Safety Issue, U.S. Nuclear Regulatory Commission Report NUREG-0744, Vol. 2, Appendix F.
35. R.A. Lula, "Ferritic Stainless Steel Corrosion Resistance and Economy," Metal Progress, July 1976, p. 25.

VI.5 Tritium Extraction and Purification

This chapter is divided into two parts. Section VI.5.1 outlines the tritium parameters in the $\text{Li}_{17}\text{Pb}_{83}$ eutectic, the blanket, the heat exchange cycle which includes an organic intermediate loop and discusses the tritium extraction scheme. Section VI.5.2 describes the TASKA fuel purification systems.

VI.5.1 Blanket and Heat Exchange Systems

In TASKA the main reactor breeding blanket consists of HT-9 tubes through which the liquid lithium-lead breeding material is circulated. The lithium-lead is a eutectic of composition 17 atom % Li and 83 atom % Pb which melts at 235°C. The $\text{Li}_{17}\text{Pb}_{83}$ is operated at temperatures between 300 and 400°C and serves as the heat transfer agent to an organic intermediate loop. The blanket and coolant characteristics in the primary and intermediate loop are summarized in Tables VI.5-1 and VI.5-2.

The low solubility of tritium in $\text{Li}_{17}\text{Pb}_{83}$ results in low inventories and presents the possibility of extracting the tritium by allowing it to permeate through the breeding blanket tubes. This in-situ extraction method is feasible if an appropriate tritium barrier is present on the organic coolant side of the heat exchange loop.

VI.5.1.1 Blanket Inventory

In order to determine the tritium inventory in the breeding material the solubility of tritium in $\text{Li}_{17}\text{Pb}_{83}$ at the reactor temperatures (300-400°C) must be known. The solubility of hydrogen in dilute solutions is expressed by the Sievert's constant (K_s) where:

Table VI.5-1. Characteristics of the Primary Heat Exchange Cycle

Blanket Parameters:

Structure	HT-9
Tube Thickness	.227 cm
Temperature	
High	440°C
Low	300°C
Average	370°C
Surface Area	1234 m ²

Primary Coolant:

Composition	Li ₁₇ Pb ₈₃
Temperature	
High	400°C
Low	300°C
Average	350°C
Li Vapor Pressure (350°C)	1.2 x 10 ⁻¹⁰ torr
Pb Vapor Pressure (350°C)	1.3 x 10 ⁻⁸ torr
Density (350°C)	9.46 g/cm ³
Volume in blanket	39.3 m ³
Mass (Blanket and Ext. Piping)	5.7 x 10 ⁵ kg
Flow Rate	2.9 x 10 ⁶ g/sec

Table VI.5-2. Characteristics of the Intermediate Loop

IM Loop:

Composition	HT-9
Tube Thickness	.227 cm
Temperature	
High	385°C
Low	285°C
Average	335°C
Surface Area	895 m ²

Intermediate Coolant:

Composition	HB-40
Temperature	
High	371°C
Low	271°C
Average	321°C
Mass	1.4 x 10 ⁴ kg
Flow Rate	169.1 kg/s

$$K_s = \frac{N}{p^{1/2}}$$

where N = the concentration of hydrogen in the alloy (appm), and

P = the hydrogen pressure above the alloy (torr).

The Sievert's constant for deuterium in Li-Pb alloys has been determined by Ihle et al.⁽¹⁾ at 677 and 767°C, much higher temperatures than the reactor conditions. The accuracy of this data is questionable and direct extrapolation to lower temperatures results in unreasonable solubility values. The solubility has also been predicted from models.⁽¹¹⁾ E. Veleckis⁽²⁾ at Argonne National Laboratory is conducting Sievert's constant experiments on lithium-lead alloys in the temperature range of 400 to 600°C. The value obtained for hydrogen in Li₁₇Pb₈₃ is $(7.1 \pm 1.5) \times 10^3 \text{ atm}^{1/2} (\text{at.fr.H})^{-1}$ which corresponds to 5.1 appm H/torr^{1/2}. Preliminary results also indicate that in this temperature range the Sievert's constant is independent of temperature within experimental error.

The low value and temperature independence of the solubility seem to be consistent with the thermodynamic and physical properties of the lithium-lead system. A comparison of the hydrogen solubility of pure lithium⁽³⁾ and lead⁽⁴⁾ to that of other metals^(5,6,7) (Fig. VI.5-1) shows that lithium has one of the highest hydrogen solubilities of any known metal while lead has one of the lowest hydrogen solubilities. Therefore, when hydrogen dissolves in the alloy it interacts exclusively with the lithium, because lead-hydrogen interactions are weak. The degree to which the lithium is available for bonding is related to the activity coefficient for lithium in lithium-lead. Activity measurements on the alloy^(1,8,9,10) indicate very low activities of

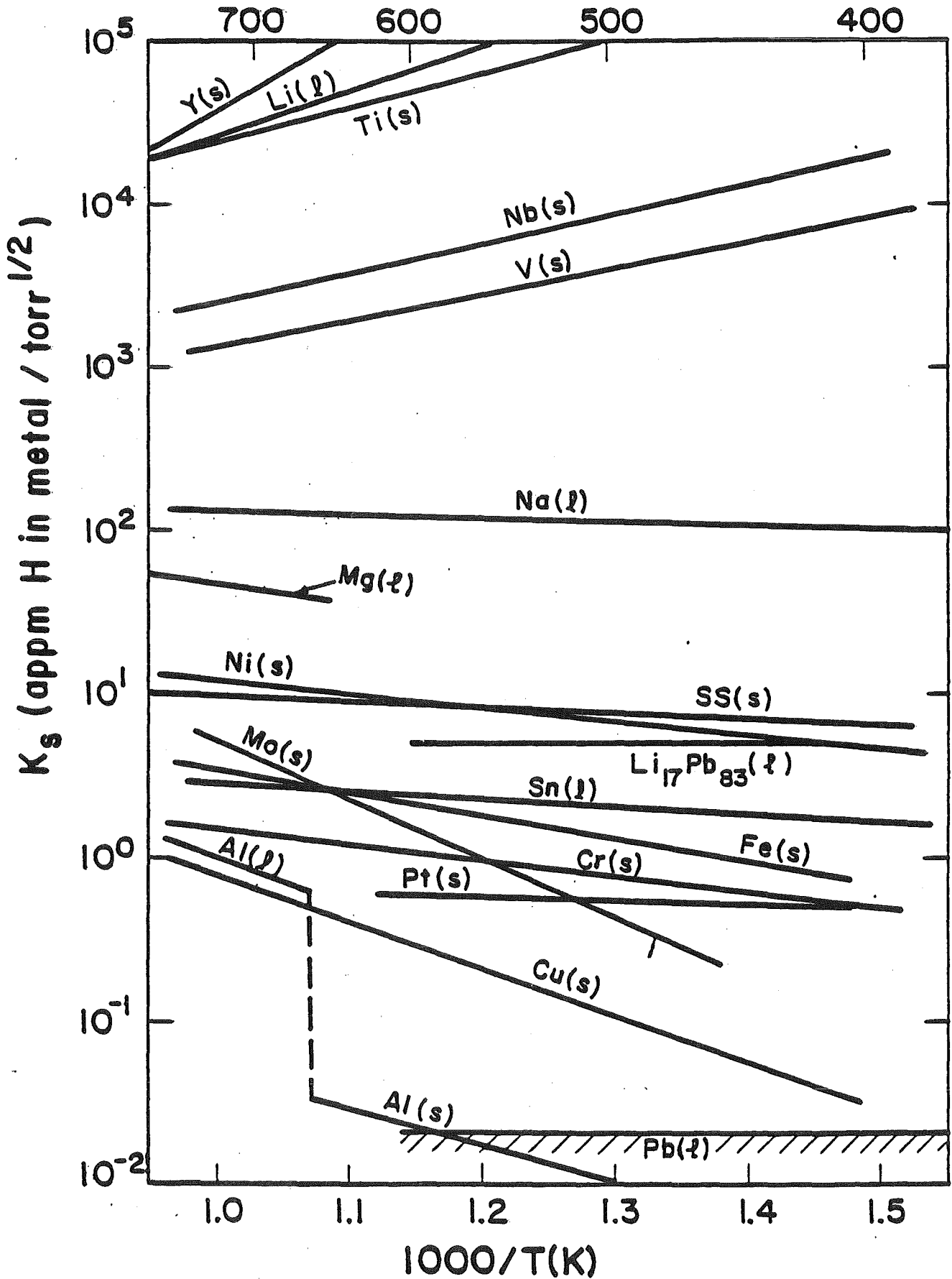


Figure VI.5-1. THE SOLUBILITY OF HYDROGEN IN SELECTED METALS AND ALLOYS AS A FUNCTION OF TEMPERATURE.

lithium in the $\text{Li}_{17}\text{Pb}_{83}$ eutectic (1.3×10^{-4} at 500°C) which predicts low solubilities.

The temperature independence also appears reasonable on examination of Fig. VI.5-1. Lithium dissolves hydrogen exothermically while metals with low solubilities, (such as lead) generally dissolve hydrogen endothermically. This probably leaves Li-Pb alloys in an intermediate category showing little temperature dependence. (11)

For TASKA, the Sievert's constant for hydrogen ($5.1 \text{ appmH/torr}^{1/2}$) is converted to tritium units by assuming the $\sqrt{3}$ dependence as observed in the pure lithium hydrogen isotope solubility studies. The resulting value is

$$0.051 \frac{\text{wppm T in Li}_{17}\text{Pb}_{83}}{\text{torr}^{1/2}} .$$

To determine the blanket inventory the tritium pressure above the coolant must be specified. The pressure required for the tritium to be extracted at the breeding rate can be calculated from the permeability of tritium through HT-9(12) given in Eq. (VI.5-1):

$$P = \frac{65.3}{\sqrt{3}} \exp\left(\frac{-11100}{RT}\right) \frac{\text{mol T}_2 \cdot \text{mm}}{\text{d} \cdot \text{m}^2 \cdot \text{torr}^{1/2}} . \quad (\text{VI.5-1})$$

For the TASKA parameters:

$$P = 1.3 \times 10^5 \text{ Ci/d (breeding rate)}$$

$$T = 350^\circ\text{C}$$

$$\text{Area} = 1234 \text{ m}^2$$

$$\text{Thickness} = 0.227 \text{ cm,}$$

the resulting pressure is 0.39 torr. At a pressure of 0.39 torr the solubility is 0.032 wppmT in $\text{Li}_{17}\text{Pb}_{83}$. For a total Li-Pb mass of 5.7×10^5 kg, the tritium inventory in the blanket is 18.2 g T.

At this high tritium pressure, we also need to determine the tritium inventory in the structural material. The hydrogen solubility in HT-9⁽¹²⁾ is given by Eq. (VI.5-2):

$$K_s = \frac{2.3 \times 10^{-4} \exp\left(\frac{-7500}{RT}\right)}{\sqrt{3}} \frac{\text{mol } {}_2\text{H}}{\text{cm}^3 \text{ metal} \cdot \text{atm}^{1/2}} \quad (\text{VI.5-2})$$

At 370°C and 0.39 torr for 3.84 m³ of metal the inventory is 0.12 g T. The tritium blanket parameters are summarized in Table VI.5-3.

VI.5.1.2 Tritium Extraction

From the previous section it is apparent that with the low Sievert's constant the tritium pressure can be allowed to build up to a fairly high pressure (0.39 torr) and still maintain a relatively modest blanket inventory (18.32 g T). A way to take advantage of this phenomenon is to allow the tritium to permeate through the blanket tubing into the reactor vessel⁽¹³⁾ where it will be pumped and recovered along with the exhaust gases. This scheme necessitates an effective containment scheme to prevent losses to the heat exchanger. For TASKA, the containment is provided by the use of an organic coolant in the intermediate loop (IM loop) of the heat exchange cycle. Tritium permeating into the organic will exchange slowly with hydrogen and be effectively contained. The flux of tritium into the organic must be minimized to prevent gross decomposition of the coolant.

The tritium permeation into the organic IM loop can be calculated from Eq. (VI.5-1) assuming the same wall thickness, temperature, and tritium

Table VI.5-3. Blanket Tritium Parameters

Breeding Ratio	1.0
Breeding Rate	1.3×10^5 Ci/d
Tritium Flow Rate	9.28×10^{-2} g T/sec
Tritium Partial Pressure (@ 350°C)	0.39 torr
Tritium Concentration in $\text{Li}_{17}\text{Pb}_{83}$	0.032 wppm
Blanket Tritium Inventory:	
$\text{Li}_{17}\text{Pb}_{83}$ Coolant	18.2 g
HT-9 Structure	<u>0.12 g</u>
Total:	18.32 g

pressure assuming no tritium barrier is present. A barrier that will provide a factor of ~ 150 or more reduction in tritium permeation is necessary to reduce the permeation to less than 500 Ci/d. The tritium permeation should be minimized to prevent high decomposition rates in the organic.

VI.5.1.3 Tritium Barriers

Tritium barriers are commonly invoked to reduce permeation to the steam cycle. For example in STARFIRE⁽¹⁴⁾ a barrier factor of 150 is used for both the 316 SS blanket (500°C) and the Inconel (300°C) in the steam generator. The most common barrier is the oxide coating that is present on the steam-side of the heat exchange tubing. Table VI.5-4 illustrates the magnitude of permeation barriers for steels at 660°C. A factor of 150 for a barrier seems reasonable.

There are many factors that affect the magnitude of the oxide barrier. The oxidation temperature is important. Stainless steel membranes oxidized at 750°C for 200 hrs had 20 times lower permeation rates than those oxidized at 550°C for an equivalent time period.⁽¹⁷⁾ Surface analyses revealed that Mn and Cr oxides formed on the surface of the high temperature membranes and Fe oxides have been formed at lower temperatures. After prolonged operation, 6000 to 24000 hrs at 500 to 600°C, Mn/Cr oxide coatings were observed at HEDL. These data imply that for steam generators running at low temperatures (<500°C), oxide coatings may have to be preformed at higher temperatures to obtain the more resistant barrier. Studies also show that the permeability does not necessarily decrease linearly with oxide thickness.⁽¹⁸⁾ Thick oxides (>1 μm) often showed permeabilities with activation energies close to that of the substrate. This indicates that cracks or defects form in the oxide which permit hydrogen access to metal surfaces.^(18,19)

Table VI.5-4. Permeation Barrier Factors of Ferritic and Austenitic Steels Produced by Steam Oxidation of the Downstream Side

	<u>Ferritic Fe-2-1/4 Cr-1 Mo</u>	<u>Ferritic SS 406</u>	<u>Austenitic SS 316</u>
Reference	16	15	15
Temperature (°C)	472	660	660
Steam Pressure (atm)	2	0.94	0.94

Factors by Which Permeabilities are Reduced

Time			
0.33 d	10	13	---
1 d	25	72	1.6
6 d	100	144	2.8
24 d	170	291	3.8
40 d		434	4.3

Experiments with palladium over oxides indicate that a Pd coating on the oxide has an effect on the permeability on the upstream face, but that very little difference is observed if the downstream face is coated.⁽¹⁸⁾ This suggests that surface effects on the upstream side are rate controlling. The difference between the two measurements, however, was less than a factor of two.

The liquid-metal side of the steam generator tubing is not capable of maintaining an oxide coating. A nickel-aluminide layer has been developed which shows a reduction in diffusion rate of two orders of magnitude for 304 SS at 550°C and 10 torr H₂.⁽¹⁷⁾ The pressure dependence of the diffusion rate appears to be linear. This indicates that for the low tritium pressure expected in fusion heat exchangers, the Ni-Al barrier will lower the permeation by several orders of magnitude. This barrier can be formed in-situ by addition of Al to the coolant and it is resistant to attack by hot sodium and lithium. In TASKA, the blanket and heat exchange material is HT-9, which is very low in nickel and not expected to form the Ni-Al layer. To form this barrier a different structural material with a higher nickel concentration would have to be chosen for the heat exchanger. The resistant coating would then form on the heat exchange tubing while a low Ni alloy would be used in the blanket to allow permeation. Experimentation is needed to verify the barrier effectiveness at low pressures.

Multilayered metal laminates containing at least one layer with a relatively low hydrogen permeability have been studied⁽²⁰⁾ and the use of double walled tubes with an oxidizing purge gas in the gap⁽²¹⁾ have been proposed. The cost and feasibility of constructing these types of special tubing may be prohibitive. The use of double walled tubes is an especially effective

tritium barrier, as tritium in the gap is converted to the oxide, reducing the HT partial pressure to $\sim 10^{-16}$ torr.

The use of $\text{Li}_{17}\text{Pb}_{83}$ as a coolant in any design will result in a high tritium partial pressure and thus a containment problem. For TASKA, the organic IM loop acts as a tritium getter and, therefore, tritium permeating to the organic will not be released to the environment. However, the permeation into the organic must be minimized to prevent decomposition. Oxide coatings have been shown to be effective barriers, reducing permeation by 2 to 3 orders of magnitude. A conservative barrier assumption of 150 will result in 370 Ci/d lost to the IM loop.

VI.5.1.4 Organic Intermediate Loop

The intermediate loop contains a mixture of partially hydrogenated terphenyls with the proprietary name of the Monsanto Company HB-40. The coolant is a pale yellow liquid at room temperature and has the characteristics of a light lubricating oil. After exposure to heat and radiation the coolant is opaque black and contains $\sim 30\%$ high boiling (HB) decomposition products as well as $\sim 1\%$ hydrogen and gaseous hydrocarbons and $\sim 5\%$ volatile ($\text{C}_6\text{-C}_{12}$) hydrocarbons. The AECL (Atomic Energy of Canada Limited) has done considerable work in the development and use of organic terphenyls as heat transfer media for nuclear reactors. In particular, the AECL has over 8 years of operating experience with a heavy water moderated, organic cooled reactor, WR-1, at the Whiteshell Nuclear Research Establishment. There is a vast amount of literature available on the Canadian experience (see Summary Report, Ref. 22). In this section a few of the characteristics of the organic that impact the tritium processes are outlined.

It is difficult to ascertain the effects of tritium leakage into the organic. The organic decomposes in both radiation and thermal environments and the coolant is periodically vented and partially replaced. The organic that is removed from the IM loop and the vented gases can be oxidized to CO₂ and H₂O and the isolated tritiated water is then sent to a water recovery unit. The thermal decomposition rate of the organic is 1.4 kg/hr. If the tritium intake for the primary coolant is 370 Ci/d and the coolant inventory is 1.4×10^4 kg HB-40, then the tritium concentration in the coolant is 11 Ci/kg and the total inventory in the IM loop is 15g T.

The terphenyls are also known to form fouling films on heat transfer surfaces. The effect of these films on the tritium permeation and the oxide barrier is unknown. However, experience with organic coolants and zirconium alloys has shown that if 50 mg water/g is added to the coolant the fouling is reduced and the integrity of the oxide layer is maintained. The organic must also be sent through purification cycles to remove any chlorine species originally present in the organic. Chlorine can be absorbed into the oxide film and can destroy its protective characteristics. Therefore, by careful chemical control of chlorine species and addition of water, it is felt that the oxide barrier can be maintained in the presence of fouling films.

An initial analysis indicates that the organic in the intermediate loop may serve as a possible tritium getter in the steam cycle. The radiolytic damage due to tritium decay must be quantified and the safety aspects involved in using a flammable organic should be addressed.

VI.5.2 Purification Systems

The design of the purification systems for TASKA is patterned after the Tritium Systems Test Assembly (TSTA).⁽²³⁻²⁵⁾ The philosophy of the TASKA

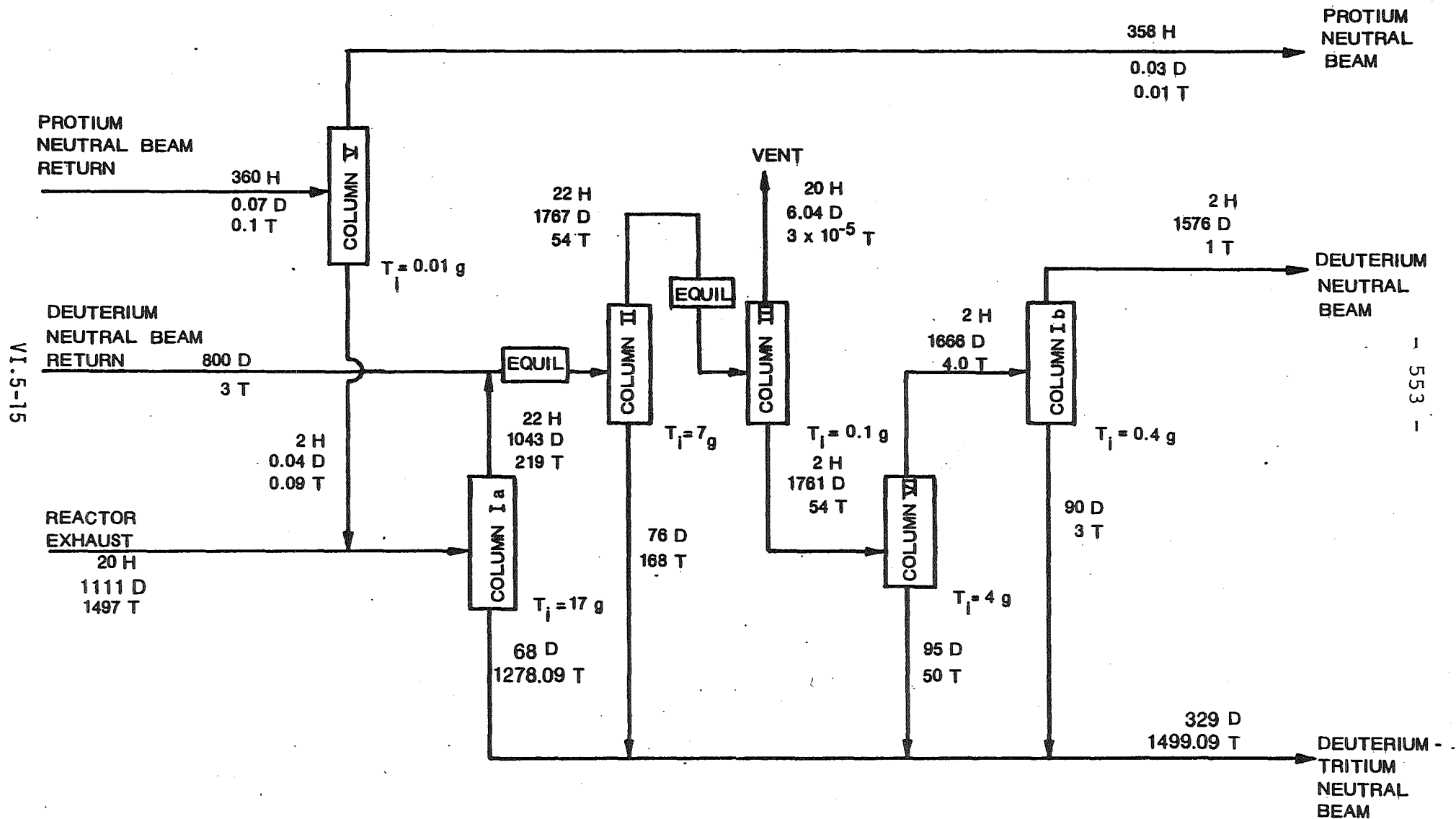
purification system is to provide gases for the neutral beam lines free of impurities (O,N,C) in order to maintain the predicted efficiencies and component lifetimes of the injection system and getter panels, to provide D-T fuel of the appropriate mixture, to limit tritium losses and to attempt to produce a simplified yet efficient design.

VI.5.2.1 Purification of NB Recycle Gases Deuterium and Proton NBI

The gases that are regenerated from the Zr-Al getter panels in the deuterium and proton NB lines are expected to contain small amounts of tritium impurities. It is possible to recycle only a fraction of these beam lines and to let the tritium level build up to a certain maximum (~5%). Although this would have a very small impact on the tritium inventory, it would increase losses to the dump coolants. In order to minimize these losses, the entire gas load is continuously sent to the reactor isotopic separation unit (ISU). The Zr-Al panels are effective getters for oxygen, nitrogen and CO, and somewhat less effective getters for water and hydrocarbons. These impurities are chemically trapped in the getter. No re-emission of N₂, CO, CO₂, or O₂ occurs at regenerations below 1100°C.⁽²⁶⁾ Therefore, the recycled isotope gases can be sent directly to the cryogenic systems where helium is removed and then to the reactor ISU. Alternatively, the gases can pass through liquid nitrogen cooled charcoal beds before being sent to the cryogenic system if further purification proves necessary. The deuterium recycle from the LE-NB (low energy-neutral beam) and the HE-NB (high energy-neutral beam) are combined and the proton stream is kept separate. These two streams are injected into the isotopic separation columns as shown in Fig. VI.5-2. Purified gases (~99.9%) are returned to the NBI systems.

Fig. VI.5-2
 TASKA ISOTOPIC SEPARATION UNIT

(Flow rates in g/d)



VI.5-15

553

The mixed DT beam will contain helium as its main impurity after being released from the getter panels. Hydrogen impurities from backstreaming are expected to be very small. A small side stream of the DT gas can be sent to the ISU periodically if there is any hydrogen buildup. It is unnecessary, in general, to send the recycle gases from this beam to the ISU.

The DT recycle gases can be purified simply by sending them over uranium beds to absorb the deuterium and tritium and separate helium. The purified DT recycle stream receives purified gases from the ISU to achieve the appropriate fuel mixture. The inventory in the DT fuel cleanup unit is approximated as 33 g T.

VI.5.2.2 Purification of Reactor Exhaust

The reactor exhaust is composed of unburned and bred tritium (1500 g/d), unburned deuterium (1111 g/d), hydrogen from the plug neutral beam (20 g/d), helium (35 g/d), and impurities produced in the harsh reactor environment.

The hydrogen isotopes and helium are pumped from the surface of the thermal dump with compound cryopumps. It has been demonstrated that a compound pump can simultaneously pump hydrogen isotopes and helium. The separation of the hydrogen on the condensation panel from helium on the cryo-sorption panel is extremely sharp. Thus, separation of the hydrogen isotopes from the helium ash is accomplished at this step. The helium panel is first regenerated, after which the cryocondensation panel is warmed to remove the hydrogen isotopes from the pump.⁽²⁴⁾ The hydrogen isotopes are then sent to the fuel cleanup unit.

The fuel cleanup unit serves to purify the hydrogen isotopes from any tritiated water, methane, ammonia, argon or any other species which would freeze out at the liquid hydrogen temperatures employed in the isotope

separation system.⁽²³⁻²⁵⁾ Impurity levels must be maintained below 1 ppm to ensure safe, long-term operation of the isotope separation system.⁽²⁵⁾

The tritiated water and ammonia are condensed out of the hydrogen isotope stream, after which the low melting impurities are separated from the hydrogen molecules by adsorption on molecular sieve beds at 75 K. The recovered impurities are then catalytically oxidized to form tritiated water and tritium-free compounds. The water is finally condensed out and electrolyzed to recover the tritium.⁽²⁵⁾ For a 500 mole T/day flow rate TSTA has estimated an inventory of 14 g.⁽²³⁾ In TASKA the exhaust cycles 1500 g T/d (500 moles T/d) and should, therefore, have the same inventory.

From the fuel cleanup unit the gases are sent to cryogenic distillation (Fig. VI.5-2). Cryogenic distillation columns are used to separate the hydrogen isotopes into 4 streams: HD waste which is vented to the atmosphere, high purity D₂ for the deuterium neutral beam injector, D-T stream for the use in the DT-NBI and high purity H₂ for use in the end plug neutral beam injectors. The cryogenic distillation columns are modeled on the separation scheme used in WITAMIR⁽¹²⁾ with minor modifications. Since the breeding ratio in TASKA is 1.0, minor redistribution of tritium into the pure deuterium gas flow from the columns has two consequences: (1) a small amount of tritium must be supplied to the DT beams or (2) assume that the tritium in the deuterium beams will fulfill the fueling requirements. A sixth column is used to reduce the amount of tritium sent to the deuterium beam lines. A breeding ratio of ~ 1.1 would compensate for this small redistribution effect. The tritium inventory in the columns is estimated as 28 g.

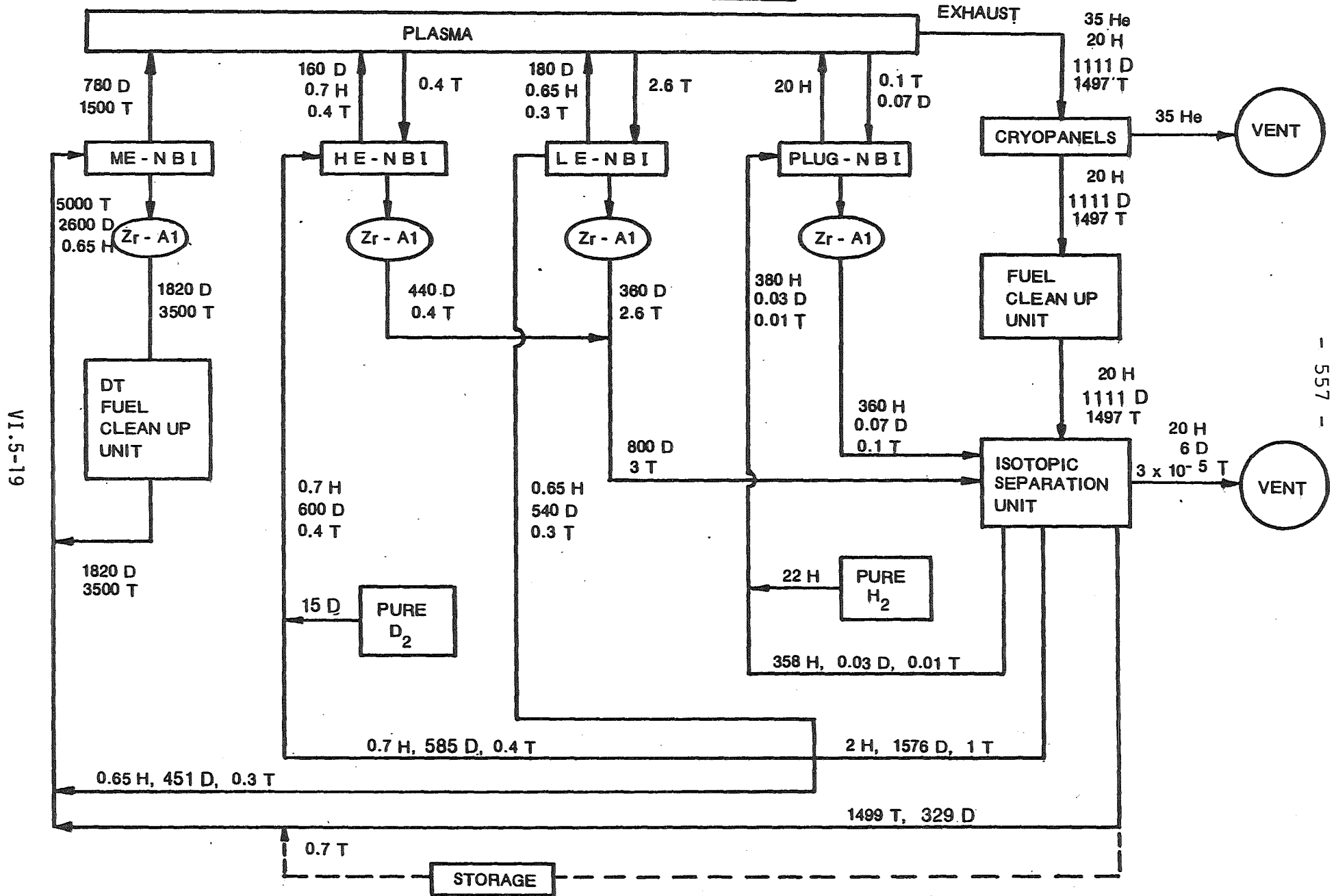
VI.5.3 Summary of the Total Tritium Inventory and Comments

The overall hydrogen isotope pathways and the total tritium inventory in the fuel cycle (IV.5.2) and the blanket and purification systems are given in Fig. VI.5-3 and Table VI.5-5. The total inventory is 5347 g T (5.3×10^7 Ci).

Further investigation for TASKA should include details of the water recovery unit and the secondary and tertiary containment systems.

Fig. VI.5-3

HYDROGEN ISOTOPE PATHWAYS IN TASKA



VI.5-19

- 557 -

Table VI.5-5. Total TASKA Tritium Inventory

Fuel and Exhaust Cycle (g)		385
NBI Getter Panels	259	
Cryopanel	125	
Dumps	0.52	
Blankets (g)		18.32
Li ₁₇ Pb ₈₃	18.2	
HT-9	0.12	
Organic IM loop (g)	15.0	15.0
Purification (g)		
Fuel Cleanup		75.0
DT-NBI Recycle	33.0	
Exhaust Recycle	14.0	
Cryogenic Distillation	28.0	
Subtotal		493
Storage (g)	5000	<u>5000</u>
Total		5493

References for Section VI.5

1. H. R. Ihle, A. Neubert and C. H. Wu, "The Activity of Lithium, and the Solubility of Deuterium, in Lithium-Lead Alloys," Proc. Tenth Symp. Fusion, Padova, Italy, September 4-9, 1978, Pergamon Press, New York, (1979) 639-644.
2. E. Veleckis, Argonne National Laboratory, private communication.
3. F. J. Smith, A. M. Batistoni, G. M. Begun, J. F. Land, "Solubility of Hydrogen Isotopes in Lithium," Report 1976, Conf. 760631-1.
4. W. Hofmann and J. Maatsch, "Loslichkeit von Wasserstoff in Aluminium, Blei und Zinkschmelzen," Z. Metallkunde 47, (1956) 89-95.
5. M. Hansen. Constitution of Binary Alloys, Second Edition, McGraw-Hill Book Co., Inc., New York, (1958) 789-790.
6. V. A. Maroni and E. H. Van Deventer, "Materials Considerations in Tritium Handling Systems," J. Nucl. Mater. 85 & 86, (1969) 257-269.
7. S. D. Clinton and J. S. Watson, "The Solubility of Tritium in Yttrium at Temperatures from 250 to 400°C," J. Less Common Met. 66, (1979) 51-57.
8. M. L. Saboungi, J. Marr and M. Blander, "Thermodynamic Properties of a Quasi-Ionic Alloy from Electromotive Force Measurements - The Li-Pb System," J. Chem. Phys. 68, (1978) 1375-1384.
9. A. I. Demidov, A. G. Morachevskii and L. N. Gerasimenko, "Thermodynamic Properties of Liquid Lithium-Lead Alloys," Sov. Electrochem. 9, (1973) 813-814.
10. S. P. Yatsenko and E. A. Saltykova, "Thermodynamic Properties of Liquid Lithium-Lead Alloys," Russ. J. Phys. 50, (1976) 1278.
11. E. M. Larsen, M. S. Ortman and K. E. Plute, "Comments on the Hydrogen Solubility Data for Liquid Lead, Lithium and Lithium-Lead Alloys and Review of a Tritium Solubility Model for Lithium-Lead Alloys," University of Wisconsin Fusion Design Memo, UWFDM-415, (May 1981).
12. B. Badger et al., "WITAMIR-I - A Tandem Mirror Reactor Study," University of Wisconsin Fusion Design Memo, UWFDM-400, Chapter XI (Dec. 1979).
13. D. K. Sze, "In-Situ Tritium Recovery from $Li_{17}Pb_{83}$ Breeding Blanket," Ninth Symposium on Engineering Plasma Problems of Fusion Research, 26-29 October 1981, Chicago, IL (UWFDM-445).
14. C. C. Baker et al., "STARFIRE, A Commercial Tokamak Fusion Power Plant Study," Argonne National Laboratory, (Sept. 1980) ANL/FPP-80-1, Chapter 14.

15. J. T. Bell, J. D. Redman and H. F. Bittner, "Tritium Permeability of Structural Materials and Surface Effects on Permeation Rates," Proceedings: Tritium Technology in Fission, Fusion and Isotopic Applications, Dayton, Ohio, April 29 - May 1, 1980, CONF-800427, American Nuclear Society (1980) 48-53.
16. T. A. Renner and D. J. Raue, "Tritium Permeation Through Fe-2-1/4 Cr-1 Mo Steam Generator Material," Nucl. Technol. 42 (1979) 312-319.
17. J. C. McGuire, "Hydrogen Permeation Resistant Layers for Liquid Metal Reactors," Proceedings: Tritium Technology in Fission, Fusion and Isotopic Applications, Dayton, Ohio, April 29 - May 1, 1980 CONF-800427, American Nuclear Society (1980) 64-68.
18. W. A. Swansiger and R. Bastasz, "Tritium and Deuterium Permeation in Stainless Steels: Influence of Thin Oxide Films," J. Nuclear Mat. 85 and 86 (1979) 335-339.
19. M. R. Piggot and A. C. Siarkowski, "Hydrogen Diffusion through Oxide Films on Steel," J. of the Iron and Steel Institute, (Dec. 1972) 901-905.
20. V. A. Maroni et al., "Experimental Studies of Tritium Barrier Concepts for Fusion Reactors," Proceedings Radiation Effects and Tritium Technology for Fusion Reactors, Gatlinburg, Tennessee, Oct. 1-3, 1975, CONF-750989, Vol. IV, 329-361.
21. A. B. Johnson, Jr., and T. J. Kabebe, "Tritium Containment in Fusion Reactors," Topical Meeting on Technology of Controlled Nuclear Fusion, Richland, Washington, Sept. 21, 1976, CONF-760935, 1319-1328.
22. J. L. Smee et al., "Organic Coolant Summary Report," Atomic Energy of Canada Limited, Whiteshell Nuclear Research Establishment, Panawa, Manitoba (Aug. 1975) AECL-4922.
23. J. L. Anderson and R. H. Sherman, "Tritium Systems Test Assembly Design for Major Device Fabrication Review," LA-6855-P, Los Alamos Scientific Lab., (June 1977).
24. J. L. Anderson, "Design and Construction of the Tritium Systems Test Assembly," Proceedings: Tritium Technology in Fission, Fusion and Isotopic Applications, Dayton, Ohio, April 29 - May 1, 1980, CONF-800427, American Nuclear Society (1980) 341-346.
25. E. C. Kerr, J. R. Bartlit and R. H. Sherman, "Fuel Cleanup System for the Tritium Systems Test Assembly: Design and Experiments," Proceedings: Tritium Technology in Fission, Fusion and Isotopic Applications, Dayton, Ohio, April 29 - May 1, CONF-800427, American Nuclear Society (1980) 115-118.

26. T. Giorgi and F. Ricca, "On the Residual Pressure of Nitrogen, Carbon Monoxide and Hydrogen over Bulk Getters of Thorium and Zirconium Alloys," *Supplemento al Nuovo Cimento*, Vol. 1, No. 2, (1963) 613-625.

VI.6 Heat Removal Cycle

VI.6.1 Introduction

The heat removal cycle for TASKA has the primary objective of demonstrating practical power production while operating with the highest possible reliability together with the desired flexibility required for an experimental facility.

While meeting the above requirements has top priority, it appears (whenever possible and practical) that the system should have features which will provide valuable experience needed to produce better, more efficient power cycle designs for later generations of TASKA (emphasizing power production to a greater degree). It is also desirable to identify power cycle refinements applicable to these later generation plants so that component design and configuration options available in the TASKA cycle can be used intelligently.

The purpose of this subsection is to describe the proposed 45 MW_t power module cycle and its major components with the above objectives in mind and then to identify unique power cycle refinements suitable for later generations of this concept.

VI.6.2 TASKA Power Cycle

The power cycle temperatures are set to comply with the steam generating system temperature diagram shown in Fig. VI.7-2. Though not fully optimized, these temperatures appear to provide the following:

- A 29°C (52°F) log mean temperature difference in the intermediate heat exchanger. This appears to be a practical value from the standpoint of limiting IHX heating surface (a tritium diffusion path) and

retaining sufficient ΔT for a power cycle similar to those used for pressurized water reactors.

- A 138°C (280°F) final feedwater temperature. This lower than normal temperature will allow steam generation at 6.55 MPa (950 psia) using a pinch point ΔT of 13.9°C (25°F). This steam pressure is typical of pressurized water reactor power cycles.

This is desirable since it makes much PWR steam plant technology available to the project in fields such as water chemistry, steam turbine designs, steam generator designs, etc. In later designs, the lower feed temperature used to reach the desired steam pressure can be avoided by methods described later in this subsection.

- A steam temperature of 343°C (650°F) making full use of the HB-40 temperature (max.) of 371°C (700°F) and capable of providing improved PWR power cycle performance. A simplified turbine schematic is shown in Fig. VI.6-1.
- A moisture separator reheater shown here is optional. Its use will bring the cycle closer to preferred PWR cycle operating conditions and experience.

The steam generating equipment (see Section VI.7) will consist of separate heat exchanger units for the pre-boiler (economizer), evaporator and superheater. This allows use of more reliable heat exchanger configurations which, in addition, are required for the more advanced cycle features to be described below in this subsection.

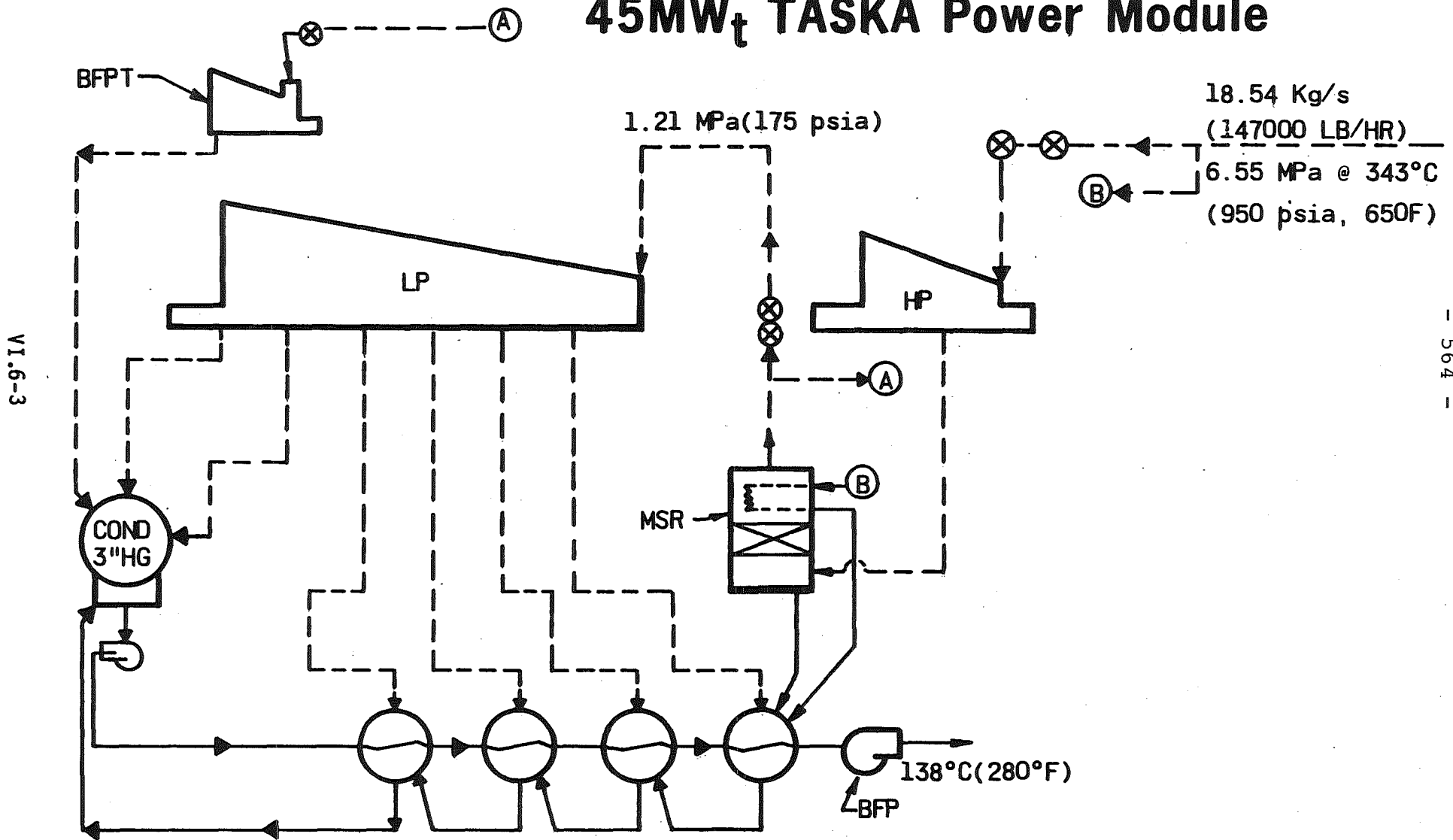
VI.6.3 Future Steam Cycle Improvements

It is believed desirable to identify methods of improving steam cycle efficiency applicable to later versions of TASKA to help confirm the organic

Turbine Power Cycle Schematic

for

45MW_t TASKA Power Module



VI.6-3

- 564 -

Fig. VI.6-1

cooled intermediate loop as an attractive approach to fusion power reactor design.

Heat made available from a fusion or fission source at relatively low temperatures poses various problems in effectively using a suitable power cycle (Rankine) to achieve adequate thermal efficiency.

In the study to increase efficiency, it was assumed that PbLi and HB-40 maximum loop fluid temperatures could each be increased about 50°C above the values assumed for TASKA. These hot and cold PbLi temperatures would be 450° (842°F) and 350°C (662°F), respectively. Similarly, HB-40 hot and cold temperatures become 421°C (790°F) and 321°C (610°F). These improved system temperatures will permit use of the power cycles listed in Table VI.6-1.

The cycle shown in the first column would use heat exchange components arranged in a manner typical of present day PWR plants. There is no HB-40 heated pre-boiler or superheater. Thus, the HB-40 would be cooled from 421° C to 321°C in the evaporator. All heat would then be transferred at saturated steam temperature. This would put the evaporator pinch point ΔT at the cold end of the temperature diagram so that the permissible steam pressure would be about 8.28 MPa (1,200 psia). Such a power cycle would yield a thermal efficiency of about 35 per cent at the generator terminals in a large plant (1,000 MWe).

In PWR practice, a "once-through" steam generator capable of providing pre-boiler and superheat surface (as well as evaporator surface) will produce a temperature diagram in which the pinch point (at the low temperature end of the evaporator surface) will move to the right. This effect can be realized more fully with separate heat exchangers for the pre-boiler, evaporator, and

Applicable STM Cycles for Advanced TASKA

<u>CYCLE PARAMETERS</u>	<u>SINGLE STM HTD RH NO ECONOMIZER NO SUPERHEATER</u>	<u>SINGLE STM HTD RH HB-40 HTD ECON. HB-40 HTD SH</u>	<u>DOUBLE HB-40 HTD RH HB-40 HTD SH HB-40 HTD ECON</u>
● STEAM PRESS @ T.T. ~ MPa (psia)	8.27,(1200)	12.41,(1800)	16.55(2400)
● FINAL FEED TEMP. ~ °C (°F)	227,(440)	227,(440)	246,(475)
● STEAM TEMP. @ T.T. °C(°F)	297,(567)	399,(750)	385,(725)
● RH NO. 1 STM. TEMP. °C(°F)	282,(540)	313(595)	343,(650)
● RH NO. 2 STM. TEMP. ~°C(°F)	-	-	343(650)
● EST. CYCLE EFF (NET @ GEN)	-35	-37	-39

VI.6-5

- 566 -

Table VI.6-1

superheater functions. Consequently, a scheme such as this was selected for the TASKA facility and is shown in Fig. VI.6-1.

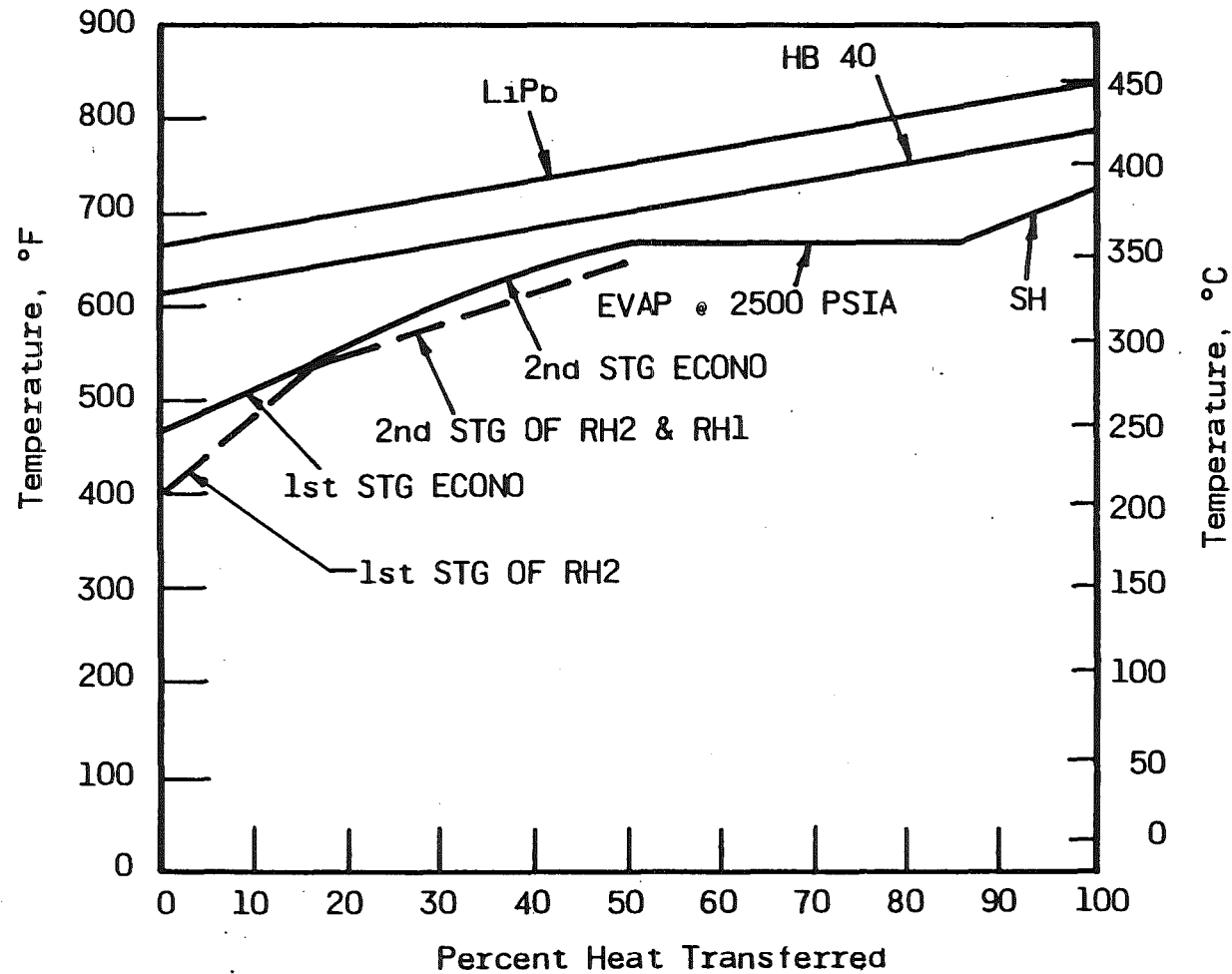
When applied to the HB-40 temperature levels used in Table VI.6-1, it is possible to increase steam pressure to 12.41 MPa (1,800 psia) as shown in the second column of this table. These improved steam conditions produce a rise in plant thermal efficiency of two percentage points to 37 per cent as shown.

Past work on steam cycles at B&W has shown that steam pressure can be raised further if the pre-boiler temperature curve slope can be decreased so that the pinch point is moved further to the right of the temperature diagram. It was found that reheat steam conditions could be slightly adjusted so that reheat begins at a temperature within the pre-boiler water temperature range (final feed to saturation). If some HB-40 is used to perform this reheat function, there will be less HB-40 available for the pre-boiler. This reduced HB-40 flow in the pre-boiler will reduce the slope of the corresponding water temperature curve and push the pinch point to the right on the temperature diagram, thereby allowing an increase in steam pressure.

To maximize this effect in a steam cycle suitable for future power producing versions of TASKA, it was decided to use a double reheat power cycle as shown in Fig. VI.6-2 with characteristics as listed in Column 3 on Table VI.6-1. This should permit an unprecedented thermal efficiency rise to about 39 per cent and a steam pressure of 16.55 MPa (2,400 psia).

Figure VI.6-3 shows the required arrangement of pre-boiler and reheater stages and stage sections. This more complicated arrangement should be justified by the resulting increase in plant MWe output, especially in view of the high balance of plant capital costs that are apparently characteristic of fusion power systems.

Proposed Future TASKA Power Cycle and Temperature Diagram

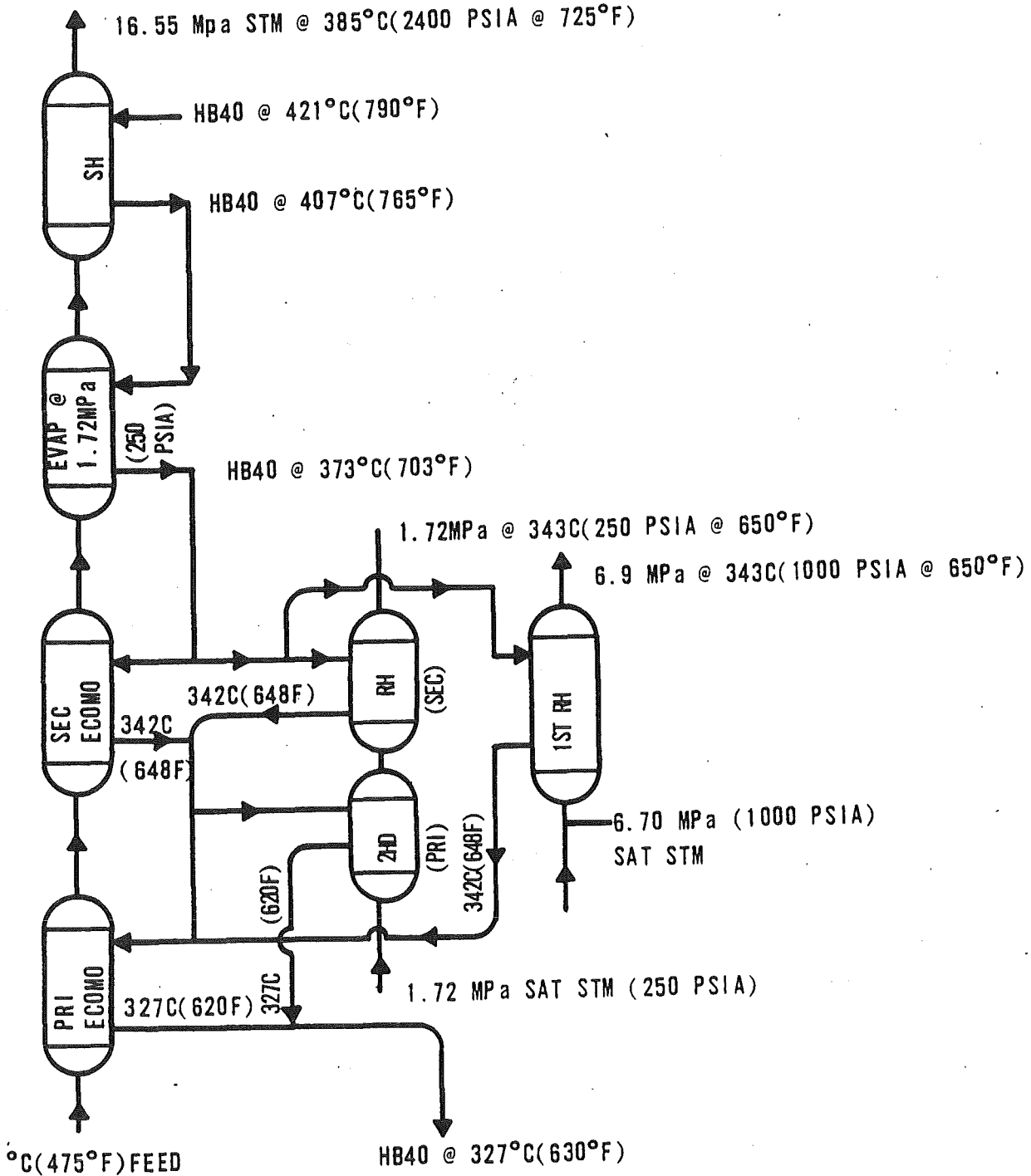


VI.6-7

Fig. VI.6-2

Fig. VI.6-3

Steam Generator Flow Diagram for Advanced TASKA Tandem Mirror Power Cycle



This potential future advantage helps justify the use of separate heat exchangers in the TASKA system for the pre-boiler, evaporator and superheater.

VI.7 Electricity Production

VI.7.1 Introduction

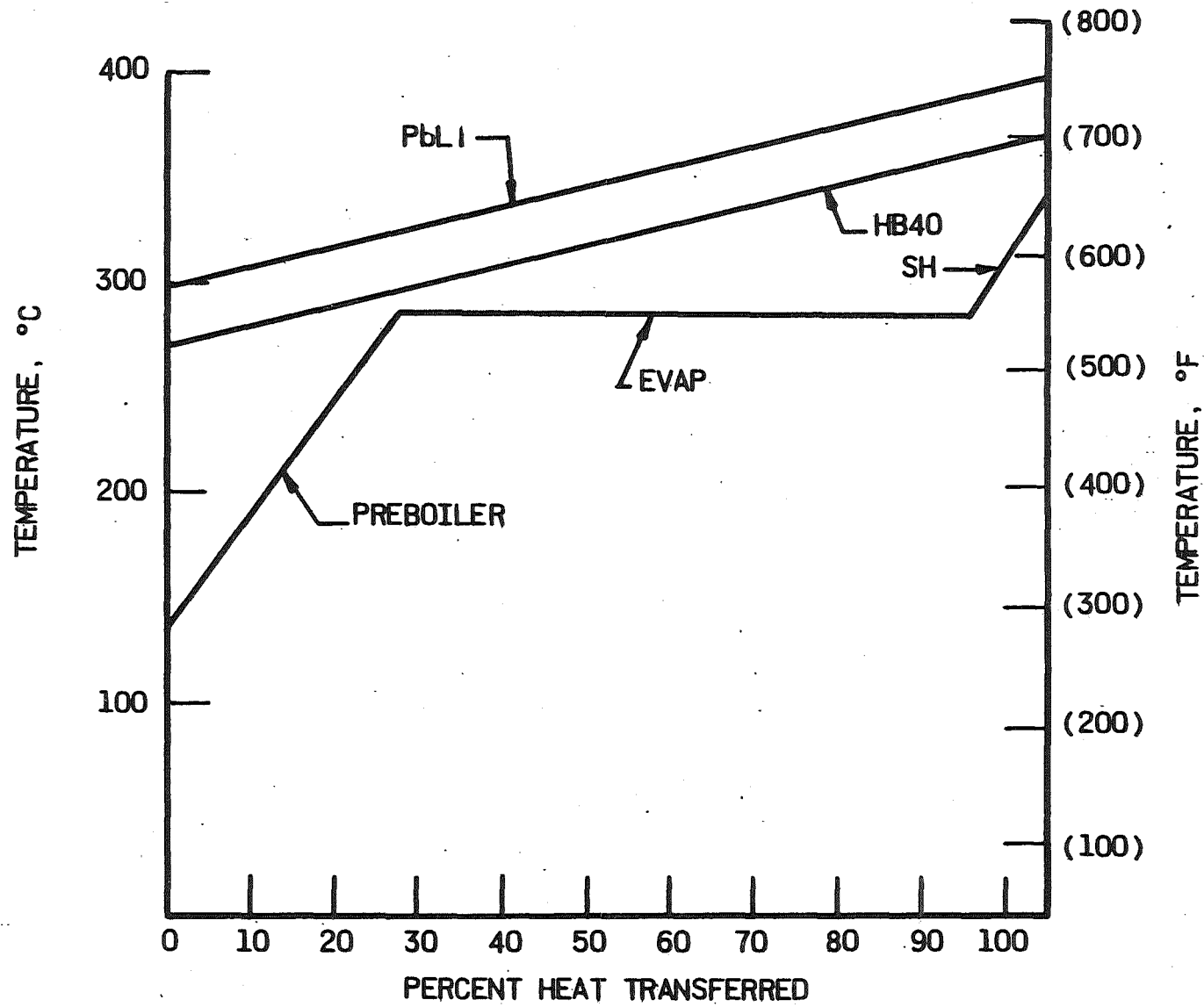
The objective of this study is to design a heat transport system to remove heat from the reactor blanket and provide steam to a conventional turbo-generator system. Many of the major features of heat transport systems and components, conceived for fusion reactors, are dictated by the need to provide a barrier to tritium diffusion. For the WITAMIR-I project, the reactor coolant was transported directly to the steam generator which utilized double wall tubes in its design as a tritium barrier. For the purposes of the present study, an optional position was taken to utilize more conventional steam generator design requiring some other means for preventing tritium diffusion. The method chosen was the use of an organic coolant loop to absorb tritium which diffuses from the PbLi loop. A basic requirement of the system is, therefore, to provide an intermediate loop of organic fluid between the PbLi reactor coolant and the steam generating system.

VI.7.2 General System Requirements

Schematics of the heat transport system and its temperature diagram are shown on Figs. VI.7-1 and VI.7-2, respectively. The requirements dictated by the primary system are that the heat removal rate from the reactor blanket be 45 MW_t with inlet and outlet operating temperatures of 300°C (572°F) and 400°C (752°F), respectively. Heat is transferred to the organic coolant via an intermediate heat exchanger (IHX) utilizing a horizontal U-tube, U-shell arrangement. The organic fluid, HB-40, has been successfully used as an experimental reactor coolant in Canada. The organic fluid flows in series

Power Module Temp. Diagram

VI.7-3



- 573 -

Fig. VI.7-2

through the superheater, evaporator and pre-boiler components of the steam generator system before being pumped back to the IHX. Steam conditions of 6.55 MPa (950 psia), 343°C (650°F) were chosen which would meet the requirements of small turbines designed for conditions close to those of PWR systems and still permit practical LMTD's in the respective heat exchange components.

Before sizing the components, the organic fluid flow rate and operating temperatures were selected. The temperature limits were determined after a study was made to trade-off the IHX surface against the steam generator surface.

VI.7.3 Steam Generation System

The major components of the steam generation system are the superheater, evaporator, pre-boiler, steam drum, and recirculating pump. A pumped circulating system for the evaporator was chosen over natural circulation primarily because of its flexibility of operation which makes it especially attractive for use in small pilot plants. Pumped circulation systems are often used in the power industry where frequent startups or major load swings need to be accommodated. A circulation ratio of 3.3 was chosen to avoid the transition from nucleate boiling to film boiling within the evaporator. By avoiding the transition, the probability of tube wall corrosion (tubeside) due to deposits is greatly diminished.

Most of the components can be mounted horizontally at one elevation. The only exception is the steam drum which would require some additional elevation above the evaporator to insure positive head on the pump. The horizontal orientation, as opposed to vertical orientation, provides an opportunity to save costs, both in the support of the components and in building height.

A separate pre-boiler has been designed to minimize the total heat transfer surface of the pre-boiler and evaporator. While the pre-boiler and evaporator may be combined in one unit, the total surface will increase. For the purpose of this study, a separate pre-boiler was assumed to provide the overall lowest cost system.

VI.7.4 Components

Heat exchanger components need to be designed to accommodate the temperature differences between the heating and cooling fluid and to withstand thermal transients imposed during operation. U-tubes are employed in all components to provide the necessary flexibility and accommodate the differential expansion between the tubes and the shell. For the evaporator and superheater, a straight shell arrangement is used to house the tube bundle. For the pre-boiler and IHX, the higher temperature differences across the unit would impose excessive thermal stresses on a single tubesheet arrangement and, therefore, a U-shell is used to house the U-tube bundle (see Table VI.7-1, Figs. VI.7-3 to VI.7-6).

Both the U-tube, U-shell and the U-tube, straight shell arrangements are conventional designs which have been used extensively for nuclear applications.

In the design of the IHX, PbLi was chosen as the shell side fluid and the HB-40 as the tubeside fluid. Putting HB-40 on the tube side was considered appropriate in this component where the HB-40 is in contact with the heating surface at temperatures approaching the limit permitted by thermal decomposition considerations. Removal of surface fouling is more easily accomplished on the tube side.

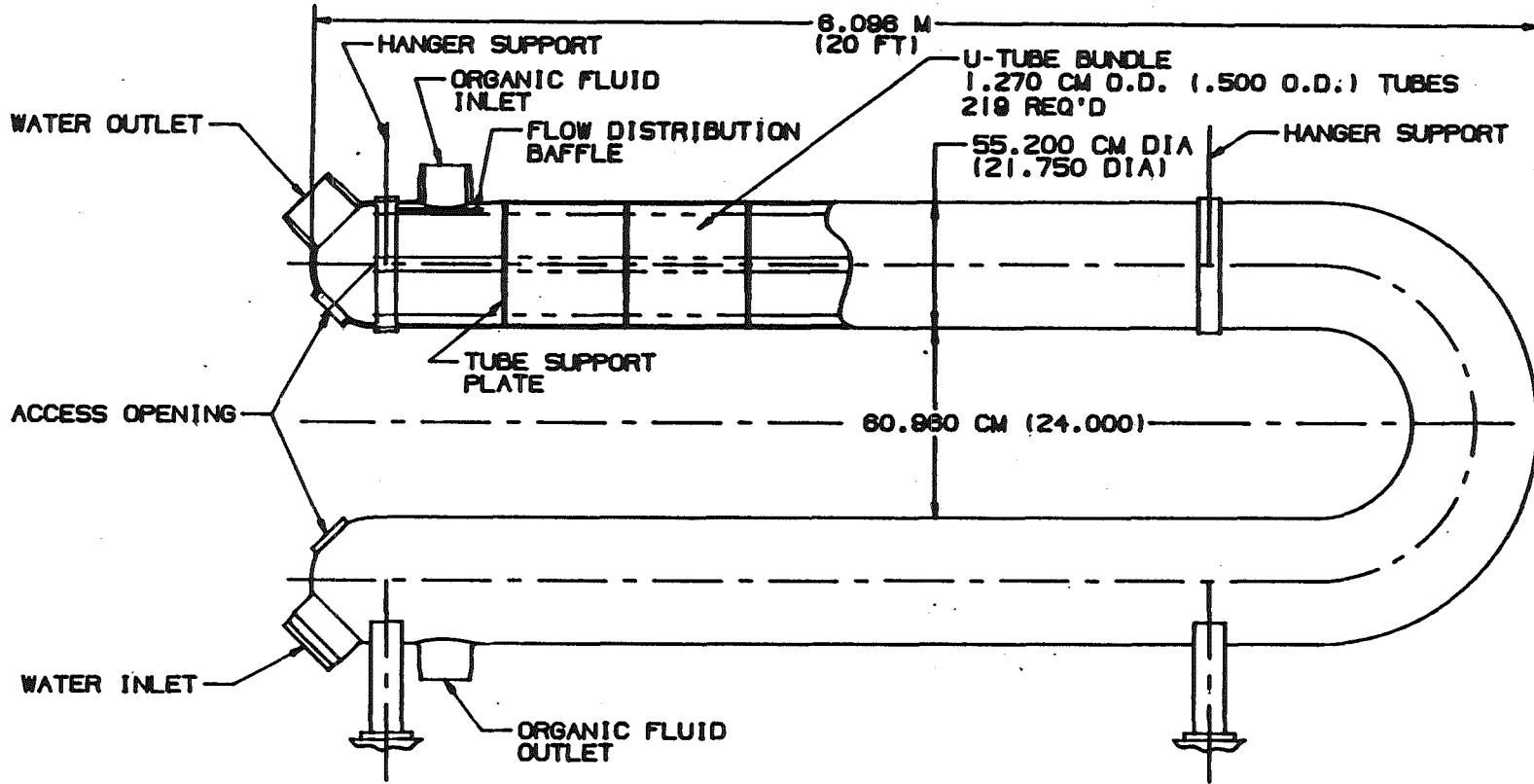
Table VI.7-1 IHX/Steam Generator Sizing (45 MWe)

	<u>Units</u>	<u>IHX</u>	<u>Pre-Boiler</u>	<u>Evaporator</u>	<u>Superheater</u>
Heat Exchanger Type		U-Tube U-Shell, Pure Counterflow	U-Tube, U-Shell Pure Counterflow	U-Tube, Straight Shell Segmented Baffle	U-Tube, Straight Shell Segmented Baffle
Material		9 Cr-1 Mo	SA-210 Carbon Steel	SA-210 Carbon Steel	2 1/4 Cr-1 Mo
Number of Tubes (All 0.5 inch O.D.)		1,235	219	772	221
Shell Side					
Fluid Type		PbLi	Organic	Organic	Organic
Temperatures					
Inlet	°C/°F	400/752	299/571	361/683	371/700
Outlet	°C/°F	300/572	271/520	299/571	361/683
Norm. Pressure	MPa/psia	.55/80(inlet)	.21/30(inlet)	.28/40(inlet)	.34/50(inlet)
Flow Rate	kg/s/lb/hr	2881/22.9x10 ⁶	169.1/1.34x10 ⁶	169.1/1.34x10 ⁶	169.1/1.34x10 ⁶
Tube Side					
Fluid Type		Organic	Water	Water/Steam	Steam
Temperature					
Inlet	°C/°F	271/520	138/280	273/535	285/545
Outlet	°C/°F	371/700	273/535	285/546	343/650
Norm. Pressure	MPa/psia	.41/60(inlet)	3.24/1,050(outlet)	6.90/1,000(outlet)	6.6/950(outlet)
Flow Rate	kg/s/lb/Hr	169.1/1.34x10 ⁶	7.24/.147x10 ⁶	7.24/.147x10 ⁶	7.24/.147x10 ⁶
Heat Transfer Surface	m ² ft ²	639/9,633	94.5/1,016	388/4,169	54.4/585
Overall Coefficient	(W/m ² °C/ BTU/hrft ² °F)	1,741/307	2,133/376	1,947/343 (boiling range)	1,704/300
Estimated Weight	kg/lb _m	17,689/39,000	4,644/10,232	4,900/22,810	5,521/12,179

VI.7-6

575

146080B-1



NOTE:
 APPROX. DRY WEIGHT - 4,644 KG (10,230 LBS)
 MATERIAL - SA-210 CARBON STEEL

THE BABCOCK & WILCOX COMPANY

REV. 1, - REVISED VESSEL DIA., TUBE QUANTITY AND WEIGHT.

PREBOILER

SCALE: DRAWN: 1 FOOT
146080B-1

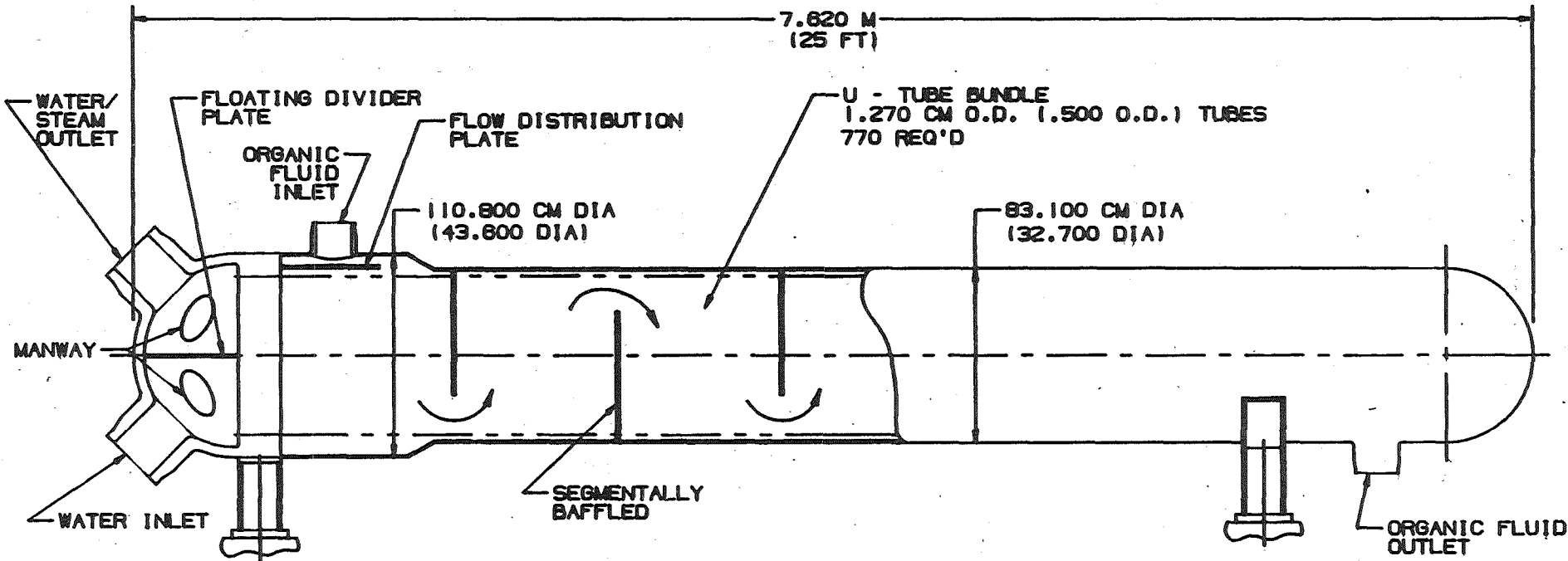
Fig. VI.7-3

VI.7-7

- 576 -

146081B

VI.7-8



NOTE:
 APPROX. WEIGHT - 10,791 KG (23,770 LBS)
 MATERIAL - SA-210 CARBON STEEL

THE BRIDGEMAN & WILCOX COMPANY

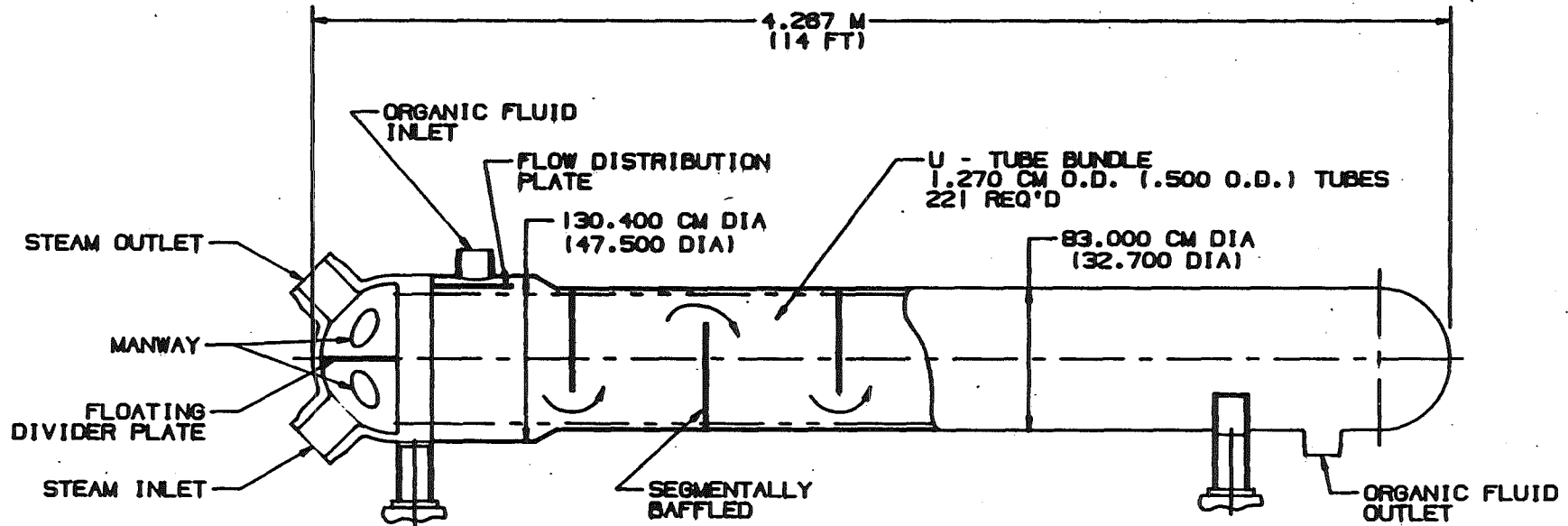
REV. 1 - REVISED VESSEL DIAMETERS, TUBE QUANTITY & WEIGHT.

DATE: _____
 BY: _____

EVAPORATOR

146081 B-1

Fig. VI.7-4



NOTE:
 APPROX. DRY WEIGHT - 5,528 KG (12,180 LBS)
 MATERIAL - 2 1/4 CR-1MO

THE BRIDGEMAN & WILCOX COMPANY

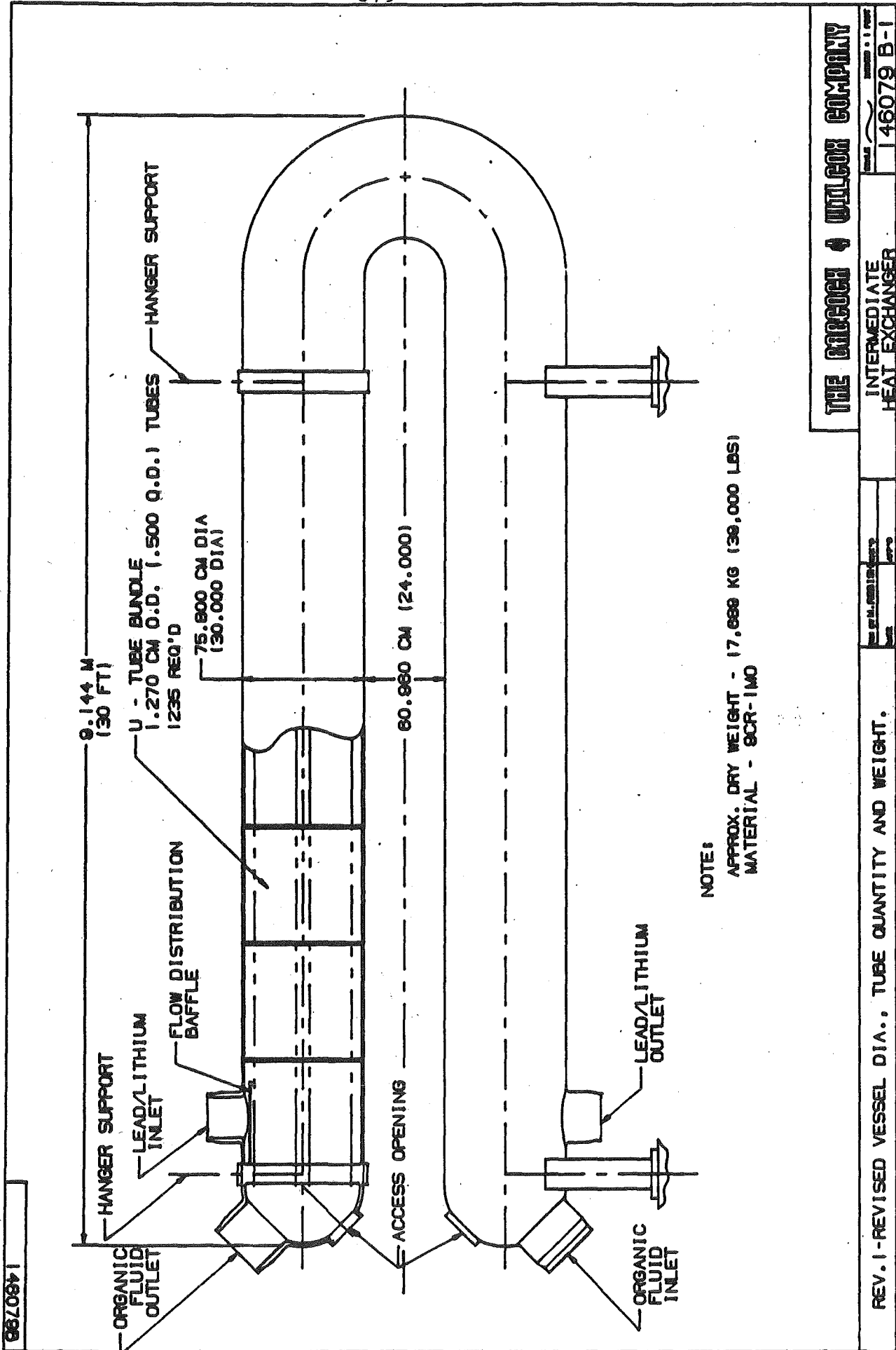
REV. 1 - REVISED VESSEL DIAMETERS, TUBE QUANTITY & WEIGHT.

DESIGNED BY	DATE
APPROVED BY	DATE

SUPERHEATER

SCALE	SHEET NO. 1 OF 1
146082 B-1	

Fig. VI.7-5



NOTE:

APPROX. DRY WEIGHT - 17,698 KG (39,000 LBS)
 MATERIAL - 9CR-1MO

THE BORGES & WILCOX COMPANY
 INTERMEDIATE HEAT EXCHANGER
 146079 B-1

REV. 1-REVISED VESSEL DIA., TUBE QUANTITY AND WEIGHT.

Fig. VI.7-6

Tube side fouling tends to be at a minimum over a velocity range of 1.8 to 3.1 meters/sec (6 to 10.0 ft/sec). A velocity of 3.1 meters/sec was chosen to improve heat transfer and thereby minimize IHX heating surface. Reduced heating surface is of course desirable to reduce tritium diffusion as much as possible.

In all of the components, shell side velocities are typical of values normally used to avoid damaging flow induced vibration. In addition, tube support plates are spaced to provide a tube natural frequency above the flow eddy force frequencies produced by turbulence at velocities. The support plates are broached to allow longitudinal passage of the shell side fluid.

Materials have been chosen to lower unit costs consistent with allowable stresses at design temperatures and with environmental compatibility. The 9 Cr-1 Mo steel was mandated for the IHX to ensure compatibility with the PbLi. For the pre-boiler and evaporator, carbon steel was chosen. For the superheater, 2 1/4 Cr-1 Mo was chosen to provide higher strength than is available with carbon steel at the required design temperatures.

VI.7.5 Component Costs

Estimated component costs are listed below:

<u>Component</u>	<u>Cost</u>
	(fob Barberton, Ohio)
Pre-Boiler	\$ 672,000
Evaporator	1,200,000
Superheater	620,000
Intermediate Heat Exchanger	3,264,000
Boiler Steam Drum	<u>124,000</u>
Total	\$5,880,000

Cost estimates for the circulating pump, valves, piping, instrumentation, controls, foundations, etc., can be made at a later phase of the project when reactor parameters are more nearly finalized.

Low pressure in the PbLi and HB-40 loops plus the respective compatibility of these fluids with 9 Cr-1 Mo and carbon or low allow steel (Table VI.7-1) will assure a relatively low component and system cost when compared with concepts using other heat transport fluids involving less favorable materials compatibility, higher operating temperatures or higher pressures.